Technische Universität München
Institut für Energietechnik

Professur für Thermofluiddynamik

Dynamics of Unsteady Heat Transfer and Skin Friction in Pulsating Flow Across a Cylinder

Armin Witte

Vollständiger Abdruck der von der Fakultät für Maschinenwesen der Technischen Universität München zur Erlangung des akademischen Grades eines

DOKTOR – INGENIEURS

genehmigten Dissertation.

Vorsitzender:
Prof. Dr.-Ing. Harald Klein
Prüfer der Dissertation:
1. Prof. Wolfgang Polifke, Ph.D.
2. Prof. Dr.-Ing. Jens von Wolfersdorf

Die Dissertation wurde am 26.04.2018 bei der Technischen Universität München eingereicht und durch die Fakultät für Maschinenwesen am 09.10.2018 angenommen.

Acknowledgments

This thesis was conceived at the Thermo-Fluid Dynamics Group of the Technical University of Munich during my time as a research assistant. Financial support was provided by Deutsche Forschungsgemeinschaft (DFG), project PO 710/15-1.

First of all, I would like to thank my supervisor Prof. Wolfgang Polifke, Ph.D. for the opportunity to study this interesting subject. He sparked my interest in system identification in addition to my already existing affinity towards CFD and numerical methods. My sincere thanks go to Prof. Dr.-Ing. Jens von Wolfersdorf for reviewing my thesis and to Prof. Dr.-Ing. Harald Klein for kindly accepting to chair the defense.

My thanks also go to my colleagues at the Thermo-Fluid Dynamics Group and the Chair of Thermodynamics of the Technical University of Munich. First and foremost, I would like to thank Kilian Förner, Malte Merk, Alexander Präbst, and Thomas Steinbacher for valuable input and discussions to this thesis. Special thanks also go to my officemates Lin Strobio Chen, Shuai Guo, and Tobias Holzinger. For their support regarding administrative tasks, I would also like to thank Helga Bassett and Sigrid Schulz-Reichwald. Moreover, my thanks go to Anja Friedrich, Margitta Witte, and Manuela Witte who made sure that this thesis does not scare off the gentle reader outside the thermo-fluid dynamics world (at least not immediately). For regular transdepartmental exchange including caffeinated beverages I am grateful to Peter Holfelder and Volker Schneider.

Complementing my tasks at the Thermo-Fluid Dynamics Group, I was teaching assistant to the Master's level course "Heat and Mass Transfer". I perfectly enjoyed working with the numerous students who came to my exercise course, the supplementary course, and office hours. I would like to thank every student who made me think harder, and I hope they put to good use the things they learned I also had the opportunity to get to know a few students who were helping me with my work and explored interesting topics surrounding and scratching the scope of this thesis. My thanks go to Patrick Brandl, Ana Cabrera, Ateş Çalak, Buddy Herath, Magnus Mechler, Viktoria Meißner, and Benedikt Wohner.

I would like to express my gratitude to Prof. Matthew Juniper who made it possible for me to visit his research group at the University of Cambridge and especially Alessandro Orchini and José Aguilar. I enjoyed the exchange and fruitful discussions.

Of course, this thesis would not have been possible without the support of my parents Maria and Otto Baumgartner as well as my sister Julia Baumgartner for which I am deeply grateful.

Most of all I would like to thank my wife, Susanne. She was with me all the way with valuable discussions and a keen eye for what is relevant despite her own thesis and despite much more important things like carrying a new life.

Kurzfassung

Untersucht wurde das dynamische Verhalten des Wärmeübergangs und der Wandschubspannung eines Zylinders in pulsierender Querströmung für kleine Störungen der Strömungsgeschwindigkeit. In diesem Regime ist der zeitlich gemittelte Wärmeübergang konstant, und Fluktuationen von Strömungsvariablen können als lineares, zeitinvariantes System beschrieben werden. Es wurde ein großer Bereich von Reynolds-Zahlen $0.1 \leq \mathrm{Re} \leq 3900$ mit Schwerpunkt auf die Regime ohne Wirbelablösung untersucht ($\mathrm{Re} \leq 40$). Letztere sind besonders interessant für Anwendungen wie das Rijke-Rohr und die Hitzdrahtanemometrie.

Methoden der Systemidentifikation in Kombination mit CFD-Simulation (CFD/SI) wurden zur Datengenerierung verwendet. Die Übertragungsfunktionen von Geschwindigkeitspulsationen zu Pulsationen in Wärmeübergang und Wandschubspannung wurden mit drei verschiedenen Methoden bewertet: Anregung einer numerischen Simulation mit der Sprungfunktion, Breitbandanregung von CFD-Simulationen kombiniert mit linearer Systemidentifikation und Lösen der linearisierten Navier-Stokes-Gleichungen im Frequenzbereich. Für Untersuchungen bei unterkritischer Strömung wurden LES-Simulationen verwendet.

Die Dynamik des Wärmeübergangs und der Wandschubspannung wird von mehreren Zeitskalen bestimmt. Diese entsprechen den jeweiligen Reaktionszeiten des Geschwindigkeitsfeldes und des Temperaturfeldes. Es gibt jedoch keine einfache Analogie wie die Reynolds-Analogie für stationäre Strömungen. Die Wechselwirkung der verschiedenen Zeitverzögerungen führt zu einer nicht trivialen Abhängigkeit der Frequenzantwort des Wärmeübergangs und der Wandschubspannung von Strouhal-Zahlen und Reynolds-Zahlen. In der Literatur verfügbare Modelle für das dynamische Verhalten von Wärmeübergang und Wandschubspannung stimmen nur bis zu einem gewissen Grad mit den simulierten Daten überein. Diese Arbeit liefert ein Meta-Modell niedriger Ordnung, das den Wärmeübergang bei Reynolds-Zahlen in der Größenordnung von 10 besonders gut abbildet.

Quantitative Ergebnisse werden für einen großen Bereich von Reynolds-Zahlen und Strouhal-Zahlen angegeben. Andere möglicherweise relevante Parameter wie absolute Temperaturdifferenzen, temperaturabhängige Eigenschaften und hohe Amplituden wurden nicht erschöpfend behandelt. Das sehr vielseitige Verfahren kann jedoch für weitere Untersuchungen in dieser Hinsicht adaptiert werden.

Abstract

The dynamic behavior of heat transfer and skin friction of a cylinder in pulsating crossflow for small perturbations of flow velocity was investigated. In this regime, the time-averaged heat transfer is constant, and fluctuations of flow variables can be described as linear, time-invariant dynamics. A wide range of Reynolds numbers $0.1 \leq \mathrm{Re} \leq 3900$ was studied with emphasis on the regimes without vortex shedding ($\mathrm{Re} \leq 40$). The latter are of particular interest for applications like the Rijke tube and hot-wire anemometry.

Using system identification techniques in combination with CFD simulation (CFD/SI) for data generation, the transfer functions from velocity pulsations to pulsations in heat transfer and skin friction were assessed with three different methods: Step excitation of a numerical simulation, broadband excitation of CFD simulations combined with linear system identification, and solving the linearized Navier–Stokes equations in the frequency domain. For investigations in subcritical flow, LES simulations were used.

The heat transfer and skin friction dynamics are governed by several time scales. These correspond to the respective response times of the velocity field and the temperature field. However, no simple analogy, like the Reynolds analogy for steady flow, exists. The interaction of the different time lags leads to a non-trivial dependence of the frequency response of heat transfer and skin friction on Strouhal numbers and Reynolds numbers. Available analytical models for the dynamic behavior of skin friction and heat transfer match the simulated data only up to a point. This thesis provides a low-order meta-model, which excels at Reynolds numbers of order 10.

Quantitative results are given for a wide range of Reynolds numbers and Strouhal numbers. Other possibly relevant parameters, such as absolute temperature differences, temperature-dependent properties, and high amplitudes were not covered exhaustively. However, the very versatile procedure can be very useful for further investigations in this regard.

Teile der vorliegenden Dissertationsschrift wurden vom Autor bereits vorab auf Konferenzen vorgetragen und als Konferenz- und Zeitschriftenbeiträge veröffentlicht (Strobio Chen et al., 2015; Witte et al., 2016a,b; Witte and Polifke, 2015, 2016, 2017a,b, 2019). Alle Vorveröffentlichungen sind entsprechend der gültigen Promotionsordnung ordnungsgemäß gemeldet. Sie sind deshalb nicht zwangsläufig im Detail einzeln referenziert. Vielmehr wurde bei der Referenzierung eigener Vorveröffentlichungen Wert auf Verständlichkeit und inhaltlichen Bezug gelegt.

Parts of this Ph.D. thesis have been presented by the author at conferences and published beforehand in conference proceeding or journal papers (Strobio Chen et al., 2015; Witte et al., 2016a,b; Witte and Polifke, 2015, 2016, 2017a,b, 2019). All of these prior printed publications are registered according to the current doctoral regulations. For this reason, they are not quoted explicitly at all pages. Whether these personal prior printed publication were referenced, depend on maintaining comprehensibility and providing all necessary context.

Contents

List of Figures **xiii**

List of Tables **xvii**

Nomenclature **xix**

1 Introduction **1**
1.1 Motivation . . . 1
1.1.1 Energy Conversion and Environmental Aspects . . . 1
1.1.2 Transformation Between Thermal Energy and Acoustic Energy 2
1.1.3 Heat Transfer Dynamics in Unsteady Flow . . . 4
1.1.4 Modeling and Modeling Techniques . . . 5
1.2 Aims . . . 5
1.3 Scope . . . 6

2 Flow Around a Circular Cylinder **9**
2.1 Cylinder in Steady Crossflow . . . 9
2.1.1 Phenomenology . . . 10
2.1.2 Heat and Momentum Transfer . . . 11
2.1.3 Flow Separation and Turbulence . . . 19
2.2 Governing Equations . . . 21
2.2.1 Navier–Stokes Equations . . . 22
2.2.2 Fluid Properties . . . 22
2.2.3 Dimensional Analysis . . . 25
2.2.4 Non-Dimensionalized Navier–Stokes Equations . . . 27
2.2.5 Incompressible Navier–Stokes Equations . . . 28
2.2.6 Vorticity Stream Function Formulation . . . 30
2.2.7 Potential Flow . . . 31
2.3 Transfer Analogies . . . 32
2.3.1 Analogy of Heat and Mass Transfer . . . 32
2.3.2 Reynolds' Analogy . . . 33
2.4 Cylinder in Unsteady Crossflow . . . 34
2.4.1 Perturbation Approach and Small Amplitudes . . . 34
2.4.2 Pulsations . . . 35

2.4.3 Transfer Function and Frequency Response 38

3 Cylinder in Pulsating Flow—Literature Review 39
3.1 Early Works on Unsteady Flows and Thermoacoustics 39
3.1.1 Thermoacoustics 40
3.1.2 High Frequency Oscillations over a Flat Plate 40
3.1.3 Motion of a Sphere 42
3.2 Perturbation Boundary Layer Equations 43
3.2.1 Boundary Layer Equations 44
3.2.2 Lighthill 45
3.2.3 Lin 51
3.2.4 Gersten 52
3.2.5 Telionis and Romaniuk 57
3.3 Approximation for low Reynolds Numbers 58
3.3.1 Oseen Equation 58
3.3.2 Bayly 58
3.4 Navier-Stokes Equations 59
3.4.1 Apelt and Ledwich 61
3.4.2 Linearized Navier-Stokes Equations 61
3.4.3 Hantschk and Vortmeyer 62
3.4.4 Time Series Analysis 63
3.5 Further Literature on Heat Transfer in Unsteady Flow 64
3.5.1 Experimental Investigations of Unsteady Flow 64
3.5.2 Oscillating Flow 65
3.5.3 Nonlinearity of Heat Transfer 65
3.5.4 Heat Transfer Enhancement 66
3.6 Rijke Tube 67
3.6.1 Modeling Approaches 67
3.6.2 Time Constant 68
3.6.3 Literature Survey 69

4 Linear Dynamic Systems 73
4.1 Linear Time Invariant Systems 74
4.1.1 Definition 75
4.1.2 Properties 75
4.1.3 Convolution Model and Impulse Response 76
4.1.4 Transfer Function 77
4.1.5 Disturbances 78
4.2 Data Basis 81
4.2.1 Continuous and Discrete Time Data 81
4.2.2 Frequency Domain 82
4.2.3 Transformations Between Laplace- and Z-Domain 84
4.3 Representations of LTI Systems 84

4.3.1 Continuous Time Transfer Function . . . 84
4.3.2 Discrete Time Transfer Function . . . 86
4.3.3 Unit Impulse Response . . . 87
4.3.4 Unit Step Response . . . 87
4.3.5 Frequency Response . . . 88
4.3.6 Differential/Difference Equation . . . 89
4.4 System Identification . . . 91
4.4.1 Identification Procedure . . . 91
4.4.2 Parameter Estimation . . . 93
4.4.3 Influence of Disturbances . . . 97
4.4.4 Identification of Discrete Time Models . . . 99
4.4.5 Identification of Continuous Time Models . . . 104
4.5 Model Validation . . . 108
4.6 Dynamics of Heat Transfer and Skin Friction . . . 112

5 Data Generation 113
5.1 Basic Setup . . . 113
5.1.1 Boundary Conditions . . . 113
5.1.2 Domain and Basic Mesh Topology . . . 115
5.1.3 Grid Study . . . 116
5.2 Laminar Time Domain Simulation . . . 121
5.2.1 Excitation Signal Generation . . . 121
5.2.2 Computational Procedure . . . 123
5.2.3 Data Acquisition . . . 125
5.3 Large Eddy Simulation . . . 126
5.3.1 Computational Domain and Grid . . . 127
5.3.2 Turbulence Modeling . . . 130
5.3.3 Computational Procedure . . . 132
5.3.4 Data Acquisition . . . 133
5.4 Linearized Navier Stokes Equations . . . 133
5.4.1 Computational Domain and Grid . . . 133
5.4.2 Perturbation Equation in Vorticity–Stream Function Form . . . 134
5.4.3 Finite Difference Approach . . . 138
5.4.4 Computational Procedure . . . 139
5.4.5 Acquisition of Frequency Domain Data . . . 141
5.4.6 Discussion and Outlook . . . 141

6 Transfer Function Identification 143
6.1 Step Response . . . 144
6.1.1 Heat Transfer . . . 145
6.1.2 Skin Friction . . . 148
6.1.3 Characterization of Dynamic Behavior . . . 150
6.1.4 Transfer Function from Step Simulation Data . . . 152

6.2 Transfer Function from LNSE . . . 154
6.2.1 Identification from Frequency Response Data . . . 155
6.2.2 Results . . . 156
6.3 CFD/SI . . . 157
6.3.1 Data Preparation . . . 159
6.3.2 Development of Discrete Time Models . . . 167
6.3.3 Development of Continuous Time Models . . . 171
6.3.4 Model Validation . . . 173
6.3.5 Identification in the Presence of Tonal Noise and Turbulence . 179
6.4 Results from Transfer Function Identification . . . 181
6.4.1 Heat Transfer . . . 182
6.4.2 Skin Friction . . . 189
6.5 Discussion . . . 195
6.5.1 Identification Method . . . 195
6.5.2 Heat Transfer . . . 197
6.5.3 Skin Friction . . . 200

7 Flow Field Representations 203
7.1 Steady State . . . 203
7.2 Step Response . . . 205
7.2.1 Common Features and Behavior . . . 205
7.2.2 Behavior at Different Mean Flow Reynolds Numbers . . . 206
7.3 Representations of the Linearized Flow Field . . . 214
7.3.1 Amplitude of Vorticity and Temperature Fluctuation . . . 214
7.3.2 Amplitude and Phase Fields of Temperature Fluctuation . . . 222
7.4 Circumferential Distribution of Heat Transfer and Skin Friction . . . 224
7.5 Discussion . . . 228

8 Low Order Parametrized Model for Heat Transfer 231
8.1 Low Order Models . . . 232
8.1.1 $n-\tau$ Model . . . 232
8.1.2 PT1 Model . . . 232
8.1.3 $n-\tau$ Model as Linearization of First Order Lag . . . 233
8.1.4 Comparison of Low Order Parametrized Models . . . 234
8.2 Parametrized First Order Time Lag Model . . . 235
8.3 Limitations and Corrections of the PT1 Model . . . 236
8.3.1 Influence of Prandtl Number . . . 236
8.3.2 Influence of Absolute Temperature . . . 238
8.3.3 High Amplitudes . . . 240
8.3.4 Discussion . . . 242

9 Aspects of Applications **243**
9.1 Rijke Tube . . . 243
9.1.1 Mode of Operation . . . 243
9.1.2 Significance of the Heat Transfer Model . . . 248
9.1.3 Justification of the Assumptions . . . 249
9.1.4 Limitations . . . 253
9.2 Hot-Wire Anemometry . . . 254
9.2.1 Mode of Operation . . . 255
9.2.2 Justification of Assumptions . . . 255
9.2.3 Fluctuation of Angle of Attack . . . 256
9.2.4 Interactions of Dynamic Subsystems . . . 257
9.3 Heat Exchanger in Domestic Boilers . . . 259
9.3.1 Temperature Difference . . . 260
9.3.2 Low Frequency Limit . . . 260

10 Conclusions and Outlook **263**
10.1 Summary . . . 263
10.2 Implications for Further Research . . . 265

Supervised Theses **267**

References **269**

Appendix **287**

A Complementary Identification Results **287**

List of Figures

2.1 Sketch of a Cylinder in Steady Crossflow 10
2.2 Coordinate Systems for the Cylinder 12
2.3 Sketch of a Cylinder in Steady Crossflow 13
2.4 Steady-State Friction and Pressure Coefficient Distributions 15
2.5 Mean Friction Coefficient and Correlations 15
2.6 Nußelt Number Distribution 17
2.7 Nußelt Number and Correlations 18
2.8 Energy of Turbulent Structures 21
2.9 Sketch of a Cylinder in Pulsating Crossflow 35

3.1 Velocity Profiles of Oscillating Flow Close to a Surface 42
3.2 Frequency Response of Skin Friction for the HL (Lighthill, 1954) . . . 48
3.3 Frequency Response of Skin Friction for the BL (Lighthill, 1954) . . . 49
3.4 Frequency Response of Heat Transfer (Lighthill, 1954) 50
3.5 Frequency Response of Skin Friction for the HL (Gersten, 1965) 55
3.6 Frequency Response of Skin Friction for the BL (Gersten, 1965) 55
3.7 Frequency Response of Heat Transfer for the HL (Gersten, 1965) . . . 56
3.8 Frequency Response of Heat Transfer for the BL (Gersten, 1965) . . . 57
3.9 Frequency Response of Heat Transfer (Bayly, 1985) 60
3.10 Amplitude of the Frequency Response (Kwon and Lee, 1985) 62

4.1 Representation of a General (Open) System 74
4.2 Representation of a General (Open) System with Disturbance 78
4.3 Representation of a General Model for an LTI System 79
4.4 Overview of Different Domain Representations 85
4.5 Amplitude and Phase of the Transfer Function $1/(1+0.2s)$ 90
4.6 Flowchart of the Identification Procedure 92
4.7 Block Diagram of the Output-Error Model 102
4.8 Block Diagram of a Box-Jenkins Model 104

5.1 Overview of Different Approaches to Determine the Transfer Function 114
5.2 Sketch of the Computational Domain 115
5.3 Mesh Topology of Exemplary Mesh 116
5.4 Detail of an Exemplary Mesh 117

5.5 Topology of LES Mesh in Spanwise Direction 129
5.6 Measure of Turbulence Resolution 132
5.7 Mesh for LNSE Approach 134
5.8 Flowchart of the Steady-State Solver 140

6.1 Unit Step Response of Nußelt Number 146
6.2 Unit Step Response of Heat Transfer for Individual Sectors 147
6.3 Unit Step Response of Skin Friction 148
6.4 Unit Step Response of Individual Sectors 149
6.5 Frequency Response of Heat Transfer from Step Simulation 154
6.6 Frequency Response of Skin Friction from Step Simulation 155
6.7 Frequency Response of Heat Transfer from LNSE 156
6.8 Frequency Response of Skin Friction from LNSE 157
6.9 Diagram of the CFD/SI Approach 158
6.10 Flowchart of the CFD/SI Procedure 160
6.11 Input Time Series (Reynolds Number) 162
6.12 Output Time Series (Nußelt Number) 164
6.13 Output Time Series (Friction Coefficient) 166
6.14 Coherence (Welch's Estimate) of Input and Outputs 167
6.15 Identified Model Parameters of Polynomials B and F 169
6.16 Impulse Response and Step Response of OE Model 169
6.17 Poles and Zeros of the Transfer Function 170
6.18 Identified Model Parameters of Nominator and Denominator of $G(s)$ 172
6.19 Impulse Response and Step Response of Transfer Function from VF . 173
6.20 Poles and Zeros of the Continuous Transfer Function 174
6.21 Time Series of Residuals (Nußelt Number) 175
6.22 Scatter Plot of Residuals and Output 177
6.23 Whiteness Test 177
6.24 Independence Test 178
6.25 Excerpt of Time Series for Comparison 179
6.26 Amplitude of the Heat Transfer Frequency Response ($\mathrm{Re}_0 \leq 40$) 185
6.27 Phase of the Heat Transfer Frequency Response ($\mathrm{Re}_0 \leq 40$) 186
6.28 Frequency Response of the Heat Transfer ($\mathrm{Re}_0 > 40$) 187
6.29 Noise Spectrum of Heat Transfer Pulsations ($\mathrm{Re} > 40$) 188
6.30 Amplitude of Skin Friction Frequency Response 192
6.31 Phase of Skin Friction Frequency Response 192
6.32 Frequency Response of the Skin Friction ($\mathrm{Re}_0 > 40$) 193
6.33 Noise Spectrum of Skin Friction Pulsations ($\mathrm{Re}_0 > 40$) 194
6.34 Comparison of Heat Transfer Frequency Response (Amplitude) . . . 198
6.35 Comparison of Heat Transfer Frequency Response (Phase) 198
6.36 Skin Friction Frequency Response 201

7.1 Representation of the Steady-State Flow Field for $Re_0 = 0.4$ 204
7.2 Representation of the Steady-State Flow Field for $Re_0 = 4$ 204
7.3 Representation of the Steady-State Flow Field for $Re_0 = 40$ 204
7.4 Flow Field Representation of the Step Response ($Re_0 = 0.4$) I 208
7.5 Flow Field Representation of the Step Response ($Re_0 = 0.4$) II 209
7.6 Flow Field Representation of the Step Response ($Re_0 = 4$) I 210
7.7 Flow Field Representation of the Step Response ($Re_0 = 4$) II 211
7.8 Flow Field Representation of the Step Response ($Re_0 = 40$) I 212
7.9 Flow Field Representation of the Step Response ($Re_0 = 40$) II 213
7.10 Linearized Flow Field Representation for $Re_0 = 0.4$ I 216
7.11 Linearized Flow Field Representation for $Re_0 = 0.4$ II 217
7.12 Linearized Flow Field Representation for $Re_0 = 4$ I 218
7.13 Linearized Flow Field Representation for $Re_0 = 4$ II 219
7.14 Linearized Flow Field Representation for $Re_0 = 40$ I 220
7.15 Linearized Flow Field Representation for $Re_0 = 40$ II 221
7.16 Flow Field Representation of Θ_1 for $Re_0 = 4$ and $Sr = 0.5$ 222
7.17 Flow Field Representation of Θ_1 for $Re_0 = 40$ and $Sr = 0.5$ 222
7.18 Flow Field Representation of Θ_1 for $Re_0 = 4$ and $Sr = 7$ 223
7.19 Flow Field Representation of Θ_1 for $Re_0 = 40$ and $Sr = 7$ 223
7.20 Nußelt Number Distribution at $Re_0 = 4$ 225
7.21 Nußelt Number Distribution at $Re_0 = 40$ 226
7.22 Friction Coefficient Distribution at $Re_0 = 4$ 227
7.23 Friction Coefficient Distribution at $Re_0 = 40$ 228

8.1 Frequency Response of PT1 and $n-\tau$ 233
8.2 Impulse Response of PT1 and $n-\tau$ 234
8.3 NRMSE-Fit of Different Models 236
8.4 Frequency Response of Heat Transfer at $Re_0 = 4$ and Various Pr 237
8.5 Frequency Response of Heat Transfer at $Re_0 = 40$ and Various Pr . . . 237
8.6 Frequency Response of Heat Transfer at $Re_0 = 4$ and Different ΔT . . 239
8.7 Frequency Response of Heat Transfer at $Re_0 = 40$ and Different ΔT . 240
8.8 Nußelt Number for Sinusoidal Fluctuations of $Sr = 0.5$ at $Re_0 = 40$ . . . 241

9.1 Sketch of a Rjike Tube 244
9.2 Acoustic Pressure and Velocity in a Tube (Time Domain) 245
9.3 Acoustic Pressure and Velocity in a Tube (Frequency Domain) 246
9.4 Normalized Rayleigh Index 247
9.5 Comparison of the Normalized Rayleigh Index 249
9.6 Frequency Response of Heat Transfer to Re and Angle of Attack 257
9.7 Frequency Response Magnitudes for Hot-Wire Anemometry 259

List of Tables

2.1 Cylinder Flow Regimes (Hucho, 2011) 11
2.2 Reynolds Numbers Examined in this Thesis 11
2.3 Separation Angle 20
2.4 Dimension Matrix 26

3.1 Survey of the Recent Literature on the Rijke Tube 71

5.1 Results of the Steady-State Domain Size Study 118
5.2 Results of the Steady-State Cell Size Study 119
5.3 Results of the Dynamic Cell Size Study 120
5.4 Results of the Dynamic Time Step Size Study 121
5.5 Results of the Steady-State Domain Size Study (LES Case) 127
5.6 Results of the Cell Size Study (LES Case) 128
5.7 Different Meshes Used in the LNSE Approach 135

6.1 Step Response Characteristics of Heat Transfer 150
6.2 Step Response Characteristics of Skin Friction 151
6.3 NRMSE-Fit of the Identified Transfer Functions of Heat Transfer . . . 183
6.4 Estimated Coefficients of the Transfer Function of Heat Transfer . . . 184
6.5 NRMSE-Fit of the Identified Transfer Functions of Skin Friction . . . 189
6.6 Estimated Coefficients of the Transfer Function of Skin Friction . . . 191
6.7 Values for the Steady-State Gain K_{Nu} 200

9.1 Exemplary Properties and Conditions for a Heated Wire in a Rijke Tube 252
9.2 Exemplary Properties and Conditions for a Hot-Wire Anemometer . . 255
9.3 Exemplary Properties and Conditions for a Heat Exchanger 262

A.1 NRMSE-Fit of the TF of the Heat Transfer (CFD/SI with VF) 287
A.2 NRMSE-Fit of the TF of the Heat Transfer (LNSE with VF) 287
A.3 NRMSE-Fit of the TF of the Skin Friction (CFD/SI with VF) 288
A.4 NRMSE-Fit of the TF of the Skin Friction (LNSE with VF) 288
A.5 Estimated Coefficients of the TF of the Heat Transfer (CFD/SI with VF) 289
A.6 Estimated Coefficients of the TF of the Heat Transfer (LNSE with VF) 290
A.7 Estimated Coefficients of the TF of the Skin Friction (LNSE with VF) . 291

Nomenclature

Roman letters

$\dot{n}_A$	Specific flux of species A
$\dot{q}$	Heat flux density
i	Imaginary unit
$\mathbf{x}$	Coordinate direction
$\vec{n}$	Surface normal vector
A	Area/Transfer function polynomial/System matrix
a	Speed of sound/Coefficient
A_S	Constant
B	Transfer function polynomial/Transfer function polynomial/Right-hand side vector
b	Coefficient/Body forces/Convective velocity
C	Constant/Transfer function polynomial
c	Specific heat capacity
c_τ	Time constant
c_A	Concentration of component A
c_d	Drag coefficient
c_f	Friction coefficient
c_p	Pressure coefficient
c_v	Isochoric specific heat capacity
D	Transfer function polynomial/Denominator/Tube diameter
d	Diameter/Constant additive component
D_{AB}	Coefficient of diffusion
E	Energy
e	Stochastic disturbance
F	Transfer function polynomial/Force
f	Coefficient/Arbitrary variable/Linear operator
F_B	Basset force
F_d	Drag force
F_s	Sampling frequency
G	Transfer function/Frequency response
g	Impulse response/Gravitational accileration

H	Model for stochastic part
h	Heat transfer coefficient
h	Step response/Heat transfer coefficient/Enthalpy
h_m	Convective mass transfer film coefficient
I	Identity matrix
i	Index
K	Steady state gain/Kernel
k	Time increment/Thermal conductivity/Turbulent kinetic energy
K_ρ	Isobaric expansion ratio
L	Length/Linear filter
l	Counter/Length
M	Measure of turbulence resolution
m	Exponent
N	Total number of datapoints/Number of cells/Numerator
n	Interaction index/order of polynomial
P	Kinematic pressure
p	Pressure
Q	Factor Matrix
q	Time shift operator
R	Specific gas constant/Factor matrix/Correlation
r	Radius/Residue
S	Constant/Strain rate tensor
s	Parameter (frequency)/Entropy
T	Temperature
t	Time
T_S	Temperature constant
T_s	Sampling time
U	Outer flow velocity
u	Velocity/Internal energy/Model input
V	Volume/Cost function
v	Disturbance
W	Weighting matrix
w	Input disturbance
x	Disturbance-free output
x	Noise free model output
x, y, z	Coordinates
y	Model output
y^+	Non-dimensional wall distance
Z	Z-standardized quantity
z	Variable of z-space

Greek letters

α	Thermal diffusivity/Roots/Angle of attack
β	Thermal expansion coefficient/Zeros/Profil coefficient
β	Thermal expansion coefficient
χ	Thermal diffusivity
Δ	Difference
δ	Perturbation parameter/Boundary layer thickness/Difference to steady state/Dirac function
δ_{ij}	Kronecker Delta
$\dot{\omega}$	Heat source density
ϵ	Small parameter/Amplitude/Turbulent energy dissipation
η	Similarity variable/Modified radial coordinate
Γ	Regularization matrix
γ	Ratio of the specific heats/Ensemble average of the power spectral density
γ_E	Euler constant
κ	Wavenumber/Coherence
λ	Secondary (bulk) viscosity/Scaling factor/Wavelength
μ	Dynamic viscosity
ν	Kinematic viscosity
ω	Angular frequency
Φ	NRMSE-fit/Dissipation function/Observation matrix
ϕ	Polar angle/flux
Π	Ratio of viscosities
Ψ	Regressor matrix/Flux limiter function
ψ	Stream function
ρ	Density
σ	Growth rate/Standard deviation
τ	Time constant/Shear stress
Θ	Dimensionless temperature difference/Heaviside step function
θ	Parameter vector
ε	Prediction error
φ	Velocity potential/Vector of regressors
ξ	Instrumental variable
ζ	Vorticity

Dimensionless Groups

Bi	Biot number
CFL	CFL number
Ec	Eckert number

Eu	Euler number
Fo	Fourier number
Fr	Froude number
He	Helmholtz number
Le	Lewis number
Ma	Mach number
Nu	Nußelt number
Pr	Prandtl number
Re	Reynolds number
Ri	Richardson number
Sc	Schmidt number
Sh	Sherwood number
Sr	Strouhal numgber
Wo	Womersley number
KC	Keulegan–Carpenter number

Superscripts

$*$	Surface-aligned frame of reference
$\hat{}$	Estimated/Fourier transform
$\bar{}$	Temporal average
ref	Reference
$\tilde{}$	Dimensionless
$''$	Turbulent fluctuation
$'$	Fluctuating
^{T}	Estimated

Subscripts

0	Steady-state/Initial
1	Pulsating
∞	Ambient
ϕ_p	Angular
c	Cylinder/Cutoff
d	Domain
f	Fluid
i	Index
j	Index
m	Mean
p	Particle
r	Radial
s	Solid/Step/Streaming
sep	Separation

u	Upstream
w	Surface (wall)
Ny	Nyquist
St	Stockes

Abbreviations

ARX model	Autoregressive with exogenous input model
BIBO	Bounded input bounded output
BJ model	Box-Jenkins model
BL	Blasius layer
BLUE	Best linear unbaised estimator
CCA	Constant current anemometer
CD	Central scheme
CDF	Cumulative distribution function
CFD	Computational fluid dynamics
CLS	Constrained least squares
CTA	Constant temperature anemometer
CVA	Constant voltage anemometer
DFT	Discrete Fourier Transform
DNS	Direct numerical simulation
DTFT	Discrete time Fourier transform
FFT	Fast Fourier transform
FIR	Finite impulse response
FOH	First-order hold
GWN	Gausian white noise
HL	Hiemenz layer
HX	Heat exchanger
IFFT	Inverse fast Fourier transform
LES	Large eddy simulation
LNSE	Linearized Navier–Stokes equations
LS	Least squares
LTI	Linear time invariant
MIMO	Multi-input multi-output
MISO	Multi-input single-output
MMSE	Minimum mean square error estimator
MSE	Mean square error
MVUE	Minimum variance unbaised estimator
NLS	Nonlinear least squares
NRMSE	Normalized root mean square error
OE model	Output-error model
OLS	Ordinary least squares

OVF	Orthonormal vector fitting
PEM	Prediction error method
PEM-QC	Quadratic-criteria prediction error method
PISO	Pressure implicit with splitting of operator
PSD	Power spectral density
PT1	Proportional with first order time lag model
QuadVF	Quadratic vector fitting
RE	Richardson extrapolation
RI	Rayleigh index
RMS	Root Mean Square
RMS	Root mean square
SGS	Subgrid scale
SI	System identification
SIMO	Single-input multi-output
SIMPLE	Semi-implicit method for pressure linked equations
SISO	Single-input single-output
SK	Sanathanan-Koerner
SNR	Signal-to-noise ratio
TAL	Total artificial lung
US	Upwind scheme
VF	Vector fitting
WLS	Weighted least squares
ZOH	Zero-order hold

1 Introduction

1.1 Motivation

1.1.1 Energy Conversion and Environmental Aspects

Energy conversion is one of the most important factors in the history of humankind. Fire, which is the conversion of some type of fuel to chemical products, light, and heat by oxidation, was harnessed even in prehistoric times. Later, more sources of primary energy—natural sources of energy—were used and converted into mechanical energy, e.g. in windmills, water wheels for gristmills, and trip hammers. The industrial revolution, starting in the second half of the 18th century, was made possible by the increasing use of steam power with coal as the primary energy source.

From an engineering perspective, the conversion of energy from one form to another is one of the main tasks. Energy is needed for electricity, heat, transportation, and the manufacturing of goods. In 2014, the supplied primary energy for the whole world was 13 699 million tons of oil equivalent (Mtoe) which amounts to 159 319 TWh (International Energy Agency, 2016). Oil, coal, and natural gas, all of which are fossil fuels, made up more than 80 % of all fuel shares (International Energy Agency, 2016). A total of 108 043 TWh was consumed in 2014, 29.4 % of which by industry and 28.3 % by transportation. A share of 8.9 % of the consumed primary energy was put to non-energy use, e.g. chemical products (International Energy Agency, 2017). The total generation of electricity and heat in power stations was 23 816 TWh (International Energy Agency, 2016) and 3815 TWh, respectively (International Energy Agency, 2017). With losses of 32 203 TWh, this leads to an overall efficiency for the conversion of primary energy to electricity and heat of 46.2 %.

The use of carbon (coal) or hydrocarbons (oil and natural gas) as energy source bears—among others—two main problems: During the combustion process nitrous oxides (NO_x) and carbon dioxide (CO_2) are generated in considerable amounts. NO_x is associated with negative consequences for the health of humans (WHO Regional Office for Europe, 2003) and is a precursor for other pollutants such as acid rain. CO_2 plays a major role in the greenhouse effect determining earth's surface temperature (Rodhe, 1990; Lacis et al., 2010). The anthropogenic greenhouse effect is caused to 60 % by the man-made emission of CO_2 (Rodhe, 1990). In the last 200 years, the concentration of CO_2 in the atmosphere rose from about 280

parts per million (ppm) to over 400 ppm (Houghton and Intergovernmental Panel on Climate Change, 2001). CO_2 is besides water one of the main products of the combustion process and can only be reduced by increasing efficiency.

To counteract the negative effect of the energy sector on the environment, the United Nations Summit in Brasil 1992 published objectives for the "energy development, efficiency and consumption" in the "Agenda 21" United Nations (1994):

> The basic and ultimate objective of this programme area is to reduce adverse effects on the atmosphere from the energy sector by promoting policies or programmes, as appropriate, to increase the contribution of environmentally sound and cost-effective energy systems, particularly new and renewable ones, through less polluting and more efficient energy production, transmission, distribution and use. This objective should reflect the need for equity, adequate energy supplies and increasing energy consumption in developing countries, [...], and the situations of countries highly vulnerable to adverse effects of climate change.

This paragraph emphasizes the need for more efficient energy production and new energy systems. Both goals can only be achieved through research on existing machinery and principles as well as on new approaches.

1.1.2 Transformation Between Thermal Energy and Acoustic Energy

One energy conversion mechanism that has to be taken into consideration is the conversion from thermal energy to acoustic energy and vice versa. Research in this area offers possibilities to achieve both objectives from the United Nations Summit: higher efficiency of existing technology and new approaches to energy conversion. Although known for about two centuries, this conversion mechanism has been neglected and came into focus again rather recently. The term thermoacoustics was coined to describe this effect which was first reported by Higgins (1802) and Rijke (1859). Higgins (1802) discovered that a hydrogen flame placed in a tube would emit sound. This setup is now known as the "singing flame". Later a similar phenomenon was found by Rijke (1859) who was experimenting with a heated wire mesh inside a resonator tube. He also experienced a clear sound that was emitted from the open ends of the resonator. The device is now called the Rijke tube. Credit is also due to Rayleigh (1896) who was the first to put thermoacoustics on a firm theoretical foundation. He recognized that the dynamics of the heat transfer between flame or heated wire and the fluid in the tube is the essential ingredient. At the time of these discoveries, these pioneers could not possibly image which importance their research might have for energy systems today.

Thermoacoustic Instabilities in Energy Systems

An example of a well-established energy system is the stationary industrial gas turbine. Modern gas turbines for electricity generation operate with lean and premixed combustion (Keller, 1995). Air is compressed to pressures as high as 30 times the environmental pressure (Jansohn, 2010). Subsequently, the air is mixed with natural gas in a plenum and oxidized at a high air–fuel ratio in the burner. The combustion products enter the turbine section at temperatures up to 1400 °C (Jansohn, 2010). The turbine converts the energy of the hot flue gas into mechanical energy driving the compressor and an electric generator to produce electrical energy.

Gas turbines have a severe impact on the environment. A portion of 21.6 % of the total electricity was produced from natural gas (International Energy Agency, 2016) and mostly in gas turbines. In predictions for the year 2040, this share is expected to rise to 27.5 % (U.S. Energy Information Administration, 2016). The optimal operating point, especially the flame temperature, is determined by the amount of carbon monoxide (CO) and NO_x produced in the combustion process. Lean premixed combustion is however prone to thermoacoustic instabilities (Keller, 1995; Paschereit and Polifke, 1998; Jansohn, 2010; Laera et al., 2014). If such an instability occurs, small fluctuations in pressure and fluid velocity are amplified greatly. This amplitude can be as high as 1 % of the mean operating pressure of the combustion (Paschereit and Polifke, 1998). This has a negative impact on efficiency and the life cycle of the gas turbine (Laera et al., 2014). In turn, the amount of carbon dioxide (CO_2) emitted by the power plant is directly related to its efficiency. Moreover, thermoacoustic oscillations disallows certain working conditions, e.g. turndown, that would allow a more flexible energy generation. Increasing the efficiency and flexibility of gas turbines for power generation would have a positive effect on their environmental impact.

Domestic boilers, used for heat production on a household level are also prone to thermoacoustic instabilities. Large pulsations can be harmful to the device and impede efficiency similar to the gas turbine. In domestic boilers, the heat exchanger, which holds the water to be heated by the flue gas from the combustion, also influences the thermoacoustic stability of this system (Strobio Chen et al., 2015). The heat exchanger is a cold, coiled tube placed in the hot flue gas stream in a cross-flow configuration. The heat transfer between the gas and the heat exchanger tubes can dampen or drive pressure oscillations. Of particular importance to this effect is the time lag between heat transfer and pressure oscillation. This phase lag decides whether acoustic fluctuations are dampened or excited.

Harnessing the Thermoacoustic Effect

In the above-mentioned examples of the gas turbine and the domestic boiler, the thermoacoustic effect, where thermal energy is converted into pressure fluctuations and acoustic velocity fluctuations, are harmful and thus unwanted. However, the thermoacoustic effect can be harnessed in devices such as a thermoacoustic engine or a thermoacoustic refrigerator. In the thermoacoustic engine, strong temperature gradients are created—most often through the use of heat exchangers—at a component called stack or regenerator. The working gas moves back and forth through the temperature gradient. It absorbs heat closer to the hot side, leading to an expansion of the gas and releases the heat to the stack at the cold end and thus the gas is compressed. Periodic compression and expansion of the working gas is acoustic energy, which can be converted to mechanical energy or electrical energy or be transmitted to a second thermoacoustic stage. This second stage also has a stack and two heat exchangers. At the second stack, a temperature gradient develops caused by the acoustic oscillation. The hot end is cooled against ambient conditions allowing the cold side to assume temperatures below ambient conditions. This is called a thermoacoustic refrigerator. It does not necessarily have to be implemented as a second thermoacoustic stage but can also be driven, e.g. by a piston. These configurations are rather simple to build and very robust. The basic body is usually a rigid resonator tube with closed ends. However, as of today, devices harnessing the thermoacoustic effect suffer from low efficiency.

1.1.3 Heat Transfer Dynamics in Unsteady Flow

The configurations mentioned in the previous sections in which thermoacoustics play a vital role can be divided into two groups. In the “singing flame” and the gas turbine, the combustion process is driving the instabilities. In contrast, in the Rijke tube, in domestic boilers, as well as in thermoacoustic engines and refrigerators the fluctuations are driven by the heat transfer between the fluid (working gas) and a solid body. This makes the heat transfer between a solid body in fluctuating flow worthwhile investigating. Moreover, configurations with solid–gas heat transfer, like the Rijke tube, are often used in the basic research of combustion instabilities. The Rijke tube, in particular, is the prototype of a thermoacoustic device (Rijke, 1859; Raun et al., 1993). It has gained interest for the study of the phenomenon of thermoacoustic oscillations in the last decades although there are little direct applications in industry. It is a cheap tool to study thermoacoustic phenomena as they occur, as a potentially harmful byproduct, in stationary gas turbines for power generation (Benoit and Nicoud, 2005).

In the case of the Rijke tube, for example, the centerpiece is a heated wire, usually in the form of a loosely wound coil or mesh. A resonator tube, hence the name Rijke

tube, sets the conditions for fluctuations to grow in strength. This makes the configuration of a cylinder in pulsating crossflow the perfect specimen for basic research in this area. The single cylinder stands for the wire, and the acoustic wave inside the tube is represented by the pulsations.

An additional practical example, where the effect of a bluff body in fluctuating crossflow plays a vital role is hot-wire anemometry (Bruun, 1996). For this method for flow measurement, turbulence and its effect on the heat transfer are important. Here, the pulsations are due to fluctuations occurring in turbulent flow.

Closely related to the transfer of heat between solid body and fluid is the transfer of momentum. It appears as the skin friction on the surface of the solid body. Although of lesser importance for cylindrical configurations, the effect of its dynamic behavior can be seen as the Basset history force in the case of a solid spherical particle Basset (1888). It significantly influences the trajectory of a particle in unsteady flow or if the particle experiences acceleration.

1.1.4 Modeling and Modeling Techniques

In the case of any complex phenomenon, there is a desire for modeling. A model, often in the form of mathematical formulas, is a vehicle to understand phenomena, to place them in a greater perspective and can ultimately serve as a design tool. Hence, this thesis is also motivated by the desire to find an adequate procedure to acquire a model for the dynamic behavior of heat transfer and skin friction of a cylinder in pulsating crossflow and to provide models for cases like the Rijke tube. This has never been done in such detail using data based modeling techniques.

The models presented in this thesis refer to the heated wire in the Rijke tube mostly and can directly be used in research activities involving a Rijke tube. Additionally, the techniques refined and assessed in this thesis can be applied on similar configurations like domestic boilers and thermoacoustic engines and refrigerators. It is also of interest in research directly related to gas turbines. This thesis tries to make a step towards a sustainable and ecologically sensitive energy production by improving the models and modeling techniques in the area of thermoacoustics.

1.2 Aims

This thesis had three main goals: The first objective was to give an exhaustive qualitative and quantitative description of the linear dynamic behavior of heat transfer and skin friction of a cylinder in pulsating crossflow in different flow regimes (Reynolds numbers). In particular, Reynolds numbers $\mathrm{Re} \leq 40$ are of interest for

the Rijke tube and hot-wire anemometry. Implications for these pulsating flow configurations are drawn. The limitations of previous studies of this problem, e.g. by Lighthill (1954), are scrutinized. Crucial assumptions are identified and compared to solutions from computational fluid dynamics (CFD). This way, a much more comprehensive understanding of the complex flow physics was achieved.

The assessment of techniques for system identification (SI) in combination with CFD simulation for data generation in the scope of skin friction and heat transfer was the second aim. This procedure not only supplements the first goal but also provides a framework for further studies in this field using SI techniques.

The final objective was to develop low-order models for skin friction and heat transfer. Transfer functions—as they often appear in control theory—are well founded in theory and provide a concise representation of the results. A parametrized low-order model for the heat transfer dynamics is of avail in the modeling of the Rijke tube for further studies on thermoacoustic oscillations. Particular attention was given to two phenomena: peak gain that occurs at low but non-zero frequencies and the phase difference at high frequencies.

1.3 Scope

This thesis is based on techniques and methods introduced by Föller et al. (2008) for the investigation of this problem, but represents a significant advancement over previous computational studies (Apelt and Ledwich, 1979; Kwon and Lee, 1985; Nicoli and Pelcé, 1989; Payne, 1958; Föller et al., 2008). The heat transfer of a heated cylinder in pulsating crossflow was analyzed through state-of-the-art CFD methods focusing on flow at Reynolds numbers of Re = 0.4, Re = 4, Re = 40, Re = 120, Re = 240, and Re = 3900. Reynolds numbers below the vortex shedding threshold (Re ≤ 40) are examined in even more detail. The dynamics are quantified using SI techniques. This approach to combine CFD simulations for data generation and SI methods to acquire models for the transfer behavior is called CFD/SI method. It represents the foundation for this thesis.

After introducing the phenomena of a cylinder in steady crossflow, governing equations are given, and simplifications are discussed in Chapter 2. Methods and results from previous studies of a cylinder in pulsating crossflow reported in the scientific literature are presented in Chapter 3. Special consideration is given to the widely acknowledged work by Lighthill (1954) and succeeding analytical papers. Chapter 4 deals with linear dynamic systems that are used to describe the dynamic nature of heat transfer and skin friction of a cylinder in pulsating crossflow. The framework is introduced, and the methods employed in later chapters are shown in detail. The methods and settings of CFD techniques are presented in Chapter 5. In Chapter 6,

heat transfer and skin friction dynamics of a cylinder in crossflow are quantified using data from CFD/SI method. The results are tabulated as transfer functions and presented as step responses and frequency responses of the linear system. Different approaches to acquire the transfer function are assessed and finally compared. To improve the understanding of the underlying flow physics, Chapter 7 offers a detailed view of the flow field and the spatial distribution of skin friction and heat transfer. Low order models are presented in Chapter 8, designed to be valid for a broad range of Reynolds numbers including corrections for different conditions. Applications, namely the Rijke Tube, hot-wire anemometry, and heat exchangers, are outlined in Chapter 9. In Chapter 10, conclusions are drawn, and an outlook for further areas of research is provided.

2 Flow Around a Circular Cylinder

A circular cylinder is one of the most basic shapes in geometry. Its surface is defined by all points in a fixed distance r from an (infinitely long) straight line, which is called axis. Fluid flow around a circular cylinder, perpendicular to its axis, and heat transfer between cylinder[1] and fluid is one of the archetypal problems of thermo-fluid dynamics (King, 1914; Collis and Williams, 1959; Tritton, 1959; Fornberg, 1980; Sparrow et al., 2004; Baehr and Stephan, 2011; Bergman et al., 2011; Hucho, 2011). It is a geometrically simple example for external flow, i.e. flow around a *bluff body*. The steady-state flow was assessed very thoroughly in the past (Zdravkovich, 1997) and is an important vantage point for further analyses. In this section, the case of a cylinder in steady crossflow is surveyed first. Subsequently, governing equations are given and the concept of small perturbations in free-stream flow velocity, i.e. pulsations, is introduced.

2.1 Cylinder in Steady Crossflow

A cylinder, placed in a stream of fluid with constant and uniform velocity, disturbs the flow. The fluid can neither pass through the cylinder nor slip along its surface. At the most upstream point of the cylinder, the fluid is at rest, and the kinetic energy of the fluid is converted into enthalpy, i.e. pressure. This location is called the *forward stagnation point*. Along a streamline close to the surface of the cylinder, the favorable pressure gradient forces the fluid to accelerate along the circumference of the cylinder. It reaches a velocity higher than the velocity of the approaching flow in a short distance to the surface of the cylinder. The pressure gradient reverses at the lee side of the cylinder, causing the flow to decelerate until reaching the *rear stagnation point*. Velocity profiles at different positions along the cylinder circumference are sketched in Figure 2.1.

Under the assumption that the flow of a Newtonian fluid[2] is isothermal and incompressible, the velocity field around a cylinder is determined by four reference quantities: cylinder diameter d, free-stream velocity u_∞, dynamic viscosity μ_{ref}, and density ρ_{ref}. This relationship can be written as

$$u = f(d, u_\infty, \mu_{\text{ref}}, \rho_{\text{ref}}) . \tag{2.1}$$

[1] For reasons of readability, cylinder in this thesis always refers to a circular cylinder.

[2] A fluid where the viscous forces are linearly dependent on the strain rate (White, 2007).

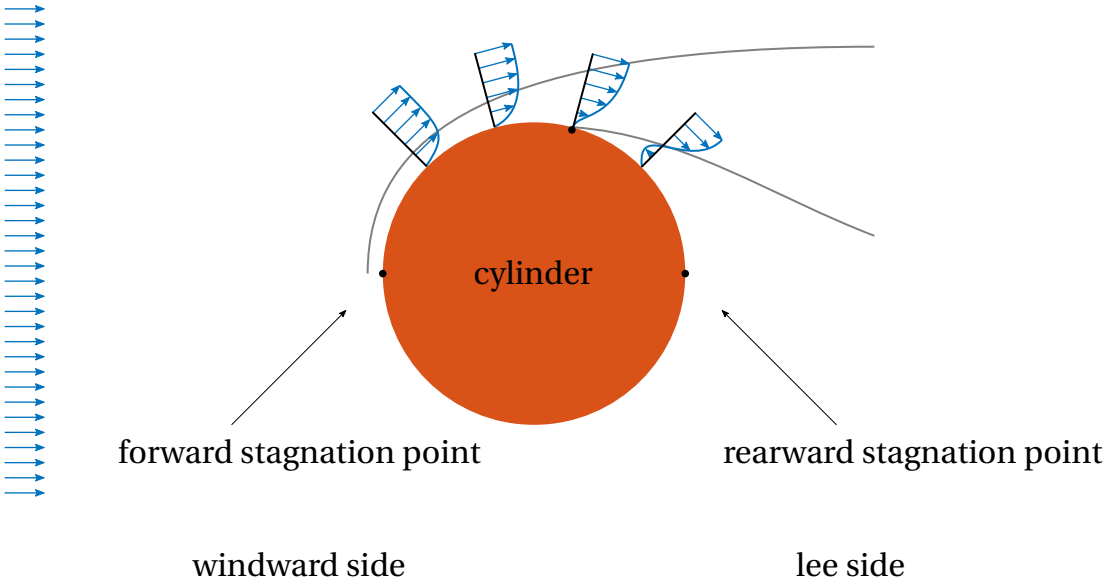

Figure 2.1: Sketch of a Cylinder in Steady Crossflow. Velocity profiles are shown as blue arrows. Grey lines signify the thickness of the boundary layer and the zone of flow separation.

The basic dimensions involved are mass, length, and time. Following a dimensional analysis, there is one parameter group describing the relationship between these quantities. This dimensionless quantity is known as *Reynolds number* and is defined as

$$\mathrm{Re} = \frac{u_\infty d}{\nu} \tag{2.2}$$

with the kinematic viscosity $\nu_{\mathrm{ref}} = \mu_{\mathrm{ref}}\rho_{\mathrm{ref}}$. The Reynolds number can also be interpreted as the ratio between inertial forces and viscous forces, i.e. the ratio of convective momentum transport to diffusive momentum transport (Bergman et al., 2011).

Different velocity profiles lead to characteristic patterns, or regimes, of the flow especially downstream of the cylinder, where the adverse pressure gradient is governing the flow. Theses patterns are characterized by the Reynolds number (Zdravkovich, 1997), as explained in a short survey of the physical phenomena in the following section.

2.1.1 Phenomenology

Several authors gave comprehensive lists of flow regimes of cylinders in crossflow (Gersten, 1965; Zdravkovich, 1997; Hucho, 2011). The regimes identified by Hucho (2011) are reproduced in Table 2.1.

Reynolds number range				Regime
		Re $\rightarrow$	0	creeping flow
		Re $<$	50	closed wake
50	$<$	Re $<$	140 – 200	Kármán vortex street
200	$<$	Re $<$	260	transition in far wake
260	$<$	Re $<$	1×10^3	transition in near wake
1×10^3	$<$	Re $<$	2×10^5	transition in shear layer
2×10^5	$<$	Re $<$	4×10^5	critical
4×10^5	$<$	Re $<$	1×10^6	post-critical
1×10^6	$<$	Re		trans-critical

Table 2.1: Cylinder Flow Regimes (Hucho, 2011).

Regime	Re
creeping flow	0.4
attached flow	4
closed vortex pair	40
Kármán vortex street	120
transition in wake	240
subcritical	3900

Table 2.2: Reynolds Numbers Examined in this Thesis. The range Re $\leq$ 40 is examined in more detail.

Recent numerical simulations by Rajani et al. (2009) assessed the flow past a cylinder in the laminar regime. Flow separation and the formation of a closed wake are reported to occur at Re > 6.1. For the wake instability, Rajani et al. (2009) found the onset of *vortex shedding* to occur at 48 < Re < 49. This is close to the value of Re = 47 reported by Norberg (2003). Rajani et al. (2009) also found that the distortion of the spanwise vorticity (z-direction) occurs at Re > 250 and Re > 200 in streamwise direction (x-direction). The flow is two-dimensional for Re < 200. Similarly, Norberg (2003) reported this onset of three-dimensional structures to occur at Re > 190.

In this thesis, one exemplary Reynolds number is chosen for every regime. Table 2.2 lists the flow regimes encountered at the flow conditions examined in this thesis.

2.1.2 Heat and Momentum Transfer

To quantify the flow around a cylinder, a frame of reference has to be set. In this thesis, three different coordinate systems are used. The Cartesian coordinate system is the most important one. The x_1-direction is parallel to the undisturbed flow. The

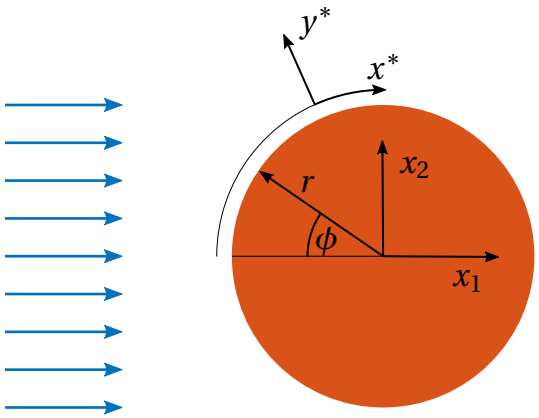

Figure 2.2: Coordinate Systems for the Cylinder.

x_2-coordinate and the x_3-coordinate are normal to the first so that the x_3-direction is parallel to the axis of the cylinder. Hence, for flow with a negligible contribution in the axial direction, the coordinate system is reduced to $[x_1\ x_2]^T$. The second frame of reference used is polar coordinates ($[r\ \phi]^T$). The origin is located in the center of the cylinder, but against the usual convention, the angle is chosen in such way that the forward stagnation point is located at $\phi = 0$. The last coordinate system introduced in this thesis is denoted by $[x^*\ y^*]^T$. The x^*-direction follows the contour of the cylinder starting at the forward stagnation point. Accordingly, y^* is the height above the surface of the cylinder. All three coordinate systems are depicted in Figure 2.2.

If a cylinder (or any object for that matter) is submerged in a fluid and relative movement between cylinder and fluid occurs, momentum is transferred. This momentum transfer, for a quasi-two-dimensional object like the cylinder, is quantified by drag and lift. Drag forces act in the direction of the flow. Lift forces occur normal to the direction of the flow and the axis of the cylinder. The lift force is not considered further in this thesis, as the problem is symmetric and therefore the net contribution is zero. Fluctuations in the lift exist due to vortex shedding (Norberg, 2003), but are not the scope of this thesis, as they are not caused by forced pulsations. Similar to the momentum transfer, heat transfer occurs when a temperature difference between the cylinder and the fluid exists.

Directly at the surface of the cylinder, the flow velocity is zero (no-slip condition). At this position, momentum transfer occurs only through *skin friction* and pressure differences. Skin friction is quantified through surface shear stress τ_w is given by

$$\tau_w = \mu \left.\frac{\partial u}{\partial y^*}\right|_{y^*=0} \tag{2.3}$$

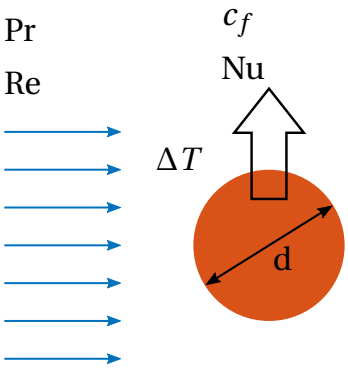

Figure 2.3: Sketch of a Cylinder in Steady Crossflow.

assuming an isotropic and incompressible Newtonian fluid. The constant of proportionality is the dynamic viscosity μ. Similarly, the *heat transfer rate* at the surface $\dot{q}_w$ is given by Fourier's law for heat conduction written as

$$\dot{q}_w = -k \left. \frac{\partial T}{\partial y^*} \right|_{y^*=0} \tag{2.4}$$

with thermal conductivity k.

Figure 2.3 shows a sketch of the problem with the relevant dimensionless parameters which will be developed below.

Drag

At the surface of the cylinder, the fluid is at rest. Heat and momentum transfer occur through viscous forces and pressure gradients. Conjointly, they amount to the drag force F_d acting on the bluff body. They solely depend on the fluid parameters u_∞, ρ_{ref}, and μ_{ref} as well as the geometric quantity d. This drag force is denoted by

$$F_d = f(d, u_\infty, \rho_{\text{ref}}, \mu_{\text{ref}}) . \tag{2.5}$$

Through dimensional analysis, this can be written as

$$\frac{F_d}{1/2\, A\, \rho_{\text{ref}}\, u_\infty^2} = f(\text{Re}) \tag{2.6}$$

where A is a reference area and $1/2\, \rho\, u_\infty^2$ is the dynamic pressure. The dimensionless group on the left hand side is called drag coefficient. It is given by

$$c_d = \frac{F_d}{1/2\, A\, \rho_{\text{ref}}\, u_\infty^2} . \tag{2.7}$$

The drag is a combination of form drag, also called pressure drag, caused by the cylindrical shape and the skin friction drag, caused by the friction on the surface.

hence, the drag coefficient is the linear combination of the pressure coefficient and the skin friction coefficient and hence reads

$$c_d = c_p + c_f \tag{2.8}$$

where c_p represents the average pressure coefficient and c_f is the average *skin friction coefficient.*

Friction Coefficients and Pressure Coefficients

The pressure coefficient is evaluated from the relative pressure at each point on the surface of the cylinder. This is written as

$$c_{p,\phi}(\phi) = \frac{p(\phi) - p_{\text{ref}}}{1/2\,\rho_{\text{ref}} u_\infty^2}. \tag{2.9}$$

Accordingly, the friction coefficient is calculated from the surface normal gradient of the flow parallel to the surface. This is denoted by

$$c_{f,\phi}(\phi) = \frac{\nu}{1/2\,u_\infty^2} \left.\frac{\partial u_\phi}{\partial r}\right|_{r=d/2}. \tag{2.10}$$

The frictional part of the drag is also referred to as skin friction. Unlike the pressure, which adjusts instantaneously in an incompressible fluid, the skin friction has a convective nature, much like the heat transfer. Figure 2.4 shows the local pressure and friction coefficients for a cylinder in steady crossflow with Re = 0.4, Re = 4, and Re = 40.

The average friction and pressure coefficients are given by

$$c_f = \frac{\nu}{1/2\,u_\infty^2} \frac{1}{2\pi} \int_0^{2\pi} \left.\frac{\partial u_\phi}{\partial r}\right|_{r=d/2} \mathrm{d}\phi = \frac{2}{\text{Re}} \frac{d}{u_\infty} \frac{1}{2\pi} \int_0^{2\pi} \left.\frac{\partial u_\phi}{\partial r}\right|_{r=d/2} \mathrm{d}\phi \tag{2.11}$$

and

$$c_p = \frac{1}{\pi\,\rho_{\text{ref}}\,u_\infty^2} \int_0^{2\pi} \big(p(\phi) - p_{\text{ref}}\big)\,\mathrm{d}\phi. \tag{2.12}$$

Figure 2.5 depicts pressure coefficient and friction coefficient as well as their combination, the drag coefficient, over a range of Reynolds numbers. A simple empirical correlation for c_d, valid for $1 \lesssim \text{Re} \lesssim 2.5 \times 10^5$ was reported by White (2007). It is given by

$$c_d = 1 + \frac{10.0}{\text{Re}^{(2/3)}}. \tag{2.13}$$

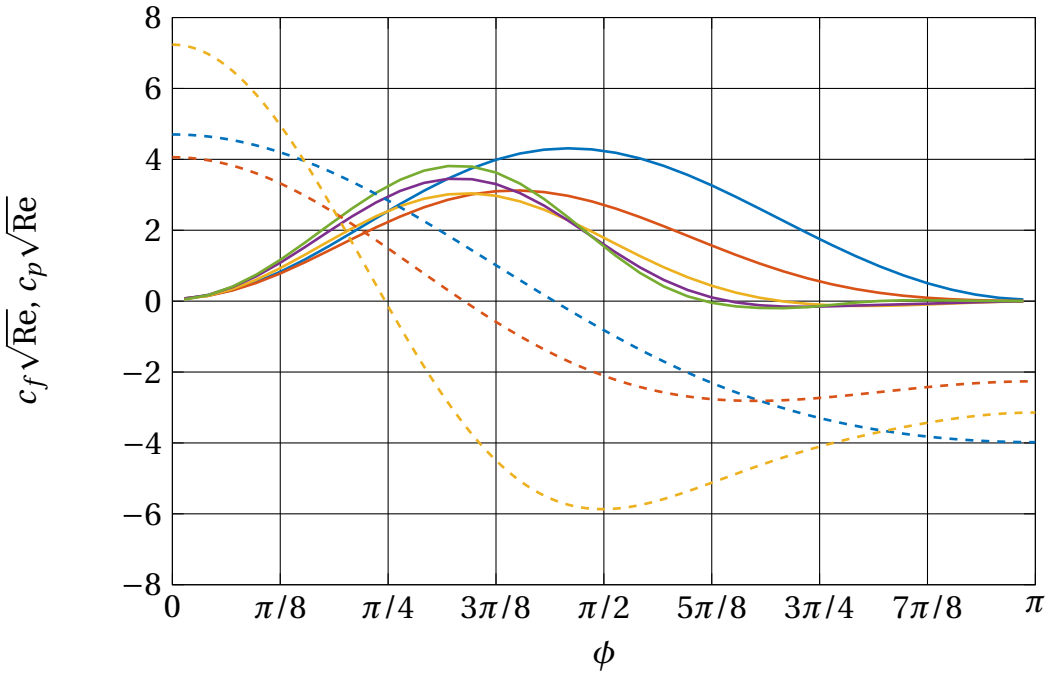

Figure 2.4: Steady-State Friction and Pressure Coefficient Distributions. The coefficients are scaled with $\sqrt{\mathrm{Re}}$. Friction coefficient: Re = 0.4 (——), Re = 4 (——), Re = 40 (——), Re = 120(——), and Re = 240 (——). Pressure coefficient: Re = 0.4 (- - -), Re = 4 (- - -), and Re = 40 (- - -).

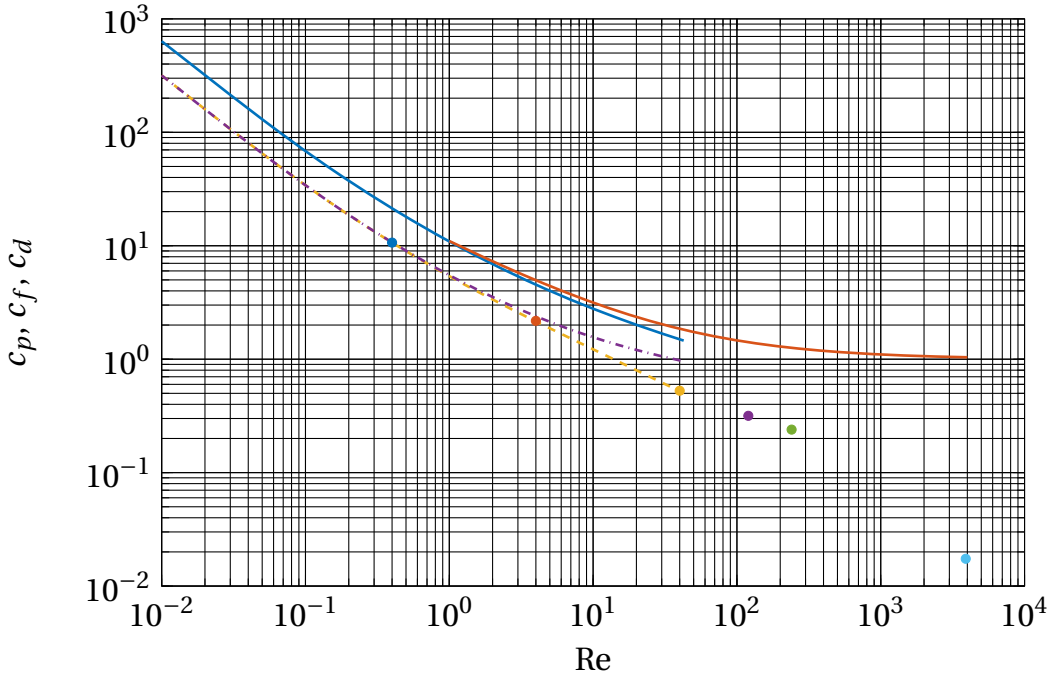

Figure 2.5: Mean Friction Coefficient and Correlations. Drag coefficient: Numerical simulation (——), correlation (White, 2007) (——). Friction coefficient (- - -). Pressure coefficient (-·-·-). The dots mark the values of c_f for Re = 0.4 (●), Re = 4 (●), Re = 40 (●), Re = 120 (●), Re = 240 (●), and Re = 3900 (●).

Heat Transfer

In cases of a temperature difference between the fluid and the cylinder, heat transfer occurs. It is determined by the heat conduction at the surface, the heat conduction within the fluid, and the enthalpy transport by the flow. The involved thermodynamic reference quantities are heat transfer rate $\dot{q}$, the temperature difference between the cylinder and the free-stream ΔT, isobaric specific heat capacity $c_{p,\mathrm{ref}}$, as well as thermal conductivity k_{ref}. These parameters are accompanied by three fluid dynamic quantities: velocity u_∞, density ρ_{ref}, and dynamic viscosity μ_{ref}. The geometric quantity is the cylinder diameter d.The heat transfer rate can thus be inferred from

$$\dot{q} = f(d, u_\infty, \rho_{\mathrm{ref}}, \mu_{\mathrm{ref}}, c_{p,\mathrm{ref}}, k_{\mathrm{ref}}, \Delta T)\,. \tag{2.14}$$

With the basic parameters—mass, length, time, and temperature—the heat transfer is determined by four dimensionless groups of reference quantities to describe the process

$$\frac{\dot{q}}{k_{\mathrm{ref}}/d\,\Delta T} = f(\mathrm{Re}, \mathrm{Pr}, \mathrm{Ec})\,. \tag{2.15}$$

In addition to the Reynolds number, two other dimensionless groups appear. The Prandtl number

$$\mathrm{Pr} = \frac{\nu_{\mathrm{ref}}}{\alpha} \tag{2.16}$$

with thermal diffusivity $\alpha = k_{\mathrm{ref}}/(\rho_{\mathrm{ref}}\, c_{p,\mathrm{ref}})$. It is the ratio of the diffusive momentum transport to the diffusive heat transfer. The group

$$\mathrm{Ec} = \frac{u_\infty^2}{c_{p,\mathrm{ref}}\,\Delta T} \tag{2.17}$$

is called Eckert number and characterizes heat dissipation by the ratio of kinetic energy to flow enthalpy difference.

Under the assumption of small velocities, the Eckert number vanishes $\mathrm{Ec} \to 0$. Using Newton's law of cooling $\dot{q} = h\,\Delta T$, the heat transfer reduces to

$$\frac{h}{k_{\mathrm{ref}}/d} = f(\mathrm{Re}, \mathrm{Pr}, \mathrm{Ec})\,. \tag{2.18}$$

With the *Nußelt number* given by

$$\mathrm{Nu} = \frac{h\,d}{k_{\mathrm{ref}}}, \tag{2.19}$$

this further simplifies to

$$\mathrm{Nu} = f(\mathrm{Re}, \mathrm{Pr})\,. \tag{2.20}$$

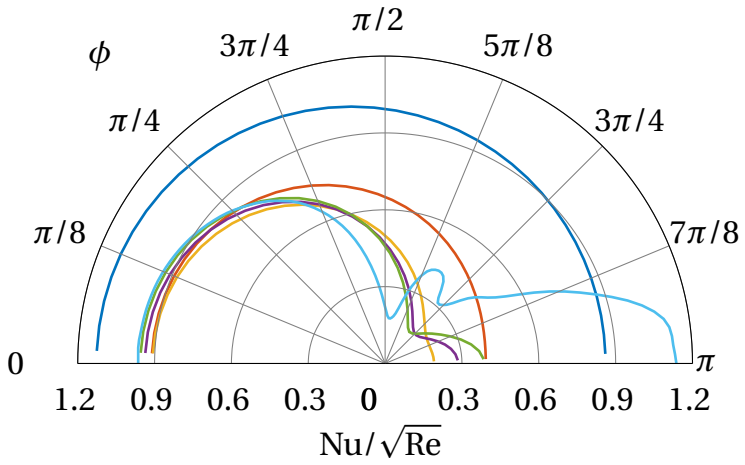

Figure 2.6: Nußelt Number Distribution. Re = 0.4 (—), Re = 4 (—), Re = 40 (—), Re = 120 (—), Re = 240 (—), Re = 3900 (—).

Nußelt Number

The temperature gradient at the cylinder can be non-dimensionalized using a characteristic length and a characteristic temperature difference. In this case, the characteristic length is the cylinder diameter d, and the characteristic temperature difference is measured between undisturbed fluid and cylinder. The resulting dimensionless group is called Nußelt number and defined by

$$\mathrm{Nu}_\phi(\phi) = \frac{d}{\Delta T}\left.\frac{\partial T}{\partial r}\right|_{r=d/2}. \tag{2.21}$$

In Figure 2.6, the Nußelt number distribution along the surface of the cylinder ($0 \leq \phi \leq \pi$) is shown for three different Reynolds numbers. The average Nußelt number is given by

$$\mathrm{Nu} = \frac{d}{\Delta T}\frac{1}{2\pi}\int_0^{2\pi}\left.\frac{\partial T}{\partial r}\right|_{r=d/2}\mathrm{d}\phi. \tag{2.22}$$

Similarity considerations show that identical Reynolds numbers and Prandtl numbers yield similar temperature distributions and thus identical Nußelt numbers (Bergman et al., 2011). The average Nußelt number of a cylinder in steady crossflow can be evaluated using correlations of the form $\mathrm{Nu} = f(\mathrm{Re}, \mathrm{Pr})$ (cf. Equation (2.20)).

A number of correlations for the average Nußelt number exists with different domains of validity and accuracy (Bergman et al., 2011; Collis and Williams, 1959; Sparrow et al., 2004). Two correlations, for negligible temperature differences and

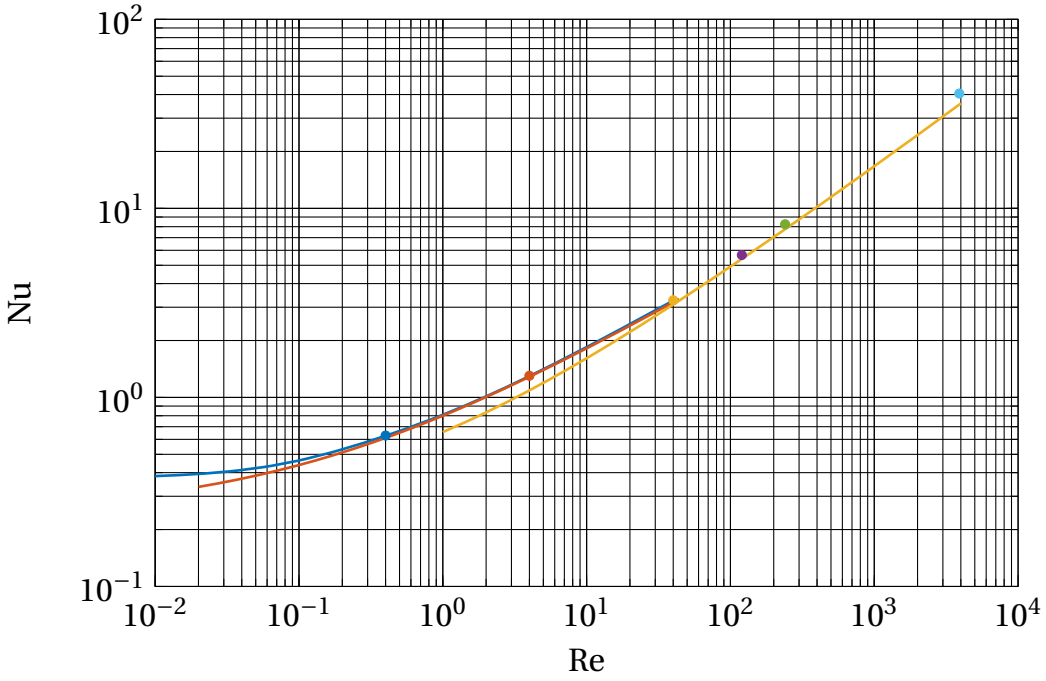

Figure 2.7: Nußelt Number and Correlations. Numerical simulation (—), correlation by Collis and Williams (1959) (—), and correlation by Sparrow et al. (2004) (—). The dots mark the values of Re = 0.4 (•), Re = 4 (•), Re = 40 (•), Re = 120 (•), Re = 240 (•), and Re = 3900 (•).

a Prandtl number of Pr = 0.7, as well as point values for several Reynolds numbers under consideration are shown in Figure 2.7.

Collis and Williams (1959) developed a correlation especially for air flow (Pr ≈ 0.7) and low Reynolds numbers ($0.02 \leq \mathrm{Re} \leq 44$). It is given as a power law by

$$\mathrm{Nu} = \left(0.24 + 0.56\,\mathrm{Re}^{0.45}\right)\left(\frac{T_m}{T_\infty}\right)^{0.17}. \tag{2.23}$$

The Reynolds number is evaluated at the arithmetic mean temperature T_m between the temperature of the cylinder and the inbound fluid with T_∞. A correction for the temperature dependence of the fluid parameters, e.g. viscosity, density, and thermal conductivity, is introduced with the term $(T_m/T_\infty)^{0.17}$. It can be rewritten as $[1 + \Delta T/(2\,T_\infty)]^{0.17}$ to incorporate the temperature difference between fluid and cylinder.

For higher Reynolds numbers ($1 \leq \mathrm{Re} \leq 1.0 \times 10^5$), the correlation by Sparrow et al. (2004) can be used. It is given by

$$\mathrm{Nu} = 0.25 + \left(0.4\mathrm{Re}^{1/2} + 0.06\mathrm{Re}^{2/3}\right)\mathrm{Pr}^{0.37}\left(\frac{\mu}{\mu_{\mathrm{wall}}}\right)^{1/4}. \tag{2.24}$$

In this case, fluid properties are evaluated at the free-stream temperature T_∞. The correction term μ/μ_{wall} adjusts the Nußelt number to accommodate different cylinder temperatures.

2.1.3 Flow Separation and Turbulence

According to Rajani et al. (2009), an important regime change occurs at Re ≈ 6.1. In this case, and for any higher Reynolds number, the inertia of the fluid is not strong enough to overcome the adverse pressure gradient. Hence, the flow separates and detaches from the surface of the cylinder.

In numerical simulations, the angle at the surface of the cylinder where separation occurs was evaluated. The smallest Reynolds number for which separation was detected in this case is Re ≈ 6.4. The angle ϕ_{sep} at which separation occurs at different Reynolds numbers is shown in Table 2.3. At higher Reynolds numbers, no steady recirculation zone exists, but vortices are shed periodically at both sides. The separation angle changes with time. Cycle averaged values are also given Table 2.3. Flow separation creates a wake that is no longer confined to a defined area, but the vortices are convected downstream. Turbulence develops downstream of the cylinder as a result of hydrodynamic instabilities within these flow structures.

In laminar flows, small scale disturbances of the flow are immediately dampened out by the effect of viscosity dominating over inertia. However, flow with higher inertial forces and smaller viscous forces tends to accommodate slowly decaying chaotic three-dimensional flow structures. These are called turbulence. Enhanced mixing due to turbulence increases momentum and heat transfer (Davidson, 2004). Hence, effectively increased viscosity and thermal conductivity determine the friction coefficient and the Nußelt number.

The Reynolds number is often used as an indicator whether the flow is laminar or turbulent. Low Reynolds numbers point towards laminar flow and large values characterize turbulent flow. This can also be seen in Table 2.1. Flow separation is a precursor to turbulence.

A quantity subject to turbulence can be characterized by the mean value and the turbulent fluctuation. As an example, this is written for a component of the velocity vector as

$$u_i = \overline{u}_i + u_i'' \,. \tag{2.25}$$

Re	ϕ_{sep} in °
10	151
20	137
40	127
120	~116
240	~111
3900	~ 89

Table 2.3: Separation Angle. Angle of flow separation at different Reynolds numbers.

The mean value is denoted by $\overline{u}$ and u_i'' is the fluctuation.[3] Turbulent structures carry energy in form of turbulent kinetic energy given by (Pope, 2000)

$$E = \frac{1}{2}\left(u_i'' u_i''\right). \tag{2.26}$$

Turbulence can be observed as flow structures. These structures can be seen as eddies of a certain wavenumber κ. This wavenumber may be interpreted as the reciprocal of a turnover time. Figure 2.8 depicts the relation between energy and wavenumber qualitatively.

Turbulence gains kinetic energy at the largest scales (production process). This energy is transferred to smaller scales, i.e. higher wavenumbers, and finally dissipated at the smallest scales (Kolmogorov scales). This process is called the energy cascade.

Figure 2.8 distinguishes three regions in the lifecycle of an eddy passing through the energy cascade. Region I is the region of the largest eddies described by the integral time scale and length scale. In the context of a cylinder in crossflow, these scales are determined by the flow velocity and the diameter of the cylinder. The eddies, contributing to this region, carry the major part of the energy and most energy is produced. Region II is called the inertial range. Energy is neither produced nor dissipated but transferred to Region III. The energy spectrum in Region II is characterized by

$$E(\kappa) = C\epsilon^{2/3}\kappa^{-5/3} \tag{2.27}$$

where C is a universal constant and ϵ is the dissipation rate. It is often referred to as Kolmogorov's $-5/3$ spectrum (Pope, 2000). The dissipation of the eddies occurs in Region III. This regime is characterized by the Kolmogorov length scale ($\sim \mathrm{Re}^{-3/4}$) and time scale ($\sim \mathrm{Re}^{-1/2}$) (Pope, 2000). Region II and Region III form the universal equilibrium range where the influence of the integral scales is weak. This range can be described by universal principles.

[3] The notation with double prime signs $''$ was chosen to distinguish turbulent from "acoustic" fluctuations.

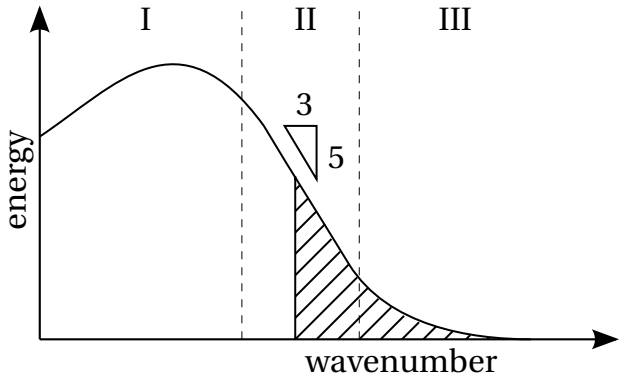

Figure 2.8: Energy of Turbulent Structures. Diagram adapted from Pope (2000).

Resolving these smallest scales is in many cases computationally very costly or even impossible considering today's computational capabilities. A practical and efficient way is therefore to model turbulence (Pope, 2000).

2.2 Governing Equations

Fluid flow in the limit of small Knudsen numbers can be described by the continuum mechanics formulation of fluid dynamics (Pope, 2000). In three spatial dimensions x_i ($\boldsymbol{x} = [x_1\ x_2\ x_3]^T$) and time t, the flow field is defined by a velocity vector u_i with one component for every spatial direction, pressure p, and temperature T. Therefore, five balance equations for continuity, momentum for all three spatial directions, and energy have to be solved. Additionally, fluid properties are required, which are generally dependent on temperature and pressure. Assuming an isotropic Newtonian fluid, stress tensors and strain rate have a linear dependence, and Fourier's law for heat conduction can be applied. In this case, the so-called transport properties are the first and the second coefficient of viscosity $\mu(T,p)$ and $\lambda(T,p)$, respectively, and the thermal conductivity $k(T,p)$. They are accompanied by the thermodynamic properties density $\rho(T,p)$ and isobaric specific heat capacity $c_p(T,p)$. Moreover, body forces b_i can act on the fluid. The most complete set of equations is the *Navier–Stokes equations*[4] which have been shown to represent experimental observations exceptionally well (Schlichting and Gersten, 2006).

[4]The designation Navier–Stokes equations is used in this thesis for the full set of equations including continuity equation and energy equation.

2.2.1 Navier–Stokes Equations

The full compressible Navier–Stokes equations include the continuity equation, momentum, and energy transport, and an equation of state. The following equations are given in index notation making use of the Einstein summation convention. Furthermore, δ_{ij} is the Kronecker delta $\delta_{ij} = 1$ for $i = j$ and $\delta_{ij} = 0$ for $i \neq j$. The Navier–Stokes equations (Schlichting and Gersten, 2006; White, 2007; Davidson, 2004; Landau et al., 1959) can be written by

$$\frac{\partial \rho}{\partial t} + u_j \frac{\partial (\rho\, u_j)}{\partial x_j} = 0 \tag{2.28}$$

$$\frac{\partial (\rho\, u_i)}{\partial t} + \frac{\partial (\rho\, u_i\, u_j)}{\partial x_j} = \rho b_i - \frac{\partial p}{\partial x_i} + \frac{\partial \tau_{ij}}{\partial x_j} \tag{2.29}$$

$$\tau_{ij} = \mu \left(\frac{\partial u_i}{\partial x_j} + \frac{\partial u_j}{\partial x_i} \right) + \delta_{ij} \lambda \frac{\partial u_l}{\partial x_l} \tag{2.30}$$

$$\frac{\partial (\rho\, c_p\, T)}{\partial t} + \frac{\partial (u_j\, \rho\, c_p\, T)}{\partial x_j} = \beta\, T \left(\frac{\partial p}{\partial t} + u_j \frac{\partial p}{\partial x_j} \right) + \frac{\partial}{\partial x_j} \left(k \frac{\partial T}{\partial x_j} \right) + \Phi \tag{2.31}$$

$$\Phi = \tau_{ij} \frac{\partial u_i}{\partial x_j} \tag{2.32}$$

where τ_{ij} is the stress tensor and Φ denotes the dissipation function.

2.2.2 Fluid Properties

Fluid properties can be classified in transport properties and thermodynamic properties. In general, fluid properties depend on the thermodynamic state, i.e. on pressure and temperature. They can be interpolated from tabulated values or assessed with expressions. Most important is the notion of an *ideal gas* where the fluid properties do not depend on its pressure but temperature, only.

Transport Properties

The first and second coefficient of viscosity, also called dynamic viscosity μ and bulk viscosity λ, are used to calculate the stress tensor τ (cf. Equation (2.30)). The

dynamic viscosity can be evaluated using Sutherland's law for the temperature dependency. It can be written as

$$\mu = \frac{A_S \sqrt{T}}{1 + T_S/T} \tag{2.33}$$

with the constants A_S and T_S depending on the fluid (White, 2007). For air, these constants are $A_S = 1.458 \times 10^{-6}\,\mathrm{kg/(m\,s\,K^{1/2})}$ and $T_S = 110.4\,\mathrm{K}$. Sutherland's law is often given with three constants T_0, μ_0, and S. In this case, the coefficients for Equation (2.33) are $T_S = S$ and $A_S = (T_0 + S)\mu_0 / T_0^{3/2}$. Both viscosities are related by Stokes' hypothesis.

The thermal conductivity of a polyatomic gas can be evaluated using the modified Eucken formula (Poling et al., 2001). The formula was deduced from elementary arguments on the degrees of freedom of a gas molecule. It is given by

$$k = \mu(c_p - R)\left(1.32 + \frac{1.77}{c_p/R - 1}\right) \tag{2.34}$$

where R denotes the specific gas constant. This constant is $R = 287.058\,\mathrm{J/(kg\,K)}$ for air.

Thermodynamic Properties

Fluid flows without chemical reactions or sudden changes, e.g. shock waves, exhibit only minor deviations from the thermodynamic equilibrium. It is, therefore, common to assume that ordinary equilibrium thermodynamics are applicable (White, 2007). The most important thermodynamic properties are pressure, temperature, density, enthalpy, entropy, and internal energy. Considering the known equations of state, only two properties are independent. The most common choice is to use p and T (White, 2007). These are the variables solved for in the transport equations given above (Equation (2.28)–(2.32)).

From these primary thermodynamic variables, secondary thermodynamic properties can be derived. These are the isobaric specific heat capacity given by

$$c_p = \left.\frac{\partial h}{\partial T}\right|_p, \tag{2.35}$$

where h denotes the enthalpy, and the isochoric specific heat capacity written as

$$c_v = \left.\frac{\partial u}{\partial T}\right|_v. \tag{2.36}$$

The internal energy is denoted by u. The ratio of the specific heats is

$$\gamma = \frac{c_p}{c_v}. \tag{2.37}$$

This ratio is close to 1.0 for nearly incompressible fluids and usually does not exceed 1.7 for any fluid (White, 2007).

A quantity of similar importance, especially in gases, is the speed of sound, defined as

$$a^2 = \left.\frac{\partial p}{\partial \rho}\right|_s = \gamma \left(\frac{\partial p}{\partial \rho}\right)_T . \tag{2.38}$$

The thermal expansion coefficient is given by

$$\beta = -\frac{1}{\rho}\left(\frac{\partial \rho}{\partial T}\right)_p . \tag{2.39}$$

If pressure changes are small, the thermodynamic properties depend on temperature only. For specific isobaric heat capacity, enthalpy, and entropy, polynomial expressions in temperature have been developed (Chase, 1998). The respective quantity is evaluated using

$$c_p(T) = R\left(a_1 + a_2 T + a_3 T^2 + a_4 T^3 + a_5 T^4\right), \tag{2.40}$$

$$h(T) = R\left(a_1 T + (a_2 T^2)/2 + (a_3 T^3)/3 + (a_4 T^4)/4 + (a_5 T^5)/5 + a_6\right), \tag{2.41}$$

$$s(T) = R\left(a_1 ln T + a_2 T + (a_3 T^2)/2 + (a_4 T^3)/3 + (a_5 T^4)/4 + a_7\right), \tag{2.42}$$

where $a_1, \ldots, a_7$ are tabulated coefficients for a large number of fluids (Chase, 1998).

Ideal Gas Law

The ideal gas law is the equation of state for an ideal gas derived from kinetic theory. For many cases, e.g. air at ambient conditions, the ideal gas law is a good approximation (Stephan et al., 2013; White, 2007). With the pressure and the temperature known from the transport equations, density is evaluated by

$$\rho = \frac{p}{R\,T} . \tag{2.43}$$

Inserting Equation (2.43) in Equation (2.38), the speed of sound for an ideal gas is given by

$$a = \sqrt{\gamma\, R\, T} . \tag{2.44}$$

For ideal gases, the specific enthalpy includes the internal energy and the pressure–volume work $h = u + R\,T$. Therefore, the isobaric specific heat capacity can be evaluated by

$$c_p = c_v + R = \frac{\gamma}{\gamma - 1} R . \tag{2.45}$$

Isobaric Perfect Gas

Under the assumption that the spatial and the temporal pressure changes are small, the formulation for an isobaric perfect gas expressed as

$$\rho = \frac{p_{\text{ref}}}{RT} \tag{2.46}$$

can be used. R and p_{ref} are constants and hence the density only depends on the temperature.

This approximation has several consequences: Compression and expansion can only occur through changes in temperature. Small changes in local pressure and density are not coupled, and thus there is no wave propagation, and the speed of sound approaches infinity $a \to \infty$. Moreover, an isobaric temperature change will not result in a change in volume or density and thus $c_p = c_v = c$. This also implies $\gamma = 1$. If a gas is considered incompressible, i.e. in the limit of low Mach numbers, still the isobaric specific heat capacity has to be considered $c = c_p$ (White, 2007).

2.2.3 Dimensional Analysis

To identify relevant parameters and acquire independence from actual physical dimensions, a dimensional analysis was carried out.

Buckingham's Π-Theorem

The idea of finding the relationship between physical quantities from their characteristic dimensions and units was formalized by Buckingham (1914). The Π-theorem makes it possible to derive an equation that only contains products of variables and single non-dimensional products (Zierep, 1991).

In the case of the Navier–Stokes equations (Equation (2.28)–(2.32)), 11 reference quantities are involved: velocity u_{ref}, density ρ_{ref}, cylinder diameter d, gravitational acceleration g, ambient pressure p_{ref}, primary viscosity μ_{ref}, secondary viscosity λ_{ref}, specific heat capacity $c_{p,\text{ref}}$, temperature T_{ref}, coefficient of thermal expansion β_{ref}, and thermal conductivity k_{ref}. These reference quantities are accompanied by four base units for length (m), time (s), mass (kg), and temperature (K). The dimension matrix, representing the powers of each base units occurring in the reference quantities is given in Table 2.4. The matrix is of full rank and thus Buckingham's Π-theorem yields $11 - 4 = 7$ dimensionless groups.

	u_{ref}	ρ_{ref}	d	g	p_{ref}	μ_{ref}	λ_{ref}	$c_{p,\text{ref}}$	T_{ref}	β_{ref}	k_{ref}
mass	0	1	0	0	1	1	1	0	0	0	1
length	1	−3	1	1	−1	−1	−1	2	0	0	1
time	−1	0	0	−2	−2	−1	−1	−2	0	0	−3
temperature	0	0	0	0	0	0	0	−1	1	−1	−1

Table 2.4: Dimension Matrix. Dimensional matrix for the reference quantities in the Navier–Stokes equations.

Dimensionless Quantities

With the reference quantities (cf. Table 2.4), the following dimensionless quantities are formed:

$$
\begin{aligned}
x_i &= d\,\tilde{x}_i & t &= \frac{d}{u_{\text{ref}}}\tilde{t} & u_i &= u_{\text{ref}}\,\tilde{u}_i \\
p &= \tilde{p}\,\rho_{\text{ref}}\,u_{\text{ref}}^2 + p_{\text{ref}} & \Phi &= \frac{\mu_{\text{ref}}\,u_{\text{ref}}^2}{d^2}\tilde{\Phi} & \tau_{ij} &= \frac{\mu_{\text{ref}}\,u_{\text{ref}}}{d}\tilde{\tau}_{ij} \\
\rho &= \rho_{\text{ref}}\,\tilde{\rho} & T &= T_{\text{ref}}\,\tilde{T} & \beta &= \beta_{\text{ref}}\,\tilde{\beta} \\
b_i &= g\,\tilde{b}_i & c_p &= c_{p,\text{ref}}\,\tilde{c_p} & k &= k_{\text{ref}}\,\tilde{k} \\
\mu &= \mu_{\text{ref}}\,\tilde{\mu} & \lambda &= \lambda_{\text{ref}}\,\tilde{\lambda}
\end{aligned}
\tag{2.47}
$$

If the ideal gas law is used to replace ρ_{ref} in the expression for the pressure, an alternative non-dimensionalization arises. Using the definition of the speed of sound, it is written as

$$
p = \tilde{p}\,\gamma\,\frac{p_{\text{ref}}}{a^2}\,u_{\text{ref}}^2 + p_{\text{ref}}\,. \tag{2.48}
$$

Dimensionless Numbers

Buckingham's Π-theorem yields seven dimensionless groups. These numbers can be chosen arbitrarily. A common choice is to use

$$
\text{Reynolds number:} \qquad \text{Re} = \frac{u_{\text{ref}}\,d}{\nu_{\text{ref}}} \tag{2.49a}
$$

$$
\text{Froude number:} \qquad \text{Fr} = \frac{u_{\text{ref}}^2}{g\,d} \tag{2.49b}
$$

Prandtl number: $$\mathrm{Pr} = \frac{\mu_{\mathrm{ref}}\, c_{p,\mathrm{ref}}}{k_{\mathrm{ref}}} \tag{2.49c}$$

Eckert number: $$\mathrm{Ec} = \frac{u_{\mathrm{ref}}^2}{c_{p,\mathrm{ref}}\, T_{\mathrm{ref}}} \tag{2.49d}$$

Isobaric expansion ratio: $$K_\rho = -\beta_{\mathrm{ref}}\, T_{\mathrm{ref}} \tag{2.49e}$$

Euler number: $$\mathrm{Eu} = \frac{p_{\mathrm{ref}}}{\rho_{\mathrm{ref}}\, u_{\mathrm{ref}}^2} \tag{2.49f}$$

Ratio of viscosities: $$\Pi = \frac{\lambda}{\mu} = -\frac{2}{3} \tag{2.49g}$$

Most of the dimensionless numbers are ubiquitous; e.g. the Reynolds number was already used in Section 2.1 to distinguish different flow regimes. The ratio of viscosities is $-2/3$ according to Stokes' hypothesis. The kinematic viscosity is derived from the dynamic viscosity by $\nu_{\mathrm{ref}} = \mu_{\mathrm{ref}}/\rho_{\mathrm{ref}}$.

Other dimensionless numbers are linear combinations of the quantities given above. With the ideal gas law, the relationship between Euler number, Mach number, and the ratio of specific heats is given by

$$\mathrm{Eu} = \frac{p_{\mathrm{ref}}}{\rho_{\mathrm{ref}} u_{\mathrm{ref}}^2} = \frac{a_{\mathrm{ref}}^2}{\gamma\, u_{\mathrm{ref}}^2} = \frac{1}{\gamma\, \mathrm{Ma}^2} \tag{2.50}$$

with the Mach number Ma. The Mach number is another ubiquitous dimensionless group in gas dynamics given by

$$\mathrm{Ma} = \frac{u_{\mathrm{ref}}}{a}. \tag{2.51}$$

The alternative formulation for the pressure (Equation (2.48)) can be written as

$$p = \tilde{p}\, \gamma\, p_{\mathrm{ref}} \mathrm{Ma} + p_{\mathrm{ref}}. \tag{2.52}$$

2.2.4 Non-Dimensionalized Navier–Stokes Equations

Inserting all dimensionless quantities and groups in the Navier–Stokes equations (Equation (2.28)–(2.32)) yields the non-dimensionalized Navier–Stokes equations. They serve as a basis for further adaptations in this thesis. Hereinafter, the tilde $\tilde{\cdot}$ denoting a dimensionless quantity will be dropped. All quantities are understood

to be dimensionless, if not indicated otherwise. The dimensionless governing equations are given by

$$\frac{\partial \rho}{\partial t} + u_j \frac{\partial (\rho\, u_j)}{\partial x_j} = 0 \tag{2.53}$$

$$\frac{\partial (\rho\, u_i)}{\partial t} + \frac{\partial (\rho\, u_i\, u_j)}{\partial x_j} = \frac{1}{\mathrm{Fr}} \rho\, b_i - \frac{\partial p}{\partial x_i} + \frac{1}{\mathrm{Re}} \frac{\partial}{\partial x_j} \left[\mu \left(\frac{\partial u_i}{\partial x_j} + \frac{\partial u_j}{\partial x_i} + \delta_{ij}\, \Pi \frac{\partial u_l}{\partial x_l} \right) \right] \tag{2.54}$$

$$\frac{\partial (\rho\, c_p\, T)}{\partial t} + \frac{\partial (u_j\, \rho\, c_p\, T)}{\partial x_j} = K_\rho\, \mathrm{Ec}\, \beta\, T \left(\frac{\partial p}{\partial t} + u_j \frac{\partial p}{\partial x_j} \right) + \frac{1}{\mathrm{Re}\,\mathrm{Pr}} \frac{\partial}{\partial x_j} \left(k \frac{\partial T}{\partial x_j} \right) + \frac{\mathrm{Ec}}{\mathrm{Re}} \Phi\,. \tag{2.55}$$

The ideal gas equation can be written as

$$\frac{p}{\mathrm{Eu}} + 1 = \rho\, T\,. \tag{2.56}$$

Alternatively, using Equation (2.50), this equation of state can be reformulated to

$$p\, \gamma\, \mathrm{Ma}^2 + 1 = \rho\, T\,. \tag{2.57}$$

2.2.5 Incompressible Navier–Stokes Equations

Some a priori assumptions lead to significant simplifications of the equation system. Justifications for these assumptions have to be given for the respective application. In Chapter 9, these simplifications are discussed for the Rijke tube (Section 9.1), hot wire anemometry (Section 9.2), and heat exchangers (Section 9.3).

Assumptions

The following three assumptions are made: (1) The flow velocity is much smaller than the speed of sound, i.e. $\mathrm{Ma} \to 0$. (2) The temperature exhibits only small deviations from the reference value, i.e. $T \to 1$, and hence it does not influence the flow field. Nevertheless, heat transfer is still present. (3) No body forces act on the fluid. From these assumptions, several simplifications can be deduced.

Simplifications

The general equation of state for the density is expressed as $\rho(p, T)$. A Taylor series expansion around the reference state is given by

$$\rho(T, p) = 1 + \left(\frac{\partial \rho}{\partial T} \right)_{\mathrm{ref}} (T - 1) + \left(\frac{\partial \rho}{\partial p} \right)_{\mathrm{ref}} p + \ldots\,. \tag{2.58}$$

The series is truncated after the first derivatives. This leads to a linearization around the reference state. Using the definitions of the coefficient of thermal expansion and the speed of sound yields

$$\rho(T,p) = 1 + K_\rho\,(T-1) + \gamma\,\mathrm{Ma}^2\,p\,. \tag{2.59}$$

Applying the first assumption $\mathrm{Ma} \to 0$ and neglecting terms of order $\mathcal{O}(2)$ or higher in Mach number Ma reveals

$$\rho(T) = 1 + K_\rho(T-1)\,. \tag{2.60}$$

Hence, variations in the density depend only on temperature and not on the pressure. For an ideal gas ($K_\rho = 1$), this simplifies even further to $\rho = T$.

Furthermore, the Eckert number can be rewritten as

$$\mathrm{Ec} = \mathrm{Ma}^2 \frac{a_{\mathrm{ref}}^2}{c_{p,\mathrm{ref}}\,T_{\mathrm{ref}}}\,. \tag{2.61}$$

If an ideal gas is assumed, the factor $a_{\mathrm{ref}}^2/(c_{p,\mathrm{ref}}\,T_{\mathrm{ref}}) = \gamma - 1$ is of order unity and thus Ec is of order $\mathcal{O}(\mathrm{Ma}^2)$. Therefore, also terms proportional to the Eckert number can be neglected when the Mach number is low.

From Equation (2.60) follows that if $T \to 1$ also $\rho \to 1$. In other words, if temperature differences are small, only small differences in density occur. The consequence is that density becomes constant and $\rho \to 1$. Moreover, the fluid properties, viscosity μ, thermal conductivity k, and specific heat capacity c_p are also unity.

Body forces usually arise from buoyancy or an acceleration of the reference system. Buoyancy requires a density gradients which are eliminated because of $\rho \to 1$. It is furthermore assumed that the reference system is at rest and hence the terms proportional to b_i vanish.

Incompressible Navier–Stokes Equations

The assumptions made above, in short $\mathrm{Ma} \to 0$, $T \to T_{\mathrm{ref}}$, and $b_i \to 0$ yield the three-dimensional *incompressible* Navier–Stokes equations. The energy equation is reduced to a scalar transport equation. Only a one-way coupling from the velocity field to the temperature exists but not vice versa. Temperature only occurs in derivatives, and hence a different non-dimensionalization is more elegant. Heat transfer between a surface with temperature T_w and a fluid with temperature T_∞ is commonly described using a dimensionless temperature defined by

$$\Theta \equiv \frac{T - T_\infty}{T_w - T_\infty}\,. \tag{2.62}$$

Inserting this in Equations (2.53) to (2.55) yields

$$\frac{\partial u_j}{\partial x_j} = 0 \tag{2.63}$$

$$\frac{\partial u_i}{\partial t} + u_j \frac{\partial u_i}{\partial x_j} = -\frac{1}{\rho}\frac{\partial p}{\partial x_i} + \frac{1}{\mathrm{Re}}\frac{\partial^2 u_i}{\partial x_j \partial x_j} \tag{2.64}$$

$$\frac{\partial \Theta}{\partial t} + u_j \frac{\partial \Theta}{\partial x_j} = \frac{1}{\mathrm{Re}\,\mathrm{Pr}}\frac{\partial^2 \Theta}{\partial x_j \partial x_j}. \tag{2.65}$$

These are the basic equations for the CFD simulations carried out in this thesis, except for a brief survey on the influence of the cylinder temperature T_w. In this case, the compressible Navier–Stokes equations were solved.

2.2.6 Vorticity Stream Function Formulation

Equations (2.63) to (2.65) show the Navier–Stokes equations in primitive variables. In incompressible two-dimensional flow ($\boldsymbol{x} = [x_1\ x_2]^T$), the use of the quantities stream function ψ and vorticity ζ, which are derived from velocity, is often beneficial (Schlichting and Gersten, 2006, p. 42). Vorticity is defined as the curl of the flow velocity vector. In two-dimensional cases only, the component associated with the x_3-direction is nonzero and given by

$$\zeta = \frac{\partial u_2}{\partial x_1} - \frac{\partial u_1}{\partial x_2}. \tag{2.66}$$

The stream function quantifies the volumetric flow rate through a line connecting any two points in the flow field. A line of constant stream function is considered a streamline. The velocity components are evaluated from the partial derivatives of the scalar stream function by

$$u_1 = \frac{\partial \psi}{\partial x_2} \qquad \text{and} \qquad u_2 = -\frac{\partial \psi}{\partial x_1}. \tag{2.67}$$

Using vorticity and stream function, the incompressible Navier–Stokes equations (Equation (2.63)–(2.65)) reduce to

$$\frac{\partial^2 \psi}{\partial x_1^2} + \frac{\partial^2 \psi}{\partial x_2^2} = -\zeta \tag{2.68}$$

$$\frac{\partial \zeta}{\partial t} + u_j \frac{\partial \zeta}{\partial x_j} = \frac{1}{\mathrm{Re}}\frac{\partial^2 \zeta}{\partial x_j \partial x_j} \tag{2.69}$$

$$\frac{\partial \Theta}{\partial t} + u_j \frac{\partial \Theta}{\partial x_j} = \frac{1}{\mathrm{Re}\,\mathrm{Pr}}\frac{\partial^2 \Theta}{\partial x_j \partial x_j}. \tag{2.70}$$

The transport equation for the temperature is the same as Equation (2.65). In this formulation, the Nußelt number is defined as in Equation (2.21). The skin friction coefficient can be given by

$$c_f = \frac{2}{\mathrm{Re}} \zeta_w \tag{2.71}$$

using the vorticity at the surface of the cylinder.

The main advantage of this approach is that the pressure does not appear in equations (2.68) to (2.70) and thus need not be calculated. Moreover, the equations for vorticity and temperature both have the structure of an advection–diffusion equation without sources or sinks. This form of the Navier–Stokes equations was used by many researchers in the past for investigations of flow across a cylinder, e.g. by Thom (1933), Apelt and Ledwich (1979), Fornberg (1980), and Kwon and Lee (1985).

2.2.7 Potential Flow

Potential flow represents further simplification of the Navier–Stokes equations. In addition to the incompressibility ($\rho = 1$), potential flow is inviscid, i.e. $\mu = 0$, and irrotational, i.e. $\zeta = 0$. The flow (without temperature) is hence fully described by applying the simplifications to Equation (2.68). This yields

$$\frac{\partial^2 \psi}{\partial x_1^2} + \frac{\partial^2 \psi}{\partial x_2^2} = 0 \tag{2.72}$$

which is a Laplace equation for which analytical solutions exist in simple cases.

It is named after the velocity potential φ, which is defined in such a way that the velocity is equal to the gradient of φ. Hence,

$$\frac{\partial^2 \varphi}{\partial x_1^2} = \frac{\partial^2 \psi}{\partial x_2^2}, \frac{\partial^2 \varphi}{\partial x_2^2} = -\frac{\partial^2 \psi}{\partial x_1^2}, \tag{2.73}$$

and

$$\frac{\partial^2 \varphi}{\partial x_1^2} + \frac{\partial^2 \varphi}{\partial x_2^2} = 0\,. \tag{2.74}$$

Lines of equal velocity potential and stream lines are always orthogonal. The solution of the potential flow also solves the Navier–Stokes equations except for the no-slip condition at the surface of the cylinder.

Pressure is evaluated by integrating

$$\frac{\partial p}{\partial x_1} = -\frac{\partial \psi}{\partial x_2} \frac{\partial^2 \psi}{\partial x_1 \partial x_2} - \frac{\partial \psi}{\partial x_1} \frac{\partial^2 \psi}{\partial x_2^2}\,. \tag{2.75}$$

Analogously, the pressure gradient in x_2-direction can be integrated (Fornberg, 1980).

Flow around a cylinder is represented by the superposition of a dipole (source and sink of equal strength) and parallel flow. If the dipole is located in the origin and parallel flow occurs in x_1-direction, velocity potential, and stream function are given by

$$\varphi = x_1 \left(1 + \frac{1}{4\left(x_1^2 + x_2^2\right)}\right) \qquad \text{and} \qquad \psi = x_2 \left(1 - \frac{1}{4\left(x_1^2 + x_2^2\right)}\right). \tag{2.76}$$

Transforming to polar coordinates (r, ϕ), the velocities in radial and circumferential direction read

$$u_r = \left(1 - \frac{1}{4r^2}\right)\cos\phi \qquad \text{and} \qquad u_\phi = \left(1 + \frac{1}{4r^2}\right)\sin\phi \tag{2.77}$$

respectively.

2.3 Transfer Analogies

The temperature in Equation (2.65) and also in Equation (2.70) is an advection–diffusion equation (Davidson, 2004). The temperature, in this case, is a passive scalar, i.e. it does not affect the flow field. If the boundary conditions may be formulated in a corresponding manner, temperature can be replaced by any scalar quantity to be assessed. The only adjustment necessary refers to the dimensionless group quantifying the ratio between convective and diffusive transport, e.g. Re Pr in the case of temperature. A widely used analogy is the one between heat transfer and mass transfer. As can be seen by inspecting Equation (2.69), also the transport of vorticity follows this principle.

2.3.1 Analogy of Heat and Mass Transfer

Mass transfer by diffusion from the surface of the cylinder is denoted by the specific flux of species $\dot{n}_A$ ($[\dot{n}] = \mathrm{mol/m^2\,s}$). It is described by Fick's law given by

$$\dot{n}_A = -D_{AB} \left.\frac{\partial c_A}{\partial r}\right|_{r=d/2} = h_m (c_A - c_{A,\infty}). \tag{2.78}$$

The coefficient of diffusion D_{AB} quantifies the diffusive transport in the binary mixture of components A and B. c_A is the molar concentration of component A and h_m is the convective mass transfer film coefficient. This is analogous to Fourier's law (cf. Equation (2.4)) and Newton's law of cooling.

The energy equation in the incompressible Navier–Stokes equations (2.65) has the structure of an advection–diffusion equation (Davidson, 2004) for the temperature. The temperature can, therefore, be interchanged with the dimensionless concentration c_A. Transport properties have to be adapted accordingly, and new dimensionless parameters arise for mass transfer. The Sherwood number, defined as

$$\mathrm{Sh}_\phi(\phi) \equiv \frac{d}{c_A - c_{A,\infty}} \left.\frac{\partial c_A}{\partial r}\right|_{r=d/2}, \tag{2.79}$$

quantifies the surface normal gradient of the concentration. The averaged Sherwood number is given by

$$\mathrm{Sh} \equiv \frac{h_m d}{D_{AB}}. \tag{2.80}$$

Hence, it is the mass transfer counterpart of the Nußelt number. The Prandtl number is replaced by the Schmidt number, defined as the ratio between the momentum diffusion and the species diffusion by

$$\mathrm{Sc} \equiv \frac{\nu}{D_{AB}}. \tag{2.81}$$

If Schmidt number Sc and Prandtl number Pr are equal, i.e. the Lewis number is unity $\mathrm{Le} \equiv \mathrm{Sc}/\mathrm{Pr} = 1$, the dimensionless temperature and concentration fields coincide.

The useful result of this analogy is that any correlation or consideration of the physical argument given for temperature also holds for concentration. This thesis focuses on heat transfer. However, the substitutions $T \rightarrow c_A$, $\mathrm{Nu} \rightarrow \mathrm{Sh}$, and $\mathrm{Pr} \rightarrow \mathrm{Sc}$ are valid throughout.

Investigations explicitly concerned with the mass transfer from a cylinder to pulsating flow can be found in Ohmi and Usui (1982); Sung et al. (1994); Zierenberg et al. (2006, 2007)

2.3.2 Reynolds' Analogy

Similar to the argument given for the analogy of heat and mass transfer, an analogy between heat and momentum transfer can be deducted (Bergman et al., 2011). Vorticity (cf. Equation (2.69)) is, like temperature and concentration, governed by an advection–diffusion equation. The boundary equations are different to some extent, but nevertheless, the analogy still applies with acceptable accuracy. For $\mathrm{Pr} = \mathrm{Sc} = 1$, the equalities

$$c_f \frac{\mathrm{Re}}{2} = \mathrm{Nu} = \mathrm{Sh} \tag{2.82}$$

are found. Following this argument, Reynolds' analogy can be formulated by

$$c_f \frac{\mathrm{Re}}{2} = \frac{\mathrm{Nu}}{\mathrm{Pr}} = \frac{\mathrm{Sh}}{\mathrm{Sc}}. \tag{2.83}$$

Strictly, this expression only yields good results, if Prandtl number and Schmidt number are close to unity and there is no pressure gradient. In the Chilton–Colburn analogy, this statement is further refined to

$$c_f \frac{\mathrm{Re}}{2} = \frac{\mathrm{Nu}}{\mathrm{Pr}^{1/3}} = \frac{\mathrm{Sh}}{\mathrm{Sc}^{1/3}}. \tag{2.84}$$

This is valid for a larger range of Prandtl numbers Pr and Schmidt numbers Sc, but only for favorable pressure gradients. If valid, this analogy may also be applied to surface averaged values.

2.4 Cylinder in Unsteady Crossflow

The scope of this thesis is to investigate a cylinder in unsteady crossflow. In this case, flow quantities depend on time. To cope with this additional complexity, methods to handle perturbations are established. The response to small forced perturbations in velocity is quantified with transfer functions. This concept is introduced and revisited in Chapter 4 within the framework of linear dynamic systems.

2.4.1 Perturbation Approach and Small Amplitudes

To study unsteady flow, i.e. *pulsations* in the free-stream, a perturbation approach is considered. Any arbitrary variable f consists of a time independent mean contribution and a fluctuation. This relationship is expressed by

$$f(\boldsymbol{x}, t) = \overline{f}(\boldsymbol{x}) + f'(\boldsymbol{x}, t) \tag{2.85}$$

where the bar $(\bar{\cdot})$ denotes the mean value

$$\overline{f}(\boldsymbol{x}) = \lim_{t^* \to \infty} \frac{1}{t^*} \int_0^{t^*} f(\boldsymbol{x}, t) \mathrm{d}t. \tag{2.86}$$

A prime $(\cdot')$ signifies the fluctuation. A fluctuation in the flow velocity results in fluctuations in skin friction and heat transfer.

All variables are dimensionless. Thus, they can be linearized using the same variable ϵ denoting the relative amplitude of any flow variable. The flow variables are treated

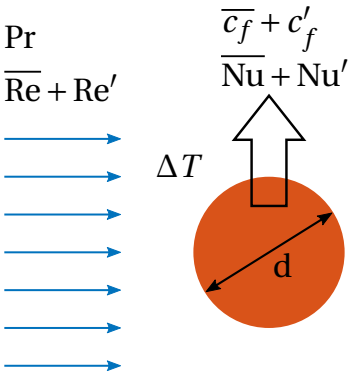

Figure 2.9: Sketch of a Cylinder in Pulsating Crossflow.

by Fourier series expansion, i.e. as a sum of complex exponential functions. This is written as

$$f(\boldsymbol{x}, t) = f_0(\boldsymbol{x}) + \epsilon \Re\left(f_1(\boldsymbol{x})\, \mathrm{e}^{\mathrm{iSr}t}\right) + \epsilon^2 \left[f_s(\boldsymbol{x}) + \Re\left(f_2(\boldsymbol{x})\, \mathrm{e}^{2\mathrm{iSr}t}\right)\right] + \ldots \tag{2.87}$$

where f is an arbitrary variable, and $\Re(\cdot)$ denotes the real part. In this case, f_0 and f_s are real-valued and f_1 and f_2 are complex-valued. The Strouhal number Sr is a dimensionless frequency and is defined by

$$\mathrm{Sr} \equiv \frac{\omega\, d}{u_{\mathrm{ref}}}. \tag{2.88}$$

The angular frequency is denoted by ω. The quantity $f_s(\boldsymbol{x})$ (with index s) signifies the streaming component. This is a nonlinear time independent contribution caused by the oscillations or pulsations.

The amplitude ϵ is assumed to be small. Terms of higher order in ϵ, e.g. ϵ^2, can thus be neglected to reasonable accuracy. An arbitrary variable f is written by

$$f(\boldsymbol{x}, t) = f_0(\boldsymbol{x}) + \epsilon \Re\left(f_1(\boldsymbol{x})\, \mathrm{e}^{\mathrm{iSr}t}\right). \tag{2.89}$$

Note that the streaming component mentioned above is a term of order $\mathcal{O}(\epsilon^2)$ and therefore neglected. This also implies that no net contribution, i.e. a positive or negative contribution, when averaged over one cycle, occurs.

2.4.2 Pulsations

The aim of this thesis is to investigate pulsations in the far field velocity and the resulting responses in skin friction and heat transfer. Figure 2.9 depicts this relationship. To investigate the transient response, pulsations in velocity are introduced and resulting fluctuations are assessed. In this thesis, the term fluctuations refers to quantities experiencing changes in time and space. The term pulsations is used for temporal variations only. The significance of this convention is that flow variables

are usually subject to fluctuations. On the other hand, lumped quantities like the mean Nußelt number Nu changes with time only and therefore is subject to pulsations.

In conjunction with unsteady flow, the term *oscillating* flow is often used, e.g. by Stokes (1851). Oscillations can be seen akin to pulsations. The difference is that it implies the reversal of the flow direction during a cycle. Peak velocities are larger than the mean flow velocity; hence, the assumption of small amplitudes does not hold in this case. This also applies to oscillations without any mean flow present.

Velocity Pulsations

The velocity field is given by the vector $\boldsymbol{u} = [u_1\ u_2\ u_3]^T$. In the far field, the influence of the cylinder is negligible. For simplicity, the velocity in the far field is chosen to have only a single contribution in x-direction and is denoted by $\boldsymbol{u}_\infty$ or simply u_∞. This restriction to solely one coordinate direction is relaxed in Section 9.2 only, where the far field velocity has a fluctuating angle of attack.

Hence, a pulsation is introduced in u_∞ in the form of

$$u_\infty(t) = \overline{u}_\infty + u'_\infty(t)\,. \tag{2.90}$$

As Fourier series expansion this reads

$$u_\infty(t) = u_{0,\infty} + \Re\left(u_{1,\infty}(\mathrm{Sr})\,\mathrm{e}^{\mathrm{i}\mathrm{Sr}t}\right). \tag{2.91}$$

The pulsations occur around a steady velocity which is also used as the reference velocity $\overline{u}_\infty = u_{0,\infty} = u_{\mathrm{ref}}$.

The velocity pulsations are the driving force for any other fluctuation. It is convenient to chose the parameter $\epsilon = u_{1,\infty}/u_{0,\infty}$. Hence, a small parameter ϵ is equivalent to assuming that the velocity pulsations are small compared to the mean velocity $u_{1,\infty} \ll u_{0,\infty}$.

The Reynolds number for a cylinder is defined with the free-stream velocity (cf. Equation (2.2)). With pulsation imposed on u_∞ also the Reynolds number exhibits pulsations of the form

$$\mathrm{Re}(t) = \overline{\mathrm{Re}} + \mathrm{Re}'(t)\,, \tag{2.92}$$

leading to a Fourier series expansion written by

$$\mathrm{Re}(t) = \mathrm{Re}_0 + \Re\left(\mathrm{Re}_1(\mathrm{Sr})\,\mathrm{e}^{\mathrm{i}\mathrm{Sr}t}\right). \tag{2.93}$$

The mean flow Reynolds number is defined by the steady-state velocity

$$\mathrm{Re}_0 = \overline{\mathrm{Re}} = \frac{u_{0,\infty}\,d}{\nu_{\mathrm{ref}}}\,. \tag{2.94}$$

Pulsations in Friction Coefficient and Nußelt Number

The friction coefficient and the Nußelt number are used to quantify skin friction and heat transfer. Pulsations are treated in the same manner as for the Reynolds number. This leads to

$$c_f(t) = \overline{c_f} + c_f'(t) \qquad \text{and} \qquad \mathrm{Nu}(t) = \overline{\mathrm{Nu}} + \mathrm{Nu}'(t)\,. \tag{2.95}$$

A Fourier series expansion yields

$$c_f(t) = c_{f,0} + \Re\left(c_{f,1}(\mathrm{Sr})\,\mathrm{e}^{\mathrm{i}\mathrm{Sr}t}\right) \quad \text{and} \quad \mathrm{Nu}(t) = \mathrm{Nu}_0 + \Re\left(\mathrm{Nu}_1(\mathrm{Sr})\,\mathrm{e}^{\mathrm{i}\mathrm{Sr}t}\right), \tag{2.96}$$

respectively.

Pulsation Frequency

The introduction of a (forced) pulsation frequency leads to another reference quantity that has to be incorporated in the dimensional analysis. The number of basic dimensions stays the same and hence one additional dimensionless group, quantifying the frequency, occurs. The *Strouhal number* as defined in Equation (2.97) is used in this thesis. With the given definition of the reference velocity, it can be written as

$$\mathrm{Sr} \equiv \frac{\omega\, d}{u_{0,\infty}}\,. \tag{2.97}$$

The Strouhal number is therefore the number of cycles divided by 2π that occur during the time it takes the fluid to cover a distance of d. For example $\mathrm{Sr} = 2\pi \approx 6.28$ means exactly one cycle of sinusoidal fluctuation takes place while at the same time the fluid advances a distance equal to the diameter of the cylinder.

Two other dimensionless groups are commonly used. As determined by the dimensional analysis, both can be given as products of the established set of dimensionless numbers. The Helmholtz number is given by

$$\mathrm{He} \equiv \frac{\omega\, d}{a} = \mathrm{Sr}\,\mathrm{Ma} \tag{2.98}$$

and will be revisited in Chapter 9. It is a crucial measure on the applicability of the incompressibility assumption. In confined flows, often the Womersley number defined by

$$\mathrm{Wo} \equiv \sqrt{\frac{\omega\, d^2}{\nu}} = \sqrt{\mathrm{Sr}\,\mathrm{Re}} \tag{2.99}$$

is used. It describes in the thickness of the unsteady boundary layer as detailed in Section 3.1.2.

2.4.3 Transfer Function and Frequency Response

The relations between the pulsations of different flow quantities,i.e. between flow velocity, heat transfer, and skin friction is quantified using *transfer functions*. Reynolds number, Nußelt number, and friction coefficient are used to quantify this dynamic behavior. Transfer functions from Reynolds number pulsations to pulsations in Nußelt number and friction coefficient are given by

$$G_{\mathrm{Nu}} = \frac{\mathrm{Nu}' \Big/ \overline{\mathrm{Nu}}}{\mathrm{Re}' \Big/ \overline{\mathrm{Re}}} \qquad \text{and} \qquad G_{c_f} = \frac{c_f' \Big/ \overline{c_f}}{\mathrm{Re}' \Big/ \overline{\mathrm{Re}}}, \tag{2.100}$$

respectively.

The angular frequency is real-valued and hence is the Strouhal number. Due to this, the quantities Re_1, Nu_1, and $c_{f,1}$ are also real-valued. Using this and Equation (2.89), the transfer behavior can be represented as the frequency responses denoted by

$$G_{\mathrm{Nu}}(\mathrm{Sr}) = \frac{\mathrm{Nu}_1(\mathrm{Sr}) \big/ \mathrm{Nu}_0}{\mathrm{Re}_1(\mathrm{Sr}) \big/ \mathrm{Re}_0} \qquad \text{and} \qquad G_{c_f}(\mathrm{Sr}) = \frac{c_{f,1}(\mathrm{Sr}) \big/ c_{f,0}}{\mathrm{Re}_1(\mathrm{Sr}) \big/ \mathrm{Re}_0}, \tag{2.101}$$

respectively.

3 Cylinder in Pulsating Flow—Literature Review

This chapter offers an overview of the literature associated with objects, in particular cylinders, in (continuously) pulsating flow. At first, the essential basic observations of the thermoacoustic effect are presented in Section 3.1, including early mathematical models. The development of the *boundary layer equations* offered a means to acquire solutions for viscous flows at high Reynolds numbers and for basic geometries. Section 3.2 shows the application of the boundary layer equations to perturbed flow. The works by Lighthill (1954) and Gersten (1965) are examined in detail as they offer the best insight into the phenomenon. Apart from the boundary layer equations, which provide a good approximation for high Reynolds number flows, another simplified solution for low Reynolds numbers was used successfully in the past. Based on the Oseen equations, Bayly (1985) developed a mathematical model for pulsating flow at low Reynolds numbers. This model is presented in Section 3.3. With the increased use of computers and CFD methods, better approximate solutions for the full Navier–Stokes equations could be obtained within reasonable time. The approach by Kwon and Lee (1985) is presented, who solve a linearized version of the Navier–Stokes equations in the frequency domain. The development of methods for time series analysis gave rise to a multitude of other approaches in which CFD simulation is combined with the adequate post-processing. The CFD/SI method, as used in this thesis, was applied by Föller et al. (2008). Studies involving the Navier–Stokes equations are presented in Section 3.4. Selected works related to the subject of pulsating flow including nonlinear effects and heat transfer enhancement is summarized in section 3.5.

3.1 Early Works on Unsteady Flows and Thermoacoustics

The first reports on thermoacoustic oscillations date back over 200 years. Subsequently, the “curio” was assessed systematically and lead to the principles and first mathematical models. They founded the basis for further investigations on heat transfer and skin friction in pulsating flows.

3.1.1 Thermoacoustics

The first experiments on pulsating flows in conjunction with heat release from combustion were carried out in the late 18th century by Higgins (1802). A hydrogen flame was observed to produce audible sound if confined in a suitable glass tube. The "singing flame" was seen as an amusement, but should prove to be a significant discovery concerning combustion instabilities occurring in rocket engines and modern gas turbines (Keller, 1995).

In pulsating or oscillating flow, heat transfer can damp, but also drive instabilities. The first observations of this thermoacoustic effect caused by heat transfer were reported by Sondhauß (1850) and Rijke (1859). Sondhauß (1850) described an effect experienced by glass blowers. In a heated glass bulb with a long neck, thermal energy is transformed into acoustic energy, which can be perceived as audible sound. This effect can be intensified by the use of a stack, a porous medium inside the neck, which extends the surface area (Swift, 2002, 2007). The important mechanisms for this self-sustaining oscillations take place in the boundary layer, which establishes in an oscillating flow at the solid surface. Kirchhoff (1868) described the influence of heat transfer on acoustic fields mathematically, and Rayleigh (1896) gave a widely accepted explanation for the thermoacoustic effect. A complete mathematical model of the Sondhauß tube was given by Kramers (1949) and eventually improved significantly by Rott (1969).

The setup examined by Rijke (1859) is similar to the Sondhauß tube. It also has a glass tube as the main corpus. As in the case of the Sondhauß tube, the tube in Rijke's case serves as a resonator in which a standing wave exists. However, in this case, it is open at both ends. A heated wire mesh, placed in the lower half of the vertical tube induces a buoyancy driven mean flow. The heat transfer at the mesh responds dynamically to fluctuations in mean flow velocity so that the heat transfer and the standing wave pressure interact constructively.

3.1.2 High Frequency Oscillations over a Flat Plate

One of the basic problems in unsteady flows is a fixed wall subject to an oscillating fluid. This is known as *Stokes' second problem* (Stokes, 1851). Later, it was also considered by Rayleigh (1911).[1] The velocity parallel to the plate can be described using the Navier–Stokes equations. In the limit of high frequencies, only the acceleration term and the viscous terms remain, and thus Equation (2.64) can be simplified to

$$\frac{\partial u_{x^*}}{\partial t} = \frac{1}{\mathrm{Re}} \frac{\partial^2 u_{x^*}}{\partial y^{*2}} . \tag{3.1}$$

[1] In the original statement, the fluid is at rest and the plate is oscillating but both configurations are equivalent.

This is in accordance with the theory of differential equations with large parameters, which states that large terms and the highest derivatives have to be retained (Lighthill, 1954). Inserting the Fourier series expansion (Equation (2.89)) yields

$$\mathrm{i}\,\mathrm{Sr}\left(u_1 - u_{1,\infty}\right) = \frac{1}{\mathrm{Re}}\frac{\partial^2 u_1 - u_{1,\infty}}{\partial {y^*}^2}. \tag{3.2}$$

At the surface, the fluid is at rest, i.e. $u_1(y^* = 0) = 0$, and approaches the undisturbed flow velocity $u_1 \to u_{1,\infty}$ in a great distance to the plate $y^* \to \infty$. This differential equation can be solved analytically. The solution is given by

$$u_1 = u_{1,\infty}\left[1 - \mathrm{e}^{-\sqrt{\mathrm{i}}\,y^*/\delta_{\mathrm{St}}}\right]. \tag{3.3}$$

The similarity variable y^*/δ_{St} uses the dimensionless thickness of the unsteady boundary layer (*Stokes layer*)

$$\delta_{\mathrm{St}} = \sqrt{\frac{2}{\mathrm{Re}\,\mathrm{Sr}}} \tag{3.4}$$

for non-dimensionalization. The index St is chosen to emphasize that this boundary layer thickness is associated with Stokes flow. By introducing an oscillating free-stream velocity $u_{1_\infty} = \epsilon\, u_{0,\infty}\cos(\mathrm{Sr}\,t)$, the solution (Schlichting and Gersten, 2006; Lighthill, 1954) written as

$$u_1 = \epsilon\, u_{0,\infty}\left[\cos(\mathrm{Sr}\,t) - \mathrm{e}^{y^*/\delta_{\mathrm{St}}}\cos(\mathrm{Sr}\,t - y^*/\delta_{\mathrm{St}})\right] \tag{3.5}$$

is achieved. Figure 3.1 shows profiles of the velocity calculated with Equation (3.5) in proximity to the plate.

The shear stress at the surface of the plate is proportional to the velocity gradient at this location. Hence, the slope of the velocity is a measure for the skin friction. The shear stress at the surface is given by

$$\tau_w = \sqrt{\mathrm{i}}\frac{u_{1,\infty}}{\delta_{\mathrm{St}}}. \tag{3.6}$$

Assuming oscillating flow as in Equation (3.5) yields

$$\tau_w = \frac{\sqrt{2}\,\epsilon\, u_{0,\infty}}{\delta_{\mathrm{St}}}\cos\left(\mathrm{Sr}\,t + \frac{\pi}{4}\right). \tag{3.7}$$

The fluid motion is driven by the pressure far away from the plate given by

$$\frac{\partial p}{\partial x^*} = -\mathrm{i}\,\mathrm{Sr}\,u_{1,\infty}\,\mathrm{e}^{\mathrm{i}\,\mathrm{Sr}\,t}. \tag{3.8}$$

It always exhibits a phase advance of $\pi/2$ in the far field. However, the boundary layer responds quicker to the pressure change, and thus close to the surface the

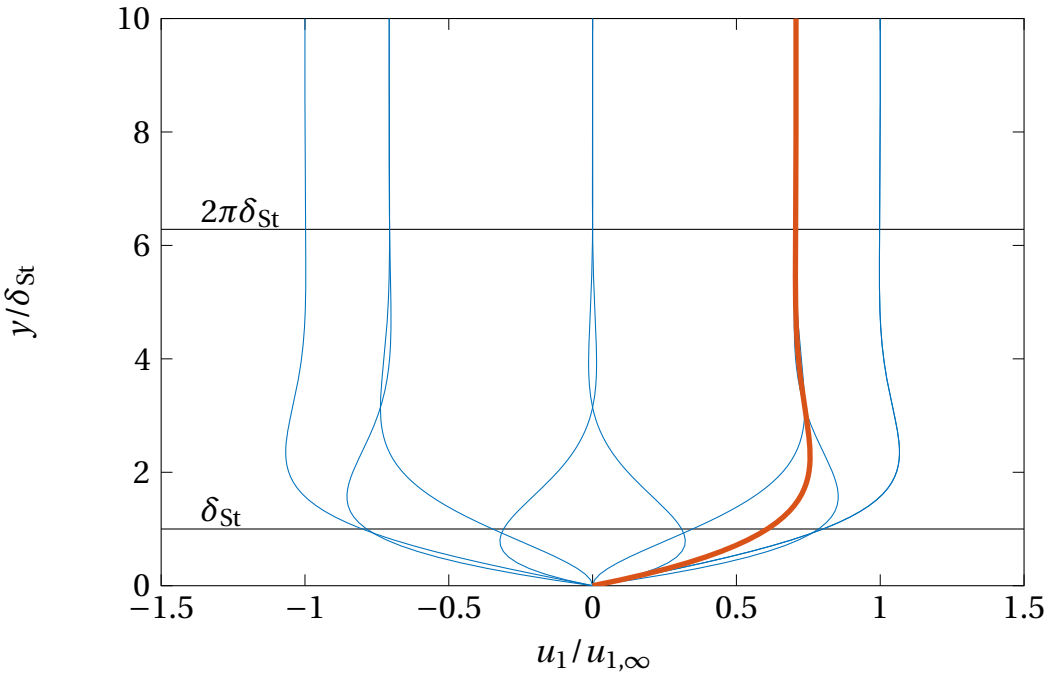

Figure 3.1: Velocity Profiles of Oscillating Flow Close to a Surface. Instantaneous values of velocity for one full period from 0 to 2π in increments of $\pi/4$ (——). Additionally, the root mean square (RMS) value of the velocity is depicted (——).

pressure leads the velocity by only $\pi/4$. This causes the phenomenon that the shear stress, for sufficiently high frequencies, is $\pi/4$ ahead of the free-stream velocity which might seem to contradict causality.

Another important aspect is the thickness of the unsteady (acoustic) boundary layer, i.e. Stokes layer thickness δ_{St}. It scales inversely with the square root of the Reynolds number and the Strouhal number. Hence, the boundary layer is thin at high Reynolds numbers and high Strouhal numbers. A fact also observed in steady boundary layers. Moreover, higher frequencies result in smaller δ_{St}. The shear stress is inversely proportional to the boundary layer thickness and therefore rises with rising Reynolds number Re and Strouhal number Sr.

3.1.3 Motion of a Sphere

Basset (1888) derived a formula for the motion of a sphere in a viscous fluid. He also accounted for the acceleration and how the evolution of the flow field affects the

motion at the present time. This resulted in the so-called *Basset force*. For a spherical particle, the Basset forces is evaluated with

$$\boldsymbol{F}_\mathrm{B} = 6\pi r_\mathrm{p}\mu_\mathrm{f} \int_{-\infty}^{t} K(t-\tau)\frac{\mathrm{d}\left(\boldsymbol{u}_\mathrm{f}-\boldsymbol{u}_\mathrm{p}\right)}{\mathrm{d}\tau}\mathrm{d}\tau\,. \tag{3.9}$$

The (convolution-) integral sums the contributions of past particle acceleration weighted with the time that has passed since the acceleration occurred. This weighting factor, or kernel $K(t-\tau)$, decays over time with $t^{-1/2}$. It is given by Basset (1888) as

$$K(t-\tau) = \frac{1}{\sqrt{\pi\nu_\mathrm{f}(t-\tau)/r_\mathrm{p}^2}}\,. \tag{3.10}$$

This kernel can be seen as the impulse response (cf. Section 4.1.3) of the skin friction at the particle surface to perturbations in the acceleration of the particle relative to the flow. The dynamics of skin friction of a sphere in (accelerated) flow is important for the motion of particles in acoustic fields or under the influence of body forces like gravity. The Basset force was revisited since 1888 by several authors, e.g. by Yang and Leal (1991) as well as Mei and Adrian (1992). It is closely linked to the dynamics of skin friction assessed numerically in this thesis. However, a spherical geometry is not in the scope of this thesis and thus will not be considered further.

3.2 Perturbation Boundary Layer Equations

The first study on the matter of a cylinder in pulsating crossflow was published by Moore (1951). Lighthill (1954) followed a similar approach and specifically tailored it for a cylinder in pulsating crossflow. This study is one of the most recognized in this field of research. Under the assumption that the dynamics of a cylinder in crossflow are mainly governed by the stagnation point flow at the front quarter, the boundary layer equations for this case (Hiemenz layer, HL) were solved approximately. This led to two solutions for skin friction and heat transfer; one for low frequencies and one for high frequencies, respectively. This study was thereafter extended to compressible flow by Gribben (1961). Glauert (1956) examined transversal movement of a cylinder in crossflow with the methods provided by Lighthill (1954).

Following this approach, Gersten (1965) solved the same equations numerically, using a series expansion in frequency. Similar results were achieved, but with more consistent values for intermediate frequencies. Especially, the description of the skin friction dynamics is more consistent. Solutions were developed for stagnation point flow and flow over a flat plate (Blasius layer, BL). A solution for compressible flow based on Gersten (1965) was again developed by Gribben (1971).

Ackerberg and Phillips (1972) investigated the flow over a flat plate using an asymptotic analysis in combination with numerical integration. The skin friction results were very similar to the solutions developed in this thesis. E.g. a characteristic dip in the phase of the friction coefficient in the transition between the initial rise and the saturation at $\pi/4$ was found and is recovered using the CFD/SI method in this thesis.

Telionis and Romaniuk (1978) solved the boundary layer equations numerically, but yet again for a different kind of flow. The boundary layer solution for Howarth flow, i.e. the flow close to a stagnation point with prior deceleration, was chosen. However, like the HL, this is also a rough approximation for the flow around a cylinder.

A yawed cylinder undergoing spanwise and chordwise oscillations was investigated by Sarma and El-Hadi (1986); Sarma and Srivastava (1986). The skin friction was assessed using the boundary layer equations (Sarma and El-Hadi, 1986). Using a compressible formulation the heat transfer for this configuration was investigated Sarma and Srivastava (1986).

3.2.1 Boundary Layer Equations

The so-called boundary layer equations can be deduced from the Navier–Stokes equations (Equation (2.63)–(2.65)). A thorough derivation was given, e.g. by Schlichting and Gersten (2006). They make use of the fact that, if the viscosity is small, a surface with no-slip condition affects the flow field only in a small region close to the surface: the boundary layer. Two main assumptions are made to derive the equations: (1) The boundary layer thickness is proportional to the square root of the viscosity $\delta \sim \sqrt{\nu}$. (2) The boundary layer thickness is much smaller than the characteristic length of the body submerged in the fluid. For a streamlined body, the characteristic length is the length along which the flow occurs. In the case of a cylinder, this is usually the diameter, i.e. $\delta \ll d$. Combining both yields

$$\frac{\delta}{d} \sim \frac{1}{\sqrt{\mathrm{Re}}} \tag{3.11}$$

and hence the boundary layer thickness tends towards zero $\delta \to 0$ for infinitely large Reynolds numbers $\mathrm{Re} \to \infty$. Quantities associated with the y-direction, i.e. y and v are proportional to δ. Therefore, when the limit $\mathrm{Re} \to \infty$ is considered, the Navier–Stokes equations reduce to the boundary layer equations.

The effect of viscosity due to the presence of the surface is captured by the boundary layer. Hence, the outer flow is governed by the Euler equations (White, 2007), which

neglect the viscous terms. The outer flow velocity is often denoted by a capital U. The momentum equation then reads

$$\frac{\partial U}{\partial t} + U\frac{\partial U}{\partial x^*} = -\frac{\partial p}{\partial x^*}. \tag{3.12}$$

The outer flow velocity U is a concept similar to the free-stream velocity u_∞. The notation with the capital letter is kept here to emphasize the relation with the boundary layer equations. The pressure gradient acting in the boundary layer is the same as in the outer flow, so Equation (3.12) can be used to replace the unknown pressure gradient in the momentum equation. Moreover, the outer flow solution serves as boundary condition and hence the full two-dimensional problem is given by

$$\frac{\partial u}{\partial x^*} + \frac{\partial v}{\partial y^*} = 0 \tag{3.13}$$

$$\frac{\partial u}{\partial t} + u\frac{\partial u}{\partial x^*} + v\frac{\partial u}{\partial y^*} = \frac{\partial U}{\partial t} + U\frac{\partial U}{\partial x^*} + \frac{1}{\mathrm{Re}}\frac{\partial^2 u}{\partial y^{*2}} \tag{3.14}$$

$$\frac{\partial T}{\partial t} + u\frac{\partial T}{\partial x^*} + v\frac{\partial T}{\partial y^*} = \frac{1}{\mathrm{Re}\,\mathrm{Pr}}\frac{\partial^2 T}{\partial y^{*2}} \tag{3.15}$$

with the boundary conditions

$$y^* = 0: \qquad u = 0, \qquad v = 0, \qquad T = T_w \tag{3.16}$$

$$y^* \to \infty: \qquad u \to U, \qquad T \to T_\infty. \tag{3.17}$$

3.2.2 Lighthill

The equations used by Lighthill (1954) are given in Section 3.2.1 as a simplification of the Navier–Stokes equations invoking the boundary layer approximations. In a landmark paper, Lighthill (1954) studied the response of laminar skin friction and heat transfer to fluctuations in the stream velocity. He presented approximate solutions for near-wall velocity and temperature profiles for the case of small pulsation amplitudes (linear regime) and evaluated the corresponding displacement thickness, skin friction, and heat flow rate, respectively. For the case of a cylinder in low Reynolds number crossflow, the heat transfer frequency response in terms of amplitude reduction and phase lag was determined. Lighthill states that his solution "applies only at Reynolds numbers for which the boundary layer approximation has some validity (say $R > 10$)" and "in the range of Reynolds number for which a laminar boundary layer exists" (Lighthill, 1954).

Lighthill (1954) already suggested that the unsteady response of the heat transfer rate to the perturbation of free-stream velocity is determined by the adaptation time of the viscous and thermal boundary layers. For harmonic perturbation, this

time lag controls the phase of the heat transfer frequency response function. For low frequencies, the time lag of the heat transfer was estimated as one fifth of the ratio of cylinder diameter and free-stream velocity.

Perturbation Approach

Lighthill's approach was to introduce small oscillations about a steady mean in the form of (cf. Equation (2.91))

$$u(x^*, y^*, t) = u_0(x^*, y^*) + \varepsilon\, u_1(x^*, y^*)\, \mathrm{e}^{\mathrm{i}\omega t} \tag{3.18}$$

and terms collected according to different powers of ϵ. The zeroth order equations are then just equal to the boundary layer equations (Equation (3.13)–(3.14)). Evaluating the time derivative, the first order equations are given by

$$\frac{\partial u_1}{\partial x^*} + \frac{\partial v_1}{\partial y^*} = 0 \tag{3.19}$$

$$i\omega\, u_1 + u_0 \frac{\partial u_1}{\partial x^*} + u_1 \frac{\partial u_0}{\partial x^*} + v_0 \frac{\partial u_1}{\partial y^*} + v_1 \frac{\partial u_0}{\partial y^*} = i\omega\, U_1 + \frac{\mathrm{d}}{\mathrm{d}x^*}(U_0 U_1) + \nu \frac{\partial^2 u_1}{\partial y^{*2}} \tag{3.20}$$

$$i\omega\, T_1 + u_0 \frac{\partial T_1}{\partial x^*} + u_1 \frac{\partial T_0}{\partial x^*} + v_0 \frac{\partial T_1}{\partial y^*} + v_1 \frac{\partial T_0}{\partial y^*} = k \frac{\partial^2 u_1}{\partial y^{*2}} \tag{3.21}$$

with the boundary conditions

$$y^* = 0: \qquad u_1 = 0, \qquad v_1 = 0, \qquad T_1 = 0 \tag{3.22}$$

$$y^* \to \infty: \qquad u_1 \to U_1, \qquad T_1 \to 0\,. \tag{3.23}$$

Lighthill (1954) considered two limiting cases for skin friction and heat transfer, respectively. In the case of high frequencies, the acceleration terms are large compared to other contributions, and hence, only those and the derivatives of the highest order are kept. For the calculation at low frequencies, such a simplification cannot be invoked. To solve the boundary layer equations, an integral Kármán–Polhausen treatment (Schlichting and Gersten, 2006, Section 8.1) was used. The results are therefore an approximation within the accuracy of the assumptions made, e.g. the velocity profile is modeled as a fourth order polynomial in y.

Skin Friction

The momentum equation for high frequencies reduces to

$$\mathrm{i}\omega(u_1 - U_1) = \nu \frac{\partial^2 u_1}{\partial y^{*2}}\,. \tag{3.24}$$

This is equivalent to Stokes' second problem (cf. Equation (3.1)) and hence the solution is

$$u_1 = U_1 \left(1 - \mathrm{e}^{-y\sqrt{\mathrm{i}\omega/\nu}}\right). \tag{3.25}$$

The shear stress at the surface of the cylinder is given by (Lighthill, 1954, Equation (14))

$$\mu \left(\frac{\partial u_0}{\partial y^*}\right)_{y^*=0} + \epsilon\, \mathrm{e}^{\mathrm{i}\omega t}\, \mu U_0 \sqrt{\frac{\mathrm{i}\omega}{\nu}}. \tag{3.26}$$

Using the definition of the transfer function (Equation (2.100)) and inserting equation (3.26) yields

$$G_{c_f,\text{Lighthill}} = \frac{\epsilon\, \mathrm{e}^{\mathrm{i}\omega t}\, \mu U_0 \sqrt{\frac{\mathrm{i}\omega}{\nu}} \Big/ \mu \left(\frac{\partial u_0}{\partial y^*}\right)_{y^*=0}}{\epsilon\, u_1\, \mathrm{e}^{i\omega t} \Big/ u_0}. \tag{3.27}$$

For low frequencies, Lighthill arrives at the following equation (Lighthill, 1954, equation 38)

$$\mu \left(\frac{\partial u_0}{\partial y^*}\right)_{y^*=0} + \epsilon\, \mathrm{e}^{\mathrm{i}\omega t} \left[\mu \left(\frac{\partial u_s}{\partial y^*}\right)_{y^*=0} + i\omega\mu \left(\frac{\partial u_2}{\partial y^*}\right)_{y^*=0}\right] = \tau_0 + \epsilon\, \mathrm{e}^{\mathrm{i}\omega t} \left[\frac{3}{2}\tau_0 + \mathrm{i}\omega \frac{1}{2}\rho U_0 \delta_0^*\right] \tag{3.28}$$

where the fluctuating velocity is decomposed into a quasi-steady part and an acceleration dependent part, respectively, written as $u_1 = u_s + i\,\omega\, u_2$. From a comparison between Equation (3.26) and Equation (3.28), Lighthill deduces a "matching frequency" given by

$$\omega_0 = \frac{3\,\tau_0}{\rho\, U_0\, \delta_0^*} \tag{3.29}$$

where δ_0^* is the displacement thickness. At this frequency, both solutions approximately coincide in amplitude and phase as well as in their respective velocity profiles. Finally, Lighthill assessed the quantitative value of this frequency for two different types of boundary layers: the boundary layer near a stagnation point (HL) and the flat plate boundary layer (BL).

The velocity profile of the inviscid flow (potential flow) near a stagnation point is given by $U_0 = \beta^* x$ and $V_0 = -\beta^* y$. Considering the potential flow solution of a cylinder in crossflow (Equation (2.76)) at the stagnation point, the derivative of the impinging flow velocity with respect to the distance to the surface is evaluated as

$$\beta^* \frac{V}{d} = \frac{\partial V_0}{\partial y^*} = -\frac{\partial u_1}{\partial x_1} = \frac{\partial^2 \psi}{\partial x_1\, \partial x_2} = \frac{x_1 \left(x_1^2 + 3x_2^2\right)}{2\left(x_1^2 + x_2^2\right)^3}. \tag{3.30}$$

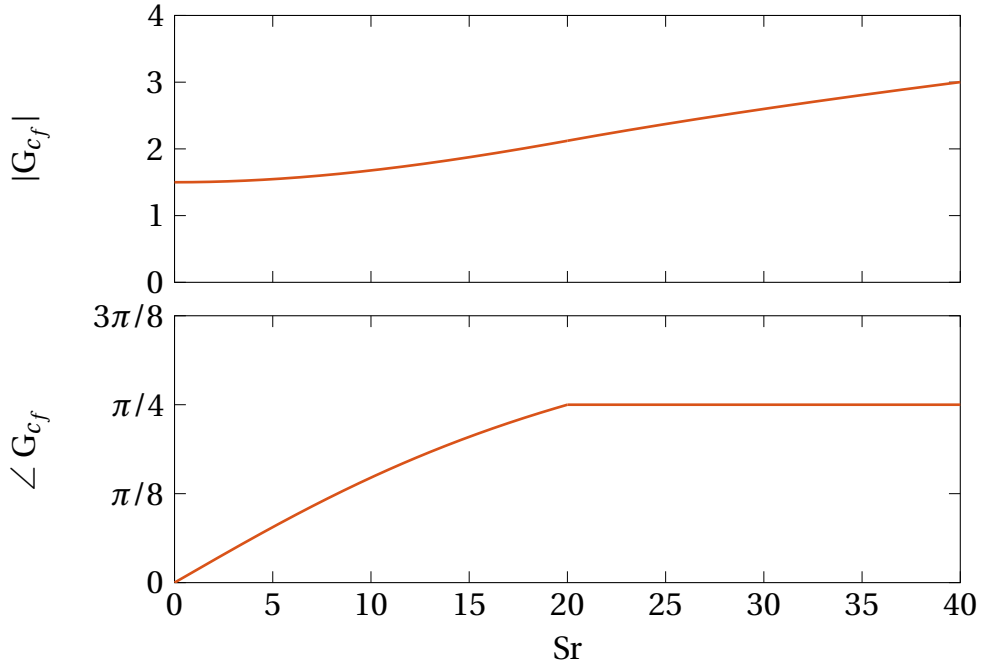

Figure 3.2: Frequency Response of Skin Friction for the HL (Lighthill, 1954). Amplitude (top) and phase (bottom).

Directly at the stagnation point, this simplifies to

$$\beta^* \frac{V}{d} = \left.\frac{\partial u_1}{\partial x_1}\right|_{(x_1=1/2, x_2=0)} = \frac{x_1^3}{2x_1^6} = -4. \tag{3.31}$$

The curvature of the cylinder causes a deviation from the pure stagnation point flow. However, this influence is minor and was accounted for by averaging the velocity, i.e. the constant factor β^*, over the first quadrant of the cylinder to yield

$$\beta \frac{V}{d} = \beta^* \frac{\pi}{2} \int_{-\pi/4}^{\pi/4} \cos(\phi) \mathrm{d}\phi \approx 3.6. \tag{3.32}$$

The matching frequency for the HL is reported to be $\omega_0 = 5.6\beta u_{0,\infty}/d$. Hence, the Strouhal number, as used in this thesis, is $\mathrm{Sr}_0 \approx 20$. Amplitude and phase of the skin friction frequency response for the HL are depicted in Figure 3.2. For the BL, the matching Strouhal number depends on the distance from the start of the flat plate and is $\mathrm{Sr}_{0,\mathrm{BL}} = 0.6\,x^*/d$. The skin friction frequency response is depicted in Figure 3.3 in terms of amplitude and phase.

At low frequencies, i.e. small values of Strouhal number Sr, Lighthill (1954) reported an "anticipation time" for the skin friction of $\tau = 0.05d/u_{0,\infty}$ for the HL and $\tau = 1.7d/u_{0,\infty}$ for the BL. The anticipation times can be given as dimensionless time constants $c_\tau = 0.05$ and $c_\tau = 1.7$, respectively. The boundary layer reacts faster to the pressure gradient necessary to accelerate the flow than the free-stream. This

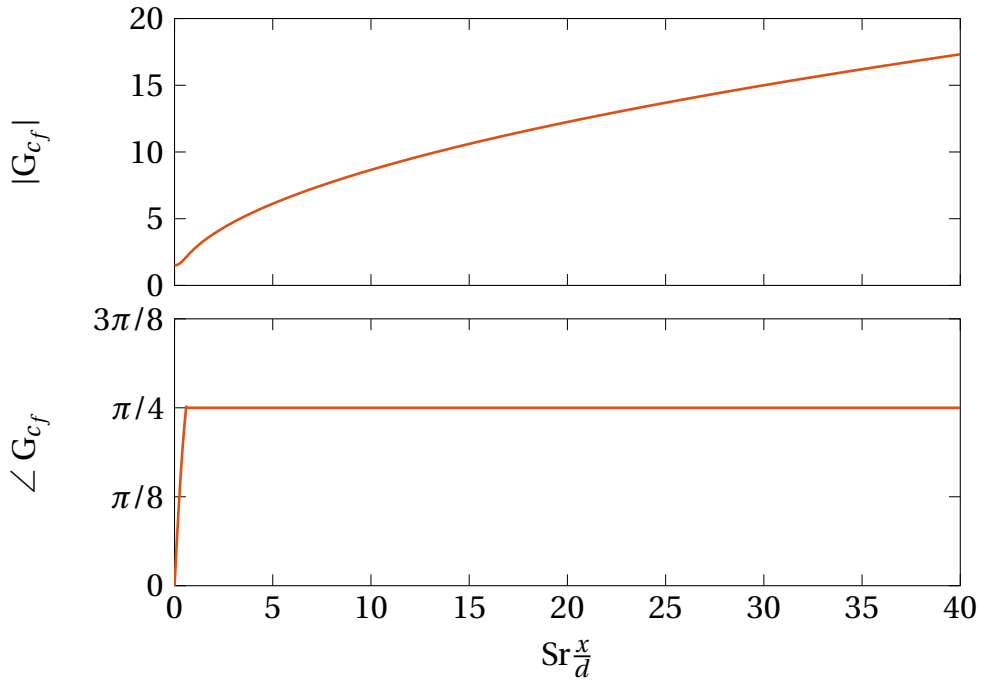

Figure 3.3: Frequency Response of Skin Friction for the BL (Lighthill, 1954). Amplitude (top) and phase (bottom).

creates the impression of the skin friction anticipating a change in velocity, which can be seen as a phase lead in the frequency response given by

$$G_{c_f} = K\,\mathrm{e}^{\mathrm{i}\,\mathrm{Sr}\,c_\tau} \tag{3.33}$$

where K is the steady-state gain. The low-frequency limits are reported as

$$\mathrm{Sr} \to 0: \qquad |G_{c_f,\mathrm{Lighthill}}| = 1.5 \qquad \angle G_{c_f,\mathrm{Lighthill}} = 0\,.$$

The steady-state gain according to Lighthill (1954) has a value of $K = 1.5$, due to the fact that $c_f \sim u_{0,\infty}^{3/2}$. It is stated that the approximation for the phase is applicable for $\mathrm{Sr} < 20$.

At high frequencies, all models agree on a square root dependence of the frequency response on the Strouhal number. This is closely related to a shear wave solution (cf. Section 3.1.2), which also predicts the constant phase lead of 45°. The limits for high frequencies are reported as

$$\mathrm{Sr} \to \infty: \qquad |G_{c_f,\mathrm{Lighthill}}| \to \infty \qquad \angle G_{c_f,\mathrm{Lighthill}} = \pi/4\,.$$

Heat Transfer

The treatment Lighthill (1954) applied to the temperature was similar to the procedure for the skin friction. Only the HL was considered as Lighthill (1954) argues that

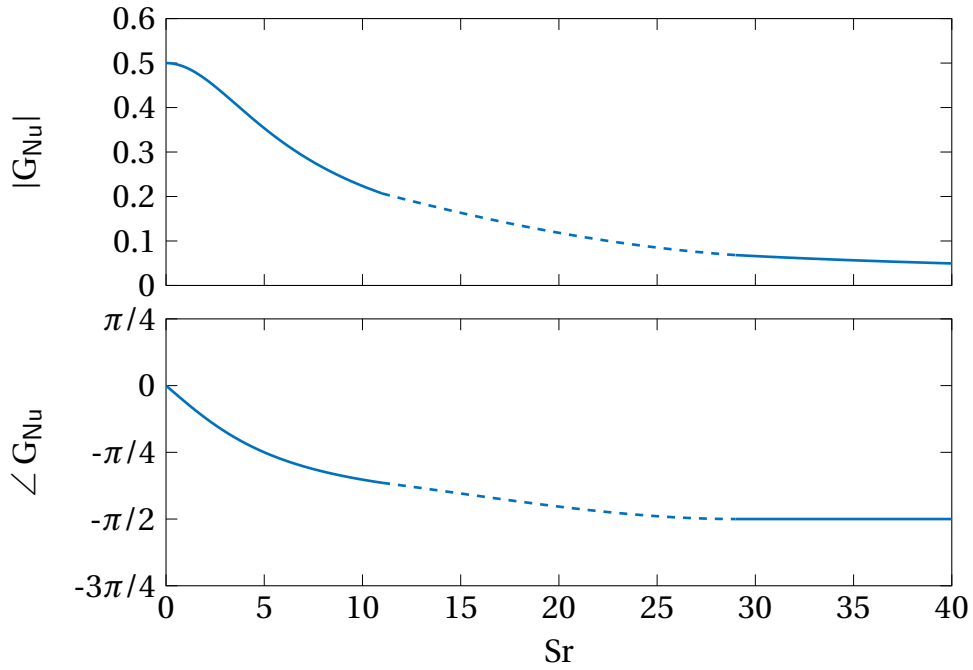

Figure 3.4: Frequency Response of Heat Transfer (Lighthill, 1954). Amplitude (top) and phase (bottom).

the major part of the heat transfer takes place at the front quadrant of the cylinder containing the stagnation point. The heat flux density is given by (Lighthill, 1954, equation 61)

$$-k\left(\frac{\partial T_0}{\partial y^*}\right)_{y^*=0} + \frac{\mathrm{i}}{\omega}\epsilon\,\mathrm{e}^{\mathrm{i}\omega t}\,k\left[\frac{\mathrm{d}U_0}{\mathrm{d}x^*}\left(\frac{\partial T_0}{\partial y^*}\right)_{y^*=0}\frac{1}{1+\mathrm{Pr}^{1/2}} - U_0\left(\frac{\partial^2 T_0}{\partial x^*\partial y^*}\right)_{y^*=0}\frac{1+2\,\mathrm{Pr}^{1/2}}{(1+\mathrm{Pr}^{1/2})^2}\right]$$

Approximate solutions for high frequencies and low frequencies were calculated from this equation. For the latter, Lighthill again applied a Kármán–Polhausen treatment. Time lag and steady-state gain according to Lighthill's approximation for low frequencies are determined to $\tau = 0.2\,d/u_{0,\infty}$ ($c_\tau = 0.2$) and $K = 0.5$, respectively. The steady-state gain is taken from a linearization of King's law (King, 1914).

The low frequency and high-frequency approximations for the heat transfer frequency response can be written as

$$G_{\mathrm{Nu,Lighthill}} = \frac{0.5}{1+0.2\,\mathrm{i}\,\mathrm{Sr}} \qquad \text{and} \qquad G_{\mathrm{Nu,Lighthill}} = \frac{2.0}{\mathrm{i}\,\mathrm{Sr}}. \tag{3.34}$$

These relations are shown in Figure 3.4 as amplitude and phase of the heat transfer frequency response.

Lighthill (1954) stated that the first expression in Equation (3.34) is only applicable if Sr < 20. However, the heat transfer shows the behavior of a low-pass filter and as the limits

$$\begin{aligned} &\mathrm{Sr} \to 0: && |G_{\mathrm{Nu,Lighthill}}| = 0.5 && \angle G_{\mathrm{Nu,Lighthill}} = 0 \\ &\mathrm{Sr} \to \infty: && |G_{\mathrm{Nu,Lighthill}}| = 0 && \angle G_{\mathrm{Nu,Lighthill}} = -\pi/2 \end{aligned}$$

indicate, high frequencies have very low gain and a phase lag of 90°, which agrees well with the high frequency approximation.

Experimental Verification

Hill and Stenning (1960) revisited the solution for the skin friction of a flat plate in pulsating flow by Lighthill (1954). They extended the treatment to boundary layers of Howarth type and conducted experiments in this regard. Lighthill's analysis for the BL agree well with measurements in the frequency range $0 < \mathrm{Sr}\, x/d < 0.6$. For higher frequencies, an intermediate regime was identified and modeled.

Conclusions

As it was unavoidable to introduce severe approximations to solve the equations of motion, Lighthill himself cautioned that his results would only be solutions of limited accuracy and range of validity and applicability. Mariappan (2012) and Moeck (2010) also found discrepancies between Lighthill's predictions and their experiments. They argued that the time lag should be larger than $\tau = 0.2\, d/u_{0,\infty}$. Lighthill's results were only validated for velocity amplitudes in the unsteady boundary layer, but never with respect to heat transfer (Hill and Stenning, 1960). Presumably, this is due to the difficulties of time resolved measurements of heat flow rates. Nevertheless, Lighthill's estimate for the time lag has since been used in many studies of the thermoacoustic instability of the Rijke tube (Hantschk and Vortmeyer, 1999; Matveev and Culick, 2003; Subramanian et al., 2010). In particular, Subramanian et al. (2010) carried out a comprehensive bifurcation analysis of thermoacoustic instability.

3.2.3 Lin

Lin (1957), in contrast to Lighthill (1954), concerned himself not only with the fluctuation but with the net change of any flow quantity due to pulsations. Lin's approach is based on the method of averaging (Telionis, 1981). Perturbed quantities in the fashion of Equation (2.85) were introduced in the boundary layer equations and subsequently averaged. This procedure is similar to Reynolds averaging (Gersten,

1965; White, 2007; Davidson, 2004) and hence it also yields Reynolds stress terms known from turbulence treatment. For closure, Lin considered the high frequency approximation given by

$$\frac{\partial u'}{\partial x^*} + \frac{\partial v'}{\partial y^*} = 0 \tag{3.35}$$

$$\frac{\partial u'}{\partial t} = \frac{\partial u_\infty}{\partial t} + \nu \frac{\partial^2 u'}{\partial y^{*2}}. \tag{3.36}$$

With $u_\infty(x^*, t) = u_\infty(x^*)\cos(\omega\, t)$, this is equivalent to Stokes' second problem and hence the solution can be written as

$$u' = u_{1,\infty}(x^*)\cos(\omega\, t) - \mathrm{e}^{-y^*\sqrt{\frac{\omega}{2\nu}}} \cos\left(\omega\, t - y^* \sqrt{\frac{\omega}{2\nu}}\right) \tag{3.37}$$

$$v' = -\int_0^y \frac{\partial u'}{\partial x^*} \mathrm{d}y. \tag{3.38}$$

This information made it possible to evaluate the nonlinear terms $u'(\partial u')/(\partial x)$ and $v'(\partial u')/(\partial y)$. The method of averaging and the model for the Reynolds stress does not require the pulsations to be small. According to Telionis (1981) this approach has not gained much attention since the 1950s.

3.2.4 Gersten

Gersten (1965) revisited Lighthill's analysis and adapted it to the Falkner–Skan equations. This form of the boundary layer equations provides a unified framework for wedge flow including stagnation point flow and flat plate flow. Gersten (1965) introduced first and second order perturbations to capture fluctuations and second order streaming effects with a non-vanishing net contribution. In contrast to Lighthill (1954), he used series expansions in the similarity variable and the frequency parameter instead of an integral Kármán–Polhausen treatment.

Falkner–Skan Equations

The Falkner–Skan equations are for wedge flows where the velocity is of the form $U_0 = \beta x^m$. In this case, the Navier–Stokes equations have self-similar solutions with the similarity variable

$$\eta = \frac{y}{l}\frac{\sqrt{\mathrm{Re}}}{x} = y\sqrt{\frac{\beta}{\nu}} x^{(m-1)/2}. \tag{3.39}$$

This includes, as special cases, stagnation point flow and flat plate flow. In the case of the HL, the exponent is $m = 1$. Thus, Lighthill's estimation to acquire β for a cylinder (cf. Equation (3.32)) can be used. In the case of the BL, $m = 0$, i.e. the velocity is constant.

To derive the Falkner–Skan equations the stream function as in Section 2.2.6 (Equation (2.67)) is used. Furthermore, two functions of the similarity variable η were introduced:

$$f(\eta) = \frac{\psi(x,y)}{\sqrt{\nu\, x\, U(x)}} \tag{3.40}$$

$$g(\eta) = \frac{T(x,y) - T_\infty}{T_w - T_\infty}. \tag{3.41}$$

The Falkner–Skan equations are ordinary differential equations of the form

$$f''' + \frac{m-1}{2} f\, f'' + m\left(1 - f'^2\right) = 0 \tag{3.42}$$

$$\frac{1}{\mathrm{Pr}} g'' + \frac{m-1}{2} f\, g' = 0. \tag{3.43}$$

The boundary conditions for steady-state wedge flow are given by

$$\eta = 0: \qquad f = 0, \qquad f' = 0, \qquad g = 1 \tag{3.44}$$

$$\eta \to \infty: \qquad f' = 1, \qquad g = 0. \tag{3.45}$$

Series Expansion

Pulsations were superimposed on the free-stream, which is denoted as outer flow by Gersten (1965). The velocity is hence described by

$$U = \overline{U}\left[1 + \epsilon \cos(\omega\, t)\right]. \tag{3.46}$$

To non-dimensionalize the frequency, the frequency parameter

$$X = \frac{\omega\, x}{U(x)} = \frac{\omega}{\beta} x^{1-m} \tag{3.47}$$

was used. The frequency parameter can be converted into a Strouhal number as defined in Equation (2.97). For the HL this yields ($m = 1$) $\mathrm{Sr} = 3.6X$ and ($m = 0$) $\mathrm{Sr} = X \cdot d/x$ for the BL.

For the two prominent cases, the HL and the BL, Gersten developed transfer functions as power series of Sr. Similar to Lighthill's approach, the solution comprises separate approximations for low and high frequencies. Furthermore, Gersten (1965) claims to have remedied a mistake by Lighthill (1954) leading to a wrong far field boundary condition for the temperature.

Skin Friction

The dynamic skin friction was reported by Gersten (1965) as

$$\frac{\tau_w}{\sqrt{\mathrm{Re}}} = f''(0) + \epsilon A_\tau(\mathrm{Sr}) \cos(\mathrm{Sr}\, t + \lambda_\tau(\mathrm{Sr}))\,. \tag{3.48}$$

The fluctuating part is given as series expansion of the frequency parameter. The coefficients of these series were tabulated. $A_\tau(\mathrm{Sr})$ and $\lambda_\tau(\mathrm{Sr})$ denote the amplitude and the phase shift of the pulsations. $f''(0)$ is the steady-state shear stress and evaluated to 1.2326 and 0.3321 for HL and BL, respectively. The transfer function for skin friction pulsation caused by pulsations of the free-stream velocity can be acquired from

$$G_{c_f} = \frac{A_\tau(\mathrm{Sr})}{f''(0)}\, \mathrm{e}^{\mathrm{i}\lambda_\tau}\,. \tag{3.49}$$

The frequency response for the HL is shown in Figure 3.5. The anticipation time evaluated by Gersten is about $\tau = 0.043 d/u_{0,\infty}$ and his model shows a smooth transition from low to high frequencies. The applicability of the low-frequency approximation is limited to $\mathrm{Sr} \lesssim 10$ in this case. The low-frequency limit is reported to be $K = 1.5$. Low and high-frequency limits are given by

$$\begin{aligned} \mathrm{Sr} \to 0: &\quad |G_{c_f,\mathrm{Gersten,HL}}| = 1.5 \quad \angle G_{c_f,\mathrm{Gersten,HL}} = 0 \\ \mathrm{Sr} \to \infty: &\quad |G_{c_f,\mathrm{Gersten,HL}}| \to \infty \quad \angle G_{c_f,\mathrm{Gersten,HL}} = \pi/4\,. \end{aligned} \tag{3.50}$$

For the BL, the anticipation time is $\tau = 1.7 d/u_{0,\infty}$ ($c_\tau = 1.7$). The frequency response for low and high frequencies are depicted in Figure 3.6. Both approximate solutions match reasonably well at $\mathrm{Sr}\, x/d \approx 0.8$. The low and high frequency limits are the same as for the HL (Equation (3.50)).

Heat Transfer

In an analogous manner, the pulsating heat transfer was given by Gersten (1965) as

$$\frac{\mathrm{Nu}}{\sqrt{\mathrm{Re}}} = g'(0) + \epsilon A_q(\mathrm{Sr}) \cos(\mathrm{Sr}\, t + \lambda_q(\mathrm{Sr}))\,. \tag{3.51}$$

The coefficients for the series expansion of the temperature gradient at the surface were tabulated and $A_q(\mathrm{Sr})$ and $\lambda_q(\mathrm{Sr})$ denote amplitude and phase shift of the series, respectively. The steady-state values $g'(0) = 0.4959$ and $g'(0) = 0.2927$ for HL and BL, respectively, are used for scaling. With the definition of the transfer function and Equation (3.51) the transfer function can be evaluated as

$$G_{\mathrm{Nu}} = \frac{A_q(\mathrm{Sr})}{g'(0)}\, \mathrm{e}^{\mathrm{i}\lambda_q}\,. \tag{3.52}$$

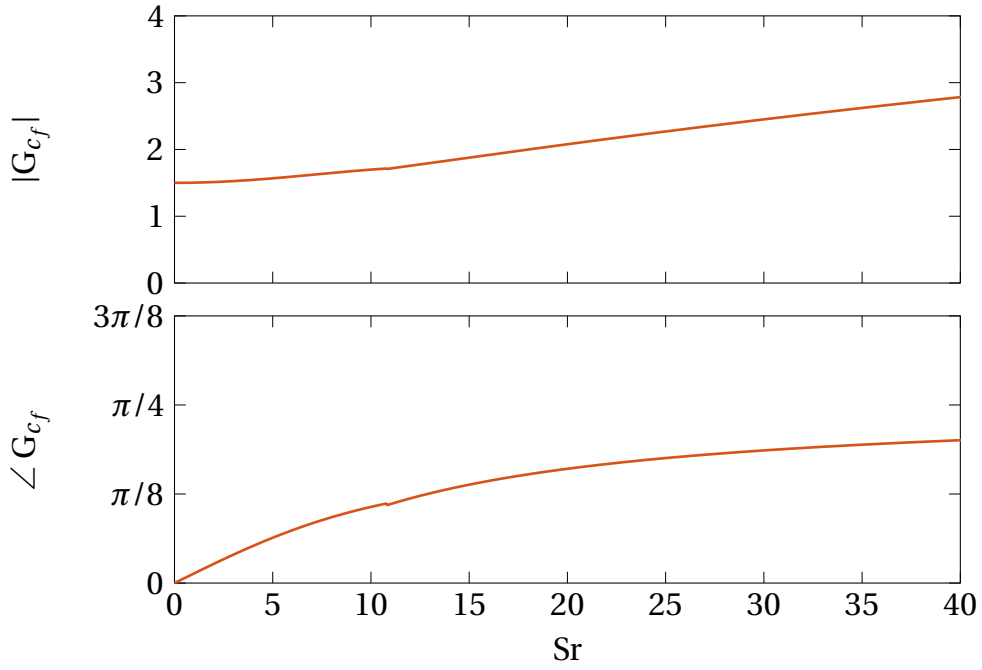

Figure 3.5: Frequency Response of Skin Friction for the HL (Gersten, 1965). Amplitude (top) and phase (bottom).

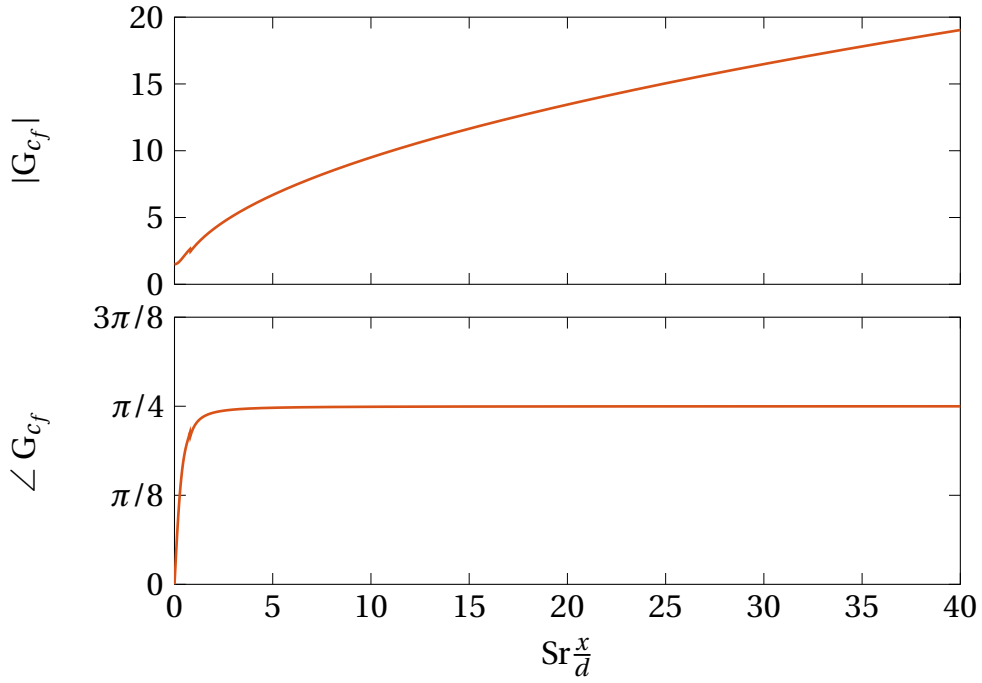

Figure 3.6: Frequency Response of Skin Friction for the BL (Gersten, 1965). Amplitude (top) and phase (bottom).

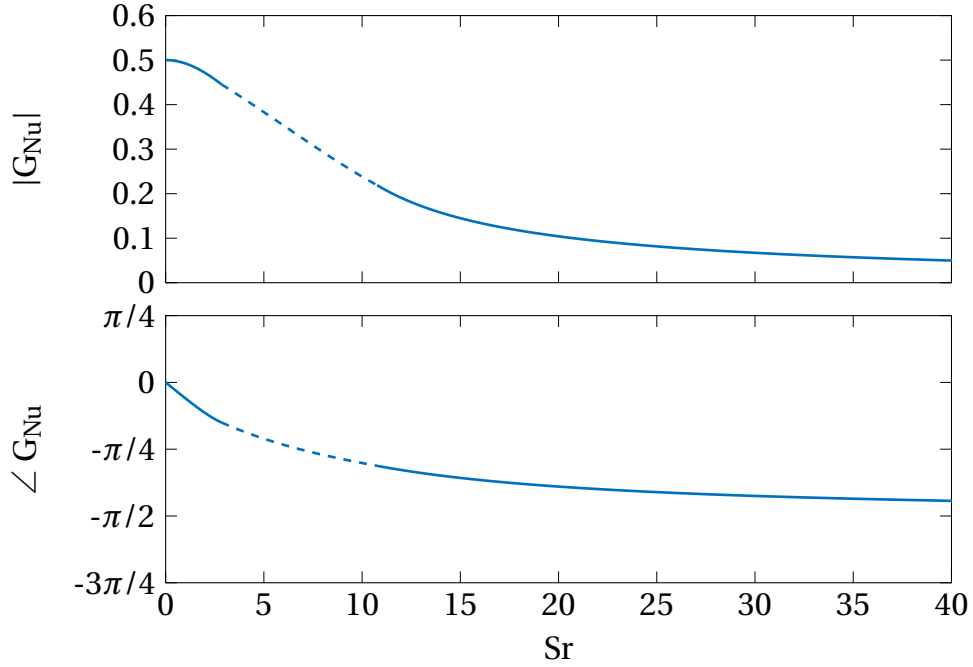

Figure 3.7: Frequency Response of Heat Transfer for the HL (Gersten, 1965). Amplitude (top) and phase (bottom).

The frequency response of the Nußelt number to pulsation in the free-stream velocity for the HL is shown in Figure 3.7. The dotted part of the graph are values from a spline interpolation connecting the approximative solutions for low frequencies and high frequencies. The limits for low and high frequencies are

$$\begin{aligned} \mathrm{Sr} \to 0: \quad & |G_{\mathrm{Nu,Gersten,HL}}| = 0.5 \quad \angle G_{\mathrm{Nu,Gersten,HL}} = 0 \\ \mathrm{Sr} \to 0: \quad & |G_{\mathrm{Nu,Gersten,HL}}| = 0 \quad \angle G_{\mathrm{Nu,Gersten,HL}} = -\pi/2 \end{aligned} \tag{3.53}$$

The results are in good agreement with the solutions of Lighthill (1954). The steady-state gain $K = 0.5$ as predicted by King (1914) and the time lag is $c_\tau = 0.188$.

The BL was not assessed with respect to heat transfer by Lighthill (1954). In contrast, Gersten (1965) reports the respective series coefficients and the resulting frequency response is depicted in Figure 3.8. Again, a dashed line is shown where a spline interpolation was necessary to match the low and high-frequency solutions. The behavior in the limit of low and high frequencies is identical to Equation (3.53), but the phase lag is approximately $c_\tau \approx 0.874 d/x$.

Conclusions

The investigation by Gersten (1965) followed the approach by Lighthill (1954) to a large extent. Therefore, the solution for $G_{\mathrm{Nu},HL}$ are almost the same in both cases. For the skin friction, the respective solutions are also in good agreement. The most

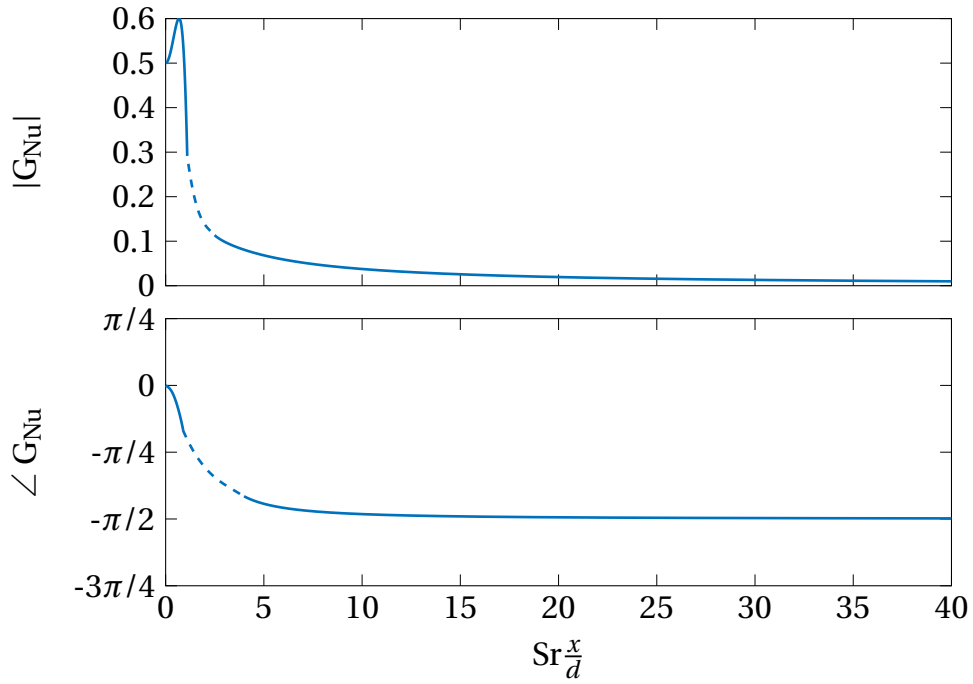

Figure 3.8: Frequency Response of Heat Transfer for the BL (Gersten, 1965).

prominent difference is visible for the phase at the frequency where low and high-frequency approximations match. The series expansion used by Gersten (1965) yields a smoother transition.

For the heat transfer in the flow over a flat plate, depicted in Figure 3.8, a peak in amplitude is visible. This *peak gain* occurs at approximately $\mathrm{Sr}\, x/d \approx 0.7$ and represents a distinct difference in the dynamic behavior compared to the flow close to a stagnation point.

With the use of a series expansion, Gersten (1965) could work around the limitations of the integral treatment used by Lighthill (1954). However, in the scope of the cylinder, the major limitations remain similar. The known solutions for wedge flow with fixed angle cannot reproduce the curvature of the cylinder and are therefore approximations for a certain region of the cylinder at best. For the Falkner–Skan equations to be valid, the mean flow Reynolds number has to be sufficiently high. Under these conditions, flow separation occurs, which cannot be handled by the current treatment. Nevertheless, the results by Gersten (1965) suggest that the dynamic behavior of a cylinder is a mixture between that of the HL and the BL.

3.2.5 Telionis and Romaniuk

Telionis (1981) summarized the advances in describing unsteady viscous flows, and a whole chapter of his book is devoted to fluctuations imposed on the steady flow.

Both the analytical and the numerical investigations applying the boundary layer equations are discussed. Most notable for the scope of this thesis is the numerical solution of the unsteady boundary equations by Telionis and Romaniuk (1978). Although no transfer function was derived, relations between fluctuating and steady temperature gradients shed some light on the heat transfer behavior. In contrast to Lighthill's solutions, but in agreement with Gersten (1965), a peak in fluctuation amplitude at low Strouhal numbers was reported.

3.3 Approximation for low Reynolds Numbers

To find an approximate solution for flow at low Reynolds numbers, Stokes' equation (Stokes, 1851) can be used. In this formulation, inertia terms, which have only a small contribution, are neglected. Better solutions are to be gained with the *Oseen equations* (White, 2007). In these equations, inertia is included with a separate convective velocity. Bayly (1985) used this simplification of the incompressible Navier–Stokes equations to derive a solution for a cylinder in pulsating crossflow at low Reynolds numbers.

3.3.1 Oseen Equation

The Oseen equations are a simplification of the incompressible Navier–Stokes equations (cf. Equation (2.63) - (2.65)). The velocity u in the convective term is replaced by an independent convective velocity $u_j(\partial u_i)/(\partial x_j) \rightarrow b_j(\partial u_i)/(\partial x_j)$. This amounts to a linearization of the Navier–Stokes equations around b_i. The convective velocity is an additional variable, and thus an equation for the outer flow is necessary to solve for all variables. Outer and inner flow are matched using a perturbation approach. The Oseen equations represent a significant improvement over Stokes' equation which neglects the convective term altogether and yield acceptable results up to higher Reynolds numbers. In the first half of the 20th century, solutions for the steady-state drag coefficient and Nußelt number were developed (White, 2007). Nevertheless, due to the linearization, this approximation leads to severely wrong results at $\mathrm{Re} \gtrsim 1$. Weisenborn and Mazur (1984) extended the approach to yield values with acceptable accuracy for the steady-state drag even up to Reynolds numbers of order ten.

3.3.2 Bayly

Bayly (1985) included the time derivatives in the Oseen equations. From this starting point, he developed a model for the unsteady heat transfer at very low Péclet

numbers, i.e. Re·Pr $\ll 1$, to be used for wires in Rijke tubes or hot-wire anemometers. Oseen's approximations allowed for the problem to be solved for a real cylindrical geometry. The skin friction was not addressed in the study by Bayly (1985).

If the Prandtl number is of order unity, the solution by Bayly (1985) is accurate for $\mathrm{Re} \to 0$. The dimensionless frequency chosen in this work is

$$\frac{\omega\, k}{\rho\, c_p\, u_{\infty,0}^2} = \frac{\mathrm{Sr}}{\mathrm{Re}\,\mathrm{Pr}}. \tag{3.54}$$

This introduces a dependence on Reynolds number not present in the models based on the boundary layer equations, e.g. by Lighthill (1954) and Gersten (1965). Introducing the perturbation parameter $\delta = [-\ln(\mathrm{Re}\,\mathrm{Pr}) + \ln(4) - \gamma_E]^{-1}$ and neglecting terms of order $\mathcal{O}(\delta^3)$ the frequency response can be written as

$$G_{\mathrm{Nu}} = \frac{\delta \ln(1 + 4\,\mathrm{i}\,\mathrm{Sr}/(\mathrm{Re}\,\mathrm{Pr}))}{4\,\mathrm{i}\,\mathrm{Sr}/(\mathrm{Re}\,\mathrm{Pr})}, \tag{3.55}$$

where $\gamma_E \approx 0.577$ is the Euler constant. The perturbation parameter is chosen in such a way that a consistent perturbation theory is achieved. Moreover, it yields the most accurate solution considering the fact that higher order terms of δ are neglected. Low and high frequency limits are given by

$$\begin{aligned} &\mathrm{Sr} \to 0: && |G| = \delta && \angle G = 0 \\ &\mathrm{Sr} \to \infty: && |G| = 0 && \angle G = -\pi/2. \end{aligned} \tag{3.56}$$

This frequency response is depicted in Figure 3.9 for three different Reynolds numbers, $\mathrm{Re}_0 = 0.01$, $\mathrm{Re}_0 = 0.05$, and $\mathrm{Re}_0 = 0.1$. Higher Reynolds numbers lead to unrealistically high values for the perturbation parameter δ, which is also the steady-state gain of the transfer function.

3.4 Navier-Stokes Equations

With the advent of CFD, it became possible to compute solutions of the full Navier–Stokes equations. Different approaches were developed. The first numerical simulations using the Navier–Stokes equations for a cylinder in unsteady flow were carried out by Apelt and Ledwich (1979). Kwon and Lee (1985) solved the linearized Navier–Stokes equations in frequency space. This provided a very efficient method for $\mathrm{Re} \lesssim 40$. A unique model was developed by Nicoli and Pelcé (1989). They solved the compressible Navier–Stokes equations in only one dimension using a series expansion with the temperature before and after the heater as expansion parameter. Hantschk and Vortmeyer (1999) carried out time domain simulations of a complete but under-resolved thermoacoustic device. A time series analysis, in the

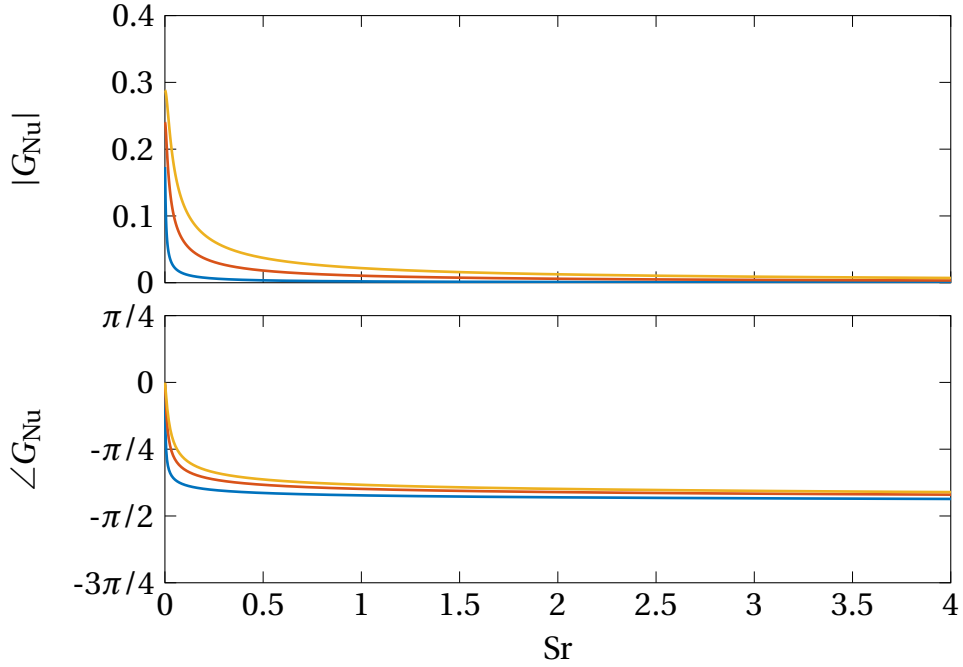

Figure 3.9: Frequency Response of Heat Transfer (Bayly, 1985). Solutions for Pr = 0.7 and three different mean flow Reynolds numbers, $Re_0 = 0.01$ (—), $Re_0 = 0.05$ (—), and $Re_0 = 0.1$ (—), are shown. The depicted range is restricted to $Sr < 4$

CFD/SI framework was conducted by Föller et al. (2008). Later, Selimefendigil et al. (2012) examined the cylinder in pulsating crossflow regarding its nonlinear behavior. Many more numerical studies touched the subject of a cylinder in unsteady flow, but in most cases, the focus was on cycle averaged behavior or on the vortex shedding at higher Reynolds numbers. Numerical studies also included oscillations of the cylinder transverse to the flow (Pham et al., 2010) and rectangular cylinders (Yu et al., 2014).

Zheng et al. (2017) examined the heat transfer and the momentum transfer numerically with a Lattice–Boltzmann code. This method is of great interest for further development because of its potential for massively parallelized computations due to its scalability to a high number of computational cores. The investigations on monofrequent pulsations at four different frequencies and four different pulsation amplitudes yielded information on the evolution of the circumferential distribution of Nußelt number and drag coefficient. Moreover, net heat transfer enhancement was investigated.

Wang et al. (2015) carried out simulations similar to Hantschk and Vortmeyer (1999). Thermoacoustic oscillations were investigated in a full-scale simulation using the Lattice–Boltzmann method. The numerical model can serve as a proof of concept but not as an accurate quantification of the physical effects.

3.4.1 Apelt and Ledwich

Apelt and Ledwich (1979) carried out the first numerical simulations of a cylinder in unsteady crossflow that also included heat transfer. The Navier–Stokes equations were solved in vorticity–stream function formulation (cf. Equation (2.68) - (2.70)) on a log-polar grid. The equations were discretized with central differences and integrated explicitly in time using a two-step method. Investigated Reynolds numbers were in the range $1 \leq \mathrm{Re} \leq 40$, i.e. below the threshold of vortex shedding. Three different cases of unsteadiness were considered: An impulsive start from rest, a sudden increase in flow velocity from a steady state (step input), and sinusoidal pulsations (monofrequent modulation) of the free-stream velocity.

Results were given as graphical representations of Nußelt number, drag coefficient, and friction coefficient over time. In response to the step input, the Nußelt number rises exponentially to its new steady-state value, similar to time lag elements in control theory. The drag coefficients drop to lower values instantaneously and slowly restore to a new steady state. For the sinusoidal pulsations only one frequency was reported, and hence only one point of the frequency response function could be acquired. For this case, the amplitude reduction and enlargement for heat transfer and skin friction were reported respectively.

3.4.2 Linearized Navier-Stokes Equations

The work of Kwon and Lee (1985) is of particular relevance for the present study. A vorticity–stream function formulation (cf. Section 2.2.6) was used to model incompressible, two-dimensional flow around a heated wire. Perturbation equations were derived for the case of small amplitude harmonic perturbations and solved numerically in a two-dimensional domain. The circumferential distribution of the oscillating heat transfer amplitude, as well as amplitude and phase of the total heat transfer rate, were evaluated for flow conditions typical for a Rijke tube. The results were used, e.g. by Matveev (2003a), because for Reynolds numbers of order unity neither Lighthill's nor Bayly's analytical solutions are valid. However, the nondimensional groups chosen in this work do not permit a detailed comparison since the inverse of the angular frequency was used as characteristic time instead of the ratio between cylinder diameter and unperturbed free-stream velocity (Lighthill, 1954; Gersten, 1965).

The results of Kwon and Lee (1985) were translated to the set of dimensionless quantities used in this thesis to facilitate comparison. The values reported by Kwon and Lee (1985) were extracted and transformed. The results provided yielded a cloud in the G_{Nu}-Re_0-Sr space and a surface, linking these points, was created using linear interpolation. The accuracy of this surface depends on the given data and is not optimal at values where the original data had to be extrapolated. Figure 3.10 shows

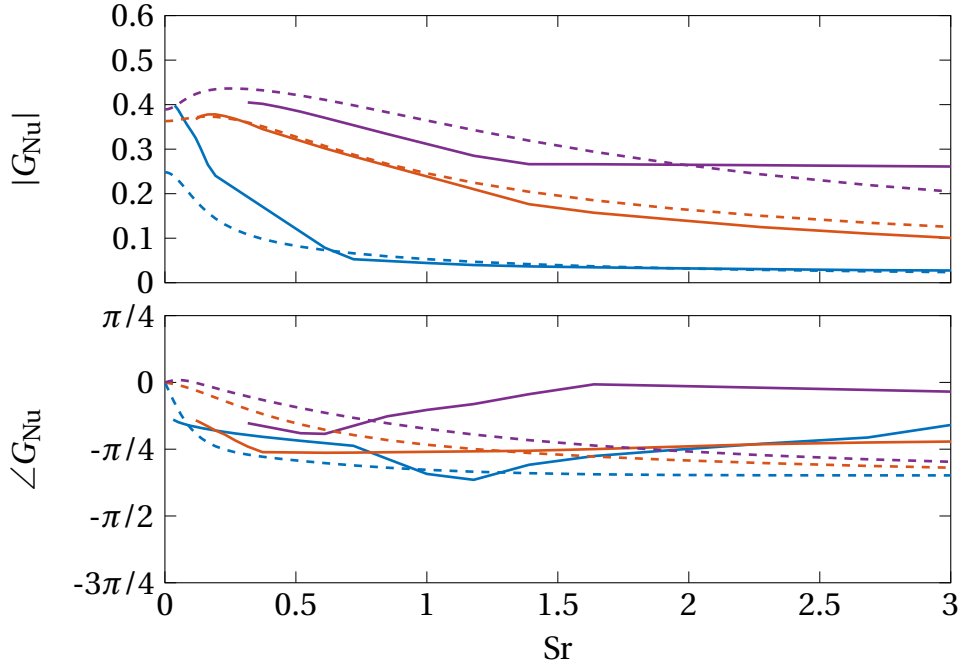

Figure 3.10: Amplitude of the Frequency Response (Kwon and Lee, 1985). $\mathrm{Re}_0 = 0.4$ (——), $\mathrm{Re}_0 = 4$ (——), and $\mathrm{Re}_0 = 10$ (——). Dashed lines represent the model developed in this thesis for $\mathrm{Re}_0 = 0.4$ (- - -), $\mathrm{Re}_0 = 4$ (- - -), and $\mathrm{Re}_0 = 10$ (- - -). The steady-state gain was adjusted. The depicted range is restricted to $\mathrm{Sr} < 3$.

the amplitude of the frequency response G_{Nu} for three slices of the interpolated surface at $\mathrm{Re}_0 = 0.4$, $\mathrm{Re}_0 = 4$, and $\mathrm{Re}_0 = 10$. Especially, the interpolated graph for $\mathrm{Re}_0 = 4$ shows the distinctive features of the dynamic behavior of the heat transfer that could also be confirmed in this thesis.

The concept of computing the linearized Navier–Stokes equations in frequency domain was revisited by Lu and Papadakis (2011, 2014). The focus of this study was on the numerical method and how to apply it to any code solving the Navier–Stokes equations iteratively in the time domain. Drag forces were computed and related to an analytical expression for oscillating flow.

3.4.3 Hantschk and Vortmeyer

Hantschk and Vortmeyer (1999) carried out numerical simulations solving the compressible Navier–Stokes equations. A complete Rijke tube like geometry was discretized in two dimensions, and the flow variables were solved using a finite volume approach. With this approach, they were able to simulate the thermoacoustic instabilities occurring in the Rijke tube including the main physical phenomena such as heat transfer and acoustic wave propagation. The numerical model is a complete

representation of the underlying mechanisms including the exponential growth of fluctuation amplitudes and the damping mechanisms causing the system to settle to a limit cycle with constant pulsations. The phase difference between velocity fluctuations and heat transfer fluctuations was determined to 64.8° in the investigated case.

The results, however, cannot be used as a model with quantitative validity. With the coarse mesh used in that study, boundary layer effects were underresolved. The grid spacing close to the heater bands was much larger than the layer thickness assessed in Section 3.1.2. Moreover, unrealistically high temperatures had to be imposed as boundary conditions to acquire the desired thermoacoustic instabilities. This might also be attributed to the lack of spatial resolution.

3.4.4 Time Series Analysis

Föller et al. (2008) investigated the unsteady heat transfer of a heated cylinder in pulsating crossflow using numerical simulations to acquire data in combination with the identification of an impulse response based on the inversion of the Wiener–Hopf equation (Polifke et al., 2001). The approach was termed CFD/SI method, as it represents a combination of CFD and system identification. Ultimately, a finite impulse response (FIR) model was acquired for the heat transfer. They showed that the heat transfer dynamics depend strongly on the response times of the boundary layers. These time scales are reported to depend on Reynolds number. A number of distinct features were identified for the frequency response of the heat transfer, such as a maximum amplitude in heat transfer rate at frequencies greater than zero. Moreover, a discrepancy in the high-frequency range in comparison to Lighthill's predictions was found. An attempt was made to physically motivate the heat transfer behavior by qualitatively assessing the flow-field response close to the cylinder to a sudden increase in inlet velocity.

Recently, Li et al. (2016b) used the online identification of a FIR model for the control of a Rijke type burner[2]. The model was built upon the pressure measurements from a microphone and hence differs from the transfer functions based on velocity pulsations in this thesis. However, the identification method is similar, and Li et al. (2016b) were able to quickly control a loudspeaker to counteract the thermoacoustic oscillations.

[2] A Rijke tube with a Bunsen burner instead of a heated wire.

3.5 Further Literature on Heat Transfer in Unsteady Flow

This section gives a brief overview of literature regarding the wider context of the dynamics of a cylinder in pulsating crossflow. Most notably, some experimental results have been obtained for similar configurations. Very similar to pulsating crossflow is oscillating crossflow. In this case, the steady mean flow component is zero, and the amplitude is determined by the fluid displacement rather than relative to the mean flow. Flow regimes and computational methodology are, however, quite different. Another aspect of a cylinder in pulsating crossflow is the nonlinear behavior of the heat transfer at high pulsation amplitudes. Although this thesis focuses on the linear regime, i.e. small amplitudes, the nonlinear behavior is of interest for some applications. Foremost, an enhancement of the net heat transfer can be caused by high amplitude fluctuations of the free-stream.

3.5.1 Experimental Investigations of Unsteady Flow

Over the course of several decades, the pulsating flow across a cylinder has been investigated experimentally several times. Not least due to the requirements of the measurement equipment, most studies were carried out for flow in the "transition in shear layer" regime (cf. Table 2.1). Hori (1963) investigated the velocity profiles at an oscillating cylinder at $3600 \leq \mathrm{Re} \leq 9000$. Quintessence of most studies was an increase in net heat transfer (heat transfer enhancement) as a result of the pulsations. Base et al. (1981) found a dependence of the heat transfer enhancement/reduction on frequency in the range $1220 \leq \mathrm{Re} \leq 4890$. Similar experiments were carried out by Perwaiz and Base (1992, $2300 \leq \mathrm{Re} \leq 13\,500$). Moreover, the evolution of the circumferential distribution was assessed by Andraka and Diller (1985, $\mathrm{Re} = 50 \times 10^3$) and Mikheev et al. (2017, $0.4 \times 10^4 \leq \mathrm{Re} \leq 1.06 \times 10^4$, $0 < \mathrm{Sr} \leq 11$). Heat transfer enhancement up to 15 % were reported, strongly dependent on the flow condition, e.g. the Strouhal number of the pulsation. The largest deviation from the steady state occurred on the lee side of the cylinder, especially at the separation point. Sung et al. (1994) investigated the circumferential distribution of the mass transfer in pulsating flow across a cylinder at $4500 \leq \mathrm{Re} \leq 12\,450$.

Investigations at lower Reynolds numbers were carried out by Li et al. (2013, $71 \leq \mathrm{Re} \leq 282$; $1.2 \leq \mathrm{Sr} \leq 16$), Li et al. (2016a, $205 \leq \mathrm{Re} \leq 822$; $1.1 \leq \mathrm{Sr} \leq 18$), and Kikuchi et al. (2000, $\mathrm{Re} = 400$, $0 \leq \mathrm{Sr} \leq 8.6$). Li et al. (2013) also assessed the heat transfer enhancement at different inclination angles. The circumferential distribution of the Nußelt number for $\mathrm{Re} = 400$ was reported by Kikuchi et al. (2000). The increase in heat transfer is attributed to flow reversal at the lee side of the cylinder. The force of pulsating flow on a cylinder was measured by Schewe (1983) at $2.3 \times 10^4 \leq \mathrm{Re} \leq 7.1 \times 10^6$.

In a unique experiment, Lin et al. (2006) investigated the influence of pulsation on a cylinder in a water tunnel. The Reynolds numbers were in the range $1 \leq \mathrm{Re} \leq 5$, i.e. the laminar regime without recirculation.

3.5.2 Oscillating Flow

This thesis deals with pulsating flow, especially with pulsations around a steady mean flow that are small compared to the mean flow itself (c.f. Section 2.4.2). Another related topic that was investigated in the past and still is of interest is a cylinder in oscillating flow. In this configuration, the mean flow velocity is zero or small compared to the peak velocities, and the amplitude is determined via the fluid displacement. Phenomenologically the largest difference to pulsating flow is that flow reversal occurs at any given amplitude.

Idiosyncratic for investigations on oscillating flow is the use of the Keulegan-Carpenter number as frequency parameter. It is usually defined as the inverse of the Strouhal number or in terms of frequency as $2\pi/\mathrm{Sr}$.

Sarpkaya (1986) investigated a cylinder in oscillating crossflow with $\mathrm{Re} = 100$ evaluated with the maximum velocity experimentally. A threshold frequency below which the shear wave model (cf. Section 3.1.2) does not yield acceptable results was found. Other experiments were conducted by Gopinath and Harder (2000) and Iwai et al. (2004). The latter also included a numerical study and was concerned with the heat transfer enhancement in oscillatory flow. Other numerical studies were conducted by Ohmi and Usui (1982), Uzunoglu et al. (2001), and Elston et al. (2006).

3.5.3 Nonlinearity of Heat Transfer

It is emphasized that the thesis is limited to relatively small oscillation amplitudes. Specifically, the amplitude of the forced velocity perturbations was below 30 % of the mean flow velocity for all cases considered. At these amplitude levels, the dynamic response of heat transfer to imposed velocity fluctuations expressed as the relative amplitude and phase of heat flow rate oscillations, is linear. Heckl (1990) as well as Hantschk and Vortmeyer (1999) reported this behavior investigating the Rijke tube phenomenon experimentally and numerically, respectively.

Selimefendigil et al. (2012) investigated the nonlinear behavior of a cylinder in pulsating crossflow with the CFD/SI method. The nonlinear regime, i.e. at fluctuation amplitudes above 30 % of the mean flow velocity is important for the achievable amplitudes of limit cycles in a Rijke tube. The developed nonlinear models were used to predict these limit cycles (Selimefendigil and Polifke, 2011).

Selimefendigil and Polifke (2011), as well as Selimefendigil et al. (2012), have studied the transition from linear to nonlinear behavior and the application of nonlinear identification methods at fluctuation amplitudes exceeding 30 % of the mean flow velocity. Algorithms for nonlinear system identification were further developed, tested and applied to problems of heat transfer by Selimefendigil and Öztop (2013, 2014). Those studies followed a "black box" approach, as is typically the case in system identification.

3.5.4 Heat Transfer Enhancement

Numerical and experimental studies on the average heat transfer in pulsating flows across a cylinder (Andraka and Diller, 1985; Al-Sumaily and Thompson, 2013; Li et al., 2016a) have shown that the influence is negligible for amplitudes smaller than one-third of the mean velocity. In the linear regime, terms that scale with the second order of oscillation amplitude may be neglected. A change in amplitude leads then to a proportional change in the response in heat transfer. Moreover, the superposition principle applies. The overall response in heat transfer to a flow perturbation can be described as a straightforward sum over contributions from different physical mechanisms.

Papadakis and Bergeles (2001) investigated the heat transfer in pulsating flow at $\mathrm{Re}_0 = 100$, i.e. in the regime of laminar periodic vortex shedding numerically. The free-steam velocity was pulsed at several forcing frequencies up to three times the natural shedding frequency $f \leq 3.5 f_{s0}$. It was found that a lock-on of the vortex shedding to the pulsation frequency occurs at pulsation frequencies $1.5 \lesssim f \lesssim 2.4 f_{s0}$. In this case, the actual vortex shedding differs from the natural shedding frequency in a steady flow and is approximately one half of the forcing frequency. Papadakis and Bergeles (2001) assessed the heat transfer at several locations on the circumference of the cylinder. Close to the forward stagnation point up to the point of separation, the pulsations result in an increase of the root mean square (RMS) value of the Nußelt number but not the mean Nußelt number. An increase in mean value was only observed downstream of the separation point; however, the contribution to the overall heat transfer is small. The largest heat transfer enhancement was reported for a forcing frequency of $f \approx 2.4 f_{s0}$.

The effect of vortex shedding can be seen as nonlinear with respect to the forcing as the frequency of the heat transfer variation is not necessarily the same as the forcing frequency (c.f. Section 4.1.1). However, during lock-on, heat transfer and velocity pulsations occur with the same frequency (twice the vortex shedding frequency) and hence some kind of linearization occurs.

The reader should bear in mind that this thesis is not concerned with an increase (or decrease) of cycle-averaged heat transfer in pulsating or reciprocating flow, which

has been observed at large pulsation amplitudes in a number of studies (Hill and Stenning, 1960; Zhao and Cheng, 1998; Dec et al., 1992; Andraka and Diller, 1985; Selimefendigil et al., 2012; Al-Sumaily and Thompson, 2013; Li et al., 2013, 2016a). The amplitude of the imposed velocity perturbations was limited to 30 % of the mean flow velocity or less, which is in fact considerably below the threshold where changes in the average heat transfer are noticeable.

3.6 Rijke Tube

The Rijke tube is the key aspect of applications in this thesis. As mentioned above, the Rijke tube was first described phenomenologically by Rijke (1859). Rayleigh (1896) explained the thermoacoustic effect in detail by a periodic transfer of heat and a phase difference that occurs between acoustic pressure pulsations and heat transfer. The first quantification of this phase difference was proposed by Lighthill (1954). Heckl (1988, 1990) revisited the existing literature to develop mathematical models which are widely used until now. Quite a few researchers have since also tackled the Rijke tube and its mathematical description.

3.6.1 Modeling Approaches

One of the most widely used equations modeling the heat transfer between a thin wire and the surrounding fluid was given by King (1914). The heat flux is given by

$$\dot{Q} = L_w \left(T_w - T_\infty\right) \left(k + 2\sqrt{\pi\, k\, c_v\, \rho \frac{d}{2} |u|} \right), \tag{3.57}$$

where L_w and T_w denote the length and the temperature of the wire, respectively. This equation is known as King's Law and adopts the square root relationship between heat transfer and flow velocity from boundary layer theory. It should be noted, that correlations for the heat transfer as provided by Collis and Williams (1959) and Sparrow et al. (2004) (cf. Equation (2.23) and Equation (2.24), respectively) offer much better accuracy than King's Law.

Heckl (1988) linearized King's Law and modified it with a time-lagged velocity fluctuation $u'(t-\tau)$ to account for the dynamics of the heat transfer. This simple model is written as

$$\dot{Q}' = L_w \left(T_w - T_\infty\right) \sqrt{\frac{\pi\, k\, c_v\, \rho\, d}{2\,\overline{u}}}\, u', \tag{3.58}$$

which is an application of the $n-\tau$ model, is called Modified King's Law.

The model by Lighthill (1954) for low frequencies (cf. Equation (3.34)) is a first order lag model (proportional with first order time lag, PT1). The parameters are the steady-state gain K and a time constant c_τ. It is used to describe the heat transfer dynamics in conjunction with the Modified King's Law where the time constant is not used in conjunction with a PT1 model, but as the time lag of the $n-\tau$ model. The significance of this, which is essentially a linearization of Lighthill's PT1 model is discussed in Chapter 8. For the original model by Lighthill, the parameters are $K = 1/2$ and $\tau = 0.2d/u_{0,\infty}$.

Heckl (1990) introduced empirical factors to the Modified King's Law to account for the heat transfer behavior at high amplitudes. These terms cause a reduction of the heat transfer amplitudes if the velocity pulsations exceed one-third of the mean flow velocity. To account for the dynamics, again the time constant $\tau = 0.2d/u_{0,\infty}$ was used. This model will be referred to as Heckl's model in this thesis and reads

$$\dot{Q} = L_w\,(T_w - T_\infty)\left[k + 2\sqrt{\pi\,k\,c_v\,\rho\frac{d}{2}}\left(\left(1-\frac{1}{3\sqrt{3}}\right)\sqrt{\overline{u}} + \frac{1}{\sqrt{3}}\sqrt{\left|\frac{\overline{u}}{3}+u'\right|}\right)\right]. \tag{3.59}$$

The fluctuating heat flux is evaluated analogous to Equation (3.58).

3.6.2 Time Constant

Essential to the description of the thermoacoustic oscillations occurring in the Rijke tube is the phase lag between acoustic pulsations and heat transfer. The Modified King's Law (Heckl, 1988) and thus Heckl's Model (Heckl, 1990) modeled this as a fixed time lag. In Lighthill's original work (Lighthill, 1954), however, the phase lag is effectuated by a PT1 model with a time constant. This time constant is given in the form

$$\tau = c_\tau \frac{d}{u_{0,\infty}}, \tag{3.60}$$

where c_τ was evaluated to 0.2.

Most literature concerned with the Rijke tube uses a different frame of reference. Instead of wire diameter d, and unperturbed inlet velocity $u_{0,\infty}$, the length of the Rijke tube L and the speed of sound a are used for non-dimensionalization. Hence, the time constant is given by

$$\tau = c_\tau^* \frac{L}{a} \tag{3.61}$$

and translates to Lighthill's frame of reference (which is also used in this thesis) by

$$c_\tau = c_\tau^* \frac{L}{d}\frac{u_{0,\infty}}{a} = c_\tau^* \frac{L}{d}\mathrm{Ma}. \tag{3.62}$$

For typical working conditions the factor $\mathrm{Ma}\,L/d$ is expected to be approximately of order one.

3.6.3 Literature Survey

The literature survey in Table 3.1 gives an overview of some of the literature on electrically heated Rijke tubes. The working conditions in terms of mean flow Reynolds number and Strouhal number are also detailed. The Reynolds number and the Strouhal number refer to the diameter of the wire. The frequency used was that of the occurring oscillations. If no specific frequency was given, the fundamental frequency of the tube used in the experiments or computations was considered.

If a model was used for the unsteady heat transfer, this is listed in the table including the time constant c_τ necessary for the dynamics of the heat transfer. Unfortunately, many publications are unspecific about the frame of reference that has been used. The column for the time constant was assembled to the best of the author's abilities.

Publication	Model for unsteady heat transfer	Re	Sr	c_τ
Kwon and Lee (1985)	CFD of wire	N/A	N/A	N/A
Heckl (1988)	Modified King's Law	19	0.8	0.2
Heckl (1990)	Heckl's model	19	0.8	0.2
Bisio and Rubatto (1999)	reference to Bayly (1985) and Kwon and Lee (1985)	N/A	N/A	N/A
Hantschk and Vortmeyer (1999)	underresolved CFD of Rijke tube	8.3	1.9	N/A
Blonbou et al. (2000)	neural network	N/A	N/A	N/A
Bittanti et al. (2002); Agostino et al. (2002)	turbulent mixing model	8	0.58	$\tau \sim d^{1/3}/u^{2/3}$
Matveev (2003a,b)	Reference to Bayly (1985) and Kwon and Lee (1985)	2.3	4.0	N/A
Culick (2006)	$n-\tau$, reference to Kwon and Lee (1985)	N/A	N/A	N/A
Deng et al. (2007)	underresolved CFD of Rijke tube	N/A	N/A	N/A
Balasubramanian and Sujith (2008)	Heckl's model	N/A	N/A	$0.31 \leq c_\tau^* \leq 1.4$

Publication	Model for unsteady heat transfer	Re	Sr	c_τ
Mariappan et al. (2010); Mariappan and Sujith (2011)	CFD of wire	20	~6.3	N/A
Subramanian et al. (2010)	Heckl's model	N/A	N/A	$0.15 < c_\tau^* < 0.85$
Juniper (2011a,b)	Heckl's model	N/A	N/A	$c_\tau^* = 0.02$
Gelbert et al. (2012)	PT1	21	0.74	0.4
Xu et al. (2012)	CFD, heater as porous medium	N/A	N/A	N/A
Subramanian et al. (2013)	Heckl's model	N/A	N/A	$0 \lesssim c_\tau^* \lesssim 1$
Gopalakrishnan and Sujith (2014)	N/A(experimental)	0.5 – 1.3	1.5 – 2.9	N/A
Sayadi et al. (2014)	Heckl's model	N/A	N/A	$0 \lesssim c_\tau^* \lesssim 1$
Surendran and Heckl (2014)	$n-\tau$, no mean flow	N/A	N/A	$\tau = 1.5 \times 10^{-4}$ s
Zhao and Reyhanoglu (2014)	Heckl's model	N/A	N/A	$c_\tau^* = 0.8, 0.025$
Olgac et al. (2014a,b); Zalluhoglu et al. (2016); Zalluhoglu and Olgac (2016a,b)	PT1	N/A	N/A	N/A
Epperlein et al. (2015)	PT1	52	1.6	N/A
Mariappan et al. (2015)	$n-\tau$	4.2	1.2	0.2
Yang et al. (2015)	Heckl's model	1.7	13	$c_\tau^* = 0.025, 0.01$
Aguilar et al. (2016)	$n-\tau$	N/A	N/A	$\tau = 0.001$ s
de Andrade et al. (2016)	discrete PT1	N/A	N/A	N/A
Gopalakrishnan et al. (2016)	Linearized $n-\tau$	N/A	N/A	N/A
Hosseini et al. (2016)	$n-\tau$	N/A	N/A	$0 \leq \tau \leq 0.003$ s

Publication	Model for unsteady heat transfer	Re	Sr	c_τ
Li et al. (2016c)	Heckl's model	16	1.2	4
Orchini et al. (2016)	Modified King's Law	N/A	N/A	0.2
Rigas et al. (2016); Jamieson et al. (2016, 2017)[3]	N/A (experimental)	3	7.9	N/A
Etikyala and Sujith (2017)	N/A (experimental)	1.3 – 7.8	1.3 – 2.5	N/A
Mohan and Mariappan (2017)	Heckl's model	6.9	2.0	0.3 – 1.5
Sui et al. (2017)	N/A (experimental)	5.8	4.4	N/A
Yang et al. (2017)	Heckl's model, reference to Lighthill (1954)	N/A	N/A	0.2

Table 3.1: Survey of the Recent Literature on the Rijke Tube.

The values in Table 3.1 show that typical Reynolds numbers for the mean flow around a heated wire investigated in studies are in the range $[1,50]$. Strouhal numbers are usually of order one but can be as high as 12.6. This underlines the necessity for a model for the heat transfer dynamics covering these ranges, which cannot be provided by the existing models, e.g. by Lighthill (1954) and Bayly (1985).

[3] Private communication, 2016

4 Linear Dynamic Systems

In science and engineering, it is in many cases beneficial to divide problems in smaller parts and concentrate on one specific part instead of trying to find a description for a phenomenon encompassing all different aspects simultaneously. Such a part is called a *system*, whereas the remaining aspects represent the environment (Pintelon and Schoukens, 2012). The concept of systems is widely used in many research areas (Söderström and Stoica, 1989), e.g. physics, biology, engineering, economics (Heij et al., 2006; Goldberger, 1991) as well as in social sciences and psychology (Köhler, 2008). Within a system, different variables influence each other on multiple time and space scales (Keesman, 2011; Ljung, 1999). A system may interact with the environment (Pintelon and Schoukens, 2012) through *signals* and is then referred to as open system (Keesman, 2011).[1] If signals change over time (Verhaegen and Verdult, 2007), the system is specified as a dynamic system.

Signals can be distinguished into *inputs*, *outputs*, and *disturbances*. Outputs y are the products or the responses of a system. Hence, they are called endogenous. These signals are observable or measurable by an agent. Inputs u are exogenous signals that can be manipulated by an agent. Disturbances cannot be manipulated. They occur from the influence of the environment on the system, within the system itself, or are caused by the errors in measurements. A representation of a system with input and output is given in Figure 4.1.

Systems can have multiple inputs and multiple outputs interacting with each other. Systems with only one input and one output are denoted single-input single-output (SISO) systems. Accordingly, multi-input multi-output (MIMO) systems have more than one input and more than one output. Analogously, systems can also be termed SIMO and MISO (Hespanha, 2009).

This thesis is mostly concerned with SIMO systems. The input is the pulsation of the freestream velocity (as Re') and outputs are heat transfer fluctuation (as Nu') and shear stress fluctuation (as c_f'). However, this particular SIMO system can be split into two SISO systems by considering only one output at a time. Therefore, descriptions are given for SISO systems, if not marked otherwise, but may also apply—with some generalization—to MIMO systems.

To understand and describe a complex system, occurring in nature or technical devices, a *model* of some sort is sought. Modeling is used in many branches of science

[1] In contrast to closed systems which do not interact with the environment according to this definition.

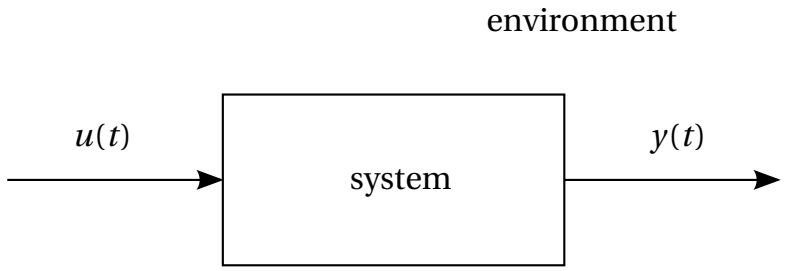

Figure 4.1: Representation of a General (Open) System. Input(s) u and output(s) y

and engineering (Söderström and Stoica, 1989). The main aims are to aid in the design process as well as to estimate, control, and monitor systems (Tangirala, 2014; Söderström and Stoica, 1989).

Söderström and Stoica (1989) distinguish three main types of models: (1) mental, intuitive or verbal models, (2) graphs and tables, and (3) mathematical models. Graphs and tables may be used to represent systems in a comprehensible manner. Differential and difference equations (and similar representations) are mathematical models. However, many different ways to classify systems exist and the above-mentioned list is by far not exhaustive.

In this chapter, basic modeling concepts of linear time invariant dynamic models are introduced in Section 4.1. Subsequently in Section 4.2, different concepts of data used in the modeling process are presented. These concepts lead to different model representations demonstrated in Section 4.3. Section 4.4 deals with the system identification process employed to build models from acquired data and finally techniques to validate identified models are shown in Section 4.5. The last section of this chapter (i.e. Section 4.6) shows how system theory is applied to the dynamics of heat transfer and skin friction of a cylinder in pulsating crossflow.

4.1 Linear Time Invariant Systems

The notion of a *linear* and *time invariant* (LTI) system is important for the application of system theory. A large set of methods exists to describe and process this type of system. The assumptions involved—linearity and time invariance—are often justified, or situations can be found when an LTI description is sufficiently accurate. In these cases, considerations based on linear theory lead to good results (Ljung, 1999).

4.1.1 Definition

An LTI system is defined by two characteristics: linearity and time invariance. Time invariance implies system characteristics do not change with time and thus its response to a certain input signal does not depend on absolute time (Ljung, 1999). This means that an arbitrary operator f, representing the system dynamics, applied to a signal shifted in time yields the same result but with the same shift in time as the signal. This can be represented by

$$\text{If } u(t) \xrightarrow{f} y(t) \text{ , then } u(t-\tau) \xrightarrow{f} y(t-\tau) \tag{4.1}$$

where u and y denote input time series and result time series of a time invariant operation f and τ is a constant shift time (Tangirala, 2014).

A system, represented by the operator f, is considered linear if its response to a linear combination (sum) of inputs is the same as the linear combination of the responses to the individual inputs (Ljung, 1999). This holds, even if a constant scaling factor is applied and can be written by

$$f(a\,u_1 + u_2) = a\,f(u_1) + f(u_2) \tag{4.2}$$

where u_1 and u_2 are the variables, f is the linear operation, and a is a constant (Tangirala, 2014). Linearity implies that the principles of homogeneity (multiplication with a constant factor) and superposition (addition of inputs) hold. The latter explicitly allows any complex time series to be decomposed into simpler signals, e.g. individual impulses.

The linearity requirement may be violated due to constant offsets in input and output. In this case, linear models can relate deviation variables that vary around a nominal operating point. These offsets are estimated (mean) and removed to achieve a linear equation, e.g.

$$(y - y_0) = f(u - u_0) \tag{4.3}$$

where y_0 and u_0 denote the (quasi-)steady state of output and input, respectively (Tangirala, 2014). Generally, the linear model may consist of a first-order Taylor's series approximation of the nonlinear system around a steady state (cf. Section 2.4) (Tangirala, 2014).

4.1.2 Properties

LTI systems exhibit two general properties important for modeling purposes: *causality/non-causality* and *stability/instability*. A suitable model has to reflect these properties, e.g. a model should be non-causal if the system is non-causal.

Causality

If the response at a certain time depends only on the input up to this instant in time, i.e. it does not depend on ”future“ values, then the system is called causal. A system in which the past, present, and future inputs are involved is referred to as non-causal (Ljung, 1999).

Stability

The assumption of stability implies that the response of a system will not grow indefinitely. More precisely, an LTI system is said to be stable, if all bounded-inputs yield bounded-outputs (Tangirala, 2014). This is the concept of a BIBO stable system which is a standard definition for LTI system. BIBO stability is denoted by

$$\|y(t)\| < \infty \quad \text{for all} \quad \|u(t)\| < \infty . \tag{4.4}$$

This is important for the modeling process as a model for a stable system should also be stable (Tangirala, 2014). If a steady state exists, this indicates that the system is stable (Tangirala, 2014).

4.1.3 Convolution Model and Impulse Response

A model should relate an input (function) to an output (function) by a mathematical operation. For an LTI system, this can be achieved using the *convolution* operation. From the pointwise multiplication of a function with another (shifted) function integrated over the shift variable a third function results. This can be written as

$$y(t) = \int_{-\infty}^{\infty} g(\tau)\, u(t-\tau) \mathrm{d}\tau = g(t) * u(t) . \tag{4.5}$$

This type of model is referred to as convolution model and is the most fundamental representation of an LTI system (Tangirala, 2014). The third function involved, $g(\tau)$, is called *impulse response function*. This is due to the fact that this is the response generated by the system when excited with a unit impulse (Dirac δ function, the neutral element of the convolution) defined by

$$\delta(t) \equiv 0 \text{ for all } t \neq 0 \text{ and } \int_{-\infty}^{\infty} \delta(t) \mathrm{d}t = 1 . \tag{4.6}$$

The impulse response exhaustively describes the dynamic behavior of an LTI system (Keesman, 2011). It is equivalent to the concept of Green's Functions (Duffy, 2001). For a causal system with zero initial conditions, the convolution model is given by

$$y(t) = \int_0^t g(\tau)\, u(t-\tau) \mathrm{d}\tau \tag{4.7}$$

using only information from a start time "0" up to the current time t.

The foundation of the impulse response function is the superposition principle. It states that the response of a linear system to the simultaneous action of several causes is obtained by first determining the effects of the separate causes and then adding them in the proper manner (cf. definition of linearity and time invariance).

If a system is BIBO stable, then the impulse response is absolutely convergent (Tangirala, 2014). This can be expressed as

$$\int_{-\infty}^{\infty} g(t) \mathrm{d}t < \infty. \tag{4.8}$$

4.1.4 Transfer Function

Causal convolution in the time domain is equivalent to multiplication in the *Laplace domain* (Keesman, 2011). Applying the Laplace transform (Phillips et al., 2008) defined by

$$F(s) = \mathscr{L}\{f(t)\} = \int_0^{\infty} f(t)\, \mathrm{e}^{-st} \mathrm{d}t \tag{4.9}$$

with the complex-valued frequency parameter $s = \sigma + i\omega$ to input $u(t)$, output $y(t)$, and impulse response function $g(t)$, Equation (4.5) can be written as

$$Y(s) = G(s) \cdot U(s)\,. \tag{4.10}$$

The frequency parameter $s \in \mathbb{C}$ is a complex-valued quantity with the angular frequency ω as imaginary part and the growth rate σ as real part. $G(s)$, which is the Laplace transform of the impulse response function $g(t)$, is called *transfer function*.

For convenience, the notation

$$y = Gu \tag{4.11}$$

is introduced. It reads "the linear operator G, representing the LTI system, is applied to u". The operator G has to be in the same domain as the signals y and u. This is the fundamental representation of dynamic behavior used in this thesis.

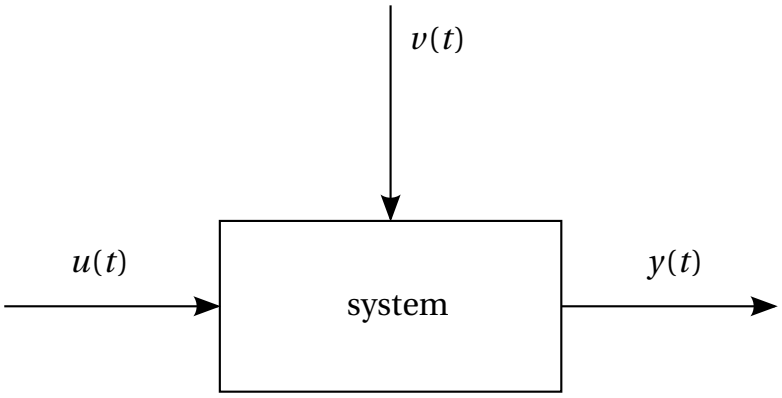

Figure 4.2: Representation of a General (Open) System with Disturbance. Input(s) u, output(s) y, and a disturbance v. Based on Söderström and Stoica (1989).

4.1.5 Disturbances

In dealing with real systems, the mapping from input to output may not be perfect, yet disturbances can influence the system. Among these disturbances are measurement noise and uncontrollable inputs. In general, they represent the influence of the environment on the system. These disturbances have to be taken into account as they effect the quality of the model.

Different authors categorize disturbances in various ways, but most distinguish two types. An input disturbance w is characterized by the fact that it is an exogenous signal originating from the environment and directly affecting the behavior of the system (Keesman, 2011). It can be measured (Ljung, 1999; Tangirala, 2014) and it has external causes (Isermann and Münchhof, 2011), i.e. the influence of the environment on the system. In contrast, the output disturbance v (Keesman, 2011) is an exogenous signal that affects the output but cannot be manipulated like the input. This disturbance is not measured (Tangirala, 2014), but may be observed due to its impact on the output (Ljung, 1999). It can also be interpreted as internal disturbance (Isermann and Münchhof, 2011). A distinction between measured disturbance w and inputs u is often less important for the system identification process (Ljung, 1999). Thus, w is omitted in the following sections.

Figure 4.1 above depicts a system that is only influenced by inputs. This corresponds to a purely *deterministic* model. However, in the scope of disturbances, a more realistic system is shown in Figure 4.2. A *stochastic* disturbance $v(t)$ is included to account for unpredictable signals.

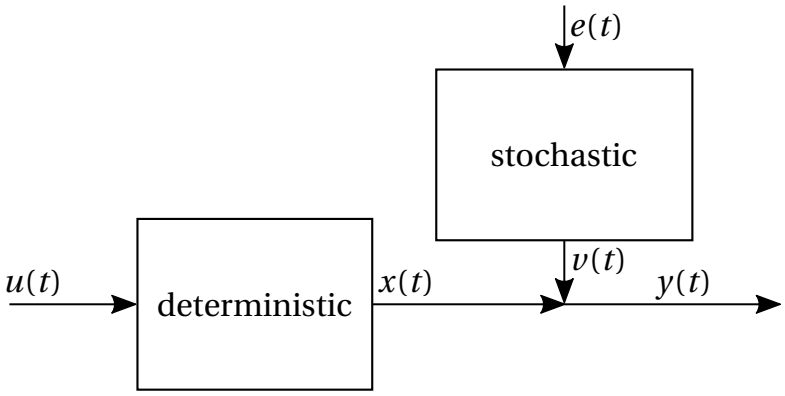

Figure 4.3: Representation of a General Model for an LTI System. Input(s) u, output(s) y, disturbance v, undisturbed output $x(t)$, and white noise $e(t)$. Based on Tangirala (2014).

Modeling a System with Disturbances

To account for disturbances in the model representations of any given LTI system, disturbances $v(t)$ are added to the right-hand side of Equation (4.5). The output $y(t)$ is then the sum of a disturbance-free output $x(t)$ and the disturbance written as

$$y(t) = x(t) + v(t)\,. \tag{4.12}$$

The noise free deterministic model is given by

$$x(t) = Gu(t) \tag{4.13}$$

where G is the representation of the deterministic part of the system, i.e. transfer function, applied to the input. The disturbance itself is unpredictable, i.e. it originates from *white noise*, but may be *colored*. This is denoted by

$$v(t) = He(t) \tag{4.14}$$

where H is a model for the noise spectrum applied to the white noise sequence $e(t)$. Figure 4.3 depicts these relationships.

Following Tangirala (2014, p. 14), the *continuous time* description is widely used for deterministic systems. Stochastic influences, i.e. disturbances, are quantified in a *discrete time* frame as they are picked up by sensors usually working in discrete time. This is in accordance with Ljung (1999, p. 233) who regards continuous time white noise descriptions as delicate mathematical objects. He suggests dealing with hybrid models, where the noise is handled in discrete time. Nevertheless, Beygi and Dounavis (2012) reported an approach to include noise modeling using an instrumental variable method. In this thesis a purely discrete time point of view was adopted whenever disturbance or noise modeling was of importance.

White Noise and Colored Noise

The disturbance v is generally any kind of signal not part of the deterministic system and therefore, by definition, unpredictable. To account for this, it is deduced from a random signal $e(t)$ and filtered by a model for the stochastic part H (c.f. Equation (4.14)).

The random signal is often modeled as white noise (Tangirala, 2014). It is a sequence of uncorrelated variables with zero mean (stationary) and finite variance. A useful assumption is that the variables follow a normal distribution $\mathcal{N}$ with variance σ_e^2. This is denoted by

$$e[k] \sim \mathcal{N}(0, \sigma_e^2) \tag{4.15}$$

and is called Gaussian white noise (GWN).

Signal–to–Noise Ratio

The *signal–to–noise ratio* (SNR) is a measure for the strength of the (true) response of the system compared to the noise. A high SNR is paramount for all estimation methods to achieve good models. The overall SNR is evaluated as the ratio of the variances of output and noise given by

$$\mathrm{SNR} = \frac{\sigma_x^2}{\sigma_v^2}. \tag{4.16}$$

A frequency dependent estimate can be found by using the asymptotic ensemble average of the *power spectral density* (PSD) γ. The SNR is defined in frequency domain as

$$\mathrm{SNR}(\omega) = \frac{\gamma_{xx}(\omega)}{\gamma_{vv}(\omega)} \tag{4.17}$$

where γ_{xx} and γ_{vv} are the PSDs of the noise-free output and the noise, respectively (Tangirala, 2014).

Coherence

The *coherence* is used to determine if a linear relationship between two signals exists. It is given by

$$|\kappa_{yu}(\omega)|^2 = \left| \frac{\gamma_{yu}(\omega)}{\sqrt{\gamma_{uu}(\omega)\gamma_{yy}(\omega)}} \right|^2 = \frac{1}{1 + 1/\mathrm{SNR}(\omega)}. \tag{4.18}$$

If the coherence is not unity $|\kappa_{yu}(\omega)|^2 \neq 1$ this can cave two reasons. (1) u and y depend on each other non-linearly or (2) the linear relationship is hidden by a high noise level. This is shown in Equation (4.18), where the coherence is linked to the SNR. These measures are used to determine a priori if good estimates can be expected at certain frequency ranges when estimating an LTI model.

4.2 Data Basis

Information on systems can be acquired from various sources and in different frameworks. Most commonly, it can be distinguished between time and frequency domain as well as between discrete and continuous data. These concepts are important for data handling and data manipulation.

4.2.1 Continuous and Discrete Time Data

Time is usually experienced as continuous and variables evolving over time are thus modeled as continuous variables. Many concepts, i.e. differential equations, are based on the notion of continuity. However, measurements are usually snapshots taken at certain instants in time. Successive measurements may be acquired distinct intervals of time apart. Thus, the variable is observed at discrete sampling instants. This concept, in contrast to continuous time, is called discrete time. In numerical computations of unsteady processes, only solutions at discrete instants in time are calculated.

Sampling

The transformation from continuous time to discrete time is called *sampling*. Discrete values are picked from a continuous time series in intervals called *sampling times*. In the case of periodic sampling, the temporal spacing between sampling instants is constant. This time T_s is referred to as the *sampling interval* with $[T_s]$ = time units per sample. It can be seen as one time unit. Any sampled instant is written in continuous time by $t = kT_s$ with $k = 0, 1, \ldots, N-1$ where N is the total number of samples. Accordingly, a sampling frequency is defined by $F_s = 1/T_s$ with $[F_s]$ = samples/time (Tangirala, 2014) and $\omega_s = 2\pi F_s = 2\pi/T_s$ for the angular frequency, respectively.

One of the most important statements in signal processing is the Nyquist-Shannon sampling theorem (Åström and Wittenmark, 1997). It states that for a given sampling frequency F_s perfect reconstruction of a signal (in continuous time) is possible for a *bandlimit* of $F_{\mathrm{Ny}} = F_s/2$. The term bandlimit refers to a finite frequency above

which the power spectral density of the signal is zero. The frequency F_{Ny} is called the *Nyquist frequency*. Similarly, the *Nyquist rate*, at which a bandlimited signal has to be sampled, is $2F_{\mathrm{Ny}}$.

If the sampling theorem is violated, *aliasing* occurs. Frequencies higher than the Nyquist frequency appear as lower frequencies falsifying the signal. This defect cannot be recovered a posteriori and has to be avoided, e.g. by low-pass filtering a signal before (down-)sampling. (Tangirala, 2014)

Sampling (with zero-order hold) has an impact on the definition of causality of a system. Although a system is still considered causal, if no future inputs affect the output, the term strict causality is introduced (Tangirala, 2014). It also excludes instantaneous effects at time $k = 0$ which are "unphysical" in a sense that if input and output are measured at the same instant, any signal would have to travel infinitely fast in order to cause a response at $k = 0$.

Reconstruction

A common way to transform a discrete time signal to continuous time is to hold the discrete value for T_s and then assume the next discrete value. This is called zero-order hold (ZOH). Analogously, the first-order hold (FOH) interpolates linearly between two successive values. This, however, is only possible, if the next value is already known.

4.2.2 Frequency Domain

In contrast to the time domain, the frequency domain does not quantify the evolution of a signal but the recurrence of patterns. The most versatile representation of the frequency domain is the *s-domain* or Laplace domain. For periodic signals, i.e. a superposition of sine waves, the Fourier transform was established. In the discrete framework, both concepts are represented by the *Z-domain* and the *discrete Fourier transform*, respectively.

Laplace Domain

A signal in s-domain is the function of a complex-valued frequency variable $s = \sigma + \mathrm{i}\omega$, where σ is a growth rate specifying the (exponential) change in amplitude and ω is the frequency. The Laplace transform converts a function in the time domain to the frequency domain. It is defined in Equation (4.9) and (originally) restricted to functions of t with $t > 0$ (unilateral Laplace transform). The inverse Laplace transform is denoted $\mathscr{L}^{-1}$.

Fourier Transform

The continuous Fourier transform is similar to the Laplace transform with two major differences: The Fourier transform is evaluated for $-\infty < t < \infty$ rather than starting at zero, which would be equivalent to a bilateral Laplace transform. Furthermore, the complex-valued argument s is reduced to $i\omega$, i.e. the growth rate $\sigma = 0$. Thus, it can only represent stable systems (Tangirala, 2014). The Fourier transform is defined as

$$\hat{f}(\omega) = \mathscr{F}\{f[k]\} = \int_{-\infty}^{+\infty} \mathrm{e}^{-\mathrm{i}\omega t} f(t)\mathrm{d}t\,. \tag{4.19}$$

The result of a Fourier transformation is called the frequency domain representation of $f(t)$. It can be interpreted as the amplitude and the phase shift at a certain frequency ω.

In discrete time, the discrete-time Fourier transform (DTFT) exists. The DTFD formally requires an infinitely long input signal. Hence, for computational purposes, the signal is assumed to be periodic, and the corresponding technique is called discrete Fourier transform (DFT) given by

$$\hat{f}_N(\omega) = \frac{1}{\sqrt{N}} \sum_{k=0}^{N-1} f[k]\,\mathrm{e}^{-\mathrm{i}\omega_d l} \tag{4.20}$$

for a sampled signal $f[k]$) with $k = 0, 1, 2, \ldots, N-1$. Discrete angular frequency is given by $\omega_d = 2\pi l/N$ with $l = 0, 1, 2, \ldots, N-1$. Several computationally very efficient algorithms called fast Fourier transform (FFT) had been developed to perform the DFT (Phillips et al., 2008).

The squared magnitude of the Fourier transform scaled with the number of samples $|\hat{f}(\omega)|^2/N$ is called *periodogram*. It is an estimate of the power spectral density (PSD) γ_{ff} of $f(t)$. Similar techniques, like Welch's PSD estimate, deliver smooth values for the PSD.

Z-Domain

Like the Laplace transform for the continuous time, a conversion from discrete time to a complex-valued frequency domain representation exists. It is called (unilateral) Z-transform and is defined by

$$F[z] = \mathscr{Z}\{f[k]\} = \sum_{k=0}^{\infty} f[k] z^{-k}\,. \tag{4.21}$$

Substituting $z = \mathrm{e}^{sT_s}$ shows that it is equivalent to the Laplace transform in discrete time. z^{-1} can be seen as e^{-sT_s}, which is the Laplace transform of a unit delay, thus z^{-1} can be interpreted as a delay operator (Keesman, 2011).

The DFT can be achieved using $z = e^{i\omega T_s}$ and the bilateral Z-transform summing from $-\infty$ to ∞.

4.2.3 Transformations Between Laplace- and Z-Domain

The transformation between the discrete Z-domain and the continuous s-domain is achieved by using numerical approximations. The most basic method is Euler's approximation (Ljung, 1999)

$$s \approx \frac{z-1}{T_s} \qquad \text{and} \qquad z \approx 1 + sT_s\,. \tag{4.22}$$

Tustin's method uses bilinear transform to approximate this relationship with (Ljung, 1999; Tangirala, 2014)

$$z \approx \frac{1+sT_s/2}{1-sT_s/2} \qquad \text{and} \qquad s \approx \frac{2}{T_s}\frac{z-1}{z+1}\,. \tag{4.23}$$

Tustin's method is a conformal mapping preserving stability. Features in the transfer function may shift in frequency but neither in gain nor phase. This frequency shift is negligible at low frequencies but substantial at frequencies close to the Nyquist frequency. An overview of the relations between different domains and transformation summarizing this section is given in Figure 4.4.

4.3 Representations of LTI Systems

Transformations between different types of data and mathematical manipulations allow various representations of LTI systems. These representations, although equivalent in most aspects, can have advantages for certain applications. All representations shown in this thesis are of input-output type. Other types, e.g. state-space representations will not be discussed here.

4.3.1 Continuous Time Transfer Function

The continuous time transfer function was introduced in Section 4.1.4 as

$$Y(s) = G(s) \cdot U(s)\,. \tag{4.10}$$

It is often used to represent deterministic systems. Disturbances are not regarded in this approach.

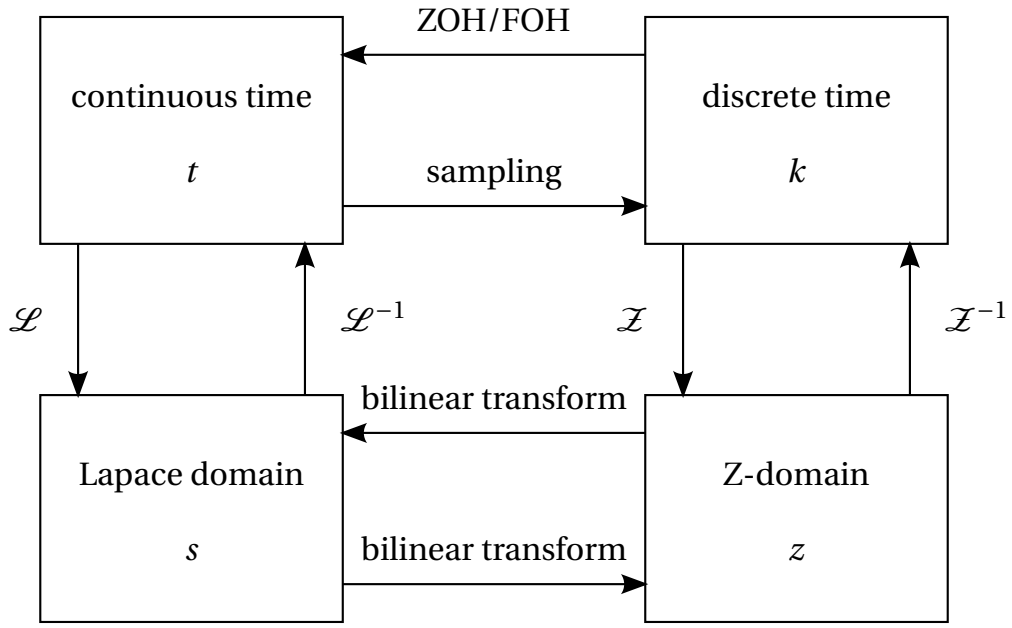

Figure 4.4: Overview of Different Domain Representations. The transforms linking these representations are included.

The most common mathematical representation is a rational function, i.e. a fraction of two polynomials in the frequency parameter s:

$$G(s) = \frac{b_m s^m + \cdots + b_1 s + b_0}{a_n s^n + a_{n-1} s^{n-1} + \cdots + a_1 s + a_0} = \frac{\sum_{i=1}^{m} b_i s^i + b_0}{\sum_{j=1}^{n} a_j s^j + a_0} \tag{4.24}$$

where $\{b_i\}$ and $\{a_j\}$ are the (usually real valued) model *coefficients* (*parameters*) of numerator and denominator, respectively.

The roots of the numerator polynomial and denominator polynomial are the *zeros* and *poles* of the transfer function, respectively. They provide insight on certain properties of the transfer function, e.g. information on stability. Factorization of Equation (4.24) yields

$$G(s) = K \cdot \frac{(s-\beta_1)(s-\beta_2)\cdots(s-\beta_m)}{(s-\alpha_1)(s-\alpha_2)\cdots(s-\alpha_n)} = K \frac{\prod_{i=1}^{m}(s-\beta_i)}{\prod_{j=1}^{n}(s-\alpha_j)} \tag{4.25}$$

where $\{\beta_i\}$ are the zeros and $\{\alpha_j\}$ the roots of the transfer function. The coefficient K represents a constant scaling factor. In contrast to the polynomial coefficients, roots and poles are often complex-valued.

Using partial fraction decomposition, the continuous time transfer function (Equation (4.24)) can be written as

$$G(s) = \frac{r_1}{s-\alpha_1} + \frac{r_2}{s-\alpha_2} + \cdots + \frac{r_n}{s-\alpha_n} + d = \sum_{j=1}^{n} \frac{r_j}{s-\alpha_j} + d\,. \tag{4.26}$$

Here, $\{\alpha_j\}$ are again the poles of the transfer function. The residues of the decomposition are denoted $\{r_j\}$ and a constant additive component d exists. It denotes the response at infinite frequency $G(s \to \infty) = d$ and is usually zero in any system occurring in nature. However, models including a non-vanishing coefficient d may be valid in a certain frequency range and may possess other desirable features like better accuracy at lower order N. Note that $d = 0$ corresponds to $b_0 = 0$ in the polynomial representation (Equation (4.24)).

4.3.2 Discrete Time Transfer Function

Similar to the continuous time approach but including disturbances, the general discrete time model is given by

$$y[k] = G(q)\,u[k] + H(q)\,e[k]\,. \tag{4.27}$$

Choosing polynomials to model the dynamics, the most general description of an input-output system in discrete time is given by

$$A(q)\,y[k] = \frac{B(q)}{F(q)}\,u[k-n_k] + \frac{C(q)}{D(q)}\,e[k] \tag{4.28}$$

with the polynomials

$$A(q) = 1 + a_1 q^{-1} + a_2 q^{-2} + \cdots + a_{n_a} q^{-n_a}\,, \tag{4.29}$$

$$B(q) = b_0 + b_1 q^{-1} + b_2 q^{-2} + \cdots + b_{(n_b-1)} q^{-(n_b-1)}\,, \tag{4.30}$$

$$C(q) = 1 + c_1 q^{-1} + c_2 q^{-2} + \cdots + c_{n_c} q^{-n_c}\,, \tag{4.31}$$

$$D(q) = 1 + d_1 q^{-1} + d_2 q^{-2} + \cdots + d_{n_d} q^{-n_d}\,, \text{ and} \tag{4.32}$$

$$F(q) = 1 + f_1 q^{-1} + f_2 q^{-2} + \cdots + f_{n_f} q^{-n_f}\,. \tag{4.33}$$

The shift operator ($q^{-n}x[k] = x[k-n]$) is used to relate to past inputs and outputs. The parameters of the model are denoted by $\{a_i\}$, $\{b_j\}$, $\{c_k\}$, $\{d_l\}$, and $\{f_m\}$. The constants n_a, n_b, n_c, n_d, and n_f are the numbers of free parameters each the polynomial. They correspond to the model orders, except in the case of B, where the order is $n_b - 1$. This is due to a free parameter, denoted by b_0, corresponding to an instantaneous feedthrough from input to output similar to d in Equation (4.26). n_k is a time delay which is assumed zero in all models here and therefore omitted henceforth.

Note that at least A or D and F must be unity in order to maintain uniqueness of the representation. Additionally, if no model for the disturbance is sought, C and D may be set to unity. The shift operator q is directly linked to the z variable of the Z transform introduced in Section 4.2.2 and any method or rule directly applies.

4.3.3 Unit Impulse Response

The *unit impulse response* is a time domain model. It shows the response to the Dirac delta function as defined in equation (4.6) in continuous time. The equivalent in discrete time is a unit impulse:

$$u_\delta[k] = \begin{cases} T_s, & k = 0 \\ 0, & k \neq 0 \end{cases}. \tag{4.34}$$

The convolution model in discrete time can be written as

$$y[k] = \sum_{n=-\infty}^{\infty} g[n]\, u[k-n]\,. \tag{4.35}$$

Physically, the impulse response can be interpreted as contribution of the input at each individual instant in time to the immediate output.

4.3.4 Unit Step Response

Similarly to the unit impulse response, the *unit step response* gives the cumulated contribution at each instant in time. The step response is the output acquired in answer to a Heaviside step function given by

$$\Theta(t) = \begin{cases} 0, & t < 0 \\ 1, & t \geq 0 \end{cases}. \tag{4.36}$$

Inserting in the convolution equation yields

$$y_\Theta(t) = \int_{-\infty}^{\infty} g(\tau)\,\Theta(t-\tau)\mathrm{d}\tau\,. \tag{4.37}$$

The Heaviside step function Θ is the integral of the Dirac delta function. Analogously, the step response is the integral of the impulse response. Assuming the system is causal ($g(t<0)=0$), the step response is given by

$$y_\Theta(t) = h(t) = \int_0^t g(\tau)\mathrm{d}\tau\,. \tag{4.38}$$

In discrete time, the unit step function is given by

$$u[k] = \begin{cases} 0, & k < 0 \\ 1, & k \geq 0 \end{cases} \tag{4.39}$$

and the step response is therefore, for a causal system, computed with

$$h[k] = \sum_{n=0}^{k} g[n] \,. \tag{4.40}$$

The step response is an important time domain model, because it is rather easy to obtain in most cases, e.g. when the SNR is not too low. In the scope of CFD, much better results are obtained using a step input instead of an impulse. The impulse response (i.e. the convolution model) can always be acquired by computing the derivative $g = (\mathrm{d}h)/(\mathrm{d}t)$, e.g. using finite differences.

$$g[k] = \frac{h[k] - h[k-1]}{T_s} \,. \tag{4.41}$$

Information on three main characteristics of a system can be deduced from the step response. The *steady-state gain* K, also referred to D.C. gain in the context of electronic circuits, is given by

$$K = h[k \to \infty] \,. \tag{4.42}$$

It is also equal to the frequency response in the low frequency limit $G(s \to 0)$.

The characteristic time constant of a system c_τ can be acquired from the *rise time*. Although multiple time scales may play a role in a system, a first order approximation, with one dominant time scale, is the time the system needs to reach 63.21 % ($1 - \mathrm{e}^{-1} = 0.6321$) of the steady-state gain K

$$c_\tau = h^{-1}[0.6321K] \,. \tag{4.43}$$

Another common definition, the rise time from 10 % to 90 % of the steady-state gain is not investigated further in this thesis.

The third important characteristic is the *time delay*, i.e. the time until the output h is significantly different from zero. No delay is expected for the systems examined in this thesis hence no attention is given to this property.

4.3.5 Frequency Response

The frequency response is based on the response to a sinusoidal input given by

$$u(t) = A\,\mathrm{e}^{\mathrm{i}\omega t} \tag{4.44}$$

with constant amplitude A and frequency ω. The response is given by

$$y_\omega(t) = A \int_{-\infty}^{\infty} g(\tau)\, \mathrm{e}^{\mathrm{i}\omega(t-\tau)}\, \mathrm{d}\tau\,. \tag{4.45}$$

Frequency Response Function

The frequency response function is deduced from Equation (4.45) by expanding the exponent of the exponential function:

$$y_\omega(t) = A\mathrm{e}^{\mathrm{i}\omega t} \int_{-\infty}^{\infty} g(\tau)\, \mathrm{e}^{-\mathrm{i}\omega\tau}\, \mathrm{d}\tau\,. \tag{4.46}$$

The term $A\mathrm{e}^{\mathrm{i}\omega t}$ is the original input and therefore the response function can be written by

$$G(\mathrm{e}^{\mathrm{i}\omega}) = \int_{-\infty}^{\infty} g(\tau)\, \mathrm{e}^{-\mathrm{i}\omega\tau}\, \mathrm{d}\tau\,. \tag{4.47}$$

It is linked to the Laplace transform of the impulse response with $s = \sigma + \mathrm{i}\omega$ through $\sigma = 0$, i.e. zero growth rate.

Bode Plot

The *Bode plot* consists of a magnitude plot $|G(\mathrm{i}\omega)|$ and a phase plot $\angle G(\mathrm{i}\omega)$ of the frequency response $G(i\omega)$. Although often depicted as log-log plot and lin-log plot, respectively, it will be shown with linear axis scaling in this thesis predominantly as it is custom for flame transfer functions (Polifke, 2014). Figure 4.5 shows the magnitude and phase of the exemplary transfer function $G(s) = 1/(1+0.2s)$. The frequency response constituting the Bode plot is highlighted in red.

4.3.6 Differential/Difference Equation

A general differential equation model can be given by

$$a_m \frac{\mathrm{d}^m y(t)}{\mathrm{d}t^m} + \cdots + a_1 \frac{\mathrm{d}y(t)}{\mathrm{d}t} + y(t) = b_0 u(t) + b_1 \frac{\mathrm{d}y(t)}{\mathrm{d}t} + b_n \frac{\mathrm{d}^n u(t)}{\mathrm{d}t^n} \tag{4.48}$$

with the parameters $\{a_m\}$ and $\{b_n\}$. In discrete time, this can be written as a *difference equation.*

$$y[k] + \sum_{m=1}^{n_a} a_m y[k-m] = \sum_{n=0}^{n_b} b_n u[k-n]\,. \tag{4.49}$$

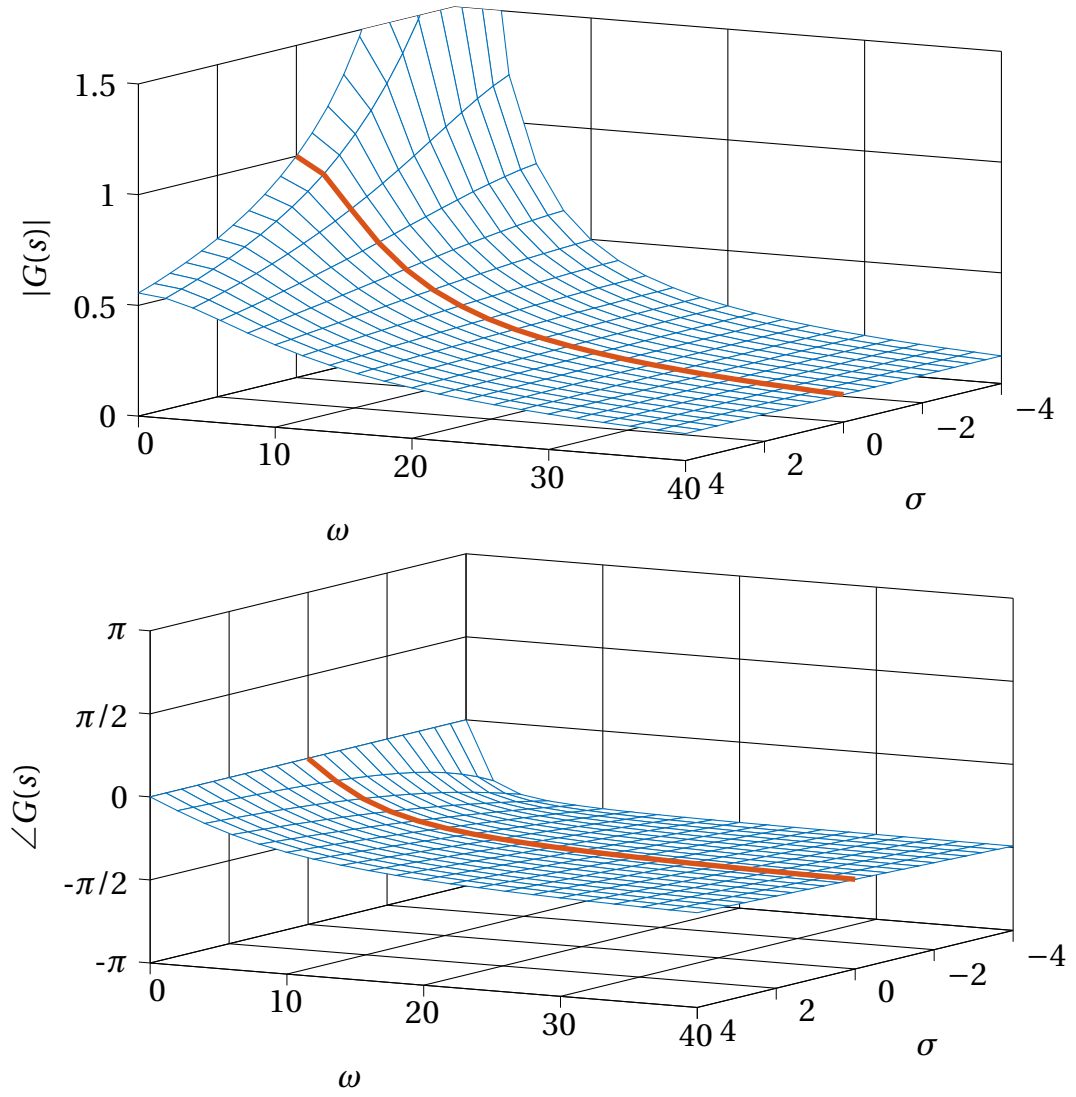

Figure 4.5: Amplitude and Phase of the Transfer Function $1/(1+0.2s)$**.** The frequency response ($\sigma = 0$) is highlighted in red.

The parameters $\{a_m\}$ and $\{b_n\}$ of the discrete time representation are not the same as in the continuous time but they are related through the sampling time.

The difference equation is a parametric model. In contrast to the convolution model, the impulse response is parametrized with $\{a_m\}$ and $\{b_n\}$. Expanding Equation (4.49) and inserting $y[k-1]$ recursively with zero initial conditions yields

$$y[k] = b_0 u[k] + (b_1 - a_1 b_0) u[k-1] + (b_2 - b_1 a_1 + a_1^2 b_0 - a_2 b_0) u[k-2] + \ldots \quad (4.50)$$

The number of past outputs that affect the system n_b is also called the input memory. Likewise, the number of past outputs n_a may be seen as the system's memory and determines the order of the parametric model (Tangirala, 2014). The difference equation representation is also able to handle time delays, i.e. the number of time

instants passing before the input affects the output. Such time delays are not relevant for the models developed in this thesis and thus will be omitted.

4.4 System Identification

A model mimics the behavior of a system with respect to certain requirements and restrictions. With a model, the output of a system can be predicted from known inputs. The subject of SI is concerned with the inverse process: To acquire a model for a system from known input and output data. In his introduction, Ljung (1999) even states that “Inferring models from observations and studying their properties is really what science is about.”

The process of SI is very general and widely known in different fields such as electrical engineering, economy, and psychology. SI is used when processes are either too complex to gain insight using first principles, i.e. physical laws, or the calculation is too costly in terms of time or resources. Its goal is to obtain an efficient and accurate model for a process from acquired data. The properties of this model can be analyzed to get insight in the process, or the model may be used for further calculations.

Overviews of a wide variety of SI methods are given in a number of books. The work of Söderström and Stoica (1989) is a very complete collection of theory on SI developed systematically since the 1960s. A milestone is the book by Ljung (1999). It includes many useful methods explained on a mathematical level. Heij et al. (2006) also approached the theme of SI from a mathematical viewpoint. The focus of Pintelon and Schoukens (2012) is on the frequency domain. Very complete and detailed insight is provided by the more recent work by Tangirala (2014). A more practical point of view is assumed by Keesman (2011) as well as Isermann and Münchhof (2011). Verhaegen and Verdult (2007) focused on state-space models but include insight also for input–output models.

4.4.1 Identification Procedure

The essential steps in SI are data acquisition, model estimation, and model validation. Data acquisition can be further divided into the design of the experiments and the execution of the experiments. The term experiment also refers to numerical simulations. Model estimation also has two components: The choice of model structure and the estimation of parameters. Figure 4.6 shows a more detailed flow chart of the procedure.

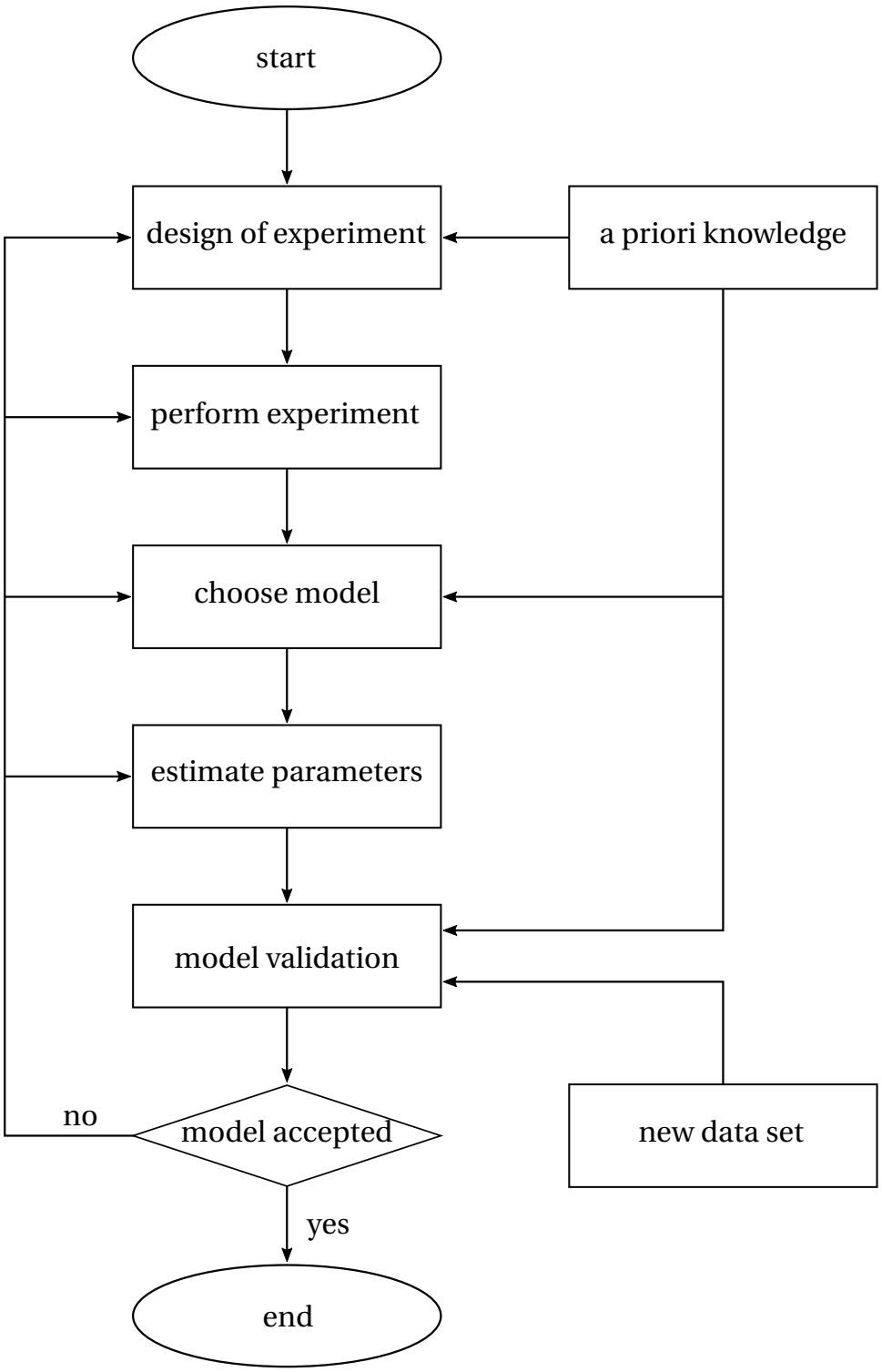

Figure 4.6: Flowchart of the Identification Procedure. Adopted from Söderström and Stoica (1989).

4.4.2 Parameter Estimation

The estimation of the parameters of the chosen model type is a key process in the SI process. A great variety of model types, i.e. representations of LTI systems, exists. Some very common model types, which are of interest in this thesis, are given in Section 4.3. The estimated output $\hat{y}(n)$ to an independent variable n of any model of these types is written as

$$\hat{y}(n) = \boldsymbol{\varphi}(n, \boldsymbol{\theta})\boldsymbol{\theta} \tag{4.51}$$

where $\boldsymbol{\varphi}(n,\theta)$ is the row vector of p *regressors* and $\boldsymbol{\theta}$ is the column vector of unknown model coefficients (parameters), one for every entry in the regressor vector. Estimated quantities are denoted by a hat ($\hat{\cdot}$), e.g. the estimated output computed from the model equation is $\hat{y}$. The independent variable is designated n here to give credit to the fact that generally any variable can be used here. In the scope of dynamic models the independent variable, however, is usually continuous time t, discrete time k or frequency Sr. The notation $\boldsymbol{\varphi}(n, \boldsymbol{\theta})\boldsymbol{\theta}$ reflects the fact that the vector of regressors may depend on the coefficients.

Measurements, e.g. an input signal, are usually available as discrete values. These values can be assembled in vectors allowing for a matrix notation of Equation (4.51). The vector of $n = 1, \ldots, N$ estimated outputs $\hat{\boldsymbol{y}}$ is then given by

$$\hat{\boldsymbol{y}} = \boldsymbol{\Psi}\boldsymbol{\theta} \tag{4.52}$$

where $\boldsymbol{\Psi}$ is the *observation* or *regressor matrix* written as

$$\boldsymbol{\Psi} = \begin{bmatrix} \boldsymbol{\varphi}(1,\theta) & \boldsymbol{\varphi}(2,\theta) & \cdots & \boldsymbol{\varphi}(N,\theta) \end{bmatrix}^T . \tag{4.53}$$

The regressor matrix is an $N \times p$ matrix comprised of the available data, e.g. the inputs and outputs of the system. Each row corresponds to one available data point and each column corresponds to one coefficient. The (linear) equation system is over-determined and cannot be solved directly. To find an approximate solution the *residuals* given by

$$\boldsymbol{\varepsilon} = \boldsymbol{y} - \hat{\boldsymbol{y}} = \boldsymbol{y} - \boldsymbol{\Psi}\boldsymbol{\theta} \tag{4.54}$$

have to be minimized. By inspecting Equation (4.54), it can be seen that $\boldsymbol{\Psi}$ is the *Jacobian matrix* of the residuals—a key feature in many optimization algorithms (Nocedal and Wright, 2006). The *least squares minimization* problem can be written as

$$\arg\min_{\boldsymbol{\theta}} \sum_{n=1}^{N} (\boldsymbol{y}(n) - \varphi(n,\theta)\boldsymbol{\theta})^2 \tag{4.55}$$

which is equal to minimizing the sum of squared residuals (hence the name).

Ordinary Least Squares

The *ordinary least squares* method (OLS), also called the linear least squares method, is a basic approach in SI that is also the underlying technique for many more advanced procedures. In this case, the regressors $\boldsymbol{\varphi}(n)$ are independent of the coefficients and the regressor matrix (Equation (4.53)) is denoted by $\boldsymbol{\Phi}$. To facilitate the estimation of the parameters $\hat{\boldsymbol{\theta}}$, a *cost function* V is defined as

$$V(\boldsymbol{\theta}) = \sum_{n=1}^{N} \varepsilon(n)^2 . \tag{4.56}$$

In vector notation, this reads

$$V(\boldsymbol{\theta}) = \boldsymbol{\varepsilon}^T \boldsymbol{\varepsilon} = \left(\boldsymbol{y}^T - \boldsymbol{\theta}^T \boldsymbol{\Phi}^T\right)\left(\boldsymbol{y} - \boldsymbol{\theta}\boldsymbol{\Phi}\right) . \tag{4.57}$$

The cost function is convex and therefore, a minimum of V can be found where its derivative with respect to the coefficients is zero:

$$\frac{\partial V(\boldsymbol{\theta})}{\partial \boldsymbol{\theta}} = -2\boldsymbol{\Phi}^T \boldsymbol{y} + 2\boldsymbol{\Phi}^T \boldsymbol{\Phi}\boldsymbol{\theta} = 0 \tag{4.58}$$

This leads to the so-called *normal equations* given by

$$\boldsymbol{\Phi}^T \boldsymbol{\Phi}\boldsymbol{\theta} = \boldsymbol{\Phi}^T \boldsymbol{y} . \tag{4.59}$$

The expression $\boldsymbol{\Phi}^T \boldsymbol{\Phi}$ denotes the *Hessian matrix* of V. Mathematically, it is also the Gramian matrix of $\boldsymbol{\Phi}$ and the product $\boldsymbol{\Phi}^T y$ is the moment matrix of regressand by regressors. The solution of the OLS problem is given by

$$\hat{\boldsymbol{\theta}} = \left(\boldsymbol{\Phi}^T \boldsymbol{\Phi}\right)^{-1} \boldsymbol{\Phi}^T \boldsymbol{y} \tag{4.60}$$

where $\boldsymbol{\Phi}^\dagger = \left(\boldsymbol{\Phi}^T \boldsymbol{\Phi}\right)^{-1} \boldsymbol{\Phi}^T$ is also known as Moore–Penrose *pseudoinverse* of the matrix $\boldsymbol{\Phi}$.

Instead of using the normal equations, the OLS problem can be solved using QR-factorization (Nocedal and Wright, 2006; Golub and Van Loan, 2013) which results in a better conditioning of the problem. The QR-factorization of the matrix $\boldsymbol{\Phi}$ which is $N \times p$ is defined as

$$\boldsymbol{\Phi} = \boldsymbol{Q}\boldsymbol{R} = \begin{bmatrix} \boldsymbol{Q}_1 & \boldsymbol{Q}_2 \end{bmatrix} \begin{bmatrix} \boldsymbol{R}_1 \\ \boldsymbol{0} \end{bmatrix} = \boldsymbol{Q}_1 \boldsymbol{R}_1 \tag{4.61}$$

where $\boldsymbol{Q}$ is an orthogonal matrix of size $N \times N$ with $\boldsymbol{Q}^T \boldsymbol{Q} = \boldsymbol{I}$. $\boldsymbol{R}$ is an upper triangular martix of size $N \times p$. Only the first p rows of $\boldsymbol{R}$ are nonzero, so a square matrix $\boldsymbol{R}_1$ with $p \times p$ can be constructed. Analogously, the matrix $\boldsymbol{Q}_1$ is $N \times p$ and contains only the first p columns of $\boldsymbol{Q}$. The solution of the OLS with QR-factorization problem is given by

$$\hat{\boldsymbol{\theta}} = \boldsymbol{R}_1^{-1} (\boldsymbol{Q}_1^T \boldsymbol{y}) . \tag{4.62}$$

Weighted Least Squares

As an addition to the OLS method, the rows of $\boldsymbol{\Phi}$ (and $\boldsymbol{y}$ accordingly) can be weighted. This is advantageous, e.g. if only a certain frequency range is of interest or variance information on measurements is available. It results in the *weighted least squares* (WLS) method (Franklin et al., 1997; Golub and Van Loan, 2013; Isermann and Münchhof, 2011; Keesman, 2011; Ljung, 1999; Pintelon and Schoukens, 2012; Tangirala, 2014; Verhaegen and Verdult, 2007). Parameter estimation is then given by

$$\hat{\boldsymbol{\theta}} = \left(\boldsymbol{\Phi}^T \boldsymbol{W} \boldsymbol{\Phi}\right)^{-1} \boldsymbol{\Phi}^T \boldsymbol{W}\, \boldsymbol{y} \tag{4.63}$$

with *weighting matrix* $\boldsymbol{W}$. Often the weighting matrix is diagonal with weights $\{\rho_i\}$, but also filter operations can be realized in $\boldsymbol{W}$. Using the WLS method is equivalent to pre-filtering the data as can be shown by

$$\left(\sqrt{\boldsymbol{W}}\boldsymbol{\Phi}\right)^T \left(\sqrt{\boldsymbol{W}}\boldsymbol{\Phi}\right)\hat{\boldsymbol{\theta}} = \left(\sqrt{\boldsymbol{W}}\boldsymbol{\Phi}\right)^T \left(\sqrt{\boldsymbol{W}}\boldsymbol{y}\right) \tag{4.64}$$

where $\left(\sqrt{\boldsymbol{W}}y\right)$ is the pre-filtered output and $\left(\sqrt{\boldsymbol{W}}\boldsymbol{\Phi}\right)$ the pre-filtered regression matrix.

Regularization

Tikhonov *regularization* is often used to solve ill-posed or ill-conditioned linear equation systems. The general solution of a regularized least squares problem reads

$$\hat{\boldsymbol{\theta}} = \left(\boldsymbol{\Phi}^T \boldsymbol{\Phi} + \boldsymbol{\Gamma}^T \boldsymbol{\Gamma}\right)^{-1} \boldsymbol{\Phi}^T\, \boldsymbol{y} \tag{4.65}$$

with the *regularization matrix* $\boldsymbol{\Gamma}$ (Söderström and Stoica, 1989; Golub and Van Loan, 2013; Isermann and Münchhof, 2011; Keesman, 2011; Ljung, 1999; Tangirala, 2014; Verhaegen and Verdult, 2007).

A special case is the so-called L_2–regularization where the regularization matrix is a scaled version of the identity matrix $\boldsymbol{\Gamma} = \lambda \boldsymbol{I}$. $\boldsymbol{I}$ is the identity matrix and λ a scalar factor determining the effect of the regularization. For the parameter estimate, this yields

$$\hat{\boldsymbol{\theta}} = \left(\boldsymbol{\Phi}^T \boldsymbol{\Phi} + \lambda^2 \boldsymbol{I}\right)^{-1} \boldsymbol{\Phi}^T\, \boldsymbol{y}. \tag{4.66}$$

Regularization can not only be used to solve ill-conditioned problems, but also to exert some control over *bias* and *variance* of the estimates of any model. Controlling bias and variance is most desirable in SI as it can prevent *overfitting* by reducing variance (Isermann and Münchhof, 2011). In many cases, one can only be minimized at the cost of the other and thus, regularization allows influencing on the trade-off between bias and variance. This is often denoted as *constrained least squares* (CLS).

Related Nonlinear Methods

The least squares methods, as mentioned above, solve estimation problems that are linear in the parameters $\boldsymbol{\theta}$. However, there are many situations in which the minimization problem is not linear and a *nonlinear least squares* (NLS) method is needed.

Several methods exist to solve nonlinear optimization, and many are related to the least squares approach applying it iteratively. The pseudo-linear regression method calculates new values for $\varphi(k,\boldsymbol{\theta})$ at each iteration using the least squares method and the parameters evaluated in the previous iteration. Similarly, the Gauss–Newton method uses the OLS method on the residuals to improve an initial guess of the parameters iteratively.

For the Gauß–Newton method, the residual of the ith iteration is given by

$$\boldsymbol{\epsilon}_i = \boldsymbol{y} - \hat{\boldsymbol{y}}\left(\boldsymbol{\theta}^{(i)}\right) \tag{4.67}$$

where the estimated output $\hat{\boldsymbol{y}}\left(\boldsymbol{\theta}^{(i)}\right)$ depends on the parameters evaluated in the ith iteration. As for the OLS method, the goal of the Gauß–Newton method is to find a minimum where the derivative of the objective function with respect to the coefficients is zero. Instead of introducing the objective function V, like in Equation (4.56), it is more convenient to use the derivatives of the estimated output evaluated by

$$\boldsymbol{\Psi}(\boldsymbol{\theta}) = \frac{\partial \boldsymbol{\epsilon}(\boldsymbol{\theta})}{\partial \boldsymbol{\theta}} = \left[\frac{\partial \boldsymbol{\epsilon}}{\partial \theta_1} \dots\right]^T \tag{4.68}$$

as defined in Equation (4.53). These are called pseudo-regressors in the nonlinear framework. In matrix form for all samples, $\boldsymbol{\Psi}$ is the Jacobian matrix of $\hat{y}(\boldsymbol{\theta})$. The iteration rule is then similar to the OLS method:

$$\boldsymbol{\theta}^{(i+1)} = \boldsymbol{\theta}^{(i)} + \left(\boldsymbol{\Psi}(\boldsymbol{\theta}^{(i)})^T \boldsymbol{\Psi}(\boldsymbol{\theta}^{(i)})\right)^{-1} \boldsymbol{\Psi}(\boldsymbol{\theta}^{(i)})^T \boldsymbol{\epsilon}_i \,. \tag{4.69}$$

The relation of the NLS method to the OLS method becomes even more apparent in the fact that if the estimator is linear, then $\boldsymbol{\Psi} \to \boldsymbol{\Phi}$ (Nocedal and Wright, 2006).

The Levenberg–Marquardt method (Nocedal and Wright, 2006) can be seen as an improved version of the Gauß–Newton algorithm. It uses a trust region approach, similar to regularization, to enhance stability and convergence. Moreover, efficient implementations involving QR-factorization are known for the Gauß–Newton and Levenberg–Marquardt methods.

The mentioned NLS methods need initial values for the search algorithm. These initial values are crucial as NLS algorithms are prone to become "trapped" in a local minimum instead of finding the true global minimum. Suitable initial values can be found, e.g. by using the OLS method.

Alternative methods for nonlinear minimization are so called derivative free optimization algorithms, e.g. the Nelder–Mead simplex-reflection method (downhill simplex algorithm) (Nocedal and Wright, 2006; Isermann and Münchhof, 2011) or genetic algorithms Isermann and Münchhof (2011).

4.4.3 Influence of Disturbances

As discussed in Section 4.1.5, disturbances have an influence on the parameter estimation. This influence can be quantified by the *mean squared error* (MSE). The MSE consists of two contributing factors: bias and variance, which can be estimated (Tangirala, 2014, p. 307, 322).

Bias

A good estimator should provide accurate estimates. Without infinitely long time series, this is only possible, if averaging over all realizations cancels out the error (Tangirala, 2014). If this is not the case, the estimate is biased. Bias is formally defined as

$$\Delta\hat{\boldsymbol{\theta}} = E[\hat{\boldsymbol{\theta}}] - \boldsymbol{\theta}_0 \tag{4.70}$$

where $\boldsymbol{\theta}_0$ is the true values of the parameters and $E[]$ denotes the expected value. Good estimators yield unbiased estimates or at least asymptotically unbiased estimates given by

$$\lim_{N\to\infty} \Delta\hat{\boldsymbol{\theta}} = 0\,. \tag{4.71}$$

An estimate for the bias of the OLS method is given by (Keesman, 2011)

$$\Delta\hat{\boldsymbol{\theta}} = E\left[\left(\boldsymbol{\Phi}^T\boldsymbol{\Phi}\right)^{-1}\boldsymbol{\Phi}^T\boldsymbol{e}\right]. \tag{4.72}$$

With the OLS method, only one minimum—the global minimum—exists and is therefore found unambiguously. However, if the residuals are not GWN, the OLS procedure will never yield the true values of $\boldsymbol{\theta}$ (Ljung, 1999). Hence, the regression model is biased whenever the equation error is colored (Tangirala, 2014).

Variance

Besides accuracy, the ability to estimate the "true" value, precision is important. Precision manifests in estimates with low variance. The variance of the parameter estimates is formally defined as

$$\sigma^2_{\hat{\boldsymbol{\theta}}} = E\left[(\hat{\boldsymbol{\theta}} - E\left[\hat{\boldsymbol{\theta}}\right])^2\right]. \tag{4.73}$$

In the scope of the OLS method, the variance is given by

$$\mathrm{Cov}(\hat{\boldsymbol{\theta}}) = E\left[\left(\boldsymbol{\Phi}^T\boldsymbol{\Phi}\right)^{-1}\boldsymbol{\Phi}^T\mathrm{Cov}(\boldsymbol{e})\boldsymbol{\Phi}\left(\boldsymbol{\Phi}^T\boldsymbol{\Phi}\right)^{-1}\right]. \tag{4.74}$$

Assuming the residuals are GWN, the covariance matrix $\hat{\boldsymbol{S}}$ is estimated using the Gramian matrix of the regressor matrix:

$$\hat{\boldsymbol{S}} = \mathrm{Cov}(\hat{\boldsymbol{\theta}}) = \hat{\sigma}_\epsilon^2\left(\boldsymbol{\Phi}^T\boldsymbol{\Phi}\right)^{-1} \tag{4.75}$$

The variance of the residuals $\hat{\sigma}_\epsilon^2$ is estimated by

$$\sigma_\epsilon^2 = \frac{1}{N-1}\sum_{n=1}^{N}\varepsilon^2(n). \tag{4.76}$$

Confidence intervals for the identified coefficients can thus be given as

$$\hat{\theta}_i - C_\alpha\sqrt{\hat{S}_{ii}} \leq \theta_{i,0} \leq \hat{\theta}_i + C_\alpha\sqrt{\hat{S}_{ii}} \tag{4.77}$$

where $\hat{S}_{ii}$ is the ith diagonal of $\hat{\boldsymbol{S}}$ and C_α is the α-level of the normal distribution for the desired confidence level, e.g. $C_\alpha = 2.58$ for 99% confidence intervals (Tangirala, 2014, p. 342).

Bootstrapping

Another method to estimate the uncertainty in the coefficient estimates (variance) is *bootstrapping* (Söderström and Stoica, 1989; Ljung, 1999; Pintelon and Schoukens, 2012; Tangirala, 2014). A new set of N regressors is drawn from the set $\{\boldsymbol{\varphi}\}$ in random order "with replacement". The new regressors form a regressor matrix $\boldsymbol{\Phi}_{(i)}$, which is used to calculate the estimate for the coefficients $\boldsymbol{\theta}_{(i)}$. From all coefficient samples, mean and covariance matrix can be computed using estimates for the sample mean and the sample covariance.

Mean Square Error

The MSE is defined as

$$\mathrm{MSE}\left(\hat{\boldsymbol{\theta}}\right) = E[\|\hat{\boldsymbol{\theta}} - \boldsymbol{\theta}_0\|_2^2] \tag{4.78}$$

where $\boldsymbol{\theta}_0$ is the true value of the estimator. In terms of bias and variance, this is expressed as (Tangirala, 2014)

$$\mathrm{MSE}\left(\hat{\boldsymbol{\theta}}\right) = \mathrm{tr}\left(\hat{S}_{\hat{\boldsymbol{\theta}}}\right) + \|\Delta\hat{\boldsymbol{\theta}}\|_2^2 \tag{4.79}$$

where $\mathrm{tr}\left(\hat{S}_{\hat{\boldsymbol{\theta}}}\right)$ denotes the trace of the covariance matrix.

The MSE is estimated calculating the sample average of the residuals

$$\hat{\mathrm{MSE}} = \frac{1}{N-1}\sum_{n=1}^{N}\varepsilon(n)\,. \tag{4.80}$$

For a consistent estimator, $\mathrm{MSE}\left(\hat{\boldsymbol{\theta}}\right) \to 0$ for $N \to \infty$.

Efficient Estimators

The most efficient estimator is the minimum variance unbiased estimator (MVUE). This implies that the estimate is unbiased and the variance is at the lowest theoretical bound (Cramer–Rao lower bound) (Tangirala, 2014, p. 332). An MVUE may not exist, and hence the best linear unbiased estimator (BLUE) is sought. The BLUE is equal to the MVUE when the observations y are governed by a linear model, and the noise e is GWN. This is known as the Gauss-Markov theorem (Tangirala, 2014, p. 332).

The MVUE or BLUE are unbiased, but can still have high variance. The minimum mean square error estimator (MMSE) tries to achieve the best trade-off between bias and variance leading to the smallest MSE. In this case, the variance can be smaller than the Cramer–Rao lower bound at the cost of bias. The MMSE is achieved, e.g. by using regularization techniques.

4.4.4 Identification of Discrete Time Models

For discrete time models, it is assumed that the output $y[k]$ can be constructed from the deterministic signal $x[k]$ and the stochastic noise $v[k]$ as in

$$y[k] = x[k] + v[k]\,. \tag{4.81}$$

The one-step ahead predictor (in this case the predictor evaluated from all inputs until the kth instant and measurements evaluated until the $(k-1)$-th instant) is given by

$$\hat{y}[k|k-1] = \hat{x}[k] + \hat{v}[k] \tag{4.82}$$

where $\hat{x}[k]$ stands for the deterministic model and $\hat{v}[k]$ for the noise model.

Coefficients for a discrete time input-output model of a priori defined structure and model orders as in Equation (4.28) can be found by minimizing the *one-step ahead prediction errors* given by

$$\varepsilon[k|k-1] = y[k] - \hat{y}[k|k-1]\,. \tag{4.83}$$

The one–step ahead prediction error is the difference between known output y and predicted output $\hat{y}$ at every instant k. These errors are also referred to as innovations Tangirala (2014). For a more general description, the prediction error sequence may be filtered by a stable linear filter $L(q)$:

$$\varepsilon_F(k,\boldsymbol{\theta}) = L(q)\varepsilon(k,\boldsymbol{\theta})\,. \tag{4.84}$$

This type of estimation method is called *prediction error method* (PEM).

For the minimization procedure, the cost function

$$V(\boldsymbol{\theta}) = \sum_{k=0}^{N-1} \varepsilon_F^2(k,\boldsymbol{\theta}) \tag{4.85}$$

is defined and minimized. Choosing the sum of the squared errors as the cost function corresponds to a minimization problem denoted by

$$\arg\min_{\boldsymbol{\theta}} \sum_{k=0}^{N-1} \varepsilon_F^2(k,\boldsymbol{\theta})\,. \tag{4.86}$$

This is called the quadratic-criteria PEM (PEM-QC).

The general discrete time model is given in Equation (4.27) as

$$y[k] = G(q)\,u[k] + H(q)\,e[k]\,. \tag{4.87}$$

This yields the *one-step ahead predictor*

$$\hat{y}[k|k-1] = H^{-1}(q)G(q)\,u[k] + (1 - H^{-1})\,y[k]\,. \tag{4.88}$$

Numerous ways to parametrize G and H exist (Tangirala, 2014). The most widely used method is shown in Section 4.3.2. The theoretical one-step ahead prediction error is the white-noise sequence (Tangirala, 2014).

Models with Linear Estimators

The *autoregressive with exogenous input* (ARX) model is a model structure often used because of its simplicity in estimating the coefficients. It is given by

$$A(q)\,y[k] = B(q)\,u[k] + e[k]\,. \tag{4.89}$$

This model is of equation error type as the error enters the equation rather than the output.[2] The one-step ahead prediction error is written by

$$\varepsilon[k|k-1] = A(q)\,y[k] - B(q)\,u[k]\,. \tag{4.90}$$

[2] As opposed to the output error models.

The innovations are linear in the coefficients $A(q)$ and $B(q)$. Therefore, the coefficient estimation is linear, and the OLS method (or WLS/CLS method respectively) can be used. This leads to one of the main advantages of this method: Only a global minimum exists which is found unambiguously by the estimation procedure (Ljung, 1999). The major drawback, however, is that the model inherently assumes that the noise is predictable with a linear predictor. Thus, the least squares procedure will not converge to the true values of the coefficients, if the equation error $\hat{v}[k] = 1/A(q)\,v[k]$ is not GWN. In this case, the estimation yields a biased estimate (Ljung, 1999).

The *finite impulse response* (FIR) model is written as

$$y[k] = B(q)\,u[k] + e[k]\,. \tag{4.91}$$

It is equal to the ARX model with $A = 1$ and thus also has a linear estimator. The FIR model is often referred to as non-parametric model (Tangirala, 2014) because the impulse response is equal to the identified coefficients and not parameterized via a denominator polynomial. It has the advantage that no model order has to be chosen, but the length of the impulse response is specified directly via the number of coefficients n_b and the sampling time step T_s. The impulse response is zero after $n_b \cdot T_s$, hence the name finite impulse response. Following Equation (4.8), FIR models are always stable. However, the pre-specified length of the impulse response is also the greatest weakness of the model. For dynamics slowly varying in time or large differences in time scales, a large number of coefficients is necessary to capture the dynamics correctly (Tangirala, 2014).

In contrast to the ARX model, the equation error in the FIR model is assumed to be unpredictable, i.e. $\hat{v}[k] = 0$ and $v[k] = e[k]$. Deterministic model $G(q)$ and noise model $H(q)$ (cf. Equation (4.27)) are parametrized independently and the deterministic model converges to the true value (Tangirala, 2014). This property is called *consistency* (Tangirala, 2014).

Before a parametric model (with a reasonable number of coefficients) is identified insight on the model order can be gained by identifying a high order FIR model. This type of model also benefits greatly from regularization, i.e. it is advantageous to use the CLS approach for coefficient estimation (Keesman, 2011).

Output-Error Model

An *output-error* (OE) model is achieved when only the deterministic part of the general discrete time input-output structure (Equation (4.28)) is sought. All other

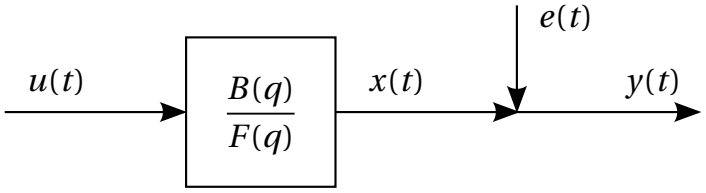

Figure 4.7: Block Diagram of the Output-Error Model.

coefficients are unity ($A = C = D = 1$) and hence not identified. This corresponds to an error term that is added to the output of the system.[3] The model takes the form

$$y[k] = \frac{B(q)}{F(q)} u[k] + e[k]\,. \tag{4.92}$$

Figure 4.7 sketches a block diagram of an OE model.

If the model structure is re-written in equation-error form given by

$$F(q)\,y[k] = B(q)\,u[k] + v[k]\,, \tag{4.93}$$

it can be shown that a least squares estimate would be biased due to $v[k] = F(q)e[k]$. Hence, a nonlinear parameter estimation method is necessary.

Using the PEM framework for the OE model, the one-step ahead prediction error can be written as

$$\varepsilon[k|k-1] = y[k] - \frac{B(q)}{F(q)} u[k]\,. \tag{4.94}$$

Introducing *instrumental variables* equal to the predicted (noise free) outputs $\xi[k] = \hat{y}[k] = B(q)/F(q)\,u[k]$, the prediction equation for a single instant k in time is given by

$$\begin{aligned}\hat{y}[k|\boldsymbol{\theta}] = &-f_1\xi[k-1] - f_2\xi[k-2] - \cdots - f_{n_a}\xi[k-n_a] \\ &+b_0\,u[k] + b_1\,u[k-1] + \cdots + b_{n_b}\,u[k-n_b]\,.\end{aligned} \tag{4.95}$$

In short, this is denoted as

$$\hat{y}[k|\boldsymbol{\theta}] = \boldsymbol{\varphi}(k,\boldsymbol{\theta})\boldsymbol{\theta} \tag{4.96}$$

where the regression vector is

$$\boldsymbol{\varphi} = \begin{bmatrix} -\xi[k-1,\boldsymbol{\theta}] & -\xi[k-2,\boldsymbol{\theta}] & \cdots & -\xi[k-n_f,\boldsymbol{\theta}] & u[k] & u[k-1]\cdots & u[k-n_b+1] \end{bmatrix} \tag{4.97}$$

[3] This is in contrast to the equation error models where the error term is included in the equation like in an ARX model.

and the vector of parameters $\boldsymbol{\theta}^T = [f_1, f_2, \ldots, f_{n_f}, b_0, b_1, \ldots, b_{n_b-1}]$. Both vectors have the length $n_b + n_f$.

The OE model can also be seen from a pre-filtering viewpoint. If input and output are filtered with a linear filter that is the inverse of the denominator polynomial $F(q)$, i.e. with $y_F[k] = 1/F(q)\,y[k]$ and $u_F[k] = 1/F(q)\,u[k]$, Equation (4.92) reads

$$F(q)\,y_F[k] = B(q)\,u_F[k] + e[k]\,. \tag{4.98}$$

This is equivalent to the ARX model structure. The coefficients of the polynomials $\{b\}$ and $\{f\}$ are found during identification by nonlinear regression. Three different algorithms arise from the descriptions given above and may be used to estimate the parameters. A linear least squares method is applied to achieve a biased estimate of the parameters. The predicted output $\hat{y}[k]$ and thus the instrumental variables $\xi[k]$ are computed. This procedure is repeated until the change in $\hat{\boldsymbol{\theta}}$ is negligible. However, convergence cannot be guaranteed (Ljung, 1999; Söderström and Stoica, 1989). This method is known as pseudo-linear regression (Tangirala, 2014). The algorithm by Steiglitz and McBride (1965) uses pre-filtering to iteratively compute a least squares estimate of the coefficients on input-output time series. The filter, which is the inverse of the denominator polynomial, is evaluated iteratively until convergence. Ultimately, the NLS method, e.g. the Gauß-Newton algorithm, can be used. The gradient necessary for the NLS method can be computed using

$$\psi[k] = \frac{1}{F(q)}\phi[k]\,. \tag{4.99}$$

The OE model, similar to the FIR model, is a consistent estimator. The deterministic part and the noise are parameterized independently and hence $B(q)/F(q)$ converges to the true value. For the initialization, when $\xi[k,\boldsymbol{\theta}]$ is yet unknown, an OLS approach is applied using the measured output $y[k]$ (ARX model). The algorithms for the identification used in this thesis are implemented in the SI toolbox of MATLAB (The MathWorks, Inc., 2016; Ljung, 2016a,b).

Box-Jenkins Model

The *Box-Jenkins* (BJ) model is an extension of the OE model. Not only the deterministic process is modeled, but also the (stochastic) noise. The use of this model type is indicated if the noise dynamics differ severely from the assumption of GWN, i.e. $H \neq 1$. The addition of a noise model offers more flexibility but at the cost of an increase in model complexity (Tangirala, 2014, p. 601). The model is given by

$$y[k] = \frac{B(q)}{F(q)}u[k] + \frac{C(q)}{D(q)}e[k]\,. \tag{4.100}$$

The block diagram of a BJ model is depicted in Figure 4.8. The one-step ahead pre-

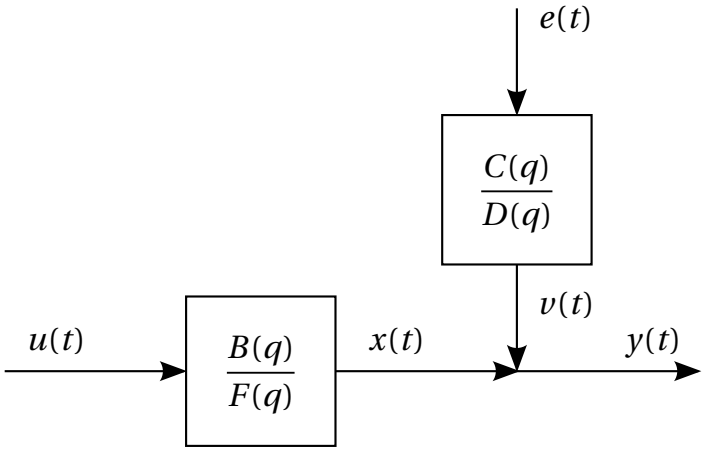

Figure 4.8: Block Diagram of a Box-Jenkins Model.

diction error for the BJ model is given by

$$\varepsilon[k|k-1] = \frac{D(q)}{C(q)}y[k] - \frac{D(q)B(q)}{C(q)F(q)}u[k]\,. \tag{4.101}$$

For the parameter estimation, similar procedures as for the OE model can be used. The most efficient method is applying one of the NLS algorithms. The Jacobian matrix, required in the NLS procedure, is evaluated by

$$\mathbf{\Psi} = \frac{D(q)}{C(q)F(q)}\mathbf{\Phi}\,. \tag{4.102}$$

The deterministic model and the stochastic model are parametrized independently as in the case of the OE model and thus converge to their true values. However, the main difference is that the model for the noise is identified and not restricted to $H(q) = 1$. The BJ model is the most versatile model structure at the cost of complexity and number of coefficients.

The BJ model includes a parametrization for the noise. It is of no use to regard the noise model as a transfer function as the input, the noise input e[k], is by definition unknown. It is therefore more useful to consider the spectrum of the noise given by $|H(\mathrm{Sr},\theta)|^2$ (Ljung, 1999, p. 202).

4.4.5 Identification of Continuous Time Models

The second method for SI that was successfully evaluated in this thesis is the identification of continuous time transfer functions from frequency domain data. Continuous time identification is an emerging branch in SI (Tangirala, 2014) and offers some advantages. Frequency domain data can, e.g. be acquired from linearized equations

in frequency space or by transforming time domain data, i.e. using the FFT method. Similar to the OE model in discrete time, only the deterministic part $G(s)$ is modeled. The noise term is omitted in this case. The goal in the identification of continuous time models is the direct identification of a rational function in powers of the frequency parameter s as shown in Section 4.3.1. The transfer function is modeled using

$$G(s) \approx \frac{N(s)}{D(s)} = \frac{\sum_{p=0}^{n_n} r_p \phi_p(s)}{\sum_{p=0}^{n_d} \tilde{r}_p \phi_p(s)} \tag{4.103}$$

where $N(s)$ and $D(s)$ represent numerator and denominator of the transfer function, respectively.

The identification of continuous time models is based on the application of least squares methods to data acquired at discrete (but not necessarily equidistant) frequencies. Early methods, including Levy's polynomial fitting (Levy, 1959), were numerically poorly conditioned, suffered from unbalanced weighting, or were likely to produce unstable models. The *Sanathanan-Koerner* (SK) iteration method (Sanathanan and Koerner, 1963) overcame the weighting problem and yielded far better results. In 1998, *vector fitting* (VF) was introduced (Gustavsen and Semlyen, 1998, 1999). VF originally used partial fractions as basis iteratively identifying poles and residues. This pole relocation method was successfully applied in the scope of thermoacoustic by Orchini et al. (2016). Stable models can easily be enforced with this method. It was further improved by to *orthonormal basis functions* (OVF) (Deschrijver et al., 2007) and by including a $\mathscr{H}_2$ error measure (QuadVF) (Drmač et al., 2015). The use of QR-decomposition to solve the least squares problem lead to better conditioning for all variants of this identification technique (cf. section 4.4.2).

The behavior of a system is characterized by n_k frequency domain data samples $(s_k,\ G_0(s_k))$, i.e. frequency and frequency response. If the acquired data is in time domain, $G_0(s_k)$ can be gained by

$$G_0(i\omega_k) = \frac{\mathrm{FFT}(\boldsymbol{y})}{\mathrm{FFT}(\boldsymbol{u})}. \tag{4.104}$$

The model parameters can be estimated using least squares techniques similar to the discrete time case. The minimization problem formulated for rational transfer function is written by

$$\underset{r_p, \tilde{r}_p}{\arg\min} \sum_{k=0}^{n_k} \left| \frac{N(s_k)}{D(s_k)} - G_0(s_k) \right|^2. \tag{4.105}$$

This is a nonlinear problem that cannot be solved by the OLS method in a straightforward manner. The two methods employed in this thesis, SK iterations and the VF approach are now explained in more detail.

Sanathanan-Koerner Iteration

A method to solve Equation (4.105) are SK iterations. The minimization problem is reformulated to

$$\underset{r_p,\tilde{r}_p}{\arg\min} \sum_{k=0}^{n_k} \frac{1}{|D(s_k)|^2} |N(s_k) - D(s_k)G_0(s_k)|^2 . \tag{4.106}$$

A WLS method is used to solve Equation (4.106) iteratively. The ith iteration is given by

$$\underset{r_p^{(i)},\tilde{r}_p^{(i)}}{\arg\min} \sum_{k=0}^{n_k} \frac{1}{\left|D^{(i-1)}(s_k)\right|^2} \left|N^{(i)}(s_k) - D^{(i)}(s_k)G_0(s_k)\right|^2 . \tag{4.107}$$

The term $1/\left|D^{(i-1)}(s_k)\right|^2$ acts as the weighting which is the denominator polynomial evaluated in the previous iteration. The remainder $\left|N^{(i)}(s_k) - D^{(i)}(s_k)G_0(s_k)\right|^2$ is linear in the coefficients $\{r_p\}$ and $\{\tilde{r}_p\}$. For the first iteration, the weighting matrix is equal to the identity matrix, i.e. no weighting is applied. This is equivalent to the approach by Levy (1959). Note the analogy to the OE model in discrete time. A linear estimator is achieved by pre-filtering with a filter equal to the denominator polynomial. The solution procedure by Steiglitz and McBride (1965) also updates the estimate for the denominator, and thus the pre-filter, iteratively.

This procedure has proven to yield fairly good results, but suffers from two drawbacks: (1) The regression matrix assembled to solve the least squares problem is a so-called Vandermonde matrix that tends to be ill-conditioned. (2) It is not guaranteed that this procedure converges to the solution of the original minimization problem (Equation (4.105)).

Vector Fitting

To overcome these deficiencies, Gustavsen and Semlyen (1998, 1999) suggested to use rational basis functions $\phi_p = 1/(s - \alpha_p)$ instead of monomial basis functions $\phi_p = s^p$. In the minimization problem Equation (4.105), numerator and denominator are replaced in a way such that no weighting is necessary. The minimization problem is written as

$$\underset{\hat{r}_p,\tilde{r}_p}{\arg\min} \sum_{k=0}^{n_k} \left|\tilde{N}(s_k) - \tilde{D}(s_k)G_0(s_k)\right|^2 \tag{4.108}$$

where

$$\tilde{D}(s) = \sum_{p=1}^{n} \frac{\tilde{r}_p}{s - \tilde{\alpha}_p} + 1 \qquad \text{and} \qquad \tilde{N}(s) = \sum_{p=1}^{n} \frac{\hat{r}_p}{s - \tilde{\alpha}_p} + d \tag{4.109}$$

are rational functions with identical poles $\{\tilde{\alpha}_p\}$. The weighting procedure from the SK iteration method is replaced by the relocation of poles. Starting values for the poles have to be given initially.

Ultimately, the transfer function is approximated by

$$G(s) \approx \frac{N(s)}{D(s)} = \left(\sum_{p=1}^{n} \frac{r_p}{s - \alpha_p} \right) + d \tag{4.110}$$

where $\{\alpha_p\}$ and $\{r_p\}$ are the poles and residues of the partial fractions, respectively. The least squares problem can be solved by expanding

$$\tilde{N}(s) = \tilde{D}(s) G_0(s) \tag{4.111}$$

which yields

$$\left(\sum_{p=1}^{n} \frac{\hat{r}_p}{s + \tilde{\alpha}_p} \right) + \tilde{d} \approx \left[\left(\sum_{p=1}^{n} \frac{\tilde{r}_p}{s + \tilde{\alpha}_p} \right) + 1 \right] G_0(s) \,. \tag{4.112}$$

This equation is linear in the residues $\{\hat{r}_p\}$ and $\{\tilde{r}_p\}$ as well as in the direct term $\tilde{d}$. It is solved using the least squares approach. Similar to Equation (4.51), the "output" in this case is the estimated transfer function given by

$$G(s_k) = \boldsymbol{\varphi}(k) \boldsymbol{\theta} \tag{4.113}$$

with the vector of regressors

$$\boldsymbol{\varphi}(k) = \left[\frac{1}{s_k - \tilde{\alpha}_1} \quad \frac{1}{s_k - \tilde{\alpha}_2} \quad \cdots \quad \frac{1}{s_k - \tilde{\alpha}_n} \quad 1 \quad \frac{-G_0(s_k)}{s_k - \tilde{\alpha}_1} \quad \frac{-G_0(s_k)}{s_k - \tilde{\alpha}_2} \quad \cdots \quad \frac{-G_0(s_k)}{s_k - \tilde{\alpha}_n} \right] \tag{4.114}$$

and the coefficient vector $\boldsymbol{\theta} = \left[\hat{r}_1 \; \hat{r}_2 \; \cdots \; \hat{r}_n \; \tilde{d} \; \tilde{r}_1 \; \tilde{r}_2 \; \cdots \; \tilde{r}_n \right]^T$.

Reformulating

$$G^{(k)}(s) = \frac{\tilde{N}^{(k)}(s)}{\tilde{D}^{(k)}(s)} = \frac{\tilde{d} + \sum\limits_{p=1}^{n} \left(\hat{r}_p^{(k)} \Big/ s - \tilde{\alpha}_p^{(k)} \right)}{1 + \sum\limits_{p=1}^{n} \left(\tilde{r}_p^{(k)} \Big/ s - \tilde{\alpha}_p^{(k)} \right)} \tag{4.115}$$

in terms of zeros and poles yields

$$G(s) = \frac{\prod\limits_{p=1}^{n} (s - \beta_p) \Big/ \prod\limits_{p=1}^{n} (s - \tilde{\alpha}_p)}{\prod\limits_{p=1}^{n} (s - \tilde{\beta}_p) \Big/ \prod\limits_{p=1}^{n} (s - \tilde{\alpha}_p)} = \frac{\prod\limits_{p=1}^{n} (s - \beta_p)}{\prod\limits_{p=1}^{n} (s - \tilde{\beta}_p)} \,. \tag{4.116}$$

This reveals that the zeros of $\tilde{D}(s)$ are the poles of $G(s)$. The new poles for every iteration of this procedure can be calculated from

$$\{\tilde{\alpha}_p\} = \{\tilde{\beta}_p\} = \text{eig}\left(\mathbf{A} - \mathbf{b} \cdot \mathbf{c}^T\right) \tag{4.117}$$

with matrix $\mathbf{A}$ including the poles $\{\tilde{\alpha}_p\}$ of the previous iteration as diagonal, a column vector of ones $\mathbf{b}$ and the residues $\{\tilde{r}_p\}$ in vector $\mathbf{c}^T$. This uses the fact that the eigenvalues are the roots of the characteristic polynomial of a matrix. If a stable model is desired, this can be enforced by flipping unstable poles, i.e. $\mathfrak{Re}\left(\{\tilde{\alpha}_p\}\right) > 0$ into the left half plane $\tilde{\alpha}_p = -\tilde{\alpha}_p$. The pole relocation procedure is repeated until $\tilde{D}(s)$ approaches 1. The poles calculated in the final iteration with $\tilde{D}(s) = 1$ are the poles of the identified transfer function $\{\alpha_p\} = \{\tilde{\alpha}_p\}$. In the second stage, the residues $\{r_p\}$ of the transfer function estimate are calculated. This is achieved by solving Equation (4.110) in a least squares sense using the final poles from the first step.

The procedure implemented in MATLAB R2016b (The MathWorks, Inc., 2016; Ljung, 2016a,b) uses the SK iteration method in the first iteration for an initial guess for the poles. All successive iterations use the OuadVF scheme by Drmač et al. (2015) with orthonormal basis functions to acquire an accurate model and to improve the conditioning of the matrix. Theoretically, it is also possible to use an NLS algorithm to solve Equation (4.105) with PEM-QC. This is numerically inferior to the VF approach (Deschrijver and Dhaene, 2006), but can be used to refine the solution acquired with VF. This approach is also implemented in MATLAB R2016b (The MathWorks, Inc., 2016).

4.5 Model Validation

There are several tests that can be performed to assess the quality of an identified model.

Least Squares Fit

The goal in SI is to find the estimate with the least MSE (cf. Section 4.4.3). The MSE is evaluated using

$$\text{MSE} = \frac{1}{N}\sum_{k=0}^{N-1}(y-\hat{y})^2 = \frac{1}{N-1}\|y-\hat{y}\|_2^2. \tag{4.118}$$

A small MSE is an indicator for a good model. However, it is complicated to compare the MSE evaluated from different models.

A suitable ramification is to normalize the MSE with using the MSE a constant model estimated with the sample mean produces. Using the square root of the MSE gives a greater sensitivity to small deviations, i.e. small errors appear amplified. This results in the *normalized root mean squared error* (NRMSE). To get a fit value with higher values signifying a better fit the NRMSE is subtracted from unity. The NRMSE-fit between output y and estimated output $\hat{y}$ is evaluated by

$$\Phi = 1 - \frac{\|y - \hat{y}\|_2}{\|y - \overline{y}\|_2}. \tag{4.119}$$

NRMSE-fit values are usually given in per cent. 100% signify a perfect fit and negative values would indicate that a constant mean value $\overline{y}$ is actually a better predictor than the estimated dynamic model.

Parameter Variance

A covariance matrix for the parameters $\boldsymbol{\theta}$ is computed during the identification process. The identified parameters should have small variances, i.e. the confidence intervals of a parameter should be narrow. This is given by

$$C_\alpha \sqrt{\hat{S}_{ii}} \overset{!}{\ll} \hat{\theta}_i \tag{4.120}$$

where C_α is a suitable constant for the α-level, e.g. $C_\alpha = 2.58$ for a 99 % confidence interval. All parameters should be significantly different from zero. Models not fulfilling this requirement are discarded as this is a sign of an unsuitable model order.

Histogram of the Residuals

The estimation procedure does not give an exact solution but reduces the prediction error ε. These prediction errors or residuals can be used as an indicator of model quality. The *histogram*, which is a graphical representation of the distribution of the residuals, is inspected visually. Many models assume the residuals to be GWN, which can be confirmed qualitatively in this manner. Moreover, neither the mean nor the maximum value of the residual vector should be too large.

Whiteness

For models with linear estimators, like the ARX model, the residuals should be GWN. Otherwise, the estimates will be biased. The test for *whiteness* is, therefore, a test for the noise model (Ljung, 1999; Keesman, 2011; Tangirala, 2014). In the case of the BJ model, residuals with the properties of white noise indicate a good noise model.

For the OE model, it is not required to achieve white noise as it will still converge to the true model values. Whiteness is tested by computing the auto-correlation of the residuals given by

$$R_{\varepsilon\varepsilon}[l] = \sum_{k=-\infty}^{\infty} \varepsilon[k]\varepsilon^*[k+l] \tag{4.121}$$

where ε^* is the complex conjugate of ε. Using the zeroth lag coefficient to standardize, the scales auto-correlation reads

$$\tilde{R}_{\varepsilon\varepsilon}[l] = \frac{R_{\varepsilon\varepsilon}[l]}{R_{\varepsilon\varepsilon}[0]}. \tag{4.122}$$

The test is passed, if all coefficients of the auto-correlation (except for the first coefficient which is unity by design) are $\tilde{R}_{\varepsilon\varepsilon} < 1/\sqrt{N}$, i.e. not significantly different from zero.

Independence

Another criterion is the *independence* of residuals and input vector (Tangirala, 2014, p. 425). Independent residuals prove that no more information on the system response to the excitation signal is included in the residuals, i.e. the identification process was able to extract all information possible from the input. Independence of residuals and inputs is assessed computing the cross-correlation function between the two time series given by

$$R_{\varepsilon u}[l] = \sum_{k=-\infty}^{\infty} \varepsilon[k]u^*[k+l]. \tag{4.123}$$

Standardization is achieved by calculating

$$\tilde{R}_{\varepsilon u}[l] = \frac{R_{\varepsilon u}[l]}{\|\boldsymbol{\varepsilon}\|_2 \cdot \|\boldsymbol{u}\|_2}. \tag{4.124}$$

A significance test is used to prove the insignificance of the cross-correlation coefficients in the range between $l = \pm 25$ lags. The cross-correlation coefficients are not significantly different from zero, if

$$\left|\tilde{R}_{\varepsilon u}[l]\right| \leq \sqrt{\frac{P_1}{N}} C_\alpha \tag{4.125}$$

where

$$P_1 = \sum_{n=-\infty}^{\infty} \tilde{R}_{\varepsilon\varepsilon}[l] \cdot \tilde{R}_{uu}[l] \tag{4.126}$$

and C_α is the α-level for the desired confidence level.

Scatter Plot of Residuals and Output

The time series of the residuals and outputs are plotted in a single graph. The abscissa and the ordinate show the output values and residuals, respectively. Each instant in time is represented by a single point in the plot forming a point cloud. The cloud is inspected visually for indicators concerning the properties of the data. The cloud is expected to be of elliptical shape with both principal axes aligned with the coordinate axes. Any deviation from this shape points towards two deficits of the model: (1) The model may not be able to capture the complete dynamics. In this case, a change of model order or type can be used as a remedy. (2) The system displays a non-negligible nonlinearity that calls for a nonlinear modeling approach (Bühner and Ziegler, 2009).

Cross-Validation

As a final performance check, a *cross-validation* test is carried out. The validation set, "fresh" data not used to develop the model parameters, serves as a data basis. The cross-validation fit is a very strong indicator of the ability of the model to represent the dynamics of the true system. Testing to a new dataset also gives information on the model's tendency to over-fit the data. In this case, the cross-validation fit would be poor although the other tests have indicated high model quality. The cross-validation fit is given as NRMSE-fit (cf. Equation (4.119)).

Pole-Zero Cancellation

Finding the right model order is an important task in SI. Insufficient model orders yield poor predictions because the dynamics are not captured sufficiently. On the other hand, too large model orders lead to over-fitting, resulting in bad predictions as well, and computational efficiency suffers. To some extent, the model order also depends on the purpose of the model and whether accuracy (sophistication) or simplicity (feasibility) is valued more (Ljung, 1999).

Except for the cross-validation, which is a test for over-fitting, none of the above can give information on the correct model order. A way to approach this is to check the parameters and their covariances in the form of poles and zeros (e.g. Equation (4.25)) for a continuous time transfer function). Surplus poles and zeros will be found to have very similar values on the real and imaginary axis. The result is that they cancel each other to reproduce the system dynamics and may therefore not be necessary. If a pole lies within the confidence region of a zero or vice versa, the model order can probably be reduced.

Validation with A Priori Knowledge

If only little of a system is known, model validation relies completely on the acquired data. However, if there is additional information available, this information can be used and interpreted with regard to the model quality. One possibility is to assess the behavior of a model in its limits. A good model has to be able to capture the low-frequency limit $\mathrm{Sr} \to 0$, which can in some cases be inferred from a quasi-steady state. The behavior in the limit of high frequencies may be given due to simplified calculations from first principles. Smoothness or the number and location of peaks in the frequency response may also be explained qualitatively from prior considerations. An example of this validation technique is the stability of a system, i.e. the behavior of the impulse response for $t \to \infty$. If a steady state exists, the impulse response has to assume and hold zero after a certain time (BIBO stability, cf. Section 4.1.2).

4.6 Dynamics of Heat Transfer and Skin Friction

In the scope of this thesis, linear models are developed representing the relationship between velocity fluctuations in the flow and heat transfer as well as skin friction. The systems are nonlinear by nature, but can be cast into the linear framework by making use of the perturbation approach (cf. Section 2.4.1). Linearization is achieved by removing the mean value of the respective quantity written as

$$\mathrm{Nu}'(t) = \mathrm{Nu}(t) - \overline{\mathrm{Nu}} \qquad \text{and} \qquad c_f'(t) = c_f(t) - \overline{c_f}\,. \tag{4.127}$$

The fluctuations are scaled with the mean and hence input and outputs are given by

$$u_{\mathrm{Re}}(t) = \frac{\mathrm{Re}'(t)}{\overline{\mathrm{Re}}}, \qquad y_{\mathrm{Nu}}(t) = \frac{\mathrm{Nu}'(t)}{\overline{\mathrm{Nu}}}, \text{ and} \qquad y_{c_f}(t) = \frac{c_f'(t)}{\overline{c_f}}\,. \tag{4.128}$$

The identified transfer functions for heat transfer and skin friction are therefore related to Nußelt number Nu and friction coefficient c_f by

$$G_{\mathrm{Nu}} = \frac{\mathrm{Nu}'/\overline{\mathrm{Nu}}}{\mathrm{Re}'/\overline{\mathrm{Re}}} \qquad \text{and} \qquad G_{c_f} = \frac{c_f'/\overline{c_f}}{\mathrm{Re}'/\overline{\mathrm{Re}}}\,. \tag{4.129}$$

This is equal to Equation (2.100). The full quantities can be recovered by

$$\mathrm{Nu} = \overline{\mathrm{Nu}}\left(1 + G_{\mathrm{Nu}}\frac{\mathrm{Re}'}{\overline{\mathrm{Re}}}\right) \qquad \text{and} \qquad c_f = \overline{c_f}\left(1 + G_{c_f}\frac{\mathrm{Re}'}{\overline{\mathrm{Re}}}\right). \tag{4.130}$$

5 Data Generation

With the computational resources available today, it is possible to determine the flow around a cylinder by solving the full (incompressible) Navier–Stokes equations numerically without the assumptions which the boundary layer equations or Oseen's method rely on.

This chapter deals with the methods used in this thesis to generate the data to assess the dynamic behavior of a cylinder in pulsating crossflow. All methods are based on the incompressible Navier–Stokes equations (Equation (2.63)–(2.65)). The use of the incompressible formulation is justified for three important applications in Chapter 9. There, also the compatibility of incompressible fluid dynamics with the inherently compressible effect of thermoacoustics is discussed. In Section 5.1, the basic simulation setup is presented. It is based on the laminar flow simulations detailed in Section 5.2 for $0.1 \leq \mathrm{Re}_0 \leq 40$ and for the laminar vortex shedding regime, i.e. $\mathrm{Re}_0 = 120$ and $\mathrm{Re}_0 = 240$. In Section 5.3, the extensions and modifications necessary to simulate flow at $Re_0 = 3900$ as an exemplary condition for subcritical flow are reported. A considerably different method to acquire frequency domain data is presented in Section 5.4. A perturbation is introduced in the Navier–Stokes equations. They are linearized around a steady state solution and transformed to the frequency domain (LNSE approach). Figure 5.1 gives an overview over different approaches to simulate a cylinder in pulsating crossflow and to determine the transfer function. The work shown here was previously published in parts in Witte and Polifke (2017a).

5.1 Basic Setup

The basic setup incorporates considerations concerning the boundary conditions, the computational domain, and the two-dimensional mesh which is in turn modified for further investigations like the Large Eddy Simulation (LES). A thorough grid independence study was carried out to investigate the spatial discretization with respect to steady-state and pulsating flow.

5.1.1 Boundary Conditions

Solving the Navier–Stokes equations is essentially the numerical integration over a given domain. The boundary conditions are necessary to evaluate the integration

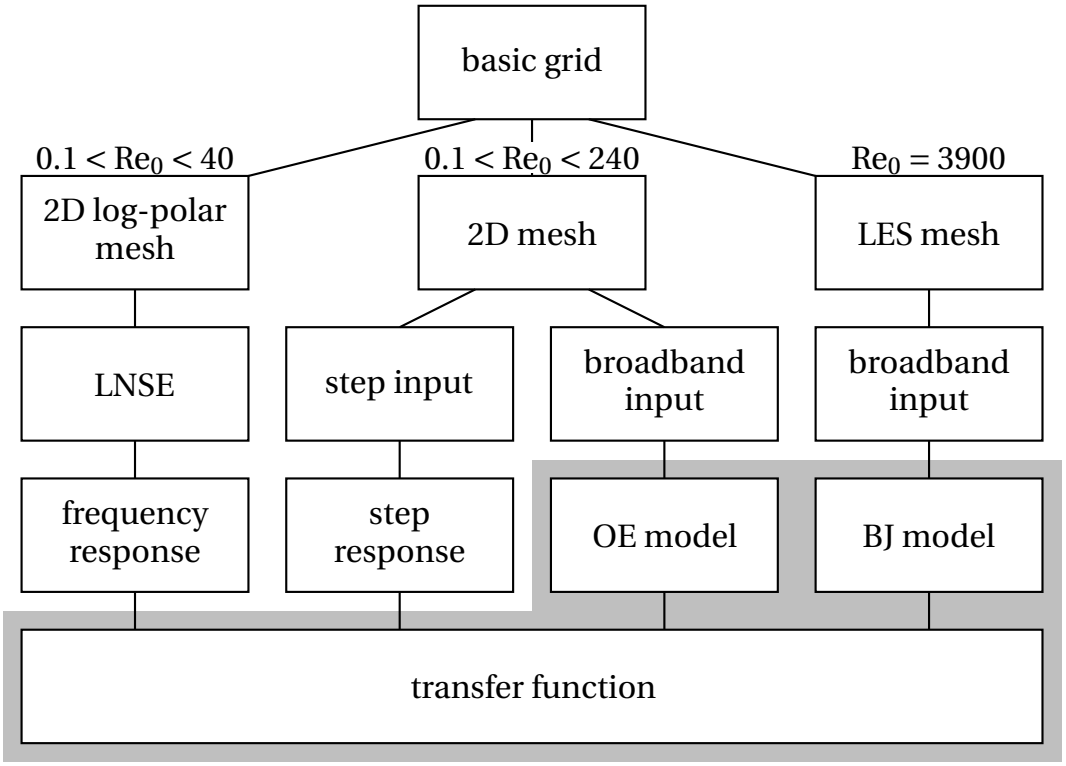

Figure 5.1: Overview of Different Approaches to Determine the Transfer Function. The gray area marks steps of the SI procedure detailed in Chapter 6.

constants, i.e. the integrals become definite integrals. The flow enters the domain at the inlet where an inlet velocity $u_\infty(t) = u_{\infty,0} + u'_\infty(t)$ is prescribed. This velocity value consists of a mean flow component $u_{\infty,0}$ and a time dependent fluctuation $u'_\infty(t)$ (cf. Equation (2.85)). The latter is either a sudden increase in velocity by 10 % at time $t = t_0$, which is then held constant to yield the step response of the heat transfer (cf. Section 6.1), or a random sequence of velocity values. This provides a broadband, colored noise input signal for the SI procedure (cf. Section 6.3). The (relative) pressure at the inlet has zero normal gradient, and the inbound fluid has a constant temperature of $\Theta = 0$.

The flow passes the cylinder, represented by a no-slip wall with a constant temperature set to $\Theta = 1$. At the outlet, the relative kinematic pressure ($P = p/\rho$) is fixed to $P = 0$ and Neumann type boundary conditions are applied for the velocity and the temperature. With such an outflow condition, flow variables are effectively extrapolated to the boundary nodes.

All other boundaries, parallel to the flow, are symmetry boundaries. Close to the cylinder, actual symmetry is enforced as justified by the symmetric flow patterns expected to occur. The symmetry condition at the far field acts as a slip wall condition. Figure 5.2 sketches the computational domain and the boundaries used in

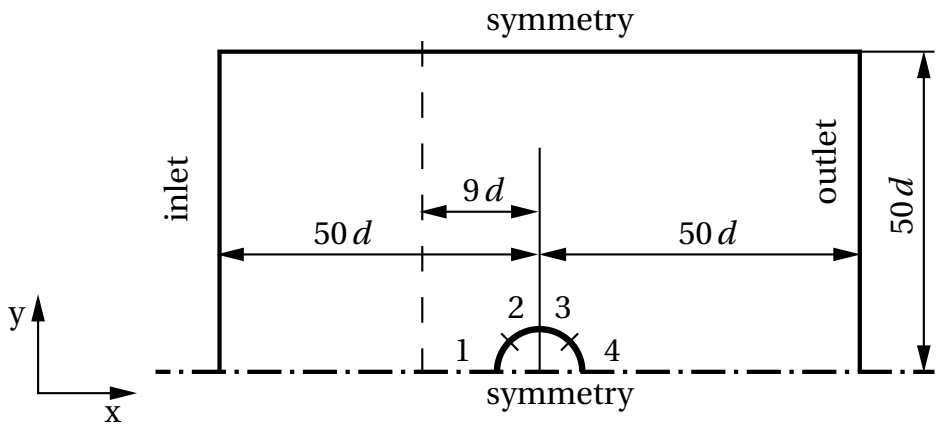

Figure 5.2: Sketch of the Computational Domain. Boundaries and the basic dimensions are marked. A dashed line represents the plane where input data is acquired. The four sectors of the cylinder used in post-processing a marked with the respective number. Representation is not to scale.

this study, including the final dimensions as determined in the grid independence study.

The boundary conditions are summarized as

$$\text{inlet} \qquad u_1 = u_\infty \qquad u_2 = 0 \qquad \frac{\partial p}{\partial x} = 0 \qquad \Theta = 0 \tag{5.1}$$

$$\text{outlet} \qquad \frac{\partial u_1}{\partial x} = 0 \qquad \frac{\partial u_2}{\partial x} = 0 \qquad p = 0 \qquad \frac{\partial \Theta}{\partial x} = 0 \tag{5.2}$$

$$\text{cylinder} \qquad u_1 = 0 \qquad u_2 = 0 \qquad \frac{\partial p}{\partial \vec{n}} = 0 \qquad \Theta = 1 \tag{5.3}$$

$$\text{symmetry} \qquad \frac{\partial u_1}{\partial y} = 0 \qquad \frac{\partial u_2}{\partial y} = 0 \qquad \frac{\partial p}{\partial y} = 0 \qquad \frac{\partial \Theta}{\partial y} = 0 \tag{5.4}$$

where $\vec{n}$ denotes the surface normal vector at the cylinder.

5.1.2 Domain and Basic Mesh Topology

The computational domain chosen to represent laminar flow across a cylinder represents the upper half of a square with a circle placed in the center (cf. Figure 5.2). This domain is discretized with a block-structured, three-dimensional mesh consisting of hexahedrons with only one cell of unit thickness in the direction of the axis of the cylinder. At the cylinder, the cells are square with respect to the plane normal to the axis of the cylinder and aligned to the curvature. Gradients aligned and normal to the surface of the cylinder are thus resolved equally. This corresponds to the nature of creeping and laminar flow. The cylindrical structure of the grid makes it possible to adjust the radial and circumferential node distribution close to the cylinder. At the same time, the near wall flow is kept aligned with the control volume

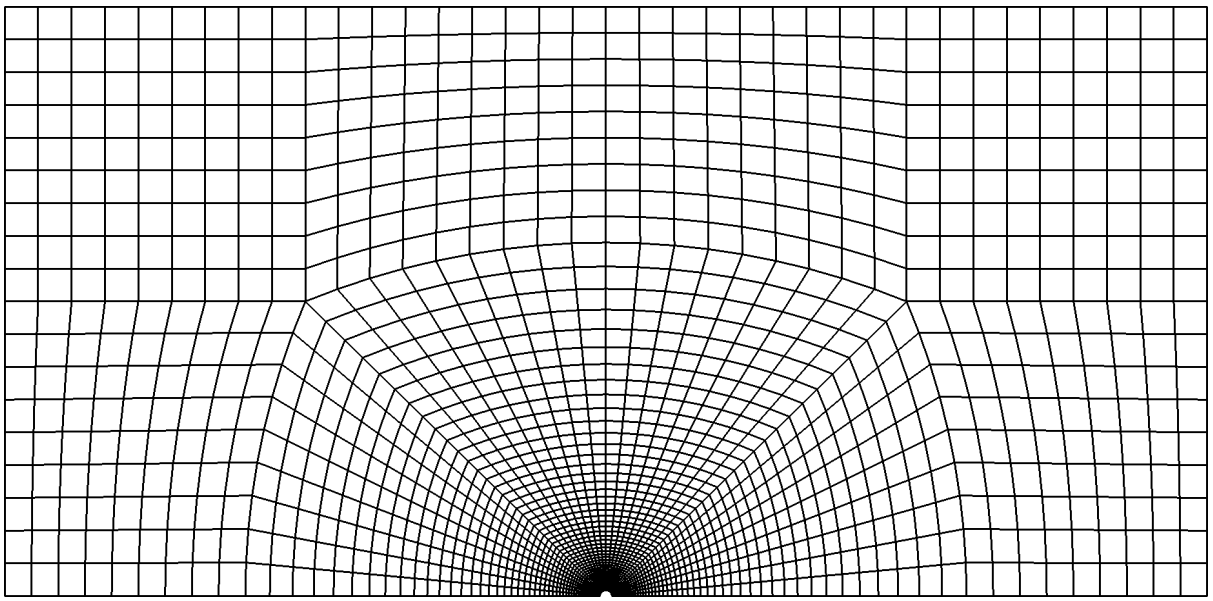

Figure 5.3: Mesh Topology of Exemplary Mesh. 36 Cells along Cylinder Perimeter. The boundaries are in a distance of $50\,d$ to the cylinder. The grids used for computations were at least four times finer.

boundaries. The surface adjacent region is strongly refined towards the surface of the cylinder to properly resolve the steep gradients. Around the inner circular block, another O-type grid is fitted to achieve a smooth transition from the cylindrical center to the outer rectangular region. The remaining blocks are of H-type with regular cell spacing. The topology of the mesh is shown in Figure 5.3. Figure 5.4 depicts a detail of the mesh close to the cylinder.

To achieve a high-quality grid with the least amount of skewness and a cell aspect ratio close to unity, square cells are enforced at the cylinder boundary. In combination with the fixed size of the H–O-transition zone, this choice determines the cell sizes throughout the domain as a function of the resolution at the cylinder. The number of cells N_c along the surface of the half cylinder is chosen as the measure of the grid resolution. The size of the surface adjacent cells in radial and circumferential direction Δx_c is therefore given by $\Delta x_c / d = \pi / (2\,N_c)$.

5.1.3 Grid Study

The insensitivity of computational results to spatial and temporal discretization was ascertained in three stages: The dependence of the solution on the domain size (1a) and the cell size (1b) was assessed for steady flow. In a second stage, a sinusoidal modulation of the inlet velocity with an amplitude of 5 % of the mean velocity and a frequency of Sr = 40 was imposed at the inlet. This represents a high frequency modulation resulting in a very thin unsteady (acoustic) boundary layer. The impact of

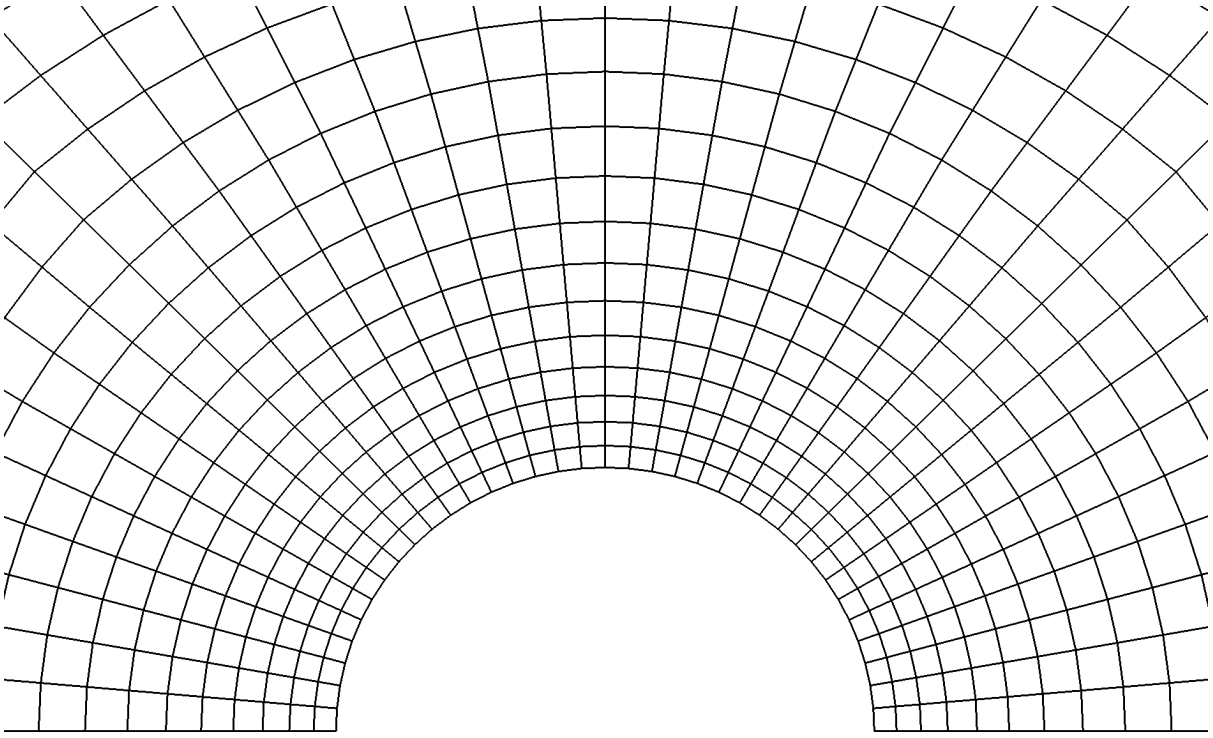

Figure 5.4: Detail of an Exemplary Mesh. 36 Cells along Cylinder Perimeter. The mesh is designed to feature almost square cells close to the cylinder. The grids used for computations were at least four times finer.

the cell size (2a) and the time step size (2b) on the heat transfer frequency response at this high frequency were assessed. Finally, grid independence for the complete SI process was demonstrated with a grid resolution chosen according to the results of the second stage and the next finer grid (3). A basic initial grid study was carried out by Brandl (2014) during the course of a bachelor's thesis, which was supervised by the author of this thesis.

Domain Size and Cell Size in Steady Flow

The size of the computational domain is characterized by a single length scale L_d, i.e. the minimal distance between the axis of the cylinder and the domain boundaries (cf. Figure 5.2). Steady-state simulations with increasing distance between the domain boundaries with boundary conditions as stated above and the cylinder were conducted at a moderate mean flow Reynolds number ($\mathrm{Re}_0 = 12.71$). The goal of this first stage was to evaluate the upstream and sideways displacement of fluid resulting from the presence of the cylinder. The inlet boundary of the computational domain was then placed at a position where such displacement was not noticeable. Similarly, the lateral domain size was chosen in such a way that the influence of the slip-wall boundaries on the flow close to the cylinder was considered insignificant, as detailed below.

L_d/d	Nu_0	Δ_d in %
15	2.064	1.31
20	2.055	0.89
30	2.047	0.49
40	2.044	0.30
50	2.041	0.20
100	2.037	—

Table 5.1: Results of the Steady-State Domain Size Study. Grid study (1a), $\mathrm{Re}_0 = 12.71$, CFL ≤ 1, $N_c = 144$, steady state $\mathrm{Sr} = 0$.

The effect of the domain size on the Nußelt number was tested in the range $15 \leq L_d \leq 100$. The computed Nußelt numbers Nu_0 and the deviations from the largest domain $\Delta_d = [\mathrm{Nu}_0(L_d) - \mathrm{Nu}_0(100\,d)]\,/\mathrm{Nu}_0(100\,d)$ are shown in Table 5.1.

Eventually, a domain size of $L_d = 50\,d$ was chosen with a relative difference in Nußelt number to the largest domain of $\Delta_d = 0.20\,\%$. This choice should ensure a very small influence of domain size $\Delta_d < 1\,\%$ at lower Reynolds numbers, where the region influenced by the presence of the cylinder is somewhat larger. The extent of the domain used in all subsequent simulations is depicted in Figure 5.2. It was confirmed that flow reversal did not occur at the outlet for any of the flow conditions considered in this study.

The results of the grid independence study for steady flow are given in Table 5.2. $\Delta_c = \left[\mathrm{Nu}_0(N_c) - \mathrm{Nu}_{0,RE}\right]/\mathrm{Nu}_{0,RE}$ is the difference in mean Nußelt number to a solution evaluated using Richardson extrapolation (RE) (Ferziger and Perić, 2002) with an estimated scheme order of 2.00. A grid with $N_c = 72$ cells along the surface of the half cylinder, corresponding to a total of about 39×10^3 finite volumes, assures very small sensitivity of steady-state heat transfer $\Delta_c < 0.1\,\%$ on the grid resolution.

Cell Size and Time Step Size for High-Frequency Harmonic Modulation

The thickness of the unsteady Stokes boundary layer $\delta_{\mathrm{St}} = (2\nu/\omega)^{1/2}$ (cf. Section 3.1.2) decreases with frequency. At high frequencies, this layer is small, but it is necessary to resolve it in order to achieve a good model with quantitative accuracy for the dynamics of the unsteady flow. The Stokes layer at high frequencies is also much smaller than the steady boundary layer, which makes this a more demanding requirement than grid independence in the steady case. In order to test for grid independence in the unsteady case, a single frequency sine wave was superimposed on the inlet velocity $u'_\infty(t) = \epsilon\, u_{\infty,0} \sin(\omega t)$. The frequency ω was chosen at the upper end of the range of interest $\mathrm{Sr} = 40$, the amplitude was set to $\epsilon = 0.05$ to remain in the linear regime at all times.

N_c	Nu_0	Δ_c in %	$\Delta x_c/d$ $\cdot 10^{-3}$	Total number of cells
36	3.2709	0.187	43.6	2466
72	3.2665	0.052	21.8	9864
144	3.2652	0.013	10.9	39456
288	3.2649	0.003	5.45	157824
576	3.2648	0.0008	2.73	631296
1152	3.2648	0.0002	1.36	2525184

Table 5.2: Results of the Steady-State Cell Size Study. Grid study (1b), $L_d = 50$, $\mathrm{Re}_0 = 40$, CFL ≤ 1, steady state $\mathrm{Sr} = 0$.

The heat transfer frequency response $G_{\mathrm{Nu}}(\mathrm{Sr} = 40)$ was evaluated at the excitation frequency using Fourier transforms of the time series and Equation (4.104). The frequency response was scaled with respect to the mean values Re_0 and Nu_0. Any constant offset was removed. Suitable reference values to assess relative differences between results computed with different meshes were chosen. These are the theoretical low-frequency limit (steady-state gain K) for the amplitude and the theoretical high-frequency limit for the phase. Relative differences in amplitude and phase were calculated using the reference values mentioned above by

$$\Delta_{|G|}(N_c) = \frac{|G(N_c)| - |G(N_c = 576)|}{K} \tag{5.5}$$

$$\Delta_{\angle G}(N_c) = \frac{\angle G(N_c) - \angle G(2N_c)}{-\pi/2}. \tag{5.6}$$

For the given mean flow Reynolds number $\mathrm{Re}_0 = 40$, the steady-state value evaluated to $K = 0.41$. The results for the frequency response and its relative change are presented in Table 5.3.

Both amplitude and phase show monotonic convergence. The amplitude value for the finest grid is slightly larger than expected from a simple extrapolation of the values at $N_c = 144$ and $N_c = 288$. This could be due to the fact that steady mean flow conditions were not fully achieved during this computationally expensive simulation. However, all amplitude differences were below $\Delta_{|G|} < 0.5\,\%$ and thus even the coarsest mesh gave good results for the transfer function amplitude at $\mathrm{Sr} = 40$. The differences in phase were slightly larger, but values $\Delta_{\angle G} < 1\,\%$ could be achieved with $N_c = 288$ or finer.

The Stokes layer thickness depends inversely on the mean flow Reynolds number and the Strouhal number $\delta_{\mathrm{St}} = d\,[2/(\mathrm{Re}_0\,\mathrm{Sr})]^{1/2}$. To transfer this finding to simulations with different Reynolds numbers, the number of surface adjacent cells within the unsteady Stokes boundary layer was kept at $N_{\mathrm{St}} \approx \delta_{\mathrm{St}}/\Delta x_c \geq 5$.

N_c	$\lvert G\rvert$	$\angle G$ in °	$\Delta_{\lvert G\rvert}$ in %	$\Delta_{\angle G}$ in %	N_{St}
144	0.042 44	−79.88	0.059 48	1.186	3
288	0.042 49	−80.49	0.047 09	0.4309	6
576	0.042 69	−80.84	—	—	12

Table 5.3: Results of the Dynamic Cell Size Study. Grid study (2a), $L_d = 50$, $\mathrm{Re}_0 = 40$, $\mathrm{CFL}_{\max} \leq 0.2$, Stokes layer size $\delta_{\mathrm{St}}(\mathrm{Re}_0 = 40, \mathrm{Sr} = 40) = 0.03536\,d$.

For a Reynolds number $\mathrm{Re}_0 = 40$, it was necessary to resolve the field close to the cylinder with $N_c = 288$ (158×10^3 cells in total). Considering the same range of Strouhal numbers, a resolution of $N_c = 144$ (39×10^3 cells in total) was sufficient for cases with $\mathrm{Re}_0 \leq 4$. Using a coarser grid for lower Re_0 is also justified by the strong low-pass behavior of the frequency response. The response at high frequencies was near zero and hence is irrelevant for most technical purposes.

The time step size of the simulation was determined by the CFL number defined by

$$\mathrm{CFL} \equiv \frac{\Delta t\, u}{\Delta x} \approx \frac{\phi\, \Delta t}{\Delta V} \tag{5.7}$$

where Δt is the time step, u the velocity in a finite volume cell, and Δx is a measure for the cell size. In the CFD code, the CFL number was approximated using the flux at the cell faces ϕ and the volume of the respective cell ΔV. The results for simulations at various maximum CFL numbers $\mathrm{CFL}_{\max}$ are given in Table 5.4. The heat transfer frequency response for a single frequency $G_{\mathrm{Nu}}(\mathrm{Sr} = 40)$ was determined and differences were computed with Equation (5.5) and Equation (5.6).

For all simulations throughout different meshes, Δt was chosen to satisfy the condition $\mathrm{CFL} \leq 0.2$ in every cell. Refining the time step size further led to changes of $\Delta_{\lvert G_{\mathrm{Nu}}\rvert}, \Delta_{\angle G} < 1\,\%$ in gain and phase.

Grid Resolution for Broadband Modulation and System Identification

In the final stage (grid study 3), simulations with broadband excitation were performed ($u'_\infty(t)$ is a specifically generated signal with certain properties, cf. Section 5.2.1). The meshes used in this stage were the ones proven to be sufficiently fine to resolve high frequency fluctuations in the previous stage ($N_c = 144$ for $\mathrm{Re}_0 = 0.4$ and $\mathrm{Re}_0 = 4$ as well as $N_c = 288$ for $\mathrm{Re}_0 = 40$) as well as the next finer grids. Only very minor differences between the two grids were detected for each of the tested mean flow Reynolds numbers. As criterion for the agreement between the frequency responses in the whole frequency range $0 \leq \mathrm{Sr} \leq 40$, the NRMSE-fit (cf. Section 4.5) evaluated at 1×10^4 equidistant frequencies was chosen. The agreement between $N_c = 144$ and $N_c = 288$ was 92.0 % and 97.4 % for $\mathrm{Re}_0 = 0.4$ and $\mathrm{Re}_0 = 4$, respectively.

$\mathrm{CFL}_{\max}$	$\lvert G\rvert$	$\angle G$ in °	$\Delta_{\lvert G\rvert}$ in %	$\Delta_{\angle G}$ in %	$\overline{\mathrm{CFL}}$
2.0	0.075 83	−89.92	26.28	17.75	0.1130
1.0	0.1409	−83.35	8.690	10.46	0.056 80
0.5	0.1662	−76.21	1.848	2.525	0.028 80
0.2	0.1732	−74.37	0.050 17	0.4724	0.011 70
0.1	0.1731	−73.94	—	—	0.005 810

Table 5.4: Results of the Dynamic Time Step Size Study. Grid study (2b), $L_d = 50$, $\mathrm{Re}_0 = 4$, $N_c = 144$, $\mathrm{Sr} = 40$.

For $\mathrm{Re}_0 = 40$, the agreement between the $N_c = 288$ and $N_c = 576$ was 97.2 %. These values were in the same range as the NRMSE-fit of the individual models to the time domain data they were trained on. As a result of the grid independence study the meshes used further featured $L_d = 50\,d$, $N_c = 288$ for $\mathrm{Re}_0 > 4$ and $N_c = 144$ for $\mathrm{Re}_0 \leq 4$, as well as $\mathrm{CFL}_{\max} \leq 0.2$.

5.2 Laminar Time Domain Simulation

This thesis endeavors to give a broad overview of the dynamic behavior of the heat transfer and skin friction of a cylinder in pulsating crossflow. Nevertheless, the main focus remains the flow at low Reynolds numbers where the steady state exists and is two-dimensional and axis-symmetric. The boundary conditions and mesh used in this investigations are without modifications those explained in Section 5.1. Prior to the simulation run, an excitation signal to be imposed on the inlet was generated.

5.2.1 Excitation Signal Generation

Three different types of excitation signal were used in the course of this study: (1) a step input to directly evaluate the step response of heat transfer and skin friction, (2) a sinusoidal wave input representing a single frequency, and (3) a broadband signal for the subsequent SI procedure. Type (2) was used during the grid independence study (cf. Section 5.1.3) and for a quick survey of the nonlinear behavior of the heat transfer in the presence of high amplitude oscillations (cf. Section 8.3.3).

For reasons of computational efficiency, the simulations were carried out with a variable time step size determined by the CFL number (cf. Section 5.1.3). Input values are supplied to the CFD solver as tabulated values of time and corresponding velocity vector in a separate file. The according boundary condition in OpenFOAM is called “uniformFixedValue”. If the table entry does not correspond to the actual time step of the simulation, a linear interpolation is performed.

Step Input

To assess the step response of the system, a small, sudden change in inlet velocity is forced in the simulation after reaching an initial stationary state. A weak perturbation ($\epsilon = 0.1$) was imposed to assure a linear response. The sudden change is applied within one time step and simulation is continued until a new stationary state (only very small changes over time) is reached. The input signal can be expressed as $\mathrm{Re}(t) = \mathrm{Re}_0 + \mathrm{Re}'(t)$ where

$$\mathrm{Re}'(t) = \begin{cases} 0 & t < t_s \\ \epsilon\,\mathrm{Re}_0 & t \geq t_s \end{cases} . \tag{5.8}$$

Sine Input

A sinusoidal input was used to evaluate the response of the heat transfer and the skin friction at a single frequency, i.e. Strouhal number. The signal is described by

$$\mathrm{Re}(t) = \mathrm{Re}_0\,(1 + \epsilon\,\sin(\mathrm{Sr}\,t)) . \tag{5.9}$$

Again, ϵ denotes the amplitude of the pulsation and is set to $\epsilon = 0.1$ to investigate the linear frequency response. This amplitude was chosen to keep well below the threshold of about $\epsilon \approx 0.3$ where the approximation of an LTI systems ceases to be valid in the case of the heat transfer (Heckl, 1990; Hantschk and Vortmeyer, 1999; Selimefendigil et al., 2012). A nonlinear response in heat transfer and even flow reversal could be achieved by $\epsilon > 1.0$.

Broadband Input

The broadband excitation is used in simulations to create and acquire the data for the SI procedure. The broadband input in combination with SI has many advantages over the step input and the sine input. In contrast to the step input, which would theoretically be sufficient to describe the LTI dynamics, a broadband signal continuously excites the system and is, therefore, less prone to disturbances influencing the response. The frequency spectrum of the input can be predefined and hence also very high frequencies, possibly interfering with the convergence of the numerical procedure, are avoided. This is also the main advantage over the sine input. With a sine wave, it is only possible to acquire the response at a single frequency.

The input signal is created using the non-Gaussian simulation algorithm by Masters and Gurley (2003). For the signal generation in the CFD/SI approach this algorithm was implemented and tested by Föller and Polifke (2011). This routine creates

a vector of random values from a given cumulative distribution function (CDF) and amplitude distribution. These distributions are taken from the properties of a Daubechies wavelet scaling function. Hence, this signal was termed wavelet based excitation signal. The prototype wavelet is designed with the desired features like a specific corner frequency.

The time series is created with the desired overall length as fluctuations in the interval $[-1, 1]$. To acquire the proper input signal for the CFD simulations, the time series was scaled, and a constant for the mean flow was added. If necessary, the time series was pre-filtered with a fifth order Butterworth filter to achieve the desired frequency spectrum. This is beneficial for CFD simulations, because the signal varies smoothly between time instances. The corner frequency chosen for this thesis corresponds to $\mathrm{Sr} \approx 60$. This is high enough so that a good power spectral density of the frequency range of interest $0 \leq \mathrm{Sr} \leq 40$ is achieved, but the changes between successive input values are small enough to not impede the convergence of the CFD simulation.

To have a sufficiently smooth input signal, a recommendation is to ensure

$$20 < \frac{\omega_s}{\omega_b} < 40 \tag{5.10}$$

where $\omega_s = 2\pi / T_s$ is the sampling frequency and ω_b is the 3 dB bandwidth of the signal (Franklin et al., 1997, Chapter 11). It was therefore reasonable to sample the input signal with $T_s = 0.001$.

An advantage of the non-Gaussian simulation is that the input signal does not follow a Gaussian distribution, but is almost uniformly distributed. This results in a comparably high crest factor (Tangirala, 2014), which is desirable for identification experiments because the amplitude extrema are assumed more often than in the case of a random Gauss signal.

5.2.2 Computational Procedure

To perform SI, time series data for the quantities of interest needed to be generated. In order to obtain these time series, a simulation over a certain period of time had to be carried out. For this simulation an algorithm that solves Equations (2.63) to (2.65) accurately for every time step was necessary. This was achieved by using the PIMPLE algorithm implemented in the OpenFOAM (OpenFOAM Foundation, 2014) framework. This algorithm is the combination of two well-known algorithms for transient simulations, PISO (Issa, 1986) and transient-SIMPLE (Patankar and Spalding, 1972; Caretto et al., 1973). It employs two so-called “correctors”, which are loops of the PISO algorithm, to compute a Laplace equation for pressure correction. Subsequently, new values for the momentum are calculated. In addition, for every time step, there are “outer correctors” corresponding to loops of the transient-SIMPLE

algorithm. In these corrector steps, also the mass flux across the faces of the finite volumes is updated. For every time step, several outer corrections were computed until a specified initial residual of 1×10^{-6} was reached for pressure, velocity, and temperature. Usually, 10 to 50 outer correctors are necessary to achieve this minimum tolerance. Each of these transient-SIMPLE loops triggered two PISO loops. This algorithm was computationally more expensive than each algorithm by itself (about a factor of two compared to PISO, which needed more iterations of the linear equation solvers). However, the PIMPLE scheme results in stable and accurate solutions.

In this application, a solution for every time step was sought that provided good results up to frequencies in the range of $\mathrm{Sr} = 40$. Small time steps were necessary to achieve this. Time step size was determined by the CFL number which was fixed to $\mathrm{CFL} \leq 0.2$. Larger CFL numbers lead to an overprediction of the amplitude of G_{Nu}, although the simulation runs stable.

Using only the PISO algorithm, yielded good values for $|G_{\mathrm{Nu}}|$ and was computationally less expensive. However, the mass flux was only updated once each time step and therefore "lagged" behind. This lag leads to overpredicted values at high frequencies in G_{Nu} or necessitates much smaller time steps.

Spatial gradients and divergence terms were approximated using a central difference scheme (termed "linear" in OpenFOAM) that is second order in space. An unbounded, second order, conservative scheme (named "corrected") was used for Laplacian terms and surface normal gradients are calculated with explicit non-orthogonal correction (named "corrected").

As the temporal scheme, a second order approximation was chosen using three time levels calculating present values from two previous time instants. For the first time step, the implicit Euler scheme (Ferziger and Perić, 2002) was used. The size of each time step was evaluated with the calculated velocities forcing the maximum CFL number to $\mathrm{CFL}_{\mathrm{max}} \leq 0.2$. The maximum time between two instances was limited to $\Delta t = 5 \times 10^{-3}$, even if the CFL number was $\mathrm{CFL}_{\mathrm{max}} < 0.2$. This ensured a specified minimum temporal resolution for the highest frequency.

The fluid properties were represented by the Prandtl number with a fixed value of $\mathrm{Pr} = 0.71$ and the Reynolds number. To achieve the desired value for Re_0, given an unperturbed inlet velocity and a cylinder diameter, the kinematic viscosity ν was set accordingly.

At least two seconds were simulated using the finite volume approach. This yielded more than 40×10^3 instances in time that were used in the identification procedure. The duration of the simulation corresponded to the unperturbed flow passing the cylinder at least 200 times.

Axis-Symmetric Flow

For mean flow Reynolds numbers below the vortex shedding threshold $\mathrm{Re}_0 \leq 40$ (cf. Section 2.1), the symmetric mesh, as described in Section 5.1, was used. Simulations were carried out for $\mathrm{Re}_0 = 0.4$, $\mathrm{Re}_0 = 4$, and $\mathrm{Re}_0 = 40$. To acquire a more information and provide a more extensive investigation, additional simulations were computed at $\mathrm{Re}_0 = 0.1$, $\mathrm{Re}_0 = 0.2$, $\mathrm{Re}_0 = 0.5$, $\mathrm{Re}_0 = 0.7$, $\mathrm{Re}_0 = 1.0$, $\mathrm{Re}_0 = 2.0$, $\mathrm{Re}_0 = 3.0$, $\mathrm{Re}_0 = 10$, $\mathrm{Re}_0 = 20$, and $\mathrm{Re}_0 = 40$.

Laminar Vortex Shedding Regime

Numerical simulations at mean flow Reynolds numbers $\mathrm{Re}_0 = 120$ and $\mathrm{Re}_0 = 240$, where periodic vortex shedding occurs, are carried out on a two-dimensional grid featuring the full cylinder. This mesh was identical to the mesh presented in Section 5.1, but mirrored at the flow aligned axis through the center of the cylinder. At $\mathrm{Re}_0 = 240$ weak three-dimensional structures are present, which cannot be represented in the two-dimensional simulation. LES simulations at this Reynolds numbers showed that those three-dimensional structures have a negligible effect on Nußelt numbers and friction coefficient.

5.2.3 Data Acquisition

To evaluate the dynamic response of the heat transfer rate and skin friction (considered as the "responses" or "outputs") to free-stream velocity fluctuations (the "signal" or "input"), CFD data was extracted at each time step for subsequent post-processing. As the flow field is considered incompressible, a perturbation in overall mass flow rate imposed at the inlet boundary propagates without delay throughout the domain. Hence, a time lag due to finite propagation speed did not have to be taken into account.

A cross-sectional area average of axial velocity $u(t)$ is acquired at a monitor plane $9\,d$ upstream of the cylinder, where the fluid is not influenced noticeably by the presence of the cylinder (cf. Figure 5.2). In order to get a dimensionless value, the velocity is scaled with the cylinder diameter and the kinematic viscosity to form an (unsteady) Reynolds number. Additionally, time is non-dimensionalized according to Section 2.2.3 using cylinder diameter and unperturbed free-stream velocity.

Temperature gradients and shear stresses were obtained as a surface average over four sub-domains "1" to "4", respectively, each representing a 45° sector of the surface of the half cylinder (cf. Figure 5.2). The sub-domains were chosen equally distributed, similar to Föller et al. (2008). Different sectors coarsely stand for different flow regimes without regard for changes in flow patterns with mean flow Reynolds

number Re_0. In sector 1, stagnation point flow, also examined by Lighthill (1954), is dominant. Sectors 2 and sector 3 might be considered more similar to flat plate flow conditions, featuring a favorable and an adverse pressure gradient in steady state, respectively. Sector 4 contains the rear stagnation point and, at higher Reynolds numbers, the recirculation region. The gradients were stored for every time step during the computation and Equation (2.21) is used to calculate the Nußelt number.

The sector-wise integration over the heat flux resolved circumferential variations of the heat transfer dynamics in a rudimentary manner. In particular, it will be shown below that sector 4, located on the lee side of the cylinder, exhibits a behavior that is qualitatively different from the upstream sectors. It would have been possible, of course, to use more sectors and thus analyze the circumferential variation of heat transfer dynamics in more detail. However, with four sectors, a good compromise between the level of detail and ease of presentation is achieved. The sum of the Nußelt number and the friction coefficient in the four sectors yields a measure for the overall heat transfer rate and shear stress, respectively.

5.3 Large Eddy Simulation

For laminar flow, no modeling of turbulence is necessary, and the simulations are inherently direct numerical simulations (DNS). If the flow becomes turbulent, it would be necessary to resolve even the smallest length and time scales to perform DNS (cf. Section 2.1.3), i.e. the cell size and the time step size have to be of the order of the smallest turbulent length scales and time scales. The Large Eddy Simulation (LES) approach can be used for turbulent flow instead. The smallest turbulent scales are universal to some extend and can hence be modeled. The majority of the energy, contained mostly in the larger scales, is still resolved. The advantage of LES is the vast reduction of computational cost. The investigation in the subcritical regime was limited to only one mean flow Reynolds number of $Re_0 = 3900$ in this thesis. It is, therefore, to be understood as proof of concept rather than a comprehensive quantitative survey of the dynamic behavior as it was carried out in the case of laminar flow. The work shown here was previously published in Witte et al. (2016a,b).

Subcritical flow across a cylinder was studied quite extensively in the past. Vidya et al. (2016) performed DNS at Re = 2000 and Liang and Papadakis (2007) investigated the case of Re = 2580 experimentally and with LES, also in the presence of a single sinusoidal frequency excitation.

A mean flow Reynolds number of $Re_0 = 3900$ is suitable for this investigation because numerous results from experiments (Meyer et al., 2010), LES (Kravchenko and Moin, 2000; Franke and Frank, 2002) and DNS (Lehmkuhl et al., 2011) are available.

Domain size	Cylinder position from the inlet	N	c_d
$30d \times 20d \times \pi d$	$10\,d$	2.96×10^6	1.066 ± 0.105
$45d \times 30d \times \pi d$	$15\,d$	3.72×10^6	1.048 ± 0.093
$60d \times 40d \times \pi d$	$20\,d$	4.79×10^6	1.065 ± 0.110

Table 5.5: Results of the Steady-State Domain Size Study (LES Case). $\mathrm{Re}_0 = 3900$, $\mathrm{CFL}_{\max} \leq 0.5$, $N_c = 108$.

Moreover, Lysenko et al. (2012) used the OpenFOAM framework to conduct LES simulations with the same turbulence modeling as used in this thesis.

5.3.1 Computational Domain and Grid

The domain and the mesh were deduced from the basic mesh (cf. Section 5.1) and adjusted to the requirements for LES. Turbulent flow structures are three-dimensional by nature, and hence the mesh is extended in the direction of the cylinder axis. Further adjustments include discretization in the axial direction, proper spatial resolution, and turbulence handling.

Domain

The computational domain was chosen smaller than in the laminar case (cf. Section 5.1). The boundary layer thickness, i.e. the part of the flow field strongly influenced by the cylinder, scales with $\mathrm{Re}^{-1/2}$. A smaller domain is hence justified by a smaller boundary layer. The direction along the axis of the cylinder is resolved in the domain spanning πd (Franke and Frank, 2002; Lysenko et al., 2012). Table 5.5 shows the domain size study for the LES case. The tested domains span $10\,d$, $15\,d$, and $20\,d$ in the directions perpendicular to the axis of the cylinder. In the direction of the outlet border, twice this value was chosen, respectively. The drag coefficient c_d (cf. Section 2.1.2) was chosen as an integral value to compare and test for convergence. Due to fluctuations in the flow, attributed to turbulence and vortex shedding, the value of c_f is fluctuating even with steady, uniform inflow. To account for this fact, also the 95 % confidence interval is reported in Table 5.5.

Mesh

The topology of the three-dimensional mesh for LES was very similar to the two-dimensional mesh for the laminar simulations shown in Figure 5.2. It was adapted

N_c	N	c_d	Δ_c in %	$\Delta x_c/d\|_\phi$ $\cdot 10^{-3}$	$\Delta x_c/d\|_r$ $\cdot 10^{-3}$	N_{St}
72	1.11×10^6	1.1164	13.8	21.8	3.63	0.987
108	3.72×10^6	1.0286	4.80	16.4	2.73	1.31
144	8.70×10^6	0.9963	1.50	10.9	1.82	1.97
180	16.6×10^6	0.9815	—	9.54	1.59	2.25

Table 5.6: Results of the Cell Size Study (LES Case). $45d \times 30d \times \pi d$, $\mathrm{Re}_0 = 3900$, $\mathrm{CFL}_{\max} \leq 0.5$, Stokes layer size $\delta_{\mathrm{St}}(\mathrm{Re}_0 = 3900, \mathrm{Sr} = 40) = 0.003\,581\,d$.

to the smaller domain size, and the spanwise direction was discretized. Three refinement steps in coaxial cylindrical regions with decreasing radius around the cylinder ensured that cells were refined in the direction of the cylinder axis. This yielded a total of 216 cells at the surface of the cylinder in the spanwise direction. Additionally, the grid close to the cylinder experienced a grading in radial direction so that the cells formed layers around the cylinder. The non-dimensional wall distance was $y^+ \approx 1$ for the innermost cell, and the aspect ratio was ~ 6. The results of the cell size study are given in Table 5.6. The difference in drag coefficient between the evaluated grid and the finest gird is quantified by $\Delta_c = [c_d - c_d(N_c = 180)] / c_d(N_c = 180)$. Moreover, the extent of the wall adjacent cells in circumferential direction (ϕ) and radial direction (r) are reported. Using the latter values, an estimate can be given how many cells N_{St} discretized the unsteady Stokes boundary layer.

The mesh chosen to conduct this study featured a domain size of $45d \times 30d \times \pi d$, i.e. the medium sized domain in Table 5.5. Although all three meshes show very similar values for c_d (all within the confidence intervals), this grid produced the smallest confidence interval and presented a good trade-off between computational cost and accuracy. The circumference of the full cylinder was discretized using $2\,N_c = 216$ cells. The same number of cells was used to discretize the spanwise direction. This lead to a total of 3.72×10^6 cells. A detail of the mesh close to the cylinder is shown in Figure 5.5.

The drag coefficient of the cylinder for the mesh used in this thesis ($c_d = 1.029$) was about 5 % higher than the drag coefficient simulated with the finest mesh ($c_d = 0.98$) and also 5 % higher than values reported in experiments ($c_d = 0.98$) (Norberg, 1994; Meyer et al., 2010). This corresponded to one standard deviation of the fluctuating quantity. Gradual refinement of the grid provided a continuous decrease in the drag coefficient towards the value of the finest mesh. The length of the recirculation zone and the vortex shedding frequency were within the range of experimental results reported in literature ($L_r = 1.19 - 1.33\,d$; $f = 0.21 - 0.22\,u_{0,\infty}/d$) (Meyer et al., 2010). Although the comparatively high Reynolds number leads to a very small Stokes layer at high frequencies, at least one cell was within a distance δ_{St} to the cylinder.

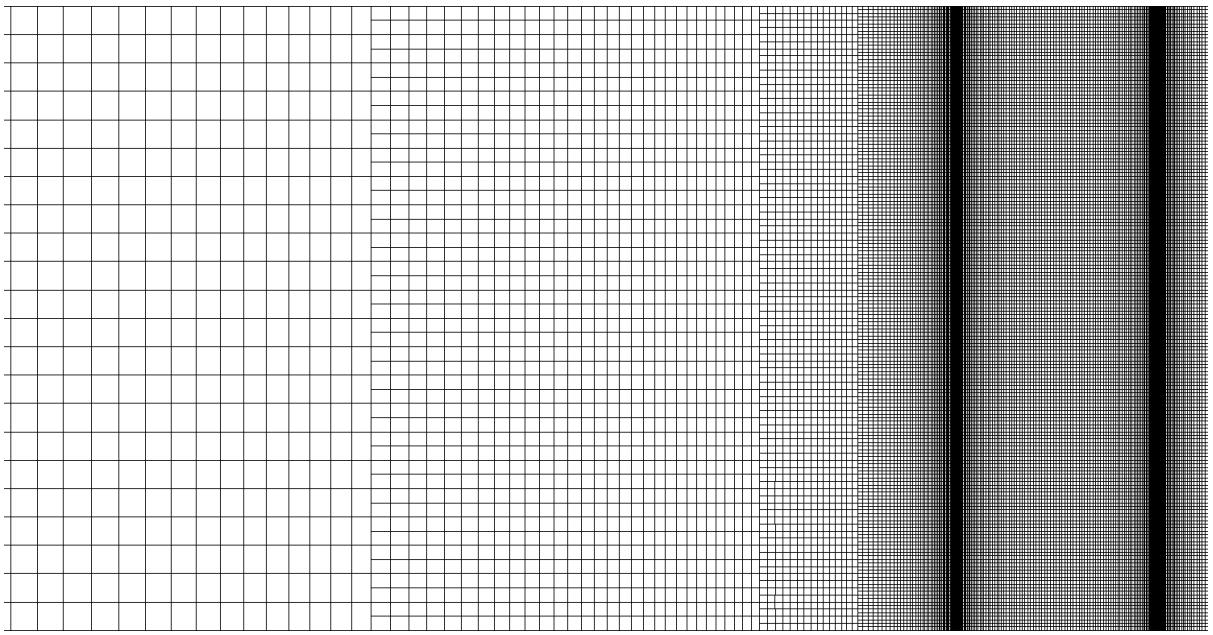

Figure 5.5: Topology of LES Mesh in Spanwise Direction. Cut through the $y = 0$-plane. The full spanwise extent is shown.

Boundary Conditions

The boundary conditions were chosen in the same way as in the two-dimensional laminar cases. Additionally, the boundaries in spanwise direction were specified as periodic boundaries. Flow leaving the domain on one of these boundaries reenters the domain at the other boundary to emulate an infinitesimally long cylinder. Two additional flow variables, the subgrid scale (SGS) turbulent kinetic energy k_{SGS} and the SGS viscosity ν_{SGS}, had to be accounted for.

It was assumed that the flow at the inlet was laminar. Hence, the free-stream turbulence was not a parameter in this investigation. The SGS turbulent kinetic energy k_{SGS} was therefore set to a small value at the inlet. At the outlet, a zero gradient boundary condition was applied.

For the boundary conditions of the SGS variables at the surface, three approaches were considered. The first strategy was to apply wall models for k_{SGS} and ν_{SGS}. However, the mesh close to the surface of the cylinder was fine enough to resolve the gradients at the wall ($y^+ \approx 1$) and hence a wall model for the SGS turbulent kinetic energy, recommended for $y^+ > 30$ is not applicable. In the second approach, the variables were chosen to $k_{\mathrm{SGS}} = 0$ and $\nu_{\mathrm{SGS}} = 0$ at the surface. These conditions are very strict and theoretically only applicable in the limit of fully resolved turbulence (DNS). The boundary conditions applied in this thesis combined both approaches. Instead of a wall model for k_{SGS}, zero gradient conditions were selected, i.e. the diffusive flux of turbulent kinetic energy through the surface is zero (Ferziger and Perić, 2002). The SGS viscosity ν_{SGS} was calculated explicitly for the whole domain

except for the cylinder boundary. At the cylinder boundary, Spalding's formula for the law of the wall (Spalding, 1961) was used. This wall function provides suitable values for the SGS viscosity over a large range of y^+ values and explicitly also for $y^+ \lesssim 1$.

5.3.2 Turbulence Modeling

In the LES approach chosen in this thesis, the computational grid acts as a filter (grid filter) separating the larger, resolved scales from the smaller, modeled scales. Hence, the size of the mesh determines the filter width $\overline{\Delta}$. The mesh was chosen in such a way that more than 80 % of the turbulent kinetic energy is part of the resolved portion, i.e. at wavenumbers smaller than the cutoff wavenumber of the filter. The SGS at higher wavenumbers included only a smaller fraction of the energy. In Figure 2.8, this SGS part is illustrated by the hatched area of the graph. As indicated in Figure 2.8, the cutoff frequency should lie in the inertial range. Then, the modeled portion is in the universal equilibrium range.

In the LES approach, the filtered Navier–Stokes equations are solved (Pope, 2000; Davidson, 2004). The quantity that needs to be modeled is the SGS stress tensor τ_{SGS}, also called residual stress tensor. A popular method is to use eddy viscosity models. An effective viscosity which is the sum of the molecular viscosity and a SGS viscosity $\nu_{\mathrm{eff}} = \nu + \nu_{\mathrm{SGS}}$ (Boussinesq hypothesis) was used in the filtered equations.

One Equation Eddy Viscosity Model

In this thesis, a dynamic subgrid kinetic energy model (Ghosal et al., 1995; Menon et al., 1996), also referred to as dynamic one equation eddy SGS model, was chosen to model the unresolved portion of turbulence. In the one equation eddy viscosity model by Deardorff (1980), the modeled turbulent kinetic energy k was calculated with an additional transport equation. The SGS stress tensor τ^{SGS} was modeled using

$$\tau_{ij}^{\mathrm{SGS}} - \frac{1}{3}\delta_{ij}\tau_{kk}^{\mathrm{SGS}} = -2C_k\Delta k^{1/2}\overline{S}_{ij}\,. \tag{5.11}$$

The strain rate tensor $S_{i,j}$ is given by

$$S_{ij} = \frac{1}{2}\left(\frac{\partial u_i}{\partial x_j} + \frac{\partial u_j}{\partial x_i}\right) \tag{5.12}$$

(cf. Newton's law $\tau_{ij} = 2\nu S_{ij}$, Section 2.2.1 and Section 2.2.5) and $\overline{S}_{ij}$ denotes its filtered value.

The transport equation for the dimensionless SGS turbulent kinetic energy is given by

$$\frac{\partial k_{\mathrm{SGS}}}{\partial t} + u_j \frac{\partial k_{\mathrm{SGS}}}{\partial x_j} = \frac{\partial}{\partial x_j}\left(\frac{1}{\mathrm{Re}_{\mathrm{eff}}}\frac{\partial k_{\mathrm{SGS}}}{\partial x_j}\right) + P - \epsilon \tag{5.13}$$

with the production rate and the dissipation defined by

$$P = \frac{2\overline{S}_{ij}\overline{S}_{ij}}{\mathrm{Re}_{\mathrm{SGS}}} \qquad \text{and} \qquad \epsilon = \frac{C_e k_{\mathrm{SGS}}^{3/2}}{\overline{\Delta}}. \tag{5.14}$$

The SGS viscosity as it appears in the effective Reynolds number $\mathrm{Re}_{\mathrm{eff}}$ is evaluated by

$$\nu_{\mathrm{SGS}} = C_k k_{\mathrm{SGS}}^{1/2} \overline{\Delta}. \tag{5.15}$$

The coefficients are determined to $C_e = 1.048$ and $C_k = 0.094$ (OpenFOAM Foundation, 2014) for the standard one equation eddy viscosity model.

In the dynamic model (Germano et al., 1991), the coefficients C_e and C_k are adapted locally and dynamically. A test filter with twice the filter width than the grid filter is applied. The constant C_k is determined by solving a variational problem (Ghosal et al., 1995).

Measure of Turbulence Resolution

The measure of turbulence resolution, often called Pope's criterion (Pope, 2000), is the ratio of modeled turbulent kinetic energy to its total value. This measure is given by

$$M = \frac{k_{\mathrm{SGS}}}{k_{\mathrm{res}} + k_{\mathrm{SGS}}} \tag{5.16}$$

where k_{res} denotes the resolved turbulent kinetic energy. The modeled turbulent kinetic energy k_{SGS} is a transported quantity and hence available as a field variable for every instant in time. Not the instantaneous value, but the mean (time averaged) quantity was used for this analysis to account for variations in time.

The resolved turbulent kinetic energy was evaluated from the filtered velocity field. Generally, the mean kinetic energy of the flow can be decomposed as

$$\langle E \rangle = E_0 + k \tag{5.17}$$

where $\overline{E} = 1/2\langle\overline{u}\rangle\langle\overline{u}\rangle$ is the kinetic energy of the mean flow and $k = 1/2\langle\overline{u}''\overline{u}''\rangle$ is the turbulent kinetic energy. Using the fact that the RMS value of a quantity is related to mean and standard deviation by $x_{\mathrm{rms}}^2 = \langle x\rangle^2 + \sigma^2 = \langle x^2\rangle$ yields

$$k_{\mathrm{res}} = \frac{1}{2}\left(\sigma_{11}^2 + \sigma_{22}^2 + \sigma_{33}^2\right) \tag{5.18}$$

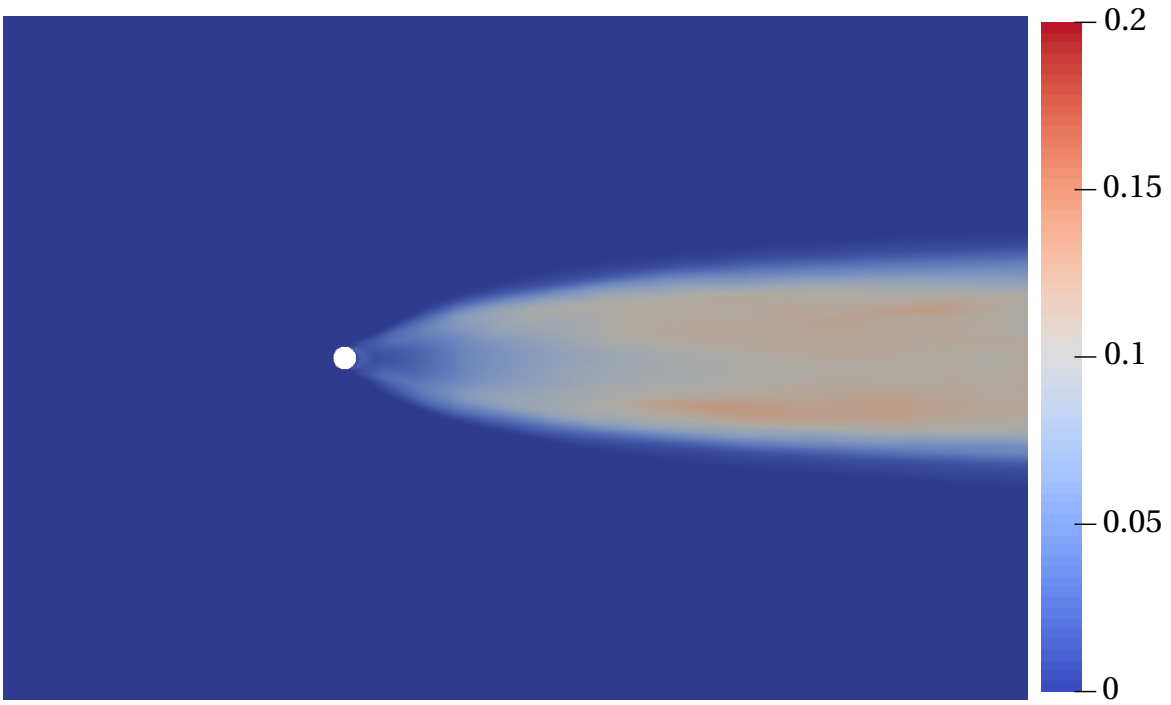

Figure 5.6: Measure of Turbulence Resolution. $M < 0.2$ is considered an adequate resolution for LES (Pope, 2000).

for the resolved turbulent kinetic energy. An estimate of $\sigma^2 = \text{var}(\overline{u})$ was calculated at every time step during the simulation.

Pope's criterion states that the measure of turbulence resolution should be small, e.g. $M < 0.2$. Figure 5.6 depicts the criterion for the simulation carried out in this thesis.

5.3.3 Computational Procedure

For the LES, a centered scheme was used for the gradients and a flux-limited scheme ("limited linear") for the divergence terms. The limiter function blends between first order schemes, e.g. upwind scheme (UD), and second order schemes, e.g. central scheme (CD), to ensure the stability of the computation. This is achieved by computing an arbitrary variable f using

$$f = f_{\text{UD}} + \Psi(r)\left(f_{\text{CD}} - f_{\text{UD}}\right) \tag{5.19}$$

with flux limiter function Ψ and the ratio of successive gradients r. The flux limiter was chosen not to follow the total variation diminishing approach (Sweby, 1984), but to tend more towards the higher order scheme. As in the two-dimensional cases, a second order time discretization was chosen. To reduce the computational time a maximum CFL number of CFL = 0.5 is applied to determine the time step size.

5.3.4 Data Acquisition

The data acquisition procedure is essentially the same as in the laminar cases (cf. Section 5.2.3). The instantaneous Reynolds number $\mathrm{Re}(t)$ is taken as an area average from the $x = -9\,d$-plane. $\mathrm{Nu}(t)$ and $c_f(t)$ are area averages from the cylinder. The spatial proportionment into sectors was discarded as turbulence not only leads to circumferential differences, but also to spanwise fluctuations. Instead only integral values for the whole cylinder were extracted and saved as tabulated time series.

5.4 Linearized Navier Stokes Equations

Another possibility to generate a linear model for the heat transfer and skin friction dynamics is to linearize the governing equations. This approach was chosen by Apelt and Ledwich (1979) to study the behavior of a cylinder in unsteady flow. Ultimately, Kwon and Lee (1985) used this approach to examine the transfer behavior of a heated wire in the scope of Rijke tube thermoacoustic oscillations.

Following the approach by Kwon and Lee (1985), a vorticity–stream function formulation was chosen for the Navier–Stokes equations. The advantage of this method is that pressure is dropped from the formulation and only three equations have to be solved in two dimensions. The dimensionless governing equations are presented in Section 2.2.6 (Equation (2.68)–(2.70)). In this approach, a steady-state solution was computed first. The perturbation equations, linearized around this steady state, were solved subsequently. To achieve good results a steady state has to exist. Hence, only $\mathrm{Re}_0 \leq 40$ was considered for this treatment. With this method, the frequency response of skin friction and heat transfer can be assessed directly without SI or other time series analysis techniques. The frequency response function can be approximated evaluating the response at multiple discrete frequencies for the same steady-state solution. The complete procedure was implemented in MATLAB (The MathWorks, Inc., 2016).

5.4.1 Computational Domain and Grid

Computational domain and grid are to a great extent based on the basic setup described in Section 5.1. Especially the resolution close to the surface of the cylinder and the domain size were chosen according to these investigations. The solver, in this case, was written for only this purpose and therefore a very efficient, but otherwise limited method could be implemented using a log-polar grid.

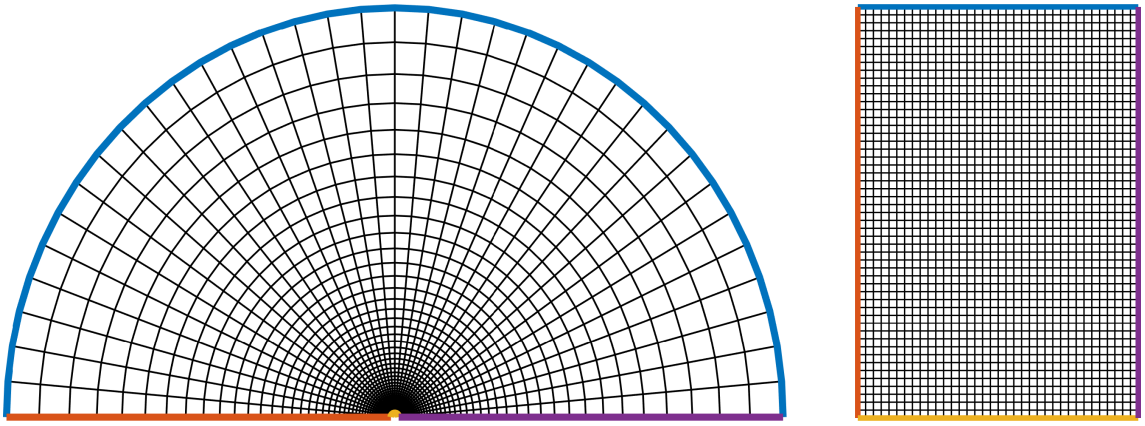

Figure 5.7: Mesh for LNSE Approach. Mesh shown in real coordinates (left) and in transformed coordinates (right). The domain boundaries are marked with colors.

Introducing modified polar coordinates η and ϕ, the so-called log-polar coordinates, yields

$$\eta = \ln\left(\frac{r}{d}\right). \tag{5.20}$$

The transformation to the x–y–system is achieved with

$$x = -\mathrm{e}^{\eta} \cdot \cos(\phi) \qquad \text{and} \qquad y = \mathrm{e}^{\eta} \cdot \sin(\phi). \tag{5.21}$$

With this transformation, concentric circles around the origin have exponentially growing radius r with linearly growing η. This type of mesh offers two advantages: On the one hand, the region close to the surface of the cylinder is greatly refined. In the far field, however, where gradients are comparably small, the mesh is rather coarse, which reduces the cell count. On the other hand, the governing equations can be formulated like in Cartesian coordinates except for a scaling factor related to the transformation. Figure 5.7 shows the grid created with this approach in x–y–coordinates (left) and in transformed coordinates (right). The mesh was created using the information acquired in the grid independence study in Section 5.1.3. Hence, the following dimensions given in Table 5.7 were used.

5.4.2 Perturbation Equation in Vorticity–Stream Function Form

To compute the frequency response to pulsations in the free-stream velocity, i.e. stream function, Equations (2.68) to (2.70) were modified. Harmonic perturbations were introduced for the flow variables stream function ψ, vorticity ζ, and temperature Θ in Equations (2.68) to (2.70). These perturbed quantities are given by

$$\psi = \psi_0 + \epsilon\psi_1 \mathrm{e}^{\mathrm{i}\mathrm{Sr}t}, \qquad \zeta = \zeta_0 + \epsilon\zeta_1 \mathrm{e}^{\mathrm{i}\mathrm{Sr}t}, \text{ and} \qquad \Theta = \Theta_0 + \epsilon\Theta_1 \mathrm{e}^{\mathrm{i}\mathrm{Sr}t}$$

N_c	N_η	$\Delta\phi$ $\cdot 10^{-3}$	$\Delta\eta/d$ $\cdot 10^{-3}$	Total number of cells
37	53	0.0849	0.0869	1961
73	106	0.0430	0.0434	7738
145	212	0.0217	0.0217	30740
289	424	0.0109	0.0109	122536

Table 5.7: Different Meshes Used in the LNSE Approach. Results of the steady-state cell size study for the log-polar grid, $L_d = 50$, $\mathrm{Re}_0 = 40$, steady state.

where ϵ denotes the perturbation amplitude. It serves as a small parameter that is used for bookkeeping in the derivation of the linearized equations, i.e. ultimately only terms of order $\mathcal{O}(\epsilon^1)$ or lower are kept. The flow variables with indices forfeit their dependence on time. The temporal derivative can be computed directly. The resulting equations were separated according to the order of the bookkeeping variable ϵ. Terms with ϵ^0, i.e. zeroth order terms, form the equations for the steady state. These equations are still nonlinear as is the nature of the flow. First order terms amount to the linearized perturbation equations. Terms with higher powers in ϵ were neglected as they become small for $\epsilon \to 0$, i.e. small fluctuation amplitudes.

Steady-State Equations

The zeroth order equations describe the steady-state flow. They are given by

$$\frac{\partial^2\psi_0}{\partial\eta^2} + \frac{\partial^2\psi_0}{\partial\phi^2} = -r^2\zeta_0 \tag{5.22}$$

$$\frac{\partial\zeta_0}{\partial\phi}\frac{\partial\psi_0}{\partial\eta} - \frac{\partial\zeta_0}{\partial\eta}\frac{\partial\psi_0}{\partial\phi} = \frac{1}{\mathrm{Re}_0}\left(\frac{\partial^2\zeta_1}{\partial\eta^2} + \frac{\partial^2\zeta_1}{\partial\phi^2}\right) \tag{5.23}$$

$$\frac{\partial\Theta_0}{\partial\phi}\frac{\partial\psi_0}{\partial\eta} - \frac{\partial\Theta_0}{\partial\eta}\frac{\partial\psi_0}{\partial\phi} = \frac{1}{\mathrm{Re}_0\,\mathrm{Pr}}\left(\frac{\partial^2\Theta_1}{\partial\eta^2} + \frac{\partial^2\Theta_1}{\partial\phi^2}\right). \tag{5.24}$$

These equations in (ϕ, η) coordinates are equal to Equations (2.68) to (2.70) in (x, y) coordinates save for the transformation parameter r. The steady-state variables do not depend on time and hence the time derivatives are dropped.

Boundary conditions given in primitive variables in Section 5.1.1 had to be translated to the solved variables. In the far field $\eta = \eta_{\max}$, the stream function was given by the potential flow solution reported in Section 2.2.7, Equation (2.76). The assumption of potential flow at this boundary also implies $\zeta = 0$. In order to allow the vorticity created at the surface of the cylinder to leave the domain, the downstream part of the far field boundary is set to zero gradient conditions $((\partial\zeta)/(\partial\eta) = 0)$. The

temperature of the flow corresponds to the temperature in the far field and thus $\Theta = 0$. In an analogous manner, the far field downstream is set to $(\partial\Theta)/(\partial\eta) = 0$.

At the surface of the cylinder, the application of a no-slip boundary is not trivial with the given variables. Both the velocity through the surface and the slip along the surface have to be zero. The first requirement is fulfilled by setting $\psi = 0$ at the boundary. The gradient of the stream function vanishes in circumferential direction which leads to $(\partial\psi)/(\partial\phi) = u_\eta = 0$. This is also in accordance with the potential flow solution. The second requirement is then formulated, by the use of Equation (2.68), in plain Cartesian coordinates as

$$\frac{\partial^2\psi}{\partial\eta^2} + \zeta = 0\,. \tag{5.25}$$

Hence, a wall vorticity enforcing the no-slip condition had to be calculated. This also shows that the surface of the cylinder is the (only) source of vorticity. Following the approach discussed in Section 2.2.5 the temperature at the surface of the cylinder is fixed and therefore $\Theta_w = 1$.

Parallel to the flow to the windward and to the lee side of the cylinder are symmetry boundaries. The flow velocity is determined by the derivatives of the stream function. No flow crosses the symmetry boundary which dictates that the stream function has to be constant along it. With the defined value of $\psi = 0$ at the surface of the cylinder, this condition also applies to the symmetry boundaries. In this position, vorticity also cancels to $\zeta = 0$ as any mirrored flow feature exhibits a vorticity with opposite sign. The temperature gradient vanishes at the symmetry condition, i.e. $(\partial\theta)/(\partial\eta) = 0$.

The boundary conditions are summarized as

$$\eta = \ln(1/2) \qquad \psi_0 = 0 \qquad \zeta_0 = \zeta_{0,w} \qquad \Theta_0 = 1 \tag{5.26}$$

$$\eta \to \infty \qquad \psi_0 = u_{0,\infty}\, r\, \sin(\phi) \qquad \frac{\partial\zeta_0}{\partial\eta} = 0 \qquad \Theta_0 = 0 \tag{5.27}$$

$$\phi = 0 \qquad \psi_0 = 0 \qquad \zeta_0 = 0 \qquad \frac{\partial\Theta_0}{\partial\phi} = 0 \tag{5.28}$$

$$\phi = 2\pi \qquad \psi_0 = 0 \qquad \zeta_0 = 0 \qquad \frac{\partial\Theta_0}{\partial\phi} = 0\,. \tag{5.29}$$

To quantify skin friction and heat transfer, the steady-state friction coefficient and the steady-state Nußelt number were computed using

$$\mathrm{Nu}_{0,\phi} = \left.\frac{\partial\Theta_0}{\partial\eta}\right|_{\eta=\ln(1/2)} \qquad \text{and} \qquad c_{f,x,0,\phi} = \frac{2}{\mathrm{Re}_0}\,\zeta_{0,w}\,\sin(\phi)\,. \tag{5.30}$$

Perturbation Equations

In the perturbation equations or first order equations, the terms of order $\mathcal{O}(\epsilon)$ are collected. The equations read

$$\frac{\partial^2\psi_1}{\partial\eta^2}+\frac{\partial^2\psi_1}{\partial\phi^2}=-r^2\zeta_1 \tag{5.31}$$

$$\mathrm{iSr}\,r^2\zeta_1+\frac{\partial\zeta_1}{\partial\phi}\frac{\partial\psi_0}{\partial\eta}-\frac{\partial\zeta_1}{\partial\eta}\frac{\partial\psi_0}{\partial\phi}+\frac{\partial\zeta_0}{\partial\phi}\frac{\partial\psi_1}{\partial\eta}-\frac{\partial\zeta_0}{\partial\eta}\frac{\partial\psi_1}{\partial\phi}=\frac{1}{\mathrm{Re}_0}\left(\frac{\partial^2\zeta_1}{\partial\eta^2}+\frac{\partial^2\zeta_1}{\partial\phi^2}\right) \tag{5.32}$$

$$\mathrm{iSr}\,r^2\Theta_1+\frac{\partial\Theta_1}{\partial\phi}\frac{\partial\psi_0}{\partial\eta}-\frac{\partial\Theta_1}{\partial\eta}\frac{\partial\psi_0}{\partial\phi}+\frac{\partial\Theta_0}{\partial\phi}\frac{\partial\psi_1}{\partial\eta}-\frac{\partial\Theta_0}{\partial\eta}\frac{\partial\psi_1}{\partial\phi}=\frac{1}{\mathrm{Re}_0\,\mathrm{Pr}}\left(\frac{\partial^2\Theta_1}{\partial\eta^2}+\frac{\partial^2\Theta_1}{\partial\phi^2}\right). \tag{5.33}$$

Time derivatives are resolved explicitly with $(\partial\zeta_1\,\mathrm{e}^{\mathrm{iSr}\,t})/(\partial t)=\mathrm{iSr}\,\zeta_1\,\mathrm{e}^{\mathrm{iSr}\,t}$ and the transformation parameter r.

The boundary conditions for the perturbation equations are very similar to those of the steady state. Besides the fact that these boundary conditions apply to the perturbed quantities ψ_1, ζ_1, and Θ_1 the main differences concern the stream function at the far field boundary and the temperature at the surface of the cylinder. The stream function is directly linked to the excitation as it decides upon the free-stream velocity. Hence, it is computed from the potential flow solution with the perturbation velocity in the far field $u_{1,\infty}=\epsilon\,u_{0,\infty}$. The temperature at the cylinder is a Dirichlet boundary condition. It is fixed to a given value and hence $\Theta_0=1$. This also dictates, that no pulsations may occur at the surface of the cylinder or otherwise this condition would be violated. It follows from this that the pulsating quantity is zero $\Theta_1=0$ at this position.

Summarizing, the boundary conditions for the periodic fluctuations are given by

$$\eta=\ln(1/2): \qquad \psi_1=0 \qquad \zeta_1=\zeta_{1,w} \qquad \Theta_1=0 \tag{5.34}$$

$$\eta\to\infty: \qquad \psi_1=u_{1,\infty}\,r\,\sin(\phi) \qquad \frac{\partial\zeta_1}{\partial\eta}=0 \qquad \Theta_1=0 \tag{5.35}$$

$$\phi=0: \qquad \psi_1=0 \qquad \zeta_1=0 \qquad \frac{\partial\Theta_1}{\partial\phi}=0 \tag{5.36}$$

$$\phi=2\pi: \qquad \psi_1=0 \qquad \zeta_1=0 \qquad \frac{\partial\Theta_1}{\partial\phi}=0\,. \tag{5.37}$$

Analogous to the steady state, the Nußelt number and the friction coefficient of the fluctuations are computed by

$$\mathrm{Nu}_{1,\phi}=\left.\frac{\partial\Theta_1}{\partial\eta}\right|_{\eta=\ln(1/2)} \qquad \text{and} \qquad c_{f,x,1,\phi}=\frac{2}{\mathrm{Re}_0}\,\zeta_{1,w}\,\sin(\phi)\,. \tag{5.38}$$

5.4.3 Finite Difference Approach

The governing equations in stream function vorticity formulation (Equation (5.22) to Equation (5.24) and Equation (5.31) to Equation (5.33)) were solved using a finite difference approach on a log-polar grid (Thom, 1933; Fornberg, 1980; Kwon and Lee, 1985).

On an equidistant, rectangular grid such as the one employed in this case (cf. Figure **??**), the finite difference formulation is equal to the finite volume formulation. Therefore, it is argued that this approach offers similar accuracy as state of the art tools using the finite volume approach, e.g. OpenFOAM.

Derivatives were approximated using central differences and thus second order accuracy in space was achieved. For any given flow variable f, the central difference is given by

$$\frac{\partial f}{\partial \eta} \approx \frac{f_{i+1,j} - f_{i-1,j}}{2\,\Delta\eta} \qquad \text{and} \qquad \frac{\partial f}{\partial \phi} \approx \frac{f_{i,j+1} - f_{i,j-1}}{2\,\Delta\phi}. \tag{5.39}$$

Second derivatives were approximated by

$$\frac{\partial^2 f}{\partial \eta^2} \approx \frac{f_{i+1,j} - 2f_{i,j} + f_{i-1,j}}{(\Delta\eta)^2} \qquad \text{and} \qquad \frac{\partial^2 f}{\partial \phi^2} \approx \frac{f_{i,j+1} - 2f_{i,j} + f_{i,j-1}}{(\Delta\phi)^2} \tag{5.40}$$

which also is a central difference. At the boundaries, one sided differences of second order were used.

Vorticity at the Surface of the Cylinder

The vorticity at the surface is an important factor in these simulations. The wall boundary conditions, i.e. no-slip and no penetration, have to be enforced. The no-slip condition is violated by the potential flow solution, and the vorticity has to be calculated to counteract. Thom (1933) developed a formula that provides first order accuracy. In this thesis, the equation

$$\zeta_w = \frac{1}{2}\frac{1}{r^2}\frac{8\psi_{i-1,j} - \psi_{i-2,j}}{(\Delta\eta)^2}$$

was used, which is second order accurate (Weinan and Liu, 1996). With this approximation, slip cannot be suppressed completely. Hence, the slip velocity $(\partial\psi)/(\partial\eta)\big|_w$ is used as a secondary criterion for convergence and quality of the results.

5.4.4 Computational Procedure

Steady State

To evaluate the linearized equations, it was first necessary to find a steady state at which the linearization is carried out. This was achieved by solving the nonlinear equations sequentially.

The nonlinear equation system was solved by using an initial velocity, calculated from the potential equations (cf. Section 2.2.7), to evaluate the stream function. The derivative of the stream function was used as the velocity in the subsequent iteration. The vorticity generated at the surface of the cylinder to fulfill the no-slip condition was propagated. This procedure was repeated until changes in the solution were small compared to the initial change. Convergence was improved through the use of a relaxation factor. Figure 5.8 depicts a flow chart of the iterative procedure. The temperature is not coupled with the other equations and could hence be calculated in a final step outside the iteration loop.

The change in vorticity normalized with the vorticity after the first iteration written as

$$\sigma = \frac{\|\boldsymbol{\zeta}^{(i)}\| - \|\boldsymbol{\zeta}^{(i-1)}\|}{\|\boldsymbol{\zeta}^{(1)}\|} \tag{5.41}$$

was used as the convergence criterion. Additionally, the slip velocity at the surface of the cylinder $(\partial\psi)/(\partial\eta)$ was evaluated to check for the fulfillment of the no-slip boundary condition.

A relaxation factor ρ was applied to the wall vorticity. The relaxed vorticity at the surface was computed for the ith iteration with

$$\zeta_w^* = \rho\zeta_w^{(i)} + (1-\rho)\zeta_w^{(i-1)}\,. \tag{5.42}$$

The relaxation factor had to be very small initially ($\rho \approx 0.05$). To find an optimum between stability and convergence, the relaxation factor was adapted. Depending on the behavior of the convergence criterion, the relaxation factor was adjusted. If σ rose from one iteration to the next, ρ was decreased to enhance stability. Vice versa, ρ was increased for even faster convergence, if σ dropped rapidly. To make this adaptive relaxation scheme robust, ρ was forced to stay in the interval $[0.001, 1]$. The simulation was restarted with a lower initial value for ρ if the solution diverged fatally.

This algorithm for the solution of the nonlinear coupled steady-state equation system, although it may seem crude, proved to be more efficient than the built-in MATLAB (The MathWorks, Inc., 2016) function provided by the optimization toolbox.

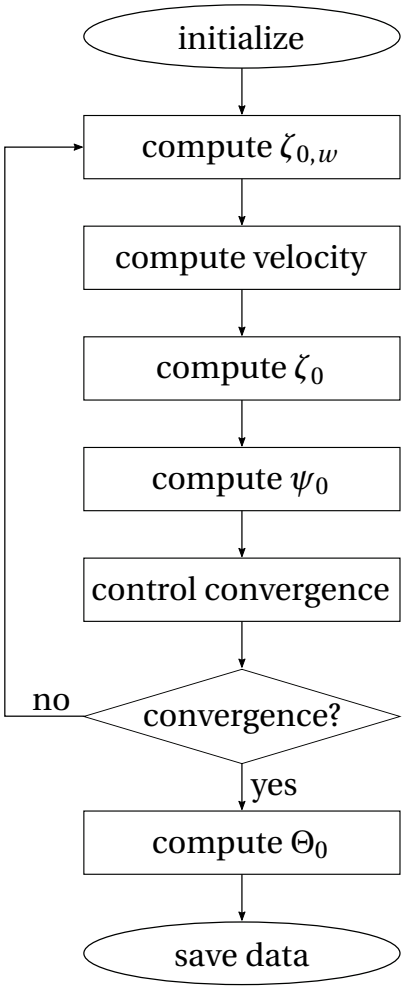

Figure 5.8: Flowchart of the Steady-State Solver.

Perturbed Quantities

The first order equations are linear and can hence be solved efficiently by using the matrix left division function from MATLAB (The MathWorks, Inc., 2016, mldivide "\"). The equations for stream function and vorticity are coupled, and they are hence collected in a single system matrix. For convenience also the temperature is induced. This is not strictly necessary and can also be calculated sequentially. The structure of the matrix can be depicted as

$$\begin{bmatrix} \boldsymbol{A}_\psi & \boldsymbol{B}_{\psi\zeta} & \mathbf{0} \\ \boldsymbol{C}_{\zeta,\psi} & \boldsymbol{A}_\zeta & \mathbf{0} \\ \mathbf{0} & \mathbf{0} & \boldsymbol{A}_\theta \end{bmatrix} \begin{bmatrix} \psi \\ \zeta \\ \Theta \end{bmatrix} = \begin{bmatrix} \psi \\ \zeta \\ \Theta \end{bmatrix}_{\delta\Omega} . \tag{5.43}$$

The finite difference stencil for the respective Equation (5.31) to (5.33) is included in $\boldsymbol{A}_\psi$, $\boldsymbol{A}_\zeta$, and $\boldsymbol{A}_\Theta$. The submatrix $\boldsymbol{B}_{\psi,\zeta}$ couples the vorticity with the stream function equations. In an analogous manner, the derivatives of the stream function (velocities) are coupled with the vorticity equation through $\boldsymbol{C}_{\zeta,\psi}$. $\delta\Omega$ denotes the boundary

conditions. The terms $\mathrm{i}\,\mathrm{Sr}\,r^2\zeta_1$ and $\mathrm{i}\,\mathrm{Sr}\,r^2\Theta_1$ serve as source terms and are included through the diagonals in $\boldsymbol{A}_\zeta$ and $\boldsymbol{A}_\Theta$.

Excitation

The excitation is equivalent to a sine wave excitation as detailed in Section 5.2.1. In time domain it is given by

$$\mathrm{Re}(t) = \mathrm{Re}_0\,(1 + \epsilon\,\sin(\mathrm{Sr}\,t))\,. \tag{5.9}$$

In the frequency domain approach with the linearized Navier–Stokes equations, this is achieved in two steps. The amplitude ϵ is specified in the boundary condition for the stream function pulsation

$$\psi_{1,\eta\to\infty} = u_{0,\infty}\,\epsilon \cdot r \cdot \sin(\phi)\,. \tag{5.44}$$

The frequency, i.e. the Strouhal number Sr, is included in the system matrix, in the $\mathrm{i}\,\mathrm{Sr}\,r^2\zeta_1$ and $\mathrm{i}\,\mathrm{Sr}\,r^2\Theta_1$ term, and can be specified according to the desired excitation.

5.4.5 Acquisition of Frequency Domain Data

The steady-state solver was used to find a solution (ψ_0, ζ_0, and Θ_0) for a specified mean flow Reynolds number Re_0 and Prandtl number Pr. These converged results were used to compute the fluctuating quantities (ψ_1, ζ_1, and Θ_1) at the same Re_0 and Pr and at specified frequencies Sr. The frequencies were chosen from the interval of interest $[0, 40]$. A smaller distance between sequential frequencies was used in regions where greater changes were assumed. The frequency response for the heat transfer and the skin friction at each Strouhal number was evaluated using Equation (2.101) in the form

$$G_{\mathrm{Nu}}(\mathrm{Sr}) = \frac{\mathrm{Nu}_1(\mathrm{Sr})/\mathrm{Nu}_0}{\epsilon} \qquad \text{and} \qquad G_{c_f}(\mathrm{Sr}) = \frac{c_{f,1}(\mathrm{Sr})/c_{f,0}}{\epsilon}\,. \tag{5.45}$$

This frequency response data serves as input for the continuous time identification procedure introduced in Section 4.4.5. Results are presented in Section 6.2.

5.4.6 Discussion and Outlook

For Reynolds numbers higher than the onset of vortex shedding, which occurs around $\mathrm{Re} \approx 47$ (cf. Table 2.1), no steady-state solution exists. The dynamics of the wake are inherently unsteady but repeat periodically. Fornberg (1980) computed steady-state solutions even beyond this threshold up to $\mathrm{Re} = 300$. However, these

solutions are found numerically by neglecting the time derivative in the Navier–Stokes equations and are not physically meaningful.

A possible approach would be to compute cycle averaged solutions for the flow fields (ψ_0, ζ_0, and Θ_0) and subsequently calculate the linearized perturbation variables. Without further improvements, this would not yield acceptable results and is thus beyond the scope of this thesis.

This approach to acquiring the frequency response of the skin friction and the heat transfer of a cylinder in pulsating crossflow proved to be very efficient. Depending on the desired accuracy, the same results as computed with the time domain computation in a matter of days was obtained in several minutes. However, this method is limited to the flow regime $\mathrm{Re}_0 \lesssim 40$, where no vortex shedding occurs. Another limitation is that the type of mesh chosen in this thesis is restricted to cylinder geometries. This can be circumvented by the use of specialized software, e.g. finite element solvers for unstructured grids. Besides this, the main advantage of this method is its high accuracy combined with low computational cost.

6 Transfer Function Identification

This section deals with different methods to identify transfer functions from free-stream velocity pulsations to heat transfer and skin friction from CFD data. A direct approach might be to simulate the system introducing an impulse in the inlet velocity. The response, acquired during the simulation, would be the impulse response, which completely quantifies the LTI system. A transfer function is achieved by applying the Laplace transform (or Z-transform in discrete time) on the unit impulse response. However, this method is not feasible. The available numerical procedures cannot conserve the forcing impulse which would lead to a deteriorated response. A better approach, from a numerical point of view, is to use step excitation instead. The post-processing of a step response is straightforward. This is shown in Section 6.1, where also methods to acquire a transfer function are discussed. Simulating a step response can often be used as a preliminary tool to gain information vital for more sophisticated identification methods.

Another approach, often used in experiments, is the excitation with a single frequency Sr_i ($u(t) = A_u \sin(\mathrm{Sr}_i\, t)$). The response for an LTI system is again a sine wave, but usually with different amplitude and shifted in time. These time series can be evaluated using the Fourier transform, so the response at this particular frequency is

$$G(\mathrm{Sr}_i) = \frac{\hat{y}(\mathrm{Sr}_i)}{\hat{u}(\mathrm{Sr}_i)}\,. \tag{6.1}$$

Repeating this procedure for multiple frequencies in the range of interest leads to a typical frequency response that can be further processed to form a transfer function. This has some advantages over an impulse excitation or step excitation and is usually directly implemented in experiments. Advantages are that the excitation amplitude can be chosen for each frequency individually and the influence of disturbances can be minimized by using several periods of the same frequency. However, use of CFD simulations in the time domain to generate the data is rather time consuming. For every frequency, a simulation has to be carried out over several periods of the given excitation frequency. In Section 5.4, a method was introduced to acquire a frequency response by simulating in the frequency domain. In Section 6.2, SI is applied to the frequency response yielding a transfer function.

Section 6.3 deals with the application of the CFD/SI approach. The data acquired from time domain simulations (cf. Section 5.2 and Section 5.3) is processed with methods introduced in Section 4.4. Instead of an impulse, a step or sine waves, per-

sistent excitation is used together with SI techniques to develop the desired transfer function.

6.1 Step Response

The adaptation of the boundary layers after changes in the free-stream velocity controls the dynamics of the transfer of momentum and heat in the unsteady case. Payne (1958) studied starting flow past a cylinder at moderate Reynolds numbers, using numerical integration of Helmholtz's vorticity equation. In a similar manner, Apelt and Ledwich (1979) studied the response of drag force and heat transfer of a heated cylinder to impulsive forcing from rest, as well as impulsive increases in velocities by 50 %. The step response technique was also used by Surendran et al. (2016) to study the dynamic behavior of a cold heat exchanger in flue gas crossflow.

In this thesis, the development of the boundary layers and the heat transfer rate and skin friction in response to a sudden, small increase of the free-stream velocity by 10 % (step forcing) are investigated. The results obtained with the step input are simpler to interpret physically than the response to periodic perturbations and can be used to elucidate effects observed in the case of the periodic velocity pulsations (see below). The work shown here was previously published in parts in Witte and Polifke (2017a).

The step response is an immediate output of the computation with data acquisition procedures as described above (cf. Section 5.2.2). For reasons of simplicity, the time instant when the step occurs was chosen to be $t_s = 0$. The response is given as reported in Equation (4.127) by

$$\mathrm{Nu}'(t) = \mathrm{Nu}(t) - \mathrm{Nu}(0) \qquad \text{and} \qquad c_f'(t) = c_f(t) - c_f(0) \tag{6.2}$$

where $\mathrm{Nu}(0) = \mathrm{Nu}_0$ and $c_f(0) = c_{f,0}$ denote the (steady-state) Nußelt number and friction coefficient before the step input, respectively.

The unit step responses were calculated with

$$h_{\mathrm{Nu}}(t) = \frac{\mathrm{Nu}'(t) \Big/ \mathrm{Nu}(0)}{\mathrm{Re}'(t) \Big/ \mathrm{Re}(0)} = \frac{\mathrm{Nu}'(t)}{\epsilon\,\mathrm{Nu}(0)} \quad \text{and} \quad h_{c_f}(t) = \frac{c_f'(t) \Big/ c_f(0)}{\mathrm{Re}'(t) \Big/ \mathrm{Re}(0)} = \frac{c_f'(t)}{\epsilon\, c_f(0)} \tag{6.3}$$

where the Nußelt number and the friction coefficient are normalized with their respective steady-state value before the step. The computed response is scaled with the strength of the perturbation ϵ to yield a unit step response, although the excitation was weaker than unity. This scaling is valid as it was assumed to be within the limits of linearity. After this step, the simulation was continued with constant input

until the output did not change anymore, i.e. the flow had adopted to a new steady state.

From the unit step response, apart from qualitative insight into the flow dynamics, the quasi-steady gain K can be assessed easily. The gain corresponds to the value of the unit step response when a new steady state is reached. This is also the limit of the unit step response for very long times $K_{\mathrm{Nu}} = h_{\mathrm{Nu}}(t \to \infty)$ and $K_{c_f} = h_{c_f}(t \to \infty)$ and again appear as low frequency limits in the frequency responses (cf. Section 6.5).

In the following sections, results for the unit step responses h_{Nu} and h_{c_f} as simulated directly are shown. Snapshots of the temperature field surrounding the cylinder at discrete instants in time at two Reynolds numbers are reported in Section 7.2. The investigated Reynolds numbers ($\mathrm{Re}_0 = 0.4$, $\mathrm{Re}_0 = 4$, and $\mathrm{Re}_0 = 40$) correspond to the three flow regimes of creeping flow, attached flow, and flow with recirculation in wake without vortex shedding. This corresponds to the flow conditions of interest for the Rijke tube and hot-wire anemometry. However, the vortex shedding phenomenon limits this approach also to $\mathrm{Re}_0 \lesssim 40$, because the changes in Nußelt number and friction coefficient due to this unsteady behavior severely impede the results. In other words, no steady state exists above the threshold for vortex shedding, which complicates the interpretation of the results drastically.

6.1.1 Heat Transfer

Full Cylinder

The temporal development of the response is depicted in Figure 6.1. The thick solid lines represent the response evaluated directly from simulations with a step input. The dashed line denotes the steady-state gain (taken at $t = 80$ for $\mathrm{Re}_0 = 0.4$ and at $t = 20$ for $\mathrm{Re}_0 = 4$ and $\mathrm{Re}_0 = 40$). For comparison, the step responses computed from a transfer function identified with the CFD/SI approach (cf. Section 6.3) are depicted as dash dotted lines.

The sudden increase in the inlet velocity leads to a rise in the heat transfer rate. For $\mathrm{Re}_0 = 40$, the heat transfer increases rapidly until a local maximum is reached near $t \approx 1.5$. At lower mean flow Reynolds numbers, this peak is less pronounced and occurs at later times ($t \approx 5$ for $\mathrm{Re}_0 = 4$) or not at all ($\mathrm{Re}_0 = 0.4$). All step responses approach a new steady-state value K_{Nu}. This value is smaller if the Reynolds number is smaller. The limits for $t \to \infty$ are $K_{\mathrm{Nu}} = 0.25$, $K_{\mathrm{Nu}} = 0.37$, and $K_{\mathrm{Nu}} = 0.42$ for Reynolds numbers $\mathrm{Re}_0 = 0.4$, $\mathrm{Re}_0 = 4$, and $\mathrm{Re}_0 = 40$, respectively.

The step response shows that at low Reynolds numbers the dynamic behavior of the heat transfer rate can be interpreted as a single, comparatively large time scale that governs the time delay until a new steady-state value is reached. Towards higher

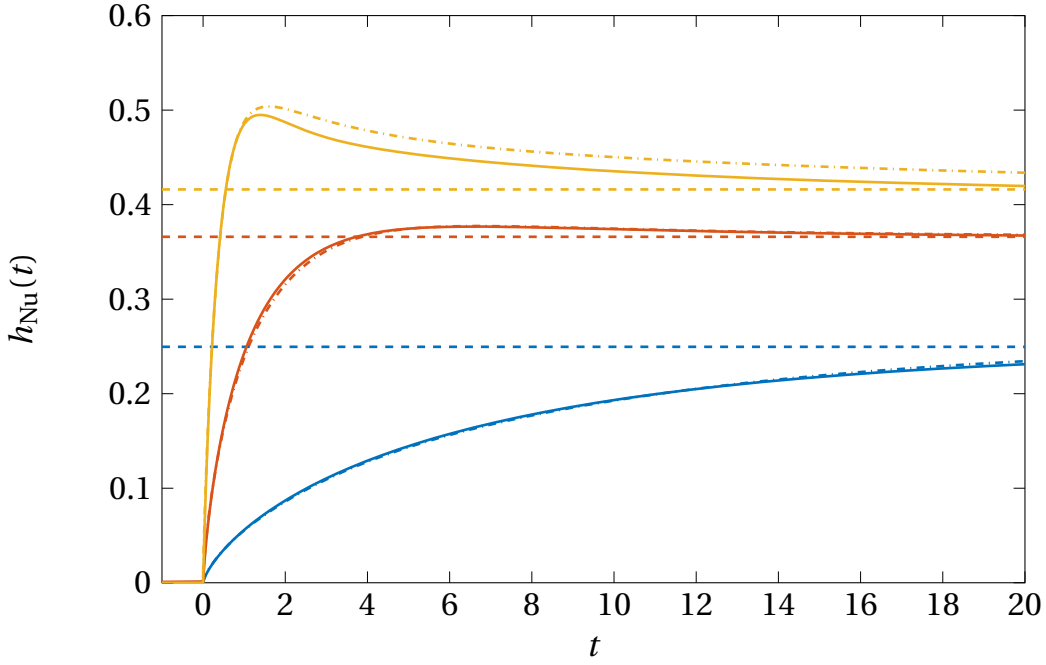

Figure 6.1: Unit Step Response of Nußelt Number. $\mathrm{Re}_0 = 0.4$ (——), $\mathrm{Re}_0 = 4$ (——), and $\mathrm{Re}_0 = 40$ (——). The dashed lines (- - -) denote the steady-state gain K_{Nu} taken at $t = 20$ for $\mathrm{Re}_0 = 4$ and $\mathrm{Re}_0 = 40$ and at $t = 80$ for $\mathrm{Re}_0 = 0.4$. Dash dotted lines (-·-·-) represent the response evaluated with the CFD/SI method.

Reynolds numbers ($\mathrm{Re}_0 = 4$), this dominant time scale becomes shorter and a second effect appears. It is visible as a local maximum in the response. This effect has a different time scale and is even stronger at $\mathrm{Re}_0 = 40$.

Circumferential Distribution

In order to gain more insight into spatial differences of the temporal development of the heat transfer, four equally sized sectors were examined separately. The sectors, as marked in Figure 5.2, are labeled 1 to 4 starting at the windward side of the cylinder. The choice is justified by the different flow regimes that are present at various locations (cf. Section 5.2.3). The step response of the individual sectors is computed with

$$h_{\mathrm{Nu},i}(t) = \frac{\mathrm{Nu}_i'(t)}{\epsilon\,\mathrm{Nu}(0)} \tag{6.4}$$

where $i = 1,2,3,4$ denotes the sector. Figure 6.2 shows the Nußelt number gain normalized with the area of the whole cylinder for Reynolds numbers $\mathrm{Re}_0 = 0.4$, $\mathrm{Re}_0 = 4$, and $\mathrm{Re}_0 = 40$. The sum of the four curves results in the graph shown in Figure 6.1.

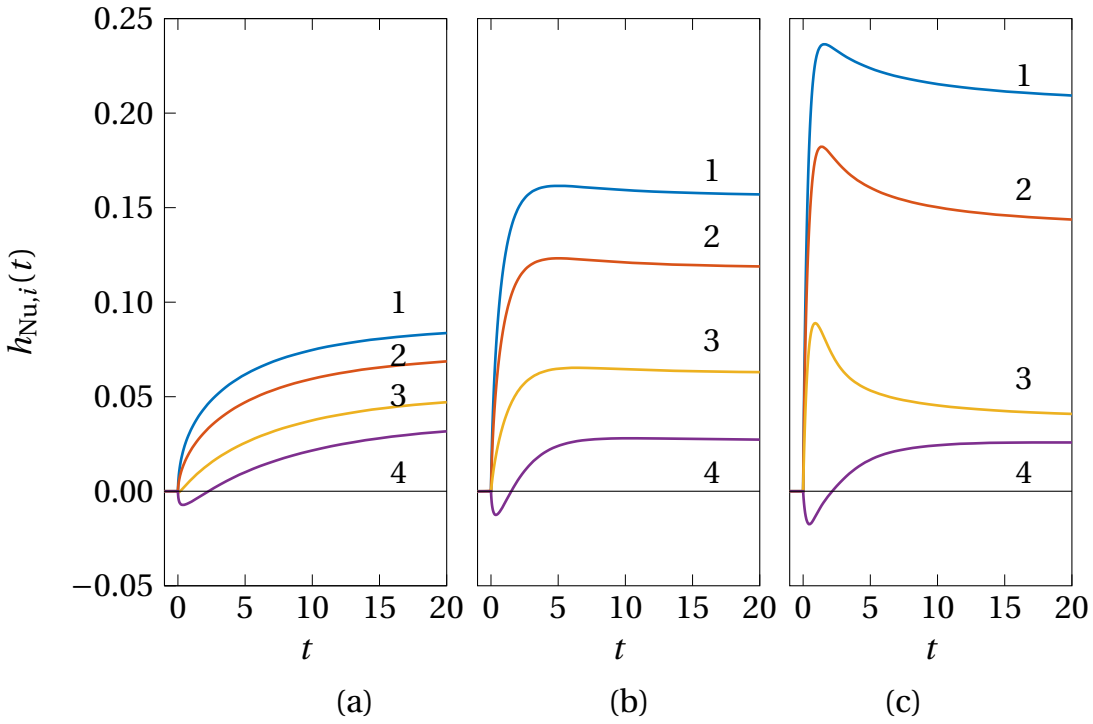

Figure 6.2: Unit Step Response of Heat Transfer for Individual Sectors. Sectors: 1 (—), 2 (—), 3 (—), and 4 (—). Mean flow Reynolds number $\mathrm{Re}_0 = 0.4$ (a), $\mathrm{Re}_0 = 4$ (b), and $\mathrm{Re}_0 = 40$ (c). The responses of the individual sectors are normalized with the heat transfer at the full (half) cylinder.

At the lowest Reynolds number ($\mathrm{Re}_0 = 4$, cf. Figure 6.2 (a)), it can be seen that sectors 1 through 3 show a behavior very similar to the complete cylinder. The sector 1 contributes most to the overall heat transfer followed by sector 2 and sector 3 and thus they show the highest gain. However, the behavior of sector 4 differs. It drops below the initial steady-state value directly after the step input occurred. At about $t = 2.5$ after the perturbation, the heat transfer becomes greater than in steady state again and settles asymptotically to a value below that of the sector 3.

The flow configurations with $\mathrm{Re}_0 = 4$ (Figure 6.2(b)) and $\mathrm{Re}_0 = 40$ (Figure 6.2(c)) show essentially the same characteristics. In contrast to $\mathrm{Re}_0 = 0.4$, a peak response occurs for $\mathrm{Re}_0 = 4$ and $\mathrm{Re}_0 = 40$ in sectors 1 to 3, which again determine the behavior of the complete cylinder to the largest extent. For higher Reynolds numbers, these maxima are more pronounced and occur shortly after the step input. The occurrence of the peak is strongest in sector 3, which includes the flow separation point. The relative contribution of the windward side of the cylinder is greater for higher Reynolds numbers.

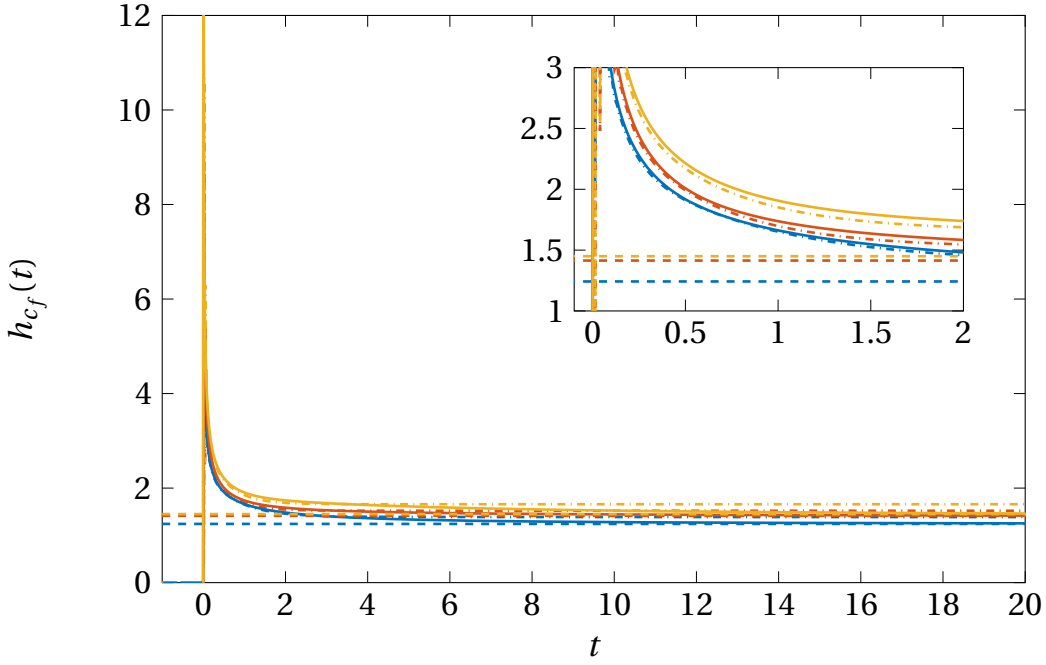

Figure 6.3: Unit Step Response of Skin Friction. $\mathrm{Re}_0 = 0.4$ (——), $\mathrm{Re}_0 = 4$ (——), and $\mathrm{Re}_0 = 40$ (——). The dashed lines (- - -) denote the steady-state gain K_{c_f} taken at $t = 80$ for $\mathrm{Re}_0 = 0.4$ and at $t = 20$ for $\mathrm{Re}_0 = 4$ and $\mathrm{Re}_0 = 40$. Dash dotted lines (-·-·-) represent the response evaluated with the CFD/SI method.

6.1.2 Skin Friction

Full Cylinder

Like the step response of the heat transfer, the temporal evolution of the skin friction is shown. Figure 6.3 depicts the normalized response of the friction coefficient to step forcing. The thick solid lines represent the response evaluated directly from simulations with a step input. The dashed line denotes the steady-state gain (taken at $t = 20$ for $\mathrm{Re}_0 = 4$ and $\mathrm{Re}_0 = 40$ and at $t = 80$ for $\mathrm{Re}_0 = 0.4$). For comparison, the step responses computed from transfer functions that were identified with the CFD/SI approach (cf. Section 6.3) are plotted as dash dotted lines.

The skin friction responds instantly to the step input by assuming large values. The following decrease is very steep as well, but slows down eventually. This restoration process is due to the transport of excess vorticity, created when the step excitation takes place, away from the surface of the cylinder. The friction coefficient settles to a new steady state above the initial conditions, but much lower than the peak. The restoration is fastest for $\mathrm{Re}_0 = 0.4$ and slowest for $\mathrm{Re}_0 = 40$. The new steady-state value, equivalent to the steady-state gain $K_{c_f} = 1.242$, $K_{c_f} = 1.414$, and $K_{c_f} = 1.450$ for $\mathrm{Re}_0 = 0.4$, $\mathrm{Re}_0 = 4$, and $\mathrm{Re}_0 = 40$, respectively.

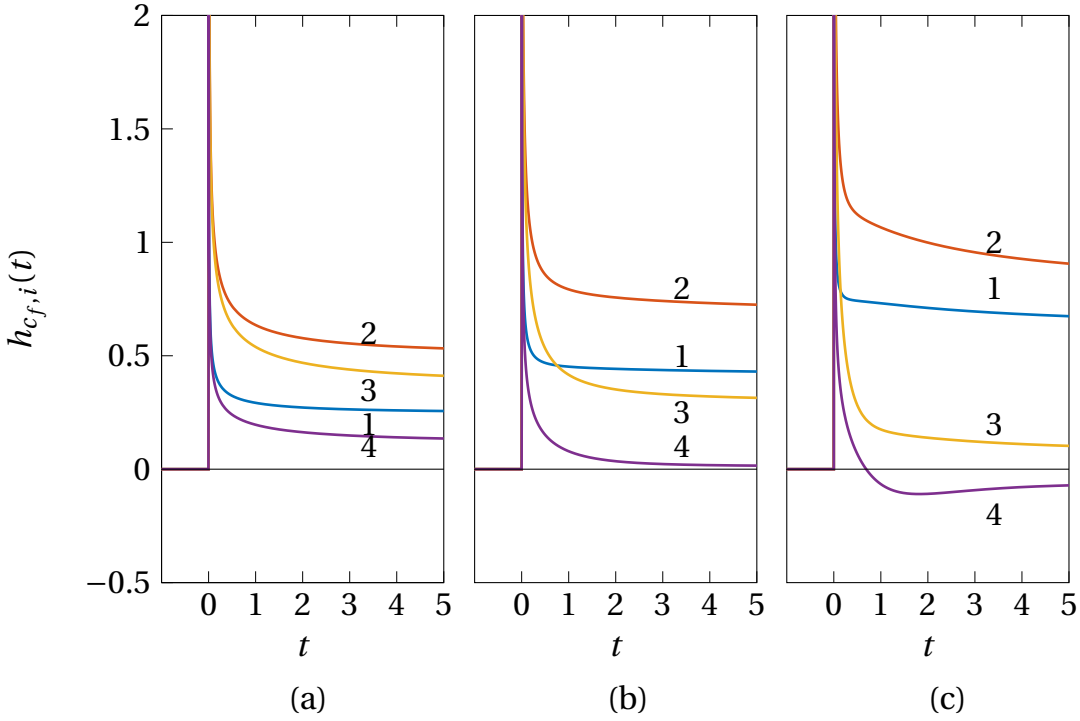

Figure 6.4: Unit Step Response of Individual Sectors. Sectors 1 to 4 (upstream–downstream) to step forcing at (a) $\mathrm{Re}_0 = 0.4$, (b) $\mathrm{Re}_0 = 4$, and (c) $\mathrm{Re}_0 = 40$. The responses of the individual sectors are normalized with the skin friction at the full (half) cylinder.

The peak values are only limited by the numerical procedure and reach such high values because an incompressible fluid is assumed. Such a harsh peak is associated with very high frequencies, for which the compactness assumption (c.f. Section 9.1.3) does not strictly hold. Nevertheless, the delay in returning to a steady state is captured adequately.

Circumferential Distribution

Figure 6.4 depicts the response of the individual sectors 1 to 4 of the skin friction coefficient to step forcing. Graphs are given for (a) $\mathrm{Re}_0 = 0.4$, (b) $\mathrm{Re}_0 = 4$, and (c) $\mathrm{Re}_0 = 40$. The behavior of each individual sector is very similar to the full cylinder given in Figure 6.3. For the heat transfer, a clear trend was apparent: Most heat is transferred close to the forward stagnation point, and the heat transfer declines towards the backward stagnation point. This is not the case for the skin friction. For all Reynolds numbers, the strongest response is observed in sector 2. This is in accordance with the position of the greatest steady-state skin friction (cf. Section 2.1.2, Figure 2.4). Immediately after the step excitation, the friction coefficient experiences the second largest change in sector 3. At Reynolds numbers $\mathrm{Re}_0 = 4$ and $\mathrm{Re}_0 = 40$, however, it is overtaken by sector 1 which adapts faster, but finally assumes

Re_0	Steady-state gain	Rise time 0 %–63.2 %	Rise time 10 %–90 %	Overshoot in %
0.4	0.2495	6.0289	16.8758	0
4	0.3649	0.9124	2.1246	2.96
40	0.4161	0.2378	0.4091	18.95

Table 6.1: Step Response Characteristics of Heat Transfer.

a new steady state with a relative change above sector 3. When a recirculation zone exists at the lee side of the cylinder, friction values are negative. This can be observed in plot (c) at $Re_0 = 40$ where the steady state of sector 4 is negative, which corresponds to a stronger recirculation in the new steady state (Re = 44). The skin friction response in sector 4 (cf. Figure 6.4 (c)) is positive until $t \approx 0.7$. This indicates that the recirculation zone collapses and is restored over time to the new steady state. The reason for this is the strong pressure gradient necessary to accelerate the flow to the new velocity from one time step in the simulation to the next. The adverse pressure gradient that leads to flow separation and hence recirculation is counteracted. The pressure becomes favorable, and the flow stays attached to the surface of the cylinder. This effect only holds as long as the acceleration occurs, i.e. as long as there is a strong external pressure gradient. In the restoration process, the pressure gradient at the cylinder switches back instantly, and the flow starts to detach again. This process becomes even more apparent in the flow-field representation in Section 7.2.

6.1.3 Characterization of Dynamic Behavior

The basic dynamic characteristics, i.e. simplified dynamics, can be quantified by a few parameters. These parameters can be gained from the step response. They include the steady-state gain, the rise time or fall time associated with a time constant, the overshoot over the final new steady state, and the dead time which is the time it takes the system to show a significant response (cf. Section 4.3.4). The latter is not relevant in the cases under investigation, as all systems respond instantaneously and is hence not considered further.

In accordance with the theory of LTI systems (cf. Section 4.1), the step response provides a complete description of the system. Characteristic quantities describing the dynamics are obtained simply by graphical evaluation. This information can also be used as prior knowledge for more sophisticated methods of SI. The characteristic quantities, as mentioned in Section 4.3.4, are given in Table 6.1 for the heat transfer.

Re_0	Steady-state gain	Time to settle to $K \cdot (1 \pm 0.1)$
0.4	1.242	3.884
4	1.414	2.421
40	1.450	5.651

Table 6.2: Step Response Characteristics of Skin Friction.

The steady-state gain and the rise time from 0 % to 63.2 % ($= 1 - \mathrm{e}^{-1}$) describe a first order time lag behavior. More accurately, they represent K_{Nu} and c_τ from the first order model $G = K_{\mathrm{Nu}}/(1 + c_\tau \,\mathrm{Sr})$ (cf. Section 8.1.2).

The rise time is a measure for the time scale of the dynamics. It can be used to determine an adequate sampling for further processing. The recommended time step sizes T_s for an impulse response model are $\tau/10 - \tau/4$ for control purposes, but might be higher depending on the application (Åström and Wittenmark, 1997). This leads to the recommended sampling time steps of $\tau_s = 0.6029$, $\tau_s = 0.0912$, and $\tau_s = 0.0238$ for $\mathrm{Re}_0 = 0.4$, $\mathrm{Re}_0 = 4$, and $\mathrm{Re}_0 = 40$, respectively. These correspond to Nyquist Strouhal numbers of Sr = 5.2109, Sr = 34.4320, and Sr = 132.1096, respectively.

A similar analysis can be carried out for the friction coefficient. Due to the shape of the skin friction step response, it is reasonable to compute a settling time instead of a rise or fall time. The settling time chosen in this thesis is defined as the time required to reach a value within some error margin around the final new steady-state value. The chosen error is 10 % and hence the settling time is the duration from the occurrence of the step until $|h_{c_f}/K_{c_f} - 1| < 0.1$. Steady-state gain and settling time for the skin friction step response of the investigated mean flow Reynolds numbers are listed in Table 6.2.

The settling times calculated from the step response of the skin friction are well within the range of the rise times of the heat transfer step response. Therefore, the derivation of the time step size still holds. It is noteworthy that the settling time does not behave monotonically like the heat transfer rise time. The case with $\mathrm{Re}_0 = 4$ is quickest to settle to a value slightly below the predicted steady-state gain of 3/2 (Lighthill, 1954). This also holds for $\mathrm{Re}_0 = 40$ although the time necessary to reach the 10 % bounds is more than twice as high. The settling time for the smallest Reynolds number is in between the other values, but the new steady-state value is lower. This effect can be attributed to the change in circumferential distribution (cf. Section 6.1.2). This corresponds to the expectation that the drag scales linearly with velocity at low Reynolds numbers (linear drag regime).

6.1.4 Transfer Function from Step Simulation Data

Within the framework of LTI systems, it is possible to acquire a transfer function for heat transfer and skin friction pulsations caused by pulsations in the free-stream velocity from a step response. Four different methods were surveyed to achieve this goal: (1) Use the time series of step input and step response to perform SI. (2) Compute a frequency response first using FFT and subsequently identify a transfer function from frequency data. From the discrete data, acquired from the CFD simulation, an impulse response can be computed with an approximation of the derivative. This leads to method (3) which uses the impulse response directly as coefficients of an FIR model. (4) Compute the frequency response from the impulse response padded with zeros and perform identification on the frequency data.

Choice of Method

Method (1), the use of the CFD/SI procedure directly on step response data, was rejected because the input signal is not optimal for SI. The PSD of the signal is significantly diminished at high frequencies, and hence inaccurate results are expected. The broadband excitation (cf. Section 6.3) provides better results at almost the same effort.

A frequency response is gained computing the element-wise (frequency-wise) quotient written as

$$G(\mathrm{Sr}) = \frac{\hat{h}}{\epsilon \hat{H}} \tag{6.5}$$

where $\hat{H}$ denotes the Fourier transform of the Heaviside step function. Continuous time identification can be used to develop a transfer function (method (2)). The frequency resolution of the FFT is determined by the length of the time series. A better resolution can be achieved by appending the last value of the times series (the new steady-state value) multiple times. This is allowed as the value should not change as long as the input is constant. A discrete Fourier transform of the Heaviside step function, however, leads to zeros at certain frequencies in the transformed quantity. This is not desirable because at these frequencies the computation of the frequency response is inaccurate or fails completely. Therefore, this method was rejected as well.

The step response $h[k]$ is the integral of the impulse response $g[k]$. Hence, the impulse response can be computed from the step response data with finite differences given by

$$g[k] = \frac{h[k] - h[k-1]}{T_s}. \tag{6.6}$$

These impulse response coefficients $g[k]$ can directly serve as the coefficients of an FIR model. Mathematically, this corresponds to the application of the Z-transform on the computed data. This method is straightforward, but the FIR model has certain disadvantages like a large number of coefficients depending on the time step size. Thus, method (3) was also rejected in favor of method (4). The most promising procedure to acquire a transfer function from step response data is detailed in the following.

Data Preparation

The time series data was acquired from the simulation as described in Section 5.2.3. The computations were performed with variable time step to ensure a constant CFL number. These time steps are usually much smaller than the desired maximum frequency to ensure a certain smoothness of the signals. For further processing, the time series were linearly interpolated to a constant sampling time step equivalent to the smallest time step of the simulation. This occurs at rates much higher than the range of interest where the PSD of the signal is low. Hence, the information loss and the aliasing introduced by the interpolation are minimal. Subsequently, an anti-aliasing filter was applied to the time series, and they are downsampled to a bandwidth Strouhal number Sr = 240. This is still six times higher than the maximum frequency of interest, but the amount of data is reduced considerably.

Frequency Response

At first, the impulse response was computed from the step response data using Equation (6.6). The final steady-state value, which is zero in the case of a BIBO stable system such as the one at hand, was appended to the original time series to enhance the frequency resolution of the Fourier transform in the consecutive step. To acquire a frequency response, it is only necessary to compute the Fourier transform of the impulse response. The Fourier transform of the unit impulse is unity, i.e. it is the neutral element in frequency space, and a frequency-wise division like in the case of the step response is not required. This avoids the problem arising in the ill-conditioned computation of the frequency response directly from the step response.

The frequency response computed from step response data is shown in Figure 6.5 for the heat transfer pulsations caused by velocity pulsations and in Figure 6.6 for the skin friction as solid lines. For comparison, the frequency response of the transfer function computed in Section 6.3 are included as dashed lines. It can be seen that indeed for the investigated mean flow Reynolds numbers $\mathrm{Re}_0 = 0.4$, $\mathrm{Re}_0 = 4$, and $\mathrm{Re}_0 = 40$ the results are very similar and only minor deviations are visible. The

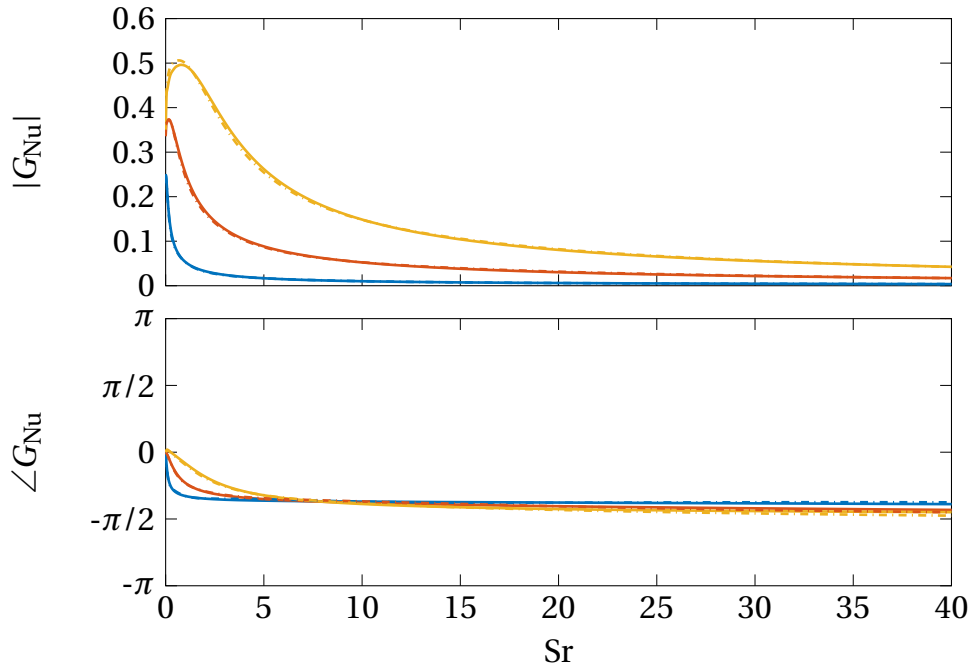

Figure 6.5: Frequency Response of Heat Transfer from Step Simulation. $Re_0 = 0.4$ (——), $Re_0 = 4$ (——), and $Re_0 = 40$ (——). Step simulation results are shown as solid lines (——). For comparison, results from CFD/SI are depicted as dash-dotted lines (-·-·-).

largest discrepancies occur for skin friction at the lowest Reynolds number and high frequencies.

Transfer Function

The frequency response can be used to compute transfer functions with the methods of identification of continuous time models (cf. Section 4.4.5) in particular VF related methods. The frequency response, computed as shown above, is acceptably smooth as can be seen in Figure 6.5 and Figure 6.6. Hence, the identification with VF is straightforward, and the results are expected to be very similar to that of the CFD/SI method. Details and results from the transfer function identification are omitted at this point and are reported in the following sections associated with the LNSE approach and the CFD/SI approach.

6.2 Transfer Function from LNSE

The LNSE provide a method to compute the frequency response directly by simulation in frequency space (Kwon and Lee, 1985). The solver and the solution pro-

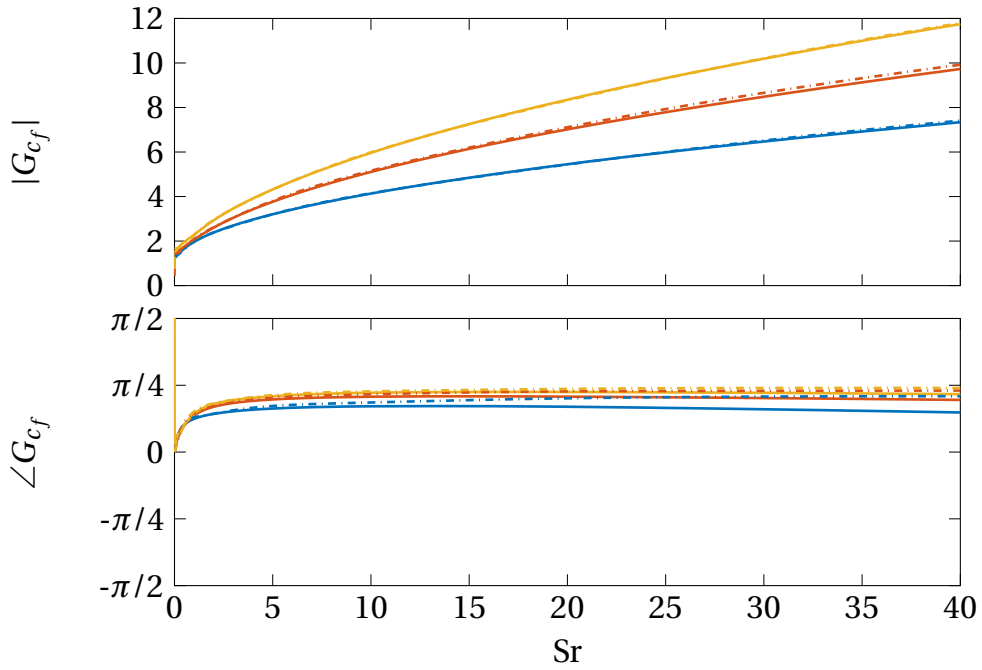

Figure 6.6: Frequency Response of Skin Friction from Step Simulation. $\mathrm{Re}_0 = 0.4$ (——), $\mathrm{Re}_0 = 4$ (——), and $\mathrm{Re}_0 = 40$ (——). Step simulation results are shown as solid lines (——). For comparison, results from CFD/SI are depicted as dash-dotted lines (-·-·-).

cedure for the LNSE were detailed in Section 5.4. The steady-state flow field was computed for a specified mean flow Reynolds number $\mathrm{Re}_0 \leq 40$ and Prandtl number $\mathrm{Pr} = 0.7123$. Based on this steady-state solutions, the linearized perturbation equations were solved for 50 logarithmically spaced Strouhal numbers in the range $[0.01, 40]$.

From the temperature fields and their derivatives in radial direction, the steady-state Nußelt Nu_0 number and the perturbed Nußelt Nu' number were calculated. The values were subsequently averaged over the circumference of the cylinder, and a frequency response was calculated (cf. Section 5.4.5). The frequency response function was approximated by the discrete values at 50 Strouhal numbers.

In an analogous manner, the friction coefficient c_f was calculated from the vorticity fields. This frequency response data was used to identify transfer functions for heat transfer and skin friction from velocity perturbation at $\mathrm{Re}_0 \in \{0.1, 0.2, 0.4, 0.5, 0.7, 1.0, 2.0, 3.0, 4.0, 10.0, 20.0, 40.0\}$.

6.2.1 Identification from Frequency Response Data

Continuous time transfer functions were identified using the VF technique detailed in Section 4.4.5. The input for the VF method is the frequency response of the

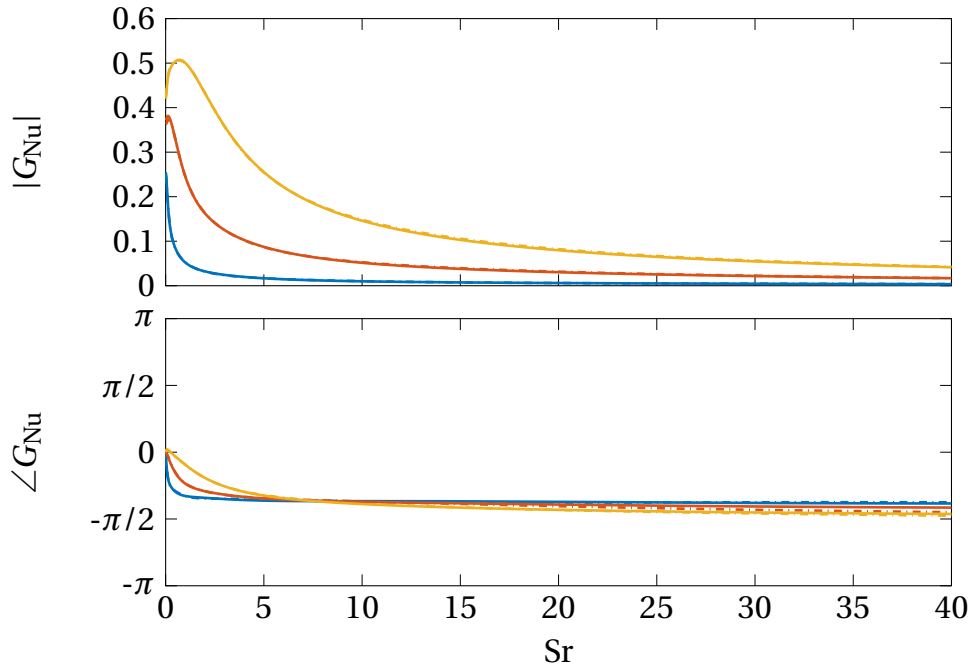

Figure 6.7: Frequency Response of Heat Transfer from LNSE. $\mathrm{Re}_0 = 0.4$ (——), $\mathrm{Re}_0 = 4$ (——), and $\mathrm{Re}_0 = 40$ (——). Step simulation (——), CFD/SI (- · - · -).

heat transfer ($G_{\mathrm{Nu}}(\mathrm{Sr})$) and the skin friction ($G_{c_f}(\mathrm{Sr})$) to pulsations in free-stream velocity, respectively. The VF method does not require the frequency samples to be evenly distributed. The frequency samples are logarithmically distributed over the Strouhal number range $[0.01, 40]$ with a higher density of samples at low frequencies. This spacing was chosen to credit the fact that changes, especially in phase, are stronger at lower frequencies. A logarithmic spacing, however, shifts more weight to low frequencies in the identification process. This is desired for the skin friction. For the heat transfer, this was partially counteracted by using the inverse frequency response gain $|1/G_{\mathrm{Nu}}(\mathrm{Sr})|$ as weighting vector. Stability of the resulting transfer functions was enforced by pole flipping.

6.2.2 Results

Figure 6.7 depicts the heat transfer frequency response $G_{\mathrm{Nu}}(\mathrm{Sr})$ of the identified transfer functions for the mean flow Reynolds numbers $\mathrm{Re}_0 = 0.4$, $\mathrm{Re}_0 = 4$, and $\mathrm{Re}_0 = 40$. For comparison, the result from the time domain CFD/SI approach are included as dash dotted lines. Both solution techniques lead to very similar results also observed in the frequency response computed from step response data in Figure 6.5.

Correspondingly, the frequency response of the skin friction $G_{c_f}(\mathrm{Sr})$ to pulsations in the free-stream velocity are depicted in Figure 6.8. The response functions, rep-

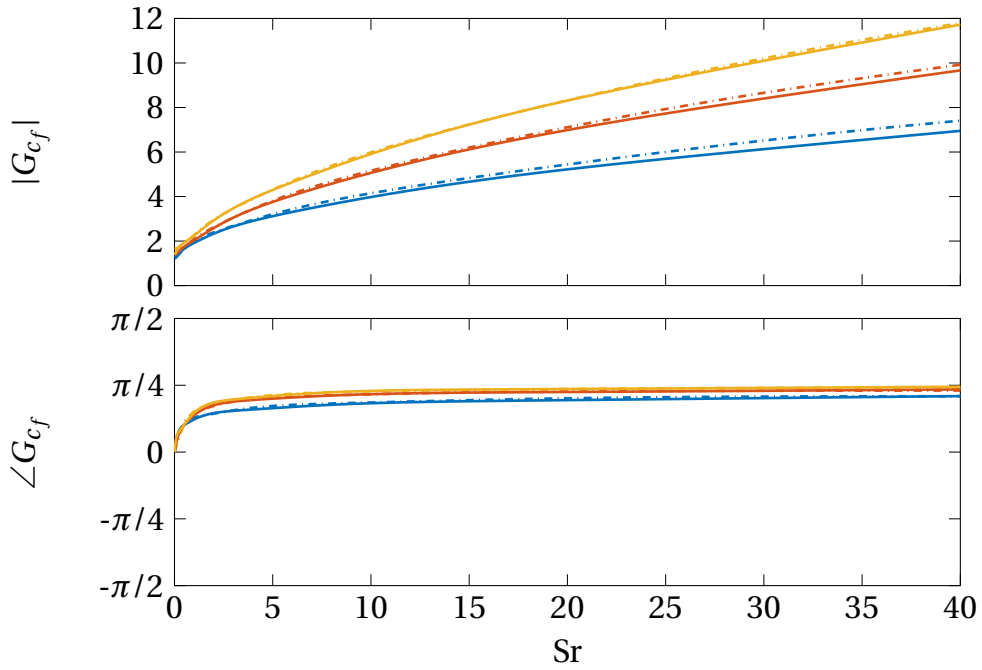

Figure 6.8: Frequency Response of Skin Friction from LNSE. $\mathrm{Re}_0 = 0.4$ (——), $\mathrm{Re}_0 = 4$ (——), and $\mathrm{Re}_0 = 40$ (——). Step simulation (——), CFD/SI (- · - · -).

resenting the transfer functions identified from data from the LNSE, matches well with the response evaluated with the CFD/SI approach (dash dotted lines).

In consideration of the good match between the models evaluated from LNSE and CFD/SI, only the results acquired from CFD/SI are reported in Section 6.4 for the parameter study. For completeness the fit values and transfer function from the LNSE approach are reported in Appendix A.

6.3 CFD/SI

The CFD/SI method, combining numerical simulation with SI was proposed by Polifke et al. (2001). It has been applied to various problems in aero-acoustics and thermo-acoustics (Polifke, 2014). The identification of the transfer function of the heat transfer was published in Witte et al. (2016a,b); Witte and Polifke (2017a).

Figure 6.9 illustrates the procedure in a flow chart: First, an unsteady CFD simulation of flow and heat transfer around the cylinder with imposed excitation of the free-stream velocity is conducted. Specifically, a spatially homogeneous, broadband perturbation signal $u_\infty(t)$ is imposed as inflow velocity. The Reynolds number of the axial velocity upstream of the cylinder Re represents the input. The Nußelt number of the heat transfer Nu, as well as the friction coefficient between the surface of the cylinder and fluid c_f, are used as the outputs. Second, a transfer function is iden-

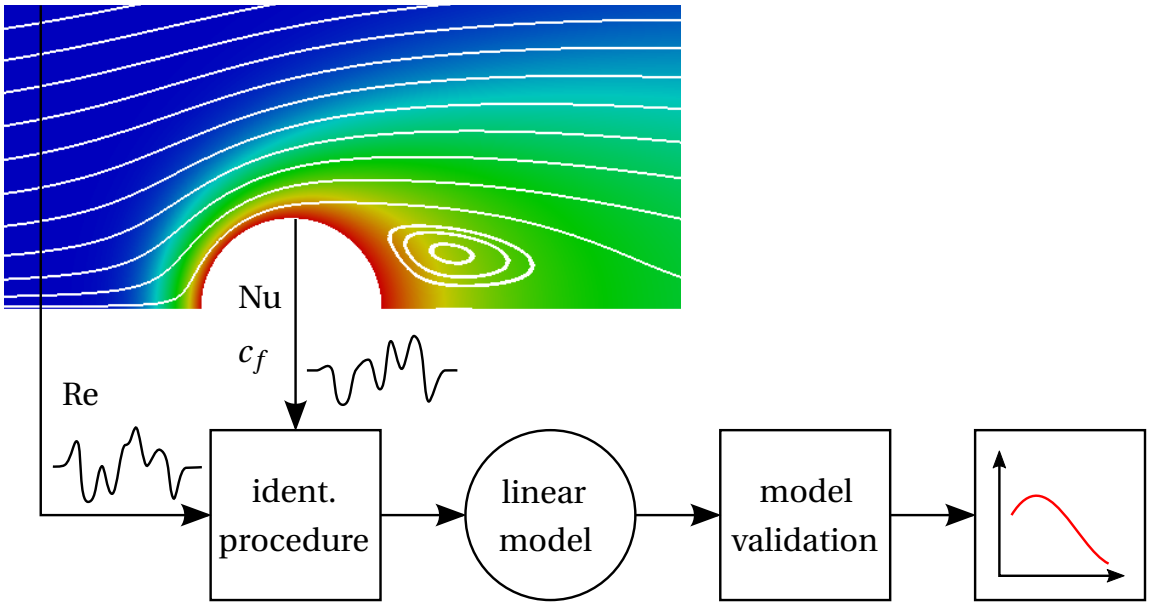

Figure 6.9: Diagram of the CFD/SI Approach.

tified from input and output data using SI methods. Continuous time and discrete time identification techniques were considered. Subsequently, the transfer function is validated, i.e. the model quality is assessed. The best model for each mean flow Reynolds number Re_0 is reported in Section 6.4.

The CFD/SI approach allows to determine the response function over a wide frequency range using data from a single CFD simulation with broadband excitation. In contrast, the FFT approach, based on forcing with a single frequency, requires one simulation per frequency. Other types of signals, e.g. sums of sinusoids, chirps, or sawtooth signals, have also been used in the past but did not perform as efficiently as broadband noise. This is due to the fact that the latter provides high and constant power spectral density over all frequencies of interest. Hence, the excitation is persistent and limited in amplitude (Tangirala, 2014). Moreover, different signal time series can be designed to be decorrelated. This allows extending the available time series for identification by simply concatenating the series of two separate experiments or simulations. For the identification with multiple inputs (MISO or MIMO systems), decorrelated excitation signals allow the SI procedure to distinguish between the inputs.

Numerous SI procedures and auxiliary tools are implemented in MATLAB (The MathWorks, Inc., 2016). The CFD/SI procedure can be divided into five main steps: After an input signal is created with the desired properties and the solver is set up to give an accurate representation of the underlying physics, this signal is used in the CFD simulation. During the computation, time advances and time series are acquired at every time step. These time series are used for parameter estimation and

for validation. This data is processed and eventually fed to the identification routine. A model based on the data is fitted by the identification algorithm, i.e. model parameters are estimated. The structure of the model as well as other settings and the choice of routines is made beforehand. The identification is followed by a model validation in which the performance and some characteristics of the model are assessed. All steps may be repeated in order to find the best model. A flowchart of the CFD/SI procedure is depicted in Figure 6.10. A priori acquired data from the step response simulation (cf. Section 6.1) and the discretization study (cf. Section 5.1) was used to aid the process in finding a suitable solver setup and model structure. Moreover, this information was employed in the validation process.

6.3.1 Data Preparation

The acquired data were pre-processed for the SI. If the simulation had to be restarted, the data series were concatenated to form a single long time series for each variable. Depending on whether the full cylinder or only parts of it should be analyzed, the data of the individual sectors were combined as desired. All time series were recorded with variable time steps as the simulation was set to keep the CFL number constant to a specific maximum value ($\mathrm{CFL}_{\max} \leq 0.2$). To achieve a constant sampling time, necessary for the identification procedure, the data were linearly interpolated to a constant sampling time step corresponding to the smallest time increment in the simulation. The PSD at frequencies associated with the smallest time step is low and hence the aliasing introduced by the interpolation is negligible.

Subsequently, the data is filtered and down-sampled to a larger sampling time T_s. A general guideline to choose the T_s in practice is about 20 to 40 samples in one settling time c_τ, where c_τ is the dominant time constant or the time constant of a first order approximation of the system (Åström and Wittenmark, 1997, Chapter 2). For $c_\tau = 0.2$ (Lighthill, 1954), this leads to $T_s = 0.005 - 0.01$. In this thesis, $T_s = 0.01309$ was chosen, which yields a Nyquist frequency of $\mathrm{Sr}_{\mathrm{Nyquist}} = 240$ six times higher than the frequency of interest. In the step response simulations, a rise time of $c_\tau = 0.2378$ for a mean flow Reynolds number $\mathrm{Re}_0 = 40$ was found. This result confirms the choice of sampling time.

The down sampling procedure removes high-frequency noise from the interpolation and keeps only information necessary for the identification procedure. The choice of $\mathrm{Sr}_{\max} = 240$ proved to yield the best results in the identification of OE models. The desired range of frequencies in terms of Strouhal number is $0 \leq \mathrm{Sr} \leq 40$, similar to Lighthill's study (Lighthill, 1954). If a transient process at the beginning of the time series was observed, this part was removed before further processing.

At this point, it would have been possible to filter the time series further to enhance desirable properties or reduce contamination and therefore aid the identification

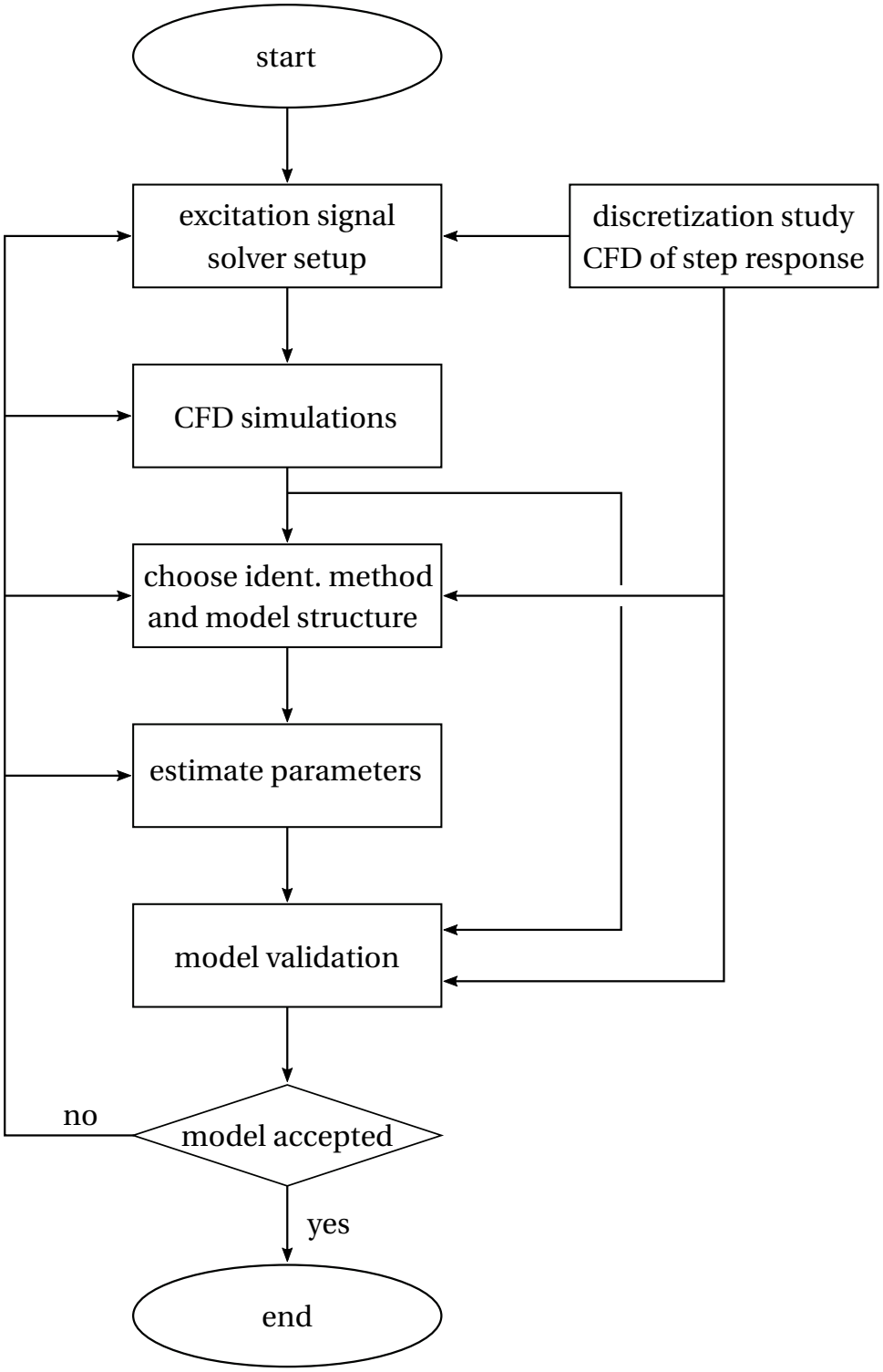

Figure 6.10: Flowchart of the CFD/SI Procedure. Adapted from Söderström and Stoica (1989) (cf. Figure 4.6).

process. Filtering the data series does not modify the transfer behavior itself, as long as both input and output are treated with the same filter. This does, however, not hold for the noise. For the transfer function identification, filtering is equivalent to weighting, but the filter changes the color of the noise and hence it is not recommended to use "pre-filtering"if a proper noise model is sought.

In the next step, the normalized pulsations of the instantaneous Reynolds number, the Nußelt number, and the friction coefficient are determined by

$$u_{\mathrm{Re}}(t) = \frac{\mathrm{Re}(t) - \overline{\mathrm{Re}}}{\overline{\mathrm{Re}}}, \qquad y_{\mathrm{Nu}}(t) = \frac{\mathrm{Nu}(t) - \overline{\mathrm{Nu}}}{\overline{\mathrm{Nu}}}, \text{ and} \qquad y_{c_f}(t) = \frac{c_f(t) - \overline{c_f}}{\overline{c_f}}. \tag{6.7}$$

The quantities $\overline{\mathrm{Re}}$, $\overline{\mathrm{Nu}}$, and $\overline{c_f}$ are the sample means of the according time series evaluated by

$$\overline{\phi} = \frac{1}{N} \sum_{n=1}^{N} \phi[n] \tag{6.8}$$

where ϕ stands for Re, Nu, and c_f. The means served as estimates for Re_0, Nu_0, and $c_{f,0}$ respectively.

Finally, input and response data were split into two sets. A larger set, containing 80 % of the complete time series, was used to estimate the model (estimation set). The rest served as a validation set, which the model output was compared to as a test on "fresh" data (cross validation). The data for every mean flow Reynolds number was collected for a simulation time of more than $t > 200$, i.e. the free-stream passes the cylinder more than 200 times. Therefore, the estimation set had at least a length of 160 and the validation set at least a length of 40. The acquired time series are examined in more detail.

Reynolds Number Time Series

For the SI procedure, the time series of the input signal was acquired over a cross-sectional plane inside the simulation domain. This was done to ensure that any effect of the simulation tool, e.g. the implementation of the inlet boundary or of the numerical procedure, affected the signal in the least possible way. In other words: This ensured that the velocity actually acting on the cylinder is acquired, which equals not necessarily exactly the imposed input signal.

Figure 6.11a shows an excerpt of the time series acquired from the CFD simulation. The signal never exceeds the interval $[-0.05, 0.05]$. This corresponds to the desired amplitude of the 5 % of the mean flow Reynolds number.

Figure 6.11b depicts Welch's estimate of the acquired input signal. The PSD is high at low frequencies and nearly constant between $0 \leq \mathrm{Sr} \leq 40$. The cutoff frequency,

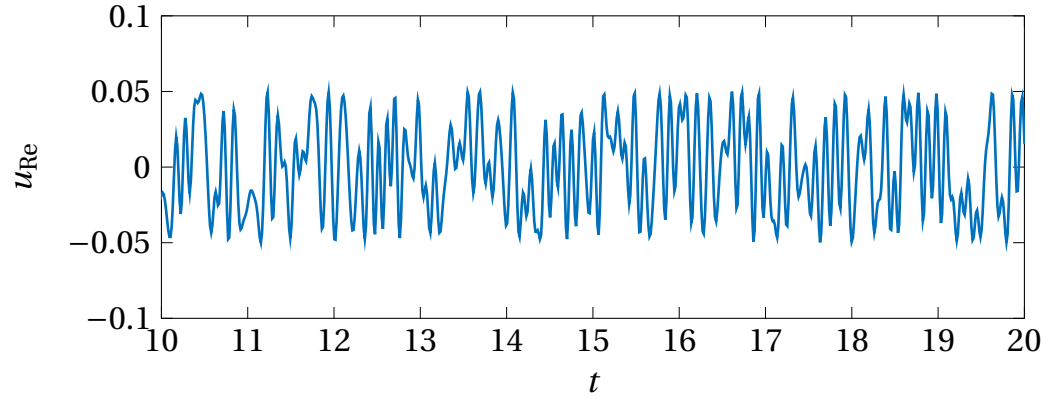

(a) Excerpt of Input Time Series

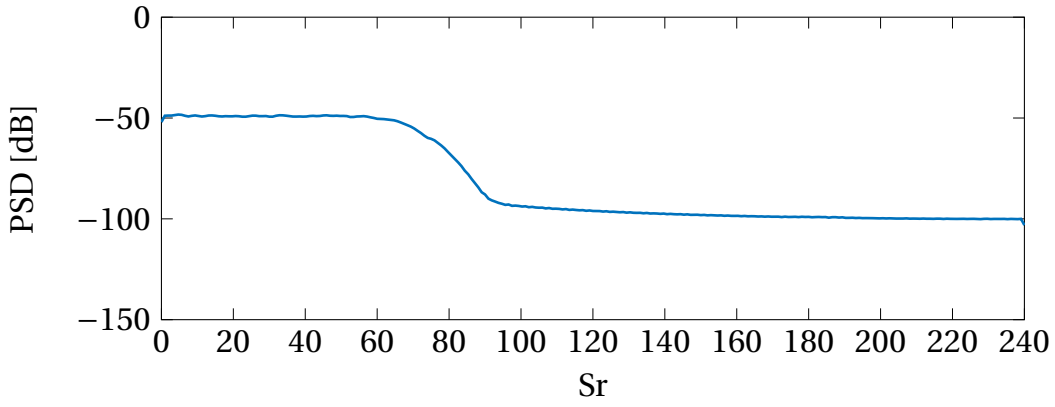

(b) PSD (Welch's Estimate) of Input Time Series

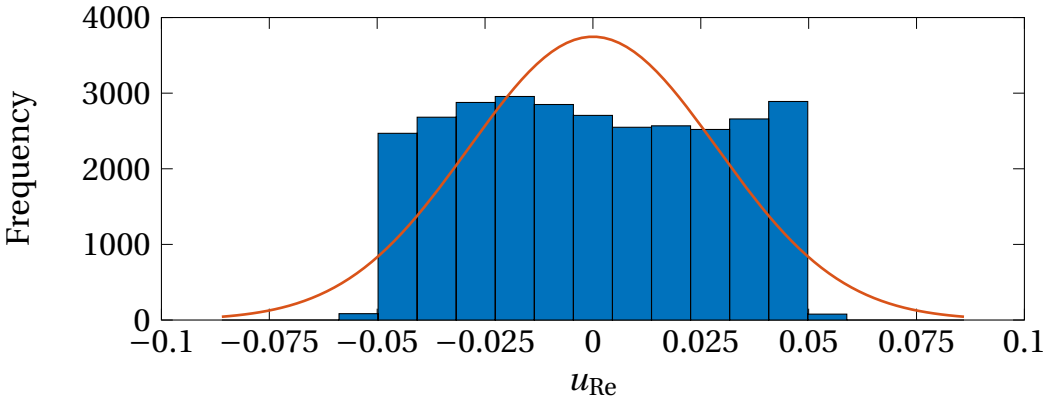

(c) Histogram of Input Time Series

Figure 6.11: Input Time Series (Reynolds Number). Bars denote the bins of the input time series. A normal distribution with the same mean and standard deviation as the data is indicated (—).

where the PSD is 3dB lower than the steady-state value, is around Sr = 60. This was also a design parameter for the input signal generation. Especially above Sr = 100, no significant power is contained in the acquired time series. The highest frequency that can be reconstructed from the signal is the Nyquist frequency $\mathrm{Sr}_{\max} = 240$, which was determined by the down sampling.

The histogram of the times series offers insight into the amplitude distribution of the data. Occurrences of values within a certain range (bin) are counted, and the final sums are shown in Figure 6.11c. The excitation signal was generated by non-Gaussian simulation (sampling). Hence, the acquired Reynolds number fluctuation does not deviate too much from the amplitude distribution created with the tool by Föller and Polifke (2011). It is almost uniform with a wave-like shape favoring positive values. The almost uniform distribution is advantageous for SI, because extreme values are reached comparably often, i.e. a good crest factor is achieved.

Nußelt Number Time Series

The Nußelt number was acquired as the time series comprising the output of the system. A similar procedure as for the input signal was applied to post-process the data. Figure 6.12a shows an excerpt of the acquired relative Nußelt number fluctuation for all sectors combined. The same period of time as in Figure 6.11a was chosen for comparison. The time series has less high amplitude peaks and also the general range is only in the range $[-0.01, 0.008]$ in this excerpt indicating the expected low-pass behavior.

This tendency to respond weaker at higher frequencies can also be seen in the PSD as depicted in Figure 6.12b. Within the frequency range of interest the PSD drops more than 20 dB in this case ($\mathrm{Re}_0 = 40$). As expected, the cutoff frequency of the input signal is visible as a sudden drop in PSD at frequencies above Sr = 60. There is no significant PSD above Sr = 100.

The amplitude distribution of the Nußelt number fluctuation in response to the excitation in Reynolds number is depicted in Figure 6.12c. In comparison to a normal distribution with zero mean value and the same standard deviation, y_{Nu} resembles a Gaussian distribution which may be explained through the Central Limit Theorem.

Friction Coefficient Time Series

The skin friction is quantified by the friction coefficient. Again, only the relative fluctuation y_{c_f} is considered for the SI procedure. The time series depicted in Figure 6.13a includes the same time range as in Figure 6.11a and Figure 6.12a. High

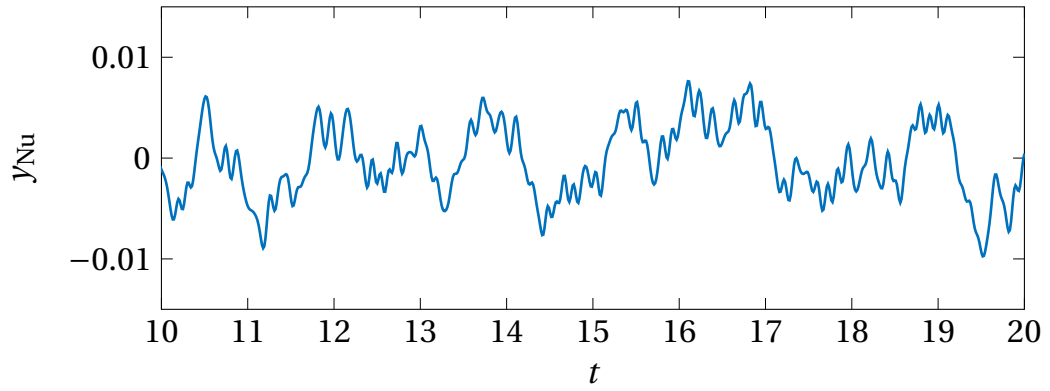

(a) Excerpt of Time Series

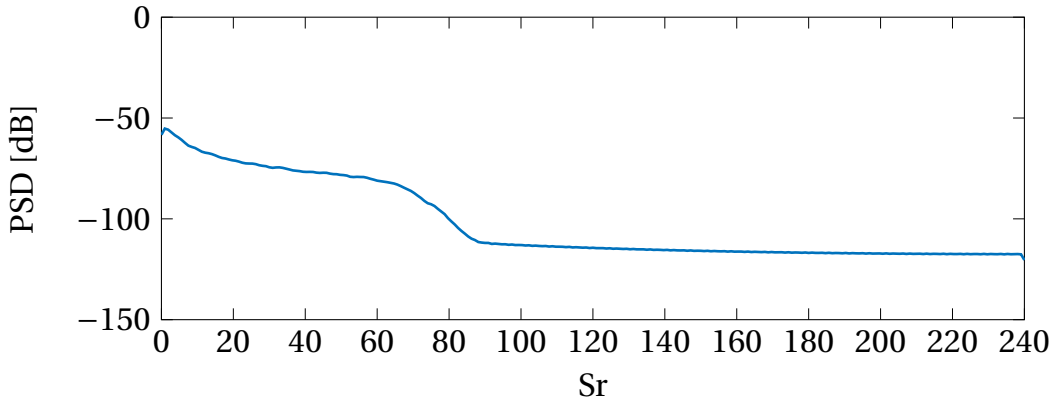

(b) PSD (Welch's Estimate) of Time Series

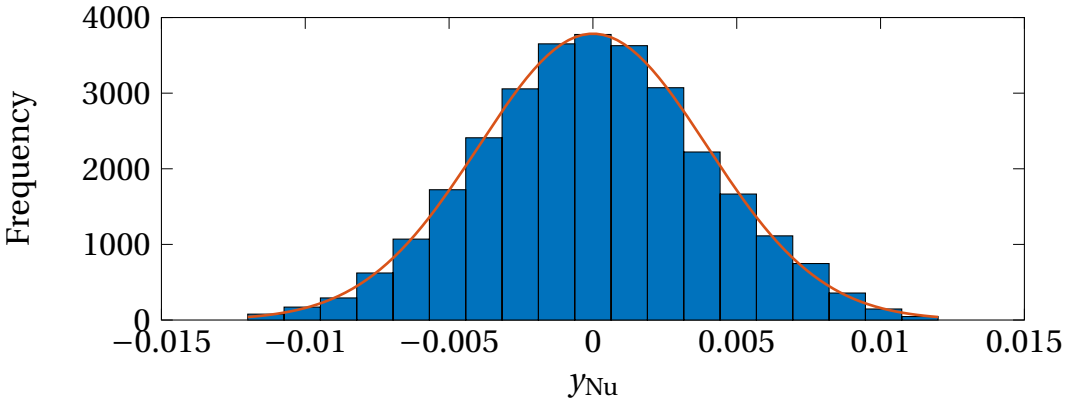

(c) Histogram of Time Series

Figure 6.12: Output Time Series (Nußelt Number). Bars denote the bins of the input time series. A normal distribution with the same mean and standard deviation as the data is indicated (—).

relative amplitudes of up to 70 % can be detected which is a lot stronger than the 5 % of the excitation.

Inspection of the PSD of the friction coefficient, as shown in Figure 6.13b, reveals that the PSD rises with the frequency until the cutoff of the input signal is reached. Comparison with the PSD of the Reynolds number fluctuation indicates a high-pass behavior. It is to be expected that the amplitude would grow indefinitely with frequency. This is in accordance with the analysis of Stoke's second problem (cf. Section 3.1.2). It predicts the shear stress pulsations to grow with the square root of the Strouhal number Sr. However, at some frequency much higher than examined in this thesis, the assumption of incompressibility will cease to be valid.

For the amplitude distribution of the friction coefficient pulsation, a similar shape as for the Nußelt number is acquired (Figure 6.13c). However, the high-pass behavior does not force the amplitude distribution to be Gaussian as does the low-pass behavior of the heat transfer.

Coherence of Input and Outputs

The coherence of the input and the output signal (cf. Section 4.1.5) is an indicator for the linearity of the system. If excitation and response share a linear relationship, the coherence is close to unity. The coherence is also linked to the signal-to-noise ratio and hence shows at which frequencies a good model is to be expected. Figure 6.14 depicts the coherence between the Nußelt number pulsations and Reynolds number pulsations as well as the coherence between the pulsation of the friction coefficient and the pulsation of the Reynolds number. For the first, the value is above 0.9 in the complete range of interest and almost unity in the range $5 \leq \mathrm{Sr} \leq 70$. At very low frequencies, coherence is not as high, which suggests a higher noise level. This can be attributed to the fact that the time series has finite length. It is therefore expected that models will show higher errors at these frequencies. Above $\mathrm{Sr} = 90$, the PSD of the excitation is at the level of the disturbances and hence coherence is low, i.e. signal-to-noise ratio is low. This is reasonable considering the PSD of the excitation signal is also very low above this frequency.

For the coherence between Reynolds number pulsation and skin friction pulsation, a very similar behavior is observed. Coherence is high in the frequency range of interest indicating, a linear relationship and a high signal-to-noise ratio. Again, like the coherence between Re' and Nu', at very low frequencies signal-to-noise ratio is not as high (~ 0.8) and identified models are expected to be less accurate in this region. Beyond the cutoff frequency of the excitation, the coherence drops, but not as fast for the heat transfer. These higher coherence levels might be due to the high-pass nature of the skin friction.

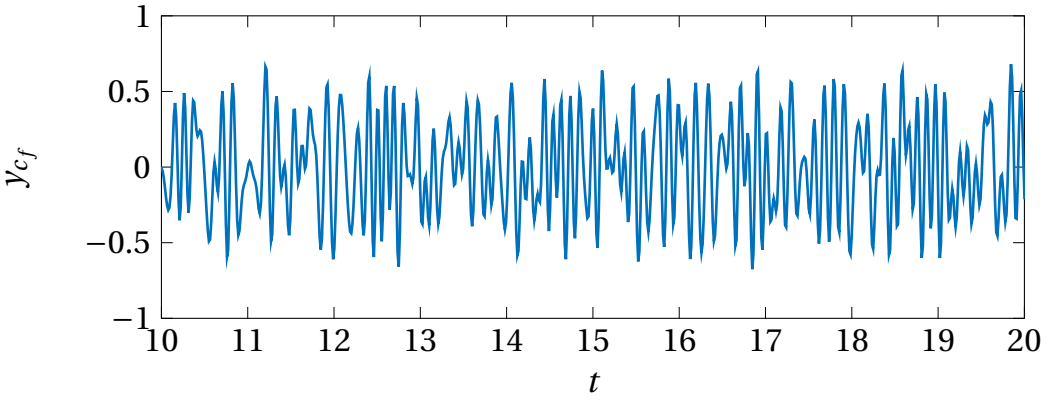

(a) Excerpt of Time Series

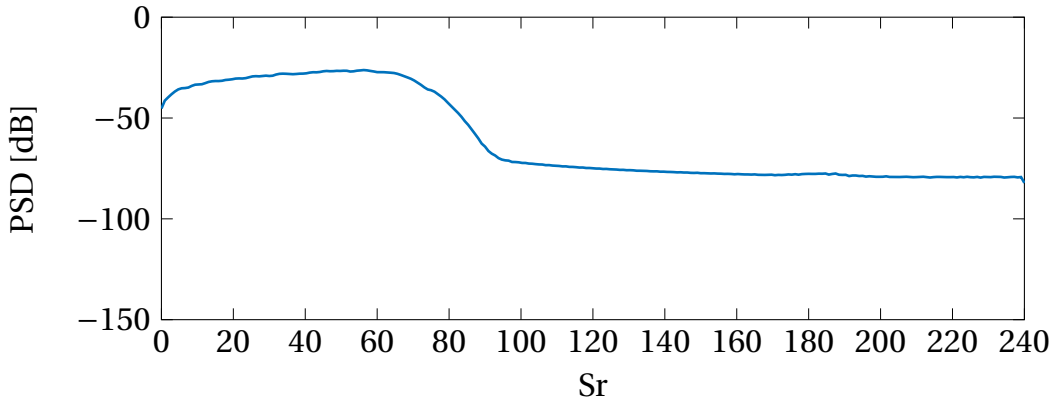

(b) PSD (Welch's Estimate) of Time Series

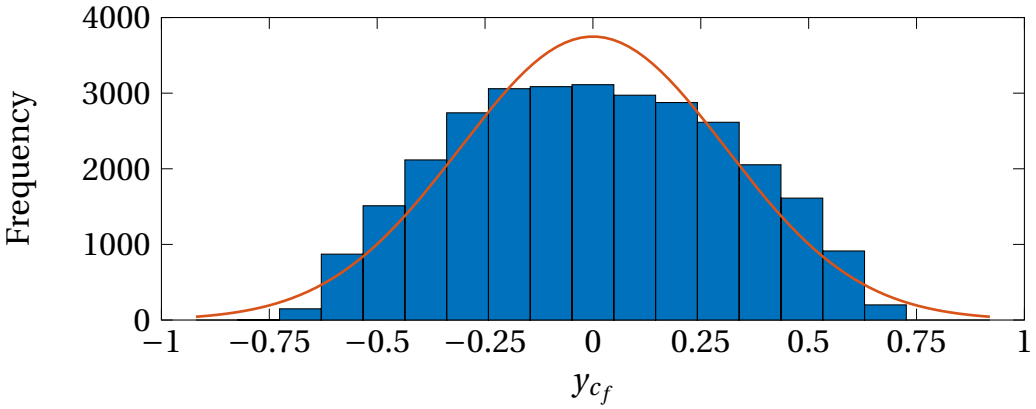

(c) Histogram of Time Series

Figure 6.13: Output Time Series (Friction Coefficient). Bars denote the bins of the input time series. A normal distribution with the same mean and standard deviation as the data is indicated (—).

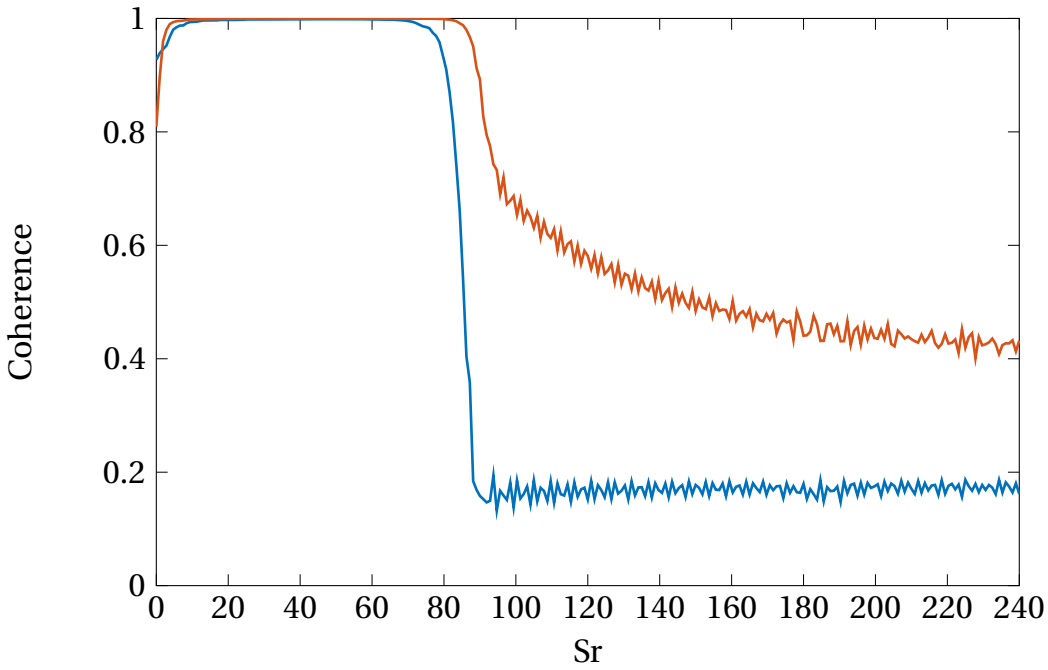

Figure 6.14: Coherence (Welch's Estimate) of Input and Outputs. Coherence of u_{Re} and y_{Nu} (——), as well as u_{Re} and y_{c_f} (——).

From the inspection of the coherence, the following conclusions can be drawn: For both the Nußelt number Nu and the skin friction c_f at the given mean flow Reynolds number Re_0 and the given excitation amplitude $A = 0.05 \cdot \mathrm{Re}_0$ the relationship to the Reynolds number fluctuation is fairly linear. The signal-to-noise ratio is high throughout the frequency range of interest, but slightly lower at very low frequencies and where the PSD of u_{Re} is low.

6.3.2 Development of Discrete Time Models

Model Structure and Parameter Estimation

The problem at hand can be described as a SISO system, and the quantities of interest can be acquired directly from CFD data. No prior knowledge of the physics involved should be used, i.e. a black-box model is sought, so the model is not restricted in this regard. Therefore, it is most convenient to identify a model in input-output structure (cf. Section 4.3.2). For $\mathrm{Re}_0 = 40$, laminar flow was assumed in the whole domain. No vortex shedding occurs even at the highest Reynolds number considered, and the routines for data extraction are not subject to "sensor noise", as would be the case for most hardware sensors. This leads to the conclusion that the level of stochastic disturbance or noise in the system is low and most likely not strongly colored. Thus, as a model structure, an OE model as sketched in Figure 4.7 was chosen.

For the identification, model orders n_b and n_f have to be chosen beforehand. The CFD simulation is a causal system, in which an instantaneous feed-through of velocity perturbations exists. The Reynolds number fluctuation at the present time has to be taken into account, and no pole may be present at the origin in the transfer function. Thus, the model orders are constrained by $n_b = n_f + 1$. A model providing the best estimate is sought, preferring models with lower orders. This was achieved with $n_b = 5$ and $n_f = 4$.

Model Representations

Different representations of the identified models are shown in the plots in Figure 6.15 to Figure 6.17 exemplary for $\mathrm{Re}_0 = 40$. The SI procedure was the same for all mean flow Reynolds numbers. During parameter estimation (cf. Section 4.4.2), the coefficients of the B polynomial and the F polynomial yielding the smallest prediction error were calculated. A graphical representation of these parameters is given in Figure 6.15. Blue dots show the coefficient values. The 99 % confidence interval calculated during parameter estimation (cf. Section 4.4.3) is indicated by the area confided by red lines around zero. A parameter within this region would indicate that this parameter is not significantly different from zero and possibly point towards a too high model order. However, in the case of the model depicted in Figure 6.15, the confidence intervals are very narrow, and it may be concluded that all coefficients provide a significant contribution to the description of the system dynamics.

As described in Section 4.1.3 and Section 4.3.3, the (unit) impulse response is an important representation. On the one hand, it facilitates physical interpretation of a process in the time domain. On the other hand, it is a simple and well-known model for linear systems.

The impulse response of the identified OE model is depicted in Figure 6.16. The heat transfer responds instantly and strongly to an impulse in the velocity. The deviation from the mean Nußelt number continues at $t > 0$, although the impulse is already in the past, but decays to even slightly negative values before settling to zero at later times. A value of zero at infinite times is in accordance with the fact that the system is BIBO stable. Stability is required because the system is also stable, which can be deduced from the fact that a steady state exists (cf. Section 4.1.2). The response at time $t = 0$ is approximately half as strong as at the next instant $t = T_s$. This is due to the discretization in the discrete time framework and not present in a continuous time model. The impulse response indicates that the OE model is to be preferred over the simpler FIR model, as often used in conjunction with the CFD/SI method in the past, due to the slow changing dynamics with large time scales compared to the sampling time. For an FIR model, a huge number of coefficients would be necessary. This tends to be problematic without proper regularization techniques.

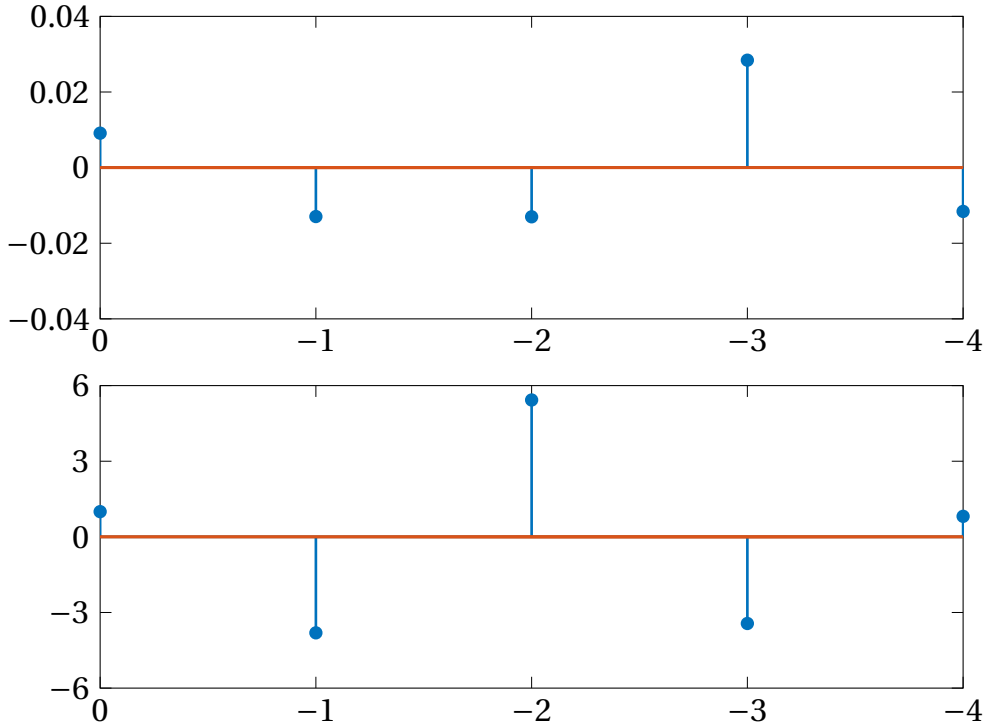

Figure 6.15: Identified Model Parameters of Polynomials *B* and *F*. The abscissa gives the exponent of the time shift operator q. Red lines mark the 99 % confidence interval.

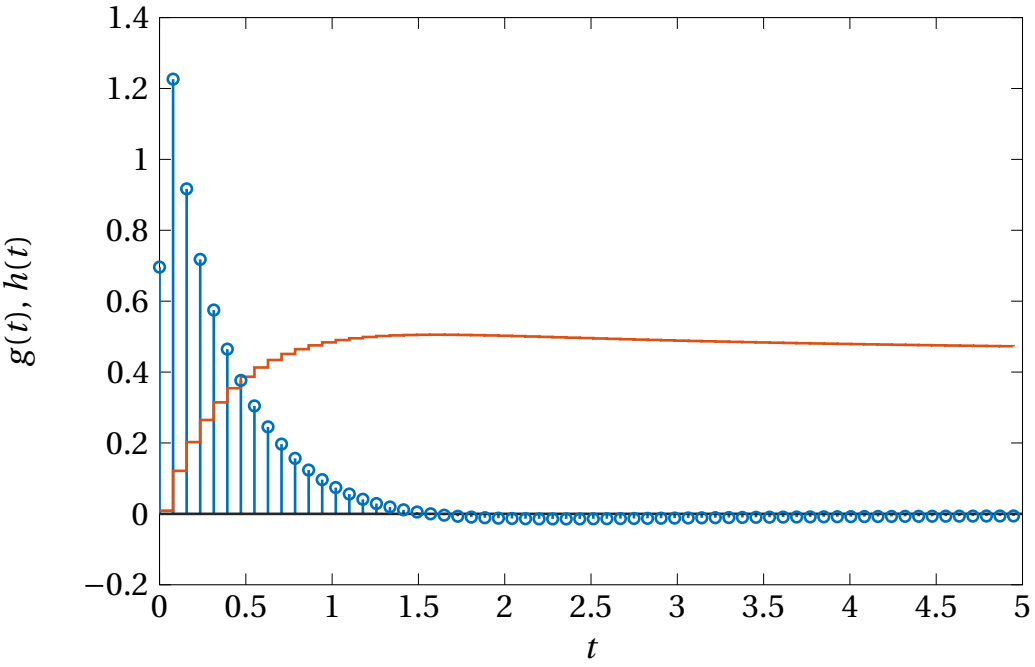

Figure 6.16: Impulse Response and Step Response of OE Model. Impulse response (∘), step response (—). For better visibility, only every sixth instant in time is shown.

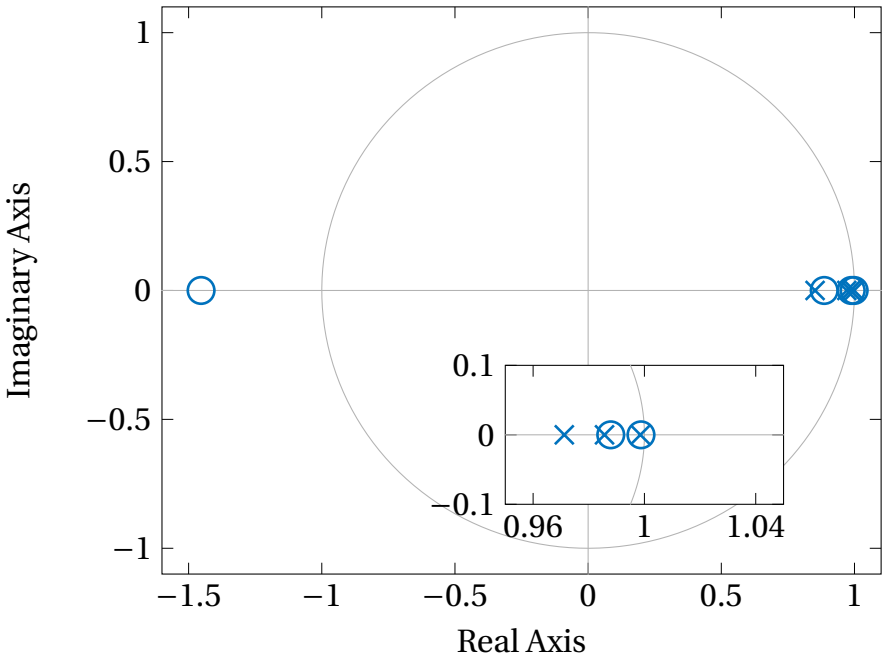

Figure 6.17: Poles and Zeros of the Transfer Function. The unit circle is marked. The insert magnifies the region close to 1 + 0i

The response of the heat transfer to a unit step in the flow velocity, also as depicted in Figure 6.16, is another time domain model (cf. Section 4.3.4). It can also be seen as the cumulative sum of all impulse responses up to a certain instant in time. Hence, no new information is acquired from the representation. However, it is possible to simulate the step response in a CFD simulation directly as shown in Section 6.1. This makes the step response an excellent tool to compare and to validate the SI procedure as shown in Section 6.1. It is, however, also limited as can be seen in the case of $\mathrm{Re}_0 = 3900$ (cf. Section 6.3.5).

The frequency response expresses the model behavior in the frequency domain. It quantifies the relation between input and output for a sinusoidal excitation at Strouhal number Sr. The complex-valued frequency response, depicted as a Bode plot with amplitude and phase of the complex-valued quantity, is reported for all identified models in Section 6.4.

The coefficients of the OE model can be transformed to poles and zeros of the rational function that is a mathematical representation of the OE model. They are shown in Figure 6.17 as crosses (poles) and circles (zeros). All poles are within the unit circle, which indicates that the discrete time model is BIBO stable. The poles are also very close to the unit circle, which is a sign of slowly varying dynamics. All poles (and zeros) are located on the real axis. Hence, no oscillating component (complex exponential) is introduced in the impulse response.

A pole–zero pair very close to the unit circle (cf. insert in Figure 6.17) indicates that a smaller model order might lead to similarly good results. Indeed, a smaller model order has proven to be sufficient at higher Reynolds numbers. At lower mean flow Reynolds numbers, a higher model order is necessary to capture the dynamics satisfactorily. The model order $n_b = 5$ and $n_f = 4$ was chosen here to be consistent with the models for other mean flow Reynolds numbers identified with the same procedure.

6.3.3 Development of Continuous Time Models

Model Structure and Parameter Estimation

As an alternative to the identification of a discrete time model like the OE model, the identification of continuous time models using Quad-VF was investigated. The best model fit was achieved using fourth-order polynomials for both the numerator and the denominator of the transfer function. The time series prepared as detailed in Section 6.3.1 were used for the identification. The major difference to the identification of an OE model is that the data was first transformed to the frequency domain using FFT. The FFT leads to data at evenly distributed frequencies. Working with frequency domain data offers some advantages: Weighting factors can easily be assigned to certain frequencies. At higher mean flow Reynolds numbers ($\mathrm{Re}_0 > 1$), lower frequencies were emphasized to accurately reflect the peak gain. At lower mean flow Reynolds numbers, the weighting shifted towards higher frequencies. This supports an accurate identification, although amplitudes are very low due to the low-pass behavior.

Any type of VF-related method is poorly conditioned if the order of the identified model becomes higher than twice the number of peaks present in the transfer function. This can be controlled to some extent by regularization, i.e. using the CLS approach to relocate the poles during the identification procedure. Regularization achieves lower variance at the cost of bias. In the case of a comparatively high model order, a small regularization factor in the order of the floating-point relative accuracy $\lambda \approx 1 \times 10^{-15}$ for an L_2-regularization proved to drastically reduce the variance with a negligible effect on the identified parameters.

Nonlinear parameter estimation methods are prone to become trapped in a local minimum and therefore rely on good initial conditions. Further improvement of the identification procedure could be achieved by successive identification of models with different mean flow Reynolds numbers using a predefined set of poles. The initial poles were taken from the model identified with a similar Reynolds number. In particular, the transfer function $G(\mathrm{Re}_0 = 40)$ was used as initial condition for $G(\mathrm{Re}_0 = 20)$ and so on. The mean flow Reynolds numbers were chosen in such a way that the changes from one model to the next were not too large. The identifica-

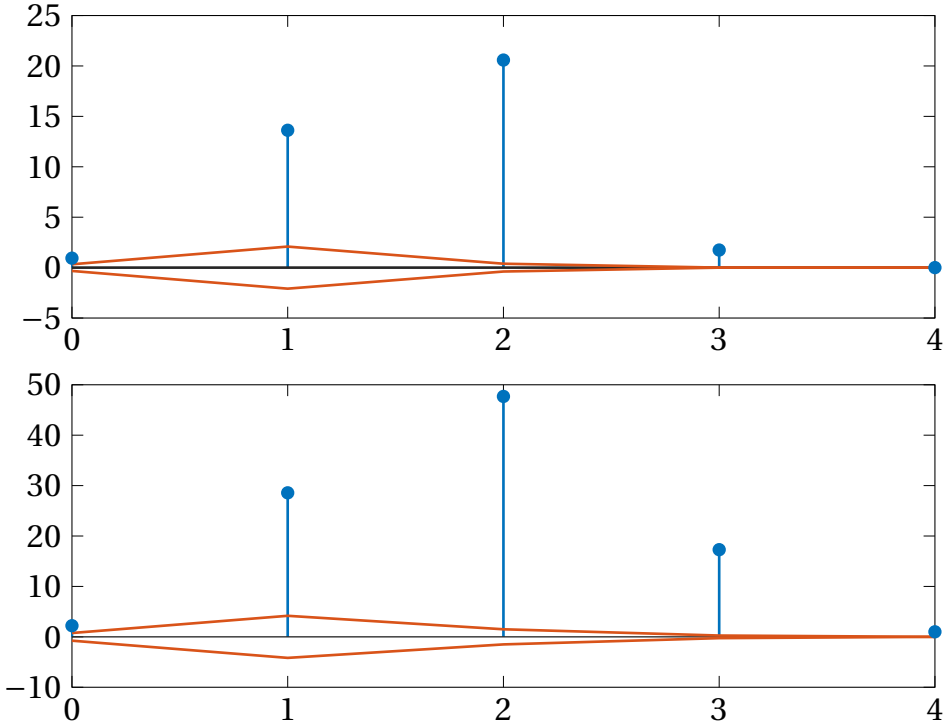

Figure 6.18: Identified Model Parameters of Nominator and Denominator of $G(s)$. The abscissa gives the exponent of the Laplace parameter s. Red lines mark the 99 %-confidence interval.

tion of a single model is not an isolated event, but the complete set of data is used to support the process. The resulting models are rational functions of the Laplace-parameter s.

Model Representations

Exemplary for all identified models, the model representations for $G_{\mathrm{Nu}}(\mathrm{Re}_0 = 40)$ are discussed in this section. The identified models are primarily represented by the model coefficients and the covariance matrix. Figure 6.18 shows the coefficients of the numerator and the denominator of the rational function that was used to model the transfer behavior. The variance of each parameter, the diagonal entries of the covariance matrix, is represented as the 99 % confidence intervals plotted in red. The abscissa indicates the power of the Laplace parameter s in the transfer function.

All parameters are significantly different from zero, and the presented model provides the best fit to the given data. However, the parameter associated with s^4 in the numerator polynomial is very small. It can be set to zero with only a minor reduction of the model fit (< 1 %). This modification yields a model with $|G_{\mathrm{Nu}}| \to 0$ for $\mathrm{Sr} \to \infty$ and is to be preferred if a well-behaved approximation of the real physics is valued over accuracy.

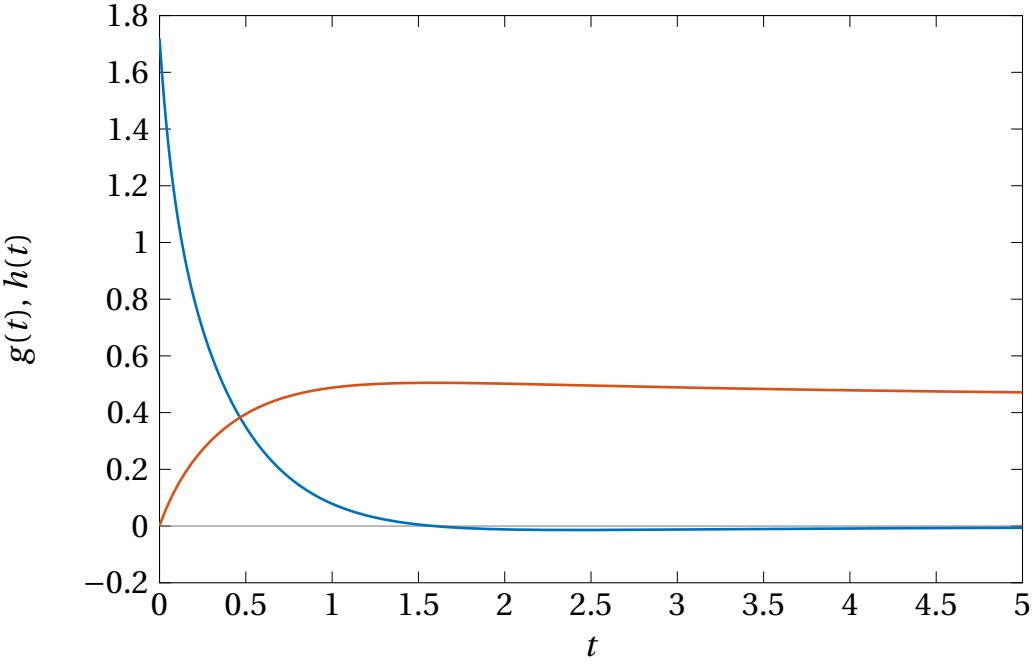

Figure 6.19: Impulse Response and Step Response of Transfer Function from VF. Impulse response (—), step response (—).

The impulse response and the step response are continuous functions in the case of a continuous model. Both response representations are depicted in Figure 6.19. The graphs are very similar to that of the discrete time model except for the discretization. The impulse response is strongest at $t = 0$ and declines in the shape of superimposed exponential functions. It becomes negative at $t \approx 1.6$ and settles to zero for $t \to 0$. Accordingly, the step response reaches its maximum at $t \approx 1.6$ and the quasi steady-state limit is $K_{\mathrm{Nu}} = 0.4235$.

For a transfer function, usually given as a rational function, poles and zeros can easily be calculated. For the case at hand, they are shown in Figure 6.20. Zeros are represented by circles and poles by crosses. All poles are located in the left half plane. Hence, the continuous time model is BIBO stable. This condition is enforced during identification by pole flipping. All poles and zeros are real-valued and no complex-valued poles, which would occur as complex conjugate pairs, are present. This also shows that no oscillatory component is present in the impulse response.

6.3.4 Model Validation

The model validation tests, introduced in Section 4.5, were performed for every identified model. Exemplary for all acceptable models, graphical representations of the validation are given for the identification procedure of the OE model for $G_{\mathrm{Nu}}(\mathrm{Re}_0 = 40)$ (cf. Section 6.3.2).

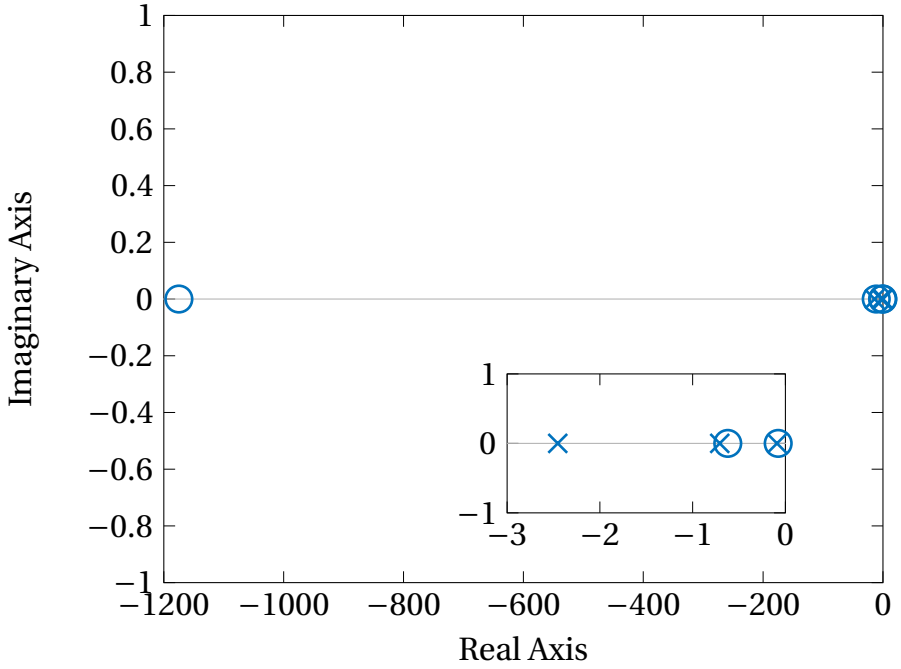

Figure 6.20: Poles and Zeros of the Continuous Transfer Function. The insert magnifies the region close to the origin $0 + 0\mathrm{i}$.

Residuals

Basic test criteria focus on the residuals of the identification process. They correspond to the prediction errors, i.e. deviations of the modeled output to the "true"(CFD simulated) output. In Figure 6.21a, an excerpt of the time series is depicted. The same interval as in the plots for the input and output data is shown. The mean value is close to zero indicating that the model is unbiased. The residuals are in the range $[-2.9 \times 10^{-4}, 2.9 \times 10^{-4}]$ which is small compared to the model output, i.e. the relative Nußelt number fluctuation ($[-0.014, 0.014]$).

Welch's estimate for the PSD of the residuals is depicted in Figure 6.21b. The noise has substantial PSD in the frequency range where also the excitation, hence the response, is strong and drops by several orders of magnitude around $\mathrm{Sr} = 80$. At very low values of the Strouhal number, the PSD is higher because of the finite length of the time series. This is in accordance with the coherence of input and outputs (cf. Figure 6.14) which shows values below unity and can thus be attributed to higher noise levels, i.e. a lower signal-to-noise ratio. Around $\mathrm{Sr} \approx 5$ a local minimum is reached. At this point, length effects are negligible, and the output y_{Nu} has a comparatively high amplitude, and hence the prediction error minimization yields best results in this region. This can be seen as a natural weighting in the case of an OE model. In cases where a noise model was identified, i.e. a BJ model structure was chosen, the model for this PSD is used to find the optimal one-step ahead predictor. The VF approach does not rely on the minimization of the prediction error but on

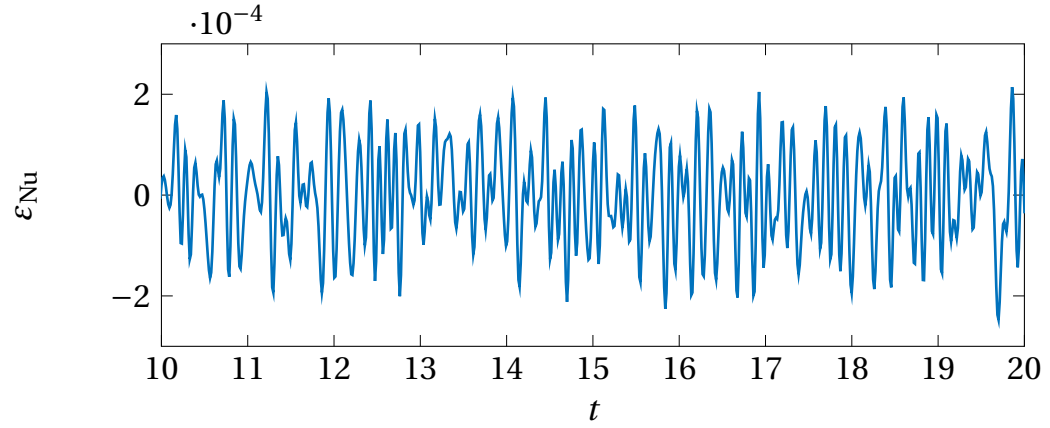

(a) Excerpt of Time Series

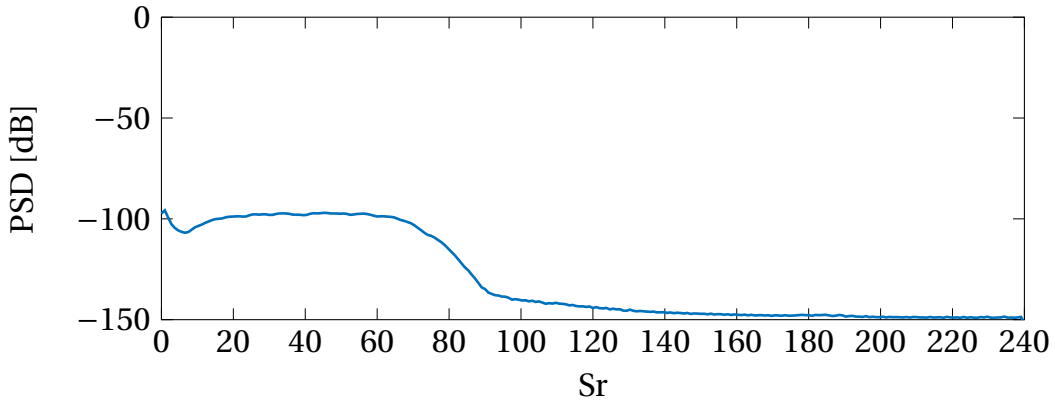

(b) PSD (Welch's Estimate) of Time Series

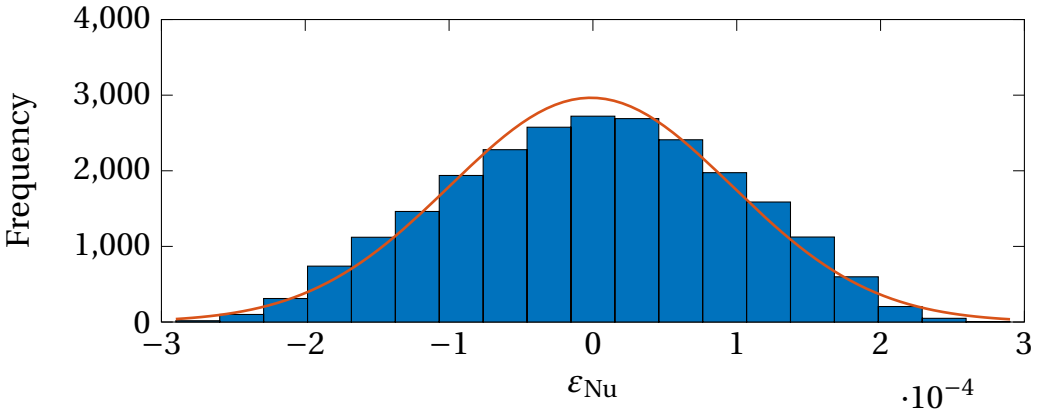

(c) Histogram of Time Series

Figure 6.21: Time Series of Residuals (Nußelt Number). Bars denote the bins of the input time series. A normal distribution with the same mean and standard deviation as the data is indicated (—).

the smart relocation of poles. For this reason, no weighting occurs in this manner in the VF procedure and residuals are often larger.

Figure 6.21c shows the histogram, i.e. the amplitude distribution of the residuals for the model estimated for $\mathrm{Re}_0 = 40$. A normal distribution derived from the sample mean and of the residual time series is included in Figure 6.21c. It can be concluded by inspection that the residuals are close to normally distributed and hence the noise, which is equal to the prediction error in case of an OE model, has a Gaussian distribution.

Figure 6.22 depicts the output y_{Nu} and the residuals $\varepsilon_{\mathrm{Nu}}$ as a scatter plot. Every instant in the time series is represented as one point. This plot can be used to detect patterns in the residuals and relations between residuals and output. The red dots mark the data of a model identified with a 5 % amplitude in excitation velocity. An excitation of 25 % was used to create the blue time series for comparison. The shape of the red cloud for the lower amplitude is elliptical with the principal axis aligned with the coordinates y_{Nu} and $\varepsilon_{\mathrm{Nu}}$. This indicates that no systematic relationship between output and residuals is present. In the case of the higher amplitude, however, the cloud exhibits a half moon shape. At extreme values of y_{Nu}, the residual also exhibits extreme and always positive values. The positive values and the curved shape indicate a (slightly) nonlinear behavior that cannot be handled by the linear model and hence condenses in the residuals. It is also strongest at extreme values, which points towards a nonlinearity associated with the excitation amplitude. For all identification procedures reported in Section 6.3, an excitation amplitude of 5 % of the mean flow velocity was used.

Correlation Tests

Two correlation tests are commonly performed during model validation: a test for whiteness and a test for independence. Before the correlations were computed the according time series were down sampled to $\mathrm{Sr}_{\mathrm{max}} = 60$. This way, the high-frequency noise did not appear in the correlation and the overall time covered by 20 samples, which is a typical number, is four times larger.

In the whiteness test (cf. Section 4.5), the auto-correlation of the residuals was computed as shown in Figure 6.23. The two red lines mark the 99 % confidence interval. Correlation coefficients within the red lines are considered not significantly different from zero. The assumption of GWN is only proven true if the auto-correlation is insignificant for every lag > 0. This is a condition hardly achieved with an OE model structure as it was in this case. However, due to the independent parametrization of the deterministic part and the noise (which is not modeled at all), this has no impact on the deterministic model.

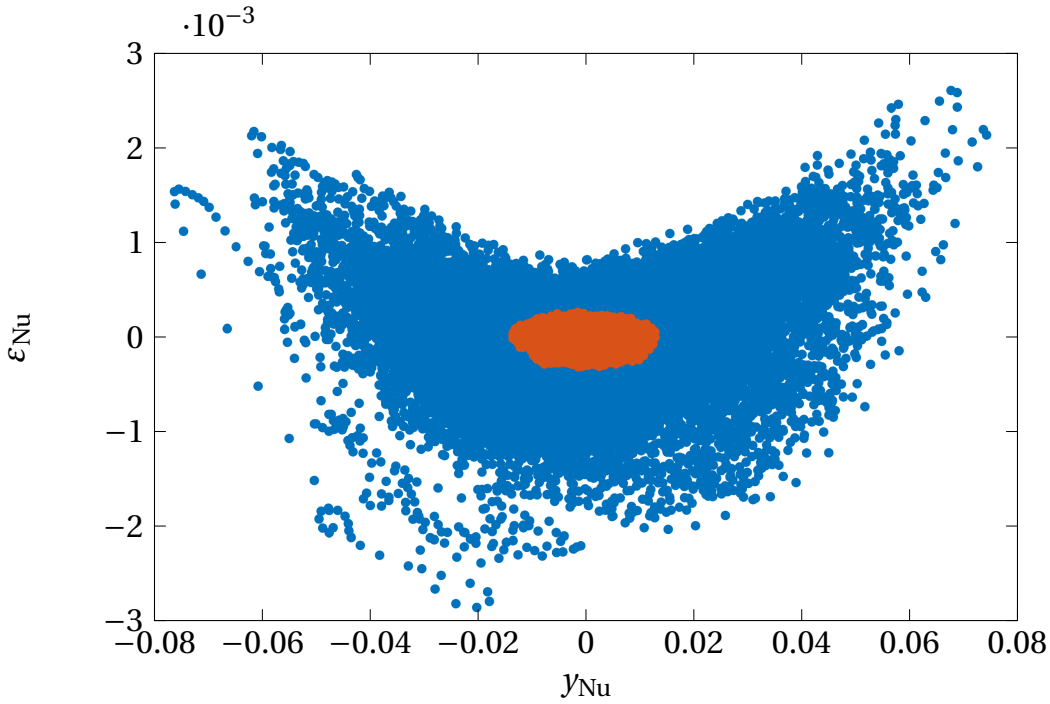

Figure 6.22: Scatter Plot of Residuals and Output. Every dot corresponds to one instant of the time series. Red dots represent data acquired from a simulation with an excitation amplitude of 5 %. Blue dots indicate 25 %.

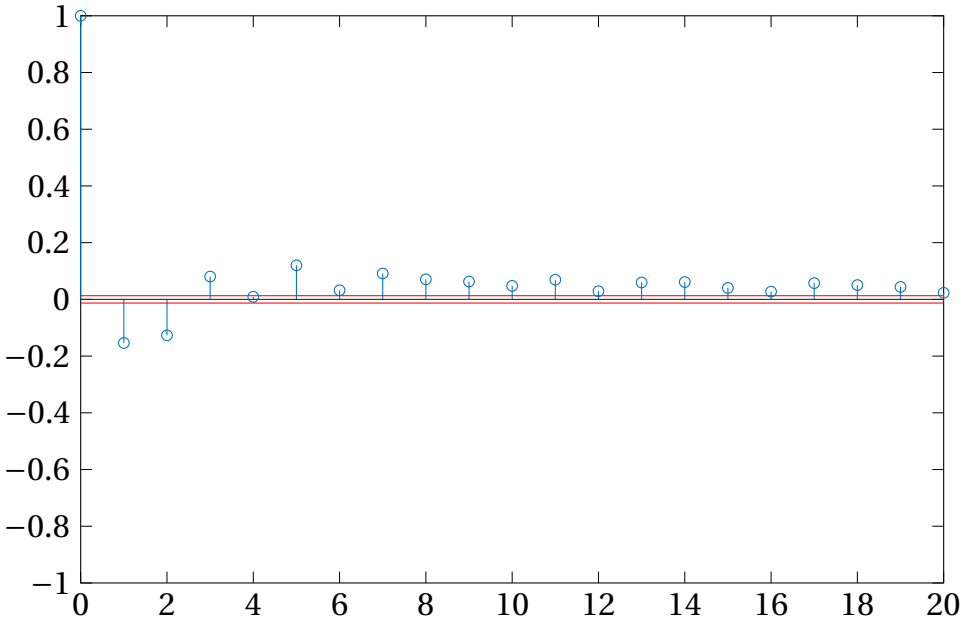

Figure 6.23: Whiteness Test. Auto-correlation of residuals.The 99 % confidence interval is indicated by red lines (—)

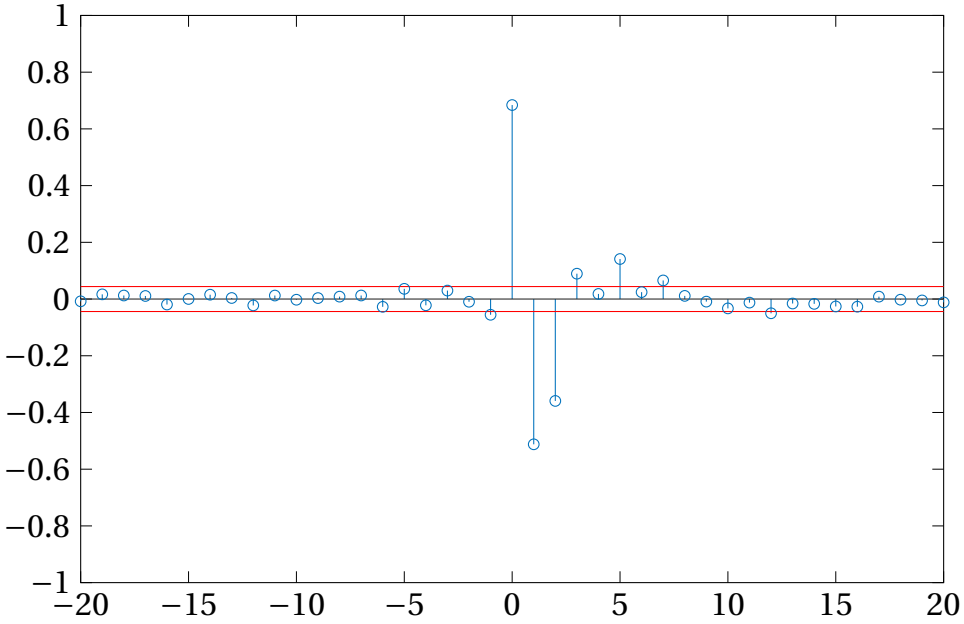

Figure 6.24: Independence Test. Cross-correlation function of residuals and input.The 99 % confidence interval is indicated by red lines (——).

The second correlation test is between the residuals and the input. If the cross-correlation between residuals and input is not significant, both time series are independent (cf. Section 4.5). This means that no information in the residuals is related to past inputs and hence all information is contained in the model output. Figure 6.24 depicts the cross-correlation between residuals of the identification of $G_{\mathrm{Nu}}(\mathrm{Re}_0 = 40)$ and the input signal used in the estimation. The 99 % confidence intervals are shown in red. There is no significant correlation at negative lags which would indicate feedback of any kind. A noticeable correlation is visible at lags 0, 1, and 2. They are associated with high frequencies and are insignificant if the time series for identification are pre-filtered with a low-pass filter, i.e. the high-frequency content is reduced beforehand.

Cross-Validation

The most important test is probably the cross-validation test. A “fresh” data set, of which input and output are known, was compared to the model response to the input provided by this validation set. This test is only applicable in this manner with high signal-to-noise ratio, i.e. in cases where stochastic disturbances have only little effect on the output. A validation time series is created for every data set, i.e. for every mean flow Reynolds number, by splitting the acquired time series into two parts. The second, much shorter part (20 % of the full time series length) is solely used for the cross-validation. Figure 6.25 shows an excerpt of the CFD simulated output. For comparison, the response computed with the model is plotted on top. The lines

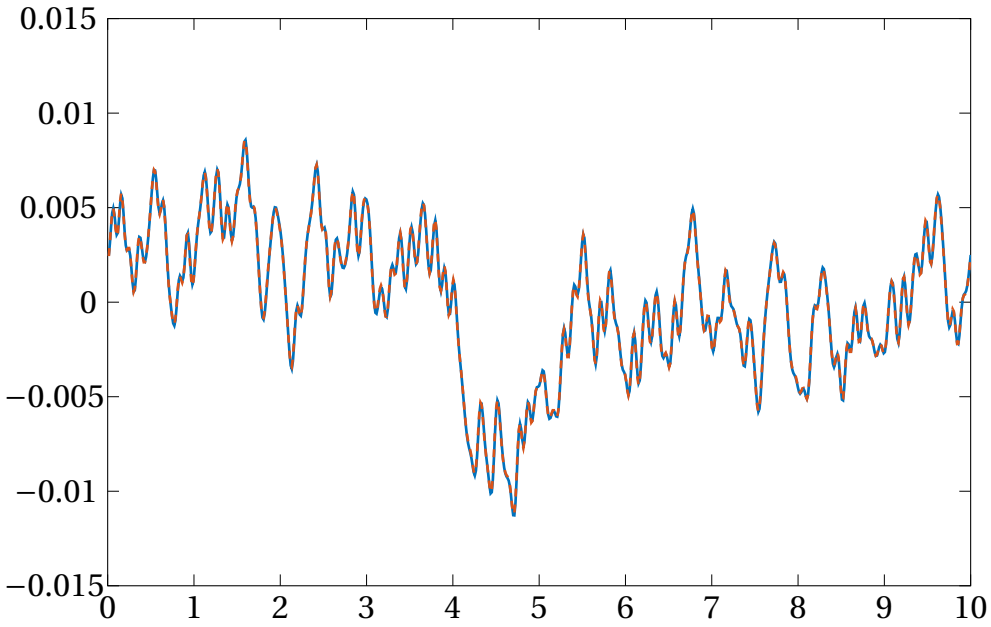

Figure 6.25: Excerpt of Time Series for Comparison. Time series from CFD simulation (——) and time series from OE model (- - -).

match very well for this case. The goodness of fit is quantified by the NRMSE-fit. The fit values for all identified models are given in Table 6.3 for the heat transfer and in Table 6.5 for the skin friction. For the continuous time identification, models and fits are reported in the appendix. All fit values are above 95 % (except for $\mathrm{Re}_0 = 1$, which has $\Phi = 94\,\%$) and hence perform excellently in the cross-validation test.

6.3.5 Identification in the Presence of Tonal Noise and Turbulence

Vortex shedding creates a tonal noise at a distinct frequency (twice the vortex shedding frequency). In this case, the noise cannot be assumed white but is strongly colored, which impedes identification. Moreover, turbulence creates broadband disturbances with a characteristic spectrum (cf. Section 2.1.3). Several measures can be taken to remedy this problem.

Tonal Noise

The influence of the vortex shedding on heat transfer and skin friction is part of the noise. As the vortex shedding occurs at a distinct frequency, the contribution to the noise is tonal. The response to vortex shedding must not be included in the deterministic model for two reasons: First, it is not a response to the input signal but also exists in the (quasi) steady state. Second, the linearity requirement is not fulfilled as the strength of the vortex shedding depends on the mean flow and not

on the excitation. The later also is detectable in the coherence between input and output.

Turbulent Noise

Disturbances in the heat transfer and the skin friction are caused by turbulent fluctuations of the flow velocity. Turbulence is by nature three dimensional, chaotic, and highly transient. It is independent of the input signal and hence clearly part of the system noise. Measuring the Reynolds number with an area average over a plane diminishes the effect of turbulence on the acquired input signal. However, the effect of turbulent structures on the heat transfer and the skin friction can only be factored out partially by calculating average values for the Nußelt number Nu and the friction coefficient c_f. It is possible to identify unbiased purely deterministic models in the presence of turbulence if the length of the time series is sufficient. In many cases, it may not be possible to acquire time series long enough through simulation. The model of choice is then the BJ model with independent parametrization for the deterministic part and the disturbances.

Approaches to Signal Processing

Due to the tonal nature of the vortex shedding influence, any deterministic model will include this effect if the model order is high enough to represent it. This results in three fundamental approaches: (1) removing the tonal noise from the response during pre-processing before parameter estimation, (2) choose a small model order so the strongly bandlimited effect cannot be represented, or (3) identify a noise model that includes this effect.

For a wide range of Reynolds numbers, the vortex shedding Strouhal number is $\mathrm{Sr}_f \approx 0.2$, evaluated with frequency $f = \omega/(2\pi)$. For smaller Re_0, it is somewhat below this value. Due to symmetry, the frequency of the tonal disturbance is twice the shedding frequency. Using the angular frequency to define the Strouhal number, as it is done throughout this thesis, yields $\mathrm{Sr} \approx 2.5$.

The vortex shedding phenomenon occurs for mean flow Reynolds numbers of $\mathrm{Re}_0 \gtrsim 47$. Hence, the investigated mean flow Reynolds numbers $\mathrm{Re}_0 = 120$, $\mathrm{Re}_0 = 240$, and $\mathrm{Re}_0 = 3900$ exhibit this periodical detaching of the recirculation zones. At $\mathrm{Re}_0 = 120$, the fluctuation in Nußelt number Nu is not as strong and can be compensated with a high signal-to-noise ratio, i.e. higher excitation amplitudes. This is not possible for higher Reynold numbers, because the strength of the tonal noise is comparable to the limit of linearity.

Tangirala[1] proposed to transform the output signal using FFT, and reduce the coefficient associated with the vortex shedding frequency. Subsequently, the signal is transformed back to time domain (using inverse fast Fourier transform IFFT). This approach does not lead to satisfactory results, because complete removal of the vortex shedding frequency, i.e. setting the FFT coefficient to zero, also leads to distortion at this frequency.

A notch filter with a very small stopband was used as another method to remove the tonal noise component. This is equivalent to factor in the vortex shedding frequency with only a small weight. The notch filter, however, is difficult to set up. A narrow filter width greatly diminishes one specific frequency but does not necessarily capture the effect of the vortex shedding satisfactorily. On the other hand, if the filter width is too broad, this influences the low frequencies to a large extent and does not yield acceptable results either.

Approaches (2) and (3) were used in combination for the identification of the models at $\mathrm{Re}_0 = 120$, $\mathrm{Re}_0 = 240$, and $\mathrm{Re}_0 = 3900$. A low-order for the deterministic model was chosen in conjunction with a high order of the noise model to successfully determine the transfer behavior.

System Identification with Noise Modeling

For the transfer function identification from LES data, a BJ model structure (cf. Section 4.4.4) was chosen. The BJ model is similar to the OE model with the addition of a parametrization for the noise. This increase in model complexity is necessary to deal with the two phenomena vortex shedding and turbulence.

A fitting of the deterministic model to the noise dynamics has to be avoided. This is especially critical in the case of the tonal noise from vortex shedding. To achieve this, a low deterministic model order is complemented by a high order for the noise model. The time series data was prepared in the same way as for the identification from laminar simulations (cf. Section 6.3.1).

6.4 Results from Transfer Function Identification

In this section, the results from the identification processes are shown. The mean flow Reynolds number Re_0 serves as a parameter. A transfer function for the heat transfer and the skin friction of a cylinder to pulsations in the flow velocity for every mean flow Reynolds number considered in this thesis was identified. The estimated coefficients of the transfer functions were tabulated. The frequency responses are

[1] Private communication, 2014

shown as Bode plots to give a graphical representation of the dynamic behavior and the differences between the models evaluated at different mean flow Reynolds numbers. The results reported here were previously published in parts in Witte et al. (2016a,b); Witte and Polifke (2017a).

The models identified with discrete time identification techniques, OE model or BJ model, are reported here. For mean flow Reynolds numbers $\mathrm{Re}_0 \leq 40$, it was possible to calculate transfer functions with three substantially different methods. The only commonality was that the data was acquired from numerical simulations solving the incompressible Navier–Stokes equations. All methods, the step response simulations, the LNSE approach and the CFD/SI method lead to results with only minor differences. Two different approaches to SI, one for discrete time and one for continuous time, were examined and the results also match within a small margin. For completeness, these models are reported in the appendix.

The coefficients of the transfer function were determined through parameter estimation during the identification process. In the discrete time framework, the models depend on the sampling time. To achieve independence from this discretization, the discrete time models were transformed to continuous time using bilinear transform (cf. Equation (4.23)). The original sampling time was short enough so that the transformation has a negligible effect on the frequency response in the range $0 \leq \mathrm{Sr} \leq 40$. $\{b_m\}$ and $\{a_n\}$ denote the model coefficients in continuous time. The general transfer function model, given as a rational function of the Laplace parameter $s = \sigma + \mathrm{i}\,\mathrm{Sr}$ (cf. Equation (4.24)), can be written as

$$G(s) = \frac{b_0 + b_1 s + b_2 s^2 + b_3 s^3 + b_4 s^4}{1 + a_1 s + a_2 s^2 + a_3 s^3 + a_4 s^4}\,. \tag{6.9}$$

The coefficients are reported for all mean flow Reynolds numbers under consideration in Table 6.4 and Table 6.6.

The BJ models for mean flow Reynolds numbers $\mathrm{Re} > 40$ can be written as

$$y = G(q)\,u_{\mathrm{Re}} + H(q)\,e[k]\,. \tag{6.10}$$

The deterministic models were transformed to a continuous time transfer function by bilinear transform. These transfer functions for heat transfer and skin friction are also reported in Table 6.4 and Table 6.6, respectively.

6.4.1 Heat Transfer

The dynamic behavior of the heat transfer of a cylinder in pulsating crossflow at different mean flow Reynolds numbers is reported as transfer functions and visualized as Bode plots of the frequency response. These results have previously been published in parts by Witte and Polifke (2017a).

Re_0	Φ in %	
	Estimation	Cross-validation
0.1	96.11	97.94
0.2	95.50	97.30
0.4	93.89	98.31
0.5	94.62	97.05
0.7	93.39	95.58
1.0	90.17	94.54
2.0	93.85	95.66
3.0	94.46	96.18
4.0	96.16	97.06
10.0	98.33	99.07
20.0	94.73	99.25
40.0	98.64	98.69
120	99.99	
240	99.99	
3900	99.93	

Table 6.3: NRMSE-Fit of the Identified Transfer Functions of Heat Transfer.

Transfer Functions

The transfer functions are transformed OE models or BJ models identified from CFD data. The goodness of fit achieved during estimation and the goodness of fit from the cross-validation test are reported in Table 6.3. For models with a mean flow Reynolds number above the threshold for vortex shedding $\mathrm{Re}_0 > 40$, for which also a noise model was identified, almost perfect fit values during estimation were achieved. This is due to the high order noise model with ten coefficients for each of the two polynomials. The computation of an infinite-step ahead prediction for cross-validation was not useful due to the strong unpredictable noise content in the data.

Table 6.4 gives the coefficients transformed to continuous time to acquire independence of the sampling time. For every mean flow Reynolds number Re_0, two rows are noted in the table. One for the numerator coefficients $\{b_n\}$ and one for the denominator coefficients $\{a_m\}$. Each column stands for one power of the Laplace parameter. The first row of coefficients includes the constant terms which are equal to the steady state limit of the transfer function $b_0 = K_{\mathrm{Nu}}$. The constant coefficient of the denominator polynomial is always one and therefore omitted. For mean flow Reynolds numbers $\mathrm{Re}_0 \leq 40$, five coefficients for the numerator $n_n = 5$ and four coefficients for the denominator $n_m = 4$ have been estimated and hence the highest power is s^4.

Re_0		s^0	s^1	s^2	s^3	s^4
0.1	b	0.2015	1.893	1.739	0.1407	0.0002416
	a		31.7	132.3	64.85	2.338
0.2	b	0.2193	1.683	1.324	0.09926	1.78×10^{-4}
	a		20.58	66.25	27.53	0.975
0.4	b	0.2561	1.228	0.7184	0.04635	8.009×10^{-5}
	a		11.98	25.1	7.98	0.263
0.5	b	0.2648	0.8961	0.3885	0.02026	2.629×10^{-5}
	a		9.102	13.96	3.382	0.09405
0.7	b	0.2806	0.6385	0.19	0.007419	6.163×10^{-6}
	a		6.483	6.814	1.168	0.02586
1.0	b	0.2921	0.5471	0.1495	0.005533	3.61×10^{-6}
	a		4.91	4.364	0.6943	0.01499
2.0	b	0.3342	99.76	74.39	5.545	0.008733
	a		300.3	739.3	259.3	10.62
3.0	b	0.3537	5.543	3.167	0.1983	2.164×10^{-4}
	a		16.45	28.6	8.078	0.2952
4.0	b	0.3662	2.846	1.895	0.1821	3.881×10^{-4}
	a		8.392	13.13	4.508	0.2586
10.0	b	0.3949	4.153	1.265	0.04329	-9.961×10^{-6}
	a		9.869	8.916	1.481	0.03482
20.0	b	0.4145	3.221	0.5823	0.01029	-1.141×10^{-5}
	a		7.007	4.28	0.4704	0.006289
40.0	b	0.4181	8.033	18	0.8508	-8.151×10^{-4}
	a		17.13	39.37	13.73	0.4533
120.0	b	0.4484	1.506×10^{-4}	-2.696×10^{-7}		
	a		0.2331	1.081×10^{-5}		
240.0	b	0.538	0.7906	−0.001383		
	a		2.602	0.4011		
3900.0	b	0.538	0.001374	-2.908×10^{-6}		
	a		0.4887	3.363×10^{-4}		

Table 6.4: Estimated Coefficients of the Transfer Function of Heat Transfer. All values are transformed to continuous time using bilinear transform.

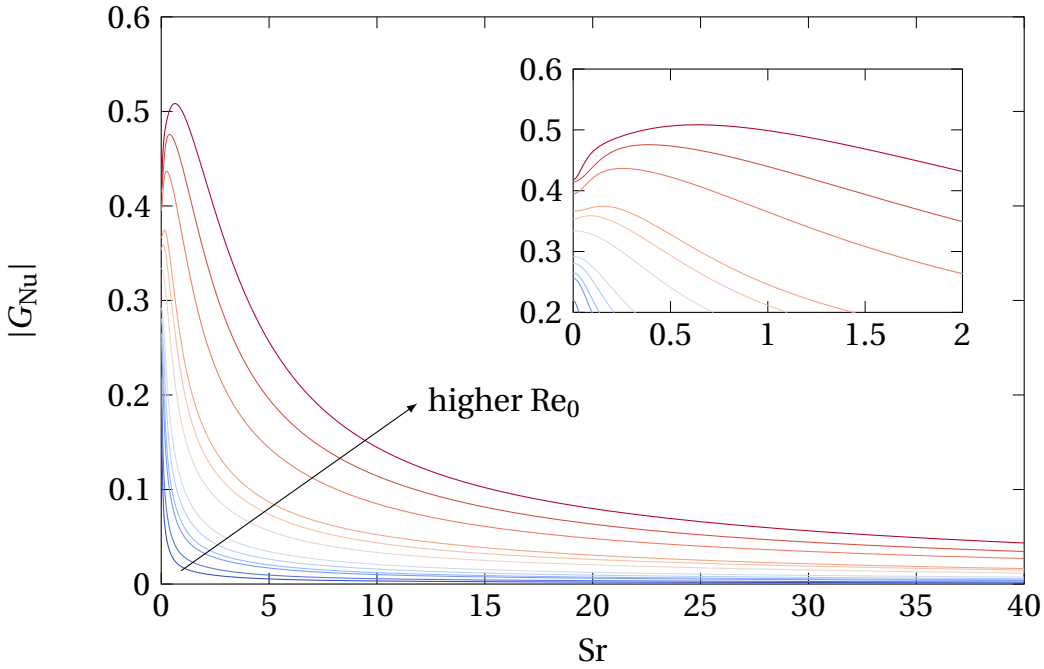

Figure 6.26: Amplitude of the Heat Transfer Frequency Response ($Re_0 \leq 40$)**.** Blue to red. Reynolds numbers: 0.1, 0.2, 0.4, 0.5, 0.7, 1, 2, 3, 4, 10, 20, and 40. The insert in the top right corner magnifies small frequencies $Sr \leq 2$.

Frequency Response at $Re_0 \leq 40$

The frequency response, as a representation of the transfer function, shows the response to continuous forcing of sine waves with a certain Strouhal number and a constant amplitude. Special attention is given to mean flow Reynolds numbers $Re_0 \leq 40$. This is the relevant range for the applications motivating this thesis, i.e. first and foremost the Rijke tube (cf. Table 3.1).

The amplitude of the frequency response depicted in Figure 6.26 shows a low-pass behavior. The response is below unity throughout all frequencies, yet high frequencies are damped more strongly. This effect is more pronounced at lower Reynolds numbers. In terms of filters, the cutoff frequency is higher for higher mean flow Reynolds numbers. The amplitude at zero frequency $Sr \to 0$ is the steady-state gain K_{Nu} also obtained through analysis of the step response (cf. Section 6.1.1 and Section 6.5.2). Again, a dependence on Reynolds number is evident and higher Reynolds number flow achieves greater gain values.

The insert in Figure 6.26 magnifies the region of small Strouhal numbers in the range of $0 < Sr < 2$, i.e. at low frequencies. For Reynolds numbers of order unity or larger, a peak in amplitude can be found in $0 < Sr < 1$, which is also in agreement with the results of the step response simulations. Again, at higher Reynolds

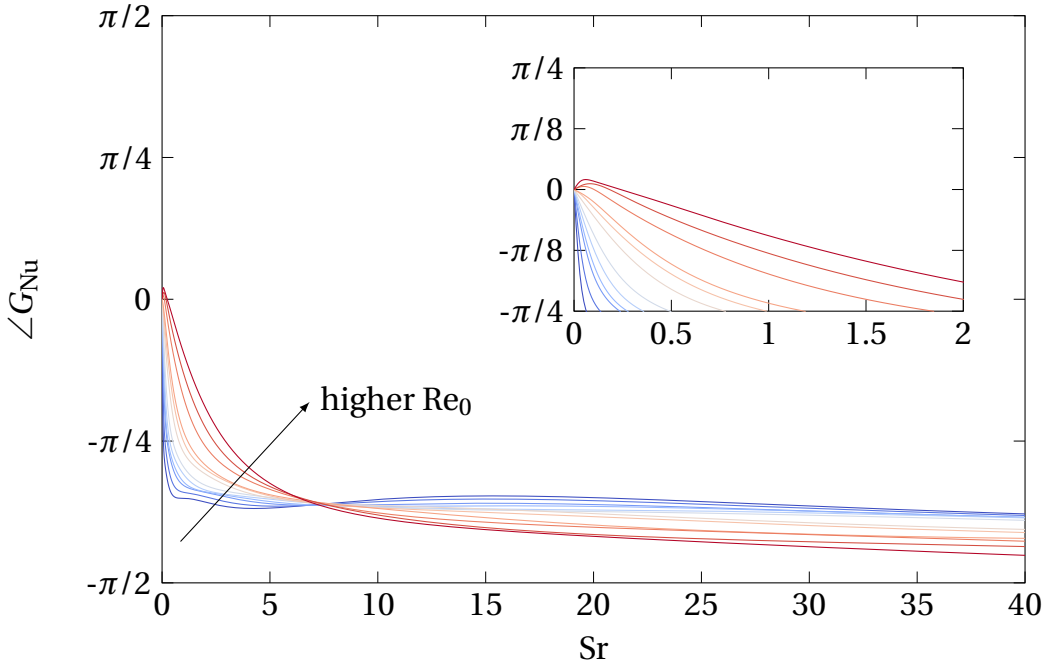

Figure 6.27: Phase of the Heat Transfer Frequency Response ($\mathbf{Re_0 \leq 40}$). Blue to red. Reynolds numbers: 0.1, 0.2, 0.4, 0.5, 0.7, 1, 2, 3, 4, 10, 20, and 40. The insert in the top right corner magnifies small frequencies $\mathrm{Sr} \leq 2$.

numbers, this effect appears in a more pronounced manner and the peak frequency moves towards higher Strouhal numbers.

Figure 6.27 shows the phase difference between normalized velocity and heat release rate fluctuations. For all Reynolds numbers, the phase starts at zero but shows a dependence on Reynolds number similar to the amplitude at $\mathrm{Sr} > 0$. In general for all mean flow Reynolds numbers, there is a strong initial decay at low frequencies that becomes less steep towards higher Sr. If the mean flow Reynolds number is lower, the descent is steeper at low frequencies and more flat-angled towards higher Sr. At intermediate mean flow Reynolds numbers ($10 \lesssim \mathrm{Re}_0 \lesssim 40$), slightly positive values (phase lead) occur at Strouhal numbers below 0.5. This effect was already predicted by Lighthill (1954), but his solution approach was not able quantify it. The insert in Figure 6.27 magnifies the values at very low Sr where this phase lead occurs.

For higher frequencies, phase values approach a value slightly larger than $-\pi/2$ for $\mathrm{Sr} \to \infty$. The theoretical high frequency limit for a first order system $\lim_{\mathrm{Sr}\to\infty} \angle G = -\pi/2$ in never reached. This is due to the flow field at the lee side of the cylinder, which could not be accounted for by the analytical investigations. In the step response in Figure 6.2, sector 4 assumes negative values leading to phase values of π, but with only a small contribution to the overall heat transfer. In the representation of the temperature fields (e.g. Figure 7.6 and Figure 7.17), this can be seen as hot zones close to the backward stagnation point of the cylinder. For the lowest mean

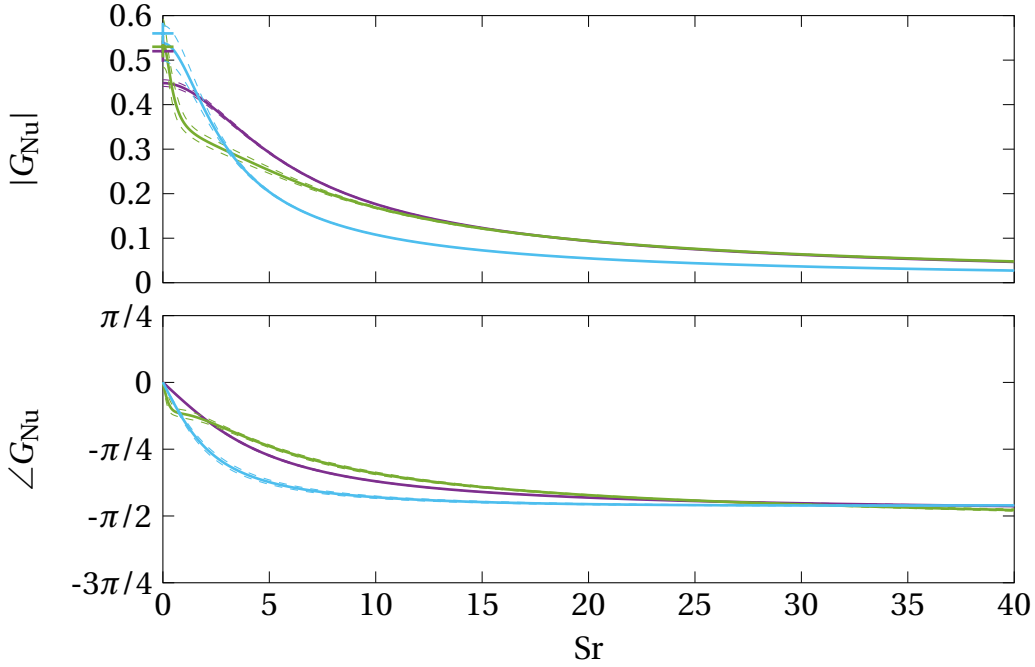

Figure 6.28: Frequency Response of the Heat Transfer ($Re_0 > 40$). $Re_0 = 120$ (——), $Re_0 = 240$ (——), and $Re_0 = 3900$ (——). Dashed lines mark the 99 % confidence intervals. The cross shows the low frequency limit evaluated from the correlation by Sparrow et al. (2004).

flow Reynolds numbers, the initial drop in heat transfer rate at sector 4 is even stronger than the increase in sector 1 through sector 3. This is the reason for the phase to have a local minimum at $Sr < 40$ and rise again towards higher frequencies. For all mean flow Reynolds numbers, the phase lags coincide at a frequency close to $Sr \approx 7$ with a value of about $-\pi/3$. The flow fields at this coincidence were inspected in Section 7.3.2, but no immediate cause could be found.

Frequency Response at Re > 40

The frequency response of the identified deterministic models for $Re_0 = 120$, $Re_0 = 240$, and $Re_0 = 3900$ is shown in Figure 6.28. The estimated 99 % confidence intervals are represented by dashed lines.

The cross sign on the y-axis marks the theoretical low frequency limit evaluated using the correlation by Sparrow et al. (2004). The steady-state gain is higher than in the case of $Re_0 = 40$ as predicted by the correlation, but no peak occurs at low frequencies. Also, no phase lead is visible and the high frequency limit is higher than in the laminar cases. No clear trend concerning the steepness of the initial decay can be made out, but the decay at $Re_0 = 3900$ is clearly stronger that at $Re_0 = 40$. All steady-state values deduced from the correlation are within the 99 % confidence

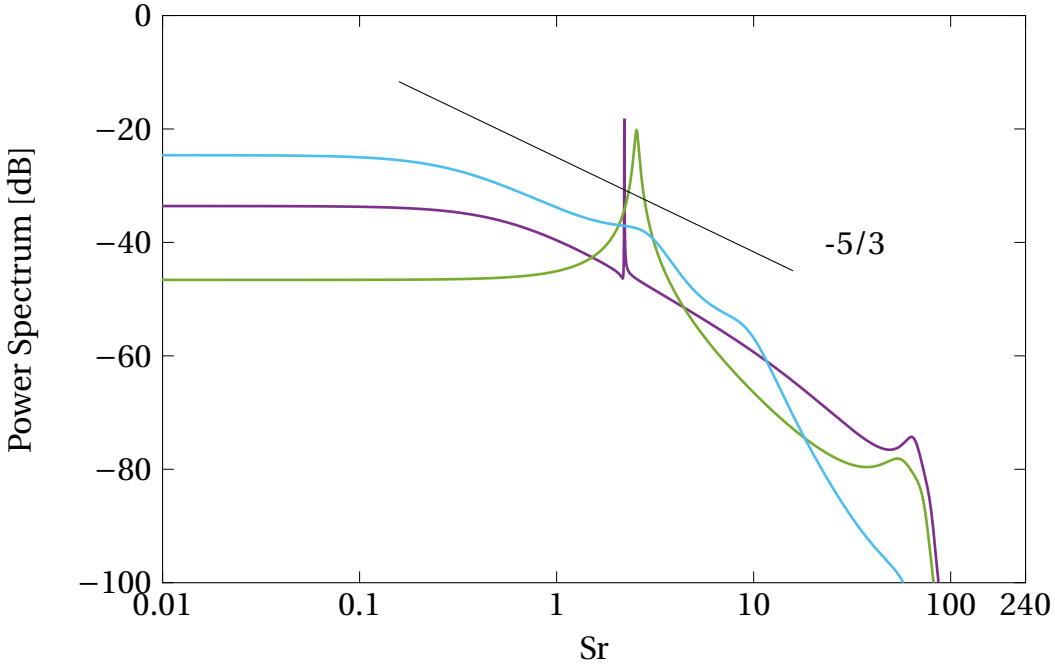

Figure 6.29: Noise Spectrum of Heat Transfer Pulsations (Re > 40). $\mathrm{Re}_0 = 120$ (—), $\mathrm{Re}_0 = 240$ (—), and $\mathrm{Re}_0 = 3900$ (—). The $-5/3$ slope is depicted to facilitate comparison with the turbulent inertial range.

intervals of the respective frequency response except for $\mathrm{Re}_0 = 120$. This is in accordance with the behavior of the phase.

At low frequencies, two impeding effects accumulate. The estimate is less accurate because the finite length of the time series and the vortex shedding, which occurs around $\mathrm{Sr} \approx 2.4$ represents strong tonal noise. For this reason, the results have to be interpreted with care.

The BJ model includes a parametrization for the noise. The spectrum of the identified noise model $|H(\mathrm{Sr})|^2$ is given in Figure 6.29 for $\mathrm{Re}_0 = 120$, $\mathrm{Re}_0 = 240$, and $\mathrm{Re}_0 = 3900$. At the lowest mean flow Reynolds number shown in this figure, the vortex shedding frequency is visible as a strong and sharp peak. At $\mathrm{Re}_0 = 240$, this peak is broader and it is only visible as a hump at $\mathrm{Re}_0 = 3900$. Moreover, the peak frequency is shifted to higher Strouhal numbers with higher mean flow Reynolds number, which is in accordance with observations reported in literature.

For comparison with the spectrum of turbulence (cf. Section 2.1.3 and Figure 2.8), a line with slope $-5/3$ representing the turbulent cascade process (inertial range) is included. Besides the vortex shedding effect, a second and very weak deviation occurs at $\mathrm{Sr} \approx 8$ and $\mathrm{Re}_0 = 3900$. This is approximately the frequency of Kelvin–Helmholtz instabilities in the free shear layer of the vortices. The exact frequency was determined by Lehmkuhl et al. (2011) to $\mathrm{Sr}_{\mathrm{KH}} = 8.42$ at $\mathrm{Re}_0 = 3900$.

Re_0	Φ in %	
	Estimation	Cross-validation
0.1	98.85	99.62
0.2	98.70	99.65
0.4	98.66	99.60
0.5	99.57	99.55
0.7	98.52	99.37
1.0	98.67	99.16
2.0	98.69	99.30
3.0	98.64	99.43
4.0	99.50	99.49
10.0	98.73	99.59
20.0	98.52	98.85
40.0	98.52	99.56
120	91.48	
240	75.62	
3900	48.33	

Table 6.5: NRMSE-Fit of the Identified Transfer Functions of Skin Friction. CFD/SI method with OE model ($Re_0 \leq 40$) or BJ model ($Re_0 > 40$).

For the validation of the results, the correlation tests were performed as shown for $Re_0 = 40$ in Section 6.3.4. It was not possible to perform a meaningful cross-validation test due to the strong unpredictable noise content. However, it is possible to refer to a priori known data like the low frequency limit evaluated from the steady-state correlation by Sparrow et al. (2004).

6.4.2 Skin Friction

The skin friction is processed and reported in a way similar to the heat transfer. The results have in parts been published previously (Witte and Polifke, 2015, 2016).

Transfer Functions

The transfer functions are transformed OE models identified from CFD data. The goodness of fit that was achieved during estimation and the goodness of fit from the cross-validation test is reported in Table 6.5.

At mean flow Reynolds numbers $Re_0 \leq 40$, fit values achieved during estimation and in comparison to the validation data set are always $\Phi > 98\,\%$. The identification of

the BJ for $\mathrm{Re}_0 > 40$ was performed with more weight on the lower frequencies. This achieves a better fit at lower frequencies, which are underrepresented due to the high-pass behavior of the skin friction, and the low-frequency limit is closer to its theoretical prediction. However, this is at the cost of higher frequencies. Because of the high amplitudes, small deviations at high frequencies lead to large prediction errors. Hence, fit values are considerably worse for the BJ models, although low-frequency limits are more realistic.

All identified transfer functions using OE model structure had five coefficients in the numerator and four coefficients in the denominator to represent the data accurately. At a mean flow Reynolds number $\mathrm{Re}_0 > 40$, BJ models were identified to cope with the tonal and turbulent noise. Table 6.6 gives the coefficients identified as an OE model and transformed to continuous time using bilinear transform. This table can be read like Table 6.4.

Frequency Response at $\mathrm{Re}_0 \leq 40$

The frequency response of the skin friction is depicted in a manner similar to the heat transfer. Figure 6.30 shows the amplitude of the complex-valued frequency response. The region of low frequencies $\mathrm{Sr} \leq 2$ is magnified in the insert on the bottom right. The low frequency values are close to the predicted steady-state gain of 3/2 (Lighthill, 1954). If the mean flow Reynolds number is higher, also the quasi steady-state value is higher. Towards larger values of Strouhal number, a rise in amplitude can be seen in a manner of a square root dependence as predicted by Stokes (1851) (cf. Section 3.1.2). A strong dependence on amplitude is visible throughout the whole range of Strouhal numbers. At the highest Strouhal number under consideration $\mathrm{Sr} = 40$, the amplitude at $\mathrm{Re}_0 = 40$ ($|G_{c_f}| = 11.8$) is approximately twice as high as at $\mathrm{Re}_0 = 0.1$ ($|G_{c_f}| = 5.88$).

Figure 6.31 depicts the phase between free-stream velocity pulsations and skin friction pulsations. Mean flow Reynolds number from $\mathrm{Re}_0 = 0.1$ (blue) to $\mathrm{Re}_0 = 40$ (red) are shown. The phase difference in the limit $\mathrm{Sr} \to 0$ is zero, like in the case of the transfer function of the heat transfer. Phase values rise towards a phase lead of $\angle G_{c_f} = \pi/4$ in the limit of high Strouhal numbers. No clear dependence on mean flow Reynolds number is visible for the initial rise starting from $\mathrm{Sr} = 0$. At about $\mathrm{Sr} \approx 0.5$, the lowest Reynolds numbers depart from the initial inclination and saturate. This saturation occurs later for higher mean flow Reynolds numbers. At $\mathrm{Sr} = 40$, the highest Strouhal number considered in this thesis, the phase of the frequency response shows a sequential order. The response of the $\mathrm{Re}_0 = 0.1$ case is substantially below $\angle G_{c_f} = \pi/4$, where the response at $\mathrm{Re}_0 = 40$ has almost reached the theoretical limit.

Re		s^0	s^1	s^2	s^3	s^4
0.1	b	1.27	2.253	0.4837	0.01882	0.0001044
	a		1.024	0.121	0.002304	4.499×10^{-6}
0.2	b	1.329	2.333	0.5046	0.01991	0.0001161
	a		0.9694	0.1128	0.002164	4.276×10^{-6}
0.4	b	1.388	2.302	0.4959	0.01966	0.0001183
	a		0.8886	0.1002	0.001891	3.45×10^{-6}
0.5	b	1.416	2.21	0.4555	0.0173	9.892×10^{-5}
	a		0.823	0.08767	0.001565	2.519×10^{-6}
0.7	b	1.397	2.292	0.5041	0.02052	0.0001296
	a		0.8502	0.09546	0.00182	3.297×10^{-6}
1.0	b	1.375	2.292	0.5066	0.02043	0.0001258
	a		0.8323	0.09132	0.00169	2.817×10^{-6}
2.0	b	1.426	2.173	0.4668	0.01863	0.0001143
	a		0.7432	0.07702	0.001385	2.246×10^{-6}
3.0	b	1.474	2.086	0.4361	0.01717	0.0001046
	a		0.6885	0.06866	0.001209	1.938×10^{-6}
4.0	b	1.521	1.997	0.3903	0.01452	8.313×10^{-5}
	a		0.6289	0.05842	9.684×10^{-4}	1.403×10^{-6}
10.0	b	1.581	2.048	0.4231	0.01696	0.0001015
	a		0.6283	0.06124	0.001067	1.334×10^{-6}
20.0	b	1.571	2.387	0.604	0.03016	0.0002389
	a		0.7755	0.09358	0.002061	4.379×10^{-6}
40.0	b	1.659	2.249	0.4783	0.02007	0.0001289
	a		0.6448	0.06432	0.001177	1.739×10^{-6}
120.0	b	1.659	1.029	0.03855		
	a		0.1575	0.001384		
240.0	b	1.528	1.044	0.04215		
	a		0.1759	0.001641		
3900.0	b	1.197	1.13	0.05315		
	a		0.1986	0.002823		

Table 6.6: Estimated Coefficients of the Transfer Function of Skin Friction. All values are transformed to continuous time using bilinear transform.

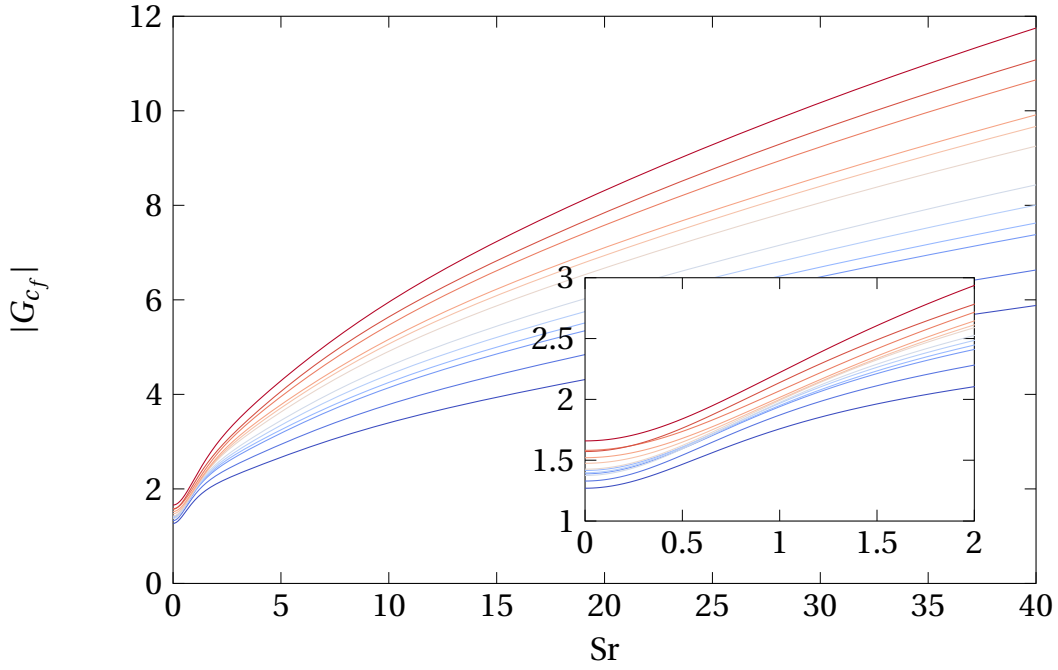

Figure 6.30: Amplitude of Skin Friction Frequency Response. Blue to red. Reynolds numbers: 0.1, 0.2, 0.4, 0.5, 0.7, 1, 2, 3, 4, 10, 20, and 40. The insert in the top right corner magnifies small frequencies Sr ≤ 2.

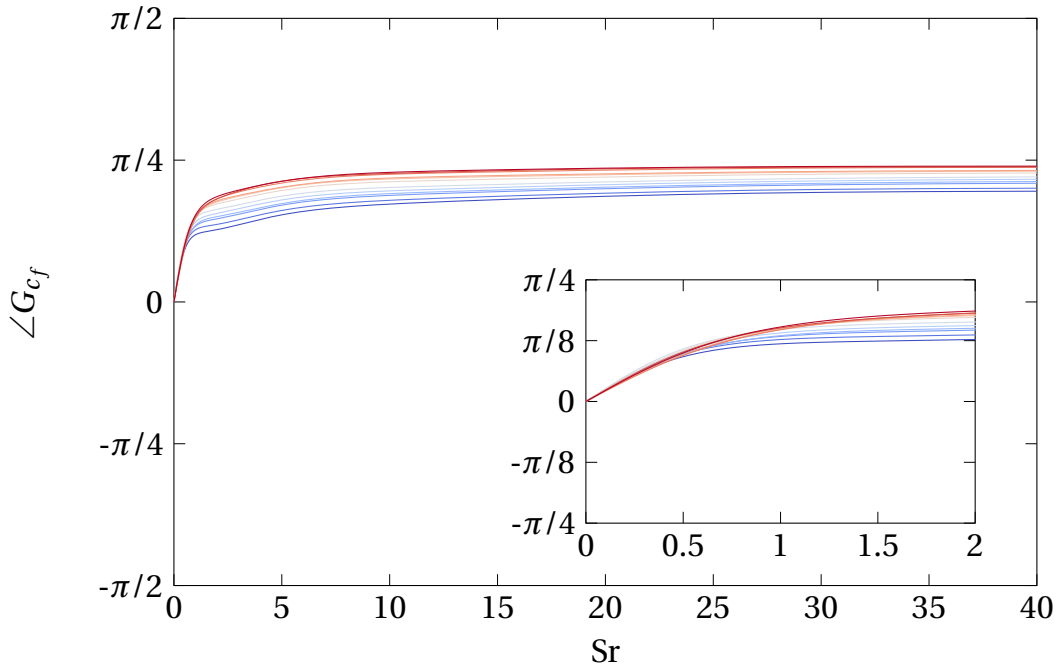

Figure 6.31: Phase of Skin Friction Frequency Response. Reynolds numbers: 0.1, 0.2, 0.4, 0.5, 0.7, 1, 2, 3, 4, 10, 20, and 40 (blue to red). The insert in the top right corner magnifies small frequencies Sr ≤ 2.

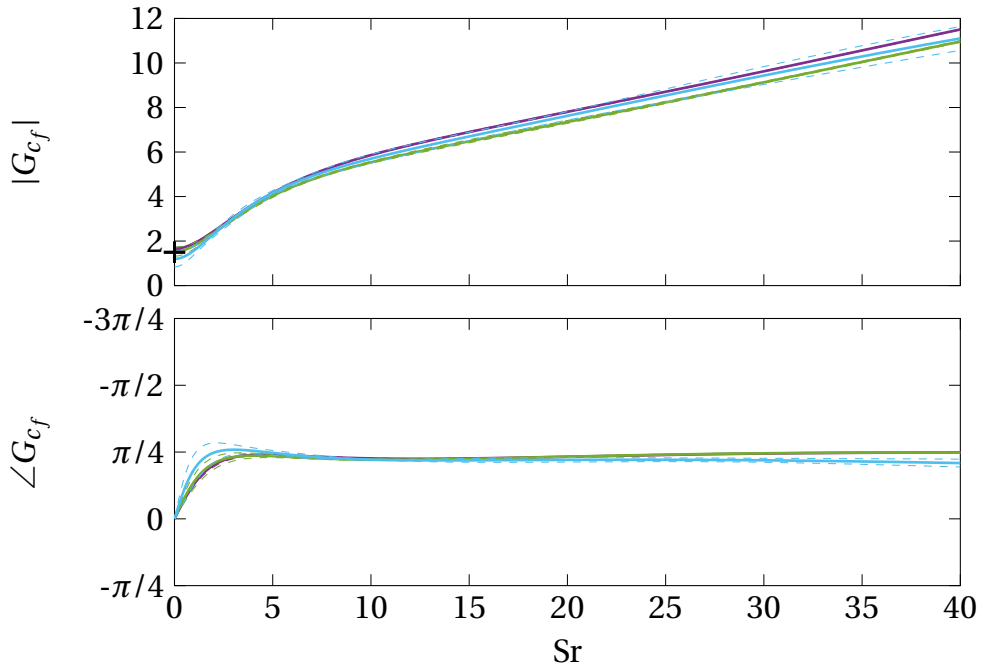

Figure 6.32: Frequency Response of the Skin Friction ($Re_0 > 40$). $Re_0 = 120$ (——), $Re_0 = 240$ (——), and $Re_0 = 3900$ (——). Dashed lines mark the 99 % confidence intervals. The cross shows the low frequency limit (Lighthill, 1954).

Frequency Response at Re > 40

The frequency responses of skin friction to pulsations in the free-stream velocity for $Re_0 = 120$, $Re_0 = 240$, and $Re_0 = 3900$ are depicted in Figure 6.32. The responses of these identified deterministic models are very similar to the $Re_0 = 40$ case (cf. Figure 6.30 and Figure 6.31). The estimated 99 % confidence intervals are shown as dashed lines. They are much larger than in the case of the laminar models, especially at $Re_0 = 3900$. This is due to turbulent disturbances and the fact that higher number of coefficients was estimated because of the noise model.

The low frequency limit of 3/2 for the amplitude (Lighthill, 1954) is underpredicted in the case of $Re_0 = 3900$ and overpredicted for $Re_0 = 120$ and $Re_0 = 240$. These deviations could be due to the low-order of the deterministic model. The amplitude rises almost linearly with frequency and all three modes do not show substantial differences. At the highest Strouhal number under consideration Sr = 40, the amplitude is approximately $|G_{c_f}| \approx 11$ for all models.

The phase of the frequency responses shows a steep rise towards the limit of $\angle G_{c_f} \approx \pi/4$ at high frequencies. The rise is steeper at higher mean flow Reynolds numbers. At $Re_0 = 3900$, a slight overshoot is visible. However, the bounds of the 99 % confi-

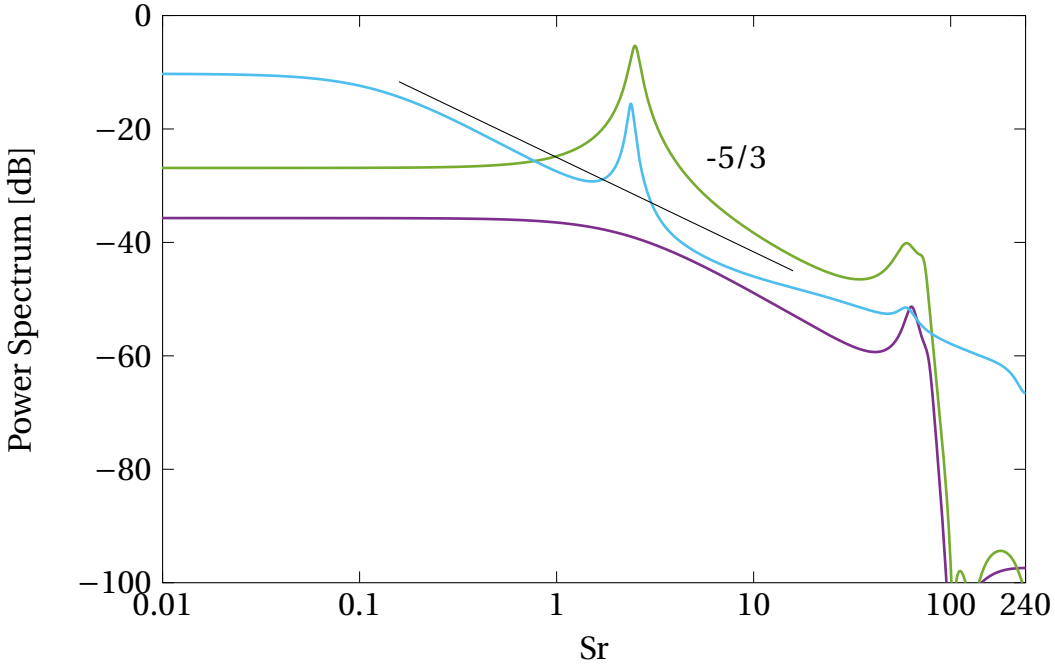

Figure 6.33: Noise Spectrum of Skin Friction Pulsations ($Re_0 > 40$). $Re_0 = 120$ (—), $Re_0 = 240$ (—), and $Re_0 = 3900$ (—). The $-5/3$ slope is depicted to facilitate comparison with the turbulent inertial range.

dence intervals are still within the limit and the overshoot may be attributed to the low-order of the deterministic model.

In the model noise spectrum, shown in Figure 6.33, a similar behavior as for the heat transfer model is visible. General noise levels are higher due to the weighting in favor of low frequencies. The spectrum was modeled with seven coefficients for the numerator polynomial and denominator polynomial for $Re_0 = 120$, $Re_0 = 240$, and $Re_0 = 3900$. Again, the $-5/3$ slope is shown to establish the connection to the turbulent energy spectrum. Indeed, the power spectrum of the noise closely resembles the turbulent spectrum for $Re_0 = 3900$.

The peak associated with vortex shedding is much more pronounced at $Re_0 = 3900$ than for the heat transfer. For $Re_0 = 120$, this effect is reversed and no peak is visible at the vortex shedding Strouhal number, where a clear maximum was visible in Figure 6.29. No distinct deviation is visible at the frequency of the Kelvin–Helmholtz instability. A small peak at $Sr \approx 60$ occurs due to perturbations in the excitation signal which has its cutoff frequency at this value.

6.5 Discussion

6.5.1 Identification Method

Three different methods were used to develop transfer functions of heat transfer and skin friction of a cylinder in pulsating crossflow. The first used the time series from the response to a step excitation. The step excitation is an important step for preliminary assessment before more complex methods are used. Nevertheless, it is possible to develop a transfer function under certain conditions. Following this path proved to be successful for $\mathrm{Re}_0 \leq 40$.

The second method reported in this chapter was processed the frequency response data from the LNSE simulations. The identification of a continuous time transfer function from the acquired data yields results with a very good fit to the raw data. The identification requires only a small amount of data preparation. Together with the efficiency of the (incompressible) LNSE approach, this is the quickest way to develop transfer functions for $\mathrm{Re}_0 \leq 40$. However, this approach, like the step response method, fails to deliver acceptable results when vortex shedding occurs due to the fact that a true steady-state solution is required. Using a time or cycle average instead of a steady-state solution might be possible together with further adjustments, but no acceptable results could be achieved in due time.

The CFD/SI method, was the third method. It used time domain data generated with broadband excitation and subsequently, a transfer function was developed. Two different identification approaches were considered.

Continuous time identification uses the time domain data transformed into frequency space to directly develop a continuous time transfer function. The identification method is basically the same as in the LNSE approach, but the frequency domain data, acquired using FFT, is not as good-natured as the frequency response data from the LNSE. The results showed the best agreement with the simulated data in cross-validation tests for mean flow Reynolds numbers $\mathrm{Re}_0 \leq 40$. The VF identification method can be used on data with $\mathrm{Re}_0 > 40$, i.e. data contaminated by tonal or turbulent noise. However, noise in discrete time domain data cannot be handled by the VF approach, and hence it competes with the OE model identification but yields inferior results compared to a BJ model in the presence of intense or strongly colored disturbances.

Discrete time identification in the framework of the CFD/SI approach proved to be the most versatile method. The identification of OE models from time domain data yielded excellent results. The time series acquired from a CFD simulation with broadband excitation can be used directly with very little pre-processing (resampling and linearization). Theoretically, the OE model identification can find the transfer function of the deterministic part even in the presence of higher noise

levels. Transformation to a continuous time transfer function is facilitated through bilinear transform. The BJ model is an OE model with parametrization of the noise and, hence, basically an extension when noise handling, e.g. in the cases with $\mathrm{Re}_0 > 40$, is necessary.

Step excitation and simulation in the frequency domain are unsuited to develop transfer functions in the presence of tonal or broadband noise. The excitation of the system with only one single step, which is superimposed by disturbances, is not enough to separate the deterministic response from the stochastic noise. Hence, the true step response cannot be inferred like in the case of laminar flow (cf. Section 6.1). This was also shown by Cabrera (2015) for the case of $\mathrm{Re}_0 = 3900$. Moreover, a single step excitation is also only of limited avail in determining step response characteristics like steady-state gain, rise time, and overshoot (cf. Section 6.1.3). Similar reasoning holds for tonal noise. No technique exists to distinguish between an overshoot or oscillations of the step response and the sinusoidal disturbance of the tonal noise. A clear distinction between deterministic system and noise would only be possible if several steps are used and the noise contribution cancels to zero across all steps due to its nature. This already leads to the principle of persistent excitation which is the idea behind broadband excitation in conjunction with SI.

In the scope of tonal noise or turbulent noise, the LNSE approach is an interesting method. Both tonal noise originating from vortex shedding and broadband noise from turbulence are transient phenomena. To be represented in the model, these effects have to be included in the solution the linearization is based upon, i.e. the "steady-state" solution. Hence, instead of a true steady-state solution, which can only be found for $\mathrm{Re}_0 \lesssim 40$, an averaged solution may be computed. In the presence of tonal noise, a cycle-average may be used at this point. This would allow simulating a frequency response giving credit to the noise through the averaged solution. A transfer function can be identified from this response at discrete frequencies without a noise model. However, in the case of the flow around a cylinder, it was not possible to compute an averaged solution that allowed for a stable solution of the linearized equations. Some stabilization technique might represent a remedy for this numerical instability, but it was not within the scope of this thesis. Moreover, in order to treat turbulent flow with this method, the LNSE solver would have to be extended to three spatial dimensions and probably a model for the turbulence.

To conclude the capabilities of each identification method in the presence of tonal or broadband noise, only OE, BJ, and the VF method remain. BJ is suited best because of the possibility to combine a low order model for the deterministic transfer function with a noise model of rather high order that is able to reproduce the characteristics of the tonal noise or broadband noise.

6.5.2 Heat Transfer

For the heat transfer, several empirical and analytical results have been reported in the literature. The analytical results by Lighthill (1954) and Bayly (1985) can be compared to the transfer functions identified in this thesis. Moreover, the steady-state heat transfer correlations, e.g. by Collis and Williams (1959) as well as Sparrow et al. (2004), can be used to deduce the response amplitude in the limit of zero frequency, i.e. the steady-state gain K.

Frequency Response

Lighthill (1954) presented a model for heat transfer fluctuations at comparatively high mean flow Reynolds numbers (Re > 10). At such Reynolds numbers, most of the heat transfer takes place close to the forward stagnation point, so only the HL is considered. The model is detailed in Section 3.2.2 and the frequency response is shown in Figure 3.4. Bayly (1985) gives an expression for the unsteady heat transfer at low Péclet numbers for the whole cylinder. The derivation of the model is sketched in Section 3.3.2 and the frequency response is depicted in Figure 3.9. A comparison between the models identified in this thesis and analytical results was given by Witte and Polifke (2019).

Lighthill's and Bayly's models are represented in Figure 6.34 and Figure 6.35 as dashed lines and dash dotted lines, respectively. Figure 6.34 depicts the amplitude and the phase is shown in Figure 6.35. Solid lines denote models for $\mathrm{Re}_0 = 0.4$, $\mathrm{Re}_0 = 4$, and $\mathrm{Re}_0 = 40$ identified in this thesis. The figures depict amplitude and phase of the frequency response of heat transfer fluctuations to velocity perturbations.

As already reported by the respective authors, the analytical models have limited applicability in the range $0.1 \leq \mathrm{Re}_0 \leq 40$. Bayly's model matches well with the identified frequency response at low Reynolds numbers. The relation given by Bayly (1985) yields fair results up to Re = 0.1 (as shown in the figure as dashed lines) but should not be used for mean flow Reynolds numbers above Re = 0.5.

Lighthill (1954) stated that his model is applicable if a laminar boundary layer exists and gave Re > 10 as a limit. This is due to the fact that the boundary layer equations used by Lighthill (1954) make use of the limiting process $\mathrm{Re} \to \infty$. Indeed, the identified frequency response at $\mathrm{Re}_0 = 40$ shows very similar low and high-frequency limits in the amplitude. Lighthill's time constant $c_\tau = 0.2$, however, is considerably smaller than the dominant time scale in the $\mathrm{Re}_0 = 40$ case from SI ($c_\tau \approx 0.3$).

This is due to the fact that only certain types of flow geometries can be handled analytically with the boundary layer equations. For flow across a cylinder with its

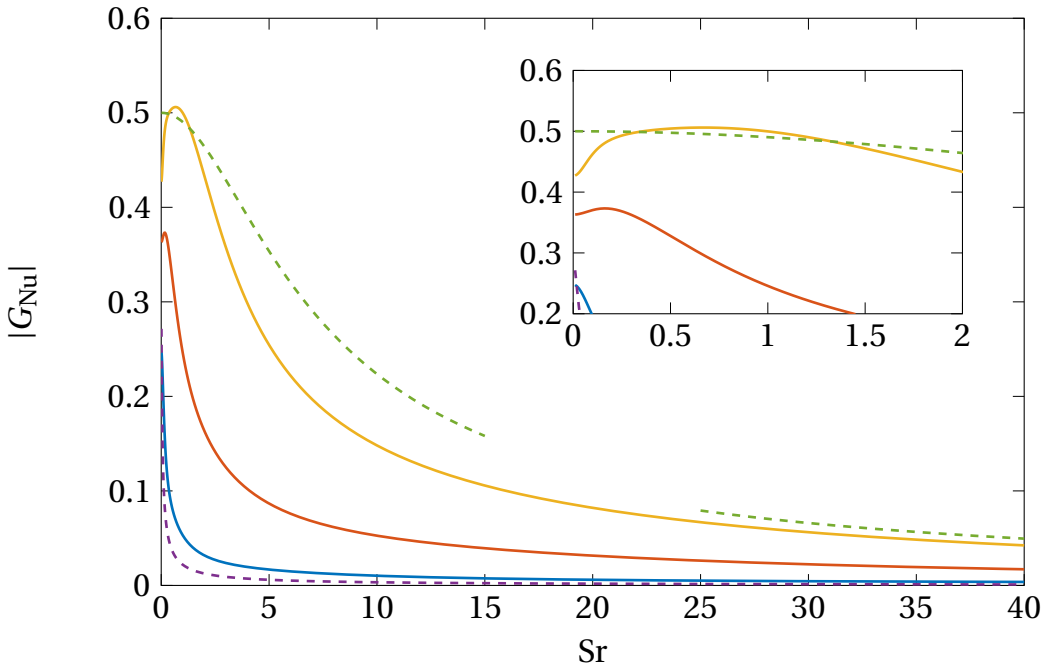

Figure 6.34: Comparison of Heat Transfer Frequency Response (Amplitude). The amplitude from CFD/SI is shown as solid lines for $\mathrm{Re}_0 = 0.4$ (——), $\mathrm{Re}_0 = 4$ (——), and $\mathrm{Re}_0 = 40$ (——). The dashed lines denote the results reported by Lighthill (1954) (- - -) and Bayly (1985) (- - -).

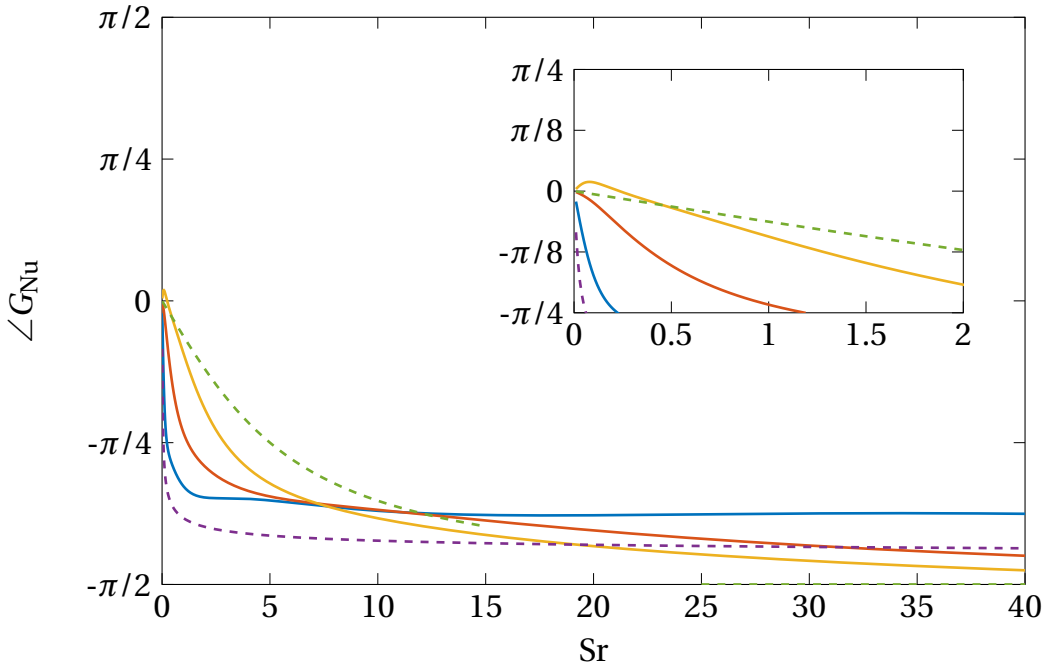

Figure 6.35: Comparison of Heat Transfer Frequency Response (Phase). The phase from CFD/SI is shown as solid lines for $\mathrm{Re}_0 = 0.4$ (——), $\mathrm{Re}_0 = 4$ (——), and $\mathrm{Re}_0 = 40$ (——). The dashed lines denote the results reported by Lighthill (1954) (- - -) and Bayly (1985) (- - -).

curvature and flow separation, further approximations were necessary. The assumption that most of the heat transfer occurs close to the forward stagnation point, as stated by Lighthill (1954), is also a very coarse approximation slightly better at higher mean flow Reynolds numbers.

On the one hand, the good match to frequency responses reported in the literature confirms the quality of the results from SI. On the other hand, a substantial improvement in accuracy was achieved. A wide range of Reynolds numbers and Strouhal numbers was covered, and the , as well as the behavior in the limit of very low and very high frequencies, was determined in superior detail. The most substantial improvement is the dependence on mean flow Reynolds number, which was determined with the CFD data based methods for a great range and and very accurately.

Low Frequency Limit

The low frequency limit K_{Nu} serves two purposes in this work. Firstly, this quasi-steady-state gain may be used as a good approximation for processes with very slow dynamics, i.e. small Strouhal numbers. The use of K_{Nu} instead of the complex transfer function might be sufficient in this case. Secondly, it is used here as validation for the identified models. The derivation of the low-frequency limit from heat transfer correlations was detailed by Witte and Polifke (2017a).

The low frequency limit or quasi-steady gain can be read from the frequency response amplitude at $\mathrm{Sr} \to 0$ (e.g. Figure 6.26) or from the step response at $t \to \infty$ (cf. Figure 6.1). However, there is a third method deriving the quantity from a steady-state Nußelt correlation like the ones given by Collis and Williams (1959) (cf. Equation (2.23)) and Sparrow et al. (2004) (cf. Equation (2.24)). A similar approach was pursued by Polifke and Lawn (2007) for premixed flames.

The steady-state correlations for the Nußelt number Nu are nonlinear functions of the Reynolds number Re. In some cases, also the Prandtl number Pr is included as a parameter and the fluid and cylinder temperatures. In this thesis, however, the Prandtl number is $\mathrm{Pr} = 0.7123$ in most cases, and absolute temperature differences are neglected. To acquire the quasi-steady-state response to pulsations in the crossflow, a rise in Reynolds number by $\Delta\mathrm{Re}$ is assumed. The correlation $\mathrm{Nu}(\mathrm{Re})$ is linearized around Re_0 and hence the new Nußelt number is given by the Taylor series

$$\mathrm{Nu}(\mathrm{Re}_0 + \Delta\mathrm{Re}) = \mathrm{Nu}(\mathrm{Re}_0) + \left.\frac{\partial \mathrm{Nu}(\mathrm{Re})}{\partial \mathrm{Re}}\right|_{\mathrm{Re}_0} \Delta\mathrm{Re} + \mathcal{O}((\Delta\mathrm{Re})^2) \tag{6.11}$$

Model	Re_0					
	0.4	4	40	120	240	3900
K_{Nu} from Collis and Williams (1959)	0.27	0.37	0.41	0.45		
K_{Nu} from Sparrow et al. (2004)	0.26	0.41	0.50	0.52	0.53	0.56
K_{Nu} from identification	0.26	0.37	0.44	0.45	0.54	0.54
K_{Nu} from step response	0.25	0.37	0.42			

Table 6.7: Values for the Steady-State Gain K_{Nu}. Calculated from linearized correlation as well as from identification and direct simulation performed in this work for different mean flow Reynolds numbers.

truncated after the first order derivative. Inserting Equation (6.11) into the definition of the transfer function G_{Nu} (cf. Equation (2.100)) yields the low frequency limit of the transfer function

$$K_{\mathrm{Nu}} = \frac{\mathrm{Re}_0}{\mathrm{Nu}_0} \left.\frac{\partial \mathrm{Nu}(\mathrm{Re})}{\partial \mathrm{Re}}\right|_{\mathrm{Re}_0} \tag{6.12}$$

which is called quasi-steady gain K_{Nu}. Using the correlation by Collis and Williams (1959) (cf. Equation (2.23)), the steady-state gain can be evaluated with

$$K_{\mathrm{Nu}} = \frac{0.252\,\mathrm{Re}^{0.45}}{0.24 + 0.56\,\mathrm{Re}^{0.45}}\,. \tag{6.13}$$

For higher Reynolds numbers, the correlation by Sparrow et al. (2004) (cf. Equation (2.24)) is recommended. The steady-state gain is then

$$K_{\mathrm{Nu}} = \frac{\mathrm{Re}^{1/2} + 0.2\,\mathrm{Re}^{2/3}}{1.25\,\mathrm{Pr}^{-0.37} + 2.0\,\mathrm{Re}^{1/2} + 0.3\,\mathrm{Re}^{2/3}}\,. \tag{6.14}$$

Considering the same Reynolds numbers as for the simulated step response (cf. Section 6.1), the results of the linearization are compared to identification and step response in Table 6.7. It can be seen that the results agree reasonably well, especially for $\mathrm{Re}_0 = 4$, with the largest discrepancy between correlation and identification for $\mathrm{Re}_0 = 40$ of about 7 %.

6.5.3 Skin Friction

A comparison between the models identified in this thesis and analytical results was given by (Witte and Polifke, 2019).

The analytical models providing the best description of the dynamic behavior of the skin friction over a wide range of frequencies were reported by Lighthill (1954) and Gersten (1965). However, no single model for the whole range of Strouhal numbers

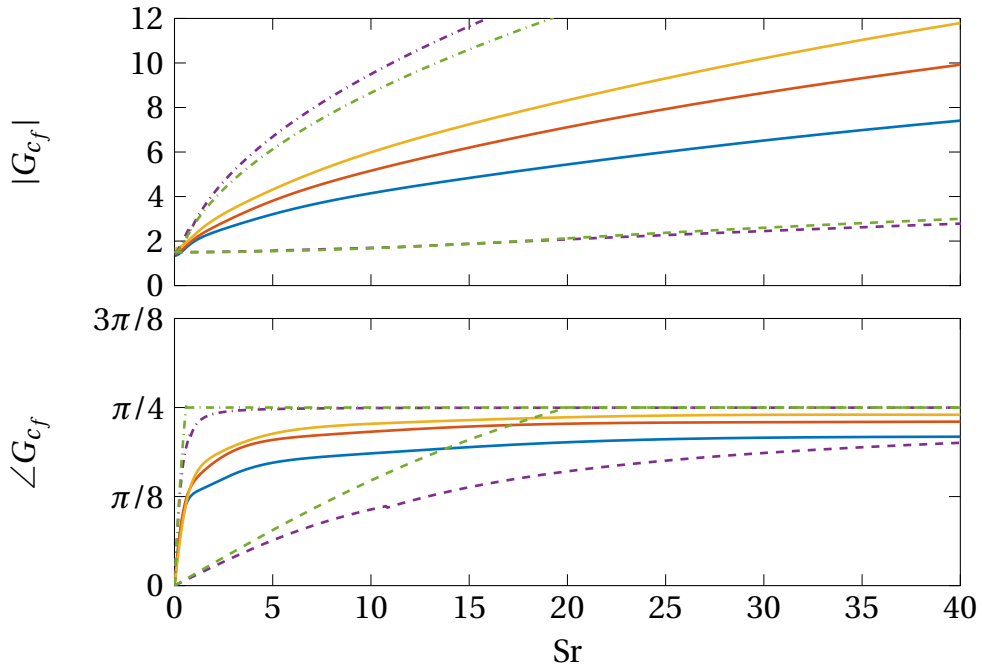

Figure 6.36: Skin Friction Frequency Response. Amplitude (top plot) and phase (bottom plot) from CFD/SI are shown as solid lines for $\mathrm{Re}_0 = 0.4$ (——), $\mathrm{Re}_0 = 4$ (——), and $\mathrm{Re}_0 = 40$ (——). Dashed lines denote the results for the HL reported by Lighthill (1954) (- - -) and Gersten (1965) (- - -) and dash-dotted lines represent the results for the BL reported by Lighthill (1954) (- - -) and Gersten (1965) (- - -).

considered exists, instead only approximations for high and low Strouhal numbers are given. Furthermore, two different types of boundary layers HL and BL were considered respectively by both authors (cf. Section 3.2). Flat plate flow was evaluated with the frequency parameter $\mathrm{Sr}\, x/d$.

Figure 6.36 shows amplitude and phase of the complex-valued frequency response of the skin friction to pulsation in the free-stream velocity. Solid lines denote identified models for $\mathrm{Re}_0 = 0.4$, $\mathrm{Re}_0 = 4$, and $\mathrm{Re}_0 = 40$. The model by Lighthill (1954) was detailed in Section 3.2.2. The frequency responses for HL and BL are shown in Figure 3.2 and Figure 3.3, respectively. They are represented in Figure 6.36 in green. The frequency response developed by Gersten (1965) is shown in Figure 3.5 and Figure 3.6 for the HL and the BL, respectively. Section 3.2.4 outlines the derivation. Lines associated with the results developed by Gersten (1965) are colored purple. The graphs of the HL solution is dashed, and the BL solution is shown dash dotted for $x/d = 1$.

At low frequencies, i.e. small values of Strouhal numbers Sr, the results from Lighthill (1954) and Gersten (1965) match well. The steady-state gain derives from the fact that the drag force depends on velocity by $F_d \sim u^{(3/2)}$ in the boundary layer approximation. In the results from SI, the low frequency limits are changing

with Reynolds number with values only slightly above unity for small mean flow Reynolds numbers (regime of linear drag) and approaching a value of two at higher Re_0 ($F_d \sim u^2$) (Polifke and Lawn, 2007).

Lighthill (1954) and Bayly (1985) reported an anticipation time for the skin friction of $c_\tau = 0.05$ for the HL and $c_\tau = 1.7x/d$ for the BL. The pressure gradient necessary to accelerate the flow acts faster on the boundary layer than on the free-stream. This creates the impression of the skin friction anticipating a change in velocity, which manifests itself as a phase lead. Lighthill (1954) stated that the approximation is applicable for $\mathrm{Sr} > 20$. Hence, at this Strouhal number, the low frequency solution merges with the high frequency approximation. Gersten's series expansion yields a smoother transition between low and high frequency approximation. CFD/SI results show an approximate anticipation time of $c_\tau = 0.7$, which is not depending on Reynolds number.

At low Strouhal numbers, neither the HL solution nor the BL solution is comparable to the identified frequency response. This is due to the fact that neither limiting case of the wedge flow is particularly fitting for the skin friction at the cylinder. This is supported by the examination of the circumferential distribution of the skin friction pulsations (cf. Section 7.4). At low frequencies, the gross of the skin friction fluctuations occur at an angle of $\phi \approx \pi/4$ which is exactly in between the HL ($\phi \approx 0$) and the BL ($\phi \approx \pi/2$).

7 Flow Field Representations

To shed light on the dynamic processes in the flow field around the cylinder, various representations of flow patterns and temperature distributions are presented in this chapter. To provide a reference, the steady-state flow fields for mean flow Reynolds numbers $\mathrm{Re}_0 = 0.4$, $\mathrm{Re}_0 = 4$, and $\mathrm{Re}_0 = 40$ are depicted in Section 7.1. Section 7.2 shows changes in the velocity field and the temperature field caused by a sudden increase in the free-stream velocity by 10 %. This corresponds to the conditions of a simulated step response and the flow fields originate from the same simulations as in Section 6.1. The fields are calculated with the time domain approach (cf. Section 5.2). From the solution of the linearized Navier–Stokes equations, fluctuations in temperature and vorticity at specific frequencies can be depicted. Section 7.3 includes fields of amplitude and phase of these fluctuations for a range of frequencies. Qualitative explanations for certain occurring phenomena, like the peak gain and the phase lag at high frequencies, that differ from previously reported studies are provided. Circumferential distributions of the fluctuations of the Nußelt number and the friction coefficient are reported in Section 7.4.

7.1 Steady State

For all simulations, the steady-state solution serves as a reference point. The step response computation needs a preliminary steady state which is excited with a sudden increase in velocity. The LNSE results are linearized around a steady state and also the CFD/SI procedure requires a steady-state (or quasi-steady-state) flow field as an initial solution. This way, the influence of an initial transient, which should not be part of the solution, is minimized.

Figures 7.1 to 7.3 show the steady-state temperature distribution on the left and the velocity magnitude on the right. The plots are captured from the same simulations carried out to acquire the data for the step response detailed in Section 6.1. The excerpt extends from $-2\,d$ to $4\,d$ in x_1-direction and from 0 to $3\,d$ in x_2-direction. Black lines represent the pseudo-streamlines of the flow (from left to right). The colors indicate regions where values of dimensionless temperature $\Theta_0 = \Theta(x, y, 0)$ and values of dimensionless velocity magnitude $|\boldsymbol{u}_0| = |\boldsymbol{u}|\,(x, y, 0)$, respectively, are higher (red) or lower (blue). Figure 7.1 depicts the steady-state flow field for a mean

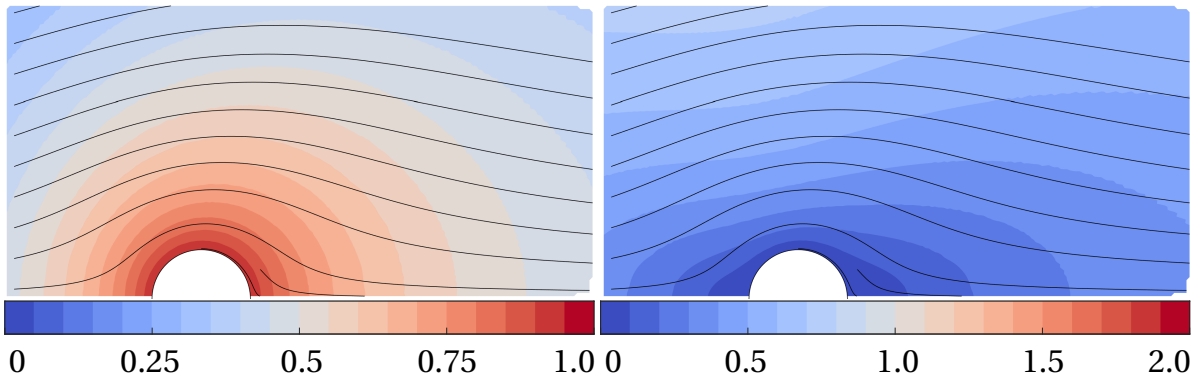

Figure 7.1: Representation of the Steady-State Flow Field for $Re_0 = 0.4$. Temperature Θ_0 (left) and velocity magnitude $|\boldsymbol{u}_0|$ (right) are represented by the coloring. Black lines depict the streamlines.

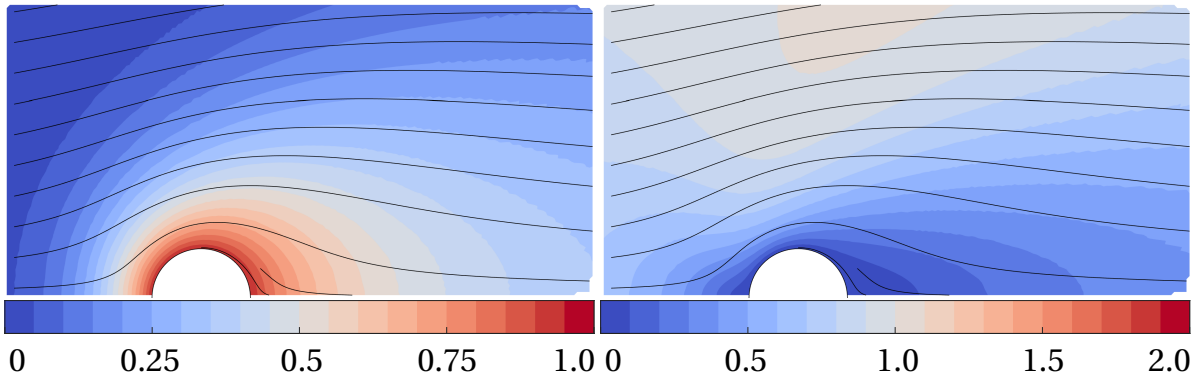

Figure 7.2: Representation of the Steady-State Flow Field for $Re_0 = 4$. Temperature Θ_0 (left) and velocity magnitude $|\boldsymbol{u}_0|$ (right) are represented by the coloring. Black lines depict the streamlines.

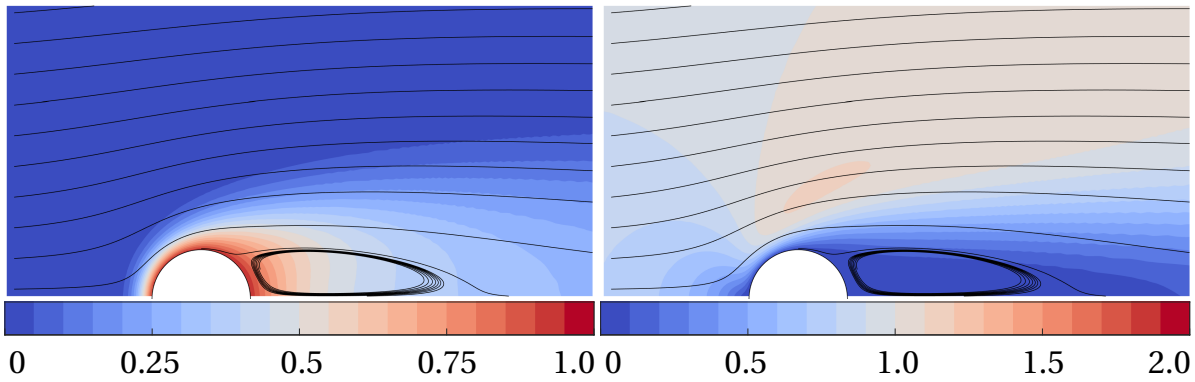

Figure 7.3: Representation of the Steady-State Flow Field for $Re_0 = 40$. Temperature Θ_0 (left) and velocity magnitude $|\boldsymbol{u}_0|$ (right) are represented by the coloring. Black lines depict the streamlines.

flow Reynolds number of $\mathrm{Re}_0 = 0.4$. The cases $\mathrm{Re}_0 = 4$ and $\mathrm{Re}_0 = 40$ are shown in Figure 7.2 and Figure 7.3, respectively.

At low Reynolds numbers and low Péclet numbers, heat conduction and viscous effects dominate over the convective transport. The flow field around the cylinder is influenced in a large area as can be seen in the case of $\mathrm{Re}_0 = 0.4$ in Figure 7.1. At higher Reynolds numbers, the area of the flow field affected by the presence of the cylinder becomes smaller (cf. Figure 7.2). This is attended by stronger gradients. At $\mathrm{Re}_0 = 40$, recirculation occurs which is visible in Figure 7.3.

7.2 Step Response

The flow around the cylinder is subject to a sudden change in flow velocity (step excitation). The Reynolds number is increased by $\epsilon = 0.1$, i.e. 10 % of the initial Reynolds number Re_0. This step response model is described in Section 6.1.

The response of the flow field is represented here as absolute differences in dimensionless temperature $\delta\Theta$ and dimensionless velocity magnitude δu at a specific time instant compared to the initial steady-state field. This can be expressed as

$$\delta\Theta(x, y, t) = \left[\Theta(x, y, t) - \Theta(x, y, 0)\right] \quad \text{and} \tag{7.1}$$

$$\delta u(x, y, t) = \left[|\boldsymbol{u}|(x, y, t) - |\boldsymbol{u}|(x, y, 0)\right] \quad . \tag{7.2}$$

The following figures (Figure 7.4 – Figure 7.9) show the flow field in proximity to the cylinder for mean flow Reynolds numbers $\mathrm{Re}_0 = 0.4$, $\mathrm{Re}_0 = 4$, and $\mathrm{Re}_0 = 40$, respectively. The plots were captured from the same simulations carried out to acquire the data for the step response detailed in Section 6.1. The excerpt extends from $-2\,d$ to $4\,d$ in x_1-direction and from 0 to $3\,d$ in x_2-direction. Black lines represent the pseudo-streamlines of the flow (from left to right). The colors indicate regions where values of temperature (left column) and values of velocity magnitude (right column) respectively are higher (red) or lower (blue) than the stationary values before the step occurs. A gray color signifies no change. In the figure series, time advances from top to bottom.

7.2.1 Common Features and Behavior

The flow fields for all of the mean flow Reynolds numbers depicted here show some common features. The hydrodynamic and the thermal boundary layer are distorted and adapt over time to the new steady-state flow. Initially, the velocity field changes drastically. The red color of the far field depicts the new velocity magnitude after the step input.

The velocity field changes instantly showing some acceleration of the flow next to the cylinder. The red spot close to the side of the cylinder relative to the flow marks noticeably higher velocities in proximity to the surface. A gray color directly at the cylinder boundary indicates no change, which reflects the fact that the no-slip condition is imposed. The flow field relaxes to the new steady state over time, to some extent reversing the sudden changes.

The drastic change instantly after the step input is due to the immediate high pressure gradient establishing to facilitate the acceleration of the flow. This favorable pressure gradient is responsible for large velocity gradients in proximity to the cylinder. Another way to interpret this is an increased generation of vorticity at the cylinder, which is subsequently transported by convection and diffusion.

A new, thinner, thermal boundary layer establishes after the step excitation, and hot fluid in proximity to the cylinder is swept away. This is indicated by the comparably cooler (blue) region that forms at the windward side of the cylinder and spreads further downstream at later instances in time. This cooler region shows that there is a higher temperature gradient at the cylinder, resulting in a rise in heat transfer rate.

In addition, a hotter zone is initially forming at the lee side of the cylinder over a time of approximately one passage time. Eventually, it is swept away downstream with the flow, and the temperature at the backward stagnation point of the cylinder is also slightly lower than before the perturbation. This is in accordance with the step response behavior of sector 4 as shown in Figure 6.2. The appearance of this hot zone is visible as a drop below the original steady-state value shortly after the step input occurred. The hotter fluid starts to move downstream between $t = 0.7$ and $t = 1.5$.

7.2.2 Behavior at Different Mean Flow Reynolds Numbers

Figure 7.4 and Figure 7.5 show the flow fields for $\mathrm{Re}_0 = 0.4$. At this low Reynolds number, the flow fields are in transition for a long time, and a new steady state is not reached at the end of the figure series, although the last flow field was captured 25 flow passage times after the step occurred. This can also be seen in Figure 6.1. However, the cold leeward zone and the hot windward zone can readily be detected. Also, the sudden change of the velocity field restores slightly and within a comparably large amount of time until the new steady state is reached.

In the case of $\mathrm{Re}_0 = 4$ (Figure 7.6 and Figure 7.7), gradients are much stronger and cold and hot zones are more pronounced. In the chosen section, it can be seen that cold and hot regions are confined spots and only extend a few cylinder diameters beyond the center. The zones are more confined than in the case of $\mathrm{Re}_0 = 0.4$. Their size is the same order of magnitude as the steady state boundary field visible in

Figure 7.2. The development of the cold zone is partially counteracted and it reaches its maximum after about $t \approx 7$ (Figure 7.7, second row). The change in heat transfer rate slows down towards the new steady-state value but still overshoots it. After $t \approx 2$, the hot zone visible in the third row in Figure 7.6 departs. This corresponds to the positive values that are assumed in the heat transfer step response of sector 4 (cf. Figure 6.2 (b)).

The step response flow field of a cylinder in crossflow with an initial Reynolds number of $\mathrm{Re}_0 = 40$ (Figure 7.8 and Figure 7.9) shows a slightly different behavior. The recirculation zone (circular pseudo-streamlines at the lee side of the cylinder) contracts suddenly at time $t = 0$ and slowly grows again until a stationary state is reached. Only a small section at the cylinder, close to the flow separation point, remains colored in gray indicating no change.

Again, the pressure gradient necessary to accelerate the flow affects the boundary layer. The adverse pressure gradient due to the curvature is counteracted by the favorable pressure gradient from the step input. This causes the separation point, where the flow cannot longer follow the curvature of the cylinder and the recirculation zone starts, to shift towards the rearward stagnation point. The recirculation zone seems to collapse and is restored when the excess of vorticity is transported downstream.

The size of the colder and hotter zones are smaller than in the case of $\mathrm{Re}_0 = 0.4$ and $\mathrm{Re}_0 = 4$, similar o the steady-state boundary field visible in Figure 7.3. Gradients are stronger (different color scales are used) and changes are faster, e.g. happen in shorter succession to the step input than at lower mean flow Reynolds numbers. Stronger gradients also indicate a greater change in heat transfer rate. While the hotter zone is washed downstream after about one passage time, the size of the colder zone peaks around $t = 2$ and shrinks until a new steady state is reached.

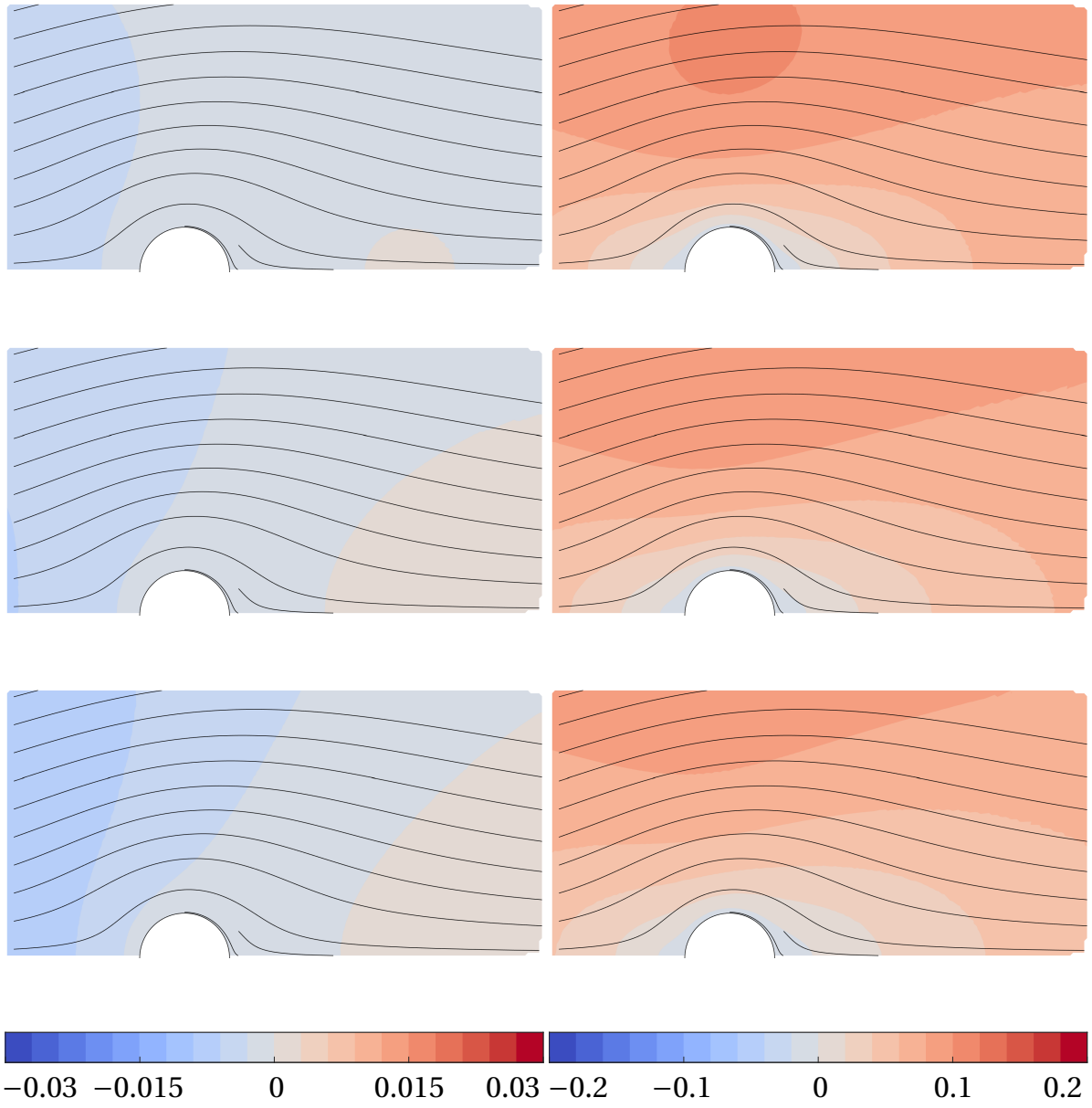

Figure 7.4: Flow Field Representation of the Step Response ($Re_0 = 0.4$) I. Left column: Fields of temperature difference $\delta\Theta$. Right column: Fields of velocity difference δu. Time instances (rows) are $t = 0.3$, $t = 0.7$, $t = 1.5$ (top to bottom). Colors range from blue (negative) to red (positive). Black lines show pseudo-streamlines.

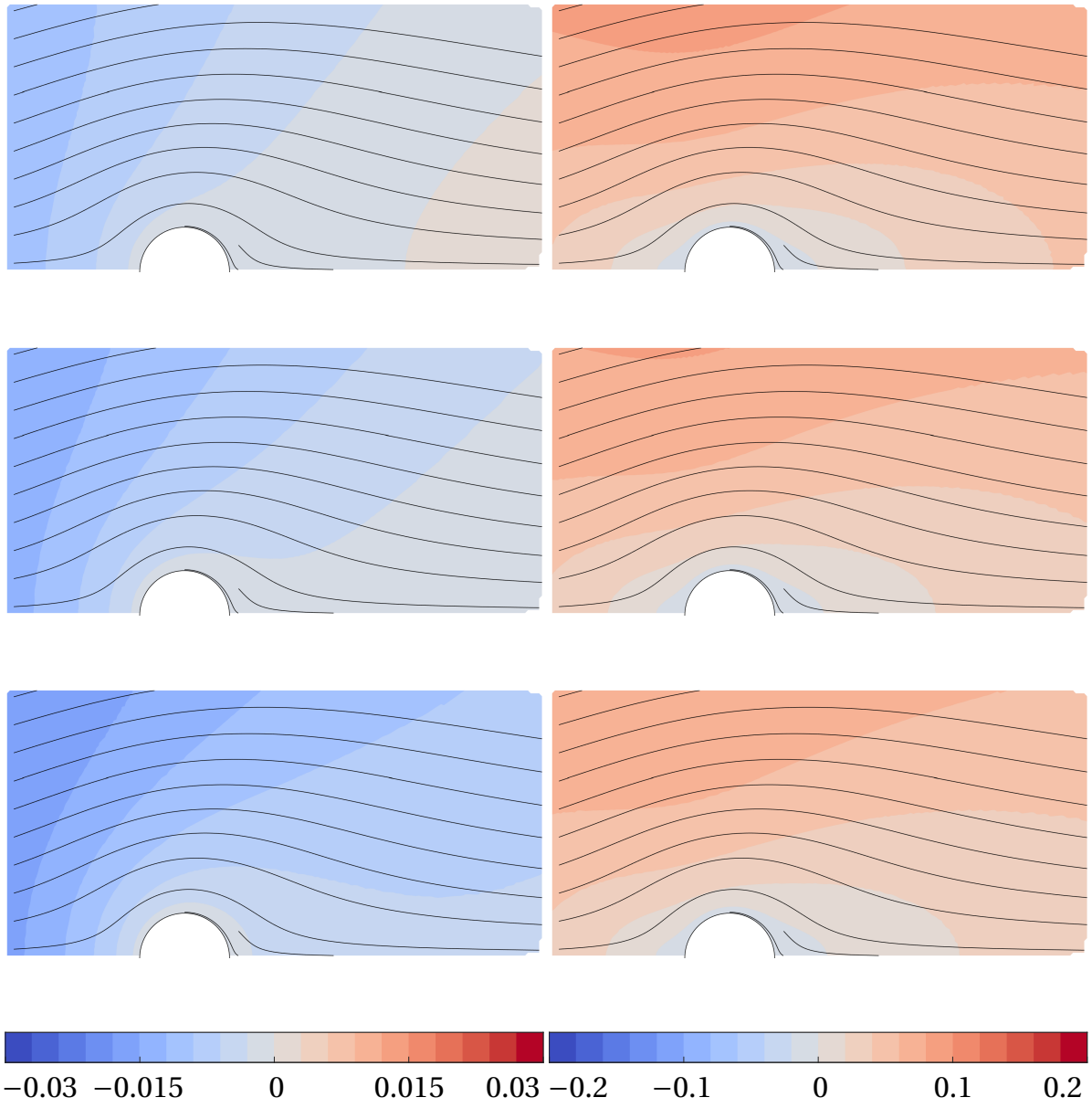

Figure 7.5: Flow Field Representation of the Step Response ($Re_0 = 0.4$) II. Left column: Fields of temperature difference $\delta\Theta$. Right column: Fields of velocity difference δu. Time instances (rows) are $t = 3$, $t = 7$ and $t = 25$ (top to bottom). Colors range from blue (negative) to red (positive). Black lines show pseudo-streamlines.

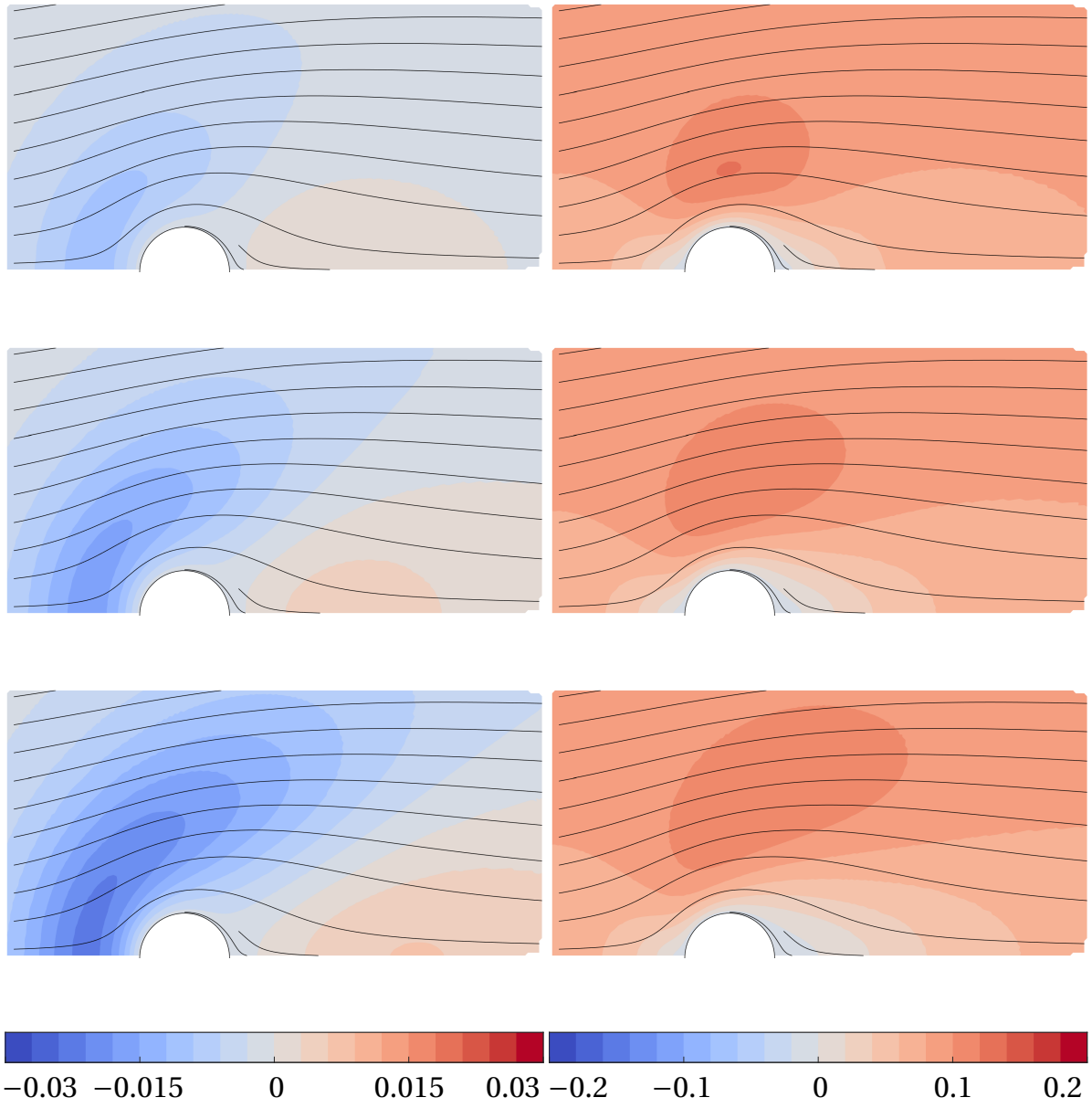

Figure 7.6: Flow Field Representation of the Step Response ($Re_0 = 4$) I. Left column: Fields of temperature difference $\delta\Theta$. Right column: Fields of velocity difference δu. Time instances (rows) are $t = 0.3$, $t = 0.7$, $t = 1.5$ (top to bottom). Colors range from blue (negative) to red (positive). Black lines show pseudo-streamlines.

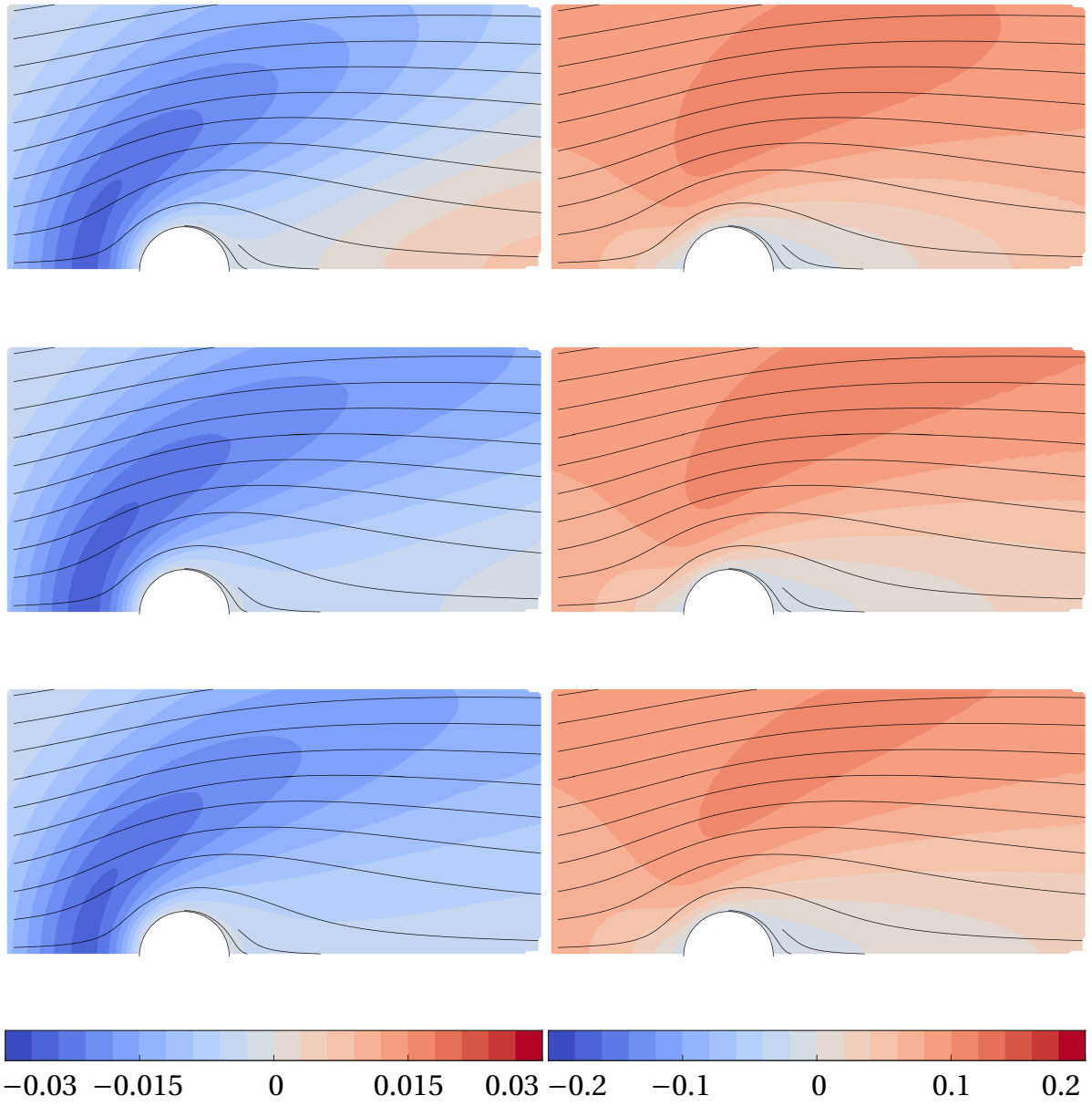

Figure 7.7: Flow Field Representation of the Step Response ($Re_0 = 4$) II. Left column: Fields of temperature difference $\delta\Theta$. Right column: Fields of velocity difference δu. Time instances (rows) are $t = 3$, $t = 7$, and $t = 25$ (top to bottom). Colors range from blue (negative) to red (positive). Black lines show pseudo-streamlines.

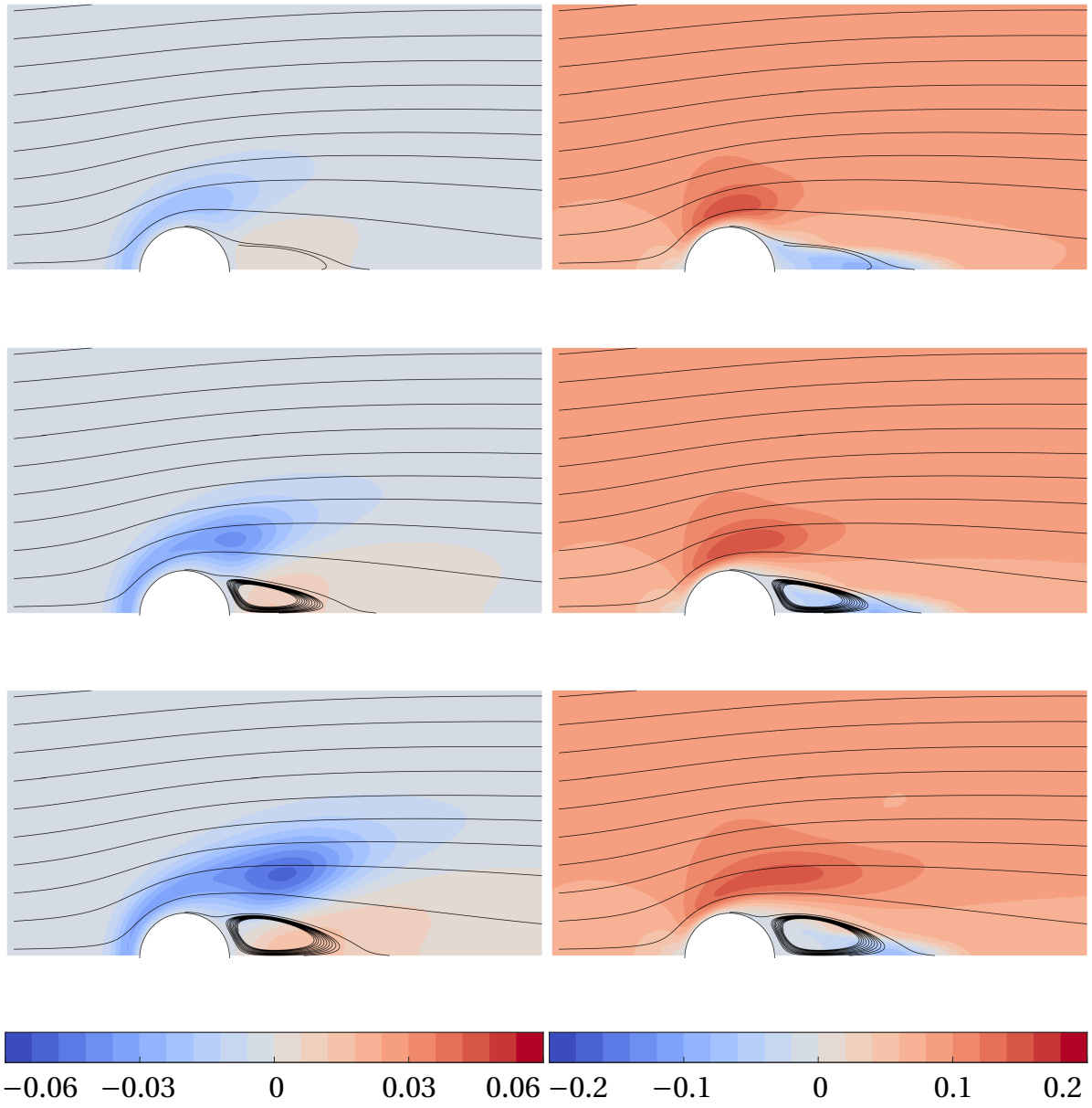

Figure 7.8: Flow Field Representation of the Step Response ($Re_0 = 40$) I. Left column: Fields of temperature difference $\delta\Theta$. Right column: Fields of velocity difference δu. Time instances (rows) are $t = 0.3$, $t = 0.7$, $t = 1.5$ (top to bottom). Colors range from blue (negative) to red (positive). Black lines show pseudo-streamlines.

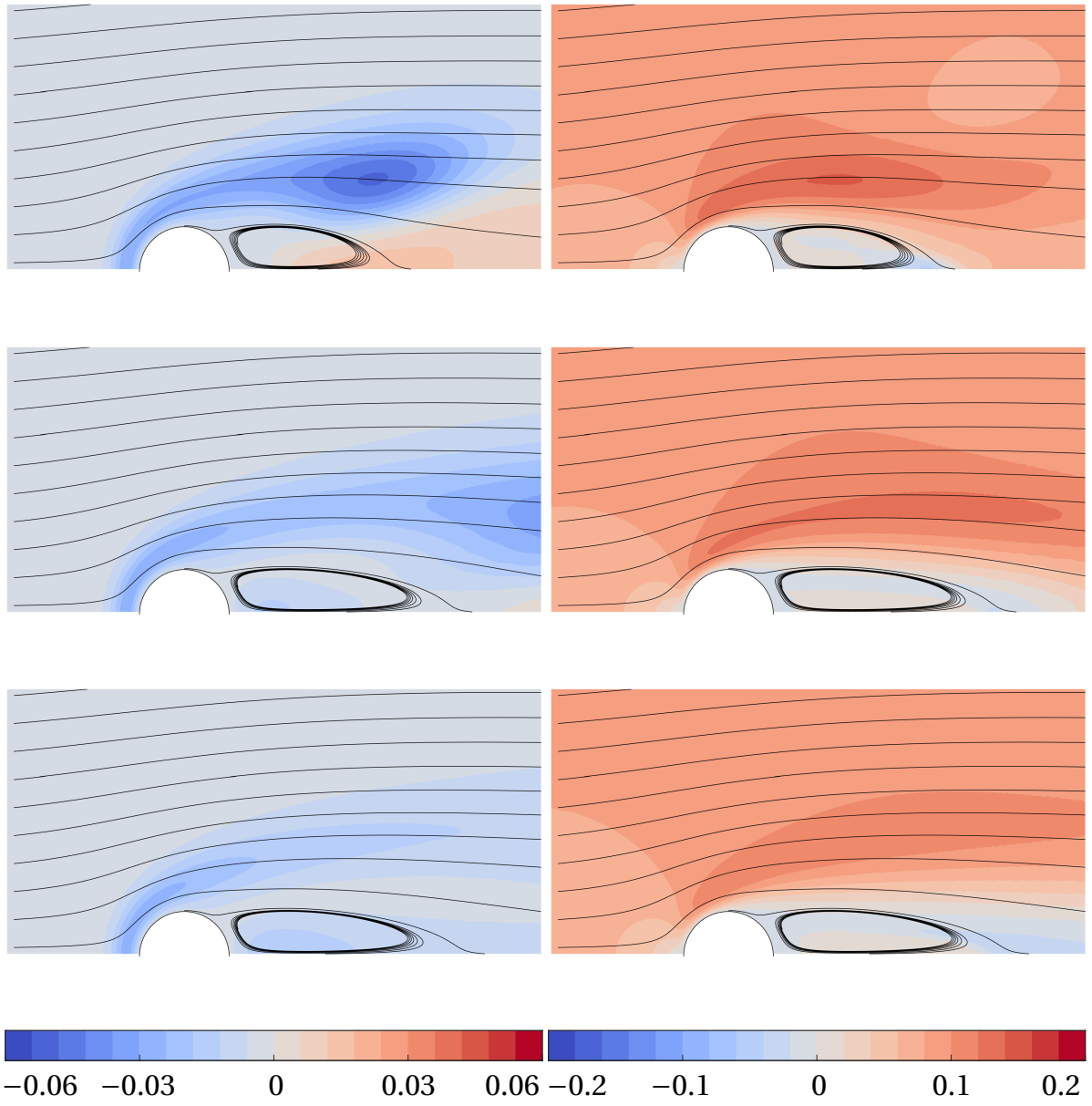

Figure 7.9: Flow Field Representation of the Step Response ($Re_0 = 40$) II. Left column: Fields of temperature difference $\delta\Theta$. Right column: Fields of velocity difference δu. Time instances (rows) are $t = 3$, $t = 7$, and $t = 25$ (top to bottom). Colors range from blue (negative) to red (positive). Black lines show pseudo-streamlines.

7.3 Representations of the Linearized Flow Field

The linearized Navier–Stokes equations solver does not only offer the possibility to acquire the frequency response of Nußelt number and skin friction at discrete predefined frequencies (cf. Section 6.2). It can also show the response of the complete (linearized) flow field around the cylinder subject to fluctuations of a specific frequency.

7.3.1 Amplitude of Vorticity and Temperature Fluctuation

In the following series of figures (Figure 7.10– Figure 7.15), the amplitude field of linearized temperature fluctuations $|\Theta_1|$ (left column) and the field of vorticity fluctuation amplitude $|\zeta_1|$ (right column) are shown. The excerpt extends from $-2\,d$ to $4\,d$ in x_1-direction and from 0 to $3\,d$ in x_2-direction. Black lines are isolines of the steady-state stream function ψ_0, i.e. they are streamlines for the mean flow from left to right.

Figure 7.10 and Figure 7.11 show the linearized temperature field and velocity magnitude field at a mean flow Reynolds number of $\mathrm{Re}_0 = 0.4$ for different Strouhal numbers $\mathrm{Sr} \in \{0.01, 0.1, 0.5, 1, 2, 5, 10, 40\}$. A Strouhal number of $\mathrm{Sr} = 0.01$ was chosen to approximate a quasi-steady state. A major outcome is that the temperature fluctuations are strong for $\mathrm{Sr} \leq 0.5$. At Strouhal numbers of $\mathrm{Sr} = 0.01$ and $\mathrm{Sr} = 0.1$, the amplitude of Θ_1 assumes large values upwind of the cylinder visible as red areas. The fluctuations at values greater than $\mathrm{Sr} > 0.5$ are comparably weak. This corresponds to the strong low-pass behavior visible in Figure 6.26.

The amplitude field of the vorticity fluctuations $|\zeta_1|$ does not change much at Strouhal numbers below the order of one. All vorticity fluctuations are generated at the cylinder and most strongly in sector 2. The frequency response of the skin friction also shows only minor changes in amplitude at low Strouhal numbers, which confirms this behavior. At higher Strouhal numbers, e.g. at $\mathrm{Sr} = 40$, the generation of vorticity fluctuations is much stronger than at low Strouhal numbers. The dynamic boundary layer thickness is small, and hence the velocity gradients are large. The maximum of the vorticity generation moves slightly downstream so that the field becomes almost symmetric to the y-axis.

Representations of the linearized flow field subject to periodic pulsations of the velocity at a mean flow Reynolds number of $\mathrm{Re}_0 = 4$ are given in Figure 7.12 and Figure 7.13. At the lowest frequency ($\mathrm{Sr} = 0.01$), the temperature fluctuations close to the forward stagnation point are strong. A localized region of approximately two diameters upstream is affected the most by the velocity fluctuations. The zone of strong fluctuations (red zone) is largest in the second row at $\mathrm{Sr} = 0.1$. This concurs with the peak gain in the transfer function of the heat transfer (cf. Section 6.2). At

Sr = 0.5, a second region of higher fluctuation amplitudes is visible on the lee side of the cylinder. This effect could also be observed for $\mathrm{Re}_0 = 0.4$ and is weaker than the fluctuations in front of the cylinder. The fluctuation amplitude is reduced with higher frequency until no fluctuation is visible in the chosen color scale for Sr = 40. The vorticity fluctuations (right column) behave again differently and are concentrated around $\phi = \pi/4$ where most of the vorticity fluctuations are generated at the surface of the cylinder. The affected region extends significantly downstream. As the fluctuations grow stronger at higher frequencies (with a peak value of $|\zeta_1|_{\max} = 26.5$ at Sr = 40), they concentrate close to the surface of the cylinder. The peak vorticity is located close to $\phi = \pi/2$, i.e. where the cylinder is thickest.

The behavior of the fluctuating quantities, temperature and vorticity, for a mean flow Reynolds number $\mathrm{Re}_0 = 40$ is shown in Figure 7.14 and Figure 7.15. Similar features occur, e.g. the temperature fluctuation at the windward side of the cylinder and the temperature fluctuation right behind the rearward stagnation point, which starts at the very low frequencies (Sr = 0.01) and is visible even at the higher Strouhal numbers. The vorticity fluctuation also behaves similarly to $\mathrm{Re}_0 = 4$ with the most substantial difference visible at the smallest frequencies where the affected region reaches further downstream. Again, the highest value ($|\zeta_1|_{\max} = 81.0$) is measured at Sr = 40.

A major difference to the behavior at the lower mean flow Reynolds numbers is the occurrence of high amplitude fluctuations downstream of the cylinder and in the shear layer next to the recirculation zone. The recirculation zone is visible as the closed streamline at the lee side of the cylinder. The temperature fluctuations in front of the cylinder are comparable in amplitude to the $\mathrm{Re}_0 = 4$ case. The smaller size of this upstream fluctuation zone leads to stronger gradients and hence to larger fluctuation amplitudes in Nußelt number. However, this third fluctuation zone located approximately at $\phi \approx 3\pi/4$ exhibits amplitudes almost twice as strong as the forward fluctuation zone. This effect is mostly visible at Sr = 0.5, Sr = 1.0, and Sr = 2.0 (third row and fourth row in Figure 7.14 and first row in Figure 7.15).

This sidewards fluctuation zone might explain why the gain of the heat transfer fluctuations exceeds the steady-state value strongly at Strouhal numbers of order one. This region is also visible in the vorticity field but much weaker and without influence on the skin friction fluctuation.

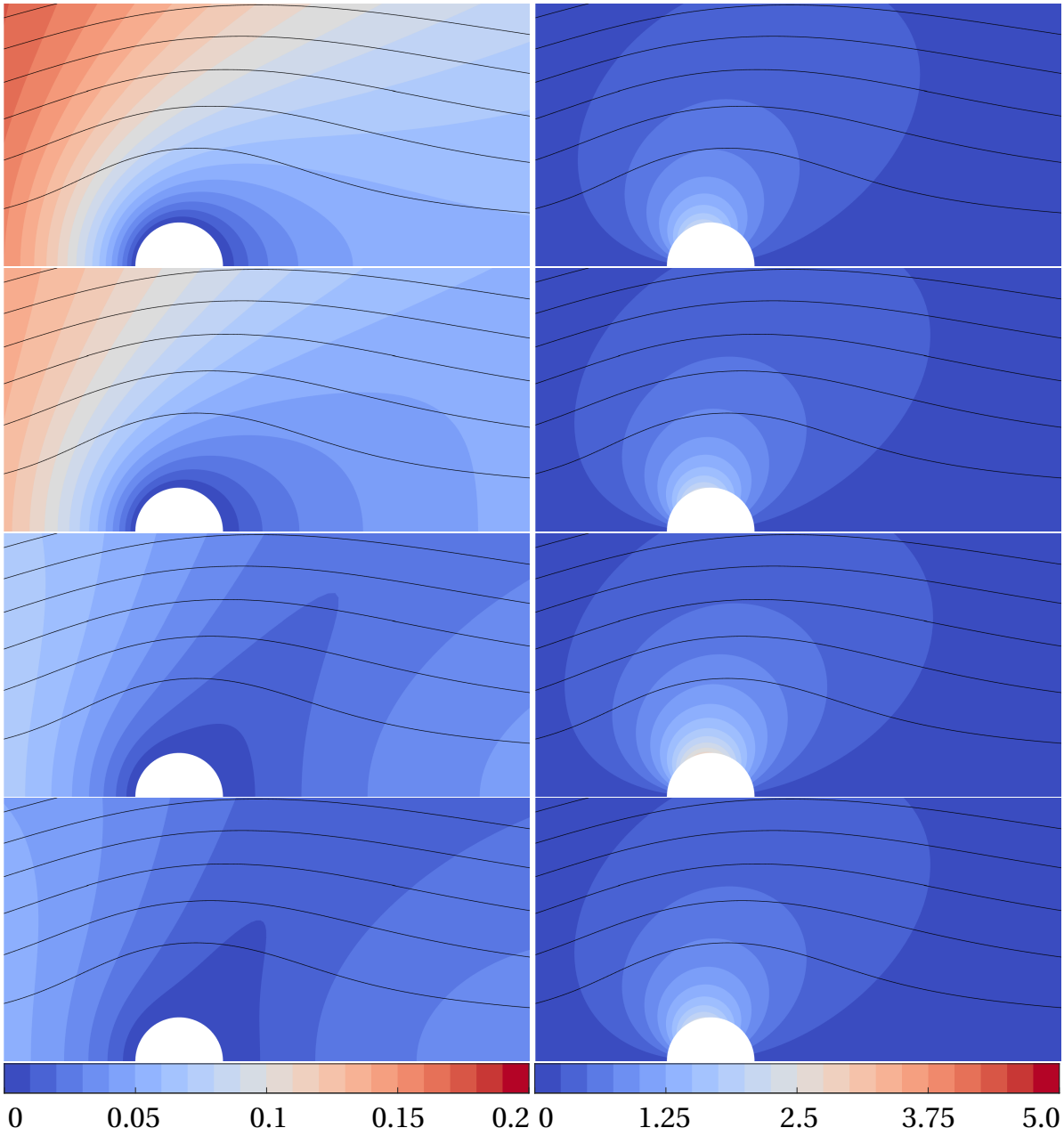

Figure 7.10: Linearized Flow Field Representation for $Re_0 = 0.4$ I. Left column: Amplitude of temperature fluctuation $\Theta_1(Sr)$. Right column: Amplitude of vorticity fluctuation $\zeta_1(Sr)$. Strouhal numbers are Sr = 2, Sr = 5, Sr = 10, and Sr = 40 (top to bottom).

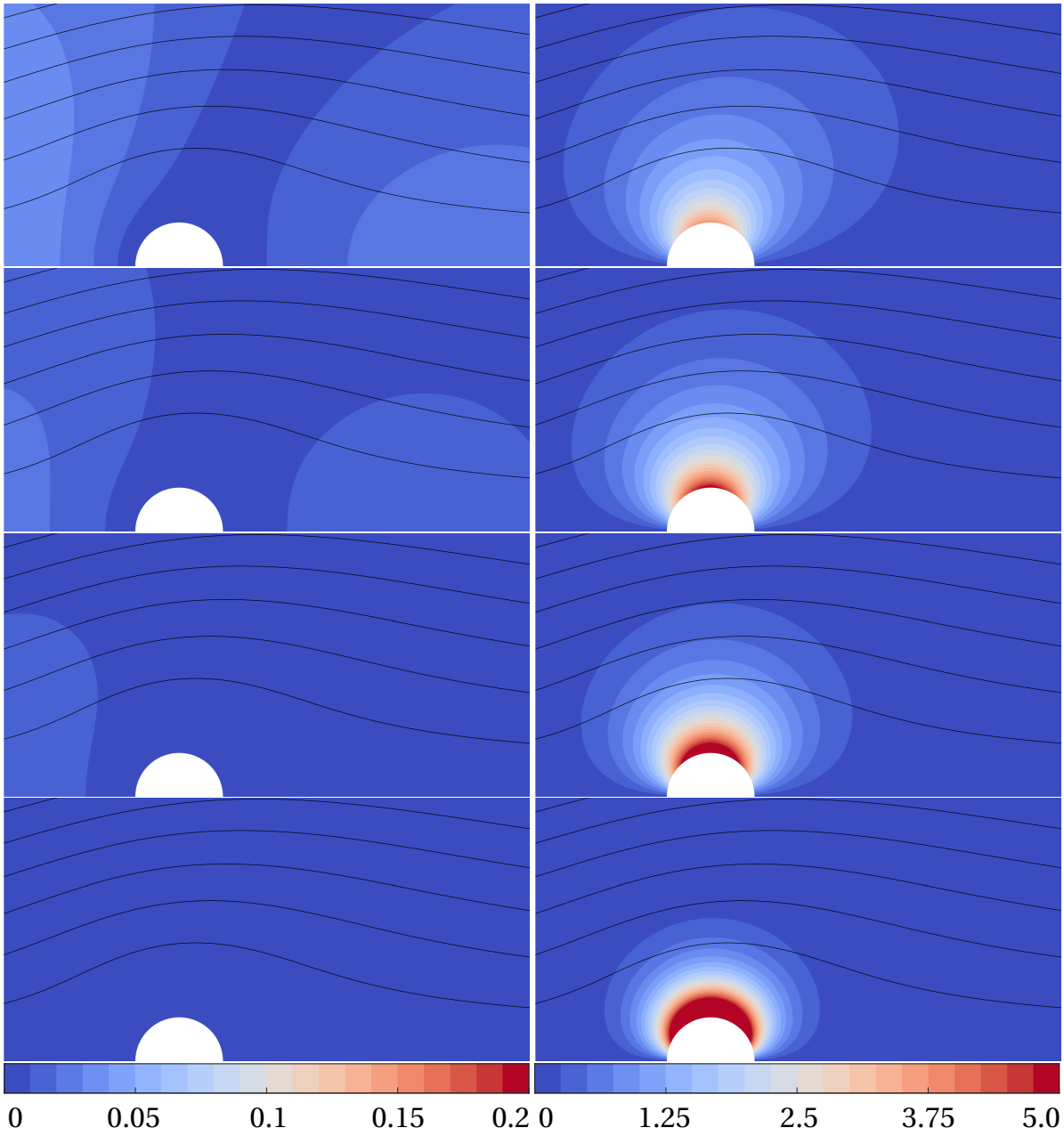

Figure 7.11: Linearized Flow Field Representation for $Re_0 = 0.4$ II. Left column: Amplitude of temperature fluctuation $\Theta_1(Sr)$. Right column: Amplitude of vorticity fluctuation $\zeta_1(Sr)$. Strouhal numbers are Sr = 2, Sr = 5, Sr = 10, and Sr = 40 (top to bottom).

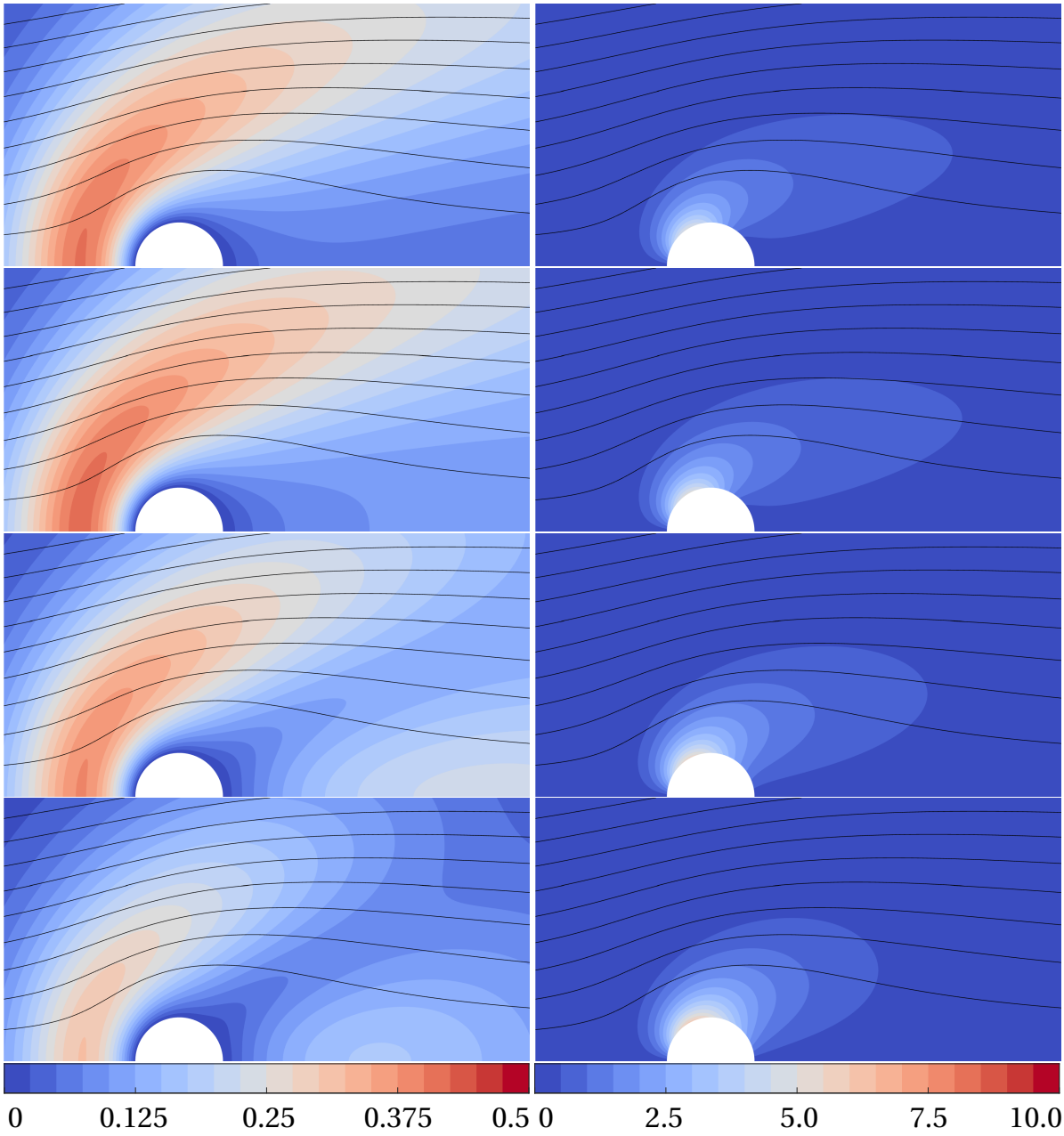

Figure 7.12: Linearized Flow Field Representation for $Re_0 = 4$ I. Left column: Amplitude of temperature fluctuation $\Theta_1(Sr)$. Right column: Amplitude of vorticity fluctuation $\zeta_1(Sr)$. Strouhal numbers are Sr = 0.01, Sr = 0.1, Sr = 0.5, and Sr = 1.0 (top to bottom).

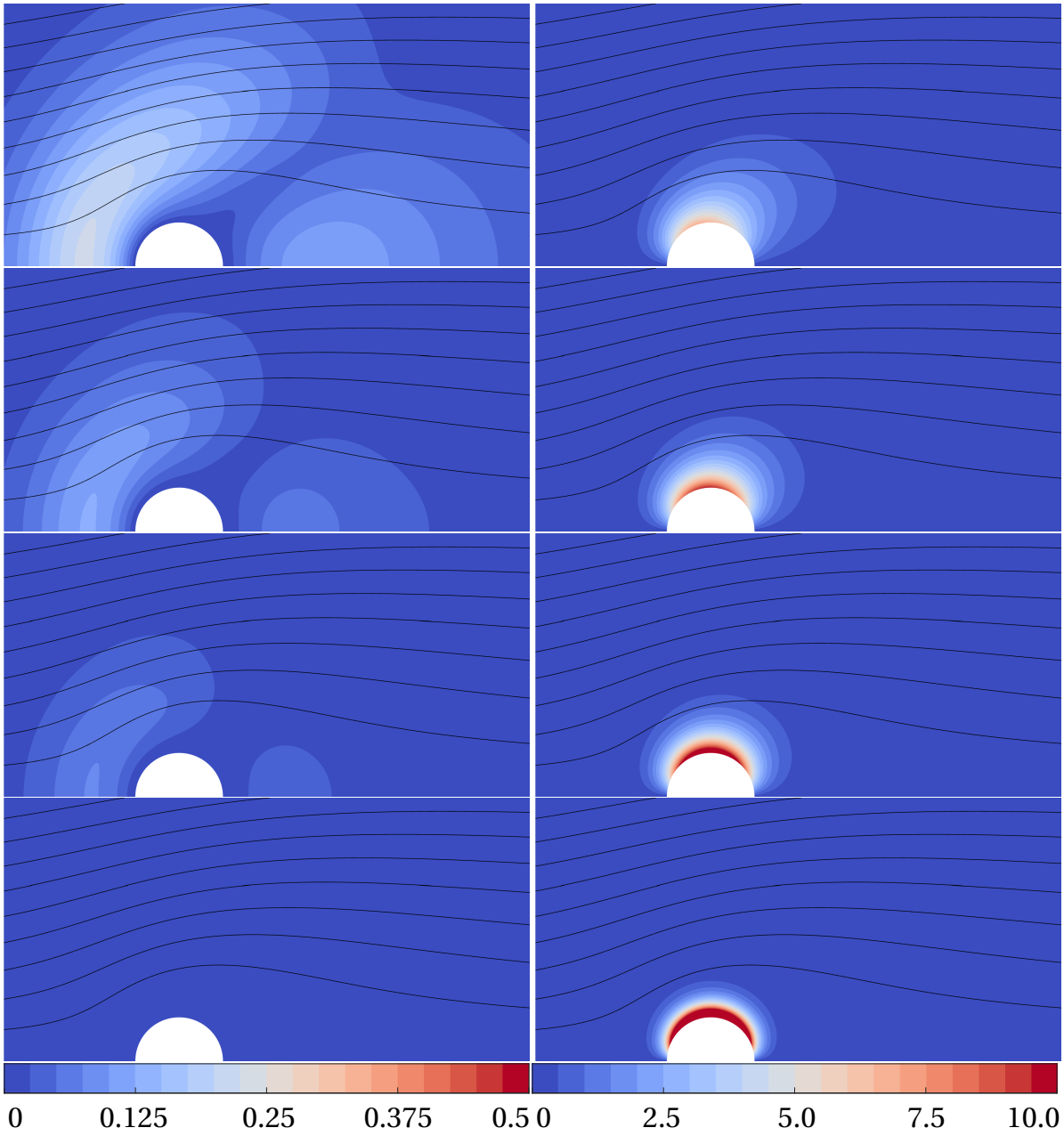

Figure 7.13: Linearized Flow Field Representation for $Re_0 = 4$ II. Left column: Amplitude of temperature fluctuation $\Theta_1(Sr)$. Right column: Amplitude of vorticity fluctuation $\zeta_1(Sr)$. Strouhal numbers are $Sr = 2$, $Sr = 5$, $Sr = 10$, and $Sr = 40$ (top to bottom).

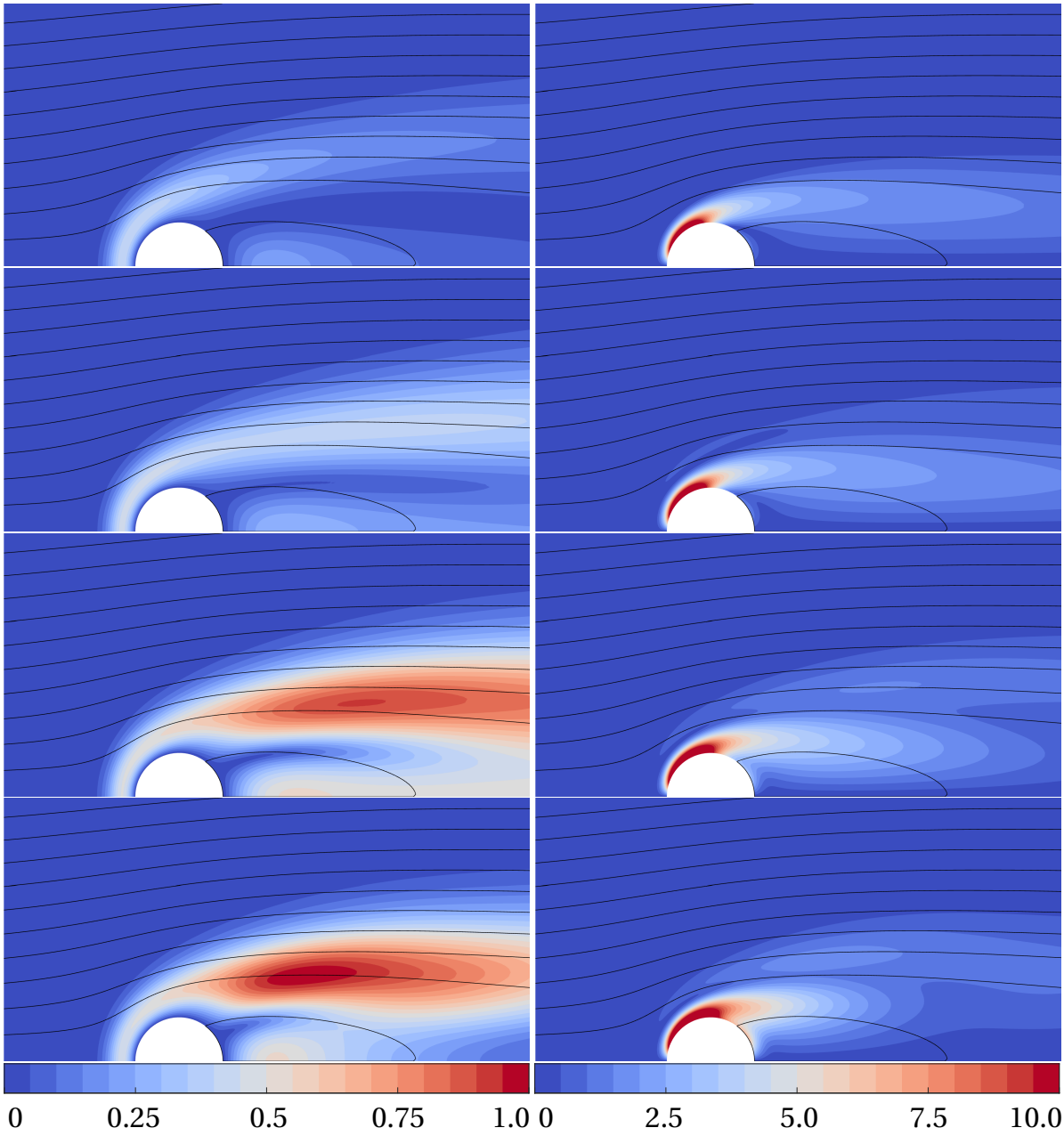

Figure 7.14: Linearized Flow Field Representation for $Re_0 = 40$ I. Left column: Amplitude of temperature fluctuation $\Theta_1(Sr)$. Right column: Amplitude of vorticity fluctuation $\zeta_1(Sr)$. Strouhal numbers are Sr = 0.01, Sr = 0.1, Sr = 0.5, and Sr = 1.0 (top to bottom).

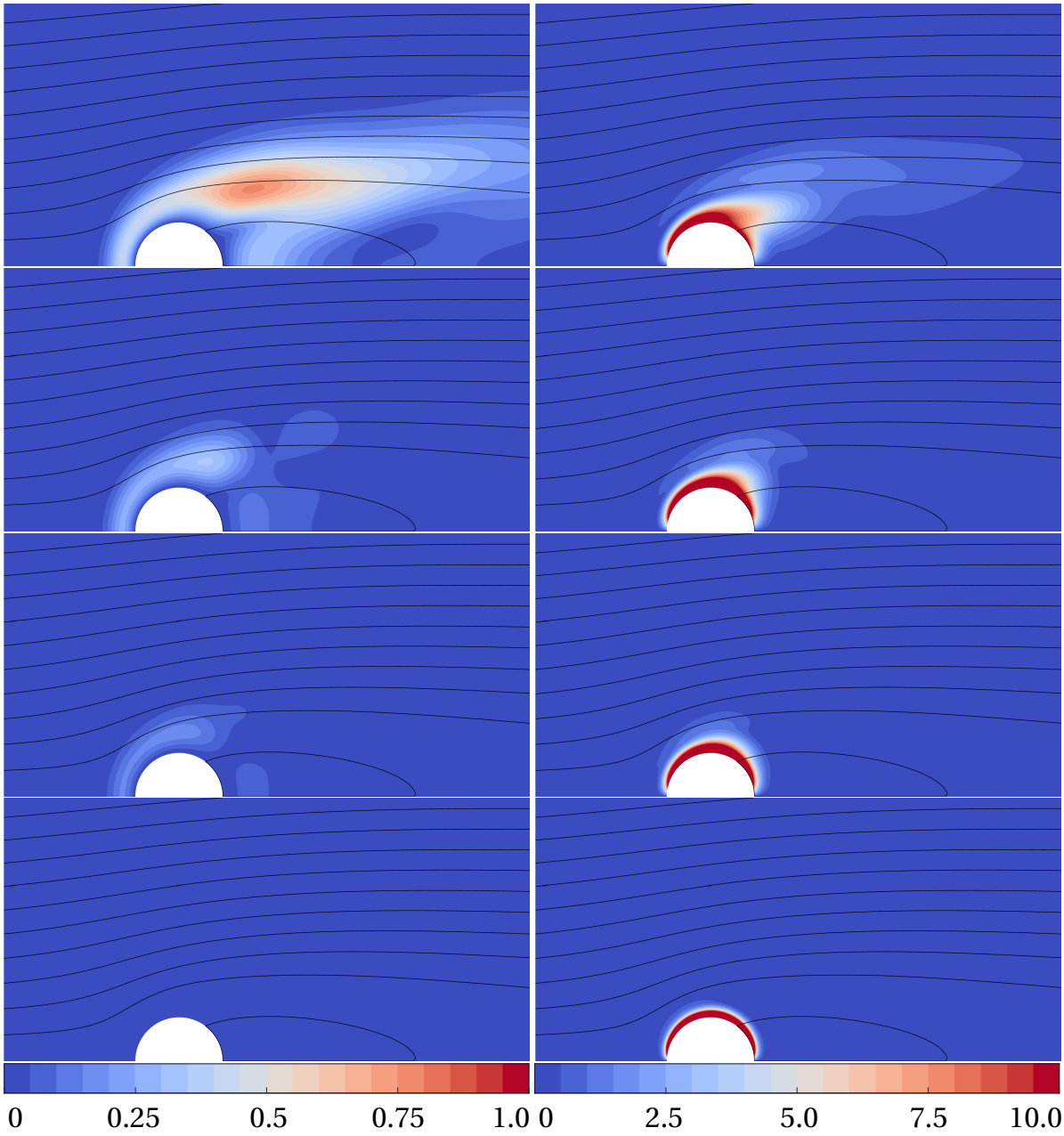

Figure 7.15: Linearized Flow Field Representation for $Re_0 = 40$ II. Left column: Amplitude of temperature fluctuation $\Theta_1(Sr)$. Right column: Amplitude of vorticity fluctuation $\zeta_1(Sr)$. Strouhal numbers are Sr = 2.0, Sr = 5.0, Sr = 10.0, and Sr = 40.0 (top to bottom).

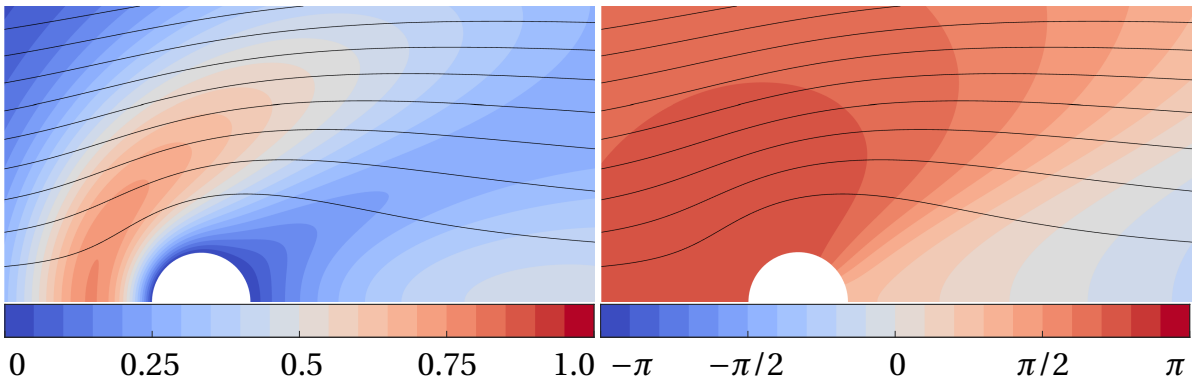

Figure 7.16: Flow Field Representation of Θ_1 for $\mathbf{Re_0 = 4}$ and $\mathbf{Sr = 0.5}$. Amplitude (left) and phase (right) of temperature fluctuation.

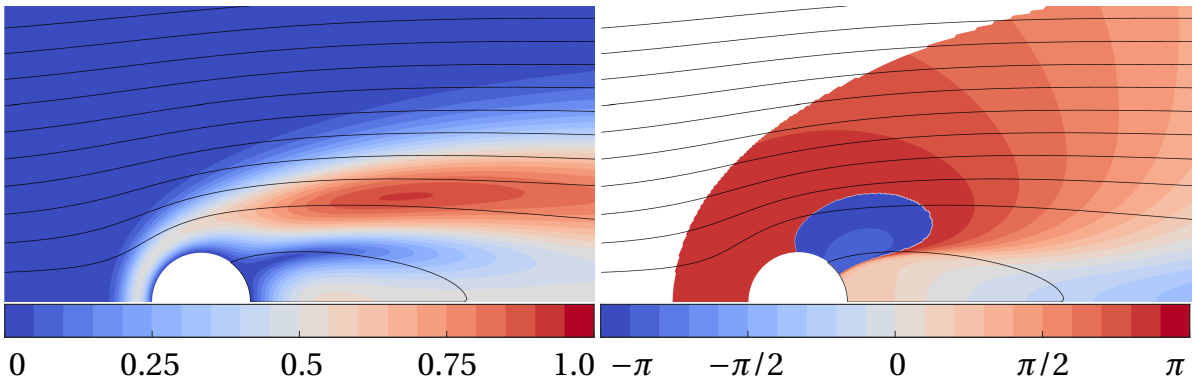

Figure 7.17: Flow Field Representation of Θ_1 for $\mathbf{Re_0 = 40}$ and $\mathbf{Sr = 0.5}$. Amplitude (left) and phase (right) of temperature fluctuation.

7.3.2 Amplitude and Phase Fields of Temperature Fluctuation

In the figure series of the previous section, only amplitude values are shown. This section links these representations to the phase field of the complex temperature fluctuations Θ_1 relative to the excitation with $e^{i\,\mathrm{Sr}\,t}$. Low frequencies, at which a peak gain $G_{\mathrm{Nu}} > K_{\mathrm{Nu}}$ occurs ($\mathrm{Sr} \approx 0.5$), are examined as well as the case of $\mathrm{Sr} \approx 7$, where all transfer functions coincide in a phase value of approximately $\angle G_{\mathrm{Nu}} \approx -3\pi/8$ (cf. Section 6.4.1).

Low Frequencies (Sr = 0.5)

Figure 7.16 shows amplitude (left) and phase (right) of the temperature fluctuations caused by periodic pulsations of the flow velocity at a mean flow Reynolds number of $\mathrm{Re}_0 = 4$ and a Strouhal number of $\mathrm{Sr} = 0.5$. The amplitude field is the same as in Figure 7.12, (third row, left column). It shows the typical windward and leeward fluctuation zones but no sideward fluctuation. The strong windward fluctuations

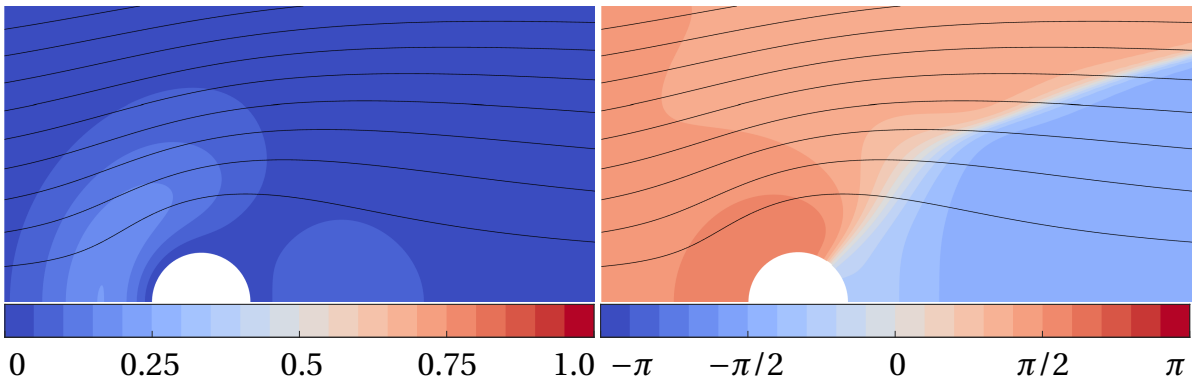

Figure 7.18: Flow Field Representation of Θ_1 for $Re_0 = 4$ and Sr = 7. Amplitude (left) and phase (right) of temperature fluctuation.

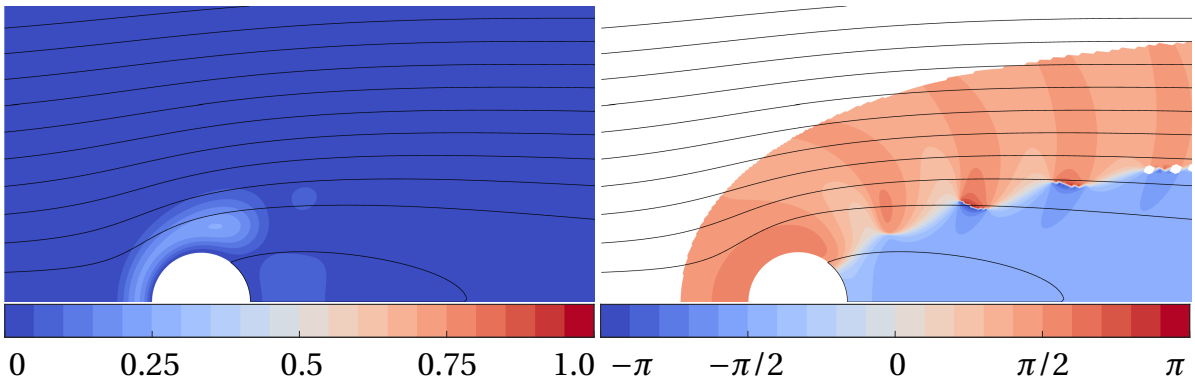

Figure 7.19: Flow Field Representation of Θ_1 for $Re_0 = 40$ and Sr = 7. Amplitude (left) and phase (right) of temperature fluctuation.

have positive phase values. In contrast, the leeward fluctuations exhibit lower, even negative phase values.

For temperature fluctuations at $Re_0 = 40$, as depicted in Figure 7.17 (cf. Figure 7.15, third row left column), the sidewards fluctuation zone is visible. For this mean flow Reynolds number, the assessed Strouhal number Sr = 0.5 is very close to the maximum of the peak gain phenomenon. The phase values, depicted on the right of Figure 7.17, are only shown in places where the amplitude is above 10^{-3}. Windward and sideward fluctuation zones are in the region with positive phase values, i.e. phase lag. The dark blue spot at an angle of $\phi \approx 3\pi/4$, indicating phase values of approximately $-\pi$, is due to phase wrapping. It occurs when values exceed π. Hence, again most fluctuations lag in phase except for the leeward zone, which shows negative values in G_{Nu}.

Intermediate Frequencies (Sr = 7)

The temperature fluctuations at an intermediate frequency (Sr = 7) and a mean flow Reynolds number $\mathrm{Re}_0 = 4$ are depicted in Figure 7.18. The amplitude values are rather small compared to lower frequencies as was to be expected from the frequency response (cf. Section 6.4.1). The phase field shows a distinct difference between the forward fluctuation zone and the leeward fluctuation zone. In the range of $\phi = 0$ to approximately $\phi = 3\pi/4$ around the circumference of the cylinder (sector 1 – sector 3), the phase exhibits a lag of approximately $\pi/2$.

The phase at $\mathrm{Re}_0 = 40$ and Sr = 7 is shown in Figure 7.19. The essential features are the same as in the case of $\mathrm{Re}_0 = 4$. Like in Figure 7.17, phase values are only depicted where the amplitude is above 10^{-3}. Partition of the field close to the surface of the cylinder is visible like in the case of $\mathrm{Re}_0 = 4$. A pattern of "phase waves" is superimposed with a wavelength of approximately one cylinder diameter. This corresponds to sinusoidal fluctuations convected with the undisturbed mean flow velocity $u_{0,\infty}$ ($\mathrm{Sr}/2\pi \approx 1$).

7.4 Circumferential Distribution of Heat Transfer and Skin Friction

Section 7.3 and Section 7.2 gave descriptions of the linearized flow field close to the cylinder. This section focuses directly on the skin friction and the heat transfer computed with the LNSE solver (cf. Section 5.4 and Section 6.2). Similar to the steady-state values for the Nußelt number and the friction coefficient, reported in Section 2.1.2, the circumferential distributions of the fluctuating quantities Nu_1 and $c_{f,1}$ are shown in polar plots. The top half of each plot represents the amplitude of the complex-valued quantity. The phase is depicted at the bottom of the figure. This viewpoint allows more insight into the influence of the cylindrical shape on the transfer behavior.

Figure 7.20 depicts the Nußelt number fluctuations at three different frequencies, Sr = 0.5 (blue), Sr = 7 (red), and Sr = 40 (yellow), for a mean flow Reynolds number of $\mathrm{Re}_0 = 4$. The amplitude of Nu_1 greatly reduces with frequency, which concurs with the low-pass behavior of the transfer function (cf. Chapter 6). From this figure, it can be seen that most of the fluctuations occur at the forward stagnation point and diminish towards larger angles. This behavior is also observed for the steady-state values (cf. Figure 2.6).

At angles of $\phi \approx 3\pi/4$, the amplitude is at its low mark. It recovers slightly towards the backward stagnation point. This change in dynamic behavior is also apparent in the phase of the Nußelt number. Phase values are always below zero for the con-

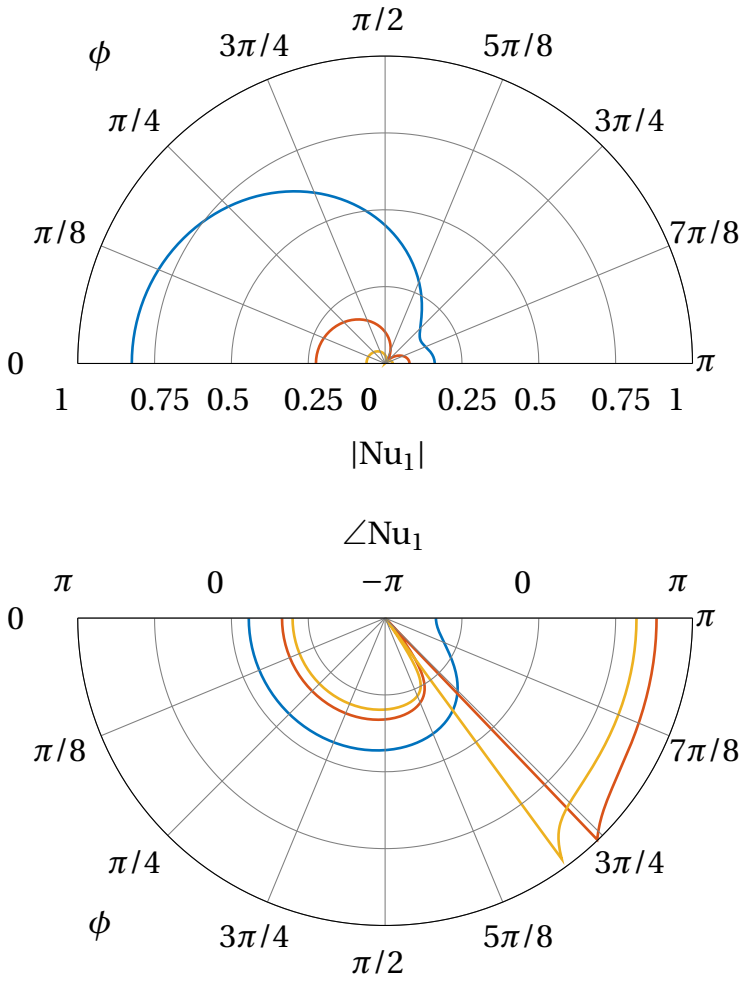

Figure 7.20: Nußelt Number Distribution at $\mathrm{Re}_0 = 4$**.** $\mathrm{Sr} = 0.5$ (——), $\mathrm{Sr} = 7$ (——), and $\mathrm{Sr} = 40$ (——).

sidered frequencies. At $\mathrm{Sr} = 7$ and $\mathrm{Sr} = 40$, phase wrapping occurs, yielding positive values. This is another indicator for the change of dynamic behavior in sector 4 of the cylinder as it can be observed in the flow fields (cf. Section 7.2 and Section 7.3) as well as in the step response (cf. Section 6.1).

At higher Reynolds numbers, the behavior is similar, yet more pronounced. Figure 7.21 shows the circumferential distribution of fluctuating heat transfer at the cylinder at a mean flow Reynolds number of $\mathrm{Re}_0 = 40$. At $\mathrm{Sr} = 0.5$, which is close to the peak gain frequency of the transfer function, the amplitude values are highest. Again, a drop to very small values is visible at an angle slightly above $\phi = 3\pi/4$. At the backward stagnation point, the amplitude rises to about 1/4 of the maximum. At angles before the amplitude minimum, the phase exhibits positive values, i.e. phase lag. In this position, the sideward fluctuation zone (cf. Figure 7.17) is located. Although the fluctuations are quite strong, the zone is far away, and hence gradients are comparatively low.

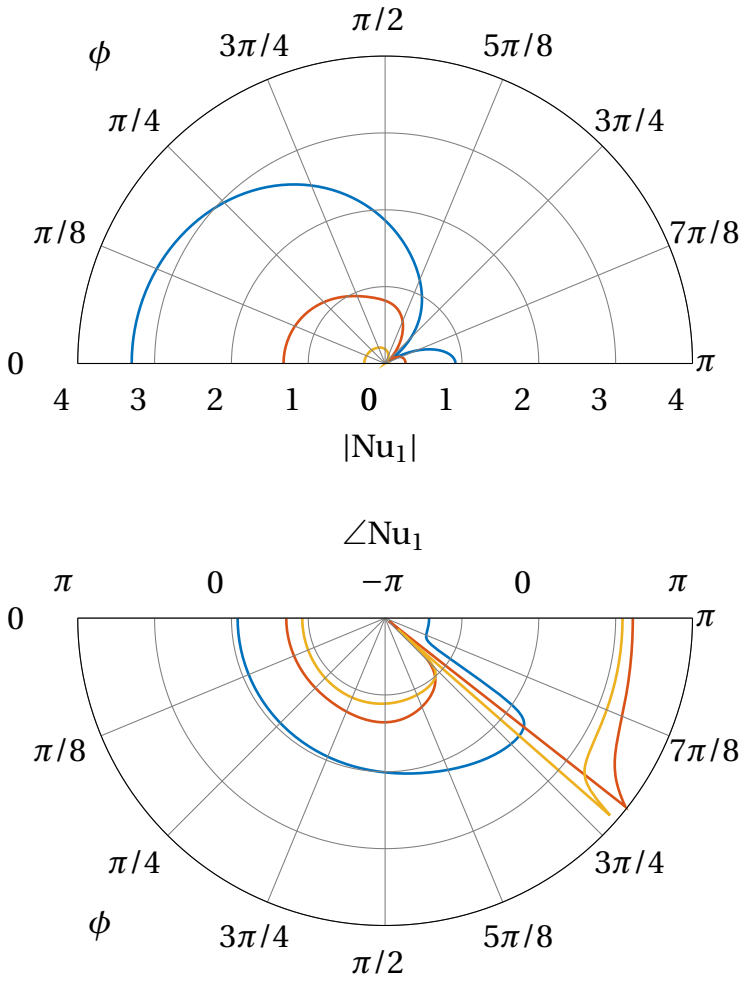

Figure 7.21: Nußelt Number Distribution at $\mathrm{Re}_0 = 40$**.** $\mathrm{Sr} = 0.5$ (——), $\mathrm{Sr} = 7$ (——), and $\mathrm{Sr} = 40$ (——).

The phase at high frequencies tends towards lower values. At a distinct angle close to $\phi = 3\pi/4$, the phase drops about an amount of π causing the phase to be wrapped in Figure 7.21. The angle at which the phase jump occurs is slightly dependent on frequency and moves towards smaller angles with rising Strouhal number.

Figure 7.22 displays the friction coefficient pulsation $c_{f,1}$, derived from the linearized flow fields for three different frequencies ($\mathrm{Sr} = 0.5$, $\mathrm{Sr} = 7$, and $\mathrm{Sr} = 40$) and a mean flow Reynolds number of $\mathrm{Re}_0 = 4$. The maximum amplitude rises with frequency as can as well be seen in the skin friction transfer function. No fluctuation occurs at the forward stagnation point. Hence, the amplitude appears egg-shaped in the polar plot. At the lowest frequency shown here ($\mathrm{Sr} = 0.5$), the maximum occurs at approximately $\phi \approx 3\pi/4$ and moves to an angle of $\phi \approx \pi/2$ at very high Strouhal numbers. The skin friction at high frequencies shows symmetry also in the direction perpendicular to the flow, which is also visible in the linearized flow field (cf. Figure 7.13). Moreover, this is reflected in the phase of $c_{f,1}$ which uniformly

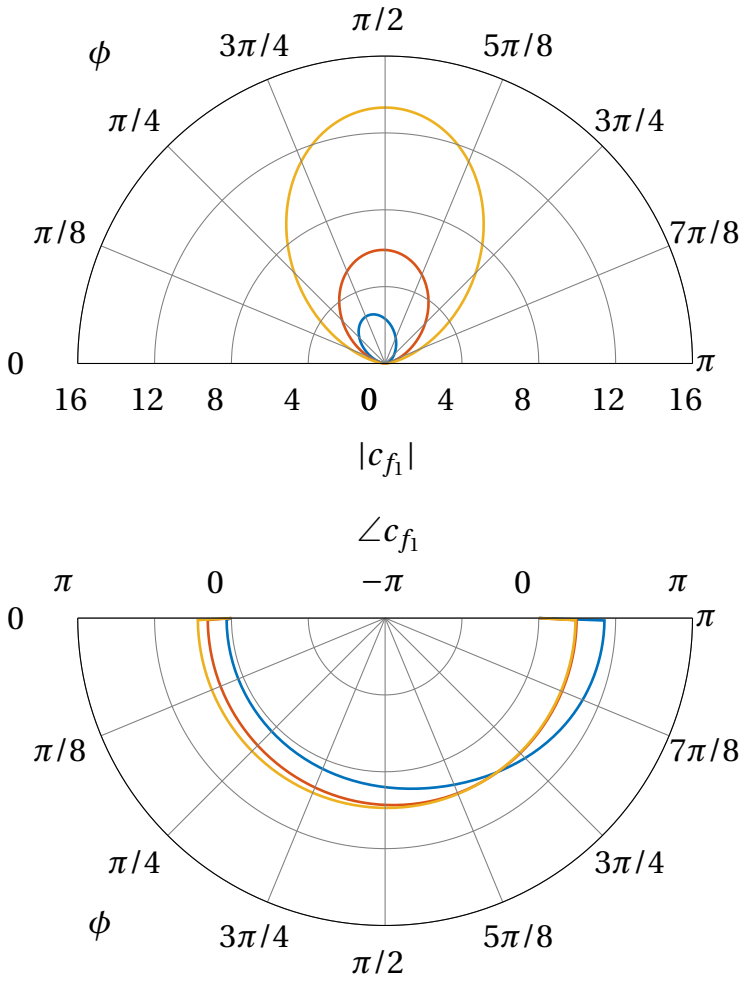

Figure 7.22: Friction Coefficient Distribution at $\mathrm{Re}_0 = 4$**.** Sr = 0.5 (—), Sr = 7 (—), and Sr = 40 (—).

approaches < $c_{f,1} = \pi/4$ at high Strouhal numbers. At Sr = 0.5, it can be seen that the phase lead close to the backward stagnation point is almost $\angle c_{f,1} = \pi/2$. This shows that only weak inertial forces act on the fluid in this region and it responds to a change in pressure, which is necessary to accelerate or decelerate the flow, almost instantly.

At a mean flow Reynolds number of $\mathrm{Re}_0 = 40$, as shown in Figure 7.23, the friction coefficient behaves in a very similar manner. The amplitudes are smaller than in the case of $\mathrm{Re}_0 = 4$, but this also applies to the steady-state value to an even larger extent. Hence, the frequency response (cf. Figure 6.26) has higher amplitudes at greater mean flow Reynolds numbers. The phase lead close to the backward stagnation point exceeds $\angle c_{f,1} = -\pi/2$, i.e. even precedes pressure fluctuations required to accelerate the flow. This is probably caused by the recirculation zone.

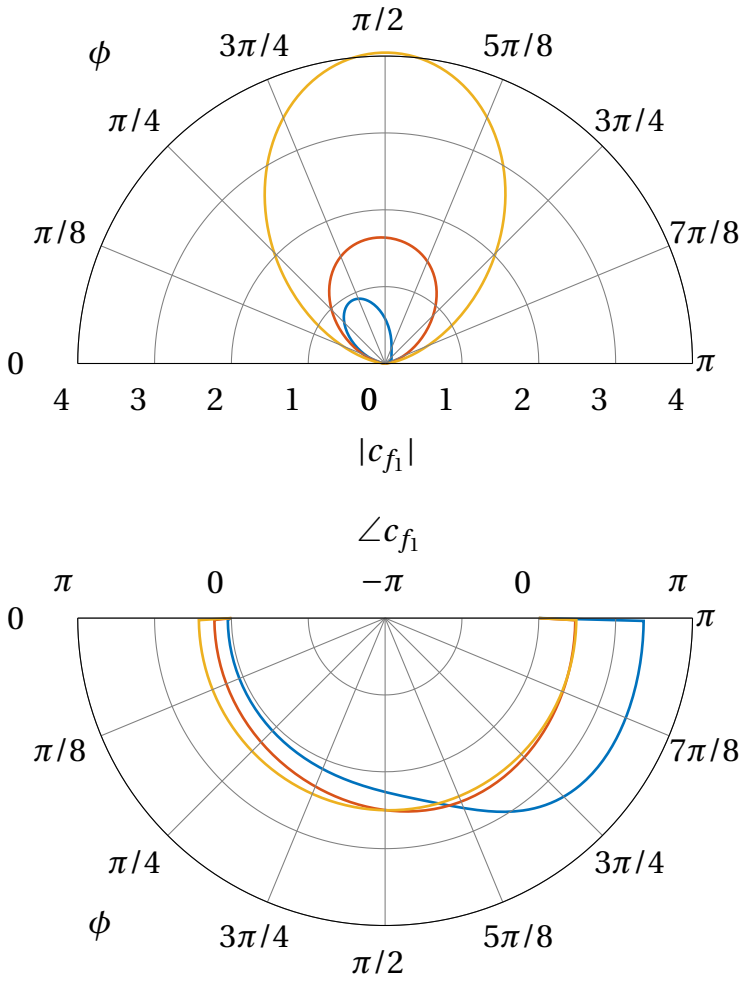

Figure 7.23: Friction Coefficient Distribution at $\mathrm{Re}_0 = 40$**.** $\mathrm{Sr} = 0.5$ (——), $\mathrm{Sr} = 7$ (——), and $\mathrm{Sr} = 40$ (——).

7.5 Discussion

Three different representations of the spatial distribution of fluctuations in flow quantities have been shown in this section. The flow fields acquired from the step response give a detailed insight into the temporal evolution of the velocity field and the temperature field close to the cylinder. The same detail is depicted for periodic forcing computed with the LNSE. This illuminates the dynamic behavior from a frequency space point of view, which is the basis for the transfer functions. Also computed with the linearized solver are the circumferential distributions of the Nußelt number and friction coefficients. They are a direct result of the surface normal gradients in the LNSE flow fields at certain Strouhal numbers. All of these representations shed light on the dynamic behavior of the heat transfer and the skin friction as well as the distinct features of the respective transfer functions.

Deviations from models reported previously, especially the model by Lighthill (1954), can be physically motivated and explained. Most notably, the peak gain phenomenon and the phase lag in the heat transfer as well as the low-frequency behavior of the skin friction. The latter is very uniquely linked in its time scales to the cylindrical shape.

In the light of these investigations, the analytical approach by Lighthill (1954, cf. Section 3.2.2) can be reassessed. In short, Lighthill's assumptions and simplifications can be summarized as follows: (1) The boundary layer equations were used to describe the flow. Lighthill (1954) then treated these equations differently for the limit of low and high frequencies. He later identified Sr = 20 as the frequency where both limiting solutions approximately matched for the skin friction. (2) High frequencies were assessed using the solution of Stokes' second problem (Stokes, 1851, cf. Section 3.1.2). (3) For low frequencies, the term including the frequency parameter (Strouhal number) could not be assumed small, and hence, simplifications similar to those made by Stokes were not possible. Instead, Lighthill used an integral Kármán–Polhausen treatment (Schlichting and Gersten, 2006). (4) The parameters for the fourth order polynomial profiles were taken from solutions for the flat plate boundary layer (Blasius layer) and the stagnation point flow (Hiemenz layer) (Schlichting and Gersten, 2006).

From the steady-state flow fields depicted in Section 7.1, it already becomes evident that the notion of a boundary layer (assumption 1) does not apply to the flow around a cylinder with mean flow Reynolds numbers of $\mathrm{Re}_0 = 0.4$ and $\mathrm{Re}_0 = 4$ (Figure 7.1 and Figure 7.2, respectively). Even at $\mathrm{Re}_0 = 40$, the zone disturbed by the flow is not only a thin layer (Figure 7.3). Lighthill (1954) stated that his approximate solution should be valid above $\mathrm{Re}_0 > 10$, but this limit has to be raised in the light of this investigation. This is noteworthy inasmuch as most Rijke tubes operate at mean flow Reynolds numbers below $\mathrm{Re}_0 < 40$ (cf. Table 3.1).

Lighthill (1954) built his model on the observation that the major part of the heat transfer occurs in the front quadrant of the cylinder (assumption 4). The findings in this thesis confirm this also for the fluctuations and even for lower Reynolds numbers. However, still a significant part of the heat transfer occurs at angles $\phi > \pi/4$. This also points to one of the main limitations in any study using the boundary layer equations to describe the flow (assumption 1).

The heat transfer at the lee side of the cylinder (sector 4 at angles $\phi > 3\pi/4$) is not negligible and has a different phase than the windward part of the cylinder (cf. Figure 7.20 and Figure 7.21). It causes the theoretical phase limit of $\angle G_{\mathrm{Nu}} > -\pi/2$ at $\mathrm{Sr} \to \infty$ predicted by Lighthill (1954) never to be reached. Using Stokes' solution for the high frequency behavior cannot represent this as Stokes developed it for a flat plate (assumption 2). Also, the low frequency approximation, which is a first order time lag system, has the same theoretical limit of $\angle G_{\mathrm{Nu}}(\mathrm{Sr} \to \infty) = -\pi/2$ and can-

not represent this phenomenon. For the skin friction at high frequencies, however, Stokes' second problem (cf. Section 3.1.2) is a good approximation even for curved geometries like the cylinder.

Föller and Polifke (2012) also reported that the limiting frequency was above $\angle G_{\mathrm{Nu}} > -\pi/2$. However, the recirculation zone, as proposed by Föller and Polifke (2012), can now be ruled out as a cause for this difference in phase because no recirculation occurs at $\mathrm{Re}_0 = 4$. The enlarged phase limit occurs predominately at low mean flow Reynolds numbers. Inspecting the solution by Bayly (1985), which specifically treats $\mathrm{Re}_0 < 1$, reveals also phase values above $\angle G_{\mathrm{Nu}} > -\pi/2$ at high Strouhal numbers. However, the limit of Bayly's formula is still $-\pi/2$ which is reached through a prolonged descent.

Assumption (3) was not assessed in further detail in this thesis. However, it can be assumed that a fully resolved solution of the incompressible Navier–Stokes equations is more accurate than the integral treatment approximating velocity profiles and temperature profiles by fourth order polynomials.

8 Low Order Parametrized Model for Heat Transfer

The identified models presented in Chapter 6 for the heat transfer show very good agreement with the data acquired from CFD simulations. Each model can be seen as the best fit for the respective mean flow Reynolds number. To acquire a model for mean flow conditions not reported in this thesis, an interpolation technique can be used: For the two models at the conditions closest to the desired one, the impulse response has to be computed. Ideally, this is done in discrete time at the desired sampling rate. Linear interpolation between two coefficients of different models representing the same time lag is subsequently used to acquire a new impulse response coefficient at every time lag. The new model can be used as an FIR model directly, or as data for the identification of a new transfer function in the desired framework. The work shown here was previously published in parts in Witte and Polifke (2016, 2019).

In this chapter, a different approach is pursued. Simple models for the dynamics of the heat transfer have been used in the past. Especially in modeling the heat transfer dynamics of the Rijke tube, two model types stand out: the n-τ model and the PT1 time lag model. In most of the literature associated with the modeling of thermoacoustic oscillations in a Rijke tube one of these models is used (cf. Table 3.1). In this chapter, a PT1 model including the mean flow Reynolds number as a parameter is proposed. The complexity is reduced to yield a model in the manner of Lighthill (1954) or Bayly (1985).

The n-τ model and the PT1 model are introduced in Section 8.1 as simple models for heat transfer behavior with some desirable properties. Both models are compared, and the strengths and weaknesses of each model type are reported. A first order time lag model parametrized with the mean flow Reynolds number is presented in Section 8.2. The chapter concludes with three case studies showing the impact of temperature dependent fluid properties, i.e. different Prandtl numbers, different cylinder temperatures, and amplitude in the order of the mean flow Reynolds number (cf. Section 8.3).

8.1 Low Order Models

Low order models are popular in the modeling of thermoacoustic devices. On the one hand, they offer certain mathematical advantages over more sophisticated methods and can be used in pen and paper calculations as well as for educated guesses. On the other hand, the accuracy provided by these low order methods is not as good as the accuracy of the individually identified models but probably still within the margins of other uncertainties.

8.1.1 $n-\tau$ Model

A model for low frequencies, very often used in thermoacoustic applications, is that of a time delayed heat transfer, the so-called $n-\tau$ model. It assumes that an output depends only on one past input which occurred some time τ in the past, scaled with the interaction index n. Time and frequency domain representations are given by

$$y_{\mathrm{Nu}} = n\, u_{\mathrm{Re}}(t - c_\tau) \quad \text{and} \tag{8.1}$$

$$G_{\mathrm{Nu}} = n\, \mathrm{e}^{-\mathrm{i}\mathrm{Sr}\, c_\tau}, \tag{8.2}$$

with the dimensionless time constant $c_\tau = \tau \cdot u_{0,\infty}/d$. The scaled pulsation in Nußelt number $\mathrm{Nu}'/\mathrm{Nu}_0$ is again denoted by y_{Nu} and likewise for the Reynolds number pulsations u_{Re}. In the frequency domain, it has a constant gain of n, and the phase decreases linearly with slope $-c_\tau$.

This model is especially interesting for computations in the time domain. As a discrete model, the impulse response has only one nonzero coefficient which considerably simplifies calculations compared to other dynamic models. It can also be used in conjunction with the theory of delayed differential equations.

8.1.2 PT1 Model

The PT1 model is a continuous time transfer function of order one. It follows the structure outlined in Equation (4.24), but with only one parameter for numerator and denominator. It reads

$$G(s) = \frac{b_0}{1 + a_1\, s}. \tag{8.3}$$

The numerator coefficient $b_0 = K$ is the steady-state gain and the coefficient of the denominator is a time constant a_1.

The PT1 model, like the $n-\tau$ model, has two parameters. Under the assumption of a positive time constant, the system is always BIBO stable. However, its impulse

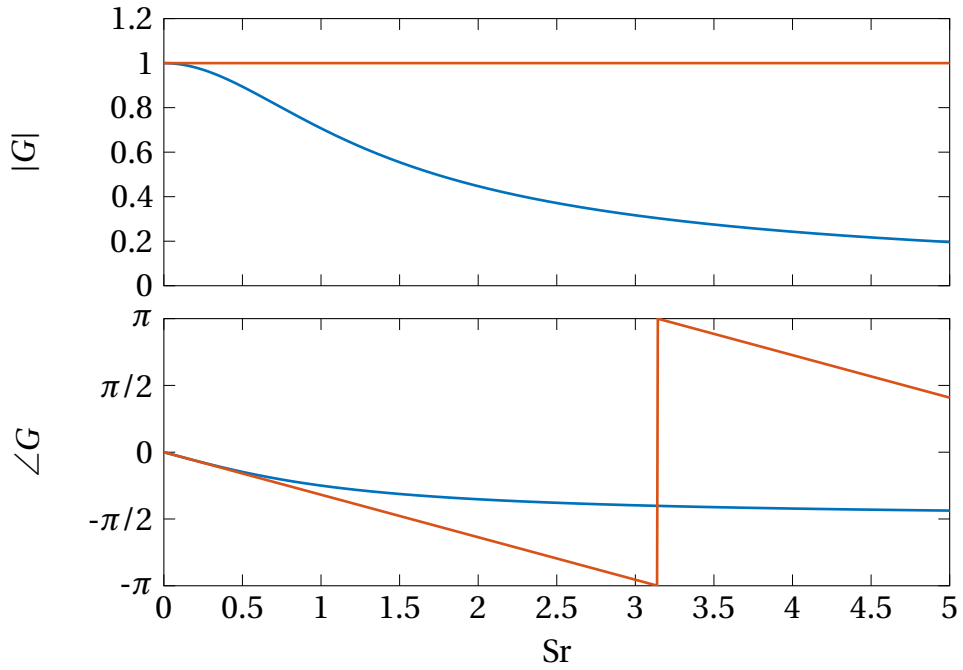

Figure 8.1: Frequency Response of PT1 and $n-\tau$. Amplitude (top plot) and phase (bottom plot) of the frequency responses with interaction index/steady-state gain $n = K = 1$ and time constant $c_\tau = 1$.

response can become arbitrarily long depending on the time constant. In the frequency domain, this is the simplest representation of a low-pass filter which fulfills the condition that the amplitude approaches zero $G(s) \to 0$ in the limit of high frequencies $s \to \infty$.

8.1.3 $n-\tau$ Model as Linearization of First Order Lag

PT1 model and $n-\tau$ model are related in that sense that the slope of the phase of the frequency response at zero frequency can be perceived as originating from a time lag c_τ. This relationship can be seen in the phase graph in the bottom plot of Figure 8.1 where both models coincide at low frequencies.

Another point of view is that the PT1 model can be acquired from a Taylor expansion of the $n-\tau$ model. The $n-\tau$ model is given in Equation (8.1). A response is caused by a signal that occurred at a dimensionless time $t-c_\tau$ in the past. This is equivalent to saying a signal will cause a response at $t+c_\tau$ in the future. Hence, the model is reformulated to

$$y_{\mathrm{Nu}}(t+c_\tau) = n\, u_{\mathrm{Re}}\,. \tag{8.4}$$

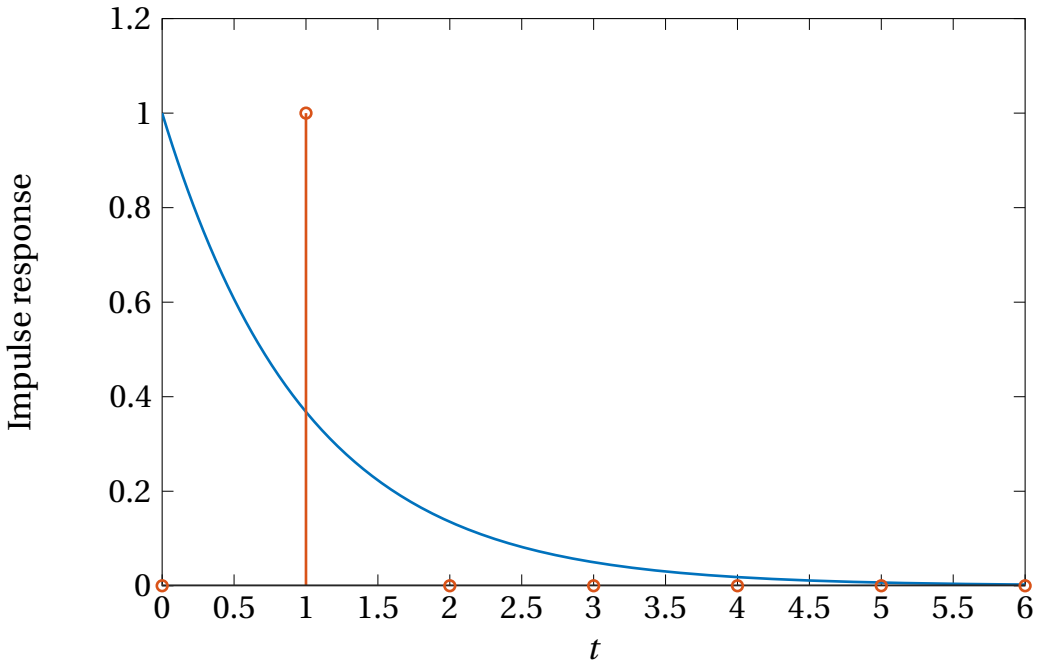

Figure 8.2: Impulse Response of PT1 and $n-\tau$. Interaction index/steady-state gain $n = K = 1$ and time constant $c_\tau = 1$.

Applying a Taylor series expansion around t and omitting terms of order $\mathcal{O}(c_\tau^2)$ and higher yields

$$y_{\mathrm{Nu}}(t) + \frac{\partial y_{\mathrm{Nu}}}{\partial t} c_\tau = n\, u_{\mathrm{Re}}(t)\,. \tag{8.5}$$

This ordinary differential equation is the time domain equivalent to the PT1 model with $n = b_0$ and $c_\tau = a_1$.

Figure 8.2 shows the impulse response of a PT1 model (continuous time) and a $n-\tau$ model (discrete time). Both the interaction index/steady-state gain and the time constant, are set to unity, i.e. $n = K = 1$ and $c_\tau = 1$, respectively.

8.1.4 Comparison of Low Order Parametrized Models

The advantage of the pure time delay model ($n-\tau$ model) is that the convolution equation, necessary to determine the heat transfer for any velocity perturbation in the time domain, is a simple multiplication and thus reduces complexity. However, compared to a first order transfer behavior, i.e. Equation (3.34) or Equation (8.3), it is important to note that the differences in amplitude and phase increase with frequency. The deviation can be assessed by analyzing the quantity $c_\tau \cdot \mathrm{Sr}$. The time constant is the inverse of the cutoff frequency of the first-order system and $\mathrm{Sr}_c = 1/c_\tau$ is the cutoff Strouhal number. Hence, $c_\tau \cdot \mathrm{Sr} = 1$ corresponds to the cutoff frequency. At this frequency, the difference in amplitude is already around 30 % relative to the

steady-state value and about 12° (0.068π) in phase. At $c_\tau \cdot \mathrm{Sr} = 3$, i.e. three times the cutoff frequency, the amplitude of the $n-\tau$ model is more than 384 % too high, and the difference in phase is greater than $\pi/2$. These values can be observed in Figure 8.1 where $n = K = 1$ and $c_\tau = 1$ and hence the cutoff frequency of the PT1 model is $\mathrm{Sr}_c = 1$.

This is noteworthy inasmuch as Rijke tubes may operate in this regime. Matveev (2003a) for example reported working conditions ($\mathrm{Re} \approx 2.3$, $\mathrm{Sr} \approx 4.0$) leading to a value of $c_\tau \cdot \mathrm{Sr} \approx 4.5$ considering Equation (8.6) for the time constant.

8.2 Parametrized First Order Time Lag Model

Following the model by Lighthill (1954, cf. Equation (3.34)) approximations to the higher order identified transfer functions are given as a PT1 model. This is possible because the dynamic behavior is governed to a large extent by only one time lag and a steady-state gain. For all mean flow Reynolds numbers, the steady-state gain and time constant were determined by identifying a transfer function with one free parameter for the numerator and the denominator respectively using continuous time identification (cf. Section 4.4.5). Through nonlinear regression over K and c_τ of 12 identified models in the range $0.1 \leq \mathrm{Re}_0 \leq 40$, respectively, the following correlations were found:

$$K = 0.25\,\mathrm{Re}_0^{0.2} \qquad \text{and} \quad c_\tau = 1.8\,\mathrm{Re}_0^{-0.8} + 0.2 \tag{8.6}$$

With these expressions the PT1 model proposed as low order model for the heat transfer oscillations caused by pulsations in free-stream velocity reads

$$G_{\mathrm{Nu}}(\mathrm{Sr}, \mathrm{Re}) = \frac{0.25\,\mathrm{Re}_0^{0.2}}{1 + \left(1.8\,\mathrm{Re}_0^{-0.8} + 0.2\right)\mathrm{i}\,\mathrm{Sr}}\,. \tag{8.7}$$

The goodness of fit (NRMSE-fit Φ) for the models by Lighthill (1954) and Bayly (1985) as well as the first order approximation presented here is shown in Figure 8.3. Additionally, the Φ-values for the best identified models (at a specific mean flow Reynolds number) are given, which correspond to the frequency responses reported in Section 6.4.

As already reported by the respective authors, Lighthill's and Bayly's models have limited validity in the range $0.1 \leq \mathrm{Re}_0 \leq 40$. Bayly's model shows high accuracy for $\mathrm{Re}_0 \to 0$, but should not be used for Reynolds numbers above $\mathrm{Re}_0 = 0.5$. Lighthill states that his model is applicable if a laminar boundary layer exists and gives $\mathrm{Re} > 10$ as the limit. However, better accuracy can be achieved by using the Reynolds number dependent model presented here.

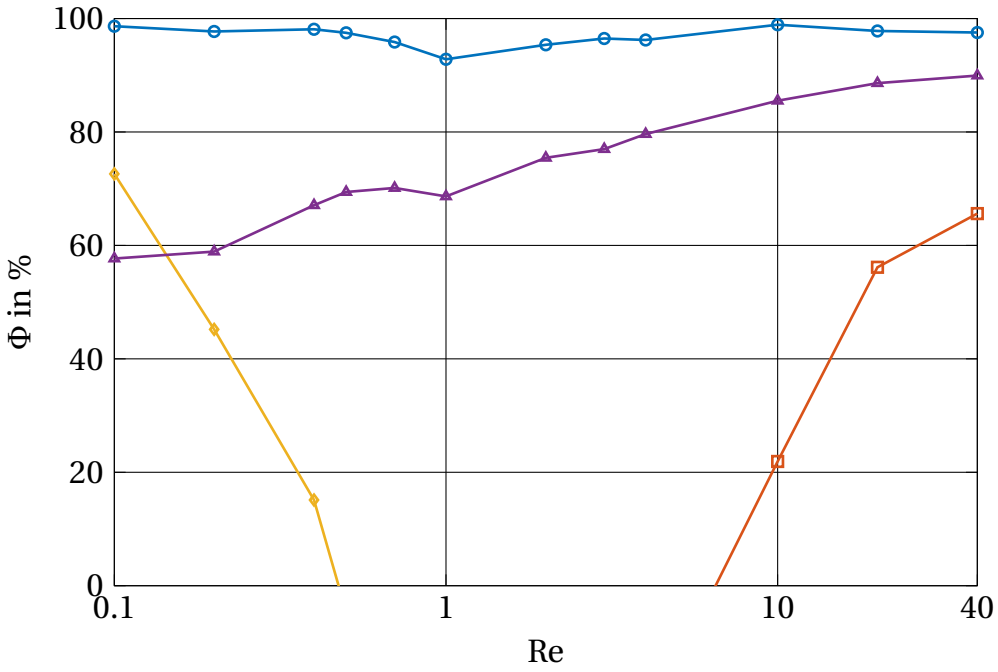

Figure 8.3: NRMSE-Fit of Different Models. Output from Lighthill (—◆—), Bayly (—□—) The first order approximation presented here (—▲—) and the identified models providing the best fit (—○—).

8.3 Limitations and Corrections of the PT1 Model

The mean flow Reynolds number is one of the most important parameters, especially in the range of low Reynolds numbers as they occur in Rijke tubes. Nevertheless, there are other parameters not explicitly accounted for in the PT1 model presented in this thesis. This includes the Prandtl number of the flow, the actual temperature difference between wire and free-stream, and the amplitude of the oscillations in the flow velocity.

8.3.1 Influence of Prandtl Number

The Prandtl number is a parameter in the incompressible Navier–Stokes equations, more precisely in the temperature equation (Equation (2.65)). It can be seen as the ratio of the boundary layer thicknesses and is therefore directly related to the dynamic behavior. All simulations for this thesis were conducted with Pr = 0.7123, which is a common value for air at ambient conditions.

Figure 8.4 and Figure 8.5 show the frequency responses of the heat transfer at mean flow Reynolds numbers $\mathrm{Re}_0 = 4$ and $\mathrm{Re}_0 = 40$, respectively, at different Prandtl numbers. The responses were evaluated with the LNSE approach (cf. Section 5.4) and for several Prandtl numbers in the range $0.5 \leq \mathrm{Pr} \leq 10$. This covers most gases and also

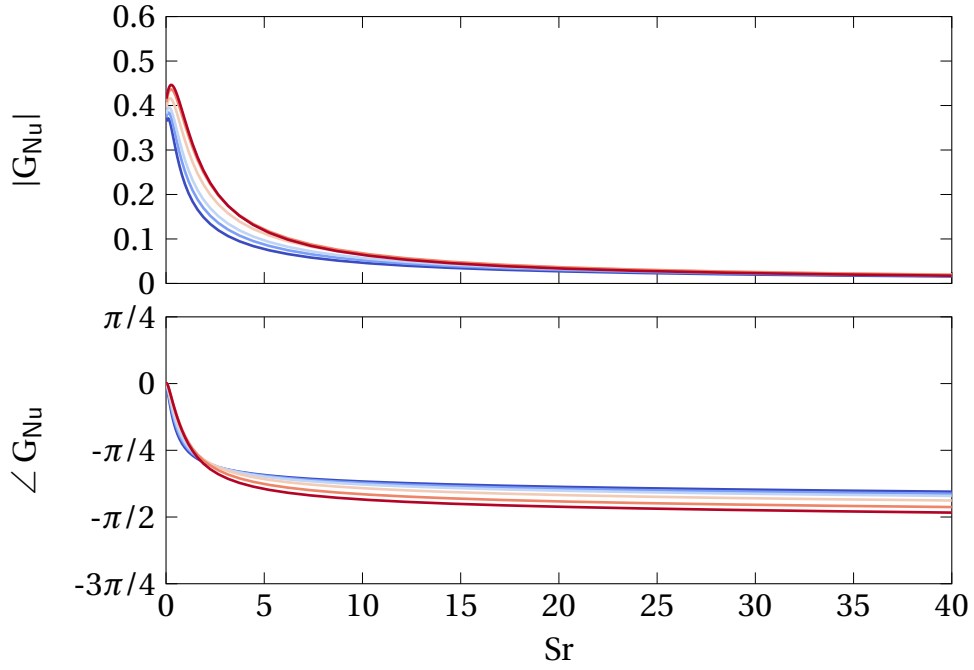

Figure 8.4: Frequency Response of Heat Transfer at $Re_0 = 4$ and Various Pr. Amplitude (top) and phase (bottom) at Pr = 0.5 (—), Pr = 0.7123 (—), Pr = 1.0 (—), Pr = 2.0 (—), Pr = 5.0 (—), and Pr = 10.0 (—).

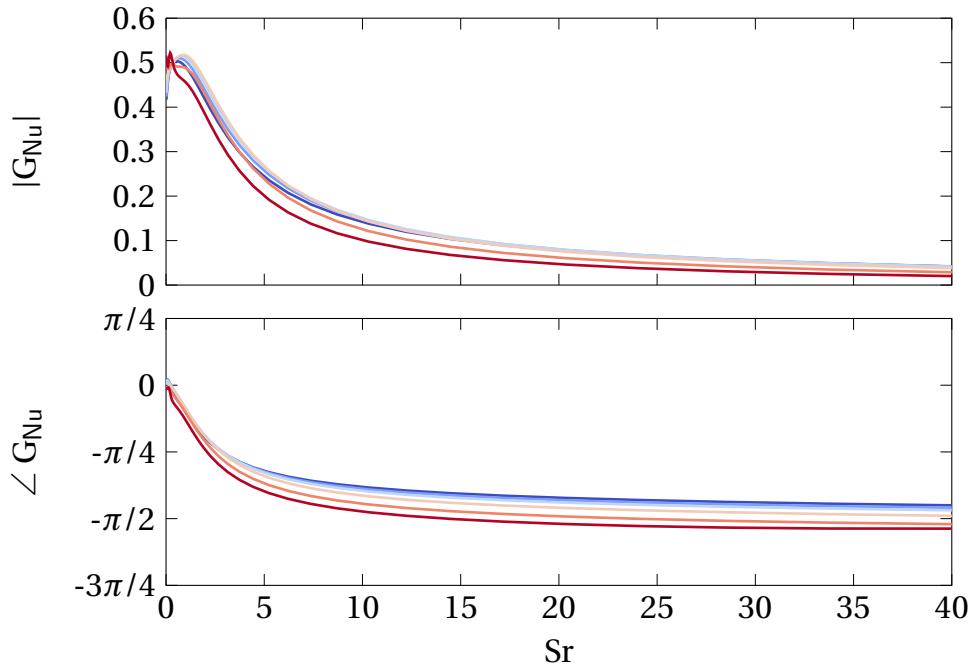

Figure 8.5: Frequency Response of Heat Transfer at $Re_0 = 40$ and Various Pr. Amplitude (top) and phase (bottom) at Pr = 0.5 (—), Pr = 0.7123 (—), Pr = 1.0 (—), Pr = 2.0 (—), Pr = 5.0 (—), and Pr = 10.0 (—).

some liquids like water. For gases, for which the Prandtl number is usually between $0.5 \leq \mathrm{Pr} \leq 1.0$, Pr has only a minor influence and may be negligible for most purposes. Higher Prandtl numbers have a similar effect as higher Reynolds numbers. The amplitude of the frequency response has a greater low-frequency limit, and the peak around $\mathrm{Sr} \approx 1$ is more pronounced. Moreover, the dominant time scale becomes smaller which manifests in the phase of the frequency response as a less steep initial descent.

8.3.2 Influence of Absolute Temperature

A much more important factor than the Prandtl number for many applications is the actual temperature difference between the surface of the cylinder and the free-stream. If the temperature at the surface of the cylinder is substantially different from the flow temperature, the fluid parameters are not constant and lead to a different dynamic behavior. The small temperature difference assumption, introduced for most computations in this thesis, allowed to reduce the complexity of the CFD simulations and to compare the results with other studies.

The influence of the cylinder temperature was surveyed using the full compressible Navier–Stokes equations (Equation (2.28)–(2.32)) together with SI (CFD/SI). The computational procedure was the same as detailed in Section 5.2 and the fluid properties were evaluated using the instantaneous temperature field as well as the laws given in Section 2.2.2 for air. An ambient temperature of 300 K was chosen for the computations, and the temperature of the cylinder was determined by a temperature difference ΔT. Four temperature differences, $\Delta T = 10\,\mathrm{K}$, $\Delta T = 100\,\mathrm{K}$, $\Delta T = 300\,\mathrm{K}$, and $\Delta T = 600\,\mathrm{K}$, were assessed at mean flow Reynolds numbers $\mathrm{Re}_0 = 4$ and $\mathrm{Re}_0 = 40$. The first ΔT is well within the limits of small temperature differences while the latter corresponds to a cylinder temperature of 626.85 °C. A heated wire would show a faint red glow at this temperature. The numerical procedure was also adapted from the incompressible simulations. This also includes the time step size, which means that acoustic waves were underresolved and the acoustic CFL number was much greater than unity.

The frequency response at different ΔT is depicted in Figure 8.6. The color of the graph indicates the temperature from blue to red. For comparison, the frequency responses assessed with the incompressible Navier–Stokes equations at $\mathrm{Re}_0 = 2$ and $\mathrm{Re}_0 = 4$ are included as dashed lines. The frequency response at the lowest temperature difference matches fairly well with the response from the incompressible Navier–Stokes equations at the same mean flow Reynolds number. The largest difference is visible in the phase at high frequencies. This is due to the fact that the assumption of acoustical compactness becomes weaker at high frequencies (high Helmholtz numbers, cf. Section 2.4.2). The time it takes for an acoustic pulsation to reach the cylinder is infinitely small in the case of the incompressible Navier–

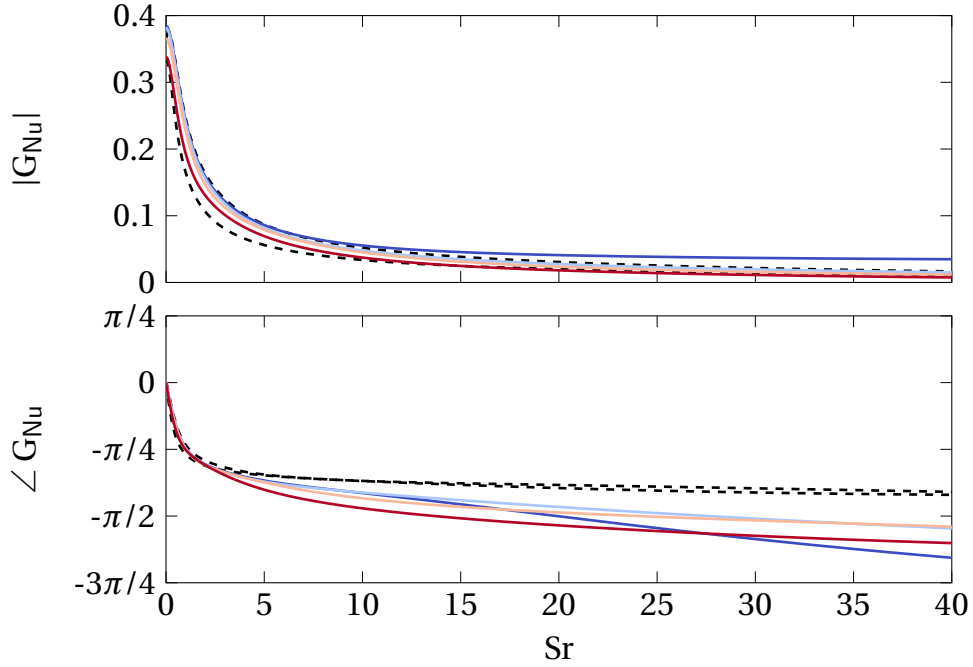

Figure 8.6: Frequency Response of Heat Transfer at $\mathrm{Re}_0 = 4$ and Different ΔT. Amplitude (top) and phase (bottom) at $\Delta T = 10\,\mathrm{K}$ (——), $\Delta T = 100\,\mathrm{K}$ (——), $\Delta T = 300\,\mathrm{K}$ (——), and $\Delta T = 600\,\mathrm{K}$ (——). For reference, the frequency response for $\mathrm{Re}_0 = 4$ and $\mathrm{Re}_0 = 2$ (incompressible) are shown (- - -).

Stokes equations. When the compressible Navier–Stokes equations are solved, the finite propagation speed leads to slightly higher phase lags. However, the complete system, consisting of data acquisition plane and cylinder with an extent of approximately $9\,d$, is still acoustically fairly compact ($\mathrm{He} \lesssim 0.1$, c.f. Section 9.1.3). Higher temperature differences, i.e. higher cylinder temperatures, lead to a reduction in amplitude of the frequency response. At $\Delta T = 600\,\mathrm{K}$, the frequency response is comparable to lower mean flow Reynolds numbers. This effect can be explained by the influence of the temperature on the fluid properties. The fluid close to the cylinder heats up substantially, resulting in a higher viscosity. This, in turn, implies a smaller Reynolds number. To account for this effect, an effective mean flow Reynolds number can be calculated from the arithmetic mean of the free-stream viscosity and the viscosity at the cylinder temperature. With this effective Reynolds number, Equation (8.7) can be used with reasonable accuracy at higher temperature differences.

At a mean flow Reynolds number of $\mathrm{Re}_0 = 40$, this tendency is reversed. As depicted in Figure 8.7, the amplitude reaches higher values, and the peak gain is more pronounced. This could be attributed to the thermal conductivity of air, which rises with rising temperature. The lowest temperature difference ($\Delta T = 10\,\mathrm{K}$) produced results with rising amplitude towards higher frequencies. This was unexpected, since higher temperature differences, as well as the quasi-isothermal simulation, do not exhibit this behavior. It is, therefore, most likely an artifact occurring at

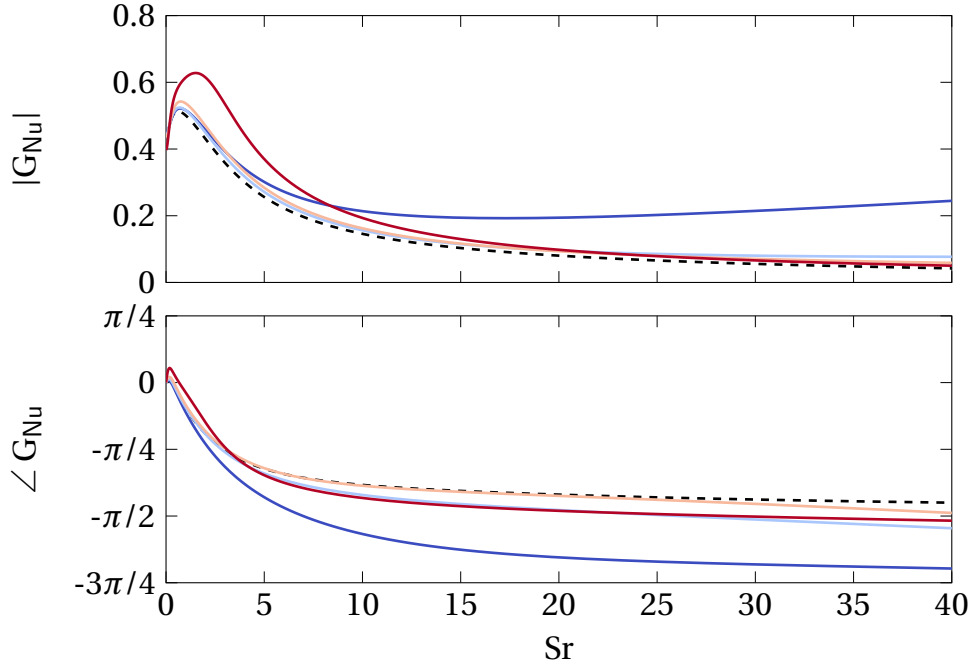

Figure 8.7: Frequency Response of Heat Transfer at $\mathrm{Re}_0 = 40$ and Different ΔT. Amplitude (top) and phase (bottom) at $\Delta T = 10\,\mathrm{K}$ (—), $\Delta T = 100\,\mathrm{K}$ (—), $\Delta T = 300\,\mathrm{K}$ (—), and $\Delta T = 600\,\mathrm{K}$ (—). For reference, the frequency response for $\mathrm{Re}_0 = 40$ (incompressible) is shown (- - -).

high frequencies and low temperature differences in fully compressible simulations. Temperature differences up to $\Delta T = 300\,\mathrm{K}$, however, match fairly well with the incompressible solution. The most distinct feature is the peak gain at $\Delta T = 600\,\mathrm{K}$ which is more pronounced and shifted towards higher frequencies than at lower temperature differences.

8.3.3 High Amplitudes

The constraint to small amplitudes, as it was chosen in this thesis to stay within the framework of an LTI system, may be too restrictive in some cases. In the Rijke tube, for example, amplitudes can be as high as the mean flow itself when a limit cycle, i.e. a state of quasi-steady high-amplitude oscillations, is reached Matveev (2003b). With an LTI model, the initial stability and growth rates can be assessed, but not the high amplitude behavior due to its nonlinear nature. Selimefendigil (2010) investigated the nonlinear behavior of the heat transfer of a cylinder in pulsating crossflow (Selimefendigil and Polifke, 2011; Selimefendigil et al., 2012). More information on the nonlinear behavior was also given by Orchini et al. (2016).

In this thesis, only a glimpse at the nonlinear behavior in the form of high-amplitude periodic oscillations is provided. The results shown here are based on

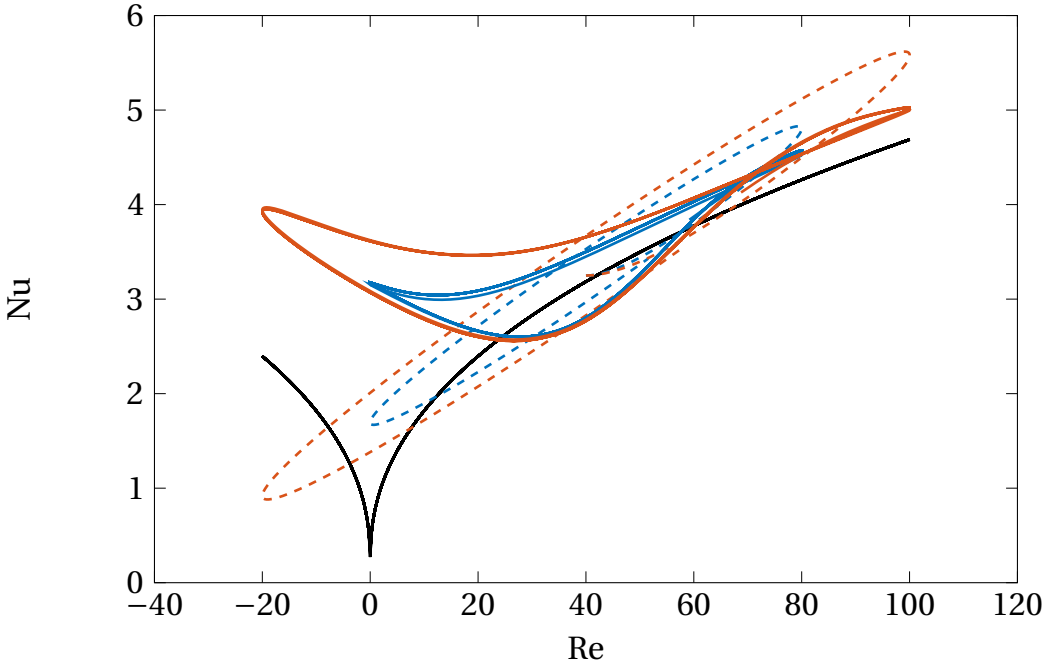

Figure 8.8: Nußelt Number for Sinusoidal Fluctuations of Sr = 0.5 at $Re_0 = 40$. Steady-state correlation by Collis and Williams (1959) (——), oscillations simulated with linear model and amplitude $\epsilon = 1.0$ (- - -), oscillations simulated with linear model and amplitude $\epsilon = 1.5$ (- - -), CFD simulation with amplitude $\epsilon = 1.0$ (——), CFD simulation with amplitude $\epsilon = 1.5$ (——).

a bachelor's thesis by Çalak (2017) supervised by the author of this thesis. Figure 8.8 depicts the Reynolds number and the Nußelt number as acquired from simulations with monofrequent modulation of the inlet velocity. The black line shows the steady-state correlation by Collis and Williams (1959) (cf. Equation (2.23)). The solid blue and red lines show the evolution of Re and Nu acquired from simulations with relative excitation amplitudes of 100 % and 150 % of the mean flow Reynolds number, respectively. The velocity was forced at Sr = 0.5 and a mean flow Reynolds number $Re_0 = 40$. The dashed lines represent the respective response from identified linear models.

Especially when the flow decelerates, i.e. at low instantaneous Reynolds numbers, the simulated response differs from the linear models and the steady state. The latter is due to the dynamic behavior in general, which at a Strouhal number of Sr = 0.5 differs considerably from the steady state. The outputs of the linear models appear as perfect ellipses with position and size determined by the input and the transfer function. The true response, however, is subject to nonlinearities which lead to a distortion of the ellipse. This distortion is already quite articulate at $Re_0 = 20$. This is in accordance with the observation , e.g. by Heckl (1990) that nonlinearities become eminent at amplitudes of 30 % and above.

From Figure 8.8, it can also be seen that dynamic response and amplitude are not interdependent. The identification of a Wiener–Hammerstein model (Tangirala, 2014, p. 781), a simple nonlinear model incorporating an OE model for the dynamics, did not yield significant improvement over purely linear models. With a Wiener–Hammerstein model, it is possible to skip the linearization and scaling steps in the data preparation, but the nonlinearity is added as one or two separate blocks, separating dynamics and nonlinearity. However, the NRMSE-fit of the linear model to data acquired from broadband simulation with amplitudes up to 150 % was still $\Phi > 80\,\%$. This means that even in the case of amplitudes higher than the linear limit, the linear models perform adequately as long as the determination of the exact pulsation amplitude is not the primary purpose. Even higher amplitudes, however, will lead to worse model fits due to the discrepancy between model output and CFD simulation data visible at low and negative Re.

8.3.4 Discussion

In this chapter, well known low order models used in the modeling of Rijke tubes were introduced. Building upon this foundation a new low order PT1 model for the heat transfer dynamics with the mean flow Reynolds number was introduced. It was developed from simulations at 12 different mean flow Reynolds numbers in the range $0.1 \leq \mathrm{Re}_0 \leq 40$ using SI methods. This newly developed model yields a better description of the time lagged dynamics than the $n-\tau$ model with just one time delay and constant amplitude. It was also shown that it performs considerably better than the analytical models reported by Lighthill (1954) and Bayly (1985) in the range of interest.

The new parametrized PT1 model was developed based on CFD simulations, performed with the incompressible Navier–Stokes equations, and identified with a linear model structure. Three different shortcomings of this approach have been addressed: Different Prandtl numbers, variable fluid properties in conjunction with large temperature differences, and high pulsation amplitudes. It was shown that the Prandtl number has a much weaker impact on the frequency response than the Reynolds number and can readily be omitted from the parametrization. Moreover, although the temperature difference between the free-stream and the surface of the cylinder has some influence on the dynamic behavior, it does not change it fundamentally and may be corrected with simple measures, e.g. an effective Reynolds number. The model is by its nature restricted to the linear regime. However, if excitation amplitudes do not exceed the mean flow too much, the parametrized PT1 model may still yield fair approximations of the true nonlinear dynamics. Excitation amplitudes up to $\epsilon = 1.5$, i.e. 150 % of the mean flow velocity, were examined. Reasonable agreement of $\Phi > 80\,\%$ was found for this case.

9 Aspects of Applications

Three different aspects of applications of a cylinder in pulsating crossflow will be presented in this chapter. The first application, detailed in Section 9.1, is the Rijke tube. This device was the main reason for the original study by Lighthill (1954) and likewise for the investigations in this thesis. Additionally, the hot-wire anemometer is discussed in this regard in Section 9.2. Not only pulsations in the magnitude of the velocity are considered but also a fluctuating angle of attack. Finally, the commonalities and differences between a cylinder in crossflow and a heat exchanger (HX) as used in domestic boilers are mentioned briefly in Section 9.3.

9.1 Rijke Tube

A Rijke tube, named after Pieter Leonard Rijke, who in 1859 was the first to describe its assembly and operation, is a prototype of a thermoacoustic device. Reviews on the subject were written by Feldman (1968) and Raun et al. (1993). A short survey of recent studies was given in Section 3.6. The response of the heat transfer between cylinder and fluid to fluctuations in flow velocity plays an important role in the Rijke tube. Thermal energy, introduced through a heated wire mesh, is transferred to acoustic energy, which can be experienced as audible sound. Prerequisites for this effect are a resonator tube, a mean flow through the tube, and proper positioning of the wire mesh. The Rijke tube is depicted schematically in Figure 9.1. A single wire of the mesh can be treated as a heated cylinder in crossflow.

A standing wave exists in the resonator tube similar to an organ pipe. The acoustic pulsations of the fluid velocity in the tube cause pulsations of the heat transfer rate. The transfer behavior between these velocity perturbations and the heat transfer is, therefore, an important parameter for the stability of thermoacoustic oscillations and the operation of the Rijke tube in general. This transfer behavior is described by the transfer functions developed in this thesis (cf. Chapter 6).

9.1.1 Mode of Operation

The mode of operation can be divided into an acoustic part, the mean flow, and the interaction of both causing thermoacoustic instabilities.

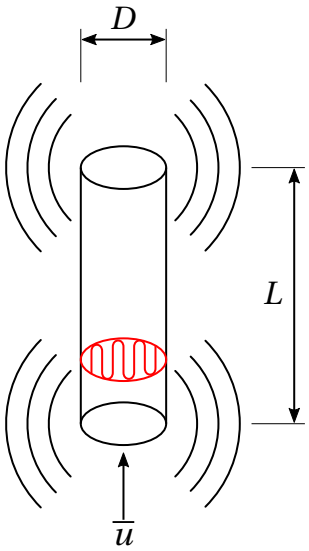

Figure 9.1: Sketch of a Rjike Tube. Basic dimensions and the mean flow are marked.

Acoustics

The Rijke tube is usually built as a short pipe from a rigid material such as aluminum, steel, or glass. Similar to an organ pipe, the gas column inside the tube has a natural frequency. Both ends of the tube are open. Hence, pressure nodes occur at the openings, and the tube serves as a half-wave resonator. The fundamental wavelength λ, neglecting end effects, is approximately twice the length of the tube $\lambda = 2L$. The Strouhal number of the fundamental frequency is hence given by

$$\mathrm{Sr} = \frac{\pi d}{L}\frac{1}{\mathrm{Ma}}. \tag{9.1}$$

Higher harmonics are integer multiples of this frequency. Although higher harmonics may occur, the focus is given to the fundamental mode only.

The temporal evolution of acoustic pressure and velocity within one cycle is shown in Figure 9.2. In the first graph, fluid exits the resonator at both ends. The velocity is positive with respect to the spatial coordinate direction x in the upper half of the resonator and negative in the lower half. The pressure in the tube decreases until the acoustic velocity reverses. This leads to a rise in pressure and in turn to the flow reversing again which closes the circle. This can be depicted in frequency space as spatial distribution of the amplitude of pressure and velocity as well as the phase shift between both (cf. Figure 9.3).

Mean Flow

In addition to the existence of a standing wave, another prerequisite is mean flow through the tube. A constant stream through the tube removes hot fluid and trans-

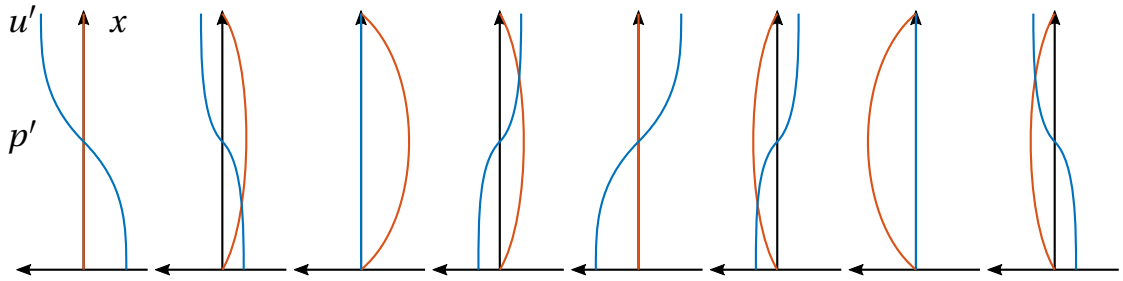

Figure 9.2: Acoustic Pressure and Velocity in a Tube (Time Domain). Time domain representation of velocity oscillations u' (blue) and pressure oscillations p' (red). One cycle is represented in eight steps corresponding to a phase difference of $\pi/4$ between each graph. Time advances from left to right ($x \in [0, L]$).

ports cold fluid to the heater. This results in a convective heat transfer between wire mesh and working medium. In other thermoacoustic devices, like the thermoacoustic engine, where no mean flow is present, this is facilitated by heat exchangers. The steady mean flow can either be forced by applying a pressure gradient or originate from buoyancy. In the first case, the Rijke tube is often arranged horizontally inducing the flow with a blower. Vertically arranged Rijke tubes usually rely on natural convection. In this case, hot fluid in the upper part of the tube has a lower density than the surroundings and is pulled upwards by buoyancy forces. This is counteracted by hydraulic losses. The temperature and thus the density of the hot fluid are determined by the heating power and the enthalpy transport caused by the flow. In both cases, flow through the tube can be quantified by a mean velocity, i.e. a mean flow Reynolds number

$$\mathrm{Re}_D = \frac{u_{0,\infty} D}{\nu} = \mathrm{Re}_0 \frac{D}{d}. \tag{9.2}$$

where D is the tube diameter. The flow is usually laminar or in the lower transitional regime.

Thermoacoustic Instability

If both prerequisites, resonator and (steady) heat transfer, are given, thermoacoustic instabilities may be excited. Rayleigh (Rayleigh, 1896) described this in what is now known as the Rayleigh criterion: If heat is added to a fluid parcel already compressed by the (acoustic) fluctuations, it will be compressed further. Thus, pressure fluctuations are amplified. In turn, if less heat is transferred to the fluid parcel during times of low pressure, i.e. compression by heating is comparatively small, pressure fluctua-

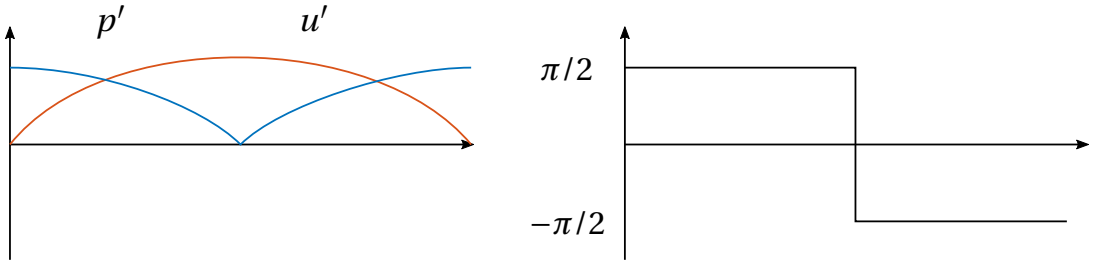

Figure 9.3: Acoustic Pressure and Velocity in a Tube (Frequency Domain). Frequency domain representation of velocity oscillations (blue) and pressure oscillations (red). Amplitude is shown on the left. The right graph represents the phase difference between p' and u'.

tions are amplified as well. This link between heat transfer and pressure demanding an in-phase behavior was later formalized as

$$RI = \oint p' \dot{Q}' \mathrm{d}t > 0\,. \tag{9.3}$$

RI is called the Rayleigh Index. In the case of the electrically heated Rijke tube, the heat flux $\dot{Q}$ is given by Newton's law of cooling by

$$\dot{Q} = \frac{\mathrm{Nu}\,k}{d}\,\pi\,d\,l_w\,(T_w - T_\infty) \tag{9.4}$$

where l_w is the length of the heated wire. Rearranging the definition of the transfer function of the heat transfer (Equation (2.100)), the Nußelt number can be written as

$$\mathrm{Nu} = \overline{\mathrm{Nu}}\left(1 + G_{\mathrm{Nu}}\frac{\mathrm{Re}'}{\overline{\mathrm{Re}}}\right). \tag{9.5}$$

Inserting Equation (9.5) in Equation (9.4) yields

$$\dot{Q} = K_Q\left(1 + G_{\mathrm{Nu}}\frac{\mathrm{Re}'}{\mathrm{Re}_0}\right) \tag{9.6}$$

with the constant factor $K_Q = \mathrm{Nu}_0\,k\pi\,l_w\,(T_w - T_\infty)$. Using only the fluctuating part of Equation (9.6), the Rayleigh integral can be rewritten to

$$RI = \frac{K_Q}{\mathrm{Re}_0}\oint p'\,G_{\mathrm{Nu}}\mathrm{Re}'\mathrm{d}t\,. \tag{9.7}$$

The Reyleigh criterion reads then

$$RI = \oint p'\,G_{\mathrm{Nu}}\mathrm{Re}'\mathrm{d}t > 0\,. \tag{9.8}$$

The Rayleigh criterion is a condition that is necessary, but not sufficient to cause instabilities.

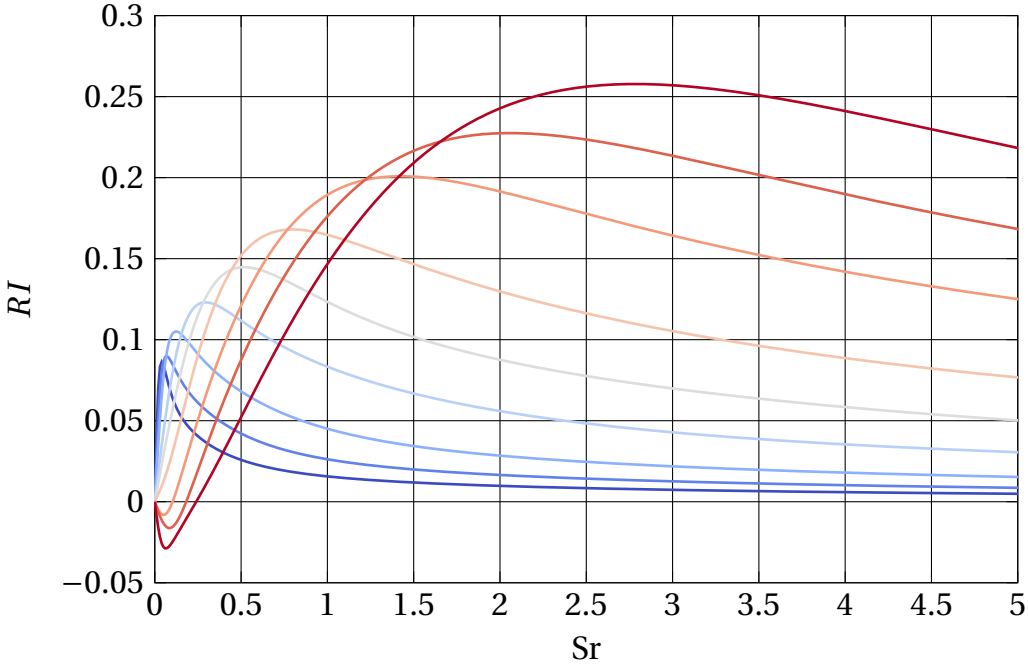

Figure 9.4: Normalized Rayleigh Index. Normalized RI computed for mean flow Reynolds numbers $\mathrm{Re}_0 \in \{0.1, 0.2, 0.4, 1, 2, 4, 10, 20, 40\}$ (blue to red).

It is evident that the transfer function G_{Nu} is an important parameter for the stability of the Rijke tube. For the following investigation, only the upstream part of the Rijke tube, where the pressure lags behind the velocity by $\pi/2$ is considered. This corresponds to the configuration of most Rijke tube test rigs where the heater is located approximately $1/4\,L$ from the inlet. However, this analysis can be made for the upper part with phase lag of $-\pi/2$ in an analogous manner. Without instantaneous heat transfer, the pressure and the velocity would be out of phase by $\pi/2$ resulting in $RI = 0$. Thus, neither infliction nor damping of thermoacoustic oscillations takes place. However, phase lag between pressure and heat transfer is $\pi/2 + \angle G_{\mathrm{Nu}}$ and hence the Rayleigh Index is positive if $-\pi < \angle G_{\mathrm{Nu}} < 0$.

To give a more detailed description, the Rayleigh Index is shown in Figure 9.4. It was computed for a series of mean flow Reynolds numbers in the range $0.1 \leq \mathrm{Re}_0 \leq 40$ and for Strouhal numbers in the range $0 \leq \mathrm{Sr} \leq 5$ with the transfer functions reported in Section 6.4.1. The amplitude of the oscillations in pressure and velocity (Reynolds number) were set to unity, so the depicted values can be seen as a normalized Rayleigh Index.

The Rayleigh Index shows similar tendencies as the amplitude of the frequency response at a certain mean flow Reynolds number, but there are several important differences owed to the phase of G_{Nu}. At low mean flow Reynolds numbers, the highest values for RI occur at small values of Sr. The maximum shifts towards higher Strouhal numbers for higher mean flow Reynolds numbers. Additionally, the higher

gain values at larger mean flow Reynolds numbers lead to higher maximum values in RI. At low Strouhal numbers and $\mathrm{Re}_0 \gtrsim 10$, the Rayleigh Index is even negative due to the phase lead in the transfer function of the heat transfer. The chart in Figure 9.4 can serve as a design criterion to achieve the desired instability in a Rijke tube. A rough estimate for the Strouhal number at which the normalized Rayleigh Index is at a maximum for a specific Reynolds number in the range $Re_0 \in [0.1, 40]$ can be given by

$$\mathrm{Sr}_{RI,\max}(\mathrm{Re}_0) = 0.44\sqrt{\mathrm{Re}_0}. \tag{9.9}$$

With this correlation, an optimal wire diameter in meters can be approximated with

$$d \approx 0.02\, L\, \mathrm{Re}_L\, \mathrm{Ma}^2, \tag{9.10}$$

where Re_L denotes the Reynolds number evaluated with the tube length L as characteristic length.

For a heater placed in the downstream half of the Rijke tube the plot in Figure 9.4 would be flipped at the abscissa. Hence, the heater dampens acoustic oscillations except for the case of $\mathrm{Re}_0 \geq 10$ and very low Strouhal numbers ($\mathrm{Sr} \approx 0.05$).

9.1.2 Significance of the Heat Transfer Model

The normalized Rayleigh Index can be used to demonstrate the significance of the dynamic heat transfer model. Figure 9.5 shows the normalized Rayleigh Index computed for different heat transfer models. Results computed with the CFD/SI method are depiced with solid lines and the same coloring as in Figure 9.4. Additionally, the normalized Rayleigh Index was computed using the PT1 model from Lighthill (1954) (dashed lines) and the $n-\tau$ model as used by Heckl (1988, dash–dotted lines). For the sake of completeness, the frequency responses of these models can be written as

$$G_{\mathrm{Nu}_i,\mathrm{Lighthill}} = \frac{0.5}{1+0.2\,\mathrm{Sr}} \qquad \text{and} \qquad G_{\mathrm{Nu}_i,n-\tau} = n\,\mathrm{e}^{-\mathrm{i}0.2\,\mathrm{Sr}}.$$

The range of Strouhal numbers was chosen to reflect the range found in the literature survey in Section 3.6, where in most cases $\mathrm{Sr} \in [0.5, 8]$.

The Rayleigh Index is an indicator for the amplification of acoustic pulsations in the Rijke tube. Other losses that are not included here would virtually increase the threshold of positive amplification to values higher than $RI = 0$. The plot shows that for lower mean flow Reynolds numbers the maximum in RI is located at lower Strouhal numbers. The results computed with the PT1 model by Lighthill (1954) and the $n-\tau$ model almost coincide due to the relationship between both models (cf. Section 8.1.3). Compared to the identified models, RI is drastically under-predicted.

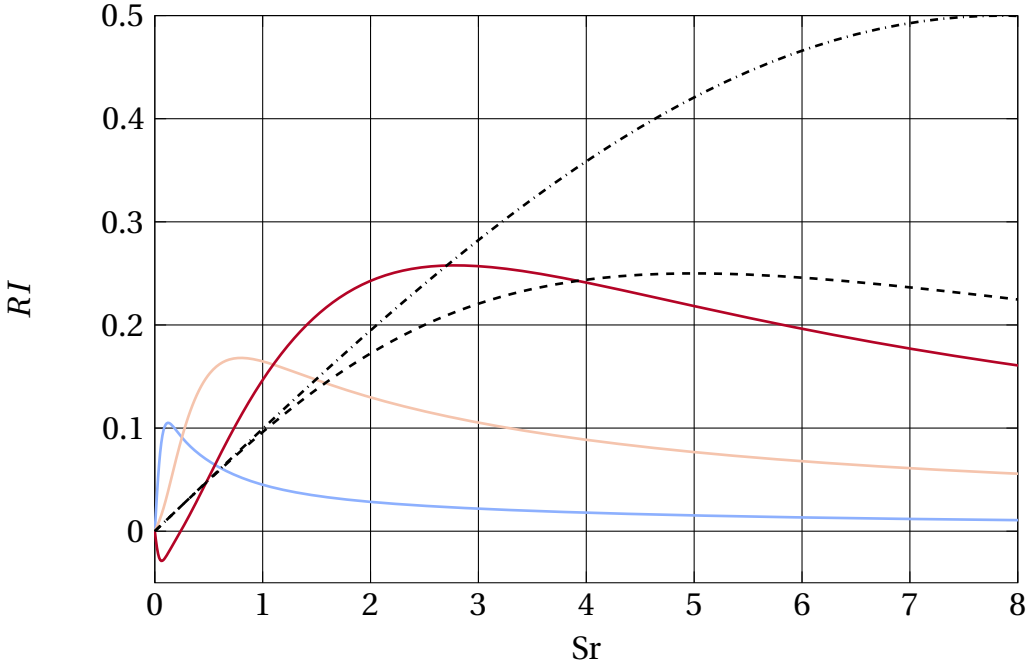

Figure 9.5: Comparison of the Normalized Rayleigh Index. Normalized RI from CFD/SI results for $\mathrm{Re}_0 = 0.4$ (——), $\mathrm{Re}_0 = 4$ (——), and $\mathrm{Re}_0 = 40$ (——), from Lighthill (1954) (- - -) and from the $n--\tau$ model (-·-·-) as used e.g. by Heckl (1988).

Towards higher Reynolds numbers, the RI computed from the identified models is more similar to the PT1 model by Lighthill (1954) and the $n-\tau$ model. However, only the identified models predict negative values of RI, which is due to the phase lead in the model. Above Sr = 3, the identified models for lower Reynolds numbers predict much lower values of RI than the PT1 and the $n-\tau$ model. The identified model for $\mathrm{Re}_0 = 40$ is fairly similar to Lighthill's PT1 model. The $n-\tau$ model, however, drastically over-predicts RI. This analysis sheds new light on results obtained with previously published models, e.g. by Lighthill (1954) and Heckl (1988) and emphasizes the significance of an accurate model for the heat transfer dynamics.

9.1.3 Justification of the Assumptions

In this thesis, certain assumptions have been invoked a priori to solve the governing equations (cf. Section 2.2.5). These assumptions are justified for the flow conditions found in Rijke tubes.

Low Mach Number

As can be seen from the Rayleigh Index in Figure 9.4, the transfer of thermal energy to acoustic energy is strongest at Strouhal numbers of order one for typical mean flow Reynolds numbers ($0.1 \leq \mathrm{Re}_0 \leq 40$). With the relationship between Mach number and Strouhal number given in Equation (9.1), the Mach number under these conditions is

$$\mathrm{Ma} \approx \frac{\pi\, d}{L}. \tag{9.11}$$

Usually, the wire diameter d is about three orders of magnitude smaller than the length of the resonator tube L. Hence, the Mach number is of order 10^{-3}, and the assumption of low Mach numbers is justified.

Low Helmholtz Number

In the case of a Rijke tube, the speed of sound is much larger than the free-stream velocity. Therefore, the Mach number is of order 10^{-3}. Indeed, even for moderate Strouhal numbers ($\mathrm{Sr} < 40$ in the present study) the Helmholtz number is also small $\mathrm{He} = \mathrm{Sr}\,\mathrm{Ma} \ll 1$. Thus, the region of heat transfer is "acoustically compact", i.e. its length is much smaller than the acoustic wavelength (Rienstra and Hirschberg, 2015; Telionis, 1981). This implies that an incompressible flow model is adequate.

Low Eckert Number

Lange et al. (1998) gave a relation between Nußelt number and viscous heating. The Nußelt number is corrected by

$$\frac{\Delta\mathrm{Nu}}{\mathrm{Nu}_0} = 0.4\mathrm{Ec}. \tag{9.12}$$

However, as it was established that $\mathrm{Ec} \sim \mathrm{Ma}^2$, viscous heating does not have a substantial influence in the case of the Rijke tube.

Overheating

The influence of the temperature difference (or overheating) ΔT is neglected in this work to ensure comparability to analytical methods. The influence in the steady state can be estimated from the correction factor of Nußelt number correlations.

Collis and Williams (1959) (cf. Equation (2.23)) gave the correction factor $(T_m/T_\infty)^{0.17}$, where T_m stands for the arithmetic mean between the temperature

of the cylinder and the inbound fluid with T_∞. This factor accounts for the temperature dependence of fluid properties like viscosity and thermal conductivity. It can be rewritten as $[1 + \Delta T/(2\,T_\infty)]^{0.17}$ indicating that low temperature differences between fluid and cylinder have negligible effect on the Nußelt number, e.g. for wire temperatures of $\Delta T = 200\,\mathrm{K}$ above a fluid temperature of $T_\infty = 300\,\mathrm{K}$ this term enlarges the Nußelt number by only 5% and less than 11% for $\Delta T = 500\,\mathrm{K}$.

In the correlation by Sparrow et al. (2004) (cf. Equation (2.24)), the correction factor is $(\mu/\mu_w)^{1/4}$. The temperature dependence of the dynamic viscosity is given by Sutherland's law (Equation (2.33)). This results in a Nußelt number reduced by 8.8 % for $\Delta T = 300\,\mathrm{K}$ and 15.5 % for $\Delta T = 500\,\mathrm{K}$ at an ambient temperature of 300 K.

Constant Wall Temperature

Heat conduction in the cylinder was not resolved. Instead, a constant temperature T_w on the surface of the cylinder was assumed. This assumption is also justified for Rijke tubes (Gelbert et al., 2012; Subramanian et al., 2010). A lumped thermal capacitance model (Baehr and Stephan, 2011; Bergman et al., 2011) is applicable, if the Biot number is much smaller than one $\mathrm{Bi} \ll 1$. The Biot number is linked to the Nußelt number by $\mathrm{Bi} = \mathrm{Nu} \cdot k_f/(2k_s)$ and thus correlates with Reynolds number by Equation (2.23) or Equation (2.24). For combinations of wire material and fluid that are common in practice as well as mean flow Reynolds numbers typical for Rijke tubes, the Nußelt numbers are of order one and the Biot numbers the order 10^{-3}, as shown in Table 9.1. Hence, a lumped thermal capacitance model may be applied with excellent accuracy, implying a spatially homogeneous temperature within the cylinder.

The equation for a lumped thermal capacitance (Bergman et al., 2011) is given by

$$V_s \rho_s c_{p,s} \frac{\partial T}{\partial t} = h A_s (T - T_\infty), \tag{9.13}$$

where V_s and A_s denote the volume and surface area, respectively. This equation can also be deduced from Equation (2.65) with Newton's law of cooling as a boundary condition. Introducing the cylindrical geometry and the definition of the Nußelt number, the time constant τ_{wire} for this first order differential equation can be given as

$$\tau_{\mathrm{wire}} = \frac{d^2 \rho_s c_{p,s}}{4\,\mathrm{Nu}\,k_f}. \tag{9.14}$$

Typical values for the time constant are given in Table 9.1.

Quantity	Value
d	0.001 m
ρ_s	19.25×10^3 kg/m^3
$c_{p,s}$	138 J/(kg K)
k_f	0.0262 W/(m K)
ν_f	1.57×10^{-5} m^2/s
Re_0	0.1 – 40
Nu	0.44 – 3.2
τ_{wire}	~ 57.8 s – 8.0 s
Sr_c	~ 0.011 – 0.000 21

Table 9.1: Exemplary Properties and Conditions for a Heated Wire in a Rijke Tube. The material properties are those of pure tungsten.

A cutoff Strouhal number Sr_c for temperature pulsations of the wire can be calculated from

$$\mathrm{Sr}_c = \frac{4\,k_f}{\nu_f\,\rho_s\,c_s}\frac{\mathrm{Nu}}{\mathrm{Re}_0}. \tag{9.15}$$

This shows that the temperature of the cylinder reacts to very low frequencies, but thermal inertia is too high at Strouhal numbers of order unity and above to substantially change due to pulsations of the flow crossflow.

Natural convection

If the Rijke tube is mounted vertically, the mean flow is driven solely by natural convection. This mean flow velocity establishing in the resonator tube can readily be converted to a Reynolds number. In the case of a horizontal Rijke tube, the forced convection in horizontal direction may superimpose with natural convection in a direction perpendicular to the tube axis and thus mixed convection occurs. The Richardson number is a measure for the relative strength of natural convection. It is given by

$$\mathrm{Ri} = \frac{\mathrm{Gr}}{\mathrm{Re}^2} \tag{9.16}$$

where the Grashof number is defined as

$$\mathrm{Gr} \equiv \frac{d^3\,g\,\beta_{\mathrm{ref}}\,(T_w - T_{\mathrm{stat}})}{\nu_{\mathrm{ref}}^2}. \tag{9.17}$$

Natural convection is negligible for $\mathrm{Ri} < 0.1$. For $\mathrm{Ri} > 10$, natural convection is dominant and forced convection may be neglected. In the intermediate region, mixed

convection should be considered (Schlichting and Gersten, 2006). According to Lange et al. (1998), the influence of natural convection is negligible, if $\mathrm{Re} \geq 2\,\mathrm{Gr}^{1/2}$.

In the Rijke tube, another factor comes into play. No net flux of fluid can occur in the direction perpendicular to the tube axis, i.e. it cannot penetrate the solid tube material. Hence, mixed convection effects are neglected in this thesis.

Radiative Heat Transfer

Radiative heat transfer was neglected in the simulations. This has two main reasons: (1) The working gas, which is air for most Rijke tubes, is transparent for radiation at wavelengths corresponding to typical wire temperatures. (2) Differences between wire temperature and ambient temperature were assumed to be small in the numerical procedure.

Nevertheless, Kopitz (2007) showed, that radiative heat transfer it not negligible concerning the overall heat transfer in the Rijke tube. In his experiments, there was significant energy exchange between the heater and the tube wall. This impeded temperature measurements and caused heat-up of the whole tube.

9.1.4 Limitations

In this thesis, the heat transfer dynamics of a Rijke tube were investigated by solving the incompressible Navier–Stokes equations for just one isolated wire. Thus, this method causes the following limitations.

Overheating

In a real Rijke tube, a certain amount of thermal power has to be introduced in order to overcome the hydraulic losses and achieve a limit cycle. Hence, the temperature of the wire has to be substantially higher than the ambient temperature. The assumption of low temperature differences is violated. It was, however, established in Section 8.3.2 that the dynamic behavior does not change fundamentally and some correction, e.g. the use of an effective mean flow Reynolds number, copes with this shortcoming.

High Amplitudes

The linear regime only describes the onset of thermoacoustic oscillations in the Rijke tube. At higher amplitudes, the nonlinearity of the heat transfer plays an im-

portant role, but it cannot be handled accurately by a linear model. Nevertheless, as shown in Section 8.3.3, the dynamics are still represented adequately to some extent even at pulsation amplitudes in the order of the mean flow velocity.

Non-Uniformity

A constant velocity profile is used in the CFD computations for a single wire. However, in the resonator tube, a boundary layer will establish, leading to a characteristic velocity profile. This is not so much of concern for a single wire, because the wire diameter is usually much smaller than the tube diameter $d \ll D$. Yet, different wires placed at a different distance from the cylinder axis experience different mean flow velocities and therefore locally different Reynolds numbers and Strouhal numbers. Moreover, oscillations in the Rijke tube do not only scale the velocity profile in the tube but also interact with the boundary layer at the tube wall and introduce additional dynamics.

Wire Pattern

As the last limitation, the isolated wire has to be mentioned. To introduce the necessary amount of thermal energy, the heated wire has to be inserted in the tube as a coil or some sort of repeating pattern. This also means that the wires interact with each other. If the distance of the wires in lateral direction is large enough, however, this interaction is negligible. Usually, this distance is several wire diameters and fulfilling the far field requirement.

A different picture can be drawn in the case of successive wires where one wire is in the (thermal) wake of the other. A simulation was conducted at a mean flow Reynolds number of $\mathrm{Re}_0 = 3$ with two successive wires at a distance of $10\,d$. The transfer function of the second wire was of the same shape as that of the first, but the amplitude values were about 10 % to 20 % smaller. This is due to the fact that the fluid arriving at the second cylinder is hotter, and hence the amount of heat transferred is smaller. The basic behavior of the heat transfer, however, is still the same as for a single wire.

9.2 Hot-Wire Anemometry

Hot-wire anemometry is used to measure velocities in laminar and turbulent flows for a wide range of velocities. A thin, electrically heated wire, mounted on prongs, is placed in the flow as a probe. An advantage of this method is that very small probes allow determining flow velocities very accurately at a specific position. Turbulent

Quantity	Value
d	$5 \times 10^{-6}\,\mathrm{m}$
ρ_w	$21.45 \times 10^{3}\,\mathrm{kg/m^3}$
$c_{p,s}$	$130\,\mathrm{J/(kg\,K)}$
k_f	$0.0262\,\mathrm{W/(m\,K)}$
Re_0	$0.1 - 40$
Nu	$0.44 - 3.2$
τ_{wire}	$\sim 1.516 \times 10^{-3}\,\mathrm{s} - 0.209 \times 10^{-3}\,\mathrm{s}$
Sr_c	$\sim 10.502 \times 10^{-3} - 0.1907 \times 10^{-3}$

Table 9.2: Exemplary Properties and Conditions for a Hot-Wire Anemometer. The material properties are those of pure platinum.

structures in the flow do not appear as mere local fluctuations, but the probe may be fully submerged detecting changes in velocity and angle of attack.

9.2.1 Mode of Operation

Different measurement methods were developed. Hot-wire devices can be classified as CCA (constant current anemometer), CVA (constant voltage anemometer) and CTA (constant-temperature anemometer) (Bruun, 1996). In the first method, changes in the wire temperature lead to changes in electrical resistance. To keep the current constant, a change in voltage is necessary and serves as a measure of the flow velocity. Similarly, in the CVA method, changes in electrical current at constant voltage are measured. The most accurate and most widely used method is CTA. In the CTA method, a controller holds the temperature of the heated wire constant. The voltage necessary to do so is again linked to the flow velocity that is to be measured.

9.2.2 Justification of Assumptions

For constant temperature anemometry, the electric current delivered by the power amplifier is controlled to maintain a constant wire temperature, so the assumption of constant surface temperature T_w is valid by design. Moreover, wire diameters are very small, and hence Helmholtz numbers are small.

A low Mach number is, however, not a necessary condition for hot-wire anemometry. On the contrary, this method is often used to examine high-velocity flows. Table 9.2 gives exemplary properties and conditions for a hot-wire probe made of platinum (Bruun, 1996).

9.2.3 Fluctuation of Angle of Attack

Hot-wire anemometers are often used to measure velocities in strongly turbulent environments. Turbulence, as detailed in Section 2.1.3, includes chaotic three dimensional fluctuations in velocity. This causes not only changes in the magnitude of the flow velocity but also fluctuations in the angle of attack. A fluctuating angle of attack was also mentioned by Lighthill (1954) in his original article as a vantage point for future investigations.

Mechler (2016), in his bachelor's thesis supervised by the author of this thesis, focused on changes in the angle of attack in the plane perpendicular to the axis of the cylinder α. The simulations were carried out on a similar setup as detailed in Section 5.1 and Section 5.2. At the inlet the velocity was excited with fluctuations in x- and y-direction. Fluctuations in velocity parallel to the inlet boundary propagate not with the speed of sound, which is infinite in the incompressible formulation used here, but with the convective velocity. This effect is similar to the shear waves described in Section 3.1.2. It poses a difficulty in the data acquisition as the signal imposed at the inlet decouples. Two changes were implemented in the computational procedure to minimize this effect: The domain boundary was chosen circular so with any inflow angle the face normals of the inlet point towards the cylinder. The second change concerned the position of the data acquisition plane. It was located as close to the cylinder as possible to acquire the actual input accurately.

Velocity fluctuations, i.e. Reynolds number fluctuations, and fluctuations in the angle of attack influence the heat transfer. Hence, the system is of MISO type, and an according model had to be identified. The identification yielded two transfer functions, which in sum determine the Nußelt number fluctuations. The dynamic influence of Reynolds number fluctuations on Nußelt number fluctuations G_{Re} is expected to be the same as G_{Nu} in Section 6.3. The transfer behavior between the angle of attack and the Nußelt number G_α shows a low gain at high frequencies where the boundary layer cannot adapt to the fast changes in the flow. In the quasi-steady limit, the adaption occurs instantly, and no change in heat transfer occurs. However, at reasonably low frequencies changes in the boundary layer affect the Nußelt number.

The relative influence of both fluctuations, Reynolds number fluctuations and fluctuations in the angle of attack, is determined by standardization of all quantities. From the standardized transfer functions conclusions can be drawn on how much of the variance in Nußelt number is explained by either Re' or α'. A standardized quantity has zero mean and a variance of unity. The quantities Re', Nu', and α' already fulfill the first requirement. The mean value was subtracted in the post-processing of the data series. The second requirement was achieved by dividing the

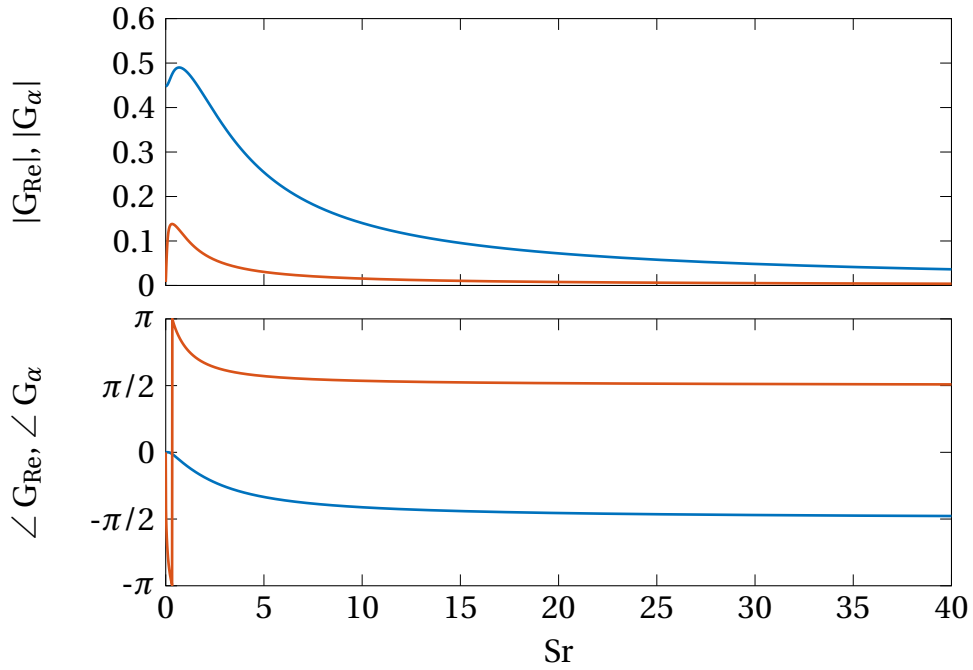

Figure 9.6: Frequency Response of Heat Transfer to Re **and Angle of Attack.** Frequency response to Re' (——) and Frequency response to α' (——).

signal by its respective standard deviation, e.g. $Z_{\mathrm{Nu}} = \mathrm{Nu}'/\sigma_{\mathrm{Nu}}$. The input-output relation with standardized quantities is thus given by

$$\frac{\mathrm{Nu}'}{\sigma_{\mathrm{Nu}}} = \frac{\overline{\mathrm{Nu}}}{\overline{\mathrm{Re}}} G^*_{\mathrm{Re}} \frac{\mathrm{Re}'}{\sigma_{\mathrm{Re}}} + \frac{\overline{\mathrm{Nu}}}{\overline{\alpha}} G^*_{\alpha} \frac{\alpha'}{\sigma_{\alpha}} \tag{9.18}$$

with the scaled transfer functions G^*_{Re} and G^*_{α} for Reynolds number and angle of attack, respectively. To achieve the original scaling for the transfer function from Re' to Nu'

$$G = \frac{\sigma_{\mathrm{Nu}}}{\sigma_{\mathrm{Re}}} G^* \tag{9.19}$$

is used. Hence, Equation (9.18) can be written as

$$\mathrm{Nu}' = \frac{\overline{\mathrm{Nu}}}{\overline{\mathrm{Re}}} G_{\mathrm{Re}} \mathrm{Re}' + \frac{\overline{\mathrm{Nu}}}{\overline{\alpha}} G_{\alpha} \alpha' \frac{\sigma_{\mathrm{Re}}}{\sigma_{\alpha}}. \tag{9.20}$$

Figure 9.6 depicts the frequency response of the identified MISO model.

9.2.4 Interactions of Dynamic Subsystems

In hot-wire anemometry, not only the dynamics of the fluid are of interest, but also the solid wire and possibly a controller. Both can be characterized by their frequency

response as well. The wire can be modeled as a first order time lag (lumped capacitance) model with time constant $c_{\tau,s}$ (cf. Equation 9.14).

As a possible controller, a critically damped second order time lag model with a cutoff frequency of 55 kHz is assumed. This represents typical values for CTA (Bruun, 1996). The natural frequency can be brought into the dimensionless framework by

$$\mathrm{Sr} = f\frac{2\,\pi\,d^2}{\mathrm{Re}_0\,\nu}\,. \tag{9.21}$$

Figure 9.7 shows the amplitude of the frequency responses in a Bode diagram in a log–log plot. This format was chosen to display a wide range of frequencies. The values were assessed for a wire probe made of platinum and air at ambient conditions. The mean flow Reynolds number is $\mathrm{Re}_0 = 40$. The cutoff Strouhal number of the CTA controller depends on the wire diameter and was evaluated for $d = 5\mu\mathrm{m}$. Thicker wires would only affect the graph of the CTA and place the cutoff frequency further to the right.

Heat conduction and storage in the solid wire are comparatively slow processes which can be seen by the low cutoff Strouhal number of the wire itself. Both the response to velocity magnitude fluctuations and fluctuations in the angle of attack can be considered quasi-stationary in this frequency range. This is also mostly true if the CTA controller is considered. Peak and drop in the gain of G_{Re} are well beyond the operating range of the controller for very thin wires. The influence of the angle of attack is negligible in the low-frequency limit. The boundary layer adapts to slow changes in the angle of attack comparably fast and therefore the gain is zero. The influence of the angle of attack becomes stronger towards the cutoff frequency of the controller. The rise in gain is about one order of magnitude. This effect would even be stronger if thicker wires were considered and the peak gain of G_α is in the pass-band of the controller. Towards even higher frequencies, the inertia of the fluid leads to a band-pass-like behavior as visible in Figure 9.7.

The comparison between the frequency ranges of the wire and the CTA controller with the frequency responses of the heat transfer fluctuations to pulsations in approaching flow velocity and angle of attack shows that anemometers operate mostly in the quasi-steady limit. Hence, the heat transfer dynamics play only a minor role. Only the response to fluctuations in the angle of attack starts to come into effect within the operating range of the CTA controller. However, the amplitude of the frequency response is small, and anemometers are usually not used for measurements at such high frequencies.

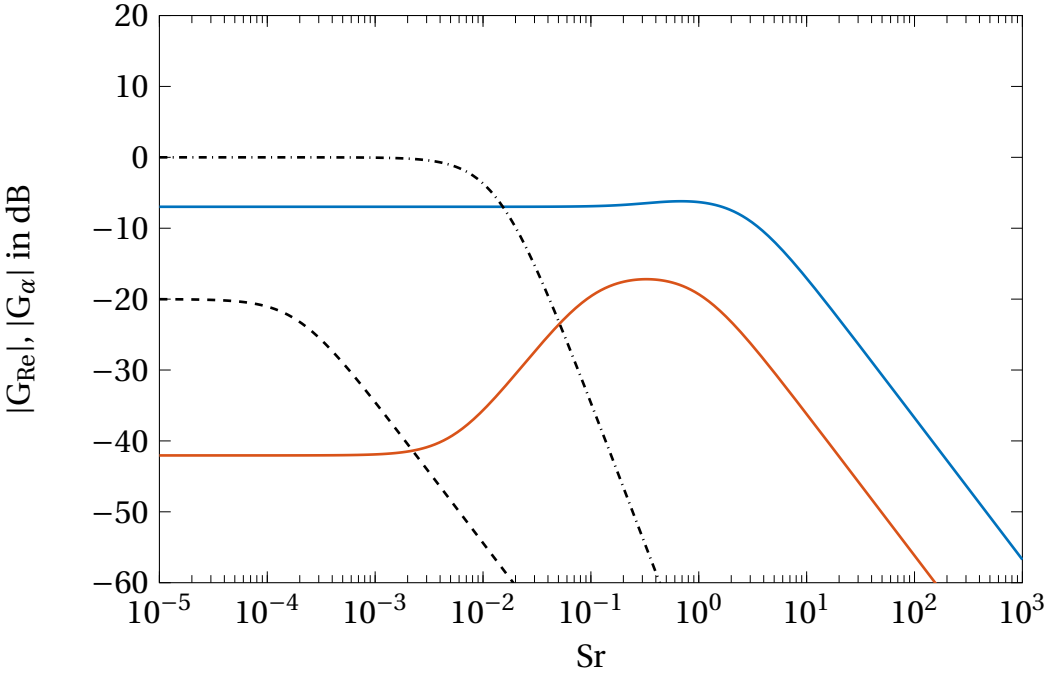

Figure 9.7: Frequency Response Magnitudes for Hot-Wire Anemometry. The amplitudes of G_{Nu} (——) and G_α (——) are compared to the wire itself (- - -) and a possible realization of a CTA controller (-·-·-)

9.3 Heat Exchanger in Domestic Boilers

Heat exchangers (HX) in domestic boilers are used to transfer the heat created in a combustion process to water for household use. Recently, the effect of an HX on thermoacoustic combustion instabilities in a heating system was investigated by Surendran and Heckl (2014, 2015). In these studies, the so-called $n-\tau$ model was used to describe unsteady heat transfer. This model corresponds to the low-frequency limit of Lighthill's results for heat transfer in pulsating crossflow: A characteristic time delay τ leads to a linearly growing phase lag in the frequency response. This approach is simple and quite popular but does not give a realistic description of the dynamics.

The HX in crossflow itself is much like the configuration investigated in this thesis, in particular, a low-pass behavior is obtained. However, the interactions between consecutive elements of an HX have a significant impact on its response function (Strobio Chen et al., 2015). Combinations of HX and flames, as found in configurations of applied interest, were investigated with respect to the dynamic heat transfer behavior from a hydrodynamic and thermoacoustic point of view by Hosseini et al. (2014b,a) and from a system point of view by Strobio Chen et al. (Strobio Chen et al., 2016). Surendran et al. (2016) determined the frequency response function of the HX in this configuration from the discrete Fourier transform of the response of the

heat transfer rate to a step input, which was determined by numerical simulation. The HX is principally very similar to the (isolated) cylinder assessed in this thesis. However, some differences arise, which are addressed in the following.

9.3.1 Temperature Difference

The temperature difference between inflow and outflow of the HX and the resulting change in fluid properties play an important role in quantifying the dynamic behavior. The qualitative behavior, however, is very similar to the heated cylinder. The most substantial difference is the arrangement. In the case of the cylinder, one bluff body is singled out surrounded by a theoretically infinite amount of fluid. The HX, in contrast, consists of tightly wound coils with only small clearances between the exchanger pipes. A specifically determined amount of fluid passes through, transferring its excess in enthalpy to the fluid in the exchanger tubes. This especially impacts the quasi-steady behavior, i.e. the low-frequency limit.

9.3.2 Low Frequency Limit

Heat transfer between a surface and a convective flow can be described by Newton's law of cooling (Bergman et al., 2011) given by

$$\dot{q} = h(T_w - T_\infty)\,. \tag{9.22}$$

In the isolated wire configuration (Rijke tube) addressed in this thesis, the enthalpy change of the flow is insignificant. Both temperatures T_w and T_∞ are constant. The low-frequency limit is determined by the heat transfer coefficient h, i.e. the Nußelt number. This is different in the case of the HX. The initially large temperature difference $(T_w - T_\infty)$ between HX surface and passing flow diminishes along the exhaust gas path until it almost vanishes. This is necessary to achieve high efficiencies. The low-frequency limit, in this case, is controlled by the enthalpy difference rather than the heat transfer.

The heat transferred in the HX is given by

$$\dot{q} = u\rho c_p(T_u - T_d) \tag{9.23}$$

where T_u and T_d are the fluid temperatures upstream and downstream of the HX. Asymptotic expansion of velocity u, downstream temperature T_d, and density ρ yields

$$\dot{q}_0 + \epsilon\dot{q}' = c_p(u_0 + \epsilon u')(\rho_0 + \epsilon\rho')\left(T_u - (T_{d,0} + \epsilon T_d')\right). \tag{9.24}$$

To leading order, Equation (9.24) is recovered with u_0, ρ_0, and $T_{d,0}$. Collecting the terms of first order in ϵ yields

$$q' = c_p\left[(T_u u_0 - T_{d,0}u_0)\rho' + (T_u\rho_0 - T_{d,0}\rho_0)u' - u_0\rho_0 T_d'\right]. \tag{9.25}$$

Assuming $\rho' = 0$ and inserting in the definition of the transfer function (Equation (2.100)) leads to

$$K_{Nu} = G_{\mathrm{Nu}}(\mathrm{Sr}=0) = \frac{u_0}{u'}\frac{c_p\left[(T_u\rho_0 - T_{d,0}\rho_0)u' - u_0\rho_0 {T_d}'\right]}{u_0\rho_0 c_p(T_u - T_{d,0})} = 1 - \frac{\frac{u_0}{u'}{T_d}'}{T_u - T_{d,0}}. \tag{9.26}$$

The downstream temperature can be inferred from a local balance. For reasons of simplicity, a constant distance s between two successive tubes is assumed. The temperature is given by

$$T_d = T_w + (T_u - T_w)\exp\left(\frac{-h\,L}{\rho\,u\,s\,c_p}\right). \tag{9.27}$$

Using the definition of the Nußelt number leads to

$$T_d = T_w + (T_u - T_w)\exp\left(\frac{-\mathrm{Nu}\,k\,L}{2\,\rho\,u\,s^2\,c_p}\right). \tag{9.28}$$

Assuming that fluctuations in temperature are only caused by velocity fluctuations, it may be argued that T can be approximated by a Taylor series

$$T(u_0 + \epsilon u') = T(u_0) + \frac{dT}{du_0}\epsilon u' + \mathcal{O}(2) = T_0 + \epsilon T'. \tag{9.29}$$

The derivative of T_d with respect to u_0 is given by

$$\frac{dT_d}{du_0} = \frac{\mathrm{Nu}\,k\,L}{2\,\rho\,u_0^2\,s^2\,c_p}(T_u - T_w)\,\exp\left(\frac{-\mathrm{Nu}\,k\,L}{2\,\rho\,u_0\,s^2\,c_p}\right). \tag{9.30}$$

Finally, the expression

$${T_d}' = \frac{\mathrm{Nu}\,k\,L}{2\,\rho\,u_0^2\,s^2\,c_p}(T_u - T_w)\,\exp\left(\frac{-\mathrm{Nu}\,k\,L}{2\,\rho\,u_0\,s^2\,c_p}\right)u' \tag{9.31}$$

can be given for the downstream temperature fluctuation.

Combining Equation (9.31) and Equation (9.26) yields

$$K_{\mathrm{Nu}} = 1 - \frac{u_0}{T_u - T_{d,0}}\frac{\mathrm{Nu}\,k\,L}{2\,\rho\,u_0^2\,s^2\,c_p}(T_u - T_w)\,\exp\left(\frac{\mathrm{Nu}\,k\,L}{2\,\rho\,u_0\,s^2\,c_p}\right) \tag{9.32}$$

for the low frequency limit.

Quantity	Value	
	Upstream	Downstream
Nu	7.54	
L	0.036 m	
s	0.8×10^{-3} m	
k	0.0764 W/(m K)	0.0262 W/(m K)
ρ	0.29 kg/m^3	1.18 kg/m^3
u_0	14 m/s	3.5 m/s
c_p	1175 J/(kg K)	1005 J/(kg K)

Table 9.3: Exemplary Properties and Conditions for a Heat Exchanger. Adapted from Strobio Chen et al. (2015)

A rough estimate can be given for the case investigated by Strobio Chen et al. (2015). Fluid properties and dimensions, taken from Strobio Chen et al. (2015), are shown in Table 9.3. With the fluid properties at the upstream side, the low-frequency limit evaluates to $K = 0.88$.

10 Conclusions and Outlook

The path towards a sustainable usage of the worlds primary energy resources leads through many intermediate landmarks. Two of which are the improvement of existing devices and the development of new technologies with high potentiality. This thesis strives to aid this process through the following findings.

10.1 Summary

The dynamic response of the heat transfer and skin friction of a cylinder in pulsating crossflow were investigated for small perturbations of flow velocity. The cycle-averaged heat transfer is independent of the fluctuations such that pulsations of flow variables can be described as LTI systems. The foundation of this study was time series data acquired from CFD simulations of a single cylinder in crossflow solving the incompressible Navier–Stokes equations. The assumptions leading to this simplified treatment are justified for the application that was the primary motivation for this thesis: the Rijke tube. The numerical procedure was designed and examined thoroughly to yield optimal results regarding the desired dynamic behavior.

The dynamic behavior was quantified by transfer functions. These are models in the framework of LTI systems known from control theory and electrical engineering. Three fundamentally different ways—with the incompressible Navier–Stokes equations as the only commonality—were implemented and compared. Transfer functions were developed from the response to a sudden rise in input velocity (step response), from a frequency domain approach, where perturbations are linearized and solved with finite differences (LNSE), and from time domain simulations with broadband excitation (CFD/SI). For the latter, discrete time identification and continuous time identification were considered. The results are in excellent agreement for all simulation and identification methods for mean flow Reynolds numbers of $\mathrm{Re}_0 \leq 40$. The CFD/SI approach offers more variability, as it does not rely on the existence of a steady state. Several improvements were easily possible such as the extension to the regime of vortex shedding and transition to turbulence in the wake $\mathrm{Re}_0 > 40$.

Continuous time identification and discrete time identification yielded comparable results as long as disturbances were well-behaved. However, in the cases where

vortex shedding occurs, and a strong tonal component is present in the noise, the OE model structure from the discrete time framework can readily be extended to a BJ model with a parametrization of the disturbance. In addition to the assessment of model types and parameter estimation methods, other advanced identification techniques, e.g. regularization and uncertainty quantification, were surveyed.

The results of the investigations were tabulated and depicted as Bode plots of the frequency responses. The heat transfer dynamics and the skin friction dynamics are governed by several time scales, corresponding to the response times of the velocity field and temperature field, respectively. The interaction of the different time lags leads to a non-trivial dependence of the respective frequency responses on Strouhal numbers and mean flow Reynolds numbers. The transfer behavior of the heat transfer appears like a low-pass filter with one dominant time scale, similar to the analytical predictions by Lighthill (1954) or Bayly (1985). However, several deviations from this behavior were found and explained, most notably the occurrence of a peak gain at $0 < \mathrm{Sr} < 1$ and the phase values at very high frequencies. The skin friction, in contrast, behaves like a high-pass filter. A strong dependence on the mean flow Reynolds number exists which is not present in the existing analytical models by Lighthill (1954) and Gersten (1965). Unification in the manner of a Reynolds analogy is not possible in the dynamic case. The present study represents also a significant advancement over previous computational studies (Apelt and Ledwich, 1979; Kwon and Lee, 1985; Nicoli and Pelcé, 1989; Payne, 1958; Föller et al., 2008). In particular, the time lag, which is of paramount importance for thermoacoustic stability in a Rijke tube, is determined with quantitative accuracy.

The advantage of CFD simulations is complete access to the flow field at any instant in time. This is used to examine the evolution of the near field of the cylinder in unprecedented detail. Step response simulations and the results from the LNSE approach allow insight in the temporal development and the behavior in the frequency domain, respectively. This was also used to show detailed circumferential distributions of the Nußelt number fluctuations and friction coefficient fluctuations at different excitation frequencies.

To make the results from this thesis readily available in tasks like the modeling of a Rijke tube, a first order parametrized model was developed. The model includes the dependence of the transfer behavior on Strouhal number and Reynolds number and can be used in the range $0.1 \leq \mathrm{Re}_0 \leq 40$ and $0 < \mathrm{Sr} \leq 40$. The steady-state gain and the time constant are given as correlations developed from the complete series of simulations in the regime without vortex shedding.

Three applications are investigated in the scope of a cylinder in pulsating crossflow: The Rijke tube, hot-wire anemometry, and an HX as an acoustic element. Special consideration was given to the Rijke tube, and the transfer functions developed in this thesis were related to the stability of thermoacoustic oscillations in the tube. For

the hot-wire anemometer, an additional fact was investigated. A fluctuating angle of attack, which originates from turbulent fluctuations of the flow to be measured, has some impact on the heat transfer dynamics and therefore on the measurement.

10.2 Implications for Further Research

Further investigations will address gas turbines as well as the Rijke tube as a prototype of a thermoacoustic device. Moreover, machinery exploiting the thermoacoustic effect, e.g. thermoacoustic engines and refrigerators, will profit from the results and methods assessed in this study. Although high amplitudes, and therefore the nonlinear heat transfer dynamics, play a vital role in this type of device, linear stability (or instability) is still a primary design criterion. Thermoacoustic prime movers are of interest, e.g. for the power generation from waste heat (Witte et al., 2015). High efficiency is of secondary importance compared to acquisition costs and service costs. These devices are predestined for this task as they are simple to build and very robust in operation once they are adequately designed. This argument also applies to thermoacoustic refrigerators. They may be used where robustness is a crucial requirement as they can be built with no moving parts. This gives these devices an advantage over conventional compression refrigerators even though the latter offer much higher efficiencies. Recent investigations in thermoacoustic devices include the possibilities to incorporate thermoacoustic prime movers or refrigerators in other assemblies. One aspect that has been studied in the past was the influence of mean flow inside the device (Holzinger et al., 2012, 2015). Such a configuration, in turn, is similar to the Rijke tube. Thermoacoustic devices are in need of much more robust design tools and smart concepts for integration in machinery that supplies heat or acoustic energy.

Although linear models, such as those assessed in this study, offer a great deal of insight and the possibility to investigate linear stability, the nonlinear behavior has to be subject to further investigations. A system may be linearly stable but nonlinear or non-normal effects may trigger high amplitudes. Moreover, if high amplitudes are desired, linear models often seize to be valid and can at most predict the coarse behavior but usually fail to recover correct amplitudes or power output.

Another application with cylinders subject to pulsating flow, which is of interest for future investigations is the total artificial lung (TAL). The TAL is a device still under development, and it aims to replace all functions of a human lung, i.e. to remove CO_2 from blood and to supply it with oxygen (O_2). To achieve this, the (pulsatile) blood flow passes small tubes from which the mass transfer occurs. Lin et al. (2006) studied these mass transfer effects in a water tunnel at very low Reynolds numbers. Numerical investigations were carried out by Zierenberg et al. (2006, 2007, $5 \leq \mathrm{Re} \leq 40, 0.25 \leq \mathrm{Wo} \leq 4, 0.25 \leq A \leq 0.75, \mathrm{Sc} = 1000$), Qamar et al. (2011, $0.33 < \mathrm{KC} < 1$,

$0.5\,d < A < d$, $5 < \mathrm{Re} < 20$), and Qamar et al. (2012, $0.2 \leq A \leq 0.6$, $0.57 \leq \mathrm{KC} \leq 2$, $\mathrm{Re} = 5, 10$). The flow conditions examined in these studies are not unlike to the range of interest in this thesis. The Reynolds numbers are in the range $1 \leq \mathrm{Re} \leq 50$ and the fluid is incompressible. The largest difference is the high Schmidt number ($\mathrm{Sc} = 1000$) which is much larger than the ratio of transport properties considered in this thesis which mainly focuses on air ($\mathrm{Pr} = 0.7$).

Besides the cylinder, another archetypal problem in thermo-fluid dynamics is a sphere in crossflow. CFD/SI methods or the LNSE can be used to investigate the impact of pulsations on the skin friction and the heat transfer. The skin friction plays an important role in the movement of small spherical particles or droplets. The movement can be described by a force balance including effects like inertia, virtual mass, and fluid drag. The latter has a "history" that has to be considered due to the dynamics of the skin friction. This history force, often called Basset force, can be identified from numerical simulations in a similar manner as the friction coefficient. The major difference is the dependence on flow acceleration instead of velocity like in this thesis. The Basset force plays an important role in the case of continuous acceleration, e.g. under the influence of gravity or in the case of droplets oscillating in an acoustic field. Moreover, the heat transfer between a droplet and the surrounding fluid plays a role in the evaporation of liquid fuels, and the heat transfer dynamics can influence the spray combustion process.

A topic explicitly excluded in this thesis are state space models. These models exist besides input–output models and have certain desirable properties, especially in conjunction with computational methods and systems with a large number of inputs and outputs. The models reported in this thesis can easily be transformed into state space models. However, in the field of SI, useful methods like balanced truncation model reduction and model order identification exist, which makes the direct identification of state space models an exciting topic for further investigations.

This thesis offers detailed models for the behavior of heat transfer and skin friction of a cylinder in pulsating crossflow. Moreover, a comprehensive procedure is given to acquire accurate results at flow conditions not investigated in detail in this thesis. The reported results allow the development of models with different levels of detail in investigations, e.g. of the thermoacoustic effect in the Rijke tube. Findings concerning the field of thermoacoustic can be transferred to other devices. On the one hand to help suppress thermoacoustic instabilities and ensure proper performance, e.g. in the case of stationary gas turbines for power generation or in domestic boilers. On the other hand, the thermoacoustic effect may be used purposefully in devices, e.g. in thermoacoustic engines and refrigerators. The ultimate goal is to contribute to maintaining the standard of living that was granted by the devices mentioned above, while most importantly reducing the toll on the environment. Specifically, to reduce noxious emissions like $\mathrm{NO_x}$ and small particles as well as greenhouse gases like $\mathrm{CO_2}$.

Supervised Theses

Im Rahmen dieser Dissertation entstanden an der Professur für Thermofluiddynamik der Technischen Universität München in den Jahren 2013 bis 2017 unter wesentlicher wissenschaftlicher, fachlicher und inhaltlicher Anleitung des Autors die im Folgenden aufgeführten studentischen Arbeiten. In ihnen wurden verschiedene Fragestellungen zur Dynamik des Wärmeübergangs und im Speziellen dessen Quantifizierung untersucht. Ergebnisse aus diesen Arbeiten sind in Teilen in das vorliegende Dokument eingeflossen. Der Autor dankt hiermit nochmals explizit allen ehemals betreuten Studentinnen und Studenten für ihr Engagement bei der Unterstützung des hier behandelten Forschungsprojekts sowie der damit verknüpften Dissertation.

Associated with the research under discussion, there are a number of different "student theses" (Semesterarbeiten, Diplomarbeiten, Bachelor theses, or Master theses). This students' contribution was prepared at the Thermo-Fluid Dynamics Group (Professur für Thermofluiddynamik) of the Technical University of Munich in the years 2013 through 2017 under the close supervision of the author of this Ph.D. thesis with regard to all academic, professional, and context-related concerns. Various issues were investigated contributing to heat transfer analysis and in particular to its quantification. Finally, the author would like to express his sincere gratitude to all formerly supervised students for their commitment and support of this research project and of the Ph.D. thesis at hand.

Student	**Title**
Patrick Brandl	*Grid Independence Study of two-dimensional, laminar, pulsating Cross-Flow around a circular Cylinder*, Bachelor's Thesis, 2014
Ana Cabrera	*Linear System Identification of the Heat Transfer Behavior of a Cylinder in Pulsating Cross-Flow at Re = 3900 Using Large Eddy Simulation*, Master's Thesis, 2015
Magnus Mechler	*Dynamic Heat Transfer Behavior of a Wire for Constant-Temperature Anemometry Applications in Cross-Flow with Fluctuating Angle of Attack*, Bachelor's Thesis, 2016
Ateş Çalak	*Identification of Wiener-Models for the Heat Transfer between a Cylinder and a Pulsating Cross Flow*, Bachelor's Thesis, 2017

References

K. J. Åström and B. Wittenmark. *Computer-Controlled Systems—Theory and Design*. Information and System Sciences. Prentice Hall, Upper Saddle River, 3rd edition, 1997. ISBN 7-302-05008-2.

R. C. Ackerberg and J. H. Phillips. The unsteady laminar boundary layer on a semi-infinite flat plate due to small fluctuations in the magnitude of the free-stream velocity. *Journal of Fluid Mechanics*, 51(1):137–157, 1972. doi: 10.1017/S0022112072001119.

F. Agostino, G. Baldini, S. Bittanti, A. De Marco, G. Poncia, W. Prandoni, and M. Scarpellini. Nonlinear identification of thermoacoustic instabilities with limit cycles in a Rijke tube. In *Proceedings of the 2002 IEEE International Conference on Control Applications*, volume 2, pages 1147–1152. IEEE, Sept. 2002. doi: 10.1109/CCA.2002.1038767.

J. G. Aguilar, L. Magri, and M. P. Juniper. Adjoint-based sensitivity analysis of low order thermoacoustic networks using a wave-based approach. In *Thermoacoustic Instabilities in Gas Turbines and Rocket Engines: Industry Meets Academia*, Garching, Germany, May 2016.

G. F. Al-Sumaily and M. C. Thompson. Forced convection from a circular cylinder in pulsating flow with and without the presence of porous media. *International Journal of Heat and Mass Transfer*, 61:226–244, 2013. doi: 10.1016/j.ijheatmasstransfer.2013.01.067.

C. E. Andraka and T. E. Diller. Heat-transfer distribution around a cylinder in pulsating crossflow. *Journal of Engineering for Gas Turbines and Power*, 107(4): 976–982, 1985. doi: 10.1115/1.3239844.

C. J. Apelt and M. A. Ledwich. Heat transfer in transient and unsteady flows past a heated circular cylinder in the range $1 \leq R \leq 40$. *Journal of Fluid Mechanics*, 95(4): 761–777, 1979. doi: 10.1017/S0022112079001683.

H. D. Baehr and K. Stephan. *Heat and Mass Transfer*. Springer, Berlin, Heidelberg, 2011. ISBN 978-3-642-20020-5.

K. Balasubramanian and R. I. Sujith. Thermoacoustic instability in a Rijke tube: Non-normality and nonlinearity. *Physics of Fluids*, 20(4): Article 044103, 2008. doi: 10.1063/1.2895634.

T. E. Base, J. M. Patel, and G. C. Valaitis. Heat transfer from cylinders in unsteady flow. *The Canadian Journal of Chemical Engineering*, 59(2):247–250, 1981. doi: 10.1002/cjce.5450590217.

A. B. Basset. *A Treatise on Hydrodynamics with Numerous Examples, Volume 2*, volume 2. Deighton, Bell and co., Cambridge, 1888. ISBN 978-1-331-95169-8.

B. J. Bayly. Heat transfer from a cylinder in a time-dependent cross fow at low Peclet number. *Physics of Fluids*, 28(12):3451–3456, 1985. doi: 10.1063/1.865298.

L. Benoit and F. Nicoud. Numerical assessment of thermo-acoustic instabilities in gas turbines. *International Journal of Numerical Methods in Fluids*, 47:849–855, 2005. doi: 10.1002/fld.886.

T. L. Bergman, A. S. Lavine, F. P. Incropera, and D. P. DeWitt. *Fundamentals of Heat and Mass Transfer*. John Wiley & Sons, Hoboken, 7th edition, 2011. ISBN 978-0-470-50197-9.

A. Beygi and A. Dounavis. An instrumental variable vector-fitting approach for noisy frequency responses. *IEEE Transactions on Microwave Theory and Techniques*, 60 (9):2702–2712, 2012. doi: 10.1109/TMTT.2012.2206399.

G. Bisio and G. Rubatto. Sondhauss and Rijke oscillations—thermodynamic analysis, possible applications and analogies. *Energy*, 24(2):117–131, 1999. doi: 10.1016/S0360-5442(98)00090-5.

S. Bittanti, A. De Marco, G. Poncia, and W. Prandoni. Identification of a model for thermoacoustic instabilities in a Rijke tube. *IEEE Transactions on Control Systems Technology*, 10(4):490–502, 2002. doi: 10.1109/TCST.2002.1014670.

R. Blonbou, A. Laverdant, S. Zaleski, and P. Kuentzmann. Active control of combustion instabilities on a Rijke tube using neural networks. *Proceedings of the Combustion Institute*, 28(1):747–755, 2000. doi: 10.1016/S0082-0784(00)80277-5.

P. Brandl. *Grid Independence Study of Two-Dimensional, Laminar, Pulsating Cross-Flow around a Circular Cylinder*. Bachelor Thesis, Technische Universität München, Munich, 2014. Supervisor: Armin Witte.

H. H. Bruun. *Hot-Wire Anemometry: Principles and Signal Analysis*, volume 7. Oxford University Press, Oxford, New York, 1996. ISBN 978-0-19-856342-6.

E. Buckingham. On physically similar systems; Illustrations of the use of dimensional equations. *Physical Review*, 4(4):345–376, 1914. doi: 10.1103/PhysRev.4.345.

M. Bühner and M. Ziegler. *Statistik für Psychologen und Sozialwissenschaftler*. PS Psychologie. Pearson, Munich, 2009. ISBN 978-3-8273-7274-1.

A. Cabrera. *Linear System Identification of the Heat Transfer Behavior of a Cylinder in Pulsating Cross-Flow at Re = 3900 Using Large Eddy Simulation*. Master Thesis, Technische Universität München, Munich, 2015. Supervisor: Armin Witte.

A. Çalak. *Identification of Wiener-Models for the Heat Transfer between a Cylinder and a Pulsating Cross Flow*. Bachelor Thesis, Technische Universität München, Munich, 2017. Supervisor: Armin Witte.

L. S. Caretto, A. D. Gosman, S. V. Patankar, and D. B. Spalding. Two calculation procedures for steady, three-dimensional flows with recirculation. In *Proceedings of the Third International Conference on Numerical Methods in Fluid Mechanics*, pages 60–68, Berlin, Heidelberg, July 1973. Springer.

M. Chase. *NIST—JANAF Thermochemical Tables*. Number 9 in Journal of Physical and Chemical Reference Data. American Chemical Society, American Institute of Physics, National Institute of Standards and Technology (NIST), Gaythersburg, 4th edition, 1998. ISBN 1-56396-831-2.

D. C. Collis and M. J. Williams. Two-dimensional convection from heated wires at low Reynolds numbers. *Journal of Fluid Mechanics*, 6(3):357–384, 1959. doi: 10.1017/S0022112059000696.

F. E. C. Culick. *Unsteady Motions in Combustion Chambers for Propulsion Systems*. Number AC/323(AVT-039)TP/103 in RTO AGARDograph AG-AVT-039. North Atlantic Treaty Organization, Research and Technology Organization, Neuilly-sur-Seine, 2006. ISBN 978-92-837-0059-3.

P. A. Davidson. *Turbulence: An Introduction for Scientists and Engineers*. Oxford University Press, Oxford, New York, 2004. ISBN 978-0-19-852948-4.

G. A. de Andrade, R. Vazquez, and D. J. Pagano. Boundary feedback control of unstable thermoacoustic ascillations in the Rijke tube. *IFAC-PapersOnLine*, 49 (8):48–53, 2016. doi: 10.1016/j.ifacol.2016.07.417.

J. W. Deardorff. Stratocumulus-capped mixed layers derived from a three-dimensional model. *Boundary-Layer Meteorology*, 18(4):495–527, 1980. doi: 10.1007/BF00119502.

J. E. Dec, J. O. Keller, and V. S. Arpaci. Heat transfer enhancement in the oscillating turbulent flow of a pulse combustor tail pipe. *International Journal of Heat and Mass Transfer*, 35(9):2311–2325, 1992. doi: 10.1016/0017-9310(92)90074-3.

K. Deng, Y. Zhong, X. Zhang, H. Li, H. Lin, and L. Cai. Numerical simulation of oscillatory flow in self-excited Rijke tube: Investigation on mechanisms of pulsation. In *Challenges of Power Engineering and Environment*, pages 1367–1371. Springer, Berlin, Heidelberg, 2007.

D. Deschrijver and T. Dhaene. Parametric identification of frequency domain systems using orthonormal rational bases. In *14th IFAC Symposium on System Identification*, Newcastle, Australia, Mar. 2006.

D. Deschrijver, B. Gustavsen, and T. Dhaene. Advancements in iterative methods for rational approximation in the frequency domain. *IEEE Transactions on Power Delivery*, 22(3):1633–1642, 2007. doi: 10.1109/TPWRD.2007.899584.

Z. Drmač, S. Gugercin, and C. Beattie. Quadrature-based vector fitting for discretized $\mathscr{H}_2$ approximation. *SIAM Journal on Scientific Computing*, 37(2):625–652, 2015. doi: 10.1137/140961511.

D. G. Duffy. *Green's Functions with Applications*. Studies in Advanced Mathematics. Chapman & Hall/CRC, Boca Raton, 2001. ISBN 1-58488-110-0.

J. R. Elston, H. M. Blackburn, and J. Sheridan. The primary and secondary instabilities of flow generated by an oscillating circular cylinder. *Journal of Fluid Mechanics*, 550:359–389, 2006. doi: 10.1017/S0022112005008372.

J. P. Epperlein, B. Bamieh, and K. J. Åström. Thermoacoustics and the Rijke tube: Experiments, identification, and modeling. *IEEE Control Systems*, 35(2):57–77, 2015. doi: 10.1109/MCS.2014.2384971.

S. Etikyala and R. I. Sujith. Change of criticality in a prototypical thermoacoustic system. *Chaos: An Interdisciplinary Journal of Nonlinear Science*, 27(2): Article 023106, 2017. doi: 10.1063/1.4975822.

K. Feldman. Review of the literature on Rijke thermoacoustic phenomena. *Journal of Sound and Vibration*, 7(1):83–89, 1968. doi: 10.1016/0022-460X(68)90159-4.

J. H. Ferziger and M. Perić. *Computational Methods for Fluid Dynamics*. Springer, Berlin, Heidelberg, 2002. ISBN 978-3-540-42074-3.

S. Föller and W. Polifke. Advances in identification techniques for aero-acoustic scattering coefficients from large eddy simulation. In *18th International Congress on Sound and Vibration (ICSV18)*, volume 4, pages 3122–3129, Rio de Janeiro, Brazil, July 2011.

S. Föller and W. Polifke. Identification of aero-acoustic scattering matrices from large eddy simulation: Application to a sudden area expansion of a duct. *Journal of Sound and Vibration*, 331(13):3096–3113, 2012. doi: 10.1016/j.jsv.2012.01.004.

S. Föller, F. Selimefendigil, and W. Polifke. Linear identification of the unsteady heat transfer of a cylinder in pulsating crossflow. In *International Conference on Jets, Wakes and Separated Flows*, Berlin, Germany, Sept. 2008. Technische Universität Berlin.

B. Fornberg. A numerical study of steady viscous flow past a circular cylinder. *Journal of Fluid Mechanics*, 98(4):819–855, 1980. doi: 10.1017/S0022112080000419.

J. Franke and W. Frank. Large eddy simulation of the flow past a circular cylinder at $re_d = 3900$. *Journal of Wind Engineering and Industrial Aerodynamics*, 90(10): 1191–1206, 2002. doi: 10.1016/S0167-6105(02)00232-5.

G. F. Franklin, J. D. Powell, and M. L. Workman. *Digital Control of Dynamic Systems*. Addison Wesley Longman, Menlo Park, 3 edition, 1997. ISBN 978-0-201-82054-6.

G. Gelbert, J. P. Moeck, C. O. Paschereit, and R. King. Feedback control of unstable thermoacoustic modes in an annular Rijke tube. *Control Engineering Practice*, 20 (8):770–782, 2012. doi: 10.1016/j.conengprac.2012.03.016.

M. Germano, U. Piomelli, P. Moin, and W. H. Cabot. A dynamic subgrid-scale eddy viscosity model. *Physics of Fluids A: Fluid Dynamics*, 3(7):1760–1765, 1991. doi: 10.1063/1.857955.

K. Gersten. Heat transfer in laminar boundary layers with oscillating outer flow. In *AGARDograph*, number 97 in AGARDograph, pages 423–475. North Atlantic Treaty Organization, 1965.

S. Ghosal, T. S. Lund, P. Moin, and K. Akselvoll. A dynamic localization model for large-eddy simulation of turbulent flows. *Journal of Fluid Mechanics*, 286:229–255, 1995. doi: 10.1017/S0022112095000711.

M. B. Glauert. The laminar boundary layer on oscillating plates and cylinders. *Journal of Fluid Mechanics*, 1(1):97–110, 1956. doi: 10.1017/S002211205600007X.

A. Goldberger. *A Course in Econometrics*. Harvard University Press, Cambridge, US, 1991. ISBN 978-0-674-17544-0.

G. Golub and C. Van Loan. *Matrix Computations*. Johns Hopkins Studies in the Mathematical Sciences. Johns Hopkins University Press, Baltimore, 4th edition, 2013. ISBN 978-1-4214-0794-4. LCCB: 2012943449.

E. Gopalakrishnan and R. Sujith. Influence of system parameters on the hysteresis characteristics of a horizontal Rijke tube. *International Journal of Spray and Combustion Dynamics*, 6(3):293–316, 2014. doi: 10.1260/1756-8277.6.3.293.

E. A. Gopalakrishnan, J. Tony, E. Sreelekha, and R. I. Sujith. Stochastic bifurcations in a prototypical thermoacoustic system. *Physical Review E*, 94(2): Article 022203, 2016. doi: 10.1103/PhysRevE.94.022203.

A. Gopinath and D. R. Harder. An experimental study of heat transfer from a cylinder in low-amplitude zero-mean oscillatory flows. *International Journal of Heat and Mass Transfer*, 43(4):505–520, 2000. doi: 10.1016/S0017-9310(99)00138-6.

R. J. Gribben. The laminar boundary layer on a hot cylinder fixed in a fluctuating stream. *Journal of Applied Mechanics*, 28(3):339–346, 1961. doi: 10.1115/1.3641709.

R. J. Gribben. The fluctuating flow of a gas near a stagnation point on a hot wall. *Journal of Applied Mechanics*, 38(4):820–828, 1971. doi: 10.1115/1.3408960.

B. Gustavsen and A. Semlyen. Simulation of transmission line transients using vector fitting and modal decomposition. *IEEE Transactions on Power Delivery*, 13(2):605–614, 1998. doi: 10.1109/61.660941.

B. Gustavsen and A. Semlyen. Rational approximation of frequency domain responses by vector fitting. *IEEE Transactions on Power Delivery*, 14(3):1052–1061, 1999. doi: 10.1109/61.772353.

C.-C. Hantschk and D. Vortmeyer. Numerical simulation of self-excited thermoacoustic instabilities in a Rijke tube. *Journal of Sound and Vibration*, 277(3):511–522, 1999. doi: 10.1006/jsvi.1999.2296.

M. A. Heckl. Active control of the noise from a Rijke tube. *Journal of Sound and Vibration*, 124(1):117–133, 1988. doi: 10.1016/S0022-460X(88)81408-1.

M. A. Heckl. Non-linear acoustic effects in the Rijke tube. *Acustica*, 72(1):63–71, 1990.

C. Heij, A. Ran, and F. van Schagen. *Introduction to Mathematical Systems Theory: Linear Systems, Identification and Control*. Birkhäuser, Basel, 2006. ISBN 978-3-7643-7549-2.

J. a. P. Hespanha. *Linear Systems Theory*. Princeton University Press, Princeton, 2009. ISBN 978-0-691-14021-6.

B. Higgins. On the sound produced by a current of hydrogen gas passing through a tube. *Journal of Natural Philosophy, Chemistry and the Arts*, 1:129–131, 1802.

P. G. Hill and A. H. Stenning. Laminar boundary layers in oscillatory flow. *Journal of Fluids Engineering*, 82(3):593–607, 1960. doi: 10.1115/1.3662672.

T. Holzinger, A. Baumgartner, and W. Polifke. A linear 1D model for the thermoacoustic effect in the presence of mean flow. In *19th International Congress on Sound and Vibration (ICSV19)*, Vilnius, Lithuania, July 2012.

T. Holzinger, A. Baumgartner, and W. Polifke. A quasi-one-dimensional model of thermoacoustics in the presence of mean flow. *Journal of Sound and Vibration*, 335:204–228, 2015. doi: 10.1016/j.jsv.2014.07.003.

E.-i. Hori. Experiments on the boundary layer of an oscillating circular cylinder. *Bulletin of JSME*, 6(22):201–209, 1963. doi: 10.1299/jsme1958.6.201.

N. Hosseini, V. Kornilov, O. J. Teerling, I. L. Arteaga, and P. de Goey. Development of a numerical model for obtaining flame transfer function in a simplified slit burner with heat exchanger. In *21st International Congress on Sound and Vibration (ICSV21)*, Beijing, China, July 2014a.

N. Hosseini, V. Kornilov, O. J. Teerling, I. Lopez Arteaga, and L. P. H. de Goey. Numerical investigations of the response of a simplified burner-heat exchanger system to inlet velocity excitations. In *Combustion Research and Application (COMBURA'14)*, Soesterberg, The Netherlands, Oct. 2014b. doi: 10.13140/2.1.2204.8001.

N. Hosseini, V. Kornilov, O. J. Teerling, I. L. Arteaga, and L. P. H. de Goey. Investigating the effects of a heat exchanger on the thermoacoustics in a Rijke tube. In *Combustion Research and Application (COMBURA'16)*, Soesterberg, The Netherlands, Oct. 2016.

J. T. Houghton and Intergovernmental Panel on Climate Change, editors. *Climate Change 2001: The Scientific Basis: Contribution of Working Group I to the Third Assessment Report of the Intergovernmental Panel on Climate Change*. Cambridge University Press, Cambridge, New York, 2001. ISBN 978-0-521-80767-8.

W.-H. Hucho. *Aerodynamik der stumpfen Körper: Physikalische Grundlagen und Anwendungen in der Praxis*. Strömungsmechanik. Vieweg+Teubner, Wiesbaden, 2nd edition, 2011. ISBN 978-3-8348-1462-3.

International Energy Agency. Key world energy statistics 2016. Technical report, International Energy Agency, France, 2016.

International Energy Agency. World balance 2014. http://www.iea.org/Sankey/, June 2017.

R. Isermann and M. Münchhof. *Identification of Dynamic Systems*. Springer, Berlin, Heidelberg, 2011. ISBN 978-3-540-78878-2.

R. I. Issa. Solution of the implicitly discretised fluid flow equations by operator-splitting. *Journal of Computational Physics*, 62(1):40–65, 1986. doi: 10.1016/0021-9991(86)90099-9.

H. Iwai, T. Mambo, N. Yamamoto, and K. Suzuki. Laminar convective heat transfer from a circular cylinder exposed to a low frequency zero-mean velocity oscillating flow. *International Journal of Heat and Mass Transfer*, 47(21):4659–4672, 2004. doi: 10.1016/j.ijheatmasstransfer.2003.08.031.

N. P. Jamieson, G. Rigas, and M. P. Juniper. Experimental sensitivity analysis as a validation for adjoint-based methods in the control of thermoacoustic oscillations. In *Thermoacoustic Instabilities in Gas Turbine and Rocket Engines: Industry Meets Academia*, Munich, Germany, May 2016.

N. P. Jamieson, G. Rigas, and M. P. Juniper. Experimental sensitivity analysis via a secondary heat source in an oscillating thermoacoustic system. *International Journal of Spray and Combustion Dynamics*, 9(4):230–240, 2017. doi: 10.1177/1756827717696325.

P. Jansohn, editor. *Modern Gas Turbine Systems*. Number 5 in Woodhead Publishing Series in Energy. CRC Press, Boca Raton, 2010. ISBN 978-1-84569-728-0.

M. P. Juniper. Transient growth and triggering in the horizontal Rijke tube. *International Journal of Spray and Combustion Dynamics*, 3(3):209–224, 2011a. doi: 10.1260/1756-8277.3.3.209.

M. P. Juniper. Triggering in the horizontal Rijke tube: Non-normality, transient growth and bypass transition. *Journal of Fluid Mechanics*, 667:272–308, 2011b. doi: 10.1017/S0022112010004453.

K. J. Keesman. *System Identification*. Advanced Textbooks in Control and Signal Processing. Springer, London, 2011. ISBN 978-0-85729-521-7.

J. J. Keller. Thermoacoustic oscillations in combustion chambers of gas turbines. *AIAA Journal*, 33(12):2280–2287, 1995. doi: 10.2514/3.12980.

Y. Kikuchi, H. Suzuki, M. Kitagawa, and K.-i. Ikeya. Effect of pulsating Strouhal number on heat transfer around a heated cylinder in pulsating cross-flow. *JSME International Journal Series B*, 43(2):250–257, 2000. doi: 10.1299/jsmeb.43.250.

L. V. King. On the convection of heat from small cylinders in a stream of fluid. *Philosophical Transactions of the Royal Society*, 214(A):373–432, 1914. doi: 10.1098/rspa.1914.0089.

G. Kirchhoff. Ueber den Einfluss der Wärmeleitung in einem Gase auf die Schallbewegung. *Annalen der Physik*, 210(6):177–193, 1868. doi: 10.1002/andp.18682100602.

T. Köhler. *Statistische Einzelfallanalyse: Eine Einführung Mit Rechenbeispielen*. Beltz, Weinheim, Basel, 2008. ISBN 978-3-621-27643-6.

J. Kopitz. *Kombinierte Anwendung von Strömungssimulation, Netzwerkmodellierung und Regelungstechnik zur Vorhersage thermoakustischer Instabilitäten*. PhD Thesis, Technische Universität München, Munich, 2007.

H. A. Kramers. Vibrations of a gas column. *Physica*, 15(11-12):971–984, 1949. doi: 10.1016/0031-8914(49)90061-0.

A. G. Kravchenko and P. Moin. Numerical studies of flow over a circular cylinder at $\mathrm{Re}_d = 3900$. *Physics of Fluids*, 12(2):403–417, 2000. doi: 10.1063/1.870318.

Y.-P. Kwon and B.-H. Lee. Stability of the Rijke tube thermoacoustic oscillation. *Journal of the Acoustical Society of America*, 78(4):1414–1420, 1985. doi: 10.1121/1.392912.

A. A. Lacis, G. A. Schmidt, D. Rind, and R. A. Ruedy. Atmospheric CO2: Principal control knob governing earth's temperature. *Science*, 330(6002):356–359, 2010. doi: 10.1126/science.1190653.

D. Laera, G. Campa, S. M. Camporeale, E. Bertolotto, S. Rizzo, F. Bonzani, A. Ferrante, and A. Saponaro. Modelling of thermoacoustic combustion instabilities phenomena: Application to an experimental test rig. *Energy Procedia*, 45:1392–1401, 2014. doi: 10.1016/j.egypro.2014.01.146.

L. D. Landau, E. M. Lifshitz, J. B. Sykes, and W. H. Reid. *Course of Theoretical Physics. Tome VI, Tome VI,*. Pergamon Press, Oxford, UK, 1959. ISBN 978-0-08-009104-4.

C. F. Lange, F. Durst, and M. Breuer. Momentum and heat transfer from cylinders in laminar crossflow at $10^{-4} \leq \mathrm{Re} \leq 200$. *International Journal of Heat and Mass Transfer*, 41(22):3409–3430, 1998. doi: 10.1016/S0017-9310(98)00077-5.

O. Lehmkuhl, I. Rodríguez, R. Borrell, C. D. Pérez-Segarra, and A. Oliva. Low-frequency variations in the wake of a circular cylinder at Re = 3900. *Journal of Physics: Conference Series*, 318: Article 042038, 2011. doi: 10.1088/1742-6596/318/4/042038.

E. C. Levy. Complex-curve fitting. *IRE Transactions on Automatic Control*, AC-4(1): 37–43, 1959. doi: 10.1109/TAC.1959.6429401.

G. Li, Y. Zheng, G. Hu, and Z. Zhang. Experimental investigation on heat transfer enhancement from an inclined heated cylinder with constant heat input power in infrasonic pulsating flows. *Experimental Thermal and Fluid Science*, 49:75–85, 2013. doi: 10.1016/j.expthermflusci.2013.04.003.

G. Li, Y. Zheng, G. Hu, Z. Zhang, and Y. Xu. Experimental study of the heat transfer enhancement from a circular cylinder in laminar pulsating cross-flows. *Heat Transfer Engineering*, 37(6):535–544, 2016a. doi: 10.1080/01457632.2015.1060758.

S. Li, Q. Li, L. Tang, B. Yang, J. Fu, C. Clarke, X. Jin, C. Ji, and H. Zhao. Theoretical and experimental demonstration of minimizing self-excited thermoacoustic oscillations by applying anti-sound technique. *Applied Energy*, 181:399–407, 2016b. doi: 10.1016/j.apenergy.2016.08.069.

X. Li, D. Zhao, X. Yang, and S. Wang. Unity maximum transient energy growth of heat-driven acoustic oscillations. *Energy Conversion and Management*, 116:1–10, 2016c. doi: 10.1016/j.enconman.2016.02.062.

C. Liang and G. Papadakis. Large eddy simulation of pulsating flow over a circular cylinder at subcritical Reynolds number. *Computers & Fluids*, 36(2):299–312, 2007. doi: 10.1016/j.compfluid.2005.10.004.

M. J. Lighthill. The response of laminar skin friction and heat transfer to fluctuations in the stream velocity. *Proceedings of the Royal Society A: Mathematical, Physical and Engineering Sciences*, 224(1156):1–23, 1954. doi: 10.1098/rspa.1954.0137.

C. Lin. Motion in the boundary layer with a rapidly oscillating external flow. In *Proceedings of the 9th International Congress on Applied Mechanics*, pages 155–167, Brussels, Belgium, Sept. 1957.

Y.-c. Lin, D. O. Brant, R. H. Bartlett, R. B. Hirschl, and J. L. Bull. Pulsatile flow past a cylinder: An experimental model of flow in an artificial lung. *ASAIO Journal*, 52 (6):614–623, 2006. doi: 10.1097/01.mat.0000235281.49204.24.

L. Ljung. *System Identification: Theory for the User*. Prentice Hall, Upper Saddle River, 2 edition, 1999. ISBN 0-13-656695-2.

L. Ljung. *System Identification Toolbox™ User's Guide*. MathWorks, Natick, 2016a.

L. Ljung. *System Identification Toolbox™ Reference*. MathWorks, Natick, 2016b.

L. Lu and G. Papadakis. Investigation of the effect of external periodic flow pulsation on a cylinder wake using linear stability analysis. *Physics of Fluids*, 23(9): Article 094105, 2011. doi: 10.1063/1.3625413.

L. Lu and G. Papadakis. An iterative method for the computation of the response of linearised Navier–Stokes equations to harmonic forcing and application to forced cylinder wakes. *International Journal for Numerical Methods in Fluids*, 74:794–817, 2014. doi: 10.1002/fld.3874.

D. A. Lysenko, I. S. Ertesvåg, and K. E. Rian. Large-eddy simulation of the flow over a circular cylinder at Reynolds number 3900 using the OpenFOAM toolbox. *Flow, Turbulence and Combustion*, 89(4):491–518, 2012. doi: 10.1007/s10494-012-9405-0.

S. Mariappan. *Theoretical and Experimental Investigation of the Non-Normal Nature of Thermoacoustic Interactions*. PhD Thesis, IIT Madras, Chennai, India, 2012.

S. Mariappan and R. I. Sujith. Modelling nonlinear thermoacoustic instability in an electrically heated Rijke tube. *Journal of Fluid Mechanics*, 680:511–533, 2011. doi: 10.1017/jfm.2011.176.

S. Mariappan, R. I. Sujith, and P. J. Schmid. Non-normal and nonlinear dynamics of thermoacoustic instability in a horizontal Rijke tube. In *n^3l - International Summer School and Workshop on Non-Normal and Nonlinear Effects In Aero- and Thermoacoustics*, Garching, May 2010.

S. Mariappan, R. I. Sujith, and P. J. Schmid. Experimental investigation of non-normality of thermoacoustic interaction in an electrically heated Rijke tube. *International Journal of Spray and Combustion Dynamics*, 7(4):315–352, 2015. doi: 10.1260/1756-8277.7.4.315.

F. Masters and K. R. Gurley. Non-Gaussian simulation: Cumulative distribution function map-based spectral correction. *Journal of Engineering Mechanics*, 129 (12):1418–1428, 2003. doi: 10.1061/(ASCE)0733-9399(2003)129:12(1418).

K. Matveev. *Thermoacoustic Instabilities in the Rijke Tube: Experiments and Modeling*. PhD Thesis, California Institute of Technology, Pasadena, 2003a.

K. Matveev. Energy consideration of the nonlinear effects in a Rijke tube. *Journal of Fluids and Structures*, 18(6):783–794, 2003b. doi: 10.1016/j.jfluidstructs.2003.07.016.

K. Matveev and F. Culick. A study of the transition to instability in a Rijke tube with axial temperature gradient. *Journal of Sound and Vibration*, 264(3):689–706, 2003. doi: 10.1016/S0022-460X(02)01217-8.

M. Mechler. *Dynamic Heat Transfer Behavior of a Wire for Constant-Temperature Anemometry Applications in Cross-Flow with Fluctuating Angle of Attack*. Bachelor Thesis, Technische Universität München, Munich, 2016. Supervisor: Armin Witte.

R. Mei and R. J. Adrian. Flow past a sphere with an oscillation in the free-stream velocity and unsteady drag at finite Reynolds number. *Journal of Fluid Mechanics*, 237:323–341, 1992. doi: 10.1017/S0022112092003434.

S. Menon, P.-K. Yeung, and W.-W. Kim. Effect of subgrid models on the computed interscale energy transfer in isotropic turbulence. *Computers & Fluids*, 25(2):165–180, 1996. doi: 10.1016/0045-7930(95)00036-4.

M. Meyer, S. Hickel, and N. A. Adams. Assessment of implicit large-eddy simulation with a conservative immersed interface method for turbulent cylinder flow. *International Journal of Heat and Fluid Flow*, 31(3):368 – 377, 2010. doi: 10.1016/j.ijheatfluidflow.2010.02.026.

N. Mikheev, V. Molochnikov, A. Mikheev, and O. Dushina. Hydrodynamics and heat transfer of pulsating flow around a cylinder. *International Journal of Heat and Mass Transfer*, 109:254–265, 2017. doi: 10.1016/j.ijheatmasstransfer.2017.01.125.

J. P. Moeck. *Analysis , Modeling , and Control of Thermoacoustic Instabilities*. PhD Thesis, Technische Universität Berlin, Berlin, 2010.

B. Mohan and S. Mariappan. Influence of non perfect impedance boundary on the bistable region in thermoacoustic interactions. *Journal of Physics: Conference Series*, 822(1): Article 012006, 2017. doi: 10.1088/1742-6596/822/1/012006.

F. K. Moore. Unsteady laminar boundary-layer flow. Technical Note 2471, National Advidory Committee for Aeronautics, Washington, 1951.

C. Nicoli and P. Pelcé. One-dimensional model for the Rijke tube. *Journal of Fluid Mechanics*, 202:83–96, 1989. doi: 10.1017/S0022112089001102.

J. Nocedal and S. J. Wright. *Numerical Optimization*. Springer Series in Operation Research and Financial Engineering. Springer, New York, 2nd edition, 2006. ISBN 978-0-387-30303-1.

C. Norberg. An experimental investigation of the flow around a circular cylinder: Influence of aspect ratio. *Journal of Fluid Mechanics*, 258:287–316, 1994. doi: 10.1017/S0022112094003332.

C. Norberg. Fluctuating lift on a circular cylinder: Review and new measurements. *Journal of Fluids and Structures*, 17(1):57–96, 2003. doi: 10.1016/S0889-9746(02)00099-3.

M. Ohmi and T. Usui. Theory of mass transfer from a sphere and a circular cylinder in pulsating flow. *Transactions of the Iron and Steel Institute of Japan*, 22(8):593–599, 1982. doi: 10.2355/isijinternational1966.22.593.

N. Olgac, U. Zalluhoglu, and A. S. Kammer. Predicting thermoacoustic instability: A novel analytical approach and its experimental validation. *Journal of Propulsion and Power*, 30(4):1005–1015, 2014a. doi: 10.2514/1.B35162.

N. Olgac, U. Zalluhoglu, and A. S. Kammer. Stability and control of a thermoacoustic device: The Rijke's tube. In *ASME 2014 Dynamic Systems and Control Conference*, volume 2, pages Article DSCC2014–5888, San Antonio, USA, Oct. 2014b. American Society of Mechanical Engineers.

OpenFOAM Foundation. OpenFOAM (Version 2.3.0). OpenFOAM Foundation, 2014.

A. Orchini, G. Rigas, and M. P. Juniper. Weakly nonlinear analysis of thermoacoustic bifurcations in the Rijke tube. *Journal of Fluid Mechanics*, 805:523–550, 2016. doi: 10.1017/jfm.2016.585.

G. Papadakis and G. Bergeles. Numerical simulation of the flow and heat transfer around a cylinder with a pulsating approaching flow at a low Reynolds number. *Proceedings of the Institution of Mechanical Engineers, Part C: Journal of Mechanical Engineering Science*, 215(1):105–119, 2001. doi: 10.1243/0954406011520463.

C. O. Paschereit and W. Polifke. Investigation of the thermo-acoustic characteristics of a lean premixed gas turbine burner. In *International Gas Turbine and Aeroengine Congress & Exposition*, ASME 98-GT-582, Stockholm, Sweden, June 1998.

S. V. Patankar and D. B. Spalding. A calculation procedure for heat, mass and momentum transfer in three-dimensional parabolic flows. *International Journal of Heat and Mass Transfer*, 15(10):1787–1806, 1972. doi: 10.1016/0017-9310(72)90054-3.

R. B. Payne. Calculations of unsteady viscous flow past a circular cylinder. *Journal of Fluid Mechanics*, 4(1):81–86, 1958. doi: 10.1017/S0022112058000318.

J. Perwaiz and T. E. Base. Heat transfer from a cylinder and finned tube in a pulsating crossflow. *Experimental Thermal and Fluid Science*, 5(4):506–512, 1992. doi: 10.1016/0894-1777(92)90037-6.

A.-H. Pham, C.-Y. Lee, J.-H. Seo, H.-H. Chun, H.-J. Kim, H.-S. Yoon, J.-H. Kim, D.-W. Park, and I.-R. Park. Laminar flow past an oscillating circular cylinder in cross flow. *Journal of Marine Science and Technology*, 18(3):361–368, 2010.

C. L. Phillips, J. M. Parr, and E. A. Riskin. *Signals, Systems, and Transforms*. Pearson/Prentice Hall, Upper Saddle River, 4th edition, 2008. ISBN 978-0-13-198923-8.

R. Pintelon and J. Schoukens. *System Identification: A Frequency Domain Approach*. John Wiley & Sons, Hoboken, 2nd edition, 2012. ISBN 978-0-470-64037-1.

W. Polifke. Black-box system identification for reduced order model construction. *Annals of Nuclear Energy*, 67:109–128, 2014. doi: 10.1016/j.anucene.2013.10.037.

W. Polifke and C. Lawn. On the low-frequency limit of flame transfer functions. *Combustion and Flame*, 151(3):437–451, 2007. doi: 10.1016/j.combustflame.2007.07.005.

W. Polifke, A. Poncet, C. Paschereit, and K. Döbbeling. Reconstruction of acoustic transfer matrices by instationary computational fluid dynamics. *Journal of Sound and Vibration*, 245(3):483–510, 2001. doi: 10.1006/jsvi.2001.3594.

B. E. Poling, J. M. Prausnitz, and J. P. O'Connell. *The Properties of Gases and Liquids*. McGraw-Hill, New York, 5 edition, 2001. ISBN 978-0-07-118971-2.

S. B. Pope. *Turbulent Flows*. Cambridge University Press, Cambridge, New York, 2000. ISBN 978-0-521-59125-6.

A. Qamar, R. Seda, and J. L. Bull. Pulsatile flow past an oscillating cylinder. *Physics of Fluids*, 23(4): Article 041903, 2011. doi: 10.1063/1.3576186.

A. Qamar, R. Samtaney, and J. L. Bull. Pulsatility role in cylinder flow dynamics at low Reynolds number. *Physics of Fluids*, 24(8): Article 081701, 2012. doi: 10.1063/1.4740504.

B. Rajani, A. Kandasamy, and S. Majumdar. Numerical simulation of laminar flow past a circular cylinder. *Applied Mathematical Modelling*, 33(3):1228–1247, 2009. doi: 10.1016/j.apm.2008.01.017.

R. Raun, M. Beckstead, J. Finlinson, and K. Brooks. A review of Rijke tubes, Rijke burners and related devices. *Progress in Energy and Combustion Science*, 19(4): 313–364, 1993. doi: 10.1016/0360-1285(93)90007-2.

J. W. S. Rayleigh. *The Theory of Sound*, volume 2. Macmillan, London, 2nd edition, 1896.

J. W. S. Rayleigh. On the motion of solid bodies through viscous liquid. *Philosophical Magazine Series 6*, 21(126):697–711, 1911. doi: 10.1080/14786440608637084.

S. W. Rienstra and A. Hirschberg. An introduction to acoustics. Technical Report IWDE 92-06, Eindhoven University of Technology, Eindhoven, 2015.

G. Rigas, N. P. Jamieson, L. K. B. Li, and M. P. Juniper. Experimental sensitivity analysis and control of thermoacoustic systems. *Journal of Fluid Mechanics*, 787, 2016. doi: 10.1017/jfm.2015.715.

P. L. Rijke. Notiz über eine neue Art, die in einer an beiden Enden offenen Röhre enthaltene Luft in Schwingungen zu versetzen. *Annalen der Physik*, 183(6):339–343, 1859. doi: 10.1002/andp.18591830616.

H. Rodhe. A comparison of the contribution of various gases to the greenhouse effect. *Science*, 248(4960):1217–1219, 1990. doi: 10.1126/science.248.4960.1217.

N. Rott. Damped and thermally driven acoustic oscillations in wide and narrow tubes. *Zeitschrift für angewandte Mathematik und Physik ZAMP*, 20(2):230–243, 1969. doi: 10.1007/BF01595562.

C. Sanathanan and J. Koerner. Transfer function synthesis as a ratio of two complex polynomials. *IEEE Transactions on Automatic Control*, 8(1):56–58, 1963. doi: 10.1109/TAC.1963.1105517.

G. N. Sarma and C. M. El-Hadi. Interaction of chord and spanwise oscillations in a flow past a yawed cylinder and asymptotic solutions. *International Journal of Engineering Science*, 24(5):675–684, 1986. doi: 10.1016/0020-7225(86)90104-7.

G. N. Sarma and R. Srivastava. Heat transfer in forced oscillatory compressible flow past a yawed cylinder. *International Journal of Heat and Mass Transfer*, 29(9): 1439–1443, 1986. doi: 10.1016/0017-9310(86)90175-4.

T. Sarpkaya. Force on a circular cylinder in viscous oscillatory flow at low Keulegan—Carpenter numbers. *Journal of Fluid Mechanics*, 165:61–71, 1986. doi: 10.1017/S0022112086002999.

T. Sayadi, V. Le Chenadec, P. J. Schmid, F. Richecoeur, and M. Massot. Thermoacoustic instability—a dynamical system and time domain analysis. *Journal of Fluid Mechanics*, 753:448–471, 2014. doi: 10.1017/jfm.2014.357.

G. Schewe. On the force fluctuations acting on a circular cylinder in crossflow from subcritical up to transcritical Reynolds numbers. *Journal of Fluid Mechanics*, 133: 265–285, 1983. doi: 10.1017/S0022112083001913.

H. Schlichting and K. Gersten. *Grenzschicht-Theorie*. Springer, Berlin, Heidelberg, 10th edition, 2006. ISBN 3-540-23004-1.

F. Selimefendigil. *Identification and Analysis of Nonlinear Heat Sources in Thermo-Acoustic Systems*. PhD Thesis, Technische Universität München, Munich, 2010.

F. Selimefendigil and H. F. Öztop. Identification of forced convection in pulsating flow at a backward facing step with a stationary cylinder subjected to nanofluid. *International Communications in Heat and Mass Transfer*, 45:111–121, 2013. doi: 10.1016/j.icheatmasstransfer.2013.04.016.

F. Selimefendigil and H. F. Öztop. Numerical study and identification of cooling of heated blocks in pulsating channel flow with a rotating cylinder. *International Journal of Thermal Sciences*, 79:132–145, 2014. doi: 10.1016/j.ijthermalsci.2014.01.010.

F. Selimefendigil and W. Polifke. A nonlinear frequency domain system model with coupled modes for limit cycle prediction of thermoacoustic systems. *International Journal of Spray and Combustion Dynamics*, 3(4):303–330, 2011. doi: 10.1260/1756-8277.3.4.303.

F. Selimefendigil, S. Föller, and W. Polifke. Nonlinear identification of unsteady heat transfer of a cylinder in pulsating cross flow. *Computers & Fluids*, 53:1–14, 2012. doi: 10.1016/j.compfluid.2011.08.012.

T. Söderström and P. Stoica. *System Identification*. Prentice Hall International Series in Systems and Control Engineering. Prentice Hall, New York, 1989. ISBN 978-0-13-881236-2.

C. Sondhauß. über die Schallschwingungen der Luft in erhitzten Glasröhren und in gedeckten Pfeifen von ungleicher Weite. *Annalen der Physik*, 155(1):1–34, 1850. doi: 10.1002/andp.18501550102.

D. B. Spalding. A Single Formula for the "Law of the Wall". *Journal of Applied Mechanics*, 28(3):455–458, 1961. doi: 10.1115/1.3641728.

E. M. Sparrow, J. P. Abraham, and J. C. Tong. Archival correlations for average heat transfer coefficients for non-circular and circular cylinders and for spheres in cross-flow. *International Journal of Heat and Mass Transfer*, 47(24):5285–5296, 2004. doi: 10.1016/j.ijheatmasstransfer.2004.06.024.

K. Steiglitz and L. McBride. A technique for the identification of linear systems. *IEEE Transactions on Automatic Control*, 10(4):461–464, 1965. doi: 10.1109/TAC.1965.1098181.

P. Stephan, K. Schaber, K. Stephan, and F. Mayinger. *Thermodynamik*. Springer-Lehrbuch. Springer, Berlin, Heidelberg, 19th edition, 2013. ISBN 978-3-642-30097-4.

G. G. Stokes. On the effect of the internal friction of fluids on the motion of pendulums. *Transactions of the Cambridge Philosophical Society*, 9, 1851. doi: 10.1017/CBO9780511702266.002.

L. Strobio Chen, A. Witte, and W. Polifke. Thermo-acoustic characterization of a heat exchanger in cross flow using compressible and weakly compressible numerical simulation. In *22nd International Congress on Sound and Vibration (ICSV22)*, Florence, Italy, July 2015.

L. Strobio Chen, N. Hosseini, W. Polifke, J. Teerling, V. Kornilov, I. Lopez Arteaga, and P. de Goey. Acoustic scattering behaviour of a 2D flame with heat exchanger in cross-flow. In *23nd International Congress on Sound and Vibration (ICSV23)*, Athens, Greece, July 2016. IIAV.

P. Subramanian, S. Mariappan, R. I. Sujith, and P. Wahi. Bifurcation analysis of thermoacoustic instability in a horizontal Rijke Tube. *International Journal of Spray and Combustion Dynamics*, 2(4):325–355, 2010. doi: 10.1260/1756-8277.2.4.325.

P. Subramanian, R. I. Sujith, and P. Wahi. Subcritical bifurcation and bistability in thermoacoustic systems. *Journal of Fluid Mechanics*, 715:210–238, 2013. doi: 10.1017/jfm.2012.514.

J. Sui, D. Zhao, B. Zhang, and N. Gao. Experimental study of Rijke-type thermoacoustic instability by using Proper Orthogonal Decomposition method. *Experimental Thermal and Fluid Science*, 81:336–344, 2017. doi: 10.1016/j.expthermflusci.2016.10.026.

H. J. Sung, K. S. Hwang, and J. M. Hyun. Experimental study on mass transfer from a circular cylinder in pulsating flow. *International Journal of Heat and Mass Transfer*, 37(15):2203–2210, 1994. doi: 10.1016/0017-9310(94)90363-8.

A. Surendran and M. A. Heckl. Analytical study of a Rijke tube with heat exchanger. In *21st International Congress on Sound and Vibration (ICSV21)*, Beijing, China, July 2014.

A. Surendran and M. A. Heckl. Passive instability control by using a heat exchnager as acoustic sink. In *22nd International Congress on Sound and Vibration (ICSV22)*, Florence, Italy, July 2015.

A. Surendran, N. Hosseini, H. Teerling, and M. Heckl. Use of heat exchanger for passive control of combustion instabilities. In *23rd International Congress on Sound and Vibration (ICSV23)*, Athens, Greece, July 2016.

P. K. Sweby. High resolution schemes using flux limiters for hyperbolic conservation laws. *SIAM Journal on Numerical Analysis*, 21(5):995–1011, 1984. doi: 10.1137/0721062.

G. Swift. Thermoacoustics. In T. D. Rossing, editor, *Springer Handbook of Acoustics*, pages 239–255. Springer, New York, 2007. ISBN 978-0-387-30425-0.

G. W. Swift. *Thermoacoustics. a Unifying Perspective for Some Engines and Refrigerators*. Acoustical Society of America, Melville, 2002. ISBN 0-7354-0065-2.

A. K. Tangirala. *Principles of System Identification: Theory and Practice*. CRC Press, Boca Raton, 2014. ISBN 978-1-4398-9599-3.

D. P. Telionis. *Unsteady Viscous Flows*. Springer, New York, 1981. ISBN 978-3-642-88569-3.

D. P. Telionis and M. S. Romaniuk. Velocity and temperature streaming in oscillating boundary layers. *AIAA Journal*, 16(5):488–495, 1978. doi: 10.2514/3.60916.

The MathWorks, Inc. MATLAB and system identification toolbox release 2016b. The MathWorks, Inc., 2016.

A. Thom. The flow past circular cylinders at low speeds. *Proceedings of the Royal Society of London. Series A, Containing Papers of a Mathematical and Physical Character*, 141(845):651–669, 1933. doi: 10.1098/rspa.1933.0146.

D. J. Tritton. Experiments on the flow past a circular cylinder at low Reynolds numbers. *Journal of Fluid Mechanics*, 6(4):547–567, 1959. doi: 10.1017/S0022112059000829.

United Nations, editor. *Agenda 21: Earth Summit: The United Nations Programme of Action from Rio*. Department of Public Information, United Nations, New York, 1994. ISBN 92-1-100509-4. OCLC: 258425533.

U.S. Energy Information Administration. International energy outlook 2016. Technical Report DOE/EIA-0484(2016), U.S. Energy Information Administration, Washington DC, 2016.

B. Uzunoglu, M. Tan, and W. G. Price. Low-Reynolds-number flow around an oscillating circular cylinder using a cell viscous boundary element method. *International Journal for Numerical Methods in Engineering*, 50(10):2317–2338, 2001. doi: 10.1002/nme.122.

M. Verhaegen and V. Verdult. *Filtering and System Identification a Least Squares Approach*. Cambridge University Press, Cambridge, New York, 2007. ISBN 978-0-521-87512-7.

M. C. Vidya, N. A. Beishuizen, and T. H. van der Meer. Direct numerical simulations of flow and heat transfer over a circular cylinder at Re = 2000. *Journal of Physics: Conference Series*, 745: Article 032018, 2016. doi: 10.1088/1742-6596/745/3/032018.

Y. Wang, D.-K. Sun, Y.-L. He, and W.-Q. Tao. Lattice Boltzmann study on thermoacoustic onset in a Rijke tube. *The European Physical Journal Plus*, 130(9), 2015. doi: 10.1140/epjp/i2015-15009-5.

E. Weinan and J.-G. Liu. Vorticity boundary condition and related issues for finite difference schemes. *Journal of Computational Physics*, 124(2):368–382, 1996. doi: 10.1006/jcph.1996.0066.

A. J. Weisenborn and P. Mazur. The Oseen drag on a circular cylinder revisited. *Physica*, 123(1):191–208, 1984. doi: 10.1016/0378-4371(84)90111-0.

F. M. White. *Viscous Fluid Flow*. McGraw-Hill Series in Mechanical Engineering. McGraw-Hill, Boston, 3rd edition, 2007. ISBN 978-0-07-124493-0.

WHO Regional Office for Europe. Health aspects of air pollution with particulate matter, ozone and nitrogen dioxide: Report on a WHO working group, Bonn, Germany 13-15 January 2003. Technical report, WHO Regional Office for Europe, Copenhagen, 2003.

A. Witte and W. Polifke. Heat transfer frequency response of a cylinder in pulsating laminar cross flow. In *17. STAB-Workshop*, Göttingen, Germany, Nov. 2015.

A. Witte and W. Polifke. Modeling the heat transfer and skin friction frequency response of a cylinder in cross-flow - a unifying perspective. In *12th International Conference on Heat Transfer, Fluid Mechanics and Thermodynamics (HEFAT)*, pages 1022–1027, Malaga, Spain, July 2016. ISBN 978-1-77592-124-0.

A. Witte and W. Polifke. Dynamics of unsteady heat transfer in pulsating flow across a cylinder. *International Journal of Heat and Mass Transfer*, 109:1111–1131, 2017a. doi: 10.1016/j.ijheatmasstransfer.2017.02.072.

A. Witte and W. Polifke. Heat transfer frequency response of a cylinder in pulsating cross flow. DFG-Abschlussbericht PO710/15-1, Technische Universität München, Garching, 2017b.

A. Witte and W. Polifke. Modeling heat transfer and skin friction frequency responses of a cylinder in cross-flow—a unifying perspective. *Heat Transfer Engineering*, 40, 2019. doi: 10.1080/01457632.2018.1457241.

A. Witte, T. Emmert, T. Holzinger, and W. Polifke. Optimization techniques for power generation from waste heat using thermoacoustic engines. In *MSE Energy Colloquium*, Garching, Germany, July 2015.

A. Witte, A. Cabrera, and W. Polifke. Identification of the heat transfer frequency response in pulsating laminar and subcritical flow across a cylinder. In *7th European Thermal-Sciences Conference (EUROTHERM)*, Krakow, Poland, June 2016a.

A. Witte, A. Cabrera, and W. Polifke. Identification of the heat transfer frequency response in pulsating laminar and subcritical flow across a cylinder. *Journal of Physics: Conference Series*, 745: Article 032055, 2016b. doi: 10.1088/1742-6596/745/3/032055.

J. Xu, W. Li, D. Zhao, and Y. Liu. Numerical simulation for thermoacoustic phenomena in Rijke tube (I)———analysis for self-oscillation and the limit period. In *Lecture Notes in Information Technology*, volume 9, Sanya, China, Feb. 2012.

S.-M. Yang and L. G. Leal. A note on memory-integral contributions to the force on an accelerating spherical drop at low Reynolds number. *Physics of Fluids A: Fluid Dynamics*, 3(7):1822–1824, 1991. doi: 10.1063/1.858202.

X. Yang, A. Turan, and S. Lei. Thermoacoustic instability in a Rijke tube with a distributed heat source. *Journal of Thermodynamics*, 2015: Article 949384, 2015. doi: 10.1155/2015/949384.

X. Yang, A. Turan, and S. Lei. Bifurcation and nonlinear analysis of a time-delayed thermoacoustic system. *Communications in Nonlinear Science and Numerical Simulation*, 44:229–244, 2017. doi: 10.1016/j.cnsns.2016.08.006.

J.-Y. Yu, W. Lin, and X.-T. Zheng. Effect on the flow and heat transfer characteristics for sinusoidal pulsating laminar flow in a heated square cylinder. *Heat and Mass Transfer*, 50(6):849–864, 2014. doi: 10.1007/s00231-014-1294-4.

U. Zalluhoglu and N. Olgac. Passive suppression of thermoacoustic instability in a Rijke tube. *IFAC-PapersOnLine*, 49(10):59–64, 2016a. doi: 10.1016/j.ifacol.2016.07.473.

U. Zalluhoglu and N. Olgac. Thermoacoustic instabilities arising from secondary modes, an analytical and experimental declaration. In *55th Conference on Decision and Control (CDC)*, pages 1417–1422, Las Vegas, USA, Dec. 2016b. IEEE.

U. Zalluhoglu, A. S. Kammer, and N. Olgac. Delayed feedback control laws for Rijke tube thermoacoustic instability, synthesis, and experimental validation. *IEEE Transactions on Control Systems Technology*, 24(5):1861–1868, 2016. doi: 10.1109/TCST.2015.2512938.

M. M. Zdravkovich. *Flow around Circular Cylinders: A Comprehensive Guide through Flow Phenomena, Experiments, Applications, Mathematical Models, and Computer Simulations*, volume 1 of *Oxford Science Publications*. Oxford University Press, Oxford UK, New York, 1997. ISBN 978-0-19-856396-9.

D. Zhao and M. Reyhanoglu. Feedback control of acoustic disturbance transient growth in triggering thermoacoustic instability. *Journal of Sound and Vibration*, 333(16):3639–3656, 2014. doi: 10.1016/j.jsv.2014.04.015.

T. S. Zhao and P. Cheng. Heat transfer in oscillatory flows. *Annual Review of Heat Transfer*, 9:359–420, 1998. doi: 10.1615/AnnualRevHeatTransfer.v9.90.

Y. Zheng, G. Li, W. Guo, and C. Dong. Lattice Boltzmann simulation to laminar pulsating flow past a circular cylinder with constant temperature. *Heat and Mass Transfer*, 53(9):2975–2986, 2017. doi: 10.1007/s00231-017-2043-2.

J. R. Zierenberg, H. Fujioka, V. Suresh, R. H. Bartlett, R. B. Hirschl, and J. B. Grotberg. Pulsatile flow and mass transport past a circular cylinder. *Physics of Fluids*, 18(1): Article 013102, 2006. doi: 10.1063/1.2164475.

J. R. Zierenberg, H. Fujioka, R. B. Hirschl, R. H. Bartlett, and J. B. Grotberg. Pulsatile blood flow and oxygen transport past a circular cylinder. *Journal of Biomechanical Engineering*, 129(2):202–215, 2007. doi: 10.1115/1.2485961.

J. Zierep. *Ähnlichkeitsgesetze und Modellregeln der Strömungslehre*. Braun, Karlsruhe, 3rd edition, 1991. ISBN 978-3-7650-2041-4.

A Complementary Identification Results

Fit Values

Heat Transfer

Re	Φ estimation	Φ validationSet
40.0	99.13	98.92
20.0	99.17	99.07
10.0	98.69	98.84
4.0	97.12	97.47
3.0	96.33	96.16
2.0	95.18	95.41
1.0	94.25	94.02
0.7	96.58	95.58
0.5	97.99	97.33
0.4	98.15	98.48
0.2	98.09	97.66
0.1	97.42	97.84

Table A.1: NRMSE-Fit of the TF of the Heat Transfer (CFD/SI with VF). Transfer functions identified with VF from CFD/SI.

Re	Φ_{Nu}	Re	Φ_{Nu}
0.1	99.47	2.0	99.16
0.2	98.97	3.0	99.39
0.4	99.08	4.0	99.54
0.5	99.26	10.0	99.60
0.7	99.57	20.0	99.14
1.0	99.58	40.0	99.67

Table A.2: NRMSE-Fit of the TF of the Heat Transfer (LNSE with VF). Transfer functions identified with VF from LNSE.

Skin Friction

Re	Φ estimation	Φ validationSet
40.0	99.43	91.30
20.0	99.64	90.80
10.0	99.31	91.40
4.0	99.32	92.73
3.0	99.30	92.71
2.0	99.31	92.52
1.0	98.99	92.96
0.7	99.48	92.99
0.5	99.69	93.37
0.4	99.70	93.41
0.2	99.63	94.21
0.1	99.55	94.55

Table A.3: NRMSE-Fit of the TF of the Skin Friction (CFD/SI with VF). Transfer functions identified with VF from CFD/SI.

Re	Φ_{c_f}	Re	Φ_{c_f}
0.1	98.92	2.0	99.17
0.2	98.97	3.0	99.18
0.4	99.07	4.0	99.19
0.5	99.09	10.0	99.20
0.7	99.12	20.0	99.18
1.0	99.14	40.0	99.21

Table A.4: NRMSE-Fit of the TF of the Skin Friction (LNSE with VF). Transfer functions identified with VF from LNSE.

Transfer Functions

Heat Transfer

$$G(s) = \frac{b_1 + b_2\,s + b_3\,s^2 + b_4\,s^3 + b_5\,s^4}{1 + f_1\,s + f_2\,s^2 + f_3\,s^3 + f_4\,s^4}$$

Re		s^0	s^1	s^2	s^3	s^4
0.1	N	0.2039	2.009	2.053	0.1875	0.0004536
	D		32.6	145.1	79.31	3.284
0.2	N	0.2139	1.504	1.155	0.09033	0.000199
	D		19.4	58.83	24.24	0.9187
0.4	N	0.2511	1.061	0.5675	0.0363	7.299×10^{-5}
	D		11.18	21.1	6.266	0.2112
0.5	N	0.259	0.8698	0.3907	0.0224	4.176×10^{-5}
	D		8.93	13.73	3.482	0.1089
0.7	N	0.2836	0.729	0.2441	0.01138	1.843×10^{-5}
	D		6.995	8.088	1.567	0.04224
1.0	N	0.3002	2.481	2.602	0.2885	0.0009421
	D		11.72	32.44	16.63	0.9465
2.0	N	0.3228	15.3	11.4	0.9206	0.001895
	D		48.01	113.1	40.42	1.826
3.0	N	0.346	8.375	4.998	0.3475	0.0005566
	D		24.3	44.05	13.05	0.5361
4.0	N	0.371	3.186	1.712	0.1147	0.0001651
	D		9.302	13.54	3.722	0.152
10.0	N	0.4051	3.206	1.186	0.05908	4.39×10^{-5}
	D		7.727	7.373	1.486	0.05046
20.0	N	0.4179	3.047	0.6752	0.02236	1.13×10^{-5}
	D		6.631	4.299	0.5855	0.01489
40.0	N	0.4235	6.162	9.311	0.7889	0.0006647
	D		12.92	21.57	7.821	0.4523

Table A.5: Estimated Coefficients of the TF of the Heat Transfer (CFD/SI with VF). Transfer functions identified with VF from CFD/SI.

$$G(s) = \frac{b_1 + b_2\,s + b_3\,s^2 + b_4\,s^3 + b_5\,s^4}{1 + f_1\,s + f_2\,s^2 + f_3\,s^3 + f_4\,s^4}$$

Re		s^0	s^1	s^2	s^3	s^4
0.1	N	0.1594	0.6932	0.3687	0.02529	9.582×10^{-5}
	D		19.18	41.9	13.33	0.5255
0.2	N	0.2181	1.595	1.262	0.1119	0.000482
	D		20.34	62.98	27.39	1.332
0.4	N	0.2544	1.276	0.7815	0.05934	0.0002117
	D		12.38	26.59	9.04	0.3835
0.5	N	0.2663	1.112	0.5965	0.04166	0.000135
	D		10.22	18.6	5.61	0.2221
0.7	N	0.2848	0.8881	0.3842	0.02334	6.382×10^{-5}
	D		7.615	10.67	2.654	0.09393
1.0	N	0.305	0.6883	0.2335	0.01204	2.663×10^{-5}
	D		5.559	5.843	1.173	0.03655
2.0	N	0.3398	9.222	7.917	0.7234	0.002106
	D		28.46	72	29.09	1.498
3.0	N	0.3587	6.173	4.174	0.3276	0.0007472
	D		17.94	34.16	11.3	0.5258
4.0	N	0.3707	5.062	2.912	0.2053	0.000386
	D		14.07	22.25	6.442	0.2798
10.0	N	0.3989	3.479	1.196	0.05844	4.739×10^{-5}
	D		8.409	7.813	1.501	0.05156
20.0	N	0.41	3.264	0.6306	0.01842	0
	D		7.12	4.405	0.539	0.01263
40.0	N	0.42	6.3	10.13	0.9059	0
	D		13.3	23.23	8.63	0.5363

Table A.6: Estimated Coefficients of the TF of the Heat Transfer (LNSE with VF). Transfer functions identified with VF from LNSE.

Skin Friction

$$G(s) = \frac{b_1 + b_2\, s + b_3\, s^2 + b_4\, s^3 + b_5\, s^4}{1 + f_1\, s + f_2\, s^2 + f_3\, s^3 + f_4\, s^4}$$

Re		s^0	s^1	s^2	s^3	s^4
0.1	N	1.118	6.725	5.056	0.6118	0.01095
	D		4.24	2.038	0.1381	0.0009137
0.2	N	1.172	6.648	4.92	0.5989	0.01093
	D		3.915	1.765	0.114	0.0007237
0.4	N	1.232	5.986	4.132	0.4889	0.008861
	D		3.302	1.326	0.07941	0.0004767
0.5	N	1.251	5.764	3.884	0.4546	0.0082
	D		3.119	1.205	0.07044	0.0004153
0.7	N	1.28	5.469	3.563	0.4104	0.007345
	D		2.882	1.055	0.05951	0.0003419
1.0	N	1.309	5.279	3.374	0.3858	0.006888
	D		2.725	0.9583	0.05264	0.0002967
2.0	N	1.357	5.356	3.475	0.4039	0.007303
	D		2.722	0.9344	0.05033	0.0002792
3.0	N	1.38	5.656	3.769	0.4462	0.00816
	D		2.877	0.9925	0.05339	0.0002953
4.0	N	1.394	5.934	4.029	0.4826	0.008893
	D		3.021	1.047	0.05631	0.000311
10.0	N	1.421	7.066	5.089	0.6346	0.012
	D		3.583	1.279	0.06939	0.0003842
20.0	N	1.424	8.79	6.949	0.9193	0.01806
	D		4.476	1.726	0.09712	0.0005499
40.0	N	1.414	12.68	11.44	1.61	0.03293
	D		6.543	2.794	0.1636	0.0009554

Table A.7: Estimated Coefficients of the TF of the Skin Friction (LNSE with VF). Transfer functions identified with VF from LNSE.